Suman Saha
A. S. Sajith
Dipti Ranjan Sahoo
Pradip Sarkar   *Editors*

Recent Advances in Materials, Mechanics and Structures

Select Proceedings of ICMMS 2022

Springer

Lecture Notes in Civil Engineering

Volume 269

Lecture Notes in Civil Engineering (LNCE) publishes the latest developments in Civil Engineering—quickly, informally and in top quality. Though original research reported in proceedings and post-proceedings represents the core of LNCE, edited volumes of exceptionally high quality and interest may also be considered for publication. Volumes published in LNCE embrace all aspects and subfields of, as well as new challenges in, Civil Engineering. Topics in the series include:

- Construction and Structural Mechanics
- Building Materials
- Concrete, Steel and Timber Structures
- Geotechnical Engineering
- Earthquake Engineering
- Coastal Engineering
- Ocean and Offshore Engineering; Ships and Floating Structures
- Hydraulics, Hydrology and Water Resources Engineering
- Environmental Engineering and Sustainability
- Structural Health and Monitoring
- Surveying and Geographical Information Systems
- Indoor Environments
- Transportation and Traffic
- Risk Analysis
- Safety and Security

To submit a proposal or request further information, please contact the appropriate Springer Editor:

– Pierpaolo Riva at pierpaolo.riva@springer.com (Europe and Americas);
– Swati Meherishi at swati.meherishi@springer.com (Asia—except China, Australia, and New Zealand);
– Wayne Hu at wayne.hu@springer.com (China).

All books in the series now indexed by Scopus and EI Compendex database!

Suman Saha · A. S. Sajith · Dipti Ranjan Sahoo ·
Pradip Sarkar

Editors

Recent Advances in Materials, Mechanics and Structures

Select Proceedings of ICMMS 2022

Editors
Suman Saha ⓘ
Department of Civil Engineering
National Institute of Technology Durgapur
Durgapur, West Bengal, India

Department of Civil Engineering
National Institute of Technology Calicut
Kozhikode, Kerala, India

Dipti Ranjan Sahoo
Department of Civil Engineering
Indian Institute of Technology Delhi
New Delhi, Delhi, India

A. S. Sajith
Department of Civil Engineering
National Institute of Technology Calicut
Kozhikode, Kerala, India

Pradip Sarkar
Department of Civil Engineering
National Institute of Technology Rourkela
Sundargarh, Odisha, India

Preface

Civil engineers are the builders of a nation. They always have played a significant role in providing the infrastructure required for the society. The ever-increasing population, rapid urbanization and industrialization, global warming and climate change, increasing incidents of natural and man-made hazards, and environmental degradation have become major concerns of the society today, and these concerns pose several challenges to the civil engineers. There has been a noticeable change in the environment within which civil engineers carry out their work. There is a growing concern about the adverse consequences of the development activities. There is a need for civil engineers to rise up to face these challenges and contribute to the development and betterment of the nation in all core areas. A multitude of threats confronts us in our effort to achieve the same. Civil engineers have always been looking for innovative tools and techniques to solve the challenging problems that they face during planning, analysis, design, and construction of civil engineering structures. In this context, the Department of Civil Engineering, National Institute of Technology, Calicut, has come out with the proposal of organizing the second edition of the *International Conference on Materials, Mechanics and Structures (ICMMS 2022).* This conference aims to provide a forum to all civil engineers to deliberate on the innovative tools and techniques that are needed to face the challenges in the fields of materials, mechanics, and structures.

We received an overwhelming response to our call for the submission of abstracts to this conference. We received more than 150 abstracts and full-length articles from across the globe. It is heartening to note that several of the contributions that we received are from young researchers/faculty. We tried our best to ensure that only quality papers were selected for presentation during the conference and for possible publication through our review process.

We hope that this book entitled *Recent Advances in Materials, Mechanics and Structures—Select Proceedings of ICMMS2022* will provide a platform, especially for young budding researchers to share their ideas and vision, notwithstanding the fact that it is being conducted in the online (virtual) mode. New and innovative technologies needed for civil engineers to face the challenges in the present world are the focus of this conference. Inclusion of several relevant themes related to

materials, mechanics, and structures is the highlight of this conference. We hope that this conference will help in building a network of researchers, faculty, and practicing engineers who will work toward the goal of achieving the same. This book is expected to highlight the current scenario on the new and innovative technologies, materials, mechanics, and structures globally, which may help researchers, faculties, and practicing engineers for achieving the solutions of the challenging problems faced during planning, analysis, design, and construction of civil engineering structures.

Durgapur, India	Dr. Suman Saha
Kozhikode, India	Dr. A. S. Sajith
New Delhi, India	Dr. Dipti Ranjan Sahoo
Sundargarh, India	Dr. Pradip Sarkar

Contents

Contents

About the Editors

Dr. Suman Saha is currently working as assistant professor at the Department of Civil Engineering, National Institute of Technology Durgapur, West Bengal, India. Prior to working at NIT Durgapur, he worked as an assistant professor at the Department of Civil Engineering, National Institute of Technology Calicut, Kerala, India. He obtained his B.E. in Civil Engineering from Jadavpur University, Kolkata; M.Tech. in Construction Technology and Management and Ph.D. from the National Institute of Technology Karnataka, Surathkal. His major areas of research interests include the alternative construction materials towards sustainability, advancement in concrete technology, etc. Association of Consulting Civil Engineers (ACCE—Bangalore Chapter) awarded his PG thesis the ACCE-Nirmana Nirvahane Puraskara—2015 for best dissertation in M.E./M.Tech. He has published several articles in peer-reviewed journals, several book chapters and presented his research work several times in the national/international conferences. He delivered several keynote lectures in various national/international events.

Dr. A. S. Sajith is currently an associate professor at the Department of Civil Engineering, National Institute of Technology Calicut, Kerala, India. He obtained his B.Tech. in Civil Engineering from College of Engineering, Trivandrum; M.E. in Structural Engineering from PSG College of Technology, Coimbatore and Ph.D. from the National Institute of Technology Calicut, Kerala. His major areas of research interests include vibration control, structural dynamics and earthquake engineering. He has published 18 papers in peer-reviewed journals and 17 papers in reputed national/international conferences. He is an active reviewer of various reputed journals and national/international conferences. He served as editor for the Proceedings of SECON'19—Structural Engineering and Construction Management published by Springer, and Proceedings of International Conference on Materials, Mechanics and Structures 2020 (ICMMS2020) published by IOP Conference Series: Materials Science and Engineering.

Dr. Dipti Ranjan Sahoo is presently working as Professor at the Department of Civil Engineering, Indian Institute of Technology Delhi, India. He obtained his B.Eng. in Civil Engineering from IGIT, Utkal University; M.Tech. in Structural Engineering and Ph.D. from the Indian Institute of Technology Kanpur, India. His major areas of research interests include hybrid testing and simulation, performance-based seismic design, passive vibration control devices, nonlinear finite element modelling of structures, seismic retrofitting and strengthening, RC and steel structures etc. He has published 86 journal papers, 92 conference papers and 13 book chapters. He applied for several patents. He was appointed as Honorary Associate Professor in University of Queensland, Australia; Associate Editor, *Indian Society of Earthquake Technology* (ISET) Journal, Roorkee; and as Guest Editor, *Indian Concrete Journal*. He received so many prestigious awards such as Fellow of The Institution of Engineers (India); outstanding reviewer awards from Elsevier journals; Young Associates (2012), Indian National Academy of Engineering (INAE), India; Young Engineers Award (2012), Indian National Academy of Engineering, India; Young Associates (2012), Indian National Academy of Engineering (INAE), India; Young Engineers Award (2012), Indian National Academy of Engineering, India, etc. He serves as editorial board member in *Structural Engineering Digest* (SED) Journal, *Journal of Civil Engineering & Construction Technology*, and *Indian Concrete Journal* (ICJ).

Dr. Pradip Sarkar is presently working as Professor at the Department of Civil Engineering, National Institute of Technology Rourkela, India. He obtained his B.E. in Civil Engineering and M.E. in Engineering Mechanics from Bengal Engineering and Science University, Shibpur, India (presently known as IIEST Shibpur) and Ph.D. from the Indian Institute of Technology Madras, India. His major areas of research interests include earthquake analysis and design of structures, structural properties of building materials. He has published 38 journal papers, 48 conference papers and nine book chapters. Best teacher award at NIT Rourkela (2018–2019), GC Mitra Memorial Gold Medal (2002), University Silver Medal (2002) were awarded to him for his extraordinary achievements in academics. He is an active reviewer of various reputed journals and the national/international conferences.

Influence on Hydration and Microstructural Properties of Low-Carbon Cementitious Binder Modified with Water-Soluble Polymer and Fly Ash

Rajesh Kumar

1   Introduction

Sustainable design is the primary need of this century to save natural sources such as water and limestone for future generation. For this purpose, the development of novel engineered materials with specific properties and low cost could only be possible by using different kinds of waste materials and chemical admixtures. In general, SCMs enhance the performance of cementing material through pozzolanic reaction with filling effect [1]. The pozzolanic activity of fly ash has bi-fold benefit. It produces additional secondary calcium silicate hydrate (C–S–H) and calcium aluminate hydrate, along with consuming $Ca(OH)_2$ which weakens the interfacial transition zone (ITZ) [2]. The degree of pozzolanic reaction depends upon the curing temperature and replacement ratio of fly ash [3].

Cement–polymer composites materials are developed by OPC with polymeric binders. Different kinds of physio-mechanical and durability properties of the composites depend on the nature and quantity of the polymer [4]. Water-soluble polymers (such as HPMC) are added to OPC mortar in order to improve workability and showed higher water retention [5]. It has been shown that the presence of HPMC also affects the hydration kinetics and the microstructure formation of OPC products too [6].

Cellulose is constituted of anhydroglucose units with β-1.4 linkages and insoluble in water. Therefore, substitution of cellulose can be occurred with methoxy groups (OCH_3), hydroxypropyl groups (POOH) and hydroxyethoxy groups (EOOH) [7].

R. Kumar (✉)
Organic Building Materials Group, CSIR–Central Building Research Institute, Roorkee, Uttrakhand 247667, India
e-mail: rajeshkumar@cbri.res.in

Department of Civil Engineering, Indian Institute of Technology (IIT) Delhi, New Delhi 110016, India

Cellulose ether is a kind of common water-retaining agent [8], viscosity modifier, and workability modifier [9]. The adsorption between cellulose ether (CEs) molecule and hydration products was the major retardation mechanism [10].

As HPMC (as water-soluble polymers) in the cementitious system improves the workability even after addition of fly ash, while fly ash was added to reduce the clinker factor and also to improve the strength of blended cement at later age. Therefore, in this attempt, the role of HPMC in the fly ash blended low-carbon cement is being studied by conducting comprehensive studies such as—normal consistency and setting time, hydration study, uniaxial compressive test, microstructural analysis using SEM, XRD study and thermal analysis.

2 Experimental Program

2.1 Materials and Composition

OPC 43 grade was used in this study. Fly ash conforming to ASTM standard C 618 was used in this investigation. Class F (siliceous type) pulverized fly ash was collected from the thermal power plant Dadri, Uttar Pradesh. Grain size distribution of fly ash and cement is depicted in Fig. 1. The physical properties of OPC 43 grade and class F fly ash is shown in Tables 1 and 2.

For this study, cellulose derivative such as hydroxypropyl methylcellulose (HPMC) with 4–6 cps apparent viscosity was used (Table 3).
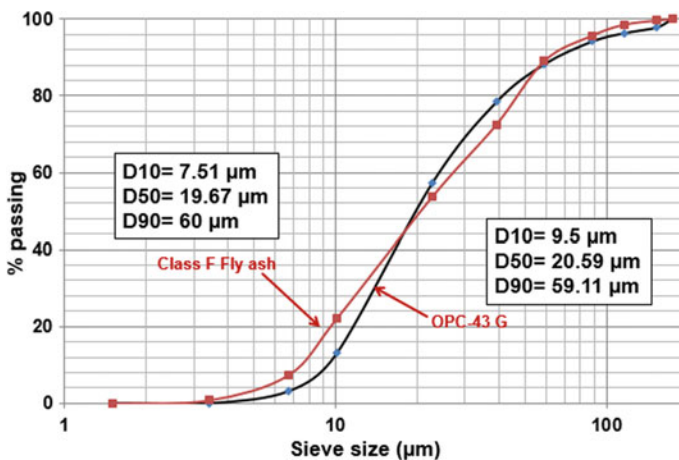
Fig. 1 Grain size distribution of OPC and fly ash

Table 1 Physical properties of OPC 43 grade

Parameters	OPC
Standard consistency	30%
Setting time (min)	
Initial	110
Final	225
Compressive strength (MPa)	
3 d	27.50
7 d	36.30
28 d	48.40
Fineness (m^2/kg)	280
Specific gravity	3.15

Table 2 Physical properties of class F fly ash

Characteristic		Class F fly ash
Fineness (m^2/kg)		538
Bulk density (kg/m^3)		2020
Bulk specific gravity		2.24
Water absorption (%)		56.9
Strength activity index	7 d	0.72
	28 d	0.74

Table 3 Typical properties of HPMC

Constituents	Quantity
Methoxy content/%OCH_3	28–30%
Hydroxypropoxyl content/%POOH	7–12%
Apparent viscosity (2% w/w)	4–6 cps
Loss on drying	10%
pH value	6.5
Appearance	White powder
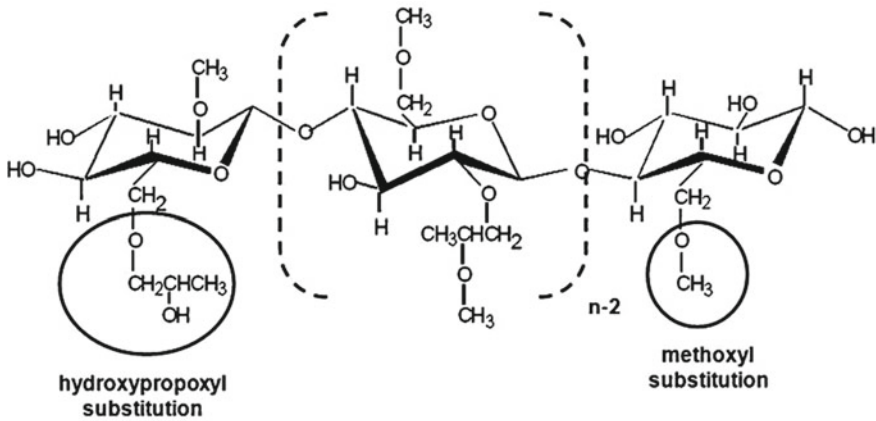
Structure of HPMC [7]

2.2 Specimen Preparation

First, cement and fly ash were mixed together in a planetary mixer for 1 min at 120 rpm. Then, HPMC were mixed with water. After that, all above raw materials were mixed for another 2 min. Fresh pastes were cast into cube molds (25 × 25 × 25 mm). The specimens were demolded and cured for 7 days at room temperature in humid environment. Then, the samples were placed in dual humidity chamber at 40 °C and 95 ± 5% RH. For this study, various types of cement paste samples were prepared at a constant w/b ratio 0.32. The unmodified paste samples and paste modified with 0.2–1.0% polymer, 10–30% of fly ash were prepared. The designed mix proportions are presented in Table 4.

2.3 Experimental Study

Fresh-state properties such as normal consistency and setting times (initial and final) with/without addition of fly ash and HPMC was determined by an automatic **Vica-matic apparatus** as per BS EN: 196-4 (Fig. 2). The cast fresh paste was maintained at 27 °C (room temperature). The heat of hydration measurement was carried out using **heat of hydration apparatus** at 28 and 90 days cured specimens, as per ASTM C186-05.

The **compressive strength** of unmodified paste samples (OPC) and paste modified with fly ash and HPMC at time interval 7, 28, and 90 days were determined by casting 25 × 25 × 25 mm cubes. The loading rate was set to 0.2 mm/min. The tests were performed using a Shimadzhu testing machine with a capacity of 100 T. For

Table 4 Mix design detail of the blended cement pastes

Mix designation	wt% of dry mix		
	OPC	PFA	HPMC
OPC	100	0	0
10FA-0HPMC	90	10	0
FA10-0.2HPMC	90	10	0.2
FA10-0.6HPMC	90	10	0.6
FA10-1HPMC	90	10	1.0
FA15-0HPMC	85	15	0
FA15-0.2HPMC	85	15	0.2
FA15-0.6HPMC	85	15	0.6
FA15-1HPMC	85	15	1.0
FA20-0HPMC	80	20	0
FA20-0.2HPMC	80	20	0.2
FA20-0.6HPMC	80	20	0.6
FA20-1HPMC	80	20	1.0
FA25-0HPMC	75	25	0
FA25-0.2HPMC	75	25	0.2
FA25-0.6HPMC	75	25	0.6
FA25-1HPMC	75	25	1.0
FA30-0HPMC	70	30	0
FA30-0.2HPMC	70	30	0.2
FA30-0.6HPMC	70	30	0.6
FA30-1HPMC	70	30	1.0
FA0-0.2HPMC	100	0	0.2
FA0-0.6HPMC	100	0	0.6
FA0-1HPMC	100	0	1.0

determination of strength; three samples were tested for each mix. For microstructural studies, the samples (taken out from > 1 mm depth) were stored in acetone up to 24 h to stop cement hydration. After that, the specimens were kept in oven at temperature of 105 °C for four hours until the mass of sample was not changed, significantly. The **scanning electron microscopy** (SEM) investigation (Carl Zeiss AG, Oberkochen, Germany) at operating voltage of 15–20 kV is carried out on hydrated paste samples. **X-ray diffraction** analysis (with a Cu_Kα radiation source (wavelength = 0.154 nm)) was used to distinguish the major solid hydrated phases in cement paste. This was performed on unmodified cement paste and modified paste after hydration stoppage with acetone. The samples were in dried state and grounded to < 45 μm. The step was carried out at a voltage 20–60 kV with an intensity 2–80 mA, and 2θ range was 5–80°.
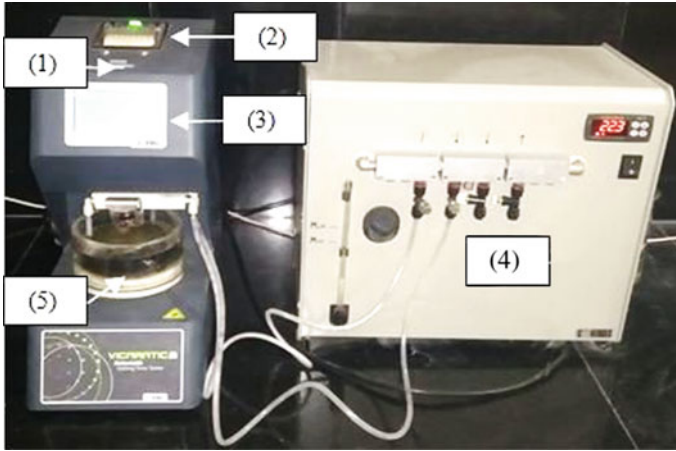
Fig. 2 Vicamatic apparatus. (1) plunger, (2) graphic printer, (3) display, (4) Water thermostatic unit, and (5) sample mold with centering ring

3 Results and Discussion

3.1 Normal Consistency and Initial–Final Setting Times

Normal consistency is calculated as the amount of water (in %) which is required to prepare OPC paste having a standard consistency [11]. The normal consistency of OPC binder system is affected by its chemical oxides, fineness (m^2/kg) along with pore %. The normal consistency and setting times of unmodified and modified paste with different ratios of fly ash and HPMC have been determined. The normal consistency of unmodified paste was 30%. The results depicted that the normal consistency of fly ash blended paste was higher than the unmodified paste. The increase in the percentage of fly ash (10–30%) leads to increase in the water demand or consistency which was due to higher fineness of pulverized fly ash. The blended paste containing HPMC content from 0.2 to 1.0% with 10 to 30% fly ash content leads to a decrease in the water demand. This was due to the viscosity modifying properties of HPMC. The initial and final setting time of unmodified OPC paste was observed as 110 and 225 min, respectively. The initial and final setting times were increased with the fly ash content from 10 to 30% in combination with 0.2–1.0% HPMC content.

Fig. 3 Degree of hydration of unmodified and modified pastes
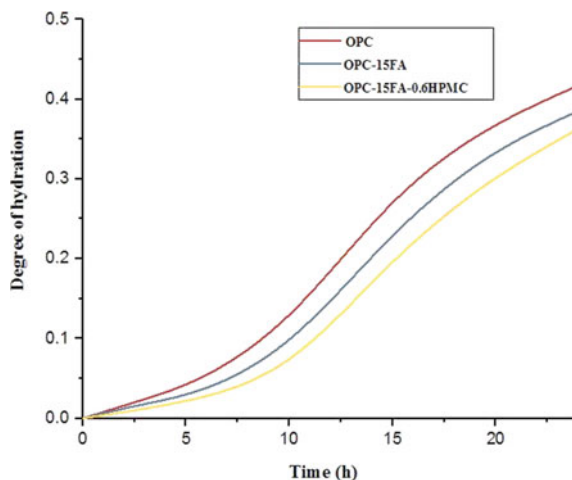
3.2 Hydration Study

Hydration is an exothermic process in which heat is released. Isothermal calorimetry is a significant tool to quantify the hydraulic and pozzolanic activity of cement and fly ash, respectively. The effect of fly ash and HPMC on degree of hydration was shown in Fig. 3. In this study, it was found that in the presence of fly ash, heat of hydration was retarded due to slow pozzolanic reaction at early ages. It has also been reported that polymer delays the induction and acceleration period of cement paste as the dosage increases. Since cellulose ether decreases the moving rate of ions into the solution and formed a film around the cement particles [12], the results clearly indicated that during the first 24 h the paste modified with FA and FA-HPMC shows the low rate of heat evolution due to the dilution effect and adsorption effect of fly ash and HPMC, respectively, than that of unmodified paste.

3.3 Uniaxial Compressive Test

The compressive strength (CS) of hardened blended OPC paste was determined at 7, 28, and 90 days. According to the results obtained, the replacement of OPC with fly ash ranging from 10 to 30% caused a decrease in CS at early ages (up to 7 days). Maximum early age CS 56.48 MPa was observed for mix with 15% fly ash after 7 days of hydration, which resulted in significant reduction in the 7 days CS than that of unmodified paste/control mix. It has been reported that at early ages of hydration slow pozzolanic reaction of fly ash and cement dilution effect was occurred. As the hydration proceeds, the pozzolanic reaction of fly ash is accelerated which was demonstrated by SEM and TG studies at the age of 28 and 90 days. Therefore,

the CS was higher after 28 and 90 days, respectively, because fly ash provided the additional C–S–H to the blended system. Singh et al. reported that organic set retarders increased the CS of OPC with later age curing [13]. HPMC and fly ash both in the combination in blended cement paste (for FA15–0.6HPMC mix) improve the CS of the system after 7 and 28 days [14]. At 28 and 90 days, CS of FA15–0.6HPMC mix was obtained as 61.11 MPa and 72.28 MPa, while, = for control mix, CS was determined as 54.32 MPa and 62.98 MPa, at 28 and 90 days, respectively.

3.4 Microstructural Analysis Using SEM

The microstructural studies of fractured surface of unmodified (OPC) and modified pastes (OPC–15%FA-0.6%HPMC) are shown in Fig. 4a, b. After curing age of 28 days, the microstructure of OPC paste was porous and heterogeneous as depicted in Fig. 4a. Figure 4b shows that some cenospheres can be seen in the microstructure of fly ash–polymer-modified paste. The pozzolanic activity of class F fly ash was activated by calcium hydroxide (CH) and speed up after 28 days, with an increase of C–S–H content [15]. The effect of polymer addition on OPC microstructure depends on interactions between HPMC with OPC grains. The cellulose ether addition also enhances the formation of inner C–S–H gel rather than unmodified pastes [16]. Fly ash and HPMC can slow down the hydration reaction due to dilution and adsorption effect, respectively. At later ages, the increase in the pozzolanic reaction was significant to improve the compactness of the paste system [17]. Therefore, it was concluded from Fig. 4b, a slight increase in the homogeneity, compactness, and modification in the hydration products of the mix of fly ash and HPMC was observed at the same age of hydration.
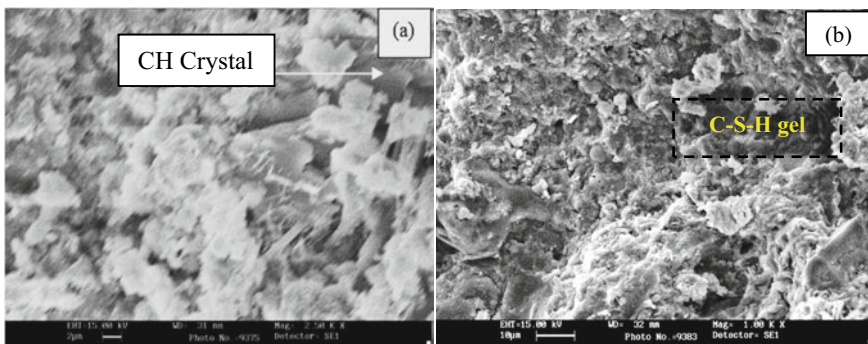
Fig. 4 SEM micrographs of sample. (**a**) OPC paste, (**b**) OPC–15%FA–0.6%HPMC after 28 days of hydration
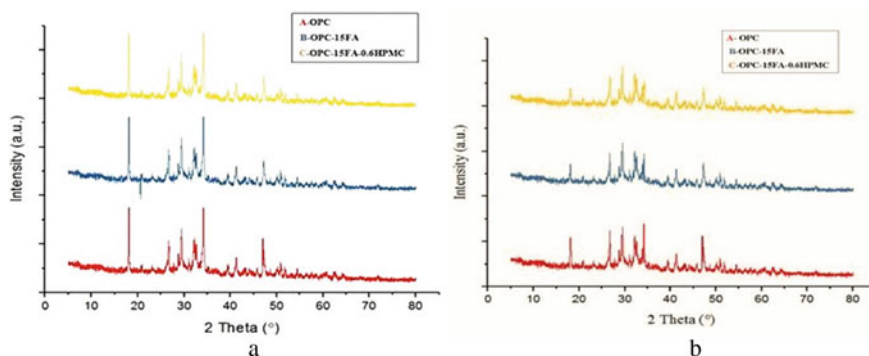
Fig. 5 XRD of (**a**) OPC, OPC–15FA and OPC–15FA–0.6HPMC blended paste at 28 days, (**b**) at 90 days of hydration

3.5 XRD Study

At curing periods of 28 and 90 days, XRD patterns of all modified and unmodified cement paste samples were recorded as shown in Fig. 5. XRD patterns showed that the main products were C–S–H at $2\Theta = 29°$–$32°$ and CH at $2\Theta = 18.0°$, $28.6°$, and $34.1°$. It is well known that CH and C–S–H are the major hydration products during the hydration reaction. It was inferred that the intensity peaks of CH in binary and ternary modified cement paste were almost similar to that of unmodified paste, because of the slow pozzolanic reaction of PFA at 28 days. After 90 days, the results showed that the CH intensity peaks were decreased with the interaction of fly ash and $Ca(OH)_2$ to form pozzolanic or secondary C–S–H products. Therefore, the intensity peak of CH for OPC–FA–HPMC mix was lower than that of control OPC paste at 90 days of curing.

3.6 Thermal Analysis

Thermo-gravimetric analysis (TGA) and DTG are more suitable methods for studying hydration at later stages [18]. The TG thermo-grams and DTG of the specimens made of unmodified cement paste and modified paste after 90 days are shown in Fig. 6a, b. The endothermic peak via mass loss was occurred in the temperature below 100 °C due to removal of free water and also in the temperature range of 100–350 °C which was attributed to the gel pores of the C–S–H, C–A–H, and hydrated calcium sulpho-aluminates [18]. The mass losses due to $Ca(OH)_2$ and $CaCO_3$ were appeared at 450 °C and 720 °C, respectively. The mass loss due to portlandite was higher in unmodified paste than modified paste at every age of hydration. The decrease in the peak intensity at 450–520 °C was occurred due to the decomposition of portlandite phase with the curing age as compared to that of control PC paste. The decrease
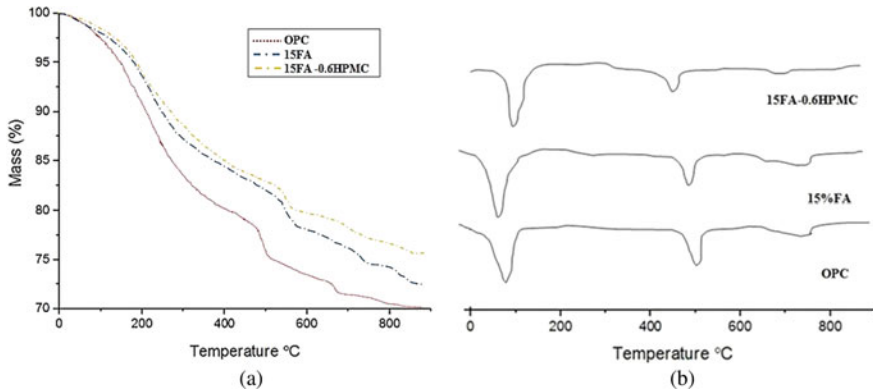
Fig. 6 TG wt% loss and DTG curves of hydrated paste at 90 days of hydration

in the intensity of calcium hydroxide phase was due to the consumption during the pozzolanic reaction of fly ash.

4 Conclusions

On the basis of the results and analysis, the following conclusions were drawn:

- Water demand of fly ash blended cement paste was higher than that of unmodified paste.
- Fly ash and HPMC reduced the rate of heat of hydration for a period of 24 h due to their retardation ability.
- The compressive strength values of modified paste are higher than the unmodified paste after 90 days of hydration.
- The SEM studies indicated that the surface morphology of the modified paste was more compact and homogeneous due to the formation of secondary C–S–H gel in the OPC system. Pores were also reduced due to the dilution of OPC with fly ash and polymer.
- Ettringite needles were very distinct near the voids after 7 days of hydration and fly ash–HPMC filled the voids by interacting with each other as the hydration proceed.
- Through the XRD studies, it can be concluded that the intensity peak of $Ca(OH)_2$ was decreased as the hydration of OPC–FA–HPMC system increased due to the consumption of $Ca(OH)_2$.

Thus, it was concluded that 28 days and 90 compressive strength of polymer-modified mix (OPC–15%FA–0.6%HPMC) was 12.5% and 14.77% higher as compared to control OPC mix. Also, HPMC polymer and fly ash SCM increased the homogeneity, compactness, and modification in the hydration products for the same

mix. Thus, mix (OPC–15%FA–0.6%HPMC) has better structural performance to be used as a building material.

References

1. Heikal M (2006) Effect of temperature on the structure and strength properties of cement paste containing fly ash alone or in combination of limestone. Ceram Silik 50(3):167–177
2. Wong Y, Lam L, Poon C, Zhou F (1999) Properties of fly ash-modified cement mortar-aggregate interfaces. Cem Concr Res 29(12):1905–1913. https://doi.org/10.1016/s0008-8846(99)00189-1
3. Narmluk M, Nawa T (2014) Effect of curing temperature on pozzolanic reaction of fly ash in blended cement paste. Int J Chem Eng Appl 5(1):31–35. https://doi.org/10.7763/ijcea.2014.v5.346
4. Rai U, Singh R (2005) Effect of polyacrylamide on the different properties of cement and mortar. Mater Sci Eng A 392(1–2):42–50. https://doi.org/10.1016/j.msea.2004.08.050
5. Knapen E, Van Gemert D (2009) Cement hydration and microstructure formation in the presence of water-soluble polymers. Cem Concr Res 39(1):6–13. https://doi.org/10.1016/j.cemconres.2008.10.003
6. Knapen E, Gemert DV (2009) Effect of under water storage on bridge formation by water-soluble polymers in cement mortars. Constr Build Mater 23(11):3420–3425. https://doi.org/10.1016/j.conbuildmat.2009.06.007
7. Pourchez J, Peschard A, Grosseau P, Guyonnet R, Guilhot B, Vallée F (2006) HPMC and HEMC influence on cement hydration. Cem Concr Res 36(2):288–294. https://doi.org/10.1016/j.cemconres.2005.08.003
8. Su L, Ma B, Jian S, Zhao Z, Liu M (2013) Hydration heat effect of cement pastes modified with hydroxypropyl methyl cellulose Ether and expanded perlite. J Wuhan Univ Technol-Mater Sci Ed 28(1):122–126. https://doi.org/10.1007/s11595-013-0652-2
9. Spychał E (2015) The effect of lime and cellulose Ether on selected properties of plastering mortar. Proc Eng 108:324–331. https://doi.org/10.1016/j.proeng.2015.06.154
10. Ou ZH, Ma BG, Jian SW (2012) Influence of cellulose ethers molecular parameters on hydration kinetics of Portland cement at early ages. Constr Build Mater 33:78–83. https://doi.org/10.1016/j.conbuildmat.2012.01.007
11. BS EN 196–4 (2016) Methods of testing cement: determination of setting times and soundness. German Standard
12. Ma BG, Su L, Jian SW, Zhao ZG, Liu M (2012) Early stage hydration process of hydroxypropyl methyl cellulose Ether modified cement pastes. Adv Mater Res 476–478:1709–1713. https://doi.org/10.4028/www.scientific.net/amr.476-478.1709
13. Singh NK, Mishra PC, Singh VK, Narang KK (2002) Effect of HPMC on the properties of cement. Indian J Chem Technol 9:112–117
14. Moon GD, Oh S, Choi YC (2016) Effects of the physicochemical properties of fly ash on the compressive strength of high-volume fly ash mortar. Constr Build Mater 124:1072–1080. https://doi.org/10.1016/j.conbuildmat.2016.08.148

15. Lee SH, Kim HJ, Sakai E, Daimon M (2003) Effect of particle size distribution of fly ash–cement system on the fluidity of cement pastes. Cem Concr Res 33(5):763–768. https://doi.org/10.1016/s0008-8846(02)01054-2
16. Qu X, Zhao X (2017) Influence of SBR LaTeX and HPMC on the cement hydration at early age. Case Stud Constr Mater 6:213–218. https://doi.org/10.1016/j.cscm.2017.04.006
17. Chindaprasirt P, Jaturapitakkul C, Sinsiri T (2007) Effect of fly ash fineness on microstructure of blended cement paste. Constr Build Mater 21(7):1534–1541. https://doi.org/10.1016/j.conbuildmat.2005.12.024
18. Kumar R (2021) Effects of high volume dolomite sludge on the properties of eco-efficient lightweight concrete: microstructure, statistical modeling, multi-attribute optimization through derringer's desirability function, and life cycle assessment. J Cleaner Prod 307:127107. https://doi.org/10.1016/j.jclepro.2021.127107

Montmorillonite Content of Expansive Soils and Its Relationship with Swelling and Consistency Properties

P. Sreekanth Reddy, Bijayananda Mohanty, and B. Hanumantha Rao

1 Introduction

Mineral quantification plays a vital role when dealing with expansive soils, as they grossly account for the consistency and swelling behavior. However, the quantification of clay minerals is a challenging issue due to their complex chemical compositions and effect of particle orientations [1, 2]. Compared to all associated minerals in expansive soils, montmorillonite is having a high surface and high cation exchange capacity. Considering it, several studies also report that mineral content can be identified indirectly from cation exchange capacity [3] and chemical balance method [4], where the latter method was successful up to the mark. On the other hand, Chittoori [5] developed a new regression model for the quantification of clay minerals based on chemical soil properties such as cation exchange capacity (CEC), total potassium, and specific surface area (SSA). Analytically, X-ray diffraction (XRD), transmission electron microscopy (TEM), infrared analysis (IR), and differential thermal analysis (DTA) are in use for the identification of clay minerals in soils [6], which are expensive and available at a limited number of laboratories [4]. Nevertheless, XRD is the only technique that in practice for the quantification of minerals from early 1960s.

Needless to state, the enormity in consistency limits of expansive soils largely depends on different parameters relevant to physical, chemical, and mineralogy [7]. But, undoubtedly, not much attention was paid to comprehend the exact influence of MMC on geotechnical properties, in particular on consistency limits. This paper is themed to address important points related to the quantification of montmorillonite content for understanding its impact on swelling behavior and consistency limits. For

P. Sreekanth Reddy (✉) · B. Mohanty · B. Hanumantha Rao
Department of Civil Engineering, NIT Mizoram, Aizawl, Mizoram 796012, India
e-mail: psreddy.civil.phd@nitmz.ac.in

B. Hanumantha Rao
School of Infrastructure, IIT Bhubaneswar, Khordha, Odisha 752050, India

the study purpose, expansive soil samples were collected from nine different regions across India. MMC, and consistency limits of these soils were determined, and appropriate interrelations were developed. The compilation of data was prompted to develop separate sets of correlations for bentonite soils (BS), having extreme consistency values, and natural expansive soils (NES), having low to very high consistency values, and the same was accomplished in the study.

2   Materials and Testing Methodology

Experimental investigations were conducted on expansive soil samples collected from different regions across India. The clay content of the soil samples was determined by hydrometer analysis (<75 µm) (ASTM D7928-17) [8], and consistency limits (liquid limit, w_L, plastic limit, w_P plasticity index, $w_{PI,}$ shrinkage limit, w_{SL} and shrinkage index, w_{SI}) were determined as per the ASTM D4318-00 [9] and ASTM D427–98 [10] standards. The swelling potential of the samples was determined as per the guidelines of ASTM D2435–04 [11]. The physical properties of soil samples used in the current study are listed in Table 1.

2.1   XRD Analysis

The mineralogy of soil samples used in the current study is analyzed by employing to D8 Advanced X-ray powder diffraction device (make, BRUKER, USA). For testing purpose, the clay content of the soil samples was separated by following the procedure

Table 1 Physical properties of soil samples used in the current study

Location	Soil properties							Classification
	Particle size distribution (%)			Consistency limits (%)			Mineralogy	
	Clay	Silt	Sand	w_L	w_P	w_{SL}	MMC (%)	USCS
Bhopal	51	43	6	68	27.52	8.5	35.61	CH
Guntur	58	31	11	93	36	8.85	19.06	CH
Kakinada	49	46	5	82	31	12	17.24	CH
Nagpur	41	43	14	61	21.92	10.62	31.59	CH
Raipur	45	39	15	76.7	25.39	9.89	31.03	CH
Vijayawada	55	33	12	92	34.32	8.65	43.97	CH
Warangal	42	30	26	70	26	15.32	33.18	CH
Mysore	53	26	21	72	28.35	8.97	28.66	CH
Kendrapara	43	38	15	60	28.29	9.85	12.19	CH

of Rao et al. [12]. The obtained samples were placed in the equipment and scanned with a voltage of 40 kV and a current of 40 mA. Further, the 2θ in the range of 5–80°, step size of 0.025°, and time interval of 0.5 s are maintained, and a copper X-ray tube (i.e., Cu-Kα radiation) was used. The presence of different minerals, especially targeting montmorillonite content (MMC) in the soil samples, was analyzed with the help of software DIFFRAC. EVA, which is already equipped with the equipment. Further, the quantity of MMC is identified by using the software TOPAS 4.2, which performs a whole pattern followed by Rietveld analysis. The MMC of soil samples determined from the analysis is listed in Table 1. The detailed procedure for the quantification of minerals can be found in Rao et al. [12].

3 Results and Discussion

Consistency limits are the mostly used parameters for identifying the presence of clay minerals in fine-grained soils. Among them, liquid limit, w_L and plasticity index, w_{PI} are the best for approximation of mineralogy of fine-grained soils [7, 13]. With this in mind, an attempt was made to deduce the relationship between consistency limits and montmorillonite content, MMC as depicted in Fig. 1a, b. The maximum values of w_L and w_{PI} of the soils used in the study are measured as 93 and 57%. In order to validate the present results, the related data have been collected from the literature and superimposed on Fig. 1.

As depicted in Fig. 1a, b, both w_L and w_{PI} increased linearly with an increase in MC. As MMC increases so does w_L and w_{PI}. Prominently, the data of Fig. 1a, b reflect both NES and BS. It is observed that the values of w_L and w_{PI} of BS are considerably higher vis-à-vis with those of NES. It is seen from Fig. 1a, b that the value of w_L as high as 993% and w_{PI} up to 950% have been reported, especially, for BS. It is, in general, seen from Fig. 1a, b that MMC in BS is reported significantly high (>50%) vis-à-vis with those of NES, for which MMC is measured below 50%. Consequently, it is prudent to make an inference that soils rich in MMC of above 50% can exhibit an average w_L of above 100% and w_{PI} of above 60%, respectively. These observations well corroborate with the results of Croft [14], who has reported that soils with w_L of greater than 60% and w_{PI} of greater than 25% evidently consist of expansive clay minerals such as montmorillonite.

As such, a linear fit model was employed to mathematically correlate w_L and w_{PI} with MMC. The empirical equations derived based on fitting functions are also printed in the same graph, alongside the values of constants. Incidentally, the values of regression coefficients, R^2, pertinent to w_L are 0.78 and 0.82 for w_{PI}. It is obvious from the trends shown in Fig. 1a, b that when MMC is extrapolated to zero, soils yet exhibited w_L of 32% and w_{PI} of 19%. Based on these observations, it can be theorized that soils without comprising of expansive minerals like montmorillonite, they still exhibit consistency behavior. This may be attributed to the fact that soils in addition to possessing minerals, like montmorillonite, might also constitute with mixed layer minerals such as illite–smectite, which would cause soils to exhibit
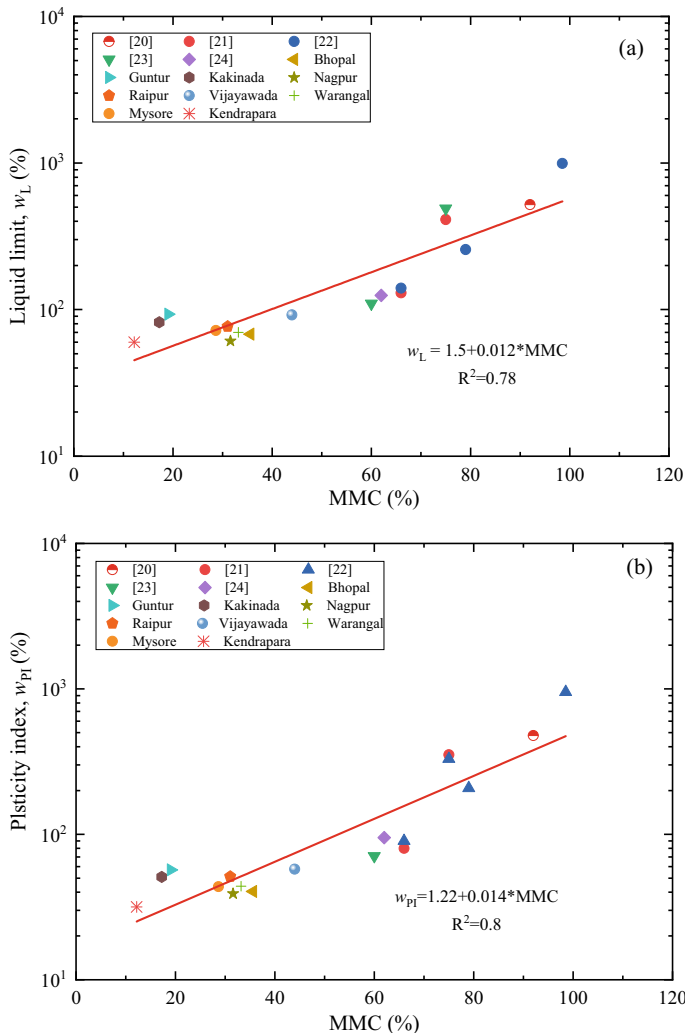
Fig. 1 Influence of MMC on liquid limit and plasticity index of soils used in the study

consistency behavior. The findings of studies by Prakash and Sridharan [13] and Reddy et al. [2], who reported that the mixed layer minerals could induce swelling to the expansive soils, excellently validate this statement.

Shrinkage index, w_{SI} of soil can be defined as the difference between plastic limit, w_{PI} and shrinkage limit, $w_{SL.}$ A close observation of Fig. 2a, b shows that w_{SL} and w_{SI} decreases with an increase in MMC. These observations are contrary to the results of Fig. 1. The maximum and minimum values of w_{SL} and w_{SI} of soils are measured as 8.5–15.32% and 46.81–110.15%, respectively. Based on the measured w_{SL} values, the volume change behavior of soils used in the study can be categorized
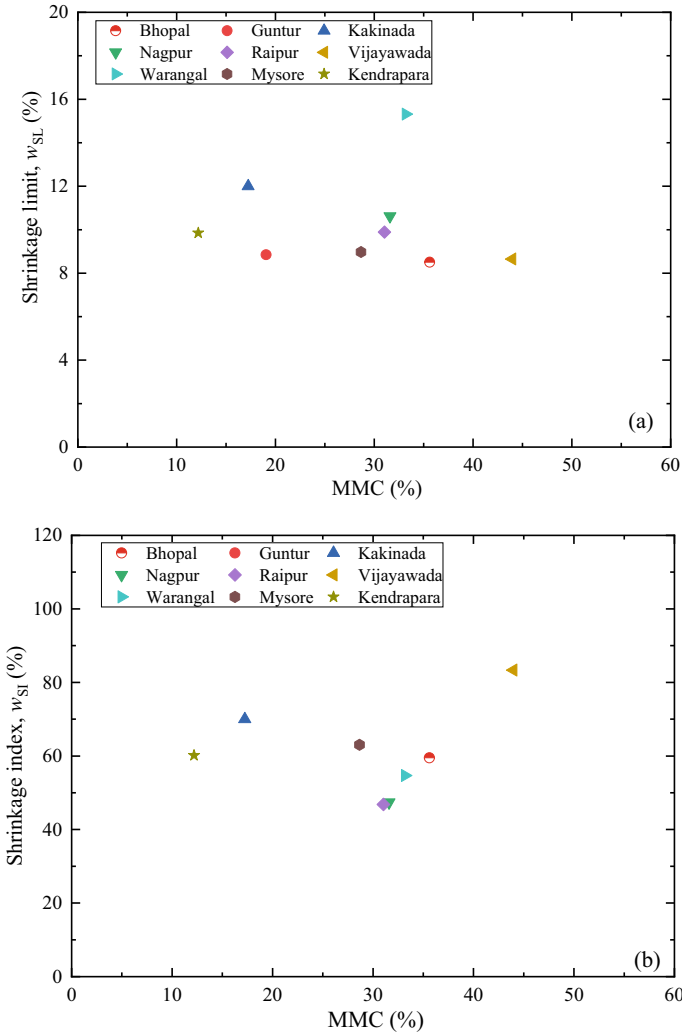
Fig. 2 Influence of MMC on shrinkage limit and shrinkage index of soils used in the study

as: non-critical to critical [15]. Furthermore, as per IS 1498 that classifies the soil based on w_{SI}, soils used in the study exhibited high to very high swell potential [16]. Many studies report that w_{SL} and w_{SI} may not be better parameters for predicting the swelling behavior of expansive or fine-grained soils. It is because these properties are not considered as plasticity characteristics, and the mechanism behind these properties is different from swelling. The swelling is due to the expansion of clay mineral lattice, whereas, in the case of $w_{SL,}$ it is chiefly managed by the relative grain size distribution of expansive or fine-grained soils [17].
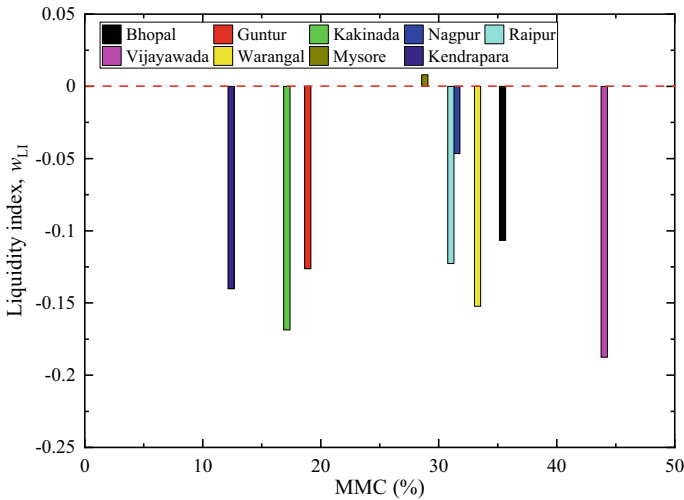
Fig. 3 Variation of liquidity index with MMC of soils used in the study

Liquidity index (w_{LI}) merely indicates the moisture condition of a soil. It becomes negative when the natural moisture content of soils lies below w_{PI}, which generally happens for overconsolidated clays or semi-plastic solids. Figure 3 depicts the relationship for w_{LI} versus MMC of respective soil samples. Observance of both +ve and −ve values is possible from Fig. 3. A close examination of Fig. 3, in general, reveals that w_{LI} could predominantly be −ve for expansive type soils. It is clearly seen that most of the data fall below zero (i.e., −ve), but a few data points are even + ve (i.e., above zero). This highlights the variability in consistency of expansive soils used in the present study. These statements well corroborate with the observation of Chen [18], who reported that expansive soils exhibit w_{LI} of −ve. It is seen from Fig. 3 that w_{LI} decreased with an increase in MMC. As such, the results presented in Fig. 3 are found to matching excellently with those reported by Shi et al. [19].

Many studies confirmed that MMC and its associated minerals, such as illite–smectite, kaolinite-smectite, which are categorized as mixed layer minerals, inherently govern the swelling behavior of expansive soils [2]. With this in mind, an attempt is made to correlate MMC with swelling potential, S_a. From Fig. 4, it can be observed that S_a increased linearly with an increase in MMC in the expansive soils. It is obvious that as MMC increases so does S_a. In order to validate the present results, the relevant data have been collected from the literature, and the same is used to validate the data produced by the present study. Additionally, a linear fit is employed, and empirical equation along with values of constants is printed in the figure. The regression coefficient, R^2, value of 0.58 was obtained for MMC versus S_a. The following observations can further be made from the results presented in Fig. 4: (a) the maximum MMC measured in NES is 42%; (b) the maximum S_a measured of these soils is 15%; (c) S_a consistently increased with MMC, for its whole measured range from 0 to 42%, and (d) MMC has a significant effect on S_a of expansive soils.
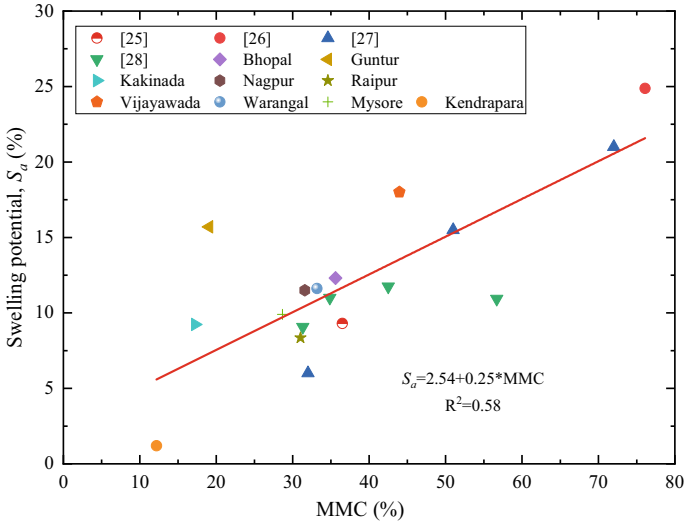
Fig. 4 Variation of swelling potential with MMC of soils used in the study

The similarity in trends of Figs. 1a, b and 4 reveals that there exists a relationship between these parameters.

4 Conclusions

In this study, different expansive soil samples were collected from different regions across India and were characterized for montmorillonite content. From the extensive experimental data, several correlations separately for natural expansive soils and mineral-rich bentonite soils were developed, and the same were validated with the literature data. Based on the correlations and further interpretations of the results, the following conclusions were derived:

1. Demonstrably, it is the montmorillonite mineral and its content is a prime controlling factor prompting consistency and swelling behavior in expansive soils.
2. Interpretation of the results evidently manifests that variability in the data of montmorillonite content, consistency limits, and swelling potential is intrinsic, in particular, pertinent to expansive soils.
3. The maximum values of MMC, w_L, w_{PI}, w_{SL}, w_{SI}, w_{LI}, and S_a of expansive soils used in the study are measured as: 44%, 93%, 57.68%, 15.32%, 110.15%, −0.05, and 18%, respectively.

References

1. Srodon J (2002) Quantitative mineralogy of sedimentary rocks with emphasis on clays and with applications to K-Ar dating. Mineral Mag 66(5):677–687
2. Reddy PS, Mohanty B, Rao BH (2020) Influence of clay content and montmorillonite content on swelling behavior of expansive soils. Int J Geosynth Ground Eng 6(1):1
3. Kaufhold S, Dohrmann RB, Ufer K, Meyer FM (2002) Comparison of methods for the quantification of montmorillonite in bentonites. Appl Clay Sci 22(3):145–151
4. Hao L, Wei Q, Zhao Y, Lu J, Zhao X (2015) Optimization method for quantitative calculation of clay minerals in soil. J Earth Syst Sci 124(3):675–680
5. Chittoori BCS (2008) Clay mineralogy effects on long-term performance of chemically treated expansive clays. Ph.D thesis, University of Texas at Arlington
6. Mitchell JK, Soga K (2005) Fundamentals of soil behavior. John Wiley and Sons, New York
7. Sridharan A, Rao SM, Murthy NS (1986) Liquid limit of montmorillonite soils. Geotech Test J 9(3):156–159
8. ASTM D7928–17 (2017) Standard test method for particle-size distribution (gradation) of fine-grained soils using the sedimentation (hydrometer) analysis. ASTM International, West Conshohocken PA, USA
9. ASTM D4318 (2010) Standard test methods for liquid limit, plastic limit, and plasticity index of soils. ASTM International, West Conshohocken PA, USA
10. ASTM D427–98 (1998) Test method for shrinkage factors of soils by the mercury method. ASTM International, West Conshohocken PA, USA
11. ASTM D2435–04 (2004) Standard test methods for one-dimensional consolidation properties of soils using incremental loading. ASTM International, West Conshohocken PA, USA
12. Rao BH, Reddy PS, Mohanty B, Reddy KR (2021) Combined effect of mineralogical and chemical parameters on swelling behaviour of expansive soils. Sci Rep 11:16562
13. Prakash K, Sridharan A (2004) Free swell ratio and clay mineralogy of fine-grained soils. Geotech Test J 27(2):220–225
14. Croft JB (1986) The problem in predicting the suitability of soils for cementitious stabilization. Eng Geol 2(6):397–424
15. Altmeyer WT (1956) Discussion. Transit ASCE 121:666–669
16. IS 1498 (1987) Indian standard classification and identification of soils for general engineering purposes. BIS, New Delhi
17. Sridharan A, Prakash K (1998) Mechanism controlling the shrinkage limit of soils. Geotech Test J 21(3):240–250
18. Chen FH (1975) Foundations on expansive soils. Elsevier Science, Amsterdam, The Netherland
19. Shi B, Jiang H, Liu Z, Fang HY (2002) Engineering geological characteristics of expansive soils in China. Eng Geol 67(1–2):63–67
20. Wang Q, Tang AM, Cui YJ, Delage P, Gatmiri B (2012) Experimental study on the swelling behaviour of bentonite/claystone mixture. Eng Geol 124:59–66
21. Tripathy S, Sridharan A, Schanz T (2004) Swelling pressures of compacted bentonites from diffuse double layer theory. Can Geotech J 41(3):437–450
22. JNC TN 2000 H12 (2000) Project to establish the scientific and technical basis for HLW disposal in Japan. (JNC TN1410 2000–003)
23. Schanz T, Nguyen-Tuan L, Datcheva M (2013) A column experiment to study the thermo-hydro-mechanical behaviour of expansive soils. Rock Mech Rock Eng 46(6):1287–1301
24. Zhang G, Germaine JT, Whittle AJ, Ladd CC (2004) Index properties of a highly weathered old alluvium. Géotechnique 54(7):441–451
25. Lin B, Cerato AB (2012) Prediction of expansive soil swelling based on four micro-scale properties. Bull Eng Geol Environ 71(1):71–78

26. Sudjianto AT, Cakrawala M, Aditya C (2012) The effects of water contents on free swelling of expansive soil. Int J Civ Environ Eng 12:13–17
27. Basma AA, Al-Homoud AS, Malkawi AI, Al-Bashabsheh MA (1996) Swelling-shrinkage behavior of natural expansive clays. Appl Clay Sci 11(2–4):211–227
28. Puppala AJ, Manosuthikij T, Chittoori BC (2004) Swell and shrinkage strain prediction models for expansive clays. Eng Geol 168:1–8

Computational Modeling of Wind Flow in an Urban Environment: A Case Study Navi Mumbai

Vigneshwaran Rajendran and J. Sivasubramanian

1 Introduction

Construction of high-rise buildings in cities fascinated the mankind due to the demand in land areas with the city limits. Advancement of lightweight material and composite method of construction have made it possible for constructing tall buildings. But tall buildings are mostly subjected to lateral loads such as wind and earthquake driven by nature. Various factors affecting the building on wind interaction are topography, internal pressure, aerodynamic pressure, and building height and its form. The analysis of wind flow behavior in an urban environment is necessary to study about the pedestrian level wind comfort to check the natural ventilation and to find the formation of the vortex. Ventilation is very much important in order to remove the pollution in an urban environment, which mainly depends on building packing and arrangement. Ventilation is used to measure the cities breathability. The computational fluid dynamics (CFD) simulations [1] for pedestrian wind comfort and wind safety in an urban area of Eindhoven University campus. The study is performed using $k–\varepsilon$ turbulence models available in Reynolds Average Navier Stoke equations (RANS). The CFD results are compared with onsite wind speed measurement for short and long durations. The researcher [2] studied a numerical analysis on the existence of venturi effect in passage between perpendicular buildings. The pedestrian wind comfort around a large football stadium in an urban environment [3]. The researcher [4] studied the wind flow around the VIT campus, Chennai using CFD.

V. Rajendran (✉)
Department of Civil Engineering, Amrita College of Engineering and Technology, Nagercoil, Tamil Nadu, India
e-mail: vignesh.rajen.93@gmail.com

J. Sivasubramanian
Department of Civil Engineering, Mepco Schlenk Engineering College, Sivakasi, Tamil Nadu, India

Further, the influence of terrain [5] and the wind flow around the building structure is also investigated by the author [6]. The investigation of wind flow around a single isolated building of different shapes, such as pentagon, Y is carried by the author [7, 8]. The investigation of the aerodynamic coefficients such as drag and lift is carried out for the building shapes pentagon, L, T, and C [9]. But in most of the scenarios, the buildings are clustered together, and the interference effects on two tall buildings are studied by the author [10]. Typically, tall buildings are provided with setbacks in order to minimize the drag and lift forces, and the study is carried out by the author [11].

The investigations such as pedestrian level wind comfort around the tall building are studied. This paper deals with the wind flow behavior of wind flow in a fast-developing urban area of sector 44A Navi Mumbai at various wind angles such as 0°, 90°, 180°, 270°, and comfort study is checked based on comfort criteria established by Penwarden and Wise for a selected area and the arrangement of sections are as follows: Sect. 1 gives a detailed introduction and report on the previous research about the study area. Section 2 gives the description about the location of site, area coverage, and common features presented in the site. Section 3 gives details of modeling, domain size, and meshing. Section 4 deals with the inlet condition. Section 5 deals with the assessment of wind comfort criteria. Section 6 presents the results and discussion of the static pressure, pressure coefficient, check for the comfort criteria as per Penwarden and Wise.

2 Description of the Site: Sector 44A Navi Mumbai

The selected area for study is Sector 44A Sea woods, Navi Mumbai located in the state of Maharashtra, India, which is elevated at 3.5276 m above the ground level. It is one of the fastest developing urban environment in the world. Figure 1a shows the satellite image of Navi Mumbai, and the red line in the figure indicates the border of the case study area. The total land coverage is about 54,042 m^2. 90% of the buildings in this area are of residential, and 10% are of commercial building. Building in

Fig. 1 shows the location (**a**) satellite view of sector 44 Navi Mumbai, red line indicates the border of the case study area (**b**), and (**c**) shows the street view taken from Ram bhau Sudama Bhoir Marg, Sector 44 Navi Mumbai (Photo Courtesy: R. Vigneshwaran)

Fig. 2 Solid works building model of sector 44A of Navi Mumbai

this area height varies from 20 to 60 m. The road width in this area is about 10 m. Figure 1b, c shows the street view pictures taken from Ram bhau Sundama Bhoir Marg, Sector 44A, Navi Mumbai.

3 Modeling

3.1 Solid Work Modeling

Modeling of the entire urban area is carried out using solid work software. With the help of earth google Website, the data are collected for each building plan, height, and distance. The models are sketched in the form of 3D. In total, there are 51 building located in the above area and numbered from 1 to 51. Further indication in this paper is done with this building numbering. Since the site has very a smaller number of trees so of short height modeling of trees are exempted. Figure 2 shows the modeling of the entire urban area with the help of solid work. Table 1 shows the various buildings with height.

3.2 Computational Domain

The size of the domain should not disturb the flow simulation. The domain should be good enough to generate vortex on the leeward side to avoid backflow of wind. The domain size is fixed based on the recommendation of [12]. The domain size is 5H at inlet, two side faces and top clearance, and 15H for the outlet. Figure 3a, b shows the plan and elevation view of the computational domain. No-slip wall is considered at building faces and bottom. The free slip wall is considered and applied for the top and bottom sides of the wall in the domain.

Table 1 Indicate the various building with height in meters

Building number	Average building height (m)
1, 2	30
3, 4	36
17, 23	16
18, 45, 46, 48	20
19, 25	24
22	70
27, 35, 38	15
28, 29, 30, 31, 32, 33, 34, 36, 37, 39, 40, 42, 43, 44	14
41, 50	26
47, 49	18
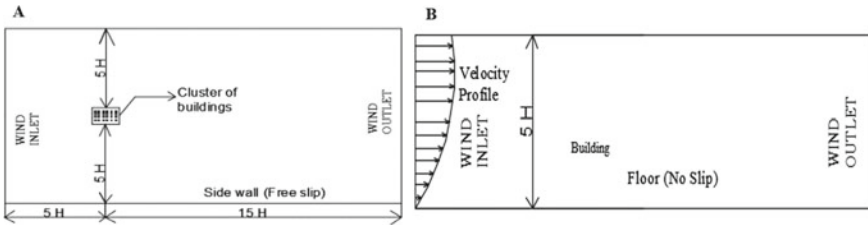
Fig. 3 Computational domain: **a** plan view, **b** elevation view

3.3 Meshing and Computational Domain Size

Meshing plays a major role in CFD analysis. The accuracy of the result depends on the meshing pattern around the building. The meshing of the domain is done with tetrahedral elements and made fine so as to have accurate wind parameters. In total, 43,297 elements and 8478 nodes were generated for the current study. Figure 4 shows the mesh refinement using ANSYS Fluent 19.2. The meshing is calculated form the Eq. (1).

$$y+ = \frac{yu*}{v} \tag{1}$$

where $y+$ is a non-dimensional number, $u*$ is shear friction velocity, y is the distance of the first grid point from the wall, v is the kinematic viscosity.
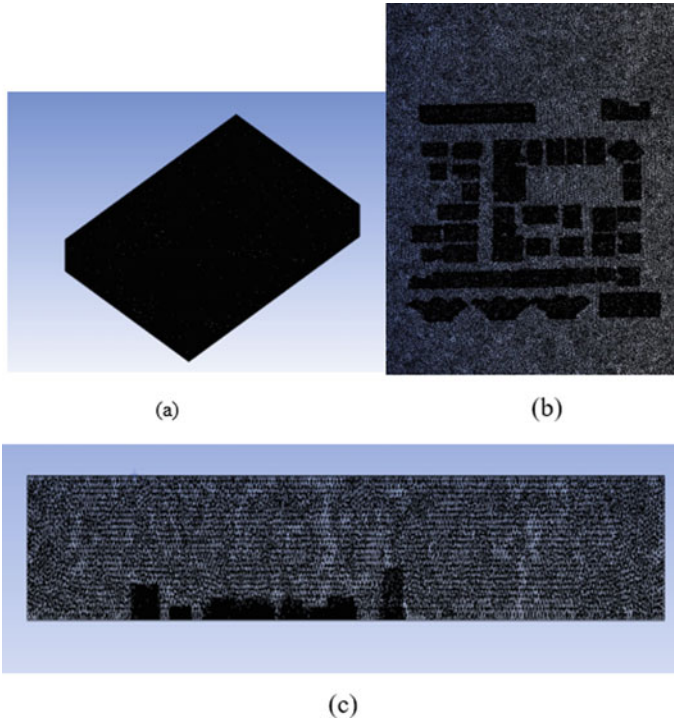
Fig. 4 Mesh refinements using ANSYS fluent. **a** Computational domain, **b** plan view of mesh, **c** front view of the domain

4 Inlet Boundary Conditions

A wind rose diagram gives the information about the wind speed and direction, typically distributed at a location at 10 m height. The velocity at the inlet for the sector 44A Navi Mumbai was fitted to a log law, and the turbulent kinetic energy k, and its dissipation rate ε, follows the usual formulation for neutral conditions. These profiles are generally simplified by assuming a constant shear stress with height.

$$U = \frac{u_\tau}{\kappa} \ln\left(\frac{z + z_0}{z_0}\right) \tag{2}$$

$$K = \frac{u_\tau^2}{\sqrt{C_\mu}} \tag{3}$$

$$\varepsilon = \frac{u_\tau^3}{\kappa\,(z + z_0)} \tag{4}$$

Table 2 Comparison of surface pressure coefficient with numerical and codal provision

Wind loading code	Face A	Face B	Face C	Face D
ANSYS fluent	0.9	−0.2	−0.86	−0.85
IS:875 (Part 3) 2015	0.8	−0.25	−0.8	−0.8

u_τ is the friction velocity, z is the vertical displacement, z_0 is the aerodynamic roughness length, κ is the von Karman constant of value 0.412, C_μ is a model constant set as 0.09.

5 Validation of CFD

Before starting the CFD analysis using ANSYS Fluent [13], validation is done for a square building and compared with various wind engineering codes. Validation is done for a square shape building of size 50 × 50 mm and a height 300 mm. It is analyzed using k–ε model in ANSYS Fluent 19.2 under uniform flow of velocity 10 m/s at the inlet. Table 2 shows the comparison of the surface pressure coefficient with numerical and codal provision.

From the result, it is observed that the ANSYS package is approximately close to the face average value of the coefficient of pressure mentioned in IS:875 (Part 3) 2015. The other code is different due to the different flow conditions.

6 Results and Discussion

In general, building usually undergoes high-wind speed at bottom level as of building height significantly taller than the surrounding. When high-wind speed passed through the opening between high-pressure and low-pressure air on windward and leeward side of the building leads to pedestrian level wind.

6.1 Wind Pressure Distribution

Simulation is carried out for sector 44A at Navi Mumbai to check the pedestrian level comfort on roads in that area. For reference purpose, these streets are numbered from 1 to 5. Table 3 shows the street name and numbers, which are used for further indication of CFD results. CFD results show a comparison between the wind in an urban area for four different wind directions such as 0°, 90°, 180°, 270°. Figure 5 shows the CFD results for of pressure around the building at different wind angle.

Table 3 Street number with present street name

Street number	Street name
1	Palm beach road (service road)
2	Ram Bhau Sudama Bhoir Marg
3	Residential main road
4	Residential park road
5	Residential road
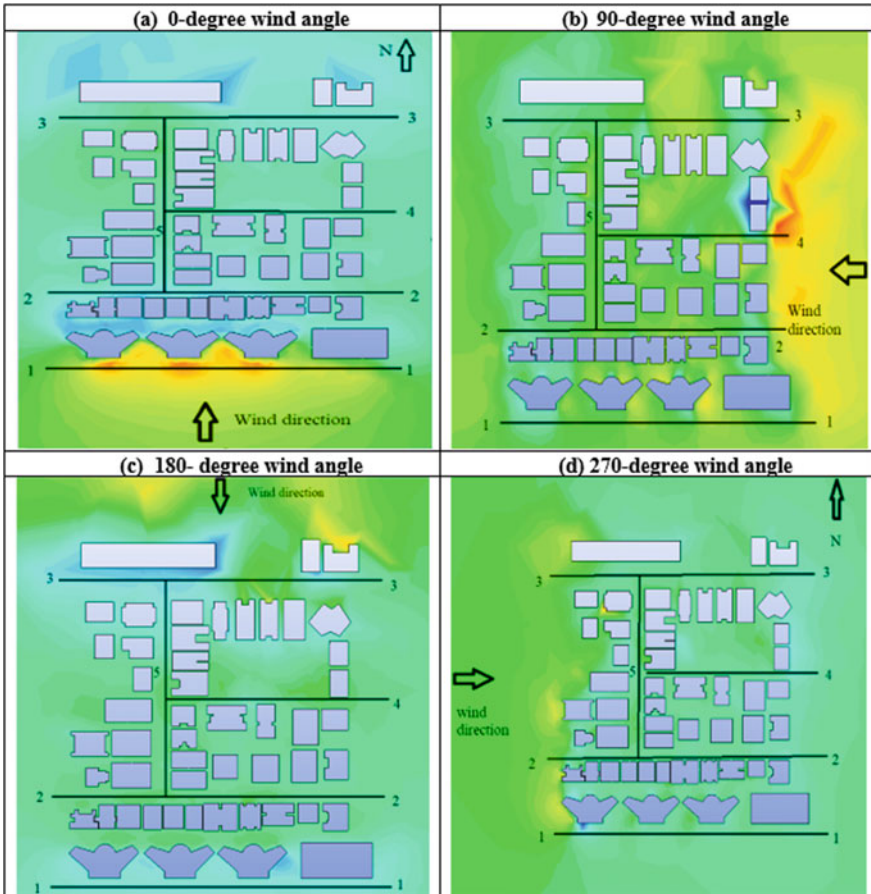
Fig. 5 Comparison of the pressure distribution around the building at different wind angles. **a** 0° wind angle, **b** 90° wind angle, **c** 180° wind angle, **d** 270° wind angle

From the post-processing of CFD results, graphs are plotted to compare the pressure distribution on various street at pedestrian level.

For 0° wind angle as shown in Fig. 5a, pressure distribution on various streets such as 1, 2, 3, 4, and 5 is indicated. High pressure is formed in the street 1 due to 0° wind directions, and wake regions are formed. In street 2 due to the presence of tall building in street 1, street 3 experienced low pressure at the beginning and ends with wake regions. Wake regions are formed because of low velocity and turbulent flow in downstream of the body. Street 4 experienced uniform low pressure. Street 5 experienced uniform wind pressure at the north face and at the junction of street 2 and 5, a wake is observed, i.e., very low pressure. Figure 5a shows the graph of pressure distribution on various streets such as 1, 2, 3, 4, and 5 for 0° wind angle. For 90° wind angle, wind pressure at the end of street 1, 2, 3, 4 experienced high-wind pressure and remaining portion of the street 5 experiences uniform wind pressure. Figure 5b shows the pressure distribution for 90° wind angle. No major wakes are created in the street for 90° wind angle. Figure 5b shows the pressure distribution for 90° wind angle. Figure 5c shows the pressure distribution for 180° wind angle. At this wind angle, the formation of wakes is large on the street because of the building 22 of height 70 m, and there is a formation of larger wake in street 3. Street 1 experiences very large wake because of the building 1, 2, 3, 4 and the remaining street 2, 4, and 5 experiences normal pressure. At the junction of street 5 and 3 experiences very low pressure. Figure 5c shows the graph for 180° wind angle. For 270° wind angle, similar pressure as 90° wind angle has been experienced. Street 5 and 3 experience varying pressure from high to low, street 1 experiences very low pressure. Street 2 and 4 experience similar pressure distribution. Figure 5d shows the pressure distribution for 270° wind angle. Figure 5d shows the graph of pressure distribution for 270° wind angle. Pressure coefficient on various faces of the building is displayed in Fig. 5.

From Fig. 6a, it is observed that for 0° wind angle, street 1 experiences large external pressure, and street 2 experiences full negative pressure. Street 3 experiences a change of negative pressure to positive pressure. Street 4 experiences positive uniform pressure. In street 5, there is a decrease in external pressure. From Fig. 6b, for a 90° wind angle, it is observed that street 1, 2, 3, 4, 5 experience change positive and negative wind pressure. From Fig. 6c for the 180° wind angle, it is observed that street 1 experiences a full negative pressure, street 2 experiences a negative to positive pressure, street 5 experiences positive to negative pressure. From Fig. 6d observed that street 1–5 experience a change of negative pressure to positive pressure.

6.2　Wind Speed and Pedestrian Discomfort

Penwarden and Wise established a comfort criterion based on the observation made on wind effect on people. The observation is taken from approximately 2 m above the ground and average over 10 min to 1 h. *V* denotes the mean wind speed measured at approximately 2 m above the ground. From the results, it is observed that buildings located in this region are subjected to various types of actions. Each face of the
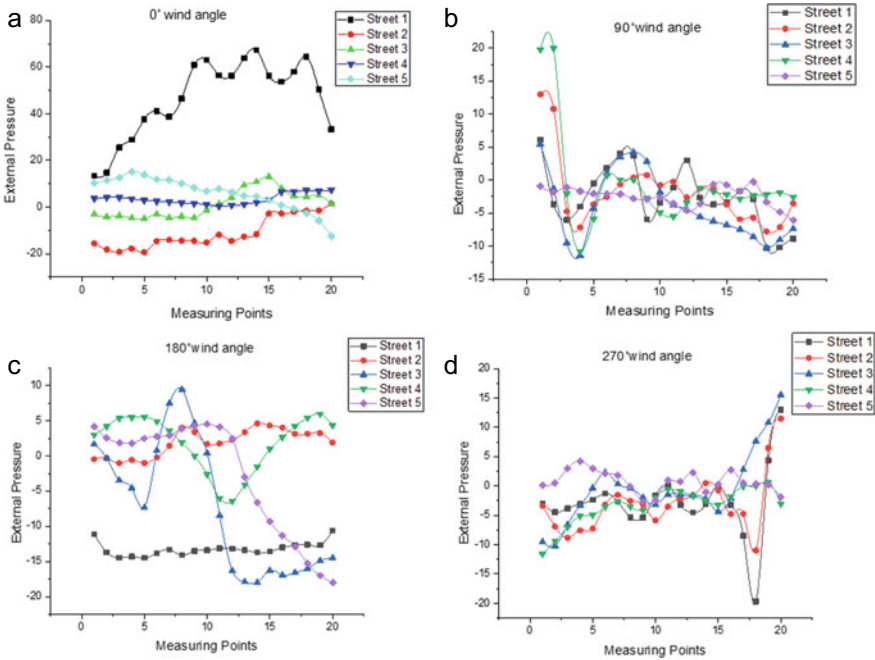
Fig. 6 C_{pe} for wind angle: **a** 0°, **b** 90°, **c** 180°, and **d** 270°

building is identified by different color which indicates the type of action. On face B, building 1 at 0° wind angle experiences an unpleasant condition. Building 2 experiences unpleasant condition for the face C, at a wind angle at 90° and 270°, similarly on face A for 90°, wind angle experiences an unpleasant condition. Building 3 on face A with 90° wind angle creates discomfort to the occupants and at face C, with a wind angle 90° and 270° experiences unpleasant condition with the occupancy. Building 4 experiences discomfort on face A at 90° wind angle and on face B, at 270° wind angle. Building 4 also experiences unpleasant condition for the faces A at 270° and at face C at 90° and 270°. Building 6 experiences only discomfort of the occupancy at 0° wind angle at face B. Building 7 experiences discomfort of the occupancy at 90° wind angle on face A and unpleasant condition on the face D at 0° wind angle. Building 8 and 9 experience unpleasant condition at face A at 90° and 270°. Building 10 and 11 experience occupancy discomfort on face A at 90° wind angle. Similarly, building 12, 13, and 14 experience occupancy discomfort on the face A at 270° wind angle. But for building 15, at face A experiences dangerous wind velocity at 270° wind angle and at 90° on the same face experience occupancy discomfort. For building 22 at on face D at 180°, wind angle building experiences occupancy discomfort. Building 23 experiences occupancy discomfort at 270° wind angle. For building 26, at an wind angle 90° and 270°, building experiences occupancy discomfort. For building 35 and 36 occupancy inside the building experiences unpleasant condition for the faces D at 180° wind angle. For the building 39 and 41

at 90˚ wind angle on face, building experiences unpleasant condition. For building 42 on face C at 90˚, wind angle experiences occupancy discomfort and at angle of 90˚ on face D experiences discomfort for occupancy. For wind angle at 90˚ on face C of the building 43 experiences occupancy discomfort. For building 5, 16, 17, 18, 19, 20, 21, 22, 24, 25, 27, 28, 29, 30, 31, 32, 33, 34, 37, 38, 40, 44, 45, 46, 47, 48, 49, 50, 51 are the building within the comfortable criteria on all the faces at various wind direction. The location at which the velocity reaches zero is the point flow separation which creates reverse flow on the surface of the body. Depending on the type of body shape, flow separation will differ.

6.3 Wake Regions

In bluff body such as buildings, the formations are wakes, i.e., separated region which are usually large because of large angle of attack. The wake depends on Reynolds Number, surface roughness, and turbulence. When the building is in the downstream side of the large structure, there is a formation of large wake and an isolated building undergo wake due to upwind force. For the case 1, i.e., for 0˚ wind angle, large wake regions are created behind the building 2, 3, 4 because of the building height 36 m, and less wake is observed behind the building 1 because of building height 30. Building presents between 5 and 15 wake regions are formed around the building. Since these buildings located in the downstream side of the large structure and the formation of wake is observed around the building. Same manner wake regions are created behind building 22, 39, 40. Size of the wake formations depends upon the breadth to height ratio of the building and velocity of the wind. For the case 2, i.e., for 90˚ wind angle, wake regions are created behind the building 42 and 43 because of less setback limit of the two buildings. Less wake is absorbed in the regions of building 4, 14, 15, 26, 16, 25, 17, 18, 19, 20, 23, 24, 21, and 22. For the case 3, i.e., for 180˚ wind angle, wake regions are created behind building 22, since the building is at a height of about 70 m, there is a formation of large and small wakes behind the building 39, 40, 35, 36, 37, 38, and 41 and large wake are absorbed in 4, 3, 2, and 1. For the case 4, i.e., for 270˚ wind angle, small wake regions are observed behind the building 31, 32, 43, 42, and 4. When the buildings natural frequency is close to the frequency of the wake turbulence, the building experiences a large resonance as well as motion. Figure 7 shows the identification of the wake regions for 0˚, 90˚, 180˚, 270˚ wind angle. When wind falls on a building, wind streams are diverged, and wind speed is reduced. The process will lead to rest of wind to flow upwards and sideways. Streep pressure is increased in edge where the flow diverges and is unable to join because of inertia. The region of recirculating disturbed flow, i.e., wake regions is formed in the leeward side. The building presented in the wake regions will lead to occupancy discomfort because of undisturbed flow creating suction (Fig. 7).
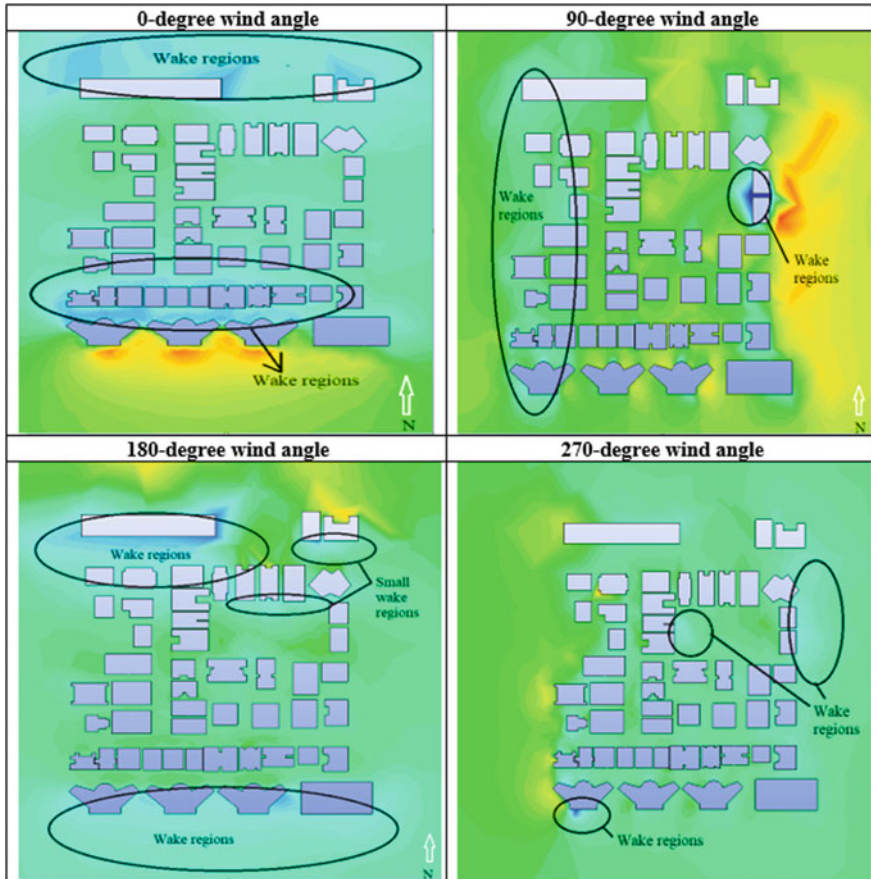
Fig. 7 Identification of wake regions at various wind directions

7   Conclusions

This paper presents a simulation for the evaluation of pedestrian wind comfort and safety in an urban area. From the selected area of sector 44A Navi Mumbai, the following results such as pressure and velocity distribution at pedestrian level were studied. Identification of wake regions, checking the comfort criteria as per the previous researcher were evaluated for the selected region.

- From the result of occupancy discomfort building number 15 on face A at 270° wind angle experiences high level of dangerous discomfort to the occupancy. Building number 1–15, 22, 35, 36, 39, and 41 experience unpleasant condition for the occupancy inside the building. Building number 3–7, 23, 26, 42, and 43 experience the condition of discomfort.

- Wake regions are studied for different wind angles, large wakes are observed in 0°
  and 180° wind angles, and for 90° and 270° wind angle, it experiences less wake.
  Upcoming new building in this area should not fall under this wake regions.
- In case of township project, low-rise building is surrounded by high-rise building,
  this type wind flow analysis is useful to study the pedestrian level occupancy
  comfort, wind flow behavior, pollution dispersion, etc.
- Future infrastructure development for the studied area can be made with the help
  of above result and the regions of wake formation can be avoided.

References

1. Blocken B, Janssen WD, Van Hooff T (2012) CFD simulation for pedestrian wind comfort
   and wind safety in urban areas: general decision framework and case study for the Eindhoven
   University campus. Environ Model Softw 30:15–34
2. Blocken B, Moonen P, Stathopoulos T, Carmeliet J (2008) Numerical study on the existence
   of the venturi effect in passages between perpendicular buildings. J Eng Mech 134:1021–1028
3. Blocken B, Persoon J (2009) Pedestrian wind comfort around a large football stadium in an
   urban environment: CFD simulation, validation and application of the new dutch wind nuisance
   standard. J Wind Eng Ind Aerodyn 97:255–270
4. Prabhaharan SA, Rajasekarababu KB, Vinayagamurthy G, Sivakumar R (2021) CFD simulation
   for pedestrian comfort and wind safety in VIT campus for wind resource management. In: IOP
   conference series: materials science and engineering, vol 1128, 1, IOP Publishing, p 012002
5. Rajasekarababu KB, Vinayagamurthy G (2020) CFD validation of wind pressure distribution on
   a tall building under the influence of upstream terrain. Prog Comput Fluid Dyn Int J 20(5):284–
   298
6. Rajasekarababu KB, Vinayagamurthy G (2019) Computational simulation of wind flow
   behavior around a building structure. In: Chandrasekhar U, Yang LJ, Gowthaman S (eds) Inno-
   vative design, analysis and development practices in aerospace and automotive engineering
   (I-DAD 2018). Lecture notes in mechanical engineering, Springer, Singapore
7. Prabavathy S, Vigneshwaran R (2021) Study of wind flow around pentagon plan shape tall
   building using CFD. J Phys: Conf Ser 1850
8. Vigneshwaran R, Prabavathy S (2022) Investigations of aerodynamic coefficient for wind flow
   around Y-plan shape tall building. Teknik Dergi 33(4):1–21
9. Rajendran V, Prabavathy, (2021) Experimental investigation on aerodynamic characteristics
   for 3D bluff bodies: pentagon, T, C and L-shape buildings. Tech Gaz 28(6):2036–2044
10. Vigneshwaran R, Prabavathy, S Interference effect study on wind pressure distribution in build-
    ings using computational fluid dynamics. In: chapter 10, recent trends in thermal engineering,
    Springer
11. Vigneshwaran R, Prabavathy S (2022) Investigation of wind loads on setback building using
    computational fluid dynamics. In: Pal I, Kolathayar S (eds) sustainable cities and resilience.
    Lecture notes in civil engineering, vol 183. Springer, Singapore

12. Franke J, Hirsch C, Jensen AG (2004) Recommendations on the use of CFD in wind engineering. In: Proceedings of international conference on urban wind engineering and building aerodynamics: COST C14: impact of wind and storm on city life and built environment, Rhode-saint-Genese, Belgium
13. ANSYS In (2019) ANSYS Fluent 19.2 user's guide

Time–Frequency Analysis of Strong Ground Motions from the 2011 Sikkim Earthquake

Shalin Mathew, Mohammed Ayub Ifan, Jayaprakash Vemuri, and K. V. L. Subramaniam

1 Introduction

The state of Sikkim in India lies in the Himalayan region and is bordered on three sides by Bhutan, Tibet, and Nepal. According to the Indian seismic zoning, Sikkim lies in the high-risk zone IV. Sikkim lies along the tectonic plate boundary where the Indian and the Eurasian plate are under collision. The Main Boundary Thrust (MBT) and Main Central Thrust (MCT) are the two major thrust faults passing through the state as shown in Fig. 1a. The region has recorded seismic activity in the past, and the distribution and damage pattern in the 2011 earthquake demonstrate attenuation features of the area [1–11] between the Main Boundary Thrust (MBT) and the Main Central Thrust (MCT). On 18th September 2011, Sikkim was struck by a Mw 6.9 earthquake which caused enormous structural damage to the built environment in the region. The earthquake exposing several structural defects and also highlighted the role of construction malpractices associated with non-engineered construction in the region. This paper analyses the ground motions of the 2011 Sikkim earthquake and describes the observed structural damage caused due to the severe ground shaking associated with this earthquake. Time–frequency analyses are performed on strong ground motion data recorded at six stations (Chungthang, Gangtok, Gezing, Melli, Mangan, and Singtam) as shown in Fig. 1b.

S. Mathew (✉) · M. A. Ifan · J. Vemuri
Ecole Centrale School of Engineering, Mahindra University, Hyderabad, Telangana 500043, India
e-mail: shalin170134@mechyd.ac.in

K. V. L. Subramaniam
Department of Civil Engineering, IIT Hyderabad, Hyderabad, Telangana 502285, India
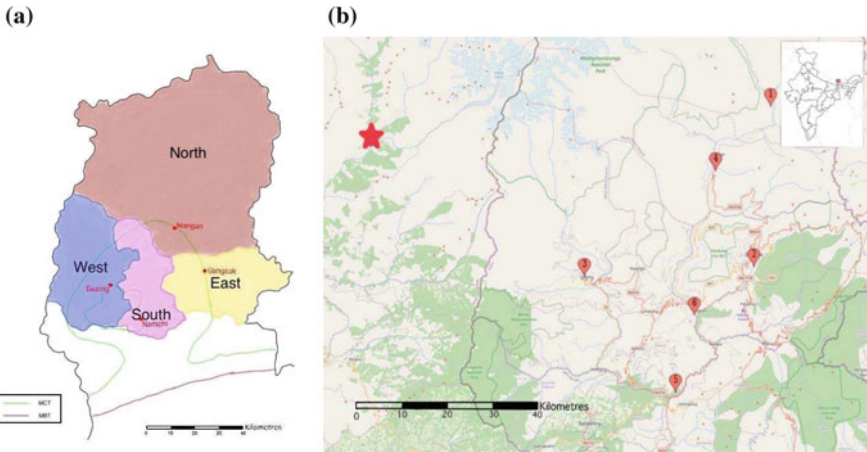
Fig. 1 **a** Location of MCT and MBT on the map of Sikkim, **b** Earthquake epicentre and recording stations. (1) Chungthang, (2) Gangtok, (3) Gezing, (4) Mangan, (5) Melli, (6) Singtam, *Epicentre

2 Observed Damage to Buildings

Several reconnaissance surveys by various researchers [12–16] were undertaken in the aftermath of the earthquake to assess structural damage. The surveys recorded the observed damage to the variety of structures prevalent in Sikkim. It was observed that damage was severe due to the non-engineered structures prevalent in the region (RC, unreinforced masonry (URM), and bamboo structures). In some towns, structural damage in engineered buildings was observed but was concentrated in low-rise buildings and the lower storeys of taller buildings. Table 1 describes the details of the wide variety in the observed structural damage due to the earthquake, as recorded in six towns of Sikkim from where strong ground motions are also available. Based on the severe damage observed in the town of Mangan, a damage intensity level of VIII+ (MMI scale) has been assigned [17]. Similarly, based on the high damage to structures in the towns of Chungthang, Gangtok, Mangan, and Singtam, the four towns were assigned a damage intensity level of VIII [17].

3 Features of Recorded Accelerograms

Table 2 shows the important characteristics of the seismic waves, namely peak ground acceleration (PGA), peak ground velocity (PGV), arias intensity (AI), mean period (T_m), and predominant time (T_p). The maximum PGA of 0.45 g was recorded at Gezing town (in the radial direction): the town was closest to the epicentre, at 50 km. The next highest PGA value of 0.39 g (in the radial direction) was recorded at Mangan town: the town is also situated at an epicentral distance of 50 km. Despite the distance

Table 1 Observed damage to buildings

S. No.	Station	Building material	Building use	Type of damage	References
1	Chungthang	Concrete	Residential, 1 storey	Damage to building due to a rolling boulder from landslides	[12]
2	Chungthang	RC framed	Storage facility building	Stiffness pattern was changed of various infill panel walls	[12]
3	Chungthang	Masonry	Chungthang Monastery, 1 storey	RRM masonry walls were damaged by collapsed by out-of-plane in corners of perimeter of the walls	[12]
4	Chungthang	RC framed	Communication structure on a 4	Damage observed in the lower storey of the building	[12]
5	Gangtok	Bamboo, mud, cement, stones	Residential, 2 storeys	Failure of load-bearing walls due to the poor transfer of earthquake inertial force	[14]
6	Gangtok	Bamboo, mud, cement, stones	Residential, 2 storeys	Shaking causing uneven settlement of the filled earth at the foundation of the house leading to tilting	[14]
7	Gangtok	Bamboo, mud, cement, stones	Residential, 2 storeys	Structures without any reinforcement or buttresses were damaged	[14]
8	Gangtok	Wooden frame, bamboo reeds, mud plaster	Residential, 1 storey	Damaged rubble masonry	[12]
9	Gangtok	RC framed	Police HQ, 3 storeys	RC elements and URM masonry infills damaged	[12]

Table 1 (continued)

S. No.	Station	Building material	Building use	Type of damage	References
10	Gangtok	Undressed stones with mud, lime-based mortar	Enchey monastery,2 storeys	Damage in the upper storey, cracks below the windowsill, local spalling, and crushing of masonry pier	[12]
11	Gangtok	RC building with masonry infills	Rey Mindu monastery, 2 storeys	Exterior and interior brick masonry walls underwent severe cracking	[16]
12	Gangtok	RC building with masonry infills	Ranka lingdum monastery, 3 storeys	One RC column in the first storey of the new building suffered severe damage	[16]
13	Gangtok	RC framed	Serney school, 3 storeys	A portion of the first storey collapsed due to the absence of tie beams at the bottom of first storey columns	[16]
14	Mangan	Masonry	Ringin monastery, 2 storeys	Rubble masonry walls were found to have out-of-plane bulging and collapse	[12]
15	Mangan	Wooden frame, bamboo reeds, mud plaster	Residential, 1 storey	Undergone 15 cm of southward shift at the base	[15]
16	Singtam	RC framed	Residential, 3 storeys	In places of poor stiffness in the plan, structure observed torsion and collapsed	[12]
17	Singtam	RC	Commercial, residential; 4 storeys	Columns failed due to buckling in the first storey	[16]

Table 2 Characteristics of the accelerograms

S. No.	Town	Component	Distance (km)	PGA (g)	PGV (cm/s)	AI (m/s)	Tp (s)	Tm (s)
1	Chungthang	Radial	55	0.36	5.69	0.45	0.10	0.11
		Transverse		0.25	4.67	0.35	0.10	0.12
		Vertical		0.11	2.20	0.08	0.10	0.11
2	Gangtok	Radial	68	0.27	5.47	1.90	0.06	0.11
		Transverse		0.28	6.44	1.41	0.06	0.14
		Vertical		0.10	2.50	0.33	0.06	0.17
3	Gezing	Radial	50	0.43	8.42	0.76	0.12	0.12
		Transverse		0.38	5.35	0.57	0.06	0.11
		Vertical		0.18	3.98	0.17	0.08	0.12
4	Mangan	Radial	50	0.38	4.81	0.66	0.06	0.08
		Transverse		0.27	5.41	0.53	0.08	0.11
		Vertical		0.12	2.44	0.14	0.06	0.14
5	Melli	Radial	78	0.26	3.31	0.63	0.06	0.07
		Transverse		0.28	3.21	0.48	0.06	0.08
		Vertical		0.18	1.67	0.28	0.04	0.08
6	Singtam	Radial	67	0.21	4.68	1.30	0.06	0.16
		Transverse		0.10	2.66	0.38	0.08	0.14
		Vertical		0.26	6.40	1.88	0.06	0.13

being similar, the difference in peak accelerations is due to the soil properties and the propagation effects of the earthquake.

Chungthang town, situated at a distance of 55 km, experienced a PGA of 0.36 g. Gangtok and Melli which are located at distances of 68 km and 78 km, respectively, recorded the same PGA of 0.28 g. The town of Singtam, which is situated at a distance of 67 km, recorded a slightly lower horizontal PGA of 0.21 g. Velocity time series are derived from the accelerograms, after applying baseline filtering (Butterworth, Bandpass) of cut frequency 0.2–80 Hz and order 4 along with second-order baseline correction. The maximum PGV of 8.42 cm/s was observed at the Gezing station in the radial direction. PGVs (in the radial direction) for Chungthang, Gangtok, Mangan, Melli, and Singtam were 5.69 cm/s, 5.47 cm/s, 4.81 cm/s, 4.68 cm/s and 3.31 cm/s, respectively. Similarly, in the transverse direction, the maximum PGV of 6.44 cm/s was observed at Gangtok, followed by Mangan at 5.41 cm/s, Gezing at 5.35 cm/s, Chungthang at 4.67 cm/s, Melli at 3.21 cm/s, and Singtam at 2.66 cm/s.

4 Fast Fourier Transforms

Fast Fourier Transforms show the frequency content in a seismic wave. Figures 2, 3, 4, 5, 6, and 7 show the FFTs obtained for the accelerograms from the six stations. It is observed that the frequencies were primarily in the range of 0–20 Hz. The radial and transverse components are designated using the symbols, *R* and *T*, respectively.
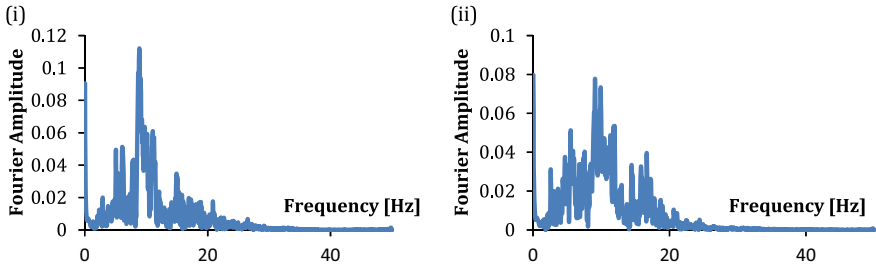
Fig. 2 FFT for Chungthang: (i) *R*, (ii) *T*
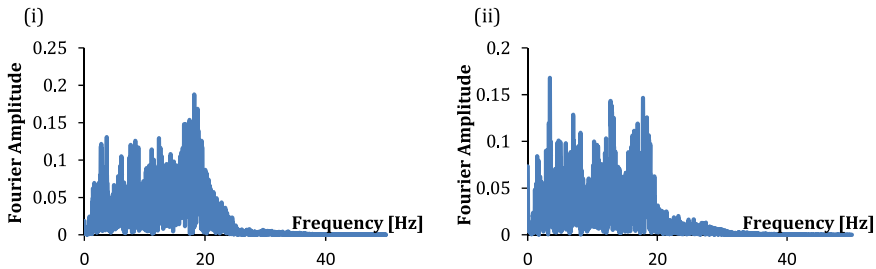
Fig. 3 FFT for Gangtok: (i) *R*, (ii) *T*
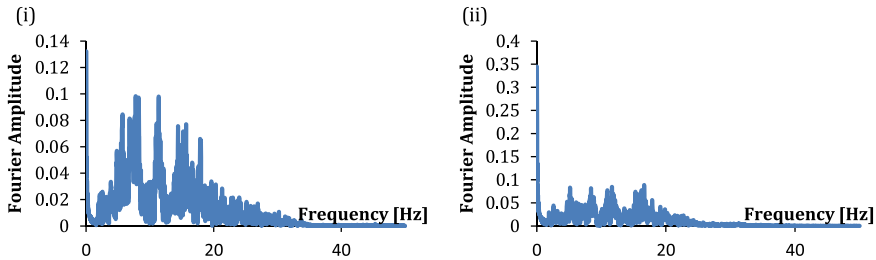
Fig. 4 FFT for Gezing: (i) *R*, (ii) *T*
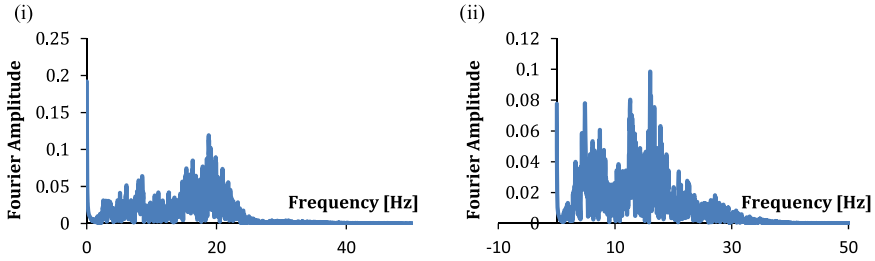
Fig. 5 FFT for Mangan: (i) *R*, (ii) *T*
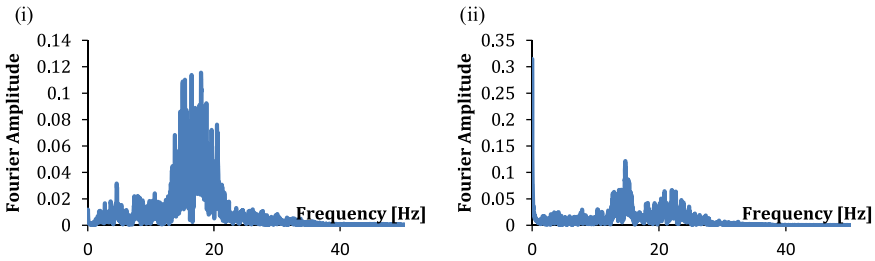
Fig. 6 FFT for Melli: (i) *R*, (ii) *T*
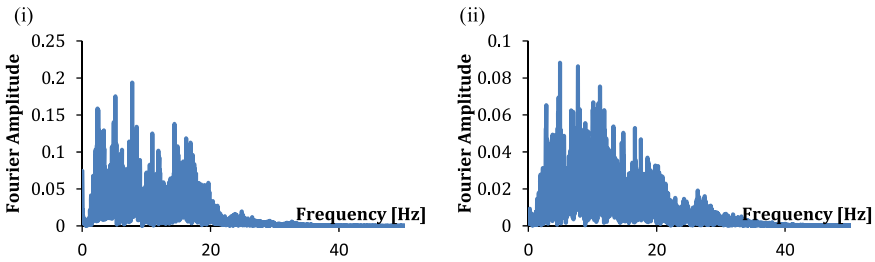
Fig. 7 FFT for Singtham: (i) *R*, (ii) *T*

5 Continuous Wavelet Transforms of Strong Ground Motions

Figures 8, 9, 10, 11, 12, and 13 (i, ii) show the CWTs for the six stations. In general, the CWT figures show the presence of high-frequency waves. In all the six towns, the high-amplitude waves contained high-frequency content of around 10 Hz, representing a low period of 0.1 s. However, in some towns, the high-amplitudes waves were observed at multiple frequency ranges. For example, the transverse record from Gezing town shows high-amplitude waves at multiple low periods, ranging from 0.04 to 0.2 s. Similarly, in the radial record from Singtam town, the high magnitude seismic waves are distributed over a low period range of 0.05–0.2 s. The damage
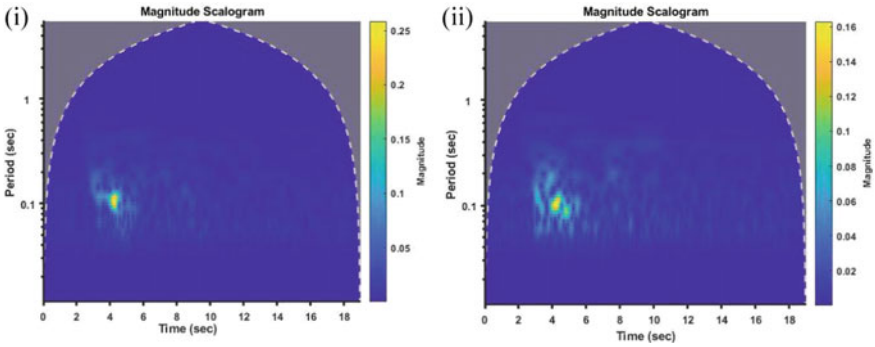
Fig. 8 CWT for Chungthang: (i) *R*, (ii) *T*
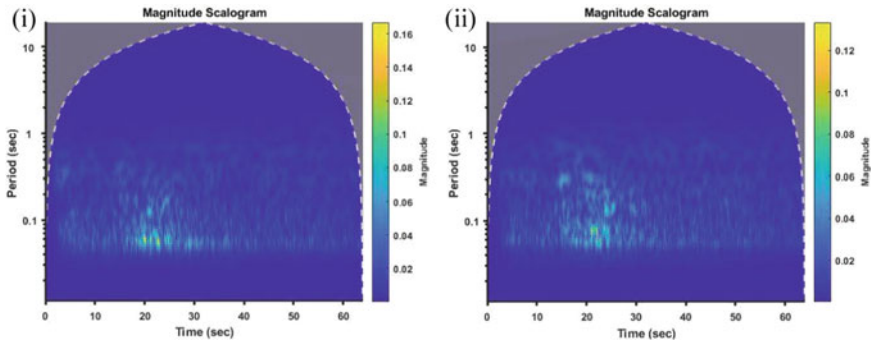
Fig. 9 CWT for Gangtok: (i) *R*, (ii) *T*
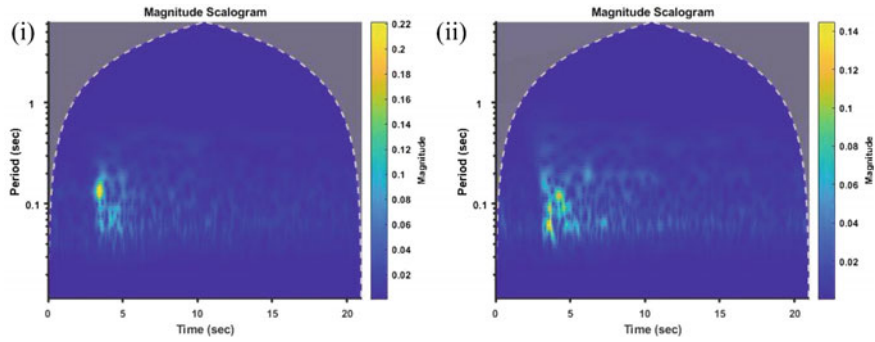
Fig. 10 CWT for Gezing: (i) *R*, (ii) *T*
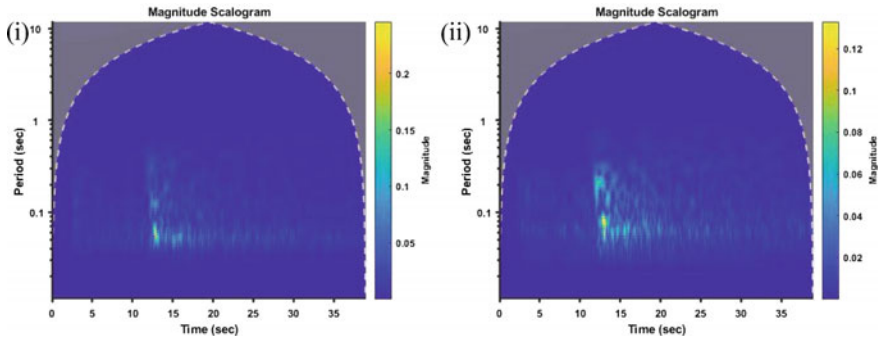
Fig. 11 CWT for Mangan: (i) *R*, (ii) *T*
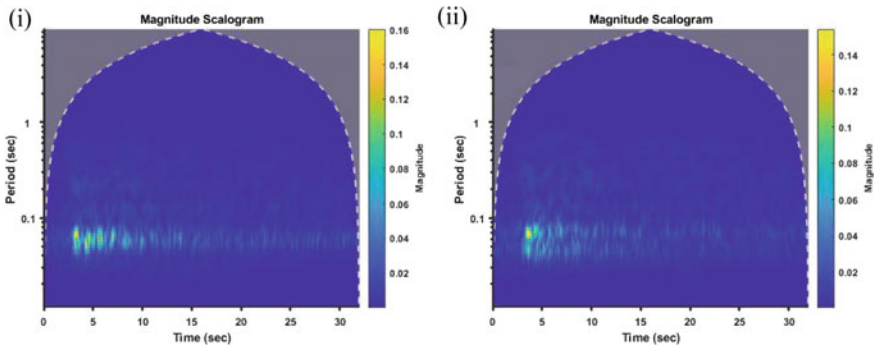
Fig. 12 CWT for Melli: (i) *R*, (ii) *T*
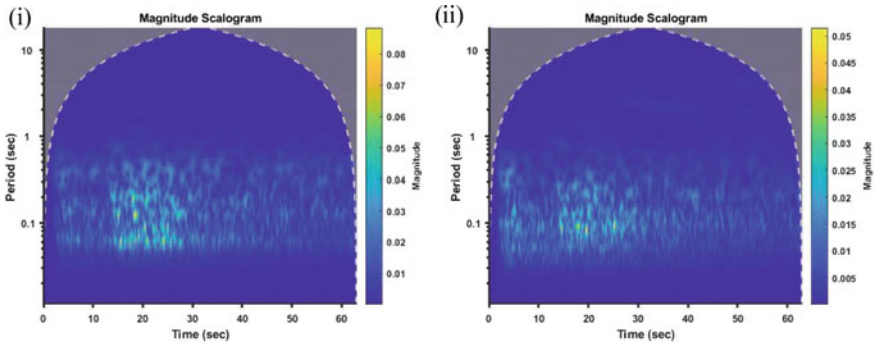
Fig. 13 CWT for Singtam: (i) *R*, (ii) *T*
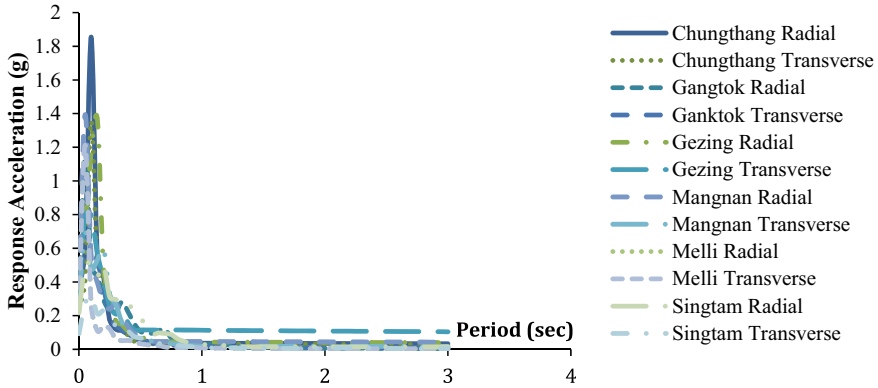
Fig. 14 Response spectra for six stations (*R* and *T* components)

due to this horizontal ground motion in Singtam town is also clearly corroborated with the observation from the reconnaissance surveys (rows 16, 17, Table 1). The CWTs of ground motions from Mangan town show high-amplitude waves having a period of 0.1–1.2 s. This is also clearly corroborated with the observed damage to 1 and 2 storey structures in Mangan town, as recorded in the reconnaissance survey (row 14–15, Table 1). Similarly, Gangtok town experienced multiple high-amplitude waves at various multiple frequencies causing damage to 1–4 storey structures (row 5–13, Table 1). In Chungthang town, the high-frequency–high-amplitude content was observed for a very short duration. Further, the response spectra as observed (Fig. 14) exhibit a peaky behaviour, corroborating the above observations. Overall, these observations indicate the high hazard to low-rise structures, prevalent in the region, which typically have low natural periods.

6   Summary and Conclusions

A massive Mw 6.9 earthquake struck the Himalayan state of Sikkim in India on 18th September 2011 causing severe damage to the built environment in several towns. In this paper, accelerograms recorded at six stations, which represent information in the time-domain, are analysed to obtain key characteristics, such as PGA, PGV, and AI of each ground motion. The response spectra of the horizontal ground motions from the six stations exhibit high peaks at very low periods and almost reduce to zero at a period of 1 sec. Fast Fourier Transforms (FFTs) of recorded ground motions from the six towns indicate that the frequency content mostly lay in the range of 0–20 Hz. The analysis of Continuous Wavelet Transforms (CWTs) correlates well with the observed damage to low-rise structures recorded in various reconnaissance surveys. It is observed that CWTs convey improved information about the destructive

nature of earthquake waves as compared to the time domain or frequency domain representations.

References

1. Baruah S, Bramha A, Sharma S, Baruah S. (2019) Strong ground motion parameters of the 18 September 2011 Sikkim earthquake MW = 6.9 and its analysis: a recent seismic hazard scenario. Nat Haz 97(3):1001–1023

2. Chopra S, Sharma J, Sutar A, Bansal BK (2014) Estimation of source parameters of Mw 6.9 Sikkim earthquake and modeling of ground motions to determine causative fault. Pure Appl Geophys 171(7):1311–1328

3. Dutta SC, Mukhopadhyay PS, Saha R, Nayak S (2015) 2011 Sikkim earthquake at eastern himalayas: lessons learnt from performance of structures. Soil Dyn Earthq Eng 75:121–129

4. Gahalaut VK (2011) M 6.9 September 18, 2011, Sikkim earthquake. Geomat Nat Haz Risk 2(4):325–328

5. Joshi A, Kumari P, Singh S, Sharma ML (2012) Near-field and far-field simulation of accelerograms of Sikkim earthquake of September 18, 2011 using modified semi-empirical approach. Nat Haz 64(2):1029–1054

6. Kumar MR, Hazarika P, Prasad GS, Singh A, Saha S (2012) Tectonic implications of the September 2011 Sikkim earthquake and its aftershocks. Curr Sci 788–792

7. Mahajan AK, Gupta V, Thakur VC (2012) Macroseismic field observations of 18 September 2011 Sikkim earthquake. Nat Haz 63(2):589–603

8. Raghukanth STG, Lakshmi Kumari K, Kavitha B (2012) Estimation of ground motion during the 18th September 2011 Sikkim earthquake. Geomat Nat Haz Risk 3(1):9–34

9. Rajendran K, Rajendran CP, Thulasiraman N, Andrews R, Sherpa N (2011) The 18 September 2011, North Sikkim earthquake. Curr Sci 1475–1479

10. Sharma ML, Sinvhal A, Singh Y, Maheshwari BK (2013) Damage survey report for Sikkim earthquake of 18 September 2011. Seismol Res Lett 84(1):49–56

11. Symans MD, Constantinou MC (1999) Semiactive control systems for seismic protection of structures: state-of-the-art review. Eng Struct 21:469–487

12. Murty CVR, Raghukanth STG, Menon A, Goswami R, Vijayanarayanan AR, Gandhi SR, Singhal V (2012) The Mw 6.9 Sikkim-Nepal border earthquake of September 18, 2011. EERI Newslett EERI Spec Earthq Rep 1–14

13. Rai DC, Mondal G, Singhal V, Parool N, Pradhan T, Mitra K (2012) Reconnaissance report of the M6. 9 Sikkim (India–Nepal border) earthquake of 18 September 2011. Geomat Nat Haz Risk 3(2):99–111

14. Tambe S, Kumar R, Arrawatia ML, Ganeriwala AK (2012) How safe are our rural structures? Lessons from the 2011 Sikkim earthquake. Curr Sci 1392–1397

15. Thakur VC, Mahajan AK, Gupta V (2012) Seismotectonics of 18 September 2011 Sikkim earthquake: a component of transcurrent deformation in eastern Himalaya. Himalayan Geol 33(1):89–96

16. Kaushik HB, Dasgupta K (2013) Assessment of seismic vulnerability of structures in Sikkim, India, based on damage observation during two recent earthquakes. J Perform Constr Facil 27(6):697–720

17. Prajapati SK, Kumar A, Chopra S, Bansal, BK (2013) Intensity map of Mw 6.9 2011 Sikkim–Nepal border earthquake and its relationships with PGA: distance and magnitude. Nat Haz 69(3):1781–1801

The Effect on Concrete Strength by Partially Replacing Cement with Brick Kiln Dust and Fly Ash

Saurabh Dubey, Deepak Gupta, and Mainak Mallik

1 Introduction

In the course of production of cement, the people generally face the problem of emission of carbon-di-oxide as pollutants which become very harmful at large, both for the society and environment. The main target is to reduce the production of cement, as during 1 ton of cement production, about 1.25 tons of carbon-di-oxide are emitted which cause greenhouse effect. Apart from cement, different waste products, namely FA and BKD also cause ecological problems. It is surveyed that India is the second large producer of brick next to China [1]. During mass production of brick, wastes like brick kiln dust are dumped in open areas, which contaminate the ground water due to the presence of different chemicals present in the BKD [2]. Also, we know that for production of concrete, cement is the main element and, in this research, we have obtained the same mechanical properties concrete by using different waste materials [3]. Literature review has given a lot of knowledge about the concrete strength and also the utilization of different waste materials in the concrete production [4]. FA, a by-product of coal combustion in power plants, and BKD, a waste product of brick kilns, are both extensively utilized to improve the mechanical properties of concrete [5]. Singh investigated that addition of BKD increases the strength of cement mortar as well as the compressive strength [6]. Rather investigated that addition of BKD with rice husk ash gives the desire strength to the concrete [7]. Singh and Bharosh investigated that BKD can be utilized effectively to generate high-quality concrete with acceptable slump and setting times [8]. Many other researchers have also made observations on materials, design mix, concrete strength and curing days. In the present work, OPC 43 grade cement is used as it is easily available in

S. Dubey (✉) · D. Gupta · M. Mallik
National Institute of Technology Arunachal Pradesh, Jote, Arunachal Pradesh, India
e-mail: saurabh.phd20@nitap.ac.in

abundance, but in the future using ordinary Portland cement of 53 grade cement can be put for use for the same research work.

2 Materials Used and Their Chemical Properties

Finding chemical property of materials is an important part of concrete production. When materials are mixed with water, they form some chemical reactions and such reactions also decide the strength of concrete.

$$Portland\ cement + Water \rightarrow Calcium\ Silicate\ Hydrate$$
$$Ca(OH)_2 + CO_2 \rightarrow CaCO_3 + H_2O$$
$$Pozzolana + Ca(OH)_2 + water \rightarrow C-H-S(Glue)\ [1]$$

The reaction with Portland cement and water gives early strength to concrete materials, later on when Pozzolana is mixed with lime and water, it will affect the early strength but provides an extra amount of concrete strength due to the presence of silica in brick kiln dust [9].

2.1 OPC 43 Grade

Cement is generally a gray powdery binding material produced by calcining of lime and clay. When the material cement is mixed together with aggregate, sand and water, it forms into concrete. In confirmation of IS 8112-2013, ordinary Portland cement (OPC) 43 grade [10] stands for cement having compressive strength of 43 N/mm^2 after curing for 28 days. When one replaces the OPC partially with some Pozzolanic materials, like, the fly ash, a new type of cement gets formed, commonly known as blended cement or Portland Pozzolana cement.

The chemical components of OPC 43 grade are displayed in Table 1, as per IS 8112-2013.

2.2 Brick Kiln Dust

BKD is generally a light red colored waste product collected from the brick kiln factory. Nowadays, construction work is taking place in large scale; therefore, the requirement of brick is increased and during production, waste like brick kiln dust is obtained. Generally, it is a combination of ash (wood and coal), and dust particles consisting of (soil and sand). The presence of alkali as a component in BKD makes

Table 1 Chemical components of cement

S. No.	Ingredients	As per IS 8112-2013
1	Total loss on ignition, % by mass	Max. 5
2	Insoluble residue	Max. 4
3	SiO_2	17–25%
4	Al_2O_3	3–8%
5	Fe_2O_3	0.5–6%
6	CaO	60–67%
7	MgO % by mass	Not more than 6%
8	SO_3, % by mass	2.0–3.5%
9	Chloride content, percent by mass	Max. 0.1%
10	Lime saturation factor (LSF), $\frac{CaO-0.7SO_3}{2.8SiO_2+1.2Al_2O_3+0.65\,Fe_2O_3}$	Min. 0.66, Max. 1.02
11	Ratio of alumina/iron oxide	Min. 0.66

Note The above data is taken from [10]

Table 2 Chemical components of BKD

S. No.	Ingredients	Test result (%)
1	SiO_2	67.43
2	Loss of ignition	1.10
3	Fe_2O_3	7.99
4	Al_2O_3	1.99
5	CaO	2.12
6	MgO	2.46
7	SO_3	0.39
8	Na_2O	0.08
9	K_2O	0.25
10	Other	7.90

Note The above data is taken from [11]

the BKD as much reactive material. The components of BKD, namely silica, Iron, alumina, etc., are displayed in Table 2.

2.3 Fly Ash

As mentioned in IS 3812 (Part 1)-2013, FA is a finely waste remainder emitted by the combustion of either sub-bituminous coal or bituminous coal during the production of electricity. Due to the large production of fly ash as a waste material, they are

Table 3 Chemical properties of fly ash

S. No.	Ingredients	As per IS 3812 part (1)-2013
1	$SiO_2 + Al_2O_3 + Fe_2O_3$, percent by mass, minimum	70
2	SiO_2, present by mass, minimum	35
3	Reactive silica present by mass, minimum	20
4	MgO, present in mass, maximum	5
5	SO_3, present by mass, maximum	3
6	Available alkalis (Na_2O), present by mass, maximum	1.5
7	Total chloride present by mass, maximum	0.05
8	Loss of ignition (LOI), present by mass, maximum	5

Note The above data is taken from [12]

nowadays used in various construction projects. The chemical components of FA are displayed in Table 3, as per IS 3812 (Part 1)-2013.

2.4 Aggregates

Confirming to IS 2386 (Part 1)-1963, IS 383-1970 and IS 460-1962, the coarse aggregate is used of size 20 mm and 10 mm and the fine aggregate below the sieve size of 4.75 mm, on the basis of grading zones I, II, III and IV (passed through 4.75 mm and clutched on to 75 μ). The findings are based on the test done in the laboratory [13, 14].

3 Physical Properties of Materials used During Research

3.1 OPC 43 Grade

As per IS 8112-1989, IS 4031(Part 1)-1996 [15], IS 4031 (Part 4)-1988, IS 4031 (Part 5)-1988 [16] and IS 4031 (Part 6)-1988 [17], some tests have been performed and their data are displayed in Table 4.

3.2 Coarse Aggregate

As per IS 383-1970, IS 2386 (Part 1)-1963, IS 2386 (Part 2)-1963, IS 2386 (Part 3)-1963, IS 2386 (Part 4)-1963, IS 2386 (Part 5)-1963, IS 2386 (Part 6)-1963 and IS 460-1962, some tests have been performed and their data are displayed in Table 5.

Table 4 Physical properties of cement

S. No.	Test	As per experiment performed	As per Indian Standard
1	Fineness test	9% Residue obtained	Residue < 10% of the total sample (100 g)
2	Consistency test	31% (5.4 mm)	5 to 7 mm penetration
3	Initial setting time	80 min	Not below 30 min
4	Final setting time	325 min	Not beyond 600 min
5	Compressive strength	44 N/mm^2	43 N/mm^2
6	Specific gravity (G)	3.15	3.11–3.16

Table 5 Physical properties of the coarse aggregate

S. No.	Test performed	As per experiment performed	As per Indian Standard
1	Fineness modulus	5.24	For all in aggregates 3.5 to 6.5
2	Flakiness index	15.1%	Up to 35%
3	Crushing value test	18.25%	Up to 45% for concrete and 30% for highways
4	Impact value test	11.45%	Up to 45% for concrete and 30% for highways
5	Specific gravity (G)	2.65	2.5 to 3.0
6	Water absorption	0.49%	Not more than 0.6% per unit weight

3.3 Fine Aggregate

As per IS 383-1970, IS 2386 (Part 1)-1963, IS 2386 (Part 2)-1963, IS 2386 (Part 3)-1963, IS 2386 (Part 4)-1963, IS 2386 (Part 5)-1963, IS 2386 (Part 6)-1963 and IS 460-1962, some tests have been performed and their data are displayed in Table 6.

Table 6 Physical properties of fine aggregate

S. No.	Test performed	As per experiment performed	As per Indian Standard
1	Fineness modulus	2.308	2.2–3.2 (FM ≤ 3.2)
2	Dry density	1.65 g/cm^3	1.49–1.6965 g/cm^3
3	Specific gravity (G)	2.59	2.65
4	OMC	12.64%	11–15

Table 7 Physical properties of BKD

S. No.	Test performed	As per experiment performed	As per Indian Standard
1	Fineness modulus	1.99	No IS code is available
2	Dry density	1.42 g/cm^3	
3	OMC	13.81%	
4	Specific gravity (G)	2.35	

Table 8 Physical properties of fly ash

S. No.	Test performed	As per experiment performed	As per Indian Standard
1	Fineness modulus	1.76	F.M < 2
2	Dry density	1.19 g/cm^3	1.01–1.78 g/cm^3
3	OMC	20.34%	11–53% (Max.)
4	Specific gravity (G)	2.18	2.1–3.0

3.4 Brick Kiln Dust

After seeking the help from different journals regarding tests, various tests were performed as displayed in Table 7.

3.5 Fly Ash

As per IS 3812 (Part 1)-2013 and from the study of journals, different tests have been performed as given in Table 8.

4 Methodology

1. In this research work, cement is partially replaced with waste materials like BKD and FA to obtain the similar target mean strength of M25 design mix concrete. The size of the cube used for determining the compressive strength is 150 × 150 × 150 (mm). In this research, five cases have been performed to achieve the target mean strength of M25 design mix concrete, in the order of replacing the cement as (0% BKD + 0% FA), (5% BKD + 5% FA), (10% BKD + 10% FA), (15% BKD + 15% FA) and (20% BKD + 20% FA). Here, one can observe that the cement is partially replaced in the order of 0%, 10%, 20%, 30% and 40% by weight, with respect to BKD and FA combined together. To attain the target, mean strength, the value of characteristic compressive strength of a different design mix and standard deviation is given in Table 8 of IS 456-2000

[18]. As per IS 456-2000 and IS 10262-2019, the design mix of M25 concrete is prepared, and then concrete compressive strength is performed after curing for 28 days.

Note The particle size of waste materials, FA and BKD, must be like that of the cement, as per Indian Standard.

2. The target mean strength, as per IS 10262-2019 of M25 deign mix concrete, is obtained using the formula:

$$fck' = fck + 1.65 \times S$$

where
fck' is the target mean strength
fck is the characteristic compressive strength
And, S is the standard deviation [16]

$$fck' = 25 + 1.65 \times 4 = 31.6 \text{ N/mm}^2 \text{ [6]}$$

5 Specification of Materials

(a) Grade of cement: OPC 43	**(f)** Exposure condition: moderate (RCC)
(b) Maximal aggregate size: 20 mm	**(g)** Method of placing: manual
(c) Minimal content of cement: 300 kg/m^3	**(h)** Maximal cement content: 450 kg/m^3
(d) Maximal ratio of water/cement: 0.50	**(i)** Chemical admixtures: none
(e) Slump: 50–100 mm	**(j)** Mineral admixture: fly ash

From the above data, an attempt has been made to obtain the values as displayed in Table 9.

Table 9 Design Mix for grade M25 for the slump value of 75 mm

Materials (Kg)	CASE I	CASE II	CASE III	CASE IV	CASE V
OPC 43	394	354.6	315.2	275.8	236.4
Fine aggregate	754	754	754	754	754
Coarse aggregate	1103	1103	1103	1103	1103
Fly ash	0	19.7	39.4	59.1	78.8
BKD	0	19.7	39.4	59.1	78.8
Water content	197	197	197	197	197
W/C	0.5	0.5	0.5	0.5	0.5

In Table 9, different parameters are reflecting about the materials which are used to perform this experiment. In CASE I, cement (0%) is partially replaced with FA (0%) and BKD (0%). In CASE II, cement (10%) is partially replaced with FA (5%) and BKD (5%) combined together. In CASE III, cement (20%) is partially replaced with FA (10%) and BKD (10%) combined together. In CASE IV, cement (30%) is partially replaced with FA (15%) and BKD (15%) combined together. In CASE V, cement (40%) is partially replaced with FA (20%) and BKD (20%) combined together.

Note A slump of 75 mm is obtained when the W/C ratio is 0.50 as done in Figs. 1, 2 and 3. As per IS 456-2000 [18], such type of workability is desirable for the

Fig. 1 Materials before mixing

Fig. 2 Mixing of materials

Fig. 3 Slump test

formation of the structural elements like that of the beams, the columns, the slabs and the foundations.

6 Result

As per IS 516-1956 [19], the cubes should be in wet condition, and measure the weight then start its compression. Table 10 gives the readings which show the replacement order of the cases and concrete compressive strength with respect to curing days. The formula used for finding the compressive strength of the concrete specimen is the force acting per unit area of the cube (150 mm × 150 mm).

Table 10 Concrete strength at 7, 14 and 28 days of curing

M25 design mix	7 days strength (N/mm^2)	14 days strength (N/mm^2)	28 days strength (N/mm^2)
CASE I	33.3	35.11	37.33
CASE II	31.11	35.66	39.55
CASE III	18.66	29.66	36.88
CASE IV	18.22	28.44	34.22
CASE V	17.77	19.11	26.66

7 Conclusion

In this experiment, the specimens are cured for 28 days for which the results for different cases from Case I to Case V have been found, such as for CASE I, the cement concrete compressive strength is obtained as 37.33 N/mm². Likewise, for the CASE II, CASE III, CASE IV and CASE V, the concrete compressive strengths were obtained as 39.55 N/mm² 36.88 N/mm², 34.22 N/mm² and 26.66 N/mm², respectively. However, as per design mix, the target mean strength of M25 design mix concrete is 31.6 N/mm². Therefore, from the above readings, it has been observed from the CASE IV that if the cement is substituted by 30% (with 15% of FA and 15% of BKD combined together), as shown in Fig. 4, the concrete gives the promising strength when it is compared with the target mean strength and the economical design mix, as per IS 10262-2019.

FA and BKD are waste products which can be used as a partial cement replacement in concrete production. The compressive strength of concrete is an important parameter which indicates the quality of concrete. Here, in this experiment, an investigation of the two input materials, FA and BKD on the effective compressive strength of concrete, was carried out. As, the chemical components of FA and BKD indicate silica (SiO_2) is the major ingredients in both the materials. It is to be observed that the function of silica during concrete production is to increase the compressive strength of concrete. Therefore, from the above readings, it has been found that up to 30% replacement of cement with FA (15%) and BKD (15%) combined together gives more strength than target mean strength, but above 30% replacement that it is further observed that the strength is decreasing due to increase in the above two inputs FA and BKD. The decrease in strength is due to increase in silica content as excessive silica swells the hygroscopic gel and increases the volume of concrete resulting to the loss of strength.
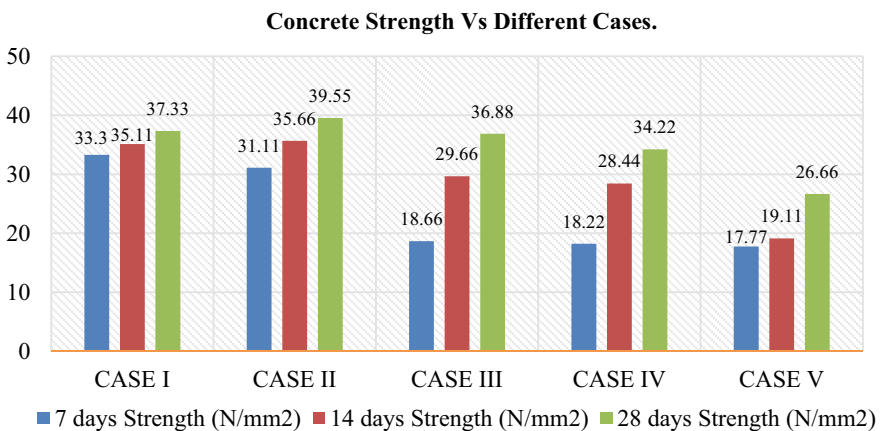
Fig. 4 Column chart showing Concrete strength Vs Different cases

Thus, the utilization of FA and BKD in concrete production turns out to be viable waste products that would reduce the emission of carbon-di-oxide as pollutants as well increase the strength of concrete.

Declaration

Compliance with Ethical Standards The work has been performed in original as per Indian Standards. No piracy is done in the research work; in fact, some data have been taken with a view to furthering my research work, the details of which have been cited in the references.

Funding NIL

Conflict of Interest No conflict of Interest.

Author's Contribution

1. **Saurabh Dubey[1]***, the corresponding author is a research scholar and his findings are based on the experiments made on the topic.
2. **Dr. Deepak Gupta[2]**, the co-author is the research supervisor of the corresponding author.
3. **Dr. Mainak Mallik[3]**, the co-author is the research supervisor of the corresponding author.

References

1. Mills SJ (2010) Coal use in the new economies of China, India and South Africa. IEA Clean Coal Centre, London
2. Gupta G, Sood H, Gupta PK (2018) Brick kiln dust waste management through soil stabilization. In: International conference on sustainable waste management through design. Springer, Cham
3. Yazici Ş, Arel HS (2012) Effects of fly ash fineness on the mechanical properties of concrete. Sadhana 37(3)
4. Rana S, Talwar K (2020) Investigating the durability of concrete filled with different ratios of glass fibre. IJERT 9(4):421
5. https://www.ijsr.net/archive/v8i7/ART20199489.pdf
6. Singh N Effects of replacement of sand by brick kiln burnt dust in mortar: a comprehensive study
7. Rather TA Partial substitution of sand & cement with brick kiln powder & rice husk ash in high strength concrete
8. Singh HP, Bharosh R (2018) Effect on properties of concrete using bricks kiln dust (BKD)
9. Nasir Ayaz Khan M et al (2018) Effect of brick dust on strength and workability of concrete. MS&E 414(1):012005
10. http://www.iitk.ac.in/ce/test/IS-codes/is.8112.2013.pdf
11. Uddin MK (2004) Use of brick dust in concrete as mineral admixture and partial replacement of cement. J Civ Eng 32(1):71
12. https://law.resource.org/pub/in/bis/S03/is.3812.1.2013.pdf
13. https://www.iitk.ac.in/ce/test/IS-codes/is.2386.1.1963.pdf

14. https://law.resource.org/pub/in/bis/S03/is.383.1970.pdf
15. https://law.resource.org/pub/in/bis/S03/is.4031.1.1996.pdf
16. https://www.iitk.ac.in/ce/test/IS-codes/is.4031.5.1988.pdf
17. https://www.iitk.ac.in/ce/test/IS-codes/is.4031.6.1988.pdf
18. https://www.iitk.ac.in/ce/test/IS-codes/is.456.2000.pdf
19. https://www.iitk.ac.in/ce/test/IS-codes/is.516.1959.pdf
20. https://law.resource.org/pub/in/bis/S03/is.10262.2009.pdf

Numerical Modelling of an Unreinforced Masonry Wall with Central Window Opening

Ruthviz Kodali, Faisal Mehraj Wani, Tariq Anwar Aquib, and Jayaprakash Vemuri

1 Introduction

Over 60% of structures in India consist of unreinforced brick masonry (URM), as per available information from the Prompt Assessment of Global Earthquakes for Response [1]. URM structures in the Indian subcontinent region are often designed only for gravity loads [2]. In several regions, these structures have load-bearing URM walls supporting a heavy roof/slab [3, 4]. URM structures are highly vulnerable to damage during earthquakes [5, 6]. However, despite the observed catastrophes, only a limited number of studies are available on the in-plane failure of URM walls [7, 8]. The high prevalence of URM structures in several regions of high seismic activity necessitates comprehensive experimental and computational studies.

A typical URM structure has several walls often with openings for accommodating doors and windows, and the size and location of the openings affect the strength and stiffness of the URM wall [9]. Several studies of the impact of openings on URM infills have been performed [10–13]. Often, these openings are misaligned in the vertical and horizontal directions [14]. Damage due to in-plane earthquake action occurs primarily in walls with openings [15]. Substantial damage to URM walls with openings was observed in the 2002 Molise, Italy earthquakes [16], and hence, specific modelling strategies for walls with openings have also been proposed [17]. Strengthening strategies for retrofitting URM walls with openings have also been proposed [18]. The M-DEM methodology has been adopted to successfully simulate the behaviour of various URM structures having openings [19]. It has also been observed that the presence of openings in URM structures, particularly irregular

R. Kodali (✉) · F. M. Wani · J. Vemuri
Ecole Centrale College of Engineering, Mahindra University, Hyderabad, India
e-mail: ruthviz18114@mechyd.ac.in

T. A. Aquib
King Abdullah University of Science and Technology, Thuwal, Saudi Arabia

openings, affects the results obtained from numerical studies which are dependent on the adopted discretization scheme [19].

In this paper, various micro-modelling techniques are used to study the in-plane behaviour of URM walls with openings, using the finite element software, DIANA 10.4 [20]. The paper presents results from the numerical modelling of two URM walls: one with a central window opening and the other being a full wall. Three numerical micro-modelling techniques, namely the total strain crack model, the engineering masonry model, and the combined cracking-crushing-shearing model, are used to model the URM wall and to understand the effect of each technique on the observed results. The load response curves are compared for both the full URM wall and a URM wall with a central opening for all three modelling techniques, and key findings are described.

2 Numerical Modelling of Unreinforced Masonry Walls

Researchers have performed numerical simulations of URM walls both at the macro-level and the micro-level [21–23]. The micro-modelling technique, first developed in 1978 [24], has been extended by several pioneers [25, 26]. The method has subsequently been adopted by researchers [27, 28] and is now available as a part of commercial software, in view of the rapid increase in computational power. In this paper, three micro-modelling techniques, (i.e.) the combined cracking-crushing-shear method, the total strain crack technique, and the recently developed engineering masonry model are used in DIANA (TNO DIANA, 2020) for modelling the full URM wall and the URM wall with a central opening, and the numerical models for which are shown in Figs. 1 and 2. The width and height of the wall are 2.2 and 2 m in both cases. The dimensions of the opening are 1×1 m. The dimensions of the brick are $0.2 \text{ m} \times 0.05 \text{ m} \times 1 \text{ m}$.

The material and geometrical properties for various numerical techniques used for analysing both the full wall and the wall with opening were adopted from the values recommended by DIANA (TNO DIANA, 2020). For numerical modelling using the linear material model, only a few properties are required: Young's modulus for brick and concrete along with their respective Poisson's ratio and mass density. These properties are listed in Tables 1 and 2. For numerical modelling using the combined cracking-shearing-crushing model, the material properties needed for bricks and concrete are taken from Tables 1 and 2. However, for modelling the interface, properties for cracking, shearing, and crushing are required. The cracking parameters are the tensile strength and the fracture energy; the crushing properties are the compressive strength, the fracture energy in compression, the equivalent plastic relative displacement; and the shearing parameters are the friction angle, cohesion, dilatancy angle, residual friction angle, confining normal stress, and exponential degradation coefficient. These properties are listed in Table 4. For the total strain crack and nonlinear model, the nonlinear properties of the brick, such as tensile behaviour and compressive behaviour, are used. These properties are listed in Table

Fig. 1 URM wall without central opening
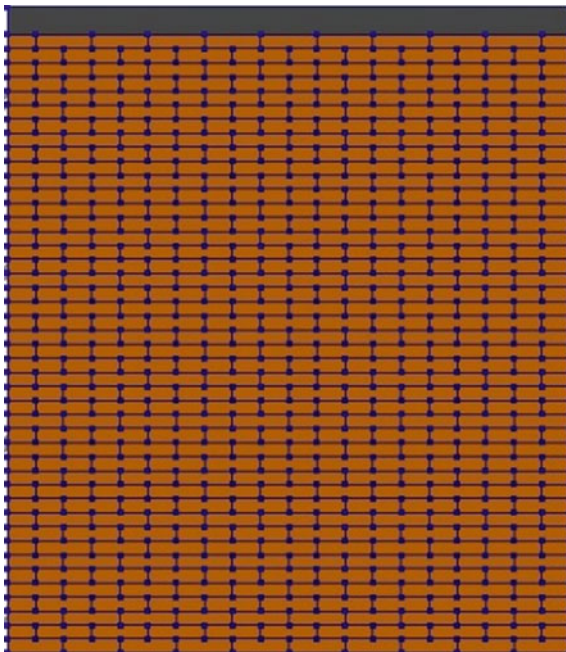
Fig. 2 URM wall with a central opening
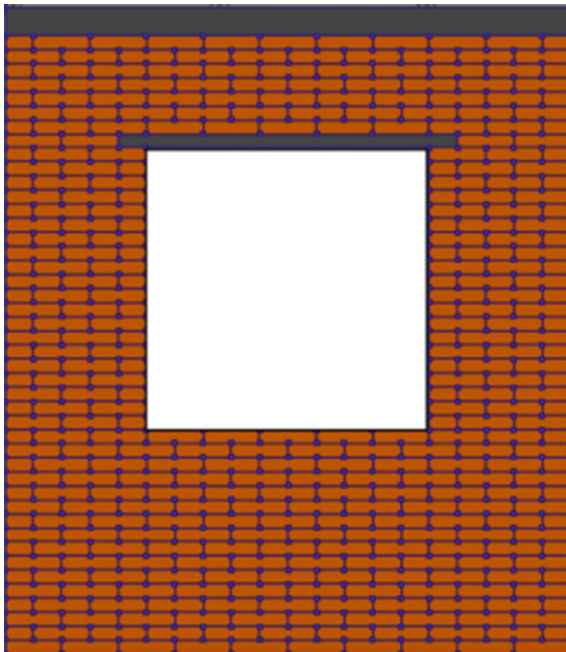
Table 1 Material properties—brick linear

Property	Value	Units
Young's modulus	1.74×10^{10}	N/m^2
Poisson's ratio	0.15	
Mass density	1700	kg/m^3

Table 2 Material properties—concrete

Property	Value	Units
Young's modulus	$3x10^{10}$	N/m^2
Poisson's ratio	0.15	
Mass density	2200	kg/m^3

5. Bed joints and head joints are modelled using a Coulomb friction model and a nonlinear elastic model, respectively. These models are referred to as *interface friction* and *interface no tension*. The properties of these models are listed in Tables 6 and 7. Finally, for numerical modelling using the engineering masonry model, the brick properties needed are Young's modulus, shear modulus, and also the cracking parameters like the bed joint tensile strength, the minimum tensile strength head joints, the residual tensile strength, the tensile strength of head joint defined by friction, the fracture energy in tension, the angle between stepped diagonal crack and bed joint, the crushing parameters like the compressive strength, the unloading factor, the fracture energy in compression, the factor to strain at compressive strength, and shear failure parameters like the friction angle, the cohesion and, the fracture energy in shear. These properties are listed in Table 8. Table 3 lists the various properties of the interface. To generate the finite element mesh for the static nonlinear analysis, we create each element of the size 0.05 m, i.e. each brick is divided into four parts. The secant method is used to perform the iterations in this numerical model and each step checks for up to 30 iterations for convergence. The displacement and force norms are used to check for convergence.

The total strain crack model is used to model brittle materials, e.g. unreinforced masonry. The models are useful for cases where the material fails primarily in cracking or crushing. The models define the behaviour of materials with a single stress–strain relationship. A key drawback is that these models were formulated for isotropic materials. However, unreinforced masonry is an anisotropic material with different stiffnesses along the bed and head joints. Another model which has been widely used is the combined cracking-shearing-crushing model. It is a composite interface model and accounts for fracture, frictional slip, and crushing along any

Table 3 Material properties—linear interface

Property	Value	Units
Normal stiffness	1×10^{12}	N/m^3
Shear stiffness	1×10^{12}	N/m^3

interface in unreinforced masonry. The new improved engineering masonry model is a smeared failure model and includes orthotropy and accounts for head joint failure, bed joint failure, and diagonal staircase cracks. The model defines four potential non-orthogonal crack orientations in each iteration.

To validate the proposed numerical methodology, analyses were carried out using the properties of a URM wall with an opening provided in standard cases in TNO DIANA. The properties used in modelling are shown in Tables 1, 2, 3, 4, 5, 6, 7, and 8. The load response curves obtained from the FEM model matched well the results from the standard cases as shown in Fig. 3. Further, the difference in the peak loads was in the range of 1–2% indicating the accuracy of the model. The methodology was then extended to various full URM walls with no openings.

Table 4 Material properties—interface plastic model

Property		Value	Units
Normal stiffness	k_n	8.3×10^{10}	N/m^2
Shear stiffness	k_s	3.6×10^{10}	N/m^2
Cracking parameters			
Tensile strength	f_t	250,000	N/m^2
Fracture energy	G_{F1}	18	N/m
Shearing parameters			
Cohesion	c	350,000	N/m^2
Friction angle	Φ	0.643501	rad
Dilatancy angle	ψ	0.54042	rad
Residual friction angle	Φ_{res}	0.643501	rad
Confining normal stress	σ_c	-1.3×10^6	N/m^2
Exponential degradation coefficient		5	
Parameter	a	0	m
Parameter	b	130	N/m
Crushing parameters			
Compressive strength	f_c	8.5×10^6	N/m^2
Factor	C_s	9	
Fracture energy in compression	G_c	15,000	N/m
Equivalent plastic relative displacement		0.93	m

Table 5 Material properties—brick nonlinear

Property		Value	Units
Young's modulus	E	1.74×10^{10}	N/m^2
Poisson's ratio	υ	0.15	
Mass density	ρ	1700	kg/m^3
Tensile behaviour			
Tensile strength	f_t	250,000	N/m^2
Ultimate strain	E_u	18	
Residual tensile strength	$f_{t,res}$	50,000	N/m^2
Compression behaviour			
Compressive strength	f_c	8.5×10^6	N/m^2
Fracture energy in compression	G_c	15,000	N/m

Table 6 Material properties—interface friction

Property		Value	Units
Normal stiffness	k_n	8.3×10^{10}	N/m^2
Shear Stiffness	k_s	3.6×10^{10}	N/m^2
Frictional behaviour			
Cohesion	C	350,000	N/m^2
Friction angle	Φ	0.643501	rad
Dilatancy angle	Ψ	0.54042	rad
Tensile strength	f_t	250,000	N/m^2
Reduced shear stiffness	$k_{s,red}$	3.6×10^6	N/m^3

Table 7 Material properties—interface no tension

Property		Value	Units
Normal stiffness	k_n	8.3×10^{10}	N/m^2
Shear stiffness	k_n	3.6×10^{10}	N/m^2
Nonlinear elasticity			
Critical normal interface opening for reduction		3×10^{-6}	m
Normal stiffness reduction factor		1×10^{-5}	
Critical shear interface opening for reduction		3×10^{-6}	m
Shear stiffness reduction factor		1×10^{-5}	

3   Results and Discussion

Figure 4 shows a comparison of the load response of the full masonry wall and the masonry wall with central opening obtained from the combined cracking-shearing-crushing model. It is observed that the lateral strength of the full wall is 93 kN which is much higher than 39 kN, which is the strength exhibited by the wall with

Table 8 Material properties—engineering masonry

Property		Value	Units
Young's modulus (X direction)	E_x	4×10^9	N/m^2
Young's modulus (Y direction)	E_y	6×10^9	N/m^2
Shear modulus	G_{xy}	2×10^9	N/m^2
Mass density	ρ	1700	Kg/m^3
Cracking parameters			
Tensile strength head joint defined by friction			
Bed joint tensile strength	f_t	250,000	N/m^2
Minimum tensile strength head joints	$f_{t,min}$	250,000	N/m^2
Fracture energy in tension	G_{F1}	18	N/m
Residual tensile strength	$f_{t,res}$	50,000	N/m^2
Angle between stepped diagonal crack and bed joint	α	0.436332	rad
Crushing parameters			
Compressive strength	f_c	8.5×10^9	N/m^2
Fracture energy in compression	G_c	15,000	N/m
Factor to strain at compressive strength	n	2	
Unloading factor	L	1	
Shear failure parameters			
Friction angle	Φ	0.642501	rad
Cohesion	c	350,000	N/m^2
Fracture energy in shear	G_{sh}	250	N/m
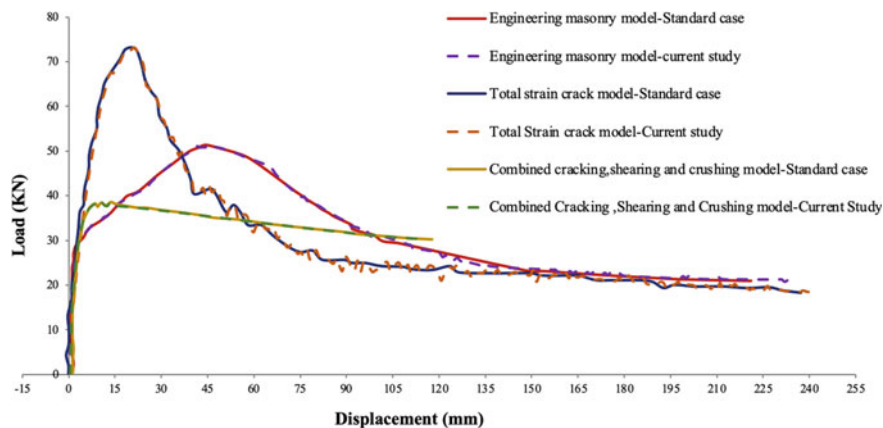
Fig. 3 Validation of load–displacement curves (current study versus standard cases in DIANA)
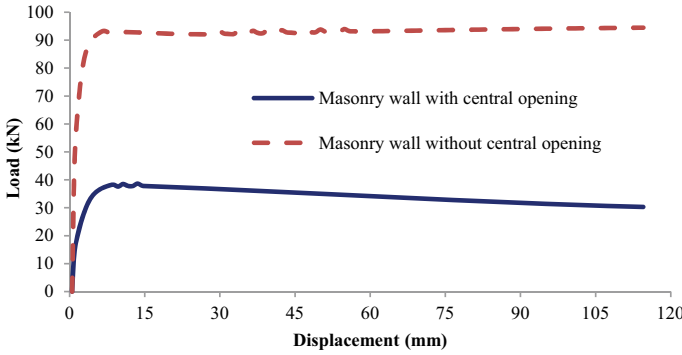
Fig. 4 Load response curves from the combined cracking-shearing-crushing model
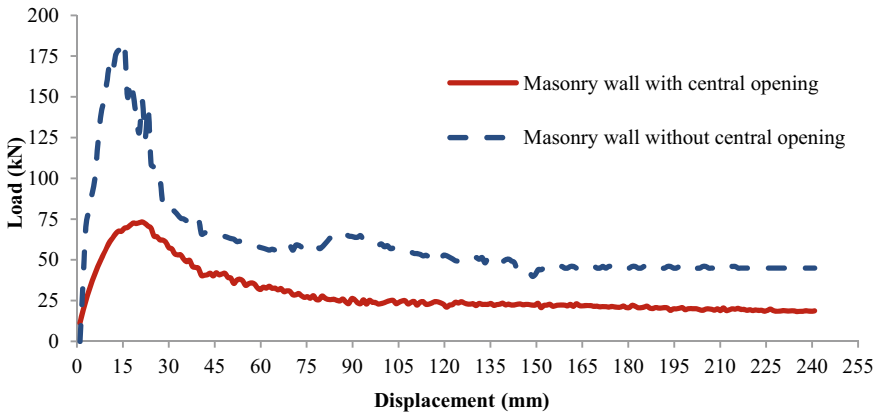
Fig. 5 Load response curves from the total strain crack and nonlinear model

an opening. Figure 5 shows the load response of the full URM wall and also the URM wall with a central opening using the total strain crack model. It is observed that the lateral strength of the full wall is 180 kN which is much higher than 70 kN, which is the strength exhibited by the wall with an opening. Figure 6 shows the load response of the full URM wall and the URM wall with a central opening using the engineering masonry model. It is observed that the lateral strength of the full wall is 120 kN which is much higher than 40 kN, which is the strength exhibited by the wall with an opening. Figure 7 shows the damage contours for the URM wall with openings, for both the engineering masonry model and the total strain crack model. It is observed that there is stress concentration near the central window opening.
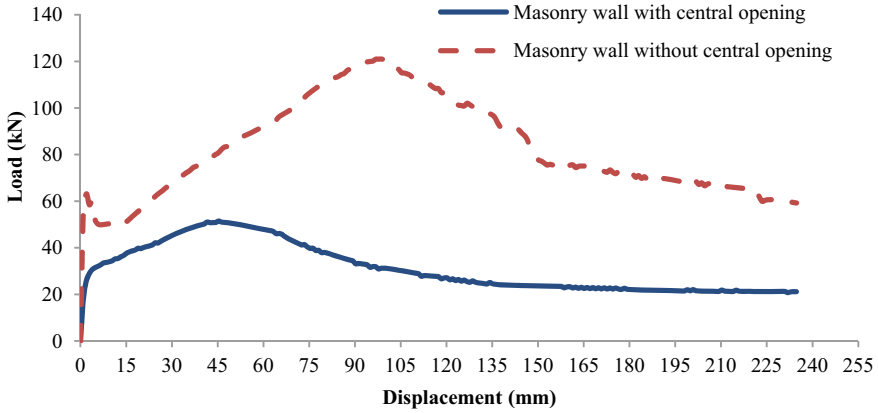
Fig. 6 Load response curves from the engineering masonry model
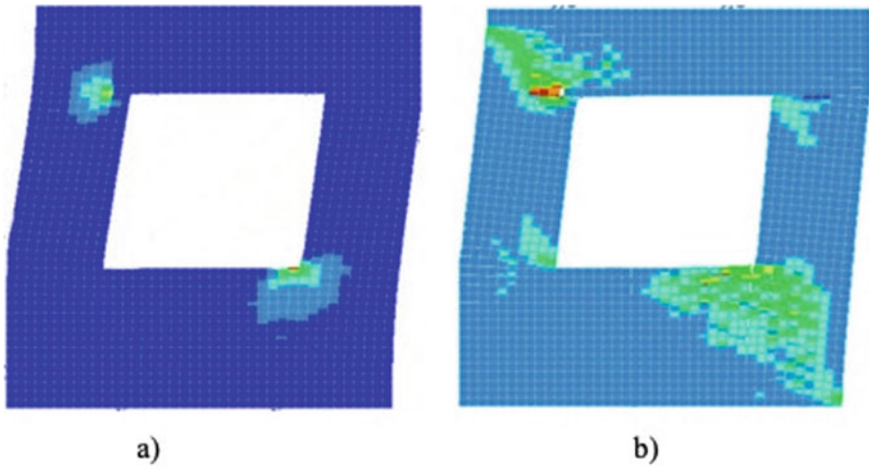
Fig. 7 Damage contours obtained from the **a** engineering masonry model and **b** total strain crack and nonlinear model

4 Conclusions

The load response curves and damage contours obtained in this study indicate that the presence of a central opening in the masonry wall causes a substantial reduction in lateral strength and stiffness. There is a substantial variation in the lateral load response obtained from the three numerical models. The strength, of a URM wall with opening as compared to a full URM wall, is reduced by a factor of 2 in the combined cracking-crushing-shearing method, while it is reduced by a factor of 2.5 using the total strain crack model and by a factor of 3 using the engineering masonry

model. Further, the peak strength is observed at a low displacement of 5 mm in the combined cracking-crushing-shearing model. In the total strain crack model, the peak strength is reached at a displacement of 15 mm for the full masonry wall and 20 mm for the corresponding wall with a central opening. In the engineering masonry model, the peak strengths are reached at 45 mm and 150 mm for the wall with a central opening and the full wall, respectively. Overall, the results from both the full URM wall and the URM wall with central openings show that the selection of the micro-modelling technique for numerical modelling has a significant influence on the observed strength, stiffness, and ductility characteristics.

References

1. WHE-PAGER Database (2007). http://pubs.usgs.gov/of/2008/1160/downloads/OF08-1160.pdf
2. Vemuri J, Ehteshamuddin S, Ravula M, Kolluru S (2020) Pushover analysis of soft brick unreinforced masonry walls using analytical and numerical approaches. Mater Today Proc 28:420–425
3. Vemuri J, Ehteshamuddin S, Kolluru S (2018) Numerical simulation of soft brick unreinforced masonry walls subjected to lateral loads. Cogent Eng 5(1):1551503
4. Vemuri J, Ehteshamuddin S, Kolluru SV (2018) Evaluation of seismic displacement demand for unreinforced masonry shear walls. Cogent Eng 5(1):1480189
5. Garg R, Vemuri JP, Subramaniam KV (2019) Correlating peak ground A/V ratio with ground motion frequency content. In: Recent advances in structural engineering, vol 2. Springer, Singapore, pp 69–80
6. Vemuri J, Kolluru S (2020) Evaluation of ground motion scaling techniques. In: Advances in computer methods and geomechanics. Springer, Singapore, pp 525–535
7. Vemuri J, Kolluru S, Chopra S (2018) Surface level synthetic ground motions for M7. 6 2001 Gujarat earthquake. Geosciences 8(12):429
8. Vemuri JP, Kolluru S (2017) Seismic analysis of unreinforced masonry walls. IDRiM J 6(2):102–115
9. Liu Z, Crewe A (2020) Effects of size and position of openings on in-plane capacity of unreinforced masonry walls. Bull Earthq Eng 18(10):4783–4812
10. Al-Chaar G, Lamb GE, Issa M (2003) Effect of openings on structural performance of unreinforced masonry infilled frames. ACI Spec Publ 211:247–262
11. Mohammadi M, Nikfar F (2012) Strength and stiffness of masonry-infilled frames with central openings based on experimental results. J Struct Eng ASCE 139:974–984
12. Asteris P (2003) Lateral stiffness of brick masonry infilled plane frames. J Struct Eng ASCE 129:1071–1079
13. Kakaletsis D, Karayannis C (2008) Influence of masonry strength and openings on infilled R/C frames under cycling loading. J Earthquake Eng 12:197–221
14. Parisi F, Augenti N (2013) Seismic capacity of irregular unreinforced masonry walls with openings. Earthquake Eng Struct Dynam 42(1):101–121
15. Ingham JM, Griffith MC (2011) The performance of unreinforced masonry buildings in the 2010/2011 Canterbury earthquake swarm. Canterbury Earthquakes Royal Commission of Inquiry, Christchurch, New Zealand
16. Augenti N, Cosenza E, Dolce M, Manfredi G, Masi A, Samela L (2004) Performance of school buildings during the 2002 Molise, Italy, earthquake. Earthq Spectra 20(S1):S257–S270
17. Augenti N (2006) Seismic behaviour of irregular masonry wall. In: Proceedings of the 1st European conference on earthquake engineering and seismology, Geneva, Paper No. 86

18. Ghobarah A, El Mandooh Galal K (2004) Out-of-plane strengthening of unreinforced masonry walls with openings. J Compos Constr 8(4):298–305
19. Malomo D, DeJong MJ (2021) A macro-distinct element model (M-DEM) for simulating the in-plane cyclic behavior of URM structures. Eng Struct 227:111428
20. Diana FEA (2020) Diana user's manual, Release 10.4. DIANA FEA BV
21. Aldemir A (2010) A simple seismic performance assessment technique for unreinforced masonry structures. MS Dissertation, Middle East Technical University, Turkey
22. Abdulla KF, Cunningham LS, Gillie M (2017) Simulating masonry wall behaviour using a simplified micro-model approach. Eng Struct 151:349–365
23. Akhaveissy AH, Desai CS (2011) Unreinforced masonry walls: Nonlinear finite element analysis with a unified constitutive model. Arch Comput Methods Eng 18:485–502
24. Arya S, Hegemier G (1978) On non-linear response prediction of concrete masonry assemblies. In: Proceedings of the North American masonry conference. Masonry Society, Boulder, pp 19.1–19.24
25. Lotfi HR, Shing PB (1994) Interface model applied to fracture of masonry structures. J Struct Eng 120(1):63–80
26. Lourenço PB, Rots JG (1997) Multisurface interface model for analysis of masonry structures. J Eng Mech 123(7):660–668
27. Berto L, Saetta A, Scotta R, Vitaliani R (2004) Shear behaviour of masonry panel: Parametric FE analyses. Int J Solids Struct 41:4383–4405
28. La Mendola L, Accardi M, Cucchiara C, Licata V (2014) Nonlinear FE analysis of out-of-plane behaviour of masonry walls with and without CFRP reinforcement. Constr Build Mater 54:190–196

A Multi-objective Optimization Framework for Sustainable Retrofit of Indian Buildings

Harshit Jain, Albert Thomas, and Tripti Singh Rajput

1   Introduction

Sustainability in buildings has been a primary subject of concern in the building sector. As the construction industry advances, energy-efficient buildings are now the primary requirement to maintain energy balance in the environment. It has been found by many studies that the building construction industry is responsible for around 40% of the final energy consumption that also results in the increase in emissions of carbon dioxide [12]. As per the report of Global Building Performance Networks (GBPN), it is predicted that globally the emissions in the building sector increased to 2% from 2017 to 2018, which reached to record high, while the final energy demand also rose 7% from 2010 [16]. In addition, it is estimated that heating and cooling energy use is expected to grow by 79% in residential buildings and 84% in commercial buildings over the period of 2010–2050 [13].

Various countries around the world have started to develop and implement policies to lower energy consumption in the building sector. Since there are various energy efficiency improvements for newly constructed buildings while for an old and existing building, the retrofitting of the building is one of the options to enhance the energy performance of the building. Asadi et al. [3] proposed the Multi-objective optimization (MOO) model and its application for building the retrofitting strategies with the use of proper decision variables to explore trade-offs between various retrofitting actions.

Jafari et al. [11] propose an optimization decision-making framework for building energy retrofit and implemented the case study model in which the economic benefit of energy retrofitting is calculated in terms of reducing the life cycle cost. Bre et al.

H. Jain (✉) · A. Thomas · T. S. Rajput
Department of Civil Engineering, Indian Institute of Technology Bombay, Powai Mumbai 400076, India
e-mail: h_jain@iitb.ac.in

[4] performed a metamodel approach-based method to carry out the Multi-objective optimization for the building performance. NSGA—Non-Sorted Genetic Algorithm method is applied along with artificial neural network (ANN), by using Energy Plus software which helped to optimize both energy efficiency and thermal comfort. It has been concluded that the application of smart sampling technique has been used to obtain Pareto optimal front. Similarly, Diakaki et al. [5] presented the Multi-objective decision-making model to enhance the building energy performance in which analysis of building energy use is carried out that allows the DM to obtain global optimum solutions. Likewise, Friedman et al. [7] analyzed the framework of Cost–Benefit to examine the potential economic benefits of building insulation envelopes in building retrofitting especially in the mild climate. Several researchers implemented the case study and developed models of Multi-objective optimization (MOO) using Genetic Algorithms and Artificial neural networks (ANN) [8–11]. The optimization technique also helps in the Life cycle assessment of buildings, Cost–benefit analysis [1], and comparison of material and energy consumptions between old and new buildings [2] which have been used in addressing the building sustainability issues.

These researchers have addressed the various problems as far as the building retrofit is considered. Most of the studies defined the list of pre-defined building solutions. In case if small solutions are defined, then there is no surety that the solution obtained is the best one from the decision-maker view while if a large count of solutions are there, it is extremely difficult to handle multiple solutions and decide which solution is the best one [3]. Various cost-effective and energy efficiency measures are taken for the retrofitting actions in the Indian buildings scenario, but the main issue is to identify the most feasible and optimal retrofitting actions considering the various factors such as budget constraint and energy consumption.

The purpose of the paper is to develop framework of Multi-objective optimization that helps in retrofitting of Indian building scenarios. Based on various parameters and objective functions, this technique can be implemented for solving the decision-making problems concerning the retrofitting cost and material energy consumption. The outcomes of best solutions of multiple objective problems with a properly defined set of decision variables along with the constraint equations are considered to get the best possible optimal and feasible solution [8]. Accordingly, this paper presents the Multi-objective optimization (MOO) techniques to quantitively assess among the various technological options in building retrofitting projects. The method provides the feasible combination of retrofit actions (such as wall plastering, flooring, windows, and internal painting) by optimizing the overall retrofitting cost and material embodied energy consumption involved in the building retrofitting. For this purpose, an illustrative residential $(G + 3)$ building model is developed in REVIT software. Through this technique, DM is capable to provide an optimal solution on retrofit cost and energy saving and the material choice at minimum retrofit cost and embodied energy consumption are identified. The paper is organized in such a manner that the proposed Multi-objective optimization model including formulating of objective functions presented in the next section which is followed by the

application case study of the proposed technique on $(G + 3)$ residential Building information modeling (BIM) for solving the decision-maker problems.

2 Theory And Methodology

2.1 Multi-objective Optimization

Multi-objective optimization is one such technique and process of decision-making in which real-life decision-making challenges are converted into mathematical objective functions formulated with constraints equations which will be solved by various optimization methods. These objective functions involve a decision variable on which optimization is carried out.

In the current study, the objective is to optimize both the cost of retrofitting actions as well as embodied energy of the materials used in retrofitting. These objectives are defined in the mathematical formulations of cost objective function (Re-Cost) and embodied energy function (EE). The decision variables used in functions reflect the whole set of alternative options for various retrofitting actions such as—flooring replacement, window replacement and internal wall painting. If the objective functions cannot be efficient without demean or affecting some of the other objective values, then such solutions are said to be non-dominated or non-inferior solutions also called Pareto Optimal (Pareto Efficient) solutions. Sometimes a single solution may not exist and in fact, there exist many Pareto optimal solutions. Such problems are called Non-Trivial Multi-Objective optimization problems. This terminology is given and described by Vilfredo Pareto [10] (Fig. 1).
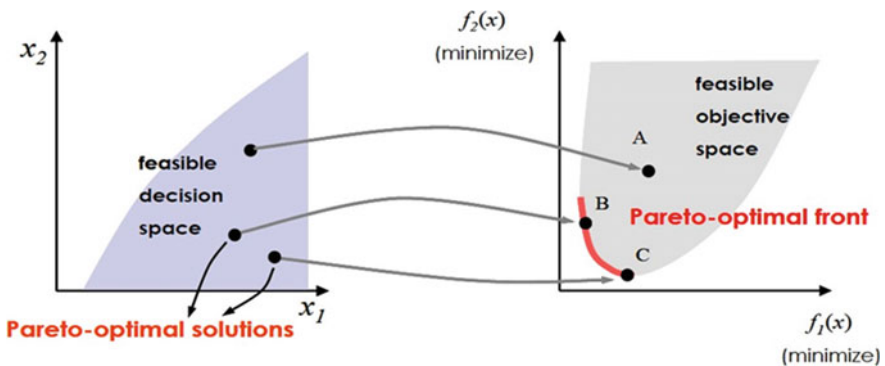
Fig. 1 Graphical description of Pareto optimal front *Source* https://medium.com/analytics-vidhya/optimization-modelling-in-python-multiple-objectives-760b9f1f26ee

2.2   Concept of Genetic Algorithm

Genetic Algorithm (GA) search is the best optimization technique based on Genetic Natural selection and is frequently used in solving the optimization problem in research and machine learning. It is depending on the concept of "Natural Selection and Genetics".

In GA-based method, we have a pool or population of possible solutions on which the combination of Crossover and Mutation operations (such as genetics) is applied and thus producing new children and over various generations, this whole procedure is repeated. Each candidate solution has given a particular value of fitness (based on its objective function value) and the better individuals are assigned more chances to mate and yield more "better" individuals. The concept is comparable to Charles Darwin's "*Theory of Survival of the Fittest*". In this method, keep "generating and evolving" fitter solutions or individuals over generations, till a certain stopping criterion is reach [17].

2.3   Decision Variables

The decision variables considered in this study concerns the various combination of retrofit choices on existing building such as wall plastering, replacement of flooring, replacement of windows, and wall painting. Although there are various retrofitting activities carried out on an existing building to enhance its condition and improve the building energy performance. In this study, the decision variables are defined based on the following retrofit actions:

(a)   Change of Wall plastering
(b)   Replacement of Flooring
(c)   Replacement of Windows
(d)   Internal Wall painting

2.4   General Method

The General method for the current research study is depicted in Fig. 2 where initially input data are gathered in form of a building information model (BIM) where quantities are taken out, and a database for a schedule of rates of each retrofitting activities and embodied energy database are taken. The quantification module is carried over the BIM model to generate the model properties. The mathematical objective functions are formulated along with the constraint equations having lower and upper bound ranges. The GA algorithm is developed for solving the optimization problem. Finally, the optimized values of cost and embodied energy are obtained and the pareto optimal plot is generated.
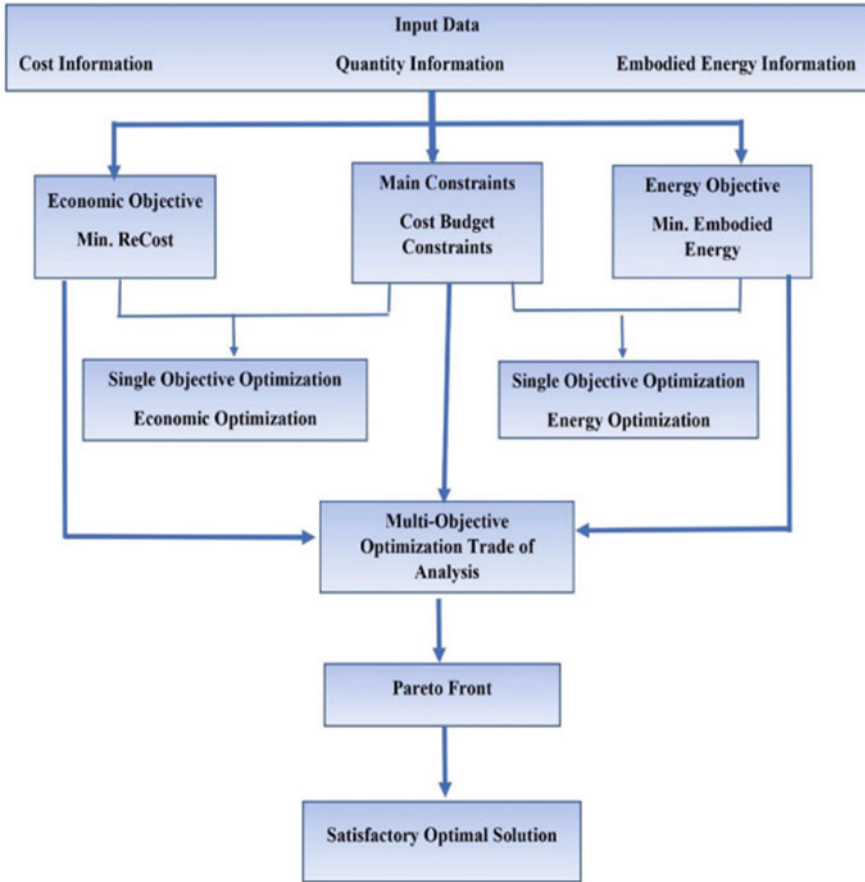
Fig. 2 Flow chart for multi-objective optimization process

2.5 Case Study

2.5.1 Building Model Implementation for Case Study

A multi-storeyed $(G + 3)$ residential 3-D building model is created in REVIT application for the case study with each floor occupied as 1 BHK flat unit as shown in Fig. 3a, b. Following are the properties of the building model.

Wall Plaster Area $= 450$ m^2
Flooring Area $= 60$ m^2
Window Opening Area $= 50$ m^2
Internal Wall Painting Area $= 450$ m^2

<center>(a)   (b)</center>
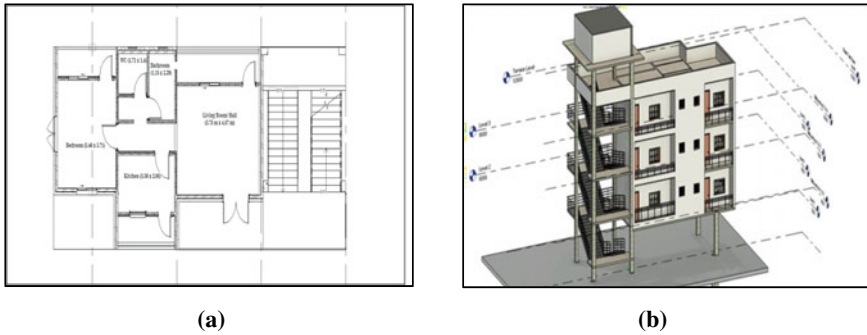
Fig. 3 a, **b** Schematic Plan of 1 BHK Residential Flat and 3-D building model created for the case study

2.6 Elements Taken in Retrofitting of Building

The Retrofitting cost objective function—Re-Cost(x) depends on the cost of work items which are to be executed on doing retrofitting of building in improving its condition and energy performance. There are various retrofitting actions to be carried out on an existing building but in this study, the following retrofitting elements are taken. The cost (in Rs/m^2) of each retrofitting action involved in retrofitting are taken based on market rates and CPWD Schedule of Rates, New Delhi (SOR) which is shown in Table 1 and accordingly the objective functions are framed involving the decision variables.

For enhancing the building energy performance, embodied energy plays a significant role. It refers to the energy consumed in manufacturing and producing of the material during its life cycle involving extraction, manufacturing, construction, maintenance, and disposal [14]. It is an inherent energy of material produced from raw stage to finished stage and for a better choice of material in building construction, there is a need to optimize EE values also. The embodied energy function (EE) is taken as a second objective function in which the EE values (in MJ/Kg) of the materials involved in retrofitting actions are taken from the report of Indian Construction Material Database published by International Finance Corporation, 2017 [15]. These

Table 1 Details of cost and embodied energy values of materials for various retrofitting actions

S. No.	Materials	Lower and upper bound ranges of Re-cost and EE	
		Cost values (in Rs./m^2)	Embodied energy values (in MJ/Kg)
A	Plastering	80 and 300	0.4 and 5
B	Flooring	750 and 1200	4.5 and 8.5
C	Window frames	1300 and 2000	60 and 290
D	Painting	60 and 120	50 and 65

values are taken as a reference for the current study in which Embodied Energy (in MJ/Kg) is taken as a second objective function as shown in Table 1.

2.7 Objective Functions

In the current study of optimization framework, the objective functions are framed which involves two objectives—the first objective is Minimization of Retrofit cost (Re-Cost) and the second objective is Minimization of Embodied Energy function (EE) along with the constraint equations. The Retrofit Cost objective function [Re-Cost] involves the following decision cost variables such as CPi, CFi, CWi, CPa. Since the overall retrofit cost is the sum of the individual cost of retrofitting actions. Hence the Eq. (1) framed as Objective-1, i.e., Re-Cost.

Similarly, in terms of the Embodied Energy function, the Embodied energy values of the materials used in the above retrofitting actions are taken as EE Pi, EE Fi, EE Wi, and EE Pa, respectively, and Eq. (2) shows the total Embodied Energy function as a sum of the Embodied energies of the materials involved in it.

$$\text{Objective 1} : \text{ReCost} = F_{\text{plastercost}} + F_{\text{flooringcost}} + F_{\text{windowcost}} + F_{\text{paintingcost}}$$

$$\text{ReCost} = (CP_i \times A_{\text{wall}}) + (CF_i \times A_f) + (CW_i \times A_{\text{win}}) + (CP_a \times A_{\text{wall}}) \quad (1)$$

$$\text{Objective 2} : \text{Embodied Energy (EE)} = \text{EE.Pi} + \text{EE.Fi} + \text{EE.Wi} + \text{EE.Pa} \quad (2)$$

where

CP_i = Cost of Plaster (Rs./m^2), EE. Pi = Embodied Energy values of Plaster (MJ/kg).

CFi = Cost of Flooring (Rs/m^2), EE. Fi = Embodied Energy values of Flooring (MJ/kg).

CWi = Cost of Window (Rs/m^2), EE. Wi = Embodied Energy values of Window (MJ/kg).

CPa = Cost of Painting (Rs/m^2), EE. Pa = Embodied Energy values of Painting (MJ/kg).

The concept of evolutionary algorithms such as Genetic algorithm (GA) has been implemented for the optimization of above objective functions in which GA algorithm has been developed in MATLAB and various parameters are taken for optimization such as number of decision variables, population size, crossover, and mutation parameters. In an algorithm, the objective functions are optimized to get data of optimized values for both functions.

2.8 Constraint Equations

The constraint equations are the conditions or the situations which are involved in the optimization process and it is formulated for both the objective functions. For embodied energy, the relationship between cost and embodied energy is taken based on the regression analysis as described in the research study [6] and as shown in Eq. (3). Considering the budget constraint scenarios of the building user or occupants, the various cases are analyzed based on the combination of different constraint equations for both cost and embodied Energy.

$$EE = 0.0235 \text{ (Cost)} + 0.0499 \tag{3}$$

Using the above relationship, the following constraint equations for various cases are developed both in terms of cost and embodied Energy. With the reduction in cost values by a particular percentage from the maximum amount, the embodied energy reduction is calculated from Eq. (3). The following cases are analyzed with the variation in Constraint equations as shown in Table 2.

The objective functions from Eq. (1) and (2) with various constraint equations shown above are solved in a GA-based algorithm in MATLAB software tool which leads to an output of optimized retrofit Cost and embodied energy values for each constraint conditions. Hence this optimal data is plotted with the help of MATLAB

Table 2 Various cases studied for cost constraint equation and embodied energy equations

S. No.	Case Condition	Cost constraint equations	Embodied energy constraint equation
1	When the user can only spend 90% of the Maximum Amount	C.Fi * 180 + C.Wi * 50 ≤ 284,400	EEWi + EE.Fi ≤ 288.94
		C.Pi * 450 + C.Pa * 450 ≤ 170,100	EE.Pi + EE.Pa ≤ 67.76
2	When the user can only spend 80% of the maximum amount	C.Fi * 180 + C.Wi * 50 ≤ 252,800	EEWi + EE.Fi ≤ 279.396
		C.Pi * 450 + C.Pa * 450 ≤ 151,200	EE.Pi + EE.Pa ≤ 65.52
3	When the user can only spend 70% of the maximum amount	C.Fi * 180 + C.Wi * 50 ≤ 221,200	EEWi + EE.Fi ≤ 269.84
		C.Pi * 450 + C.Pa * 450 ≤ 132,300	EE.Pi + EE.Pa ≤ 63.28
4	When the user can only spend 60% of the maximum amount	C.Fi * 180 + C.Wi * 50 ≤ 189,600	EEWi + EE.Fi ≤ 260.26
		C.Pi * 450 + C.Pa * 450 ≤ 113,400	EE.Pi + EE.Pa ≤ 61.03

software in which the pareto optimal points and pareto front generated are shown in results. The pareto front shown in the plot obtained between cost and EE is the set of non-dominated optimal solutions or values in such a way that none of the objective functions can be improved without sacrificing the other one.

3 Results

When running the optimization equations in MATLAB with different constraint cases, the optimized values with higher precisions for both Re-Cost and EE functions for the following cases are generated and pareto plots are shown below for various cases.

Case 1— Constraint Equation such that when the user can only spend 90% of the maximum amount of combination.

Considering the above constraint condition, the optimized values of total Retrofitting Cost come out to be Rs. 4,54,400/- while the total Embodied Energy value comes out to be is 356.699 MJ/Kg as shown in Fig. 4a. Based on this solution in the resulting output generated by the MATLAB command file, the corresponding optimized values of individual plastering cost, flooring cost, window cost, and painting cost can be selected. In such a way, the decision-maker can take a feasible decision both in terms of cost-saving and minimizing energy consumption based on their selected constraint.

Case 2—Constraint Equations such that when the user can only spend 80% of the maximum amount of the combination.

In such a case, the plot between the optimized cost fitness function and embodied energy function is shown in Fig. 4b, and the optimized value of retrofitting cost
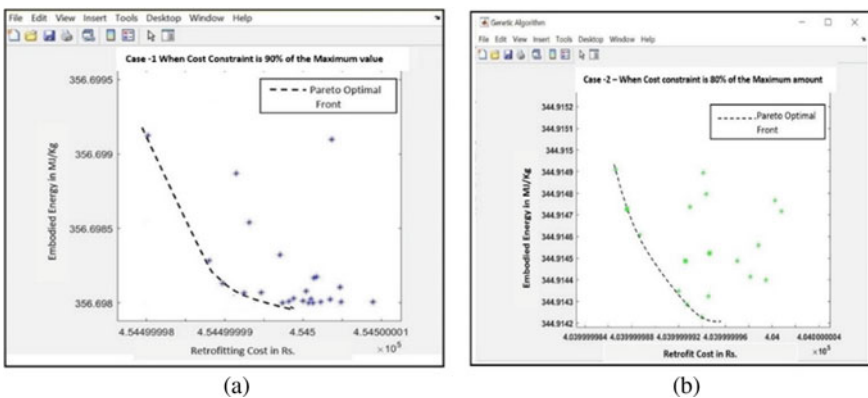
Fig. 4 Optimal plot b/w cost and embodied energy. **a** When cost constraint is 90% of the maximum amount, **b** when cost constraint is 80% of the maximum amount

comes out to Rs. 4,04,000/- and the value of embodied energy comes out to be 344.914 MJ/kg. Corresponding to this optimized retrofit cost and embodied energy values of materials can be determined.

Case 3— Constraint equations such that when the user can only spend 70% of the maximum amount of the combination.

In such a case, the optimized retrofitting cost comes out to Rs. 3,53,500/- and the value of embodied energy is 333.119 MJ/kg.

Case 4— Constraint equations such that when the user can only spend 60% of the maximum amount of the combination.

In such a case, the optimized retrofitting cost comes out to Rs. 3,14,600/- and the value of embodied energy is 321.288 MJ/kg.

4 Conclusion

(i)   To achieve the optimal and feasible solutions of various multiple objectives in building retrofitting works, there is a need to optimize the objective functions.

(ii)   From this research study, it has been concluded that in the building domain, the Multi-objective optimization techniques can also be applied and used to find optimal strategies of retrofitting actions in an existing building and identifying the feasible retrofit material choice based on constraints which helps in decision-making and achieving the potential economic benefits of retrofitting.

(iii) The current study analyses the various cases of budget constraints and obtained optimized values of both Retrofitting Cost and Embodied Energy which shows that for different conditions, the method of MOO suitably works. The proper algorithm developed in the MATLAB application using Genetic Algorithm (GA) approach which helps in optimizing the objective functions and the data obtained for optimized values of both retrofitting cost and embodied energy are plotted in MATLAB.

(iv)   Through this technique, the decision-maker can enhance the sustainability of the building by taking informed decisions as well as improving the cost feasibility of the project which is an important criterion. With the informed decision, it helps the decision-makers to select the optimal retrofitting choices which not only helps in saving the retrofitting cost of the buildings but also makes the project environmentally and economically feasible.

(v)   In future, the overall life cycle assessment of buildings can also be performed which is beneficial for the investment planners of the building.

References

1. Antipova E, Boer D, Gosalbez GG, Cabeza FL, Jimenez L (2014) Multi-objective optimization coupled with life cycle assessment for retrofitting buildings. Energy Build 82:92–99. https://doi.org/10.1016/j.enbuild.2014.07.001

2. Arpan DG, Roy M (2015) Comparing building material & embodied energy consumption between an old and a modern office building. J Mech Civil Eng (IOSR-JMCE) 12(2):36–43. https://doi.org/10.9790/1684-12233643

3. Asadi E, Silva GM, Antunes HC, Dias L (2012) Multi-objective optimization for building retrofit strategies: A model and an application. Energy Build 44:81–87. https://doi.org/10.1016/j.enbuild.2011.10.016

4. Bre F, Roman N, Fachinotti DV (2020) An efficient metamodel-based method to carry out multi-objective building performance optimizations. Energy Build 306:1–15. https://doi.org/10.1016/j.enbuild.2019.109576

5. Diakaki C, Grigoroudis E, Kabelis N, Kolokotsa D, Kalaitzakis K, Stavrakakis G (2010) A multi-objective decision model for the improvement of energy efficiency in buildings. Energy 35:5483–5496. https://doi.org/10.1016/j.energy.2010.05.012

6. Dixit MK, Lavy S, Abdagiri P (2020) The relationship of embodied energy and cost of buildings and building materials. EPiC Series in Built Environment, Associated Schools of Construction (ASC). In: Proceedings of the 56th Annual International Conference, vol 1, pp 454–462

7. Friedman C, Becker N, Erell E (2014) Energy retrofit of residential building envelopes in Israel: a cost-benefit analysis. Energy 77:183–193

8. García KI, Raslan R, Ruyssevelt P (2016) An exergy-based multi-objective optimisation model for energy retrofit strategies in non-domestic buildings. Energy 117:506–522. https://doi.org/10.1016/j.energy.2016.06.041

9. Gossard D, Lartigue B, Thellier F (2013) Multi-objective optimization of a building envelope for thermal performance using genetic algorithms and artificial neural network. Energy Build 67:253–260. https://doi.org/10.1016/j.enbuild.2013.08.026

10. Gunantara N (2018) A review of multi-objective optimization: Methods and its applications. Cogent Eng 5(1):1–16. https://doi.org/10.1080/23311916.2018.1502242

11. Jafari A, Valentin V (2017) An optimization framework for building energy retrofits decision making. Building Environ 115:118–129

12. Karmellos M, Kiprakis A, Mavrotas G (2015) A multi-objective approach for optimal prioritization of energy efficiency measures in buildings: model, software and case studies. Appl Energy 139:131–150

13. Lucon O, Ahmed ZA, Akbari USAH, Bertoldi P, Cabeza LF, Graham P, Brown M, Henry AF, Korytarova K, Ürge-Vorsatz D, Cabeza LF, Eyre N, Gadgil A, Harvey LD, Jiang Y, Liphoto E, Mirasgedis S, Murakami S, Parikh J, Pyke C, Vilariño M, Pichs-Madruga R, Sokona Y, Farahani E, Kadner S, Seyboth K, Adler A, Baum I, Brunner S, Eickemeier P, Kriemann B, Savolainen J, Schlömer S, von Stechow C, Zwickel T, Minx J (2014) Mitigation of climate change (Chap. 9). In: Buildings, Contribution of Working Group III to the Fifth Assessment Report of the Intergovernmental Panel on Climate Change

14. Praseeda KI, Reddy VB, Manic M (2015) Embodied energy assessment of building materials in India using process and input–output analysis. Energy Build 86:677–686. https://doi.org/10.1016/B978-0-12-409548-9.10188-5

15. International Finance Corporation (IFC) (2017) India construction materials database of embodied energy and global warming potential. Methodology Report

16. 2019 global status report for buildings and construction|Global Buildings Performance Network. https://library.gbpn.org/resource/2019-global-status-report-buildings-and-construction. Accessed 15 Oct 2021

17. Goldberg ED (1989) Goldberg genetic algorithm (Chap. 1). In: A gentle introduction to genetic algorithms. Addison-Wesley Publishing Company, pp 1–18

Use of IDA to Estimate Variations in Drift Demands of Irregular RCC Buildings

Nidhi J. Sitapra, Kunal P. Shukla, Tarak P. Vora, and Amit J. Thoriya

1 Introduction

Building frame configuration plays a critical role in the structural design from point of view of their seismic performance. The seismic behaviour of irregular buildings differs to a great extent as compared to regular configurations. Differential movements of different parts of the building generate unequal stresses in different members, causing extensive damage at the spots of stress concentration. There arises variation in the relative displacements of adjacent stories due to different geometric irregularities [1]. Also, ground motions that result from an earthquake rupture reflect the attributes of their seismic source such as the process of rupture, the travel path from source-to-site, and local site conditions. Therefore, the traits of ground motions nearer to an active fault significantly differ from the far-fault ones, which severely affects their damage potential. This leads to varied structural responses. So, to study the whole range of structural behaviour, analyzing the structures for different suits of ground motions is necessary as the traits of different types of ground motions differ extensively and that affects their damage potential [2]. Variations in drift ratios along the height of the buildings show the portion along the height that is more prone to suffer extensive drift and consequent damage thereof. Inter-storey displacement values are more important than the total displacement values as the former shows

N. J. Sitapra (✉)
Masters in Structural Engineering, Anjar, Kutch, Gujarat 370110, India
e-mail: nidhijaisheelsitapra313@gmail.com

K. P. Shukla · T. P. Vora
Department of Civil Engineering, Marwadi University, Morbi Road Gauridad, Rajkot, Gujarat 360003, India

A. J. Thoriya
Department of Civil Engineering, Marwadi Education Foundation Group of Institutions, Morbi Road Gauridad, Rajkot, Gujarat 360003, India

the relative displacement between two adjacent floors, which is the main cause of damage locally as well as globally [3]. As per FEMA 356 [4], there are numerous methods of seismic analysis of structures, but non-linear dynamic analysis gives more realistic results compared to other methods [5]. Incremental dynamic analysis (IDA) is an emerging process used to analyse the non-linear behaviour of structures. IDA involves evaluating the structural response and its seismic demands when subjected to increasing intensities of seismic energy input to the structure [6]. This study is focussed on comparing variations of inter-storey drift demands in geometrically irregular RCC buildings when subjected to different suits of ground motions.

2 Modelling Assumptions and Analysis Parameters

One regular and 3 irregular 10-storeyed RCC frames, as shown in Fig. 1, were considered for the analysis.

The following are the design details of the buildings:

- The bay sizes in both the directions were taken as 4 and 3 m storey height.
- Loads and load combinations were applied as mentioned in IS 875 part 1, 2, and 5 [7]
- The structures were assumed to be situated in seismic zone-V as per IS 1893:2016 [8]
- Frame hinges P-M2-M3 hinges for columns and M3 hinges for beams were assigned.
- All the frames were designed as bare frames.
- Diaphragm action was taken into account considering RCC slabs.
- All beams and columns were designed incorporating of the effective/cracked section clause introduced in the latest revision of IS 1893:2002, that is, IS 1893:2016, considering effective or gross moment of inertia to evaluate the flexural stiffness/rigidity of beams and columns for the irregular buildings considered.
- All models were designed in SAP2000 software, as per IS 456:2000 [9] to possess following member dimensions:

As stated, to study the whole range of structural behaviour, analyzing the structures for different suits of ground motions is necessary as the traits of different types of ground motions differ extensively and that affects their damage potential [2]. Therefore, a database was compiled to comprise of far-fault, near-fault, and fling-step ground motions. Details of time history records used in the analysis are mentioned in Table 2.

Table 1 Member dimensions for all buildings

Beams	230 mm × 450 mm	For all storeys
Columns	450 mm × 450 mm	For the bottom 5 storeys
	350 mm × 350 mm	For the top 5 storeys
Slab thickness	150 mm	For all storeys

Table 2 Ground motions

	Earthquake	Magnitude	Recording station	PGA (g)
Far-field	Loma Prieta, 1989	6.9	Capitola (capx)	0.42
	Chamoli, 1999	6.4	Gopeshwar (chamoli)	0.36
	Imperial Valley, 1940	6.95	El Centro Array #9 (elcx)	0.31
	Superstition Hills, 1987	6.7	El Centro Imp. Co. Centre (iccx)	0.51
	Northridge, 1994	6.7	Northridge-Saticoy St. (stcx)	0.53
Near-field	Imperial Valley, California, 1979	6.6	El Centro Array #5 (EQ11)	0.37
			El Centro Array #7 (EQ21)	0.46
	Northridge, California, 1994	6.7	Newhall (EQ31)	0.72
			Rinaldi (EQ51)	0.89
			Sylmar (EQ61)	0.73
Fling-step	Chi-chi, 1999	7.6	TCU052_NS	0.44
			TCU068_EW	0.50
			TCU074_EW	0.58
			TCU084_NS	0.42
			TCU129_NS	0.61

3 Methodology: Incremental Dynamic Analysis

Incremental dynamic analysis (IDA) is an emerging process used to analyse the non-linear behaviour of structures. IDA involves evaluating the structural response and its seismic demands when subjected to increasing intensities of seismic energy input to the structure [6, 10, 11].

General procedure of IDA consists of performing a series of non-linear runs of time history analysis on the structural model using the resultant scaled accelerograms of the selected time histories, using a set of increasing scale factors. Then, plotting IDA curves showing variation of intensity measures (IM) at increasing damage measure (DM), applying limit states there-on and interpreting the curve behaviour.

Here, IDA is used to estimate the variations in the inter-storey drift demands along the height of the buildings, to develop drift profiles at increasing seismic excitation intensities [12]. And to depict the exact intensity near which the drifts exceed the desired performance level by applying limit states on the drift profiles.

3.1 Analysis Runs

All 4 RCC buildings were modelled in SAP2000 as bare frames 3D models. A database was compiled to comprise a total of 15 time histories, 5 each belonging to of far-fault, near-fault, and fling-step ground motions. This summed up to a total of 60 models for 4 buildings subjected to 15 time histories.

Peak ground acceleration (PGA) values were considered as the intensity measure (IM) to be scaled. The scale factors to scale the PGA ranged from 0.1 to 2 at equal increments of 0.1, for far-fault and near-fault time histories, and 0.1 to 1.5, at equal increments of 0.1, for fling-step time histories.

Incremental dynamic analysis was performed by subjecting the models to a series of non-linear time history (NLTHA) runs using accelerograms scaled using increasing factors.

3.2 Post-processing

- Critical frames were identified based on the onset of formation of initial yield hinges. Storey displacements for the first mode and the hinge formation pattern were extracted considering deformed shape envelope for relative displacement for each of the load cases.
- Drift profiles were plotted for each time history record, to show the portion along the height that is more prone to suffer extensive drift and consequent damage thereof.
- Applying initial yielding as limit state on the drift profiles, the exact storeys where the drifts exceed the desired performance were identified.
- Applying limit states on the drift profiles to depicted the exact intensity near which the drifts exceed the desired performance level, and by what amounts the drifts exceed.

3.3 Considerations

- In all 3D models, 2D critical frames have been identified based on the onset of formation of initial yield hinges, that is, the frames where members reach their yield capacities first as compared to other frames of the building.
- For those cases where collapse was not reached, critical frames were identified as those that experienced maximum lateral displacement at top storey.
- The below mentioned 2D frames in each particular 3D model were considered for analysis (critical frames, marked on building models with red colour in figures shown in result section):

    – the frames at the re-enterant corners

– The frames at the offset or cut-out that create the geometric irregularities

4 Results

After completion of the analysis runs, storey displacements for the first mode and the hinge formation pattern were extracted considering deformed shape envelope for relative displacement for each of the load cases. From the roof displacement of each storey, the inter-storey drifts and the respective maximum inter-storey drift ratios were computed for each load case. At each PGA increment, for the critical frames, drift ratios profiles along the height of the buildings were plotted for each time history record, to show the portion along the height that is more prone to suffer extensive drift and consequent damage thereof. This summed up to a total of 60 such incremental drift profile graphs for 4 buildings subjected to 15 time histories. Of all resulting 60 graphs, one representative set of graphs for all 4 buildings subjected to one time history from each suit of ground motion are shown in Figs. 2, 3 and 4. Others similarly follow.

Hinge formation patterns were observed to identify critical frames and the sections reaching collapse limits. The performance limits, immediate occupancy (IO), life safety (LS), and collapse prevention (CP) based on the inter-storey drift are identified 1, 2, and 4% in FEMA 356. Here, collapse limits were determined as onset of collapse at initial yielding as per hinge rotation capacities defined in FEMA 356, that is, when initial yielding starts in the model. Drift ratios of the range of values mentioned in Table 3 were observed to have reached at various PGA levels.

Table 4 shows the comparison of PGA values where the frames reached the initial yielding for different time history records for its comparison with the IS 1893 (2016) code-indicated seismic demands to account for the specific characteristics of the actual local seismicity.
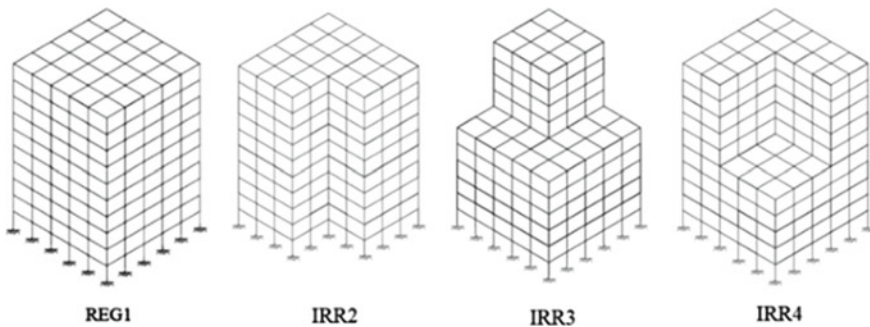
Fig. 1 Considered building configurations
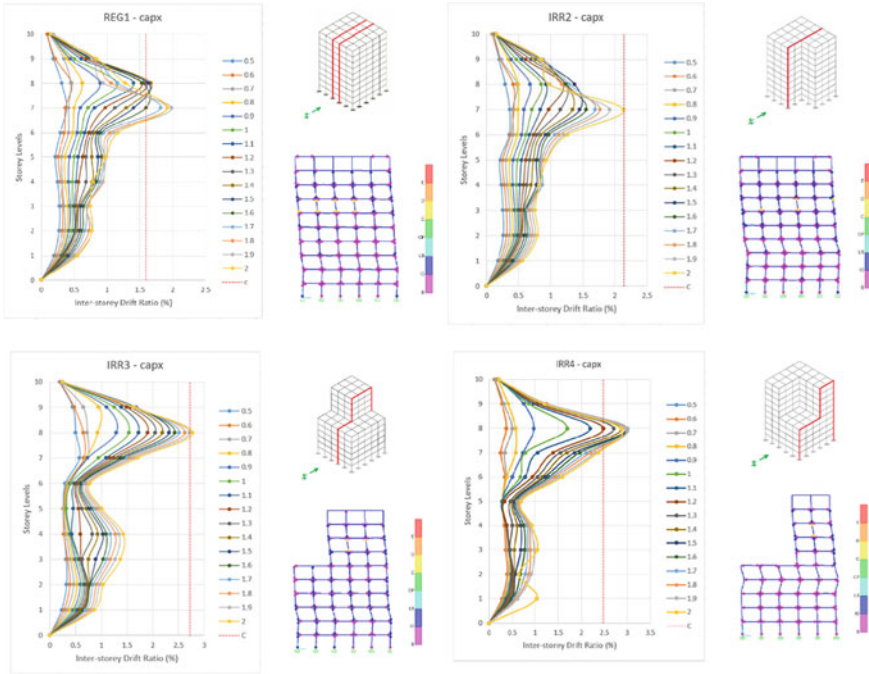
Fig. 2 Drift ratio profiles for models subjected to far-field time history record "capx"

5 Discussion of Results

The hinge formation patterns showed that the storeys having extensive drifts compared to other storeys tended to reach the collapse limit first. The results discussed here are for the critical frames.

From the comparison of drift profiles along the height of buildings showing the response and demand of each storey in terms of inter-storey drift ratios, it was observed that, by increasing the PGA, the inter-storey drift ratios increase from a linear to non-linear range. Considering the mean of the records that showed the highest damage, inter-storey drift ratio ranges at various PGA levels have been compared from the 60 drift profile graphs that resulted from the analysis.

The relationship between earthquake intensity and the drift ratio for different irregularities has been observed to follow the below described trend:

- For REG1, far-field records showed inter-storey drift ratios of the range of around 2% for PGA up to 0.5 g and 1.6% at 0.75 g and 1.75% at 1 g. Near-field records showed inter-storey drift ratios of the range of around 2% for PGA up to 0.5 g and 2.5% at 0.75 g and up to 3.75% at 1 g. Fling-step records showed inter-storey drift ratios of the range of around 3.5 to 5% for PGA up to 0.5 g and up to 11% at 0.75 g.
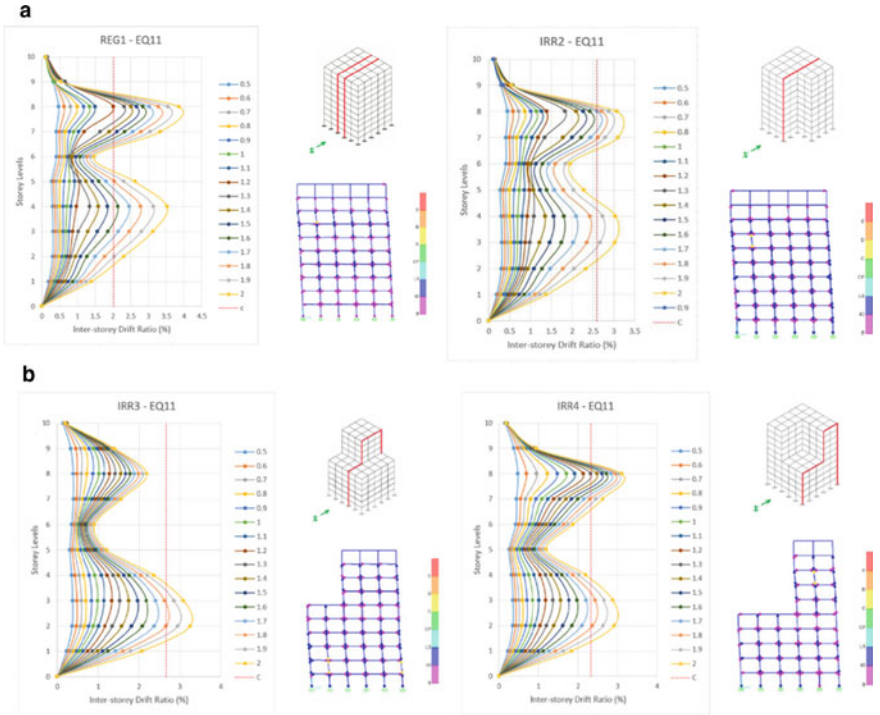
Fig. 3 **a** Drift ratio profiles for models subjected to near-field time history record "EQ11", **b** drift ratio profiles for models subjected to near-field time history record "EQ11"

- For IRR2, far-field records showed inter-storey drift ratios of the range of around 1.75% for PGA up to 0.5 g and 2% at 0.75 g and 2.2% at 1 g. Near-field records showed inter-storey drift ratios of the range of around 2% for PGA up to 0.5 g and 2.5% at 0.75 g and up to 3.25% at 1 g. Fling-step records showed inter-storey drift ratios of the range of around 3.5% for PGA up to 0.5 g and up to 13% at 0.75 g.
- For IRR3, far-field records showed inter-storey drift ratios of the range of around 2.25% for PGA up to 0.5 g and 2.75% at 0.75 g and around 3% at 1 g. Near-field records showed inter-storey drift ratios of the range of around 2% for PGA up to 0.5 g and 2.6% at 0.75 g and up to 3% at 1 g. Fling-step records showed inter-storey drift ratios of the range of around 2 to 5% for PGA up to 0.5 g and up to 11.5% at 0.75 g.
- For IRR4, far-field records showed inter-storey drift ratios of the range of around 2.5% for PGA up to 0.5 g and 2.6% at 0.75 g and about 3% at 1 g. Near-field records showed inter-storey drift ratios of the range of around 2.4% for PGA up to 0.5 g and 2.75% at 0.75 g and up to 3.5% at 1 g. Fling-step records showed inter-storey drift ratios of the range of around 2 to 4% for PGA up to 0.5 g and up to 10% at 0.75 g.
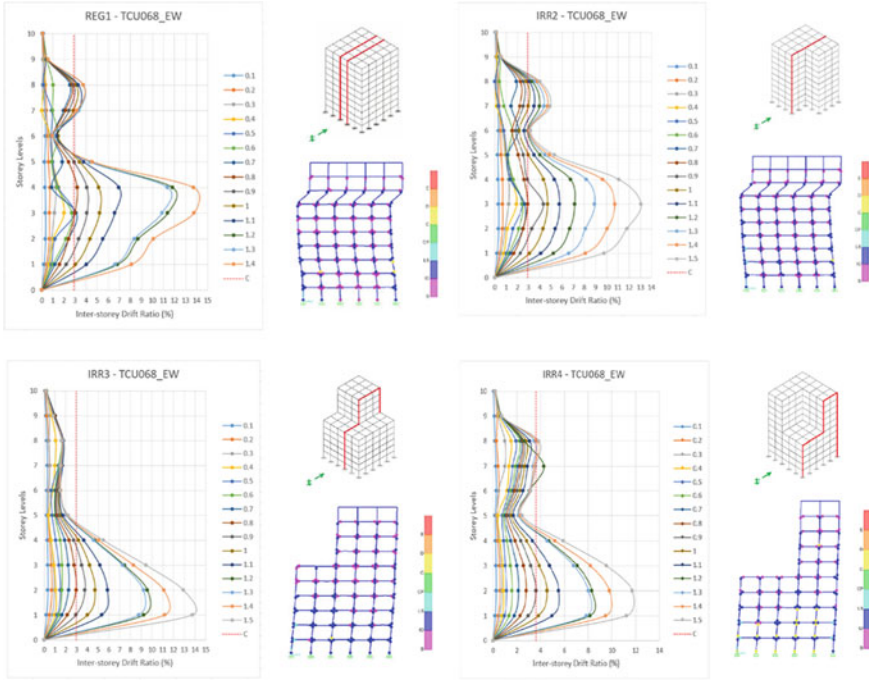
Fig. 4 Drift ratio profiles for models subjected to fling-step time history record "TCU068_EW"

Table 3 Drift values at various PGAs

Type of ground motion	PGA (g)	Drift ratios (%)			
		REG1	IRR2	IRR3	IRR4
Far-field	0.50	2.00	1.75	2.25	2.50
	0.75	1.60	2.00	2.75	2.60
	1.00	1.75	2.20	3.00	3.00
Near-field	0.50	2.00	2.00	2.00	2.40
	0.75	2.50	2.50	2.60	2.75
	1.00	3.75	3.25	3.00	3.50
Fling-step	0.50	3.50	3.50	2–5	2–4
	0.75	11.00	13.00	11.50	10.00

- When subjected to far-field ground motions and near-field ground motions without fling component, reached the collapse limits at PGA values well above the PGA of maximum considered earthquake (MCE) PGA = 0.36 g and the same buildings when subjected to fling-step ground motions, reached the collapse limit at PGA values below that of MCE but above the PGA of design basis earthquake (DBE)

Table 4 PGA values at initial yielding

Time history		PGA at which yield limit is reached (g)			
		REG1	IRR2	IRR3	IRR4
Far-field time histories	capx	0.672	0.84	0.798	0.504
	chamoli	–	–	–	0.718
	elcx	–	–	–	–
	iccx	–	–	–	–
	stcx	–	–	–	–
Near-field time histories	EQ11	0.444	0.629	0.666	0.481
	EQ21	0.690	0.874	0.874	0.598
	EQ31	–	–	–	–
	EQ51	–	–	–	–
	EQ61	–	–	–	–
Fling-step time histories	TCU052_NS	0.307	0.351	0.351	0.395
	TCU068_EW	0.250	0.401	0.401	0.451
	TCU074_EW	0.293	0.352	0.586	0.410
	TCU084_NS	0.420	0.462	–	0.546
	TCU129_NS	0.549	–	0.793	0.610

Note Empty cells in Table 4 mean that the frame did not reach collapse limit even when the original accelerogram was scaled up to twice the PGA for far-field and near-field time histories and up to 1.5 times the PGA for fling-step time histories

PGA = 0.18 g. (DBE and MCE as per the design peak ground acceleration (PGA) values as defined by IS 1893 for seismic Zone-V).

The critical storey levels identified based on the behaviour of different irregularities in the buildings for different suits of ground motions have been observed as follows:

- For far-field ground motions, 2nd, 3rd, 4th storeys showed a significant demand in REG1 and IRR2 and in IRR3 and IRR4 2nd, 3rd, 7th, 8th storeys showed a higher demand.
- For near-field ground motions, 1st, 2nd, 3rd, 4th storeys showed a significant demand in REG1 and IRR2 and in IRR3 and IRR4 2nd, 3rd, 7th, 8th storeys showed a higher demand.
- For fling-step ground motions, 7th and 8th storeys showed a significant demand all the 4 buildings.
- It was observed that drift demands in the upper stories were much more sensitive to irregularities in the lower stories than the response of lower stories affected by irregularities in the upper stories.
- Which means, near-field and fling-step ground motions affected the storeys with irregularities the most. And far-field ground motions affected the lower stories the most, irrespective of the presence or absence of any irregularities.

- Far-field ground motions caused higher inter-storey drift at higher storeys and near-field and fling-step ground motions caused higher inter-storey drift at lower storeys. This effect is a result of the proximity of the building to the epicentre of the ground motion.

6   Conclusions

Using incremental dynamic analysis, drift demands along height of the buildings were evaluated for various multi-storey RCC buildings possessing plan and vertical geometric irregularities, when subjected to various suits of ground motions. The results showed a wide range of behaviour of different irregular buildings due to different suits of ground motions, and also the parts of the buildings experiencing significant demand.

- For far-field and near-field ground motions, lower 4 storeys showed a significant demand in REG1 and IRR2 and in IRR3 and IRR4 the lower 4 and upper 3 storeys showed a higher demand. For fling-step ground motions, upper storeys showed a significant demand all the 4 buildings.
- Which means, near-field and fling-step ground motions affected the storeys with irregularities the most. And far-field ground motions affected the lower stories the most, irrespective of the presence or absence of any irregularities.
- All the models when subjected to far-field ground motions and near-field ground motions without fling component, reached the collapse limits at PGA values well above the PGA of maximum considered earthquake (MCE) and the same buildings when subjected to fling-step ground motions, reached the collapse limit at PGA values below that of MCE but above the PGA of design basis earthquake (DBE).

References

1. Dutta SC, Das P, Sengupta P (2017) Seismic behaviour of irregular structures. Struct Eng Int 27(4):526–545
2. Raji F, Naeiji A (2019) Performance of concrete mrf at near-field earthquakes compared to far-field earthquakes. Civil Eng J 5(4):759–766
3. Vamvatsikos D, Jalayer F, Cornell CA (2003) Application of incremental dynamic analysis to an RC-structure. In: FIB Symposium on Concrete Structures in Seismic Regions, Athens, Jan 2003
4. FEMA 356 (2000) Prestandard and commentary for the seismic rehabilitation of buildings, Federal Emargency Management Agency; Washington, D.C.
5. Hosseini M, Hashemib B, Safib Z (2017) Seismic design evaluation of rcc buildings for near-source earthquakes by using nonlinear time history analyse. In: X International conference on structural dynamics, EURODYN 2017, Procedia Engineering, vol 199, pp 176–181
6. Vamvatsikos D, Cornell CA (2002) Incremental dynamic analysis. Earthquake Eng Struct Dyn 2002(31):491–514

7. IS 875 Code of Practice for Design Loads (Other Than Earthquake) For Buildings And Structures, Part 1: Dead Loads—Unit Weights Of Building Material And Stored Materials, Part 2: Imposed Loads, Part 5: Special Loads And Combinations, Bureau of Indian Standards; Manak Bhavan, 9 Bahadur Shah Zafar marg, New Delhi, India
8. IS 1893 Part-1 (2016) Criteria for earthquake resistant design of structures. Bureau of Indian Standards, Manak Bhavan, 9 Bahadur Shah Zafar marg, New Delhi, India
9. IS 456:2000. Plain and Reinforced Concrete—Code of Practice, Bureau of Indian Standards; Manak Bhavan, 9 Bahadur Shah Zafar marg, New Delhi, India
10. Vamvatsikos D, Cornell CA (2002) The incremental dynamic analysis and its application to performance-based earthquake engineering. In: Proceedings of the 12th European conference on earthquake engineering 40, London, UK, Sept 2002
11. Vamvatsikos D, Cornell CA (2004) Applied incremental dynamic analysis. Earthquake Spectra, Earthquake Eng Res Inst 20(2):523–553
12. Shimpi V, Bhat G (2017) Performance evaluation of RC frame structure through incremental dynamic analysis. Indian J Sci Technol 10(3):1–8

A Simplified Incremental Dynamic Analysis Procedure Using SAP2000

Nidhi J. Sitapra

1 Introduction

According to FEMA 356, [1] a building can be analysed using linear static procedure (LSP), linear dynamic procedure (LDP), nonlinear static procedure (NSP) or nonlinear dynamic procedure (NDP) as per the suitability [2]. Buildings possessing torsional irregularities, non-orthogonal systems and tall buildings require to be analysed by dynamic procedures. Nonlinear dynamic analysis is the only method that depicts the actual behaviour of a structure during an earthquake, because the calculated internal forces are reasonable approximations of those expected during the design earthquake, as the numerical model accounts directly for effects of material inelastic response. Performance-based earthquake engineering (PBEE) approach helps derive the design of structures for a predictable seismic performance. From various NDPs, one such parametric analysis method is incremental dynamic analysis (IDA) which is emerging as an accurate tool in the field of PBEE [3].

IDA involves performing multiple nonlinear dynamic analyses of a structural model under a suite of ground motion records, each scaled to several levels of seismic intensity to force the structure through the entire range of behaviour, from elastic to inelastic and finally to global dynamic instability, where the structure reaches its ultimate capacity and essentially experiences collapse or to the extent where it reaches a certain targeted performance level [4].

As compared to other methods, IDA gives a better understanding of the changes in the nature of the structural response as the intensity of ground motion increases. Due to the dynamic and nonlinear nature of the earthquake, the results of this method in comparison with the other types of analyses are closer to the reality of structural behaviour [5]. IDA is not widely used in general, but while designing a building

N. J. Sitapra (✉)
Structural Engineer, Anjar, Kutch, Gujarat 370110, India
e-mail: nidhijaisheelsitapra313@gmail.com

for earthquake prone zones, after designing the buildings using codal provisions, it can prove to be a better decision to analyse its behaviour using performance-based analysis [6]. Also, combined IDA curves graph for different frame configurations subjected to one time history at a time, provides ease to compare the seismic behaviour of different alternative frame configurations for any proposed building.

2   Research Significance

Despite the fact that, IDA produces the most realistic results, complexities of the procedure as well as different software and system configuration required, and render it to be a computationally expensive method that is considered mostly for high cost and important structures [7]. Past literature on IDA has described the use of various different software to perform IDA analyses and studies, which are enlisted below:

1. Open Sees—a software framework for developing applications to simulate earthquakes on structures to analyse seismic performance of structural and geotechnical systems [8, 9].
2. WAVEGEN—software for conversion of the past ground motion records to match the required soil spectrum [10].
3. Ide CAD Structural 5—an integrated analysis, design and detailing software for specifically developed for tall RCC buildings [11].
4. DRAIN-2DX and DRAIN2D-UW that are modified versions of DRAIN-2D—a computer programme specifically developed to perform for the seismic analysis of inelastic two-dimensional structures [3].
5. NONLIN—software specifically for nonlinear dynamic response history analysis of structures incorporating the material and geometric nonlinearities in the structure [11].
6. IIIDAP—interactive interface for incremental dynamic analysis procedure, a software developed to perform specifically IDA only [2].
7. Seismic signal—earthquake software for signal processing of strong motion data, to scale the time history accelerograms.
8. Seismic structure—software for static and dynamic nonlinear analysis of framed structures.

As compared to the aforementioned software required for performing IDA, SAP2000 being a more commonly used tool, most of the structural engineers are well conversant with its use. Using SAP2000, nonlinear time history analysis (NLTHA) can be performed considering material and geometric nonlinearities in the structural members using hinges and modifiers. The time history functions can also be scaled up or down using scale factors in the nonlinear direct integration time history load case. Also, a series of NLTHA load cases can be defined and can be run parallelly using SAP2000 v21.1.0 and higher versions. Thus, rendering SAP2000 to be a better alternative for structural engineers to analyse buildings by IDA method.

3   IDA Basics

IDA procedure basically consists of performing nonlinear time history analysis of structures subjected to seismic excitation with certain intensity measure (IM) and record the damage measure (DM) of the structure for that intensity measure. Then, repeating the same by increasing the seismic excitation progressively taking series of increments and continue increasing the IM until a certain desired targeted performance level is reached. And then, plotting the variation of the DM as function of the IM is known as the incremental dynamic analysis (IDA) curve.

Various control parameters of IDA are as follows:

1. Scale Factors: A non-negative scalar multiplicatively applied to the acceleration time history to obtained the scaled accelerograms as a one-to-one mapping from the original accelerogram.

    Linearly, increasing scale factors at an equal interval, the simplest way to perform IDA is considered here.

2. Intensity Measure (IM): A monotonic scalable ground motion intensity measure consists of a function that depends on the original unscaled accelerogram and monotonically increases with the increasing set of scale factors. Various scalable intensity measures (IMs) are the peak ground acceleration (PGA), peak ground velocity and 5% damped spectral acceleration at the structure's first-mode period (Sa (T1; 5%)).

    Here, PGA is considered as the IM.

3. Damage Measure (DM): It is the structural state variable, a non-negative scalar, that characterizes the additional response of the structural model due to a prescribed seismic loading. It is the output of the corresponding nonlinear dynamic analysis. Various damage measures (DMs) are base shear, node rotations, peak storey ductilities, peak roof drift, peak inter-storey drift angles or the maximum peak inter-storey drift angle.

Inter-storey displacement values are more important than the total displacement values as the former shows the relative displacement between two adjacent floors, which is the main cause of damage. Therefore, maximum inter-storey drift ratios% (MIDR) have been chosen as the damage measure (DM) for the IDA in present work. Peak ground acceleration (PGA) was selected as the intensity measure (IM).

4   Simplified IDA Procedure In SAP2000

The entire IDA analysis can be mainly divided into following activities—development of the analytical model in the tool (here, SAP2000), extracting the analysis output from the tool and post-processing of that output data. The step by step detailed procedure to perform IDA in SAP2000 is described below:

4.1 Development of the Analytical Model

The step by step detailed procedure to perform IDA on RCC bare frames is described below:

STEP 1: Selection of ground motion records:

It is recommended to select and download time histories of earthquakes that have occurred at regions having similar geotechnical parameters as the site under consideration. In this way, the need of converting the response spectrum of the ground motion record to match the targeted spectrum of the site gets eliminated.

The damaging potential varies with the characteristics of ground motions for different suits, namely far field, near fault, forward directivity and fling-step ground motions [12]. Thus, time history records belonging to different suits should be selected to obtain the wide range of behaviour of the structure.

STEP 2: Modelling in SAP2000 for Nonlinear analysis:

One model for each building subjected to one time history function at a time to be prepared for simplicity in dealing with the analysis settings and results data. Bare frame model with slab to be prepared and designed as per codal design in SAP2000. For taking into account, the effective moment of inertia, the beam and column sections to be modelled by applying section modifiers in the "frame property/stiffness modification factors" dialogue box. For nonlinear analysis, frame hinges P-M2-M3 hinges for columns and M3 hinges for beams to be assigned in the members at a relative distance of 0.1 and 0.9. Hinge properties can be defined manually or as auto hinges option available in the "hinge assignment data" dialogue box.

STEP 3: Defining IDA load cases:

Time history function is to be defined for one particular time history, and for that time history, IDA load cases are to be defined along with the fundamental load cases.

As shown in Fig. 1, in the "load case data" dialogue box, geometrical nonlinearity parameter to be set to "P-delta plus large displacement". Analysis type to be selected as "nonlinear", solution type as "direct integration", history type as "transient" and initial conditions as "zero initial conditions—start from unstressed state". Now, selecting the predefined time history function, in the scale factor field, a numerical factor is to be entered to scale the time history function. Two scale factors are to be multiplicatively applied for each load case. One factor is the IDA scale factor to scale the accelerogram, say 0.1, and another factor to convert the unit of the accelerogram to match the units set in SAP2000 model. Thus, the intensity measure (IM), that is PGA of the accelerogram can be scaled directly in SAP2000 itself. Number of output time steps to be entered equal to the duration of accelerogram divided by the time period of the building. And output step size is equal to the time period of the building. Similarly, a series of load cases to be defined for all the successive scale factors of IDA, say 0.2, 0.3, 0.4…. Thus, a series of nonlinear direct integration, time history load cases are to be defined for each scale factor, as shown in Fig. 2.
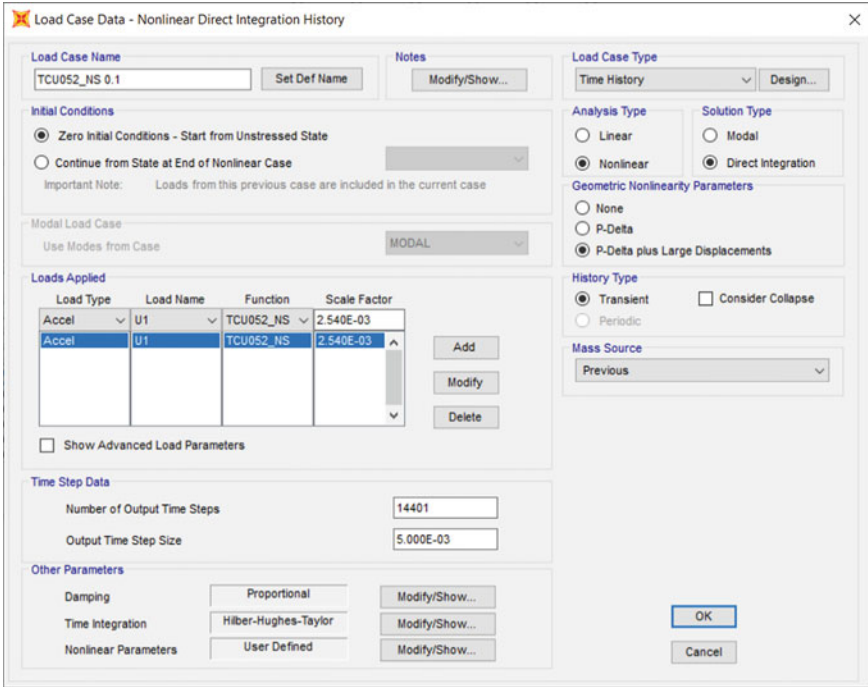
Fig. 1 "Load case data" dialogue box
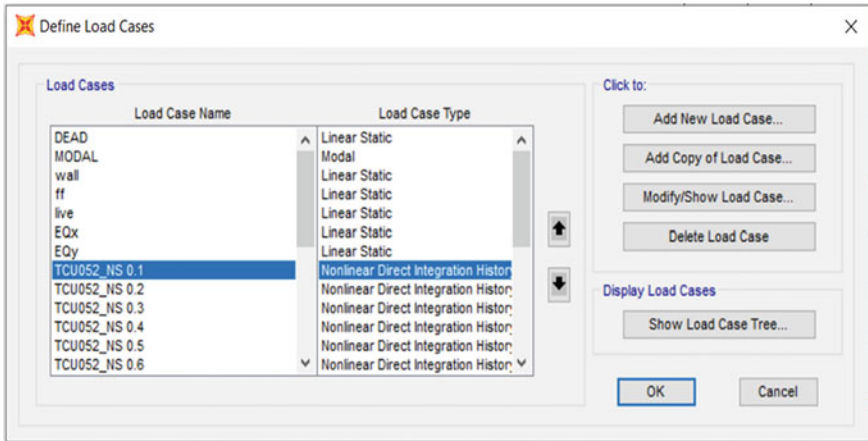
Fig. 2 "Define load cases" dialogue box

STEP 4: Performing the Analysis runs:

As said in STEP 3, for a particular time history function, there will be number of nonlinear time history analysis (NLTHA) load cases defined. For each load case, SAP2000 carries out one analysis run. So, considering IDA scale factors ranging say from 0.1 to 2.0 at equal increments of 0.1, 20 NLTHA runs to be carried out for one particular time history.

The same procedure to be repeated for a number of the time histories. Each run takes approximately 45 min in a system having the configuration Intel® Core™ i5-8250U CPU @ 1.80 GHz 4 cores, with 12.0 GB RAM. SAP2000 v21.2.0 and higher versions provide an option to run multiple load cases in parallel and also connecting multiple computers in parallel, thus minimizing the time requirement for the analysis.

4.2 Output Data Extraction and Post-processing

STEP 5: Extraction of analysis results data:

After completion of the analysis runs, storey displacements for the first mode, considering deformed shape envelope for relative displacement for each of the load cases, to be extracted to MS Excel.

The index of seismic demand is used here, that is, inter-storey drift ratio for each floor levels to be calculated as per the following expression (Figs. 3 and 4):

$$\text{Drift Ratio } (\%) = \frac{\text{Upstairs displacement} - \text{Downstars Displacement}}{\text{Storey Height}} \times 100 \quad (1)$$

Fig. 3 Specimen MIDR% excel sheet

	A	B	C	D	E	F	G
1	scale factor		0.1		0.2		0.3
2	storey	u1 disp	drift ratio	u1 disp	drift ratio	u1 disp	drift
3	10	104.64	0.103667	202.25	0.164667	269.16	
4	9	101.53	0.256	197.31	0.486667	264.3	0.59
5	8	93.85	0.408667	182.71	0.749333	246.58	0.94
6	7	81.59	0.495	160.23	0.767667	218.19	
7	6	66.74	0.387	137.2	0.674667	191.52	
8	5	55.13	0.323	116.96	0.66	167.25	0.93
9	4	45.44	0.375667	97.16	0.878	139.16	
10	3	34.17	0.417667	70.82	0.953	99.29	1.35
11	2	21.64	0.431333	42.23	0.857	58.75	1.13
12	1	8.7	0.29	16.52	0.550667	24.57	
13	GL	0		0		0	
14	max drift ratio	0.495		0.953		1.351333	
15							
16							
17	scale factor		1.1		1.2		1.3
18	storey	u1 disp	drift ratio	u1 disp	drift ratio	u1 disp	drift
19	10	584.69	0.214333	685.2	0.223333	796.73	

	A	B	C	D	E	F	G	H	I	J
1	x	y	x	y	x	y	x	y	x	y
2	TCU052_NS		TCU068_EW		TCU074_EW		TCU084_NS		TCU129_NS	
3	max story drift	PGA	max story drift	PGA	max story drift	PGA	max story drift	PGA	max story drift	PGA
4	0	0	0	0	0	0	0	0	0	0
5	0.495	0.04384	0.332333333	0.05008	0.378333333	0.05859	0.153666667	0.042	0.149666667	0.061
6	0.953	0.08768	0.704333333	0.10016	0.808333333	0.11718	0.307333333	0.084	0.299333333	0.122
7	1.351333333	0.13152	0.943333333	0.15024	1.720333333	0.17577	0.46	0.126	0.449666667	0.183
8	1.539	0.17536	1.088333333	0.20032	1.163666667	0.23436	0.605	0.168	0.606	0.244
9	1.533333333	0.2192	1.630333333	0.2504	1.191	0.29295	0.756333333	0.21	0.765	0.305
10	1.966333333	0.26304	1.659666667	0.30048	2.518	0.35154	0.905666667	0.252	0.938	0.366
11	2.414666667	0.30688	2.270333333	0.35056	1.844333333	0.41013	1.063	0.294	1.120666667	0.427
12	2.622666667	0.35072	2.966333333	0.40064	2.136666667	0.46872	1.213666667	0.336	1.286666667	0.488
13	2.510333333	0.39456	3.778666667	0.45072	2.222	0.52731	1.370333333	0.378	1.442333333	0.549
14	2.470666667	0.4384	4.728	0.5008	2.444	0.5859	1.526	0.42	1.565333333	0.61
15	3.176	0.48224	5.872	0.55088	2.69	0.64449	1.682333333	0.462	1.666666667	0.671
16	3.935666667	0.52608	9.587	0.60096	2.809333333	0.70308	1.886666667	0.504	1.741333333	0.732
17	4.752333333	0.56992	9.223666667	0.65104	2.927666667	0.76167	2.102333333	0.546	1.788333333	0.793
18	5.911666667	0.61376	11.186	0.70112	3.226	0.82026	2.353666667	0.588	1.811333333	0.854
19	7.278333333	0.6576	13.75233333	0.7512	3.425333333	0.87885	2.614	0.63	1.821333333	0.915
20										

Fig. 4 Specimen PGA versus MIDR excel sheet

STEP 6: Plotting IM Versus DM IDA curves:

From the roof displacement of each storey, the inter-storey drifts and the respective maximum inter-storey drift ratios to be computed for each load case. IDA curves, showing the variation of DM for increasing values of IM to be plotted for each time history. This results into a single record IDA curve, PGA versus MIDR. Combining a number of such single record IDA curves into one graph, results into multi-record IDA curves, as shown in Fig. 5.

Similarly, when different alternative frame configurations are thought of for any
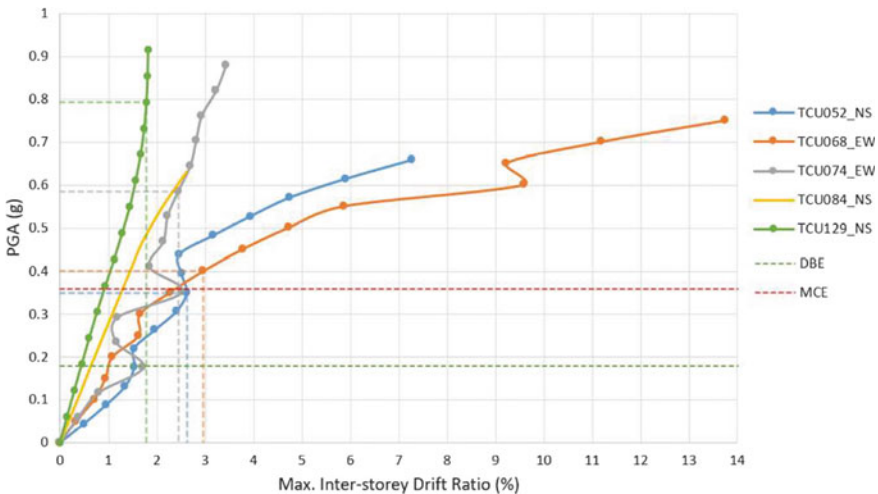
Fig. 5 Specimen multi-record IDA curve
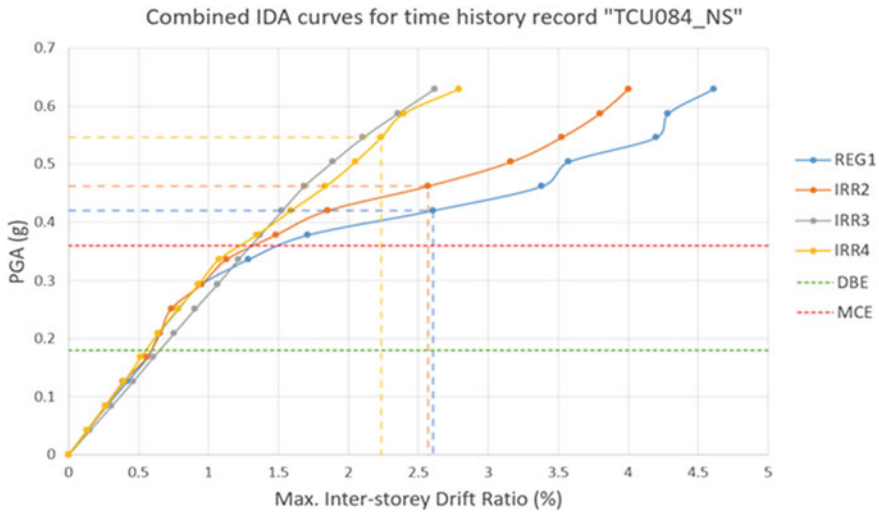
Fig. 6 Specimen combined IDA curve comparing different frame configurations of a proposed building

proposed building, the combined IDA curves as shown in Fig. 6 can facilitate comparison of the seismic behaviour for different frames under the effect of one time history at a time.

STEP 7: Plotting Drift profiles:

Drift ratio profiles showing the variation of inter-storey drift ratios along the height of the building to be plotted at every increment for each time history record.

Drift profiles to be plotted for the critical frames identified based on the onset of formation of initial yield hinges, that is, the frames where members reach their yield capacities first as compared to other frames of the building. And for those cases, where initial yielding is not reached, critical frames to be identified as those that experienced maximum lateral displacement at top storey (Fig. 7).

Thus, the results, obtained from the data extracted from this simplified incremental dynamic analysis procedure elucidated here, can be represented in the form of:

- Maximum inter-storey drift ratios at respective PGA values (for each building subjected to each time history).
- PGA versus max. inter-storey drift ratio IDA curves (time history-wise combined IDA curves comparing behaviour of all four buildings).
- Drift ratio profile along the height of building at each PGA increment (for each building subjected to each time history).
- Critical frames and sections shown by hinge formation patterns (for each building subjected to each time history).
- PGA versus max. inter-storey drift ratio IDA curves (building-wise multi-record IDA curves comparing behaviour due to different time histories).
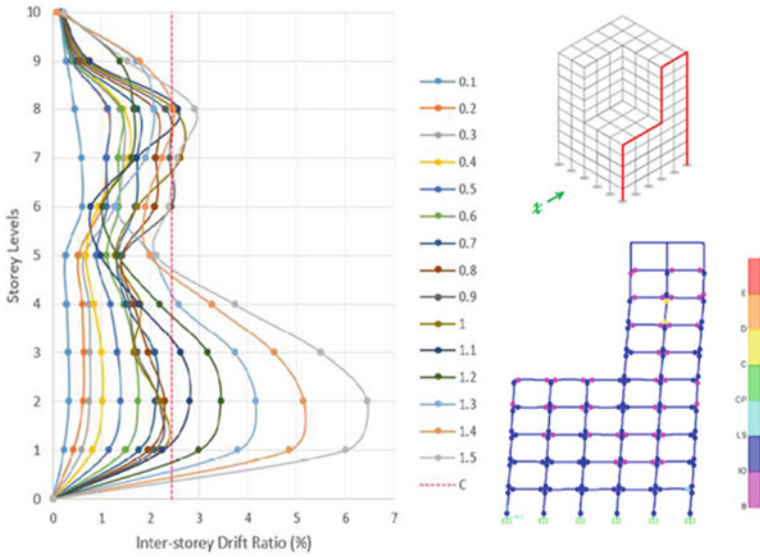
Fig. 7 Specimen drift profile graph

STEP 8: Interpreting results:

- Applying limit states on the IDA curves shows when the building reaches or crosses a certain targeted performance level.
- Applying limit states on the drift profiles shows when and at which storey levels the building reaches or crosses a certain targeted performance level. Thus, critical storeys can be identified.
- Critical members that reach or cross a certain targeted performance level can be identified by observing the hinges formed in the model.

5 Conclusion

IDA being a computationally expensive and cumbersome method is less resorted to in general. As a step by step narrative to carry out IDA in SAP2000, the paper can motivate the use of incremental dynamic analysis among the structural engineers for performance-based design of structures, which is more accurate compared to codal design. Considering the use of an easy-to-scale controlling parameter as intensity measure (IM), and scaling it within SAP2000 itself, the described procedure eliminates the requirement of an additional software for scaling the time histories. Results in the form of IDA curves help in identifying the exact intensities at which a certain targeted performance level is reached. The design can be improved by enhancing the resistance of the structural systems against lateral seismic load by postponing the collapse state to a larger drift ratio value. IDA results are useful to identify those

earthquakes that, in a probabilistic sense, inflict the most damage. The drift profiles along the height of the building enable to identify intensities at which the drift-limits are exceeded for different and the particular storeys at which it occurs. The hinge formation patterns at various intensity levels enable to identify members reaching various performance levels, to identify critical frames and members in the building where the onset of collapse occurs and to modify the structural designs accordingly to enable those members to efficiently resist the seismic damage.

References

1. FEMA 356 (2000) Prestandard and commentary for the seismic rehabilitation of buildings, Federal Emargency Management Agency; Washington, D.C.
2. Dimitrios GL. Interactive interface for incremental dynamic analysis procedure (IIIDAP) using Deteriorating Single Degree of Freedom Systems, IIIDAP manual; Lignos Research Group, License Copyright © 2009–2012
3. Vamvatsikos D, Jalayer F, Cornell CA (2003) Application of incremental dynamic analysis to an RC-structure. In: FIB symposium on concrete structures in Seismic Regions, Athens, Jan 2003
4. Vamvatsikos D, Cornell CA (2002) Incremental dynamic analysis. Earthquake Eng Struct Dyn 31:491–514
5. Vamvatsikos D, Cornell CA (2002) The incremental dynamic analysis and its application to performance-based earthquake engineering. In: Proceedings of the 12th European conference on earthquake engineering 40, London, UK, Sept 2002
6. Vamvatsikos D, Cornell CA (2004) Applied incremental dynamic analysis. Earthquake Spectra, Earthquake Eng Re Inst 20(2):523–553
7. Miari M, Nazri FM (2019) short review on incremental dynamic analysis and fragility assessment. Adv Civil Eng Tech 3(2)
8. Waghmare AA, Kawade UR (2020) Nonlinear dynamic analysis. In: International conference on emerging trends in engineering (ICETE). Learning and analytics in intelligent systems, vol 2. Springer, Berlin, pp 73–79
9. Javanpour M, Zarfam P (2017) Application of incremental dynamic analysis (IDA) method for studying the dynamic behavior of structures during earthquakes. Eng Technol Appl Sci Res 7(1):1338–1344
10. Shimpi V, Bhat G (2017) Performance evaluation of RC frame structure through incremental dynamic analysis. Indian J Sci Technol 10(3):1–8
11. Hedayat AA, Yalciner H (2010) Assessment of an existing RC building before and after strengthening using nonlinear static procedure and incremental dynamic analysis. Shock Vib 17:619–629
12. Kalkan E, Kunnath SK (2006) Effects of Fling Step and Forward Directivity on Seismic Response of Buildings. Earthq Spectra 22(2):367–390

Evaluation of Variation in Parameters of Reinforced Concrete with the Incorporation of Alccofine-1203 and Crimped Steel Fibres

Anshul Sharma and Hritick Shama

1 Introduction

The recent construction development activities and related literature show that in past decades reinforced cement concrete has emerged as a popular choice material for construction of complex and large superstructures such as bridges, buildings, highways, marine structures, pipes and conduits, tunnels. The major concern in the deterioration of reinforced cement concrete structures is the induction of corrosion in steel reinforcement bars which reduces the durability, fatigue strength, concrete rebar bond strength, ductility of rebars, shear capacity of rebars and service life of a structure [1]. The occurrence of corrosion can be observed with the physical signs such as spalling and cracking or rust staining on the surface of defected member in a structure [2]. The reasonable factors which add to the growth of corrosion in concrete structure are such as concrete quality, concrete reinforcement cover, reinforcement condition, concrete porosity, environmental effect and thawing and freezing effect. [3]. The degradation of concrete can be measured using numerous electrochemical processes such as half-cell potential technique, electrochemical impedance spectroscopy, linear polarization resistance, Galvano-dynamic polarization, potentio-dynamic cyclic polarization and gravimetry [4].

The literature highlights various studies which are involved in determination of corrosion in rebars and suitable measures taken to address the issue. Pradhan and

A. Sharma (✉)
Civil Engineering Department, National Institute of Technology, Hamirpur, Himachal Pradesh, India
e-mail: anshul.s@nith.ac.in

H. Shama
Civil Engineering Department, Jaypee University of Information Technology, Himachal Pradesh, Waknaghat, Solan, India

Bhattacharjee [5] studied chloride induced corrosion in concrete rebars with half-cell potential indicator with varying cement type, steel type and water-cement ratios. Shaikh and Sahare evaluated the variation showed by reinforcement bars corrosion rate due to application of different impressed current voltages. The variation in concrete crack pattern and rebar mass loss with time due to accelerated corrosion indicated that with increase in rebar diameter and decrease in voltage the metal mass loss increases [6]. Kumar et al. explained the role of water-cement ratio which can regulate the durability, permeability and strength in concrete. The outcomes conclude that increase in water content ratio increases pores in concrete which eventually makes the concrete susceptible to chloride ingress to deeper extent [7]. Anwar et al. studied impressed current-based protection of reinforcement bars in concrete by replacing pumice aggregate with carbon fibres. It is observed that the concrete become light weighted and more conductive with the addition of carbon fibres [8]. kavyateja studied the variation in mechanical properties of self-compacting concrete with the blending of varying fly ash and alccofine additives. The outcomes showed improvement in modulus of rupture, split tensile strength and compressive strength of self-compacting concrete [9]. Barnett et al. studied the effect on variation of flexural strength on concrete with the variation in orientation of fibres in the ultra-high performance concrete [10]. Xia et al. studied the effect of corrosion on the flexural strength of different concrete specimens with varying reinforcement bars type, diameter and water-cement ratio [11].

2 Proposed Methodology

Figure 1 shows the flowchart representing the proposed methodology procedure. The order of methodology is as such that Stage 1 deals with the determination of physical properties of construction materials such as cement, sand and aggregates by various laboratory experiments. Stage 2 includes the calculations performed for evaluating the mix designs for M20 concrete with different water-cement ratios. Stage 3 includes development of various beam specimens (reference, varying concrete depth and additives). Stage 4 includes the use of impressed current technique for corrosion initiation, half-cell potential difference method and centre point loading method application for determining the extent of corrosion and flexural strength of the specimens.

2.1 Stage 1—Physical Properties Experimental Analysis

The properties of materials used for creating M20 grade mix design are determined through laboratory tests. The *Pozzolana Portland Cement (PPC)* used in the present study is made by adding fly ash or clay which is a waste residual product obtained from thermal plants. The pozzolanic materials (clay or fly ash) add to the strength of

Fig. 1 Flowchart of the
proposed methodology
procedure
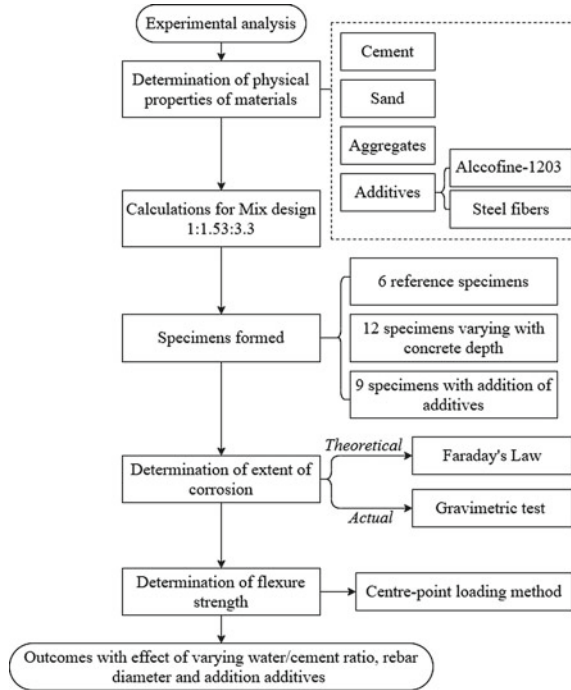
concrete due to their binding properties which evolve with the addition of water. The physical properties of 33 grade Portland Pozzolana Cement (PPC) such as normal consistency, initial setting time, final setting time and specific gravity are 34% of normal consistency, 40 min, 8 h and 2.79, respectively. The compressive strength obtained using cubes of dimensions 70.6 mm × 70.6 mm × 70.6 mm at 7 days, 14 days and 28 days are 17 MPa, 23 MPa and 35 MPa, respectively. The tensile strength obtained using briquette mould at 3 days and 7 days are 11 MPa and 16 MPa, respectively.

The *sand* used is obtained from Dumehar crusher, Himachal Pradesh, India and is tested in laboratory to obtain its physical properties. The specific gravity obtained using density bottle and pycnometer are 2.576 and 2.837, respectively. The grading of fine aggregates is done using sieves as shown in Table 1. The fineness modulus of 1.10 and aggregate particle size of 0.15 mm to 0.3 mm is obtained.

Aggregates influence the durability and quality of the concrete as they minimize the shrinkage and give volume to the concrete. The bond of cement-aggregate gets improved with the use of rough textured aggregates. The sieve analysis is performed for grading of aggregates as mentioned in IS:383–1970. The graded aggregates influence the workability and porosity (presence of voids) of the concrete. In present study, the aggregates are obtained from Dumehar crusher, Himachal Pradesh, India and is tested in laboratory to obtain its physical properties. The water absorption, effective specific gravity and apparent specific gravity of aggregates is obtained as 1.41%,

Table 1 Outcomes of sieve analysis

Sieve size (IS)	Weight retained (g)	Cumulative weight retained (g)	Cumulative weight retained (% age)	Weight passing (g)	Percentage passing (% age)
10 mm	0.00	0.00	0.00	986.10	100.00
4.75 mm	6.00	6.00	0.61	980.10	99.39
2.36 mm	8.50	14.50	1.47	971.60	98.53
1.18 mm	9.50	24.00	2.43	962.10	97.57
0.60 mm	12.70	36.70	3.72	949.40	96.28
0.30 mm	80.10	116.80	11.84	869.30	88.16
0.15 mm	775.30	892.10	90.47	94.00	9.53
Pan	94.00	986.10	Total = 110.54		
Total	986.10				

$$\text{Modulus of fineness} = \frac{\text{Cummulative weight retained}}{100} = \frac{110.54}{100} = 1.10$$

2.68 and 2.75, respectively. The fineness modulus of the aggregates show that the aggregates used fall in coarse aggregate category.

Additive is the supplementary material added to the concrete for enhancing its strength and durability. The different uses of adding additives include retarding setting time of concrete, increase freeze thaw durability by air-entraining, demands low water-cement ratio, reduces shrinkage, etc. The Alccofine-1203 and crimped steel fibres are used as additives in present study to prevent corrosion of the steel rebars in the concrete as shown in Fig. 2.

Alcofine-1203 is a supplementary material which optimizes the particle size distribution in concrete mix because of its ultra-fineness. It is slag based new generation micro fine material having smaller particle size than hydraulic materials such as silica and fly ash. It enhances the durability, performance of concrete and minimizes the permeability due to which resistance of mix to chemical attack or operational environmental conditions change increases. The physical of Alccofine-1203 additive

Fig. 2 Additives used **a** Alccofine-1203 and **b** crimped steel fibres

(a)   (b)
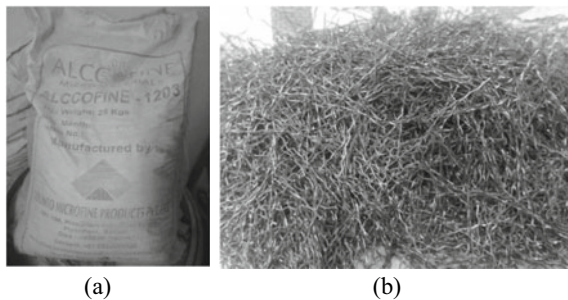
Table 2 Mix design adopted at different water-cement ratios

Water (kg/m^3)	Cement (kg/m^3)	Fine aggregate (kg/m^3)	Coarse aggregate (kg/m^3)	Water-cement ratio
153.26	340.59	587.03	1292.82	0.40
153.26	340.59	521.09	1123.94	0.45

includes specific gravity, bulk Density (kg/m^3) and particle size distribution (D 10, D 50 and D 90) as 2.9, 600–700 and 1–2, 4–5 and 8–9, respectively while the chemical properties of Alccofine-1203 additive include CaO, Al_2O_3, Slo2 and glass content as 31–33%, 23–25%, 33–35% and >90%, respectively.

The *steel fibres* are added to the concrete to concrete increase the durability of the concrete by reducing the corrosion of the reinforcement rebars. The steel fibres have larger surface area; hence, corrosion will occur to them first instead of rebars. The corroded steel fibres will provide longer time for the reinforcement bars to survive and remain intact. The aspect ratio of steel fibres used in the present study is 50 and diameter of 0.5 mm, respectively. The various physical properties of the steel fibres include crimped length, diameter, tensile strength, and appearance which are 30 mm, 0.4 mm, 800–2500 MPa (1250 MPa used) and clear-bright, respectively.

2.2 Stage-2 Specimens Mix Designs for M20 Concrete

The IS:10262–2009 code was used to design concrete mix for M20 grade concrete. The final mix design of 1:1.53:3.3 is adopted for the casting of specimens with different water-cement ratios as shown in Table 2.

2.3 Stage-3 Specimens Developed Varying Concrete Depth, w/c Ratios and Additives

Beam specimens of size 100 mm × 100 mm × 450 mm was casted to determine flexural strength and corrosion growth rate in reinforcement provided. Total 27 specimens were cast out of these six specimens were taken as reference specimens. Steel reinforcement bars of same length with three different diameters were used, i.e. 12 mm ($d1$), 16 mm ($d2$) and 20 mm ($d3$). Bars were embedded in concrete up to 350 mm length and remaining 70 mm length was kept exposed to atmosphere. A total of 27 concrete specimens was cast with two different water-cement ratios, i.e. 0.40 (p) and 0.45 (q) and two different effective concrete depths, i.e. 50 mm (x) and 45 mm (y).

Series of six mixes with concrete cover of 50 mm were kept in reference mixes. Beside reference mixes the mixes were divided into four series as shown in Table 3.

Table 3 Specimens formed from different mixes affiliations

S. No	Specimens	Diameter of reinforcement (mm)	Concrete cover depth (mm)	Water-cement ratio
Reference mixes				
1	p x d1	12	50	0.40
2	p x d2	16	50	0.40
3	p x d3	20	50	0.40
4	q x d1	12	50	0.45
5	q x d2	16	50	0.45
6	q x d3	20	50	0.45
Mixes with varying concrete cover depth				
1	p x d1	12	45	0.40
2	p y d1	12	40	0.40
3	p x d2	16	45	0.40
4	p y d2	16	40	0.40
5	p x d3	20	45	0.40
6	p y d3	20	40	0.40
7	q x d1	12	45	0.45
8	q y d1	12	40	0.45
9	q x d2	16	45	0.45
10	q y d2	16	40	0.45
11	q x d3	20	45	0.45
12	q y d3	20	40	0.45
Mixes with Alccofine-1203				
1	A F d1	12	50	0.40
2	A F d2	16	50	0.40
3	A F d3	20	50	0.40
Mixes with steel fibre				
1	S F d1	12	50	0.40
2	S F d2	16	50	0.40
3	S F d3	20	50	0.40
Mixes with both steel fibres and Alccofine-1203				
1	S F A F d1	12	50	0.40
2	S F A F d2	16	50	0.40
3	S F A F d3	20	50	0.40

First series of 12 mixes with varying concrete cover depth (45 and 40), rebar diameter (12 mm, 16 mm and 20 mm) and water-cement ratio (0.40 and 0.45). Second series of three mixes, containing replacement of 20% of cement with Alccofine-1203 with constant concrete cover depth (50 mm) and water-cement ratio (0.40). Third series of three mixes consists of addition of 3% steel fibres while remaining fourth series of three specimens were made with addition of both 1% steel fibres and replacement of 20% of cement is done with Alccofine-1203. The computed optimized concrete cover depth and water-cement ratio was used in the development of beam specimens. The curing of specimens after their achievement of final setting time is done in clean water submerging tank for 28 days. The concrete rapidly gains its maximum strength up to 28 days, and hence, this period is selected for its curing. The half-cell potential method was applied to determine the rate of corrosion in reinforcement rebars. The collected data of half-cell potential values are utilized to obtain the optimized cover depth and water-cement ratio.

2.4 Step-4 Applied Techniques

2.4.1 Impressed Current Technique

The impressed current technique is used to initiate corrosion in beam reinforcement within brief time frame by applying steady current through a DC source as shown in Fig. 3 [12]. The electrochemical process of corrosion involves oxidization of iron into iron oxides. The half-cell electric potential values can be used to quantify the amount of steel which has converted into oxides can be represented as anodic and cathodic reactions. The Faraday's law is utilized to hypothetically compute the extent of initiated corrosion, while the gravimetric test is conducted to determine the real steal mass lost due to corrosion.

The experimental set-up for prompting corrosion in reinforcement rebars through impressed current technique includes a DC power source, an electrolyte, an anode and a cathode. In present study, the anode, i.e. the steel rebars are connected to the positive terminal of the DC power source while the cathode, i.e. stainless steel is associated with the negative terminal. The 3% NaCl solution is taken as electrolyte in which specimens are dipped with constant power supply of 15 V as shown in
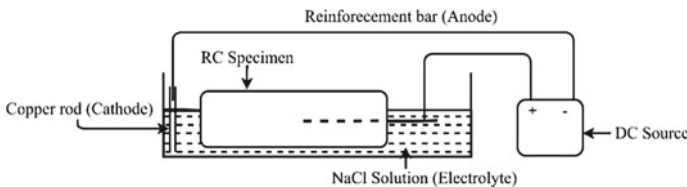
Fig. 3 Impressed current experimental method
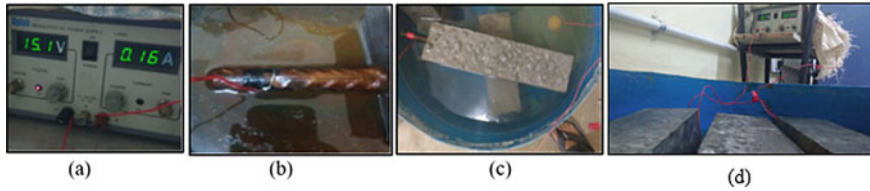
Fig. 4 Accelerated corrosion tank set-up consists of **a** power supply, **b** exposed reinforcement, **c** specimen dipped in 3% NaCl solution and **d** complete set-up
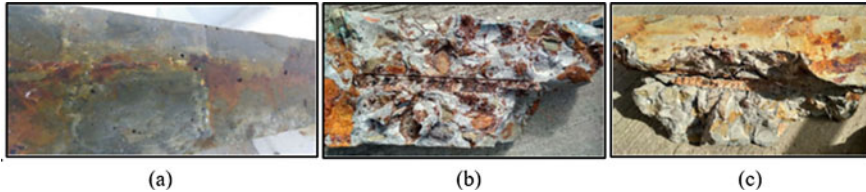
Fig. 5 Beam specimens showing **a** crack propagation, **b** corroded steel fibres and **c** corrosion in steel fibres fused with Alccofine-1203

Fig. 4. The rate of corrosion gets accelerated due to the formation of electrochemical cell and starts appearing within 5 days.

The tested specimens after response to NaCl for 5 days, where the cracks developed in the beam specimens, corroded steel fibre in specimen can be seen in Fig. 5.

2.4.2   Half-Cell Potential Method

The change in electric potential between the passive and corroded areas in concrete causes the development of a macro cell which influences the growth of corrosion in reinforcement rebars. In present study, the probability of presence of corrosion in reinforcement of concrete specimens can be determined using half-cell potential difference at the anode (steel reinforcement rebars) and cathode (copper rod) ends present in an electrolyte solution ($CuSO_4$ of 1 M) as shown in Fig. 6. Table 5 shows the relation between the changing half-cell potentials and the probability of corrosion as per ASTM C876-91. The computed half-cell potential values indicating probability of corrosion for different concrete beam specimens. The calculated potential (mV/CSE) values when varies as -200 mV $<$ E, -350 mV ≤ -200 mV and E ≤ -350 mV indicates 90% probability of zero corrosion (Initiated), medium corrosion (Intermediate) and 90% probability of corrosion (Extreme), respectively.
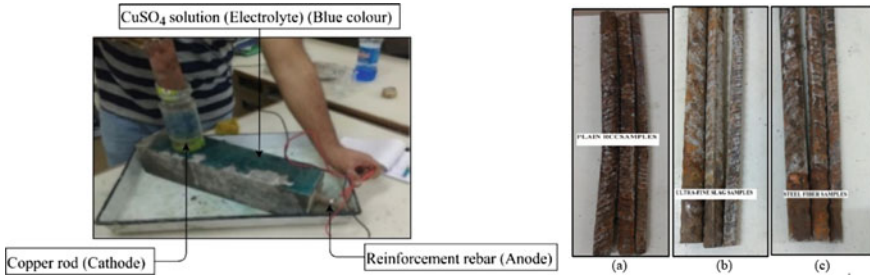
Fig. 6 Measurement of corrosion using half-cell potential method and corroded reinforcement in **a** plain RC samples, **b** ultra-fine slag samples and **c** steel fibre samples

2.4.3 Flexural Strength

The reinforced concrete beams get their flexural strength from reinforcement provided but as the corrosion in rebar's develop the strength of reinforcement weakens and ultimately the flexural strength minimizes. The flexural strength was calculated using centre point loading method for which modulus of rupture (F_r) is calculated. The flexural strength of beam specimens was calculated after half-cell potential values were measured by applying centre point load method.

3 Results and Discussions

The concrete beam specimens subjected to impressed current technique are pulled out to evaluate the loss of mass of steel due to corrosion and determine the effect of reinforcement bar diameter, concrete cover and water-cement ratio on the rate of corrosion. Further, the half-cell potential method and flexural strength tests are performed to determine the probability of corrosion and the flexural strength of different reinforced concrete specimens having varying concrete cover, reinforcement diameter, water-cement ratio and addition of additives.

3.1 Calculations of Induced Corrosion (Impressed Current Technique)

The reinforcement bars were retrieved from the specimens after first crack become visible in them as shown in Fig. 6. It is observed that concentration of corrosion is more at developed crack and exposed rebar end w.r.t whole specimen. The induced corrosion calculated varied 7.6% by weight of rebars as shown in Table 4.

It is observed that corrosion shows direct relation with the increase in reinforcement diameter while inverse relation with the increase in effective concrete cover

Table 4 Calculation of degree of induced corrosion

Specimen	Diameter of reinforcement (mm)	Concrete cover depth (mm)	Water-cement ratio	Initial weight of bar (gm) (W_i)	Final weight of the bar (gm) (W_f)	Loss (gm) ($W_f - W_i$)	Degree of induced corrosion $\left(\frac{W_f - W_i}{W_i}\right)$
Reference mixes							
p x d1	12	50	0.40	420	389	31	7.38
p x d2	16	50	0.40	680	658	22	3.24
p x d3	20	50	0.40	1100	1089	11	1.00
q x d1	12	50	0.45	420	385	35	8.33
q x d2	16	50	0.45	680	661	24	3.53
q x d3	20	50	0.45	1100	1093	14	1.27
Mixes with varying concrete cover depth							
p x d1	12	45	0.40	420	387	33	7.86
p y d1	12	40	0.40	420	385	35	8.33
p x d2	16	45	0.40	680	655	25	3.68
p y d2	16	40	0.40	680	651	29	4.26
p x d3	20	45	0.40	1100	1063	37	3.36
p y d3	20	40	0.40	1100	1061	39	3.55
q x d1	12	45	0.45	420	385	35	8.33
q y d1	12	40	0.45	420	381	39	9.29
q x d2	16	45	0.45	680	653	27	3.97
q y d2	16	40	0.45	680	650	30	4.41
q x d3	20	45	0.45	1100	1059	41	3.73
q y d3	20	40	0.45	1100	1056	44	4.00
Mixes with Alccofine-1203							
A F d1	12	50	0.40	420	411	9	2.14
A F d2	16	50	0.40	680	678	2	2.94
A F d3	20	50	0.40	1100	1098	2	1.82
Mixes with steel fibres							
S F d1	12	50	0.40	420	409	11	2.62
S F d2	16	50	0.40	680	671	9	1.32
S F d3	20	50	0.40	1100	1095	5	0.45
Mixes with both steel fibres and Alccofine-1203							
S F A F d1	12	50	0.40	420	416	4	0.95
S F A F d2	16	50	0.40	680	679.5	0.5	0.07
S F A F d3	20	50	0.40	1100	1099.6	0.4	0.04

Table 5 Half-cell potential calculated

S. No.	Specimens	Half-cell potential (mV)	Probability of corrosion
Reference mixes			
1	p x d1	−673	Extreme
2	p x d2	−585	Extreme
3	p x d3	−342	Intermediate
4	q x d1	−580	Extreme
5	q x d2	−307	Intermediate
6	q x d3	−293	Intermediate
Mixes with varying concrete cover depth			
1	p x d1	−515	Extreme
2	p y d1	−493	Extreme
3	p x d2	−428	Extreme
4	p y d2	−487	Extreme
5	p x d3	−304	Intermediate
6	p y d3	−333	Intermediate
7	q x d1	−547	Extreme
8	q y d1	−585	Extreme
9	q x d2	−418	Extreme
10	q y d2	−464	Extreme
11	q x d3	−334	Intermediate
12	q y d3	−349	Intermediate
Mixes with Alccofine-1203			
1	A F d1	−325	Intermediate
2	A F d2	−342	Intermediate
3	A F d3	−174	Initiated
Mixes with Steel fibres			
1	S F d1	−605	Extreme
2	S F d2	−598	Extreme
3	S F d3	−581	Extreme
Mixes with both steel fibres and Alccofine-1203			
1	S F A F d1	−186	Initiated
2	S F A F d2	−156	Initiated
3	S F A F d3	−143	Initiated

depth. The steel rebars with 20 mm diameter showed more loss of steel mass as compared to 16 mm or 12 mm, respectively. The appearance of cracks in higher concrete cover specimens occurred lately as compared to. It shows that resistance of more concrete cover specimens towards corrosion is more than lower concrete cover specimens. The increase in water-cement ratio also cases increase in the growth of corrosion in concrete specimen. The addition of additives Alccofine-1203 and steel fibres in concrete reduces the mass loss of the reinforcement rebars due to corrosion. The steel fibres due to their initial corrosion in a concrete sample shows appearance of stains on the surface of specimens.

3.2 Results of Half-Cell Potential Method

As per the values of half-cell potential shown in Table 5 which tells us about the probability of corrosion in specimens. More negative values of half-cell potential indicate that there will be more corrosion in the reinforcement and as the values of half-cell potential decreases with negative sign, then it shows the probability of extent of corrosion decreases. The values in Table 4 show that corrosion decreases as the diameter increases sand water-cement ratio decreases. The values of half-cell potential in steel fibres are more negative because there is little bit corrosion in steel fibres but the corrosion of reinforcement is reduced. With the combination of additives, there is improvement in the half-cell potential values as compared to the additives used in alone in the specimens, this is due to the less porosity in the specimens as all the pores in specimens are filled with additives having more flexural strength.

3.3 Results of Centre Point Loading Method for Flexural Strength

Table 6 shows the measured flexural strength for different specimens.

It is observed from Fig. 7 that the flexural strength of specimen beams decreases with the slight increase in water-cement ratio. The flexural strength increases with the increase in diameter of reinforcement bars, and there is inverse relation of water-cement ratio with flexural strength of beam specimens. The increase in concrete cover and reinforcement diameter provides greater resistance to corrosion and increases the flexural strength of specimen beams. The flexural strength of specimens with the addition of varying additive in different combinations and rebar diameters showed that the optimum water-cement ratio is 0.4 and concrete cover depth is 50 mm. The outcomes of specimens having both additives show that the corrosion rate reduces with the addition of Alccofine-1203 as the additive fills the micro pores of concrete

Table 6 Flexural strength calculated for different specimens

S. No.	Specimens	Diameter of reinforcement (mm)	Concrete cover depth (mm)	Water-cement ratio	Flexural strength (N/mm^2)
Reference mixes					
1	a x d1	12	50	0.40	21.51
2	a x d2	16	50	0.40	24.62
3	a x d3	20	50	0.40	29.88
4	b x d1	12	50	0.45	21.20
5	b x d2	16	50	0.45	23.85
6	b x d3	20	50	0.45	29.26
Mixes with varying concrete cover depth					
1	p x d1	12	45	0.40	18.00
2	p y d1	12	40	0.40	17.01
3	p x d2	16	45	0.40	19.44
4	p y d2	16	40	0.40	18.90
5	p x d3	20	45	0.40	26.85
6	p y d3	20	40	0.40	25.65
7	q x d1	12	45	0.45	17.60
8	q y d1	12	40	0.45	16.65
9	q x d2	16	45	0.45	19.20
10	q y d2	16	40	0.45	18.40
11	q x d3	20	45	0.45	26.55
12	q y d3	20	40	0.45	24.90
Mixes with Alccofine-1203					
1	A F d1	12	50	0.40	21.38
2	A F d2	16	50	0.40	25.29
3	A F d3	20	50	0.40	29.57
Mixes with steel fibres					
1	S F d1	12	50	0.40	21.02
2	S F d2	16	50	0.40	24.66
3	S F d3	20	50	0.40	29.03
Mixes with both steel fibres and Alccofine-1203					
1	S F A F d1	12	50	0.40	21.87
2	S F A F d2	16	50	0.40	25.79
3	S F A F d3	20	50	0.40	30.60
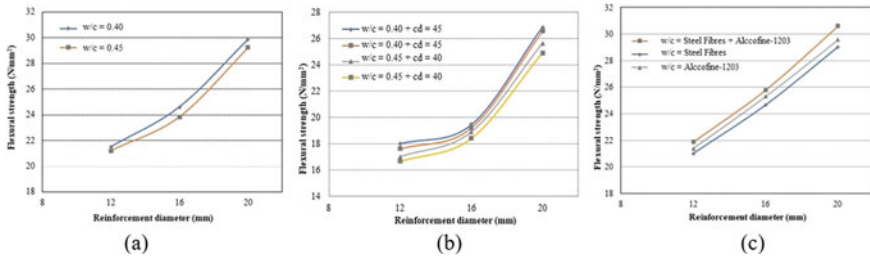
Fig. 7 Flexural strength of concrete specimen with varying **a** reinforcement diameter and w/c ratio, **b** concrete cover depth and **c** steel fibre, Alccofine-1203. *w/c = water-cement ratio, cd = concrete cover

which increases its density and strength. The incorporation of cribbed steel reinforcement also restricts the propagation of crack and increases the strength of concrete. The increase in diameter generally increases the flexural strength of concrete specimens.

4   Conclusions

1. In present study, the outcomes of the half-cell potential method shows that the increase in water-cement ratio causes reduction in half-cell potential values which further indicates the probability of presence of corrosion. The half-cell potential values for reference mixes with reinforcement diameters 12 mm, 16 mm and 20 mm varied from -673, -585, -342 to -580, -307, -293, respectively.

2. The higher diameter reinforcement rebars with more surface area has less penetration of corrosion. The induced corrosion calculated varied 7.6% by weight of rebars.

3. The rate of corrosion rate minimizes with the increase in concrete cover depth. In study for reference mixes having 0.40 water-cement ratio and 12 mm, 16 mm and 20 mm reinforcement diameter, the corrosion is induced with change in concrete cover from 45 to 40 mm the degree of induced corrosion showed increasing pattern from 7.86, 3.68, 3.36 to 8.33, 3.97, 3.73, respectively. For 0.45 water-cement ratio, the 12, 16, 20 mm reinforcement diameter specimens when induced with change in concrete cover from 45 to 40 mm the degree of induced corrosion showed increasing pattern from 8.33, 3.97, 3.73 to 9.27, 4.41, 4.00.

4. The flexural strength of concrete specimens showed 2.2% reduction with the increase in water-cement ratio; 4.24%, 5.39% increment with the increase in concrete cover at 0.40, 0.45 water-cement ratio, respectively.

5. Alccofine-1203 because of its ultra-fineness reduces the permeability of moisture and chemicals from operational environmental conditions. The steel fibres increase the surface area for rusting and thus, minimizes corrosion rate in the

rebars of reinforced beam specimens. The addition of Alccofine-1203, steel fibres show increase in flexural strength of the reinforced beam specimens by 19.2% and 17.5%, respectively. The probability of having corrosion in rebars decreases with the addition of additives as indicated by decrease in half-cell potential values.

References

1. Kere KJ, Huang Q (2019) Life-cycle cost comparison of corrosion management strategies for steel bridges. J Bridg Eng 24:1–16
2. Apostolopoulos CA, Koulouris KF, Apostolopoulos AC (2019) Correlation of surface cracks of concrete due to corrosion and bond strength (between steel bar and concrete). Adv Civil Eng 2019:1–12
3. Medeiros MHF, Rocha FC, Helene RA, Medeiros-Junior, Helene P (2017) Corrosion potential: influence of moisture, water-cement ratio, chloride content and concrete cover. Revista IBRACON de Estruturas e Materiais, vol 10, pp 864–885
4. Quraishi MA, Nayak DK, Kumar R, Kumar V (2017) Corrosion of reinforced steel in concrete and its control: An overview. J Steel Struct Construct 3:1–6
5. Pradhan B, Bhattacharjee B (2009) Half-cell potential as an indicator of chloride-induced rebar corrosion initiation in RC. J Mater Civ Eng 21:543–552
6. Shaikh N, Sahare S (2016) Effect of impressed current on corrosion of reinforcing bar in reinforced concrete. Int J Adv Mech Civil Eng 3:80–84
7. Kumar V, Singh R, Quraishi MA (2013) A study on corrosion of reinforcement in concrete and effect of inhibitor on service life of RCC. J Mater Environ Sci 4:726–731
8. Anwar MS, Sujitha B, Vedalakshmi R (2014) Light-weight cementitious conductive anode for impressed current cathodic protection of steel reinforced concrete application. Constr Build Mater 71:167–180
9. Kavyateja BV, Jawahar JG, Sashidhar C (2020) Effectiveness of alccofine and fly ash on mechanical properties of ternary blended self compacting concrete. Mater Today Proc 33:73–79
10. Barnett SJ, Lataste JF, Parry T, Millard SG, Soutsos MN (2010) Assessment of fibre orientation in ultra high performance fibre reinforced concrete and its effect on flexural strength. Mater Struct 43:1009–1023
11. Xia J, Jin WL, Li LY (2012) Effect of chloride-induced reinforcing steel corrosion on the flexural strength of reinforced concrete beams. Mag Concr Res 64:471–485
12. Caré S, Raharinaivo A (2007) Influence of impressed current on the initiation of damage in reinforced mortar due to corrosion of embedded steel. Cem Concr Res 37:1598–1612

Infilled Steel Frames Subjected to Seismic Loads

A. R. Pradeep, C. Rangaraj, and N. Jayaramappa

1 Introduction

An infilled wall substantially increases in terms of strength and rigidity of the structure. In recent days, a number of RCC and steel structures walls are built with various types of infills [1]. Masonry infills are generally used to fill the space between the vertical and horizontal components of the constructing frames with the assumption that those infills received have any role in resisting masses either axially or laterally [2]. The overall performance of the structure in an occasion of an earthquake relies upon on its form, size, and geometry and place together with the seismic forces. It has been analysed that frames with infills have additional strength and stable as compared to the bare frames and its unawareness has resulted in failure of the many of the multi-storied buildings [3]. Infill partitions are considered to be non-load bearing, but they resist wind loads applied and support their self-weight [4]. Masonry infills are usually considered as the non-structural elements in analysis and design. A review of the different methods of analysis has been presented in this paper that addresses the performance of masonry brick infills and precast panels under seismic loads.

2 Literature

In the past, attempts have been made to check the behaviour of infill walls and soft storey considerations on alternative floors for different buildings [5]. Basavaraj et al.

A. R. Pradeep (✉) · C. Rangaraj
Department of Civil Engineering, Sri Siddhartha Institute of Technology-SSAHE, Tumkur, India
e-mail: arpradeepmtech@gmail.com

N. Jayaramappa
Department of Civil Engineering, U.V.C.E, Bengaluru, India

made an effort to study the behaviour of RC frame structure using conventional bricks, CC blocks, hollow blocks, and lightweight bricks infill. Linear static and nonlinear static pushover analysis has been carried out for fixed and flexible support in different types of soil condition, to know the effect of earthquake loading [1]. Base shear, top storey displacement, natural period, and pushover results are compared to know the suitable infill material in seismic zones. From the results obtained, the lightweight brick system gives better performance than the other infill materials.

3 Objectives

1. To arrive at appropriate sections of steel beam and column for the structural model using SAP2000 software.
2. To evaluate the overall performance of steel frame with masonry infills and precast panels under seismic loading.
3. To assess the performance of the structure using seismic analysis.
4. To analyse steel frames by way of equivalent static method and response spectrum with different infills.

4 Structural Modelling and Analysis

In this study, an analytical model of G + 9 storeys was used in the analysis. Steel Bare frame, Steel Bare frame infilled with both Burnt brick masonry as infills and ferrocement precast panels as another infill with different column sections have taken for pushover analysis the number of bays and bay width in both *X* and *Y* directions are 4 m × 4 m, respectively. The total height of the building is 40 m. Storey height is 4 m were considered in the study. All columns are fixed from the base for foundations. The models are analysed as per Indian Standard Code and FEMA356 (Figs. 1 and 2; Table 1).

5 Material Properties

The materials used in the structure are steel for beam and column members and concrete for slab, respectively. Using M20 grade concrete and Fe345 steel, all the models were analysed (Table 2).

Fig. 1 Plan considered for the analysis
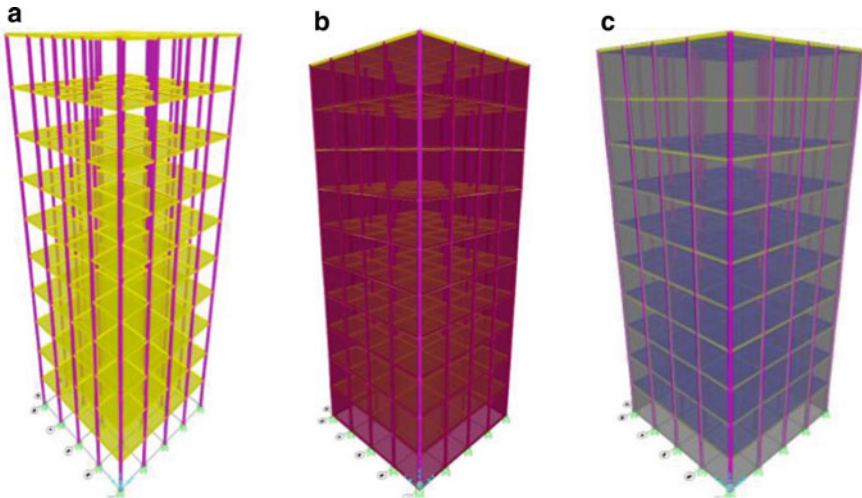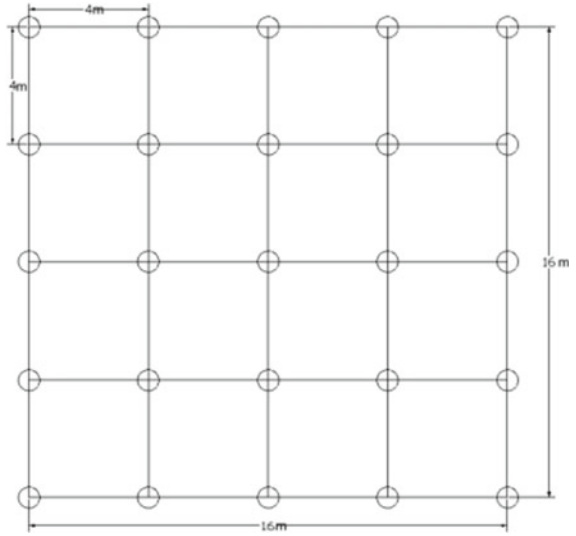
Fig. 2 **a** Bare frame, **b** Bare frame with brick infill, **c** Bare frame with ferro-cement infill

6 Analysis and Results

6.1 Base Shear

Base shear is the quantity of the highest predicted lateral pressure on the way to act because of seismic ground movement at the base of a structure. The structure is

Table 1 Models nomenclature

S. No.	Model	Nomenclature
1	Steel bare framed structure with ISNB350-3 as a column	BF 1
2	Steel bare framed structure with ISHB250-2 with top and bottom plate of 320 mm width and 25 mm thick as a column	BF2
3	Steel framed structure with Burnt brick masonry infills and ISNB350-3 as a column	BFBM1
4	Steel framed structure with Burnt brick masonry infills and ISHB250-2 with top and bottom plate of 320 mm width and 25 mm thick as a column	BFBM 2
5	Steel framed structure with Ferro-cement precast panels and ISNB350-3 as a column	BFPP1
6	Steel framed structure with Ferro-cement panels and ISHB250–2 with top and bottom plate of 320 mm width and 25 mm thick as a column	BFPP2

Table 2 Material specifications

S. No.	Model	Nomenclature
1	Slab (thickness)	150 mm
2	Beams	ISMC 200 D Steel section
		ISHB 250 with top and bottom plate of 320 mm width and 25 thick steel section
3	Precast panels (thickness)	50 mm
4	Live load	4 kN/m^2 for all the floors
5	Earthquake load	As per IS 1893 (Part-1): 2016
6	Type of soil	Type II, medium
7	Importance factor	1
8	Response reduction factor	5
9	No. of bays horizontal and vertical	4 × 4

analysed with gravity load, static earthquake loading method, and the resulting base shear is tabulated in Table 3.

Table 3 Base shear values along X and Y-direction

Structure type	Ex. (kN)	Ey (kN)
BF 1	581.150	581.150
BF2	614.066	614.066
BFBM1	1490.340	1490.340
BFBM 2	1530.206	1530.205
BFPP1	1045.780	1045.782
BFPP2	1081.639	1081.641

Table 4 Values of time period and frequency

Structure type	Period	Frequency
	S	Cycle/S
BF 1	2.100	0.472
BF2	2.187	0.453
BFBM1	0.332	3.021
BFBM 2	0.321	3.087
BFPP1	0.445	2.283
BFPP2	0.424	2.371

Table 5 Maximum storey displacement for seismic static load and response spectrum analysis

Structure type	EQx	EQy	RSx	RSy
	Along X direction	Along Y direction	Along X direction	Along Y direction
BF 1	73.75	73.75	58.43	58.43
BF2	61.36	61.34	48.70	48.70
BFBM1	3.149	3.146	2.815	2.815
BFBM 2	2.977	2.988	2.671	2.670
BFPP1	5.400	5.401	4.756	4.756
BFPP2	4.879	4.879	4.259	4.258

From Table 3, it is observed that the base shear is more for framed building with different infills compared to bare steel frame.

6.2 Time Period

The fundamental natural frequency of a structure at which shape resonates is referred to as modal frequency. Modal frequencies for first mode are obtained by performing modal analysis is tabulated in Table 4.

From Table 4, it is observed that time period is high for bare framed model compared to framed model with different infills. The frequency is more for framed building with different infills compared to bare steel frame.

6.3 Storey Displacement

The storey displacement is lateral displacement of storey with respect to the ground. The highest storey displacement along X and Y direction obtained from the equivalent static force method and response spectrum method is as given in Table 5.

Table 6 Maximum base shear for pushover load cases and all modelled buildings

Structure type	Maximum base shear (kN)		Displacement (mm)	
	Along X direction	Along Y direction	Along X direction	Along Y direction
SBFM 1	8171.148	8171.148	860.529	860.529
SBFM 2	8872.941	8872.941	632.494	632.494
SFMMI1	10,460.721	10,460.721	1375.699	1375.699
SFMMI2	5831.161	5831.161	428.504	428.504
SFMPP1	7541.302	7541.302	810.375	810.375
SFMPP2	11,221.694	11,221.694	880.855	880.855

6.4 Pushover Curves

The curves show linear behaviour of the structure until the elastic limit and then show nonlinear behaviour. In this stage, the structure forms hinges which gradually fails and finally the structure collapses.

In below figures from the pushover curves of all models, the data about displacement and base shear have obtained (Table 6).

Pushover curves for
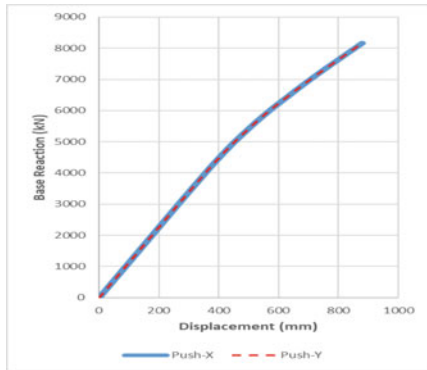
(a) SBFM1 in both X and Y direction   (b) SBFM2 in both X and Y direction
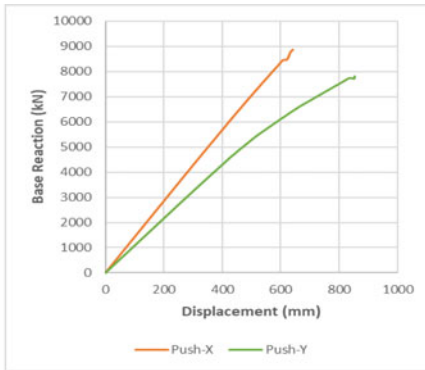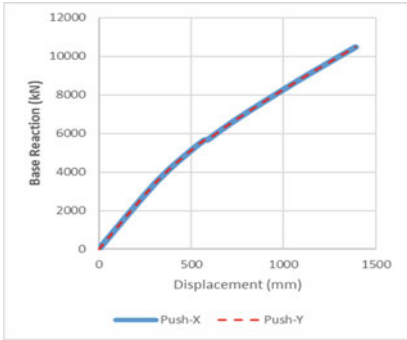
(a) BFBM1 in both X and Y direction
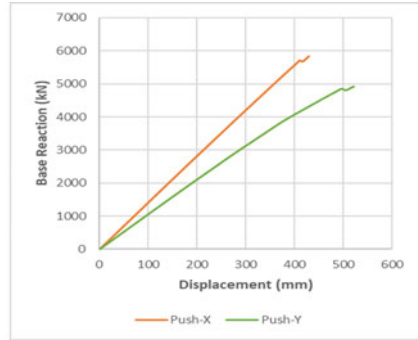
(b) BFBM2 in both X and Y direction
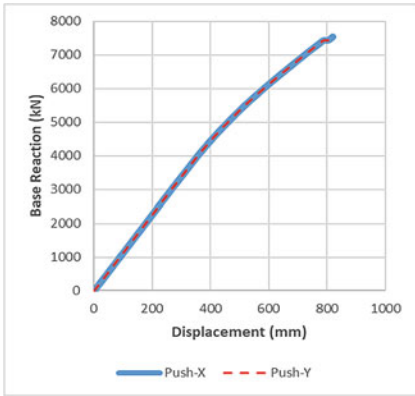
(a) BFPP1 in both X and Y direction
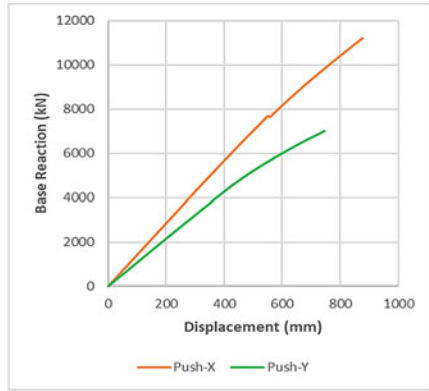
(b) BFPP2 in both X and Y direction

6.5 Response Spectrum Curves

Performance point of the structure is assessed by two methods: ATC 40 capacity spectrum method and FEMA 356 displacement coefficient method. In this case, capacity spectrum method is followed. It is helpful to calculate the overall demand and capacity of the structure useful to get the performance point of the structure. Spectrum curve of all structural models are shown below.
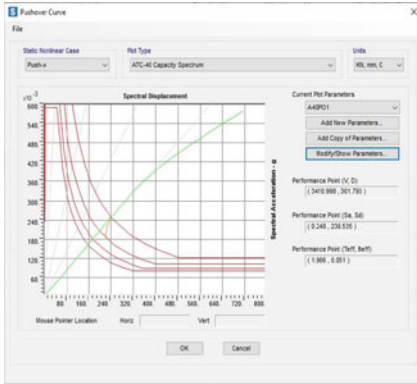
(a) SBFM 1 X direction
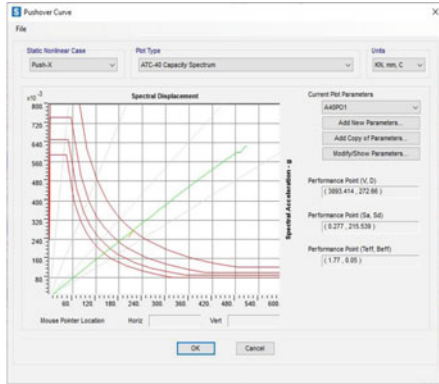
(b) SBFM2 X direction
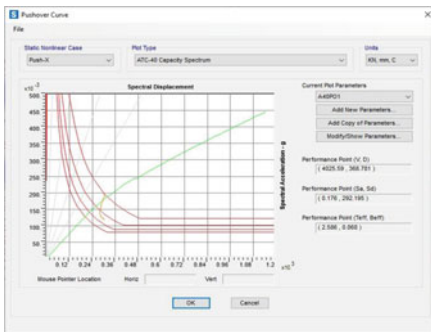
(c) BFBM1 X direction
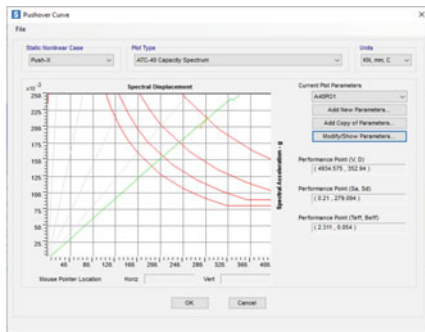
(d) BFBM2 X direction
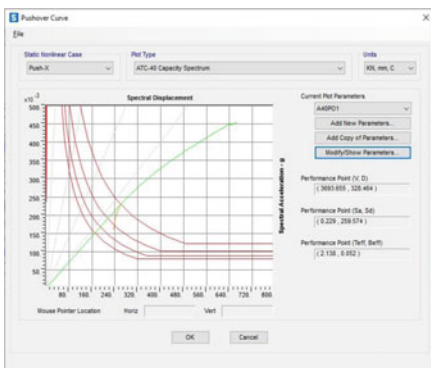
(e) BFPP1 X direction
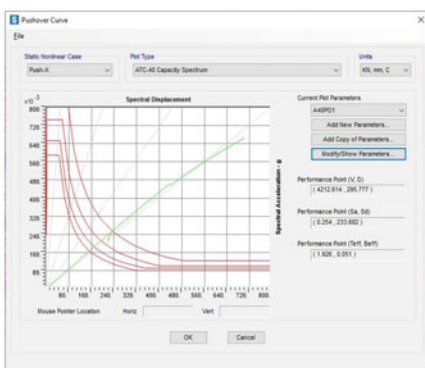
(f) BFPP2 X direction

7 Conclusions

1. For the masonry infills framed model, base shear was found maximum and reduced for framed model with precast panels and further reduced for bare steel frame from the analysis.
2. The displacement was found to be reducing for framed model with precast panels. It was further observed that decent in the displacement for framed model with masonry infills for both equivalent static condition and response spectrum condition.
3. Pushover analysis results showed that hinges formed in members at performance point are under immediate occupancy level from the SAP2000 software.
4. Framed model with masonry infills gives the minimum displacement at performance point.
5. It is concluded that framed model with masonry infills gives the maximum displacement at performance level.

References

1. Yeshodhara TS, Pradeep AR, Jayaramappa N (2021) Analysis of multistoried infilled steel structure subjected to lateral loading. Int Res J Eng Technol (IRJET) 08(04), Apr 2021. e-ISSN: 2395-0056 www.irjet.net p-ISSN: 2395-072
2. Elhelloty A (2017) Effect of lateral loads resisting systems on response of buildings subjected to dynamic loads. Int J Eng Invent 6(10):62–76
3. Malagimani BM, Cholekar SB, Sonawadekar HL (2017) Comparative study of RC structures with different types of infill walls with effect of SSI by pushover analysis. Int Res J Eng Technol 04(06):2545–2550
4. Chouhan M, Maru S (2017) Pushover analysis of steel frame structures with different types of bracing system. Int J Sci Technol Eng 4(2), 37–44
5. Basavaraj M, Malagimani BM, Swapnil B, Cholekar SB, Hemant L, Sonawadekar HL (2017) Comparative study of RC structures with different types of infill walls with effect of SSI by Pushover analysis. Int Res J Eng Technol 4(6):2545–2550
6. I.S 875 (1987) Code of Practice for Design Loads (Other Than Earthquake) for Buildings and Structures—Part 1: Dead loads – Unit weights of building materials and stored materials (Second Revision), Bureau of Indian Standards, New Delhi
7. I.S 1161 (2014) Steel tubes for structural purposes — specification (Fifth Revision). Bureau of Indian Standards, New Delhi
8. Sankhla SS, Bhati D (2016) A comparative study on the effect of infill walls on RCC frame structures. IOSR J Mech Civil Eng 13(6):01–08
9. I.S 1893 (2002) Criteria for earthquake resistant design of structures—Part 1: General provisions and buildings (Fifth Revision), Bureau of Indian Standards, New Delhi

Influence of Geometric Parameters in Self-damping Efficiency of Rectangular Liquid Storage Tanks

P. Nimisha, B. R. Jayalekshmi, and Katta Venkataramana

1 Introduction

The liquid storage tanks are essential infrastructure facility of a country. The design, development and maintenance of these storage tanks require great attention on account of the resulting loss of properties and life it may cause if any damage occurs to the structure. Failure of many liquid tank systems is reported, which even caused interruption to the emergency services [1]. Sloshing of contained liquid is a triggering factor that may result in the failure of the storage tanks under severe situations [2]. Therefore assessment of structural safety of storage tanks is essential to maintain safety against failure of such structures [3]. Housner [4] developed a two-mass model for the analysis of liquid storage tanks, which forms the basis of most of the International codes of practices. The assessment of the hydrodynamic force developed during the liquid sloshing can be done based on this mathematical model [5].

Baffles are used as an efficient structure that can be incorporated inside the liquid tanks, to reduce the slosh responses [6–10]. However, in the absence of such slosh damping structures, the viscosity of liquid imparts some fraction of slosh damping [11]. The contribution of fluid viscosity to the slosh damping is less than 0.5% even with a kinematic viscosity of more than 100 times that of water. Many studies have been reported, based on the various slosh damping techniques [12]. However, the effect of geometric configuration on slosh damping is addressed by a few researchers only [13, 14]. Therefore, the present study investigates the influence of the geometric

P. Nimisha (✉) · B. R. Jayalekshmi · K. Venkataramana
Department of Civil Engineering, National Institute of Technology Karnataka, Surathkal 575025, India
e-mail: nimisha.187cv017@nitk.edu.in

configurations of the liquid tank system on the self-damping efficiency of such structures. Pressure-based dynamic analysis of liquid tanks has been carried out considering the k-ε turbulent model, which is based on the equations for kinetic energy (k) and dissipation rate (ε). The slosh response under convective and impulsive modes of vibrations are observed and major factors to be considered for improving the self-damping efficiency of liquid tanks are pointed out.

2   Model Specifications and Methodology

The study considered tank models of the aspect ratio of 1.7, 1.0, 0.7 and 0.5 with varying horizontal and vertical dimensions. The study is carried out in three cases namely; Case-1: Varying the horizontal dimension of the tank along the direction of input motion, Case-2: Varying the horizontal dimension of the tank perpendicular to the direction of input motion, Case-3: Varying the vertical dimension of the tank. Under all the cases, the dimensions other than that of varying dimension are kept constant. Additionally, the volume of liquid is assumed to be 0.018 m^3, which is invariable under all three cases for the purpose of comparison. The base of all the models is considered to be rigidly restrained against translations and rotations in all directions. All the tank models are generated to have length of the tank in X-direction and height of the tank in Z-direction. The origin of the tank is kept at the center of the tank, keeping symmetry along ZX and ZY planes. The geometric details of the tank models considered for the study are given in Table 1.

The finite element modeling is carried using ANSYS Design Modeler. The mesh size of each model is finalized by carrying out the mesh convergence test. The tank models are assumed to be acted upon by a harmonic vibration $x(t) = 0.02\sin(\omega t)$, with the excitation frequency (ω) being equal to the natural frequency of the corresponding model. The '$x(t)$' represents the translational motion in X-direction. Volume of Fluid (VOF) [9, 15] model with two-phase Eulerian approach is used to generate liquid volume fraction and the free surface conditions. ANSYS FLUENT is used as the solver for carrying out the transient analysis. The free surface elevation and hydrodynamic pressure on the left wall of the tank, under convective and impulsive conditions are considered as the response parameters for the analysis.

Table 1   Dimensions of the tank models (in m)

Case-1	Case-2	Case-3
$0.3 \times 0.3 \times 0.5$	$0.3 \times 0.3 \times 0.5$	$0.5 \times 0.5 \times 0.85$
$0.5 \times 0.3 \times 0.5$	$0.3 \times 0.5 \times 0.5$	$0.5 \times 0.5 \times 0.5$
$0.7 \times 0.3 \times 0.5$	$0.3 \times 0.7 \times 0.5$	$0.5 \times 0.5 \times 0.35$
$1.0 \times 0.3 \times 0.5$	$0.3 \times 1.0 \times 0.5$	$0.5 \times 0.5 \times 0.25$
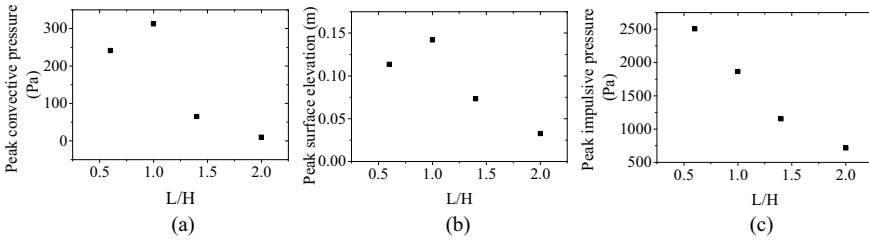
Fig. 1 Peak values of slosh response with variation in horizontal dimension parallel to input motion. **a** Convective pressure, **b** free surface elevation, **c** impulsive pressure

3 Results and Discussion

The self-damping efficiency of the liquid tank models is investigated by varying the horizontal and vertical dimensions of the tank models. The peak value of response parameters is observed under each case.

3.1 Case-1: Effect of Horizontal Dimension Along the Input Motion

The horizontal dimension of the tank models along the direction of input motion is varied as the ratio 'L/H' as shown in Fig. 1. Here, 'L' is the length of the tank and 'H' is the height of the tank. The peak value of response parameters under convective mode decreases with the increase in the length of the tank, except for the model with $L/H = 1$ (or aspect ratio = 1, in X-direction). This increase in the convective response parameters corresponding to $L/H = 1$ is due to the increase in the convective mass of liquid, which in turn increases the convective response. However, a further increase in the length of the tank models increases the length of the path traced by the slosh induced waves, which causes increased energy dissipation. However, a sudden reduction of 79% is observed for the convective pressure of the tank model with $L/H = 1.4$ (aspect ratio = 0.7). The reduction in the impulsive pressure is almost linear with the increase in the length of the tank.

3.2 Case-2: Effect of Horizontal Dimension Perpendicular to Input Motion

The horizontal dimension of the tank models perpendicular to the direction of input motion is varied as the ratio 'B/H', where 'B' is the width of the tank. The convective components of response in terms of pressure and surface elevation decrease with the
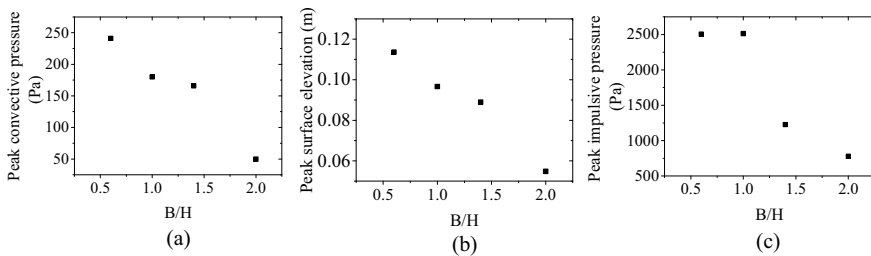
Fig. 2 Peak values of slosh response with variation in horizontal dimension perpendicular to input motion. **a** Convective pressure, **b** free surface elevation, **c** impulsive pressure

increase in the width of the tank models as shown in Fig. 2a. A similar pattern is observed in the case of impulsive response, except for the model with B/H = 1 (or aspect ratio = 1, in Y-direction) as shown in Fig. 2b. The increase in the width of the tank model causes an increase in the convective liquid mass. However, the motion of the liquid mass is constrained by the invariable length of the tank. Therefore, the convective component of response decreases. Whereas, the invariable length of the tank causes a slight increase in the impulsive mass of the liquid for the tank models with an aspect ratio of '1'. The corresponding increase in the impulsive response is noted for these models.

3.3 Case-3: Effect of Vertical Dimension

Figure 3 illustrates the effect of the vertical dimension of the liquid tank on slosh response under the convective and impulsive mode of vibration. Here, the peak value of pressure response is noted for different 'H/h' ratios, where 'h' is the height of the liquid. The response of the liquid tank decreases with an increase in the height of the tank, provided the horizontal dimensions and the volume of water being constant. Exceeding the height of the tank more than that of the horizontal dimension causes
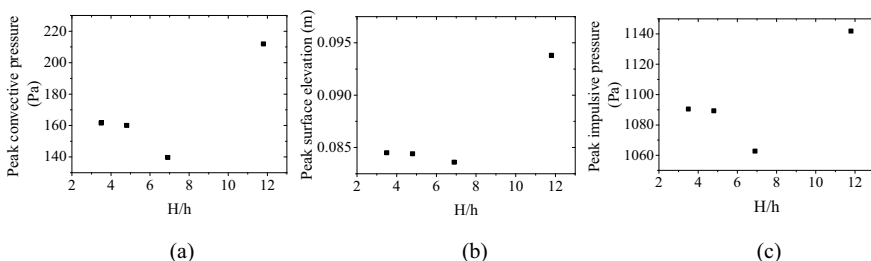
Fig. 3 Peak values of slosh response with variation in vertical dimension of the tank. **a** Convective pressure, **b** free surface elevation, **c** impulsive pressure
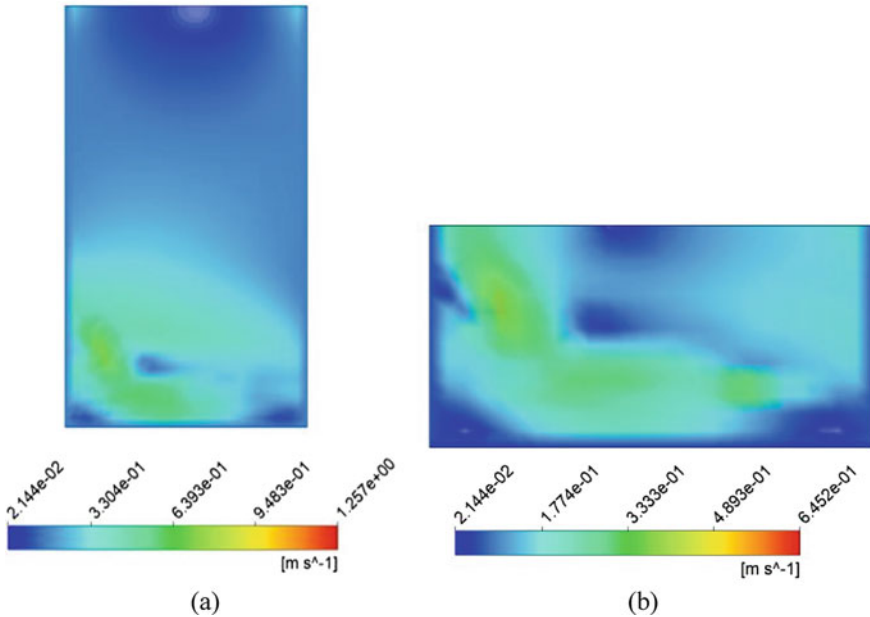
Fig. 4 Velocity of sloshing wave. **a** 0.5 × 0.5 × 0.85, **b** 0.5 × 0.5 × 0.25

an increase in the slosh response of the tank. This may be due to the increase in the sloshing wave velocity of the liquid, which is shown in Fig. 4. The velocity of liquid in the tank model 0.5 × 0.5 × 0.85 has a rotating effect, with a magnitude more than that of the model 0.5 × 0.5 × 0.25. Additionally, it is noted that the maximum reduction in the response is obtained when the vertical dimension is equal to the horizontal dimensions of the tank (aspect ratio = 1, in X and Y directions). However, the effect of vertical dimension on the slosh response of the liquid tank is less compared to that of the horizontal dimension of the tank.

3.4 Self-damping Liquid Tank Systems

Based on the parametric study on the liquid tank models, the horizontal dimension of the tank along the direction of input motion is observed as a key factor affecting the self-damping efficiency of the liquid tank systems. The horizontal dimension of the tank, which is perpendicular to the input motion also contributes to the self-damping mechanism. However, the damping efficiency imparted on the sloshing liquid is slightly less. Additionally, the effect of the vertical dimension on the self-damping efficiency is less compared to that of the horizontal dimensions. Limiting the vertical dimension to the maximum horizontal dimension will add to the self-damping mechanism of the tank. In particular, to obtain maximum self-damping
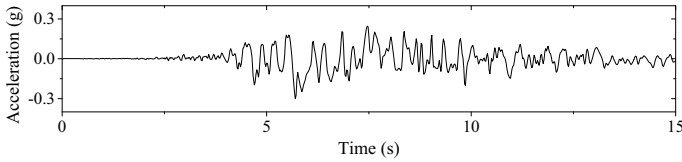
Fig. 5 Acceleration time history record of Imperial Valley ground motion
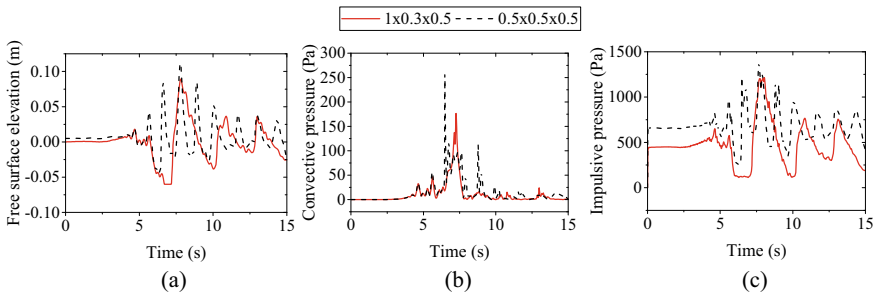
Fig. 6 Slosh response of tank models subjected to seismic ground motion. **a** Convective pressure, **b** free surface elevation, **c** impulsive pressure

efficiency of the liquid tank systems, the aspect ratio of the tank should be kept less than '1' in the direction parallel to the input motion.

In order to validate these observations, dynamic analysis has been carried out considering the tank models, $1 \times 0.3 \times 0.5$, $0.5 \times 0.5 \times 0.35$ and $0.5 \times 0.5 \times 0.5$. Imperial Valley, 1979, which is a low-frequency seismic ground motion is considered as the input motion. The major component of this ground motion is scaled down as shown in Fig. 5, and it is assumed to act along either X-direction or Y-direction of the tank model.

Figure 6 shows the comparison of slosh response of the models $1 \times 0.3 \times 0.5$ and $0.5 \times 0.5 \times 0.5$, in terms of liquid surface elevation and hydrodynamic pressure. An increased slosh damping of the tank model $1 \times 0.3 \times 0.5$ is evident under convective and impulsive modes of vibration. This is due to the longer horizontal dimension of the tank model $1.0 \times 0.3 \times 0.5$ in the direction parallel to (X-direction) the input seismic motion. Further, Table 2 shows the comparison of hydrodynamic pressure of various models. The direction of input motion is given in brackets for each model. The aspect ratio of the tank models in X and Y directions are represented as (X, Y). The maximum value of hydrodynamic pressure is obtained for the model $0.5 \times 0.5 \times 0.5$ with an aspect ratio of '1' in both horizontal directions. However, the pressure response reduces for those models with an aspect ratio less than '1' in either one or both the horizontal directions. The minimum pressure response is obtained for the model $1 \times 0.3 \times 0.5$ subjected to an input motion in Y-direction. This observation confirms that irrespective of the direction of input motion, the aspect ratio along the

Table 2 Comparison of hydrodynamic pressure of various models

Model	Aspect ratio (X, Y)	Peak hydrodynamic pressure (Pa)	
		Convective	Impulsive
0.5 × 0.5 × 0.5 (X)	1, 1	257.575	1373.372
1.0 × 0.3 × 0.5 (X)	0.5, 1.7	230.938	1214.061
0.5 × 0.5 × 0.35 (X)	0.7, 0.7	176.665	1302.637
1.0 × 0.3 × 0.5 (Y)	0.5, 1.7	135.830	731.0349
0.5 × 0.5 × 0.35 (Y)	0.7, 0.7	230.753	1302.495

length of the tank should be kept less than '1', to obtain maximum self-damping of the liquid mass.

4   Conclusions

The self-damping efficiency of the liquid tank systems is studied by carrying out the transient analysis on the tank models of different aspect ratios. The parametric study has been done based on the horizontal and vertical dimensions as the input variables. The study revealed the dominance of the major horizontal dimension of the tank in exerting the self-damping effect to the sloshing liquid mass. Major observations obtained from the study are as follows;

- The maximum damping of the slosh response is noted for the tank model with an aspect ratio of 0.5.
- The self-damping efficiency of the tank models improves by keeping the aspect ratio of the tank, less than '1' along the length of the tank.
- The vertical dimension exceeding the length of the tank models causes increased slosh response.
- These observations are validated by carrying out the dynamic analysis considering the low-frequency seismic ground motion.

From these observations, it can be noted that the maximum self-damping efficiency of the liquid tank systems is obtained by maintaining the aspect ratio of the tank, less than '1' along the length of the tank irrespective of direction of the input motion.

References

1. Soroushnia S, Tafreshim ST, Omidinasab F, Beheshtian N, Soroushnia S (2011) Seismic performance of RC elevated water tanks with frame staging and exhibition damage pattern. Procedia Eng 14:3076–3087
2. Manser WS, Touati M, Barros RC (2017) The maximum sloshing wave height evaluation in cylindrical metallic tanks by numerical means. MATEC Web Conf 95:4–8
3. Kotrasova K (2017) Study of hydrodynamic pressure on wall of tank. Procedia Eng 190:2–6
4. Housner GW (1963) The dynamic behavior of water tanks. Bull Seismol Soc Am 53:381–387
5. Housner GW (1955) Dynamic pressures on accelerated fluid containers. Bull Seismol Soc Am 15–35
6. Eswaran M, Saha UK, Maity D (2009) Effect of baffles on a partially filled cubic tank: numerical simulation and experimental validation. Comput Struct 87:198–205
7. Jin H, Liu Y, Li HJ (2014) Experimental study on sloshing in a tank with an inner horizontal perforated plate. Ocean Eng 82:75–84
8. Xue MA, Zheng J, Lin P, Yuan X (2017) Experimental study on vertical baffles of different configurations in suppressing sloshing pressure. Ocean Eng 136:178–189
9. Chu C, Wu Y, Wu T, Wang C (2018) Slosh-induced hydrodynamic force in a water tank with multiple baffles. J Ocean Eng 167:282–292
10. Ren L, Zou Y, Tang J, Jin X, Li D, Liu M (2021) Numerical modeling of coupled surge-heave sloshing in a rectangular tank with baffles. Shock Vib
11. Franklin T, Dodge (2000) The new 'dynamic behavior of liquids in moving containers. San Antonio, TX South West Res. Institute
12. Maleki A, Ziyaeifar M (2008) Sloshing damping in cylindrical liquid storage tanks with baffles. J Sound Vib 311:372–385
13. Kumar K, Maity D (2016) Pressure based Eulerian approach for investigation of sloshing in rectangular water tank. Procedia Eng 144:1187–1194
14. Nimisha P, Jayalekshmi BR, Venkataramana K (2021) Study of dynamic characteristics of circular liquid storage tanks using acoustic principles. Lect Notes Civ Eng 105:125–135
15. Kleefsman KMT, Fekken G, Veldman AEP, Iwanowski B, Buchner B (2005) A volume-of-fluid based simulation method for wave impact problems. J Comput Phys 206:363–393

Tensile and Ball Indentation Response of Am350 Steel at Room Temperature

**S. C. S. P. Kumar Krovvidi, J. Ganesh kumar, Sunil Goyal,
G. V. Prasad Reddy, M. Vasudevan, and S. Raghupathy**

Abbreviations

AM350-SA	AM350 steel in solution annealed condition
AM350-SCT1000	AM350 steel sub-cooled to -73 °C and tempered at 530 °C or 1000°F
ABI	Automated ball indentation
FCC	Face-centered cubic
FE	Finite element
SSM	Stress-strain microprobe
UTS	Ultimate tensile strength
VHN	Vickers hardness number
TRIP steels	Steels with transformation induced plasticity

1 Introduction

AM350 is precipitation-hardened stainless steel which is widely used as the material of construction for welded disk bellows in many critical applications including aerospace and nuclear applications [1, 2]. Figure 1 shows the welded disk bellows

S. C. S. P. Kumar Krovvidi (✉) · J. Ganesh kumar · G. V. Prasad Reddy · M. Vasudevan ·
S. Raghupathy
Indira Gandhi Centre for Atomic Research (IGCAR), Kalpakkam 603102, India
e-mail: krovvidi@igcar.gov.in

S. Goyal
Nuclear Fuel Complex, Kota Project, Rawatbhata 323305, India

G. V. Prasad Reddy · M. Vasudevan
Homi Bhabha National Institute (HBNI), Kalpakkam 603102, India

Fig. 1 Welded disk bellows manufactured of AM350

made up of AM350 for control rod drive mechanisms of fast breeder test reactor. AM350 in solution annealed condition is designated as AM350-SA in this paper. The microstructure of AM350-SA possesses mainly FCC austenitic structure [3]. The material is formable and weldable in AM350-SA condition. In general, after manufacturing, the components of AM350 are precipitation hardened by suitable heat treatment to get the required high strength. In the heat-treated condition referred to as SCT (sub-cooled and tempered) condition, the microstructure of the material is mostly martensitic [3]. Commercially, AM350 is available in the form of thin sheets.

As a part of the indigenous development of AM350 bellows at IGCAR Kalpakkam, it is essential to understand the mechanical and metallurgical response of the thin sheets of AM350 to develop reliable bellows. Bellows are manufactured of 0.3 mm thin sheets of AM350. This paper discusses the tensile response of thin sheets of AM350 in the solution annealed condition and in SCT1000 condition. As the tensile specimens were manufactured of 0.3 mm thick sheet, there could be chances for variation in the tensile properties obtained due to slipping in the grip, etc. Hence, the tensile properties obtained by testing thin specimens were verified by automatic ball indentation (ABI) testing. The force-depth response of the AM350 in ball indentation was analytically predicted by elastoplastic finite element analysis (FE analysis). The data obtained from the tensile testing was used as the material model in the FE analysis. This paper presents the response of the AM350 material in tensile and ABI testing, in both solution annealed (AM350-SA) and heat-treated (AM350-SCT1000) conditions. This paper also presents the numerical prediction of the force-depth response in ABI testing and comparison with the experimental results.

2 Experimental

2.1 Heat Treatment and Chemical Composition

The specimens for the investigation were extracted from 0.3 mm thick sheets of AM350-SA and AM350-SCT1000. The heat treatment of the material was done as per ASTM A693. For AM350-SA, the material was heated to 1050 °C, soaked for 15 min and water quenched. For the SCT1000 condition, the material was heated to 930 °C (soaked for 15 min) followed by water quenching to room temperature.
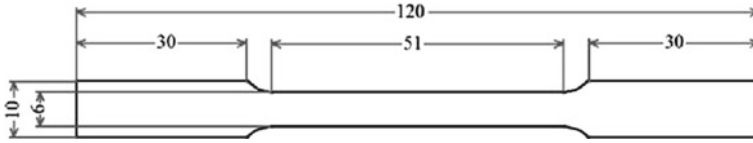
Fig. 2 Geometry of flat tensile specimen

Within 30 min of completion of this step, the material was cooled to −79 °C and held for 4 h. Subsequently, the material was tempered at 535 °C.

The chemical composition of AM350 was measured by Optical Emission Spectroscopy (OES). The specimens were extracted from 0.3 mm thick sheet of AM350. Wet chemical analysis was used for the accurate measurement of carbon content.

2.2 Tensile and Hardness Testing

Tensile testing of AM350-SA and AM350-SCT1000 was carried out on HungTa tensile testing system at room temperature at a strain rate of 3×10^{-3} s^{-1}. The geometry of the tensile specimen is given in Fig. 2. The overall length of the tensile specimen was 200 mm with a gauge length of 50 mm. The width of the specimen in the gauge length portion was 12.5 mm. The tensile specimens were extracted from 0.3 mm thick sheets by electro-discharge machining. The dimensions of the specimen were conforming to the flat tensile specimen details given in ASTM E8/8 M [4]. Microhardness of AM350-SA and AM350-SCT1000 was carried out at a load of 500 gf with a dwell time of 15 s as per ASTM E-384 [5]. In order to investigate the stain-induced martensite transformation in the steel, measurement of ferrite number was carried out using ferritescope for AS350-SA before and after tensile testing. The fractured surfaces of the tested specimens were examined in a scanning electron microscope at a higher magnification to understand the nature of the fracture under tensile loading.

2.3 ABI Testing

The stress–strain microprobe (SSM) system based on automated ball indentation (ABI) technique was employed in this investigation as described by Ganeshkumar et al. [6]. In the ball indentation tests, a SiN spherical indenter of 0.25 mm diameter was used (Fig. 3). The indenter was forced onto the test specimens for a depth of 15% of the indenter radius. The dimensions of the specimen used in the ball indentation were 10 mm × 10 mm × 0.3 mm. During testing, total depth was given in three cycles, each of 5% of the radius of the indenter.

Fig. 3 ABI test setup
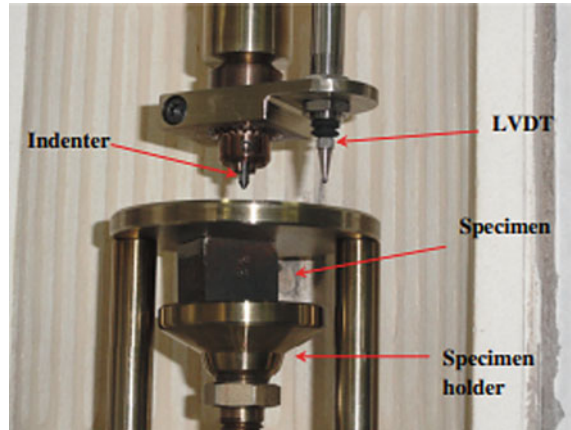
Table 1 Measured and nominal values of chemical composition of AM350

Element	Measured	As per ASTM A693
Carbon	0.082	0.07–0.10
Manganese	0.72	0.5–1.25
Silicon	0.2	< 0.5
Phosphorus	0.01	< 0.03
Sulfur	0.01	< 0.03
Chromium	16.8	16–18
Nickel	4	4–5
Molybdenum	2.21	2–3.25
Nitrogen	0.07	0.07–0.13

3 Experimental Results

3.1 Chemical Composition

The chemical composition of the steel is given in Table 1. It was found that the chemical composition of the steel is conforming to ASTM A693.

3.2 Microhardness

The microhardness measurement of AM350-SA and AM350-SCT1000 is summarized in Fig. 4. The average valve of the microhardness (VHN) in as received condition was found to be around 240 ± 10 and the VHN of AM350-SCT1000 was found to be 380 ± 5.

Fig. 4 Microhardness of AM350 and AM350-SCT1000 at room temperature
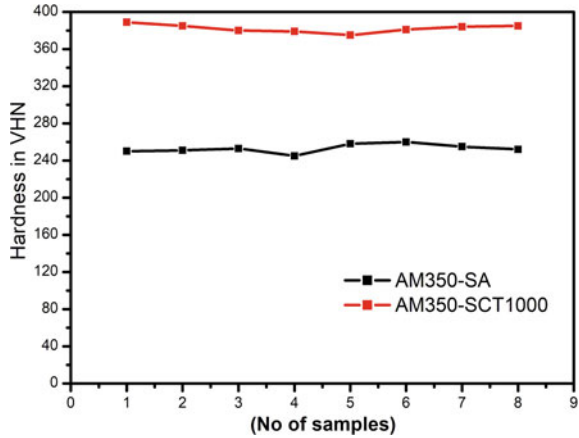
3.3 Tensile Response

The engineering stress–strain curves of AM350-SA and AM350-SCT100 are given in Fig. 5. The yield strength and UTS of AM350-SA were estimated as 475 MPa and 1090 MPa, respectively. The % elongation of AM350-SA was found to be around 35%. After heat treating to SCT1000 condition, the yield strength of the material increased significantly to 1075 MPa. The UTS of AM350-SCT1000 was found to be around 1190 MPa.

AM350-SA exhibited transgranular failure with characteristic ductile dimples on the fracture surface, as shown in Fig. 6. However, the fractographic examination of SCT1000 condition was not conclusive. Due to thin specimens used and the fracture

Fig. 5 Engineering stress strain curves of AM350 in both the heat treatment conditions
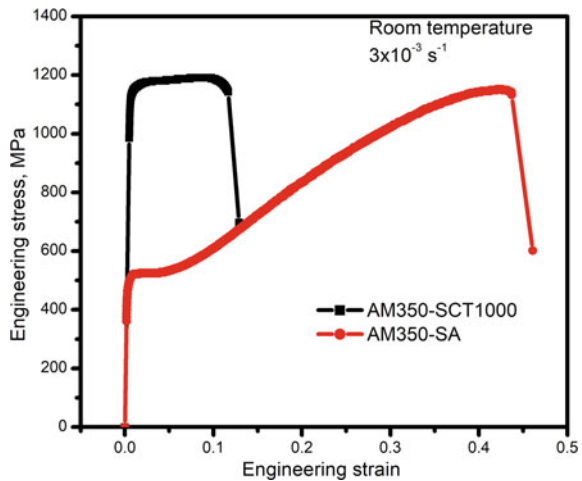
Fig. 6 Fractography of the
tensile tested specimens of
AM350-SA
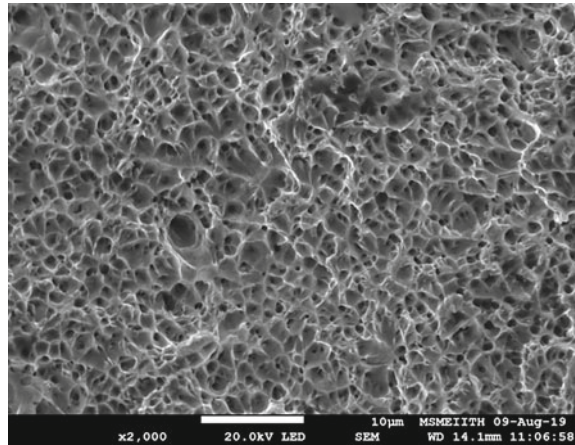
surface was inclined to the electron beam, no constructive SEM images could be
extracted during the fractographic examination of SCT1000 specimen.

3.4 ABI Response of AM350

The variation of the depth of indentation with the applied load for AM350-SA and
AM350-SCT1000 in the ABI test is shown in Fig. 8a and b. Conventionally around
24% of the indenter radius is considered as the depth of indentation. However in the
present case, as the thickness of the specimens is less, the depth of indentation was
limited to 15% of the indenter radius with a smaller diameter indenter. For the same
depth of indentation, the load applied was much higher in SCT1000 AM350-SA as
shown in Fig. 7.

4   Finite Element Analysis

4.1 FE Model and Boundary Conditions

Finite element analysis was carried out to numerically predict the ball indentation
behavior of the material. The FE model for numerical prediction of the ball inden-
tation response of the material is given in Fig. 8a. As the indenter is spherical,
axisymmetric analysis was carried out. The specimen was modeled as axisymmetric
shell. A four noded CAX4R element was used in ABAQUS [7]. Punch was modeled
as rigid. The geometry and boundary conditions are shown in Fig. 8b (Axysynnetry
was defined about the axis of the indenter and the specimen, and the bottom surface
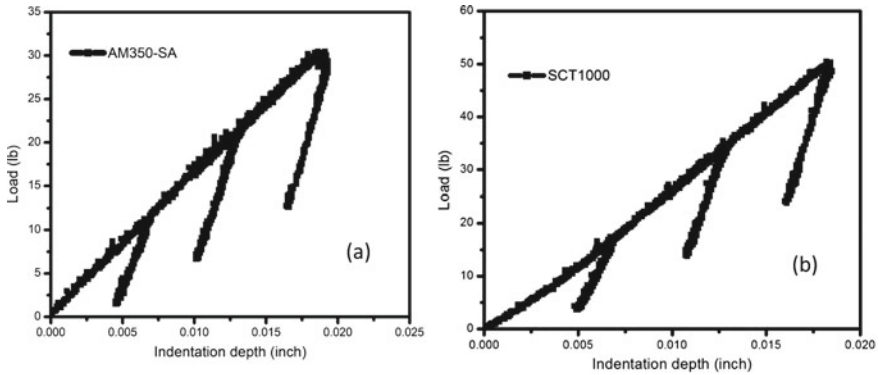
Fig. 7 Experimental observation of ball indentation of **a** AM350-SA and **b** AM350-SCT1000 at room temperature
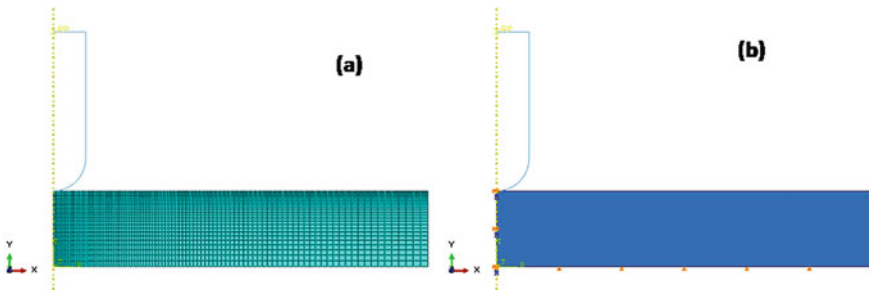
Fig. 8 Geometry and boundary conditions to predict the ball indentation

of the specimen was constrained in the *y* direction). A graded meshing was done for the AM350 specimens such that the mesh size is finer below the punch.

The Young's modulus and Poisson's ratio of the material were considered as 200 GPa and 0.3, respectively. From the experimental tensile response of the material, the variation of the true stress with the true plastic strain was computed for the material in both the heat treatment conditions and shown in Fig. 9. The data given in Fig. 9 was considered as the material model in the plastic range of AM350 in the respective heat treatment conditions. The bottom face of the shell was constrained. A reference point feature was provided on the punch on which the loading and unloading cycles were provided.

Fig. 9 True stress–strain curves in plastic range of **a** AM350-SA and AM350-SCT1000 at room temperature
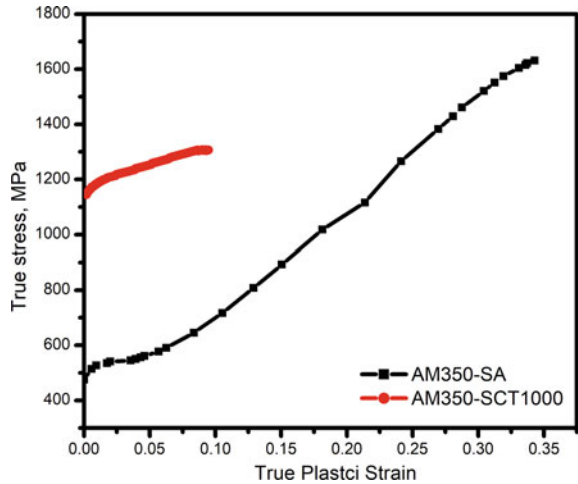
4.2 Results of Finite Element Analysis

Numerical prediction and experimental observation of the response of the AM350-SA in ABI testing are shown in Fig. 10a. It was found that the numerical estimation of the variation of the force with the depth of indentation was in close agreement with the experimental observation. At higher values of the indentation, marginal variation was found between the numerically predicted and the experimentally observed values (the predicted value of the load is more than the experimentally observed value) which can be attributed to the small thickness of the specimen and modeling the punch as a rigid material. Numerical estimation and experimental observation of the ball indentation response of the material in SCT1000 condition was also found to be in close agreement as shown in Fig. 10b. The force required for a given indentation
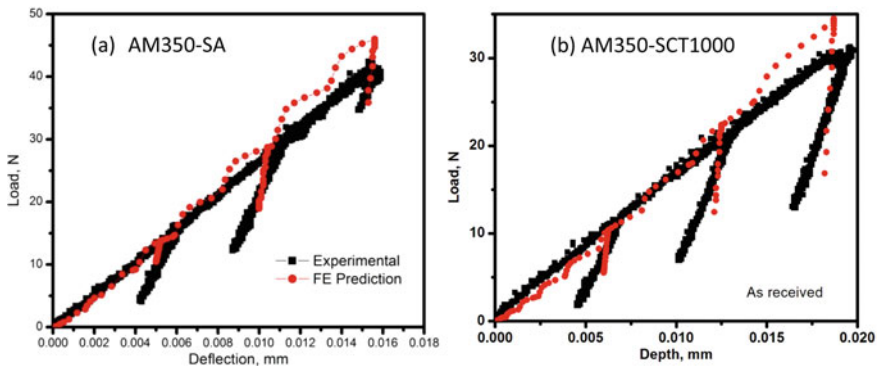
Fig. 10 Numerical prediction and experimental validation of ball indentation response of **a** AM50-SA and **b** AM350-SCT1000

in SCT1000 condition was found to be more compared to the other two grades, as the material in this condition was found to have higher hardness and mechanical strength.

5 Discussion

A significant increase in the hardness of the material due to heat treatment to SCT1000 condition is observed and is attributed to the formation of martensite. Though AM350-SA is mostly austenitic (94%) in its microstructure, it was found that the engineering stress–strain response of AM350-SA is different from other austenitic stainless steels. Austenitic stainless steels such as SS316, SS304 and their varients at room temperature exhibit exponential variation of stress with strain in the plastic range due to work hardening [8]. In the present case, the tensile response of AM350-SA showed a sigmoidal response similar to TRIP steels [9, 10]. It can also be seen from Fig. 6 that though the yield strengths of the material in solution annealed condition and SCT1000 conditions are varying, the ultimate tensile strengths of the two material conditions are closer. This suggests the formation of the strain-induced martensite in the material. Further investigation of the strain-induced martensite response of the material was carried out by measuring the ferrite number of the tensile specimens (of both AM350-SA and AM350-SCT1000) before and after testing as summarized in Table 2. The ferrite number of the specimen in the gauge length portion before tensile testing was found to be around 5–6 and the same after tensile testing was found to be around 54, indicating the formation of strain-induced martensite [11]. There was a very marginal increase in the ferrite number of the AM350-1000 after tensile testing which could be due to partial transformation of the retained martensite in SCT1000 to martensite. It may be noted from Table 2 that the transformation to martensite is very significant in the case of AM350-SA, and this transformation appeared to occur gradually concurrent with an increase in accumulated plastic strain, as indicated by the simultaneous increase in flow stress of the material during continued straining.

It was found that there is a close agreement between the numerically predicted and experimentally obtained ball indentation responses of AM350-SA and AM350-SCT1000. The close prediction of the ball indentation response of the material by FE analysis using the experimental data gives more confidence on the generated material

Table 2 Ferritescope measurements of AM350-SA and AM350-SCT1000 before and after tensile testing

	AM350-SA		AM350-SCT1000	
	Before tensile testing	After tensile testing	Before tensile testing	After tensile testing
Ferrite number	5–6	54	52	54

data from 0.3 mm thick sheets. At a higher depth of indentation, which is after a few loading and unloading cycles, a minor variation in the numerically predicted ABI response was observed. This variation is attributed to the repeated load–unload cycles in ABI which could not be captured completely with the input data from uniaxial tensile tests, thereby indicating the need for further improvement in predictions. The latter may be achieved with the test data from load–unload cycles in tensile testing and/or by using nonlinear isotropic and kinematic hardening models.

6 Conclusions

The following conclusions were derived from the present work.

- The hardness of AM350-SCT1000 was found to be more compared to that of AM350-SA.
- The tensile strength of AM350 in SCT1000 condition was found to be more compared to that of AM350-SA though the ductility was found to be less.
- AM350-SA exhibited transgranular failure with characteristic ductile dimples on the fracture surface.
- From the sigmoidal shape of the tensile curve and the ferrite scope measurements in the gauge length portion of the tensile specimen, it was found that the AM350-SA shows stain-induced martensite transformation.
- The ABI response of the material was numerically predicted and compared with the experimental response. It was found that there is a close agreement between the two, especially at low strains. Minor variation was observed at higher strains which could be due to the use of thin specimens and use of uniaxial tensile data for predicting the ABI response under cyclic loading.

References

1. Allegr P, Jacquelin R, Carbonnier JL (1979) Abstracts of paper, IWGFR-32, IAEA Specialist Meeting on sodium bellows. Tokyo
2. Kumar Krovvidi SCSP, Padmakumar G, Bhaduri AK (2017) Experience of various materials for design and manufacture of bellows for nuclear industry. J Adv Mater Proc 2(3):156–161
3. Kumar Krovvidi SCSP, Das CR, Goyal S, Arunkumar S, Mahadevan S, Albert SK, Raghupathy S, Bhaduri AK (2020) Mechanical and microstructural examination of AM350
4. ASTM E8/8M (2016) Standard test methods for tension testing of metallic materials. ASTM International, West Conshohocken, Pennsylvania
5. ASTM E384 (2017) Standard test method for microindentation hardness of materials. ASTM International, West Conshohocken, Pennsylvania
6. Nagaraju S, GaneshKumar J, Vasantharaja P, Vasudevan M, Laha K (2017) Mater Sci Eng 695:199–210. https://doi.org/10.1016/j.msea.2017.04.021
7. Smith M (2009) ABAQUS standard user's manual. Dassault Systèmes Simulia Corp, Providence, RI

8. Ganesan V, Mathew MD, Sankara Rao KB (2009) Influence of nitrogen on tensile properties of 316LN SS. Mater Sci Technol 25(5):614–618
9. Olson GB, Cohen M (1975) Kinetics of strain-induced martensitic nucleation. Metall Trans A 6:791–795
10. Olson GB, Azrin M (1978) Transformation behavior of TRIP steels. Metall Trans A 9:713–721
11. AWS A4.2M:2006 (ISO 8249:2000) Standard procedures for calibrating magnetic instruments to measure the delta ferrite content

Numerical Simulation for Design Improvement in Diffuser of Multistage Centrifugal Pump

Bhushan R. Rode and Ruchi Khare

Nomenclature

C_{m2}	Meridonal velocity at impeller outlet
g	Acceleration due to gravity (9.81 m/s^2)
H	Head generated (m)
n	Total number of stages
N	Rotational speed of impeller (rpm)
P_1	Total pressure at the pump inlet (Pa)
P_2	Total pressure at the pump outlet (Pa)
P_{in}	Input power
P_{out}	Output power
Q	Flow rate (m^3/s)
T	Total torque at pump shaft (Nm)
γ	Specific weight of water (N/m^3)
ΔH	Increase in head in each stage (m)
ΔP	Increase in pressure in each stage (Pa)
η	Hydraulic efficiency
ρ	Density of liquid (kg/m^3)
Ψ	Flow coefficient

B. R. Rode (✉)
Department of Hydro and Renewable Energy, Indian Institute of Technology Roorkee, Roorkee, Uttarakhand 247667, India
e-mail: brode23@gmail.com; bhushan_rr@hre.iitr.ac.in

R. Khare
Department of Civil Engineering, Maulana Azad National Institute of Technology Bhopal, Bhopal, Madhya Pradesh 462003, India

1 Introduction

A centrifugal pump is a work-absorbing turbo-machinery device that transforms the energy of prime mover, i.e. kinetic energy into pressure energy of the water that is being pumped, resulting in the water being elevated from lower elevation to higher elevation. It is accomplished by generating a suction pressure at the inlet and higher pressure at the outlet. About 22% of the world's energy is used by electricity [1], the pumps, therefore, have enormous energy consumption and great potential for energy savings.

To pump the water from lower elevation to a very higher elevation, a simple centrifugal pump is not survive to produce such head, therefore, a multistage centrifugal pump is used because there will be an increase in pressure in each stage of the pump, and hence, head developed is more. More and more energy-saving techniques are forcing industries and researchers to focus on improving pump efficiency. To meet the energy-saving technique, one of the method is the channel profile from the outlet of the impeller to the inlet of the next stage impeller must be optimized more and more, i.e. to bring the impeller with great efficiency into a full performance. The principle formula for total pressure head developed by the multistage centrifugal pump is given by Rode and Khare [2],

$$\sum_{0}^{n} \Delta H = \frac{\sum_{0}^{n} \Delta P}{\rho g} \tag{1}$$

Several researchers work on the profile of the impeller blades and vanes of diffuser to enhance the performance of multistage centrifugal pump. Zhou et al. [3] predicted that the performance of twisted blades is higher than that of the straight blade. Miyano et al. [4] revealed that when the trailing edge of the return vanes is set to touch condition that the fluid will stop swirling before reaching the next stage, resulting in the next impeller drawing more fluid and being able to add more power to the fluid. La Roche-Carrier et al. [5] investigated Stage 1 of a multistage centrifugal pump with three different heights of blade, i.e. 16, 23, 29 mm. When height was 29 mm, the head developed was found to be highest, and best efficiency level was highest for height 23 mm. Zhang et al. [6] introduced a new return guide vanes (RGV) which has a twisted segment that delivers efficient results than the conventional one. A different method of designing radial type vane profiles was described by Bowade and Parashar [7]. Lai et al. [8] show that the amplitudes of pressure pulsation in both diffuser and volute slowly decrease with the increase of vaned diffuser outlet diameters. Kawashima et al. [9] suggested that matching of the diffuser vane with the return vane is very important to increase the multistage pump efficiency. The performance of multistage centrifugal pump may also enhance by increasing the vaned diffuser outlet height.

In the present paper, an attempt has been made to enhance the performance of multistage centrifugal pump by using Ansys CFX viscous 3D flow simulation incorporating k–ε turbulence model. The work is analyzed for different vaned
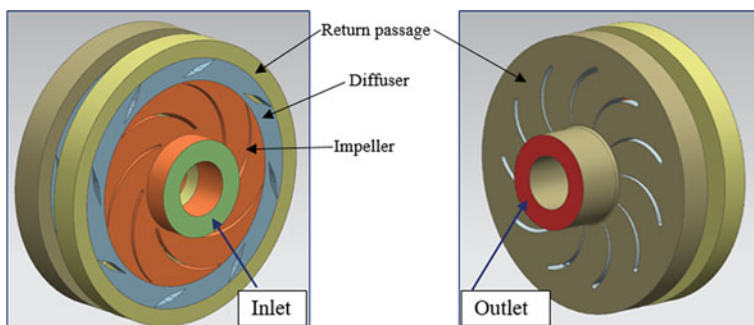
Fig. 1 3D geometry of multistage centrifugal pump

diffuser outlet heights with different rotational speeds, whilst mass flow rate of 128.8888889 kg/s is kept same.

2   Geometric Modelling

For numerical simulation, the important input is the specification of geometry of complete flow domain. Multistage centrifugal pump is basically a type of centrifugal pump which consists of more than one impeller in series keyed to a single shaft. The pump consists mainly of three main components, namely impeller, diffuser, and return channel. The numerical simulation is done on multistage (two-stage) centrifugal pump having 6 impeller blades, 8 diffuser vanes, and 11 return guide vanes. The diameter of the impeller is 412 mm. The height of the impeller blades and diffuser vanes is 23 mm and of RGV is 35 mm.

In multistage centrifugal pump, impeller is a rotating components, whereas diffuser and return guide vanes are stationary components. Hence, each domain is modelled separately in the design modeller and assembled by proper interfaces. The complete assembled modelling is Fig. 1.

3   Boundary Conditions

The results obtained in a flow domain from numerical simulation depend on the defined boundary conditions. At the inlet of the pump, static pressure of 1 atmosphere is specified as inlet boundary condition, and at the outlet of the pump, mass flow rate of 128.8888889 kg/s is specified as outlet boundary condition. The diffuser and return passage domains are set stationary. The rotational speed, i.e. 1450, 1600, 1750, 1900, 2200, and 2500 rpm is specified for impeller domain for all different diffuser outlet heights. For all walls, the boundary condition is taken as no slip boundary condition,

(a) Inlet boundary condition   (b) Outlet boundary condition
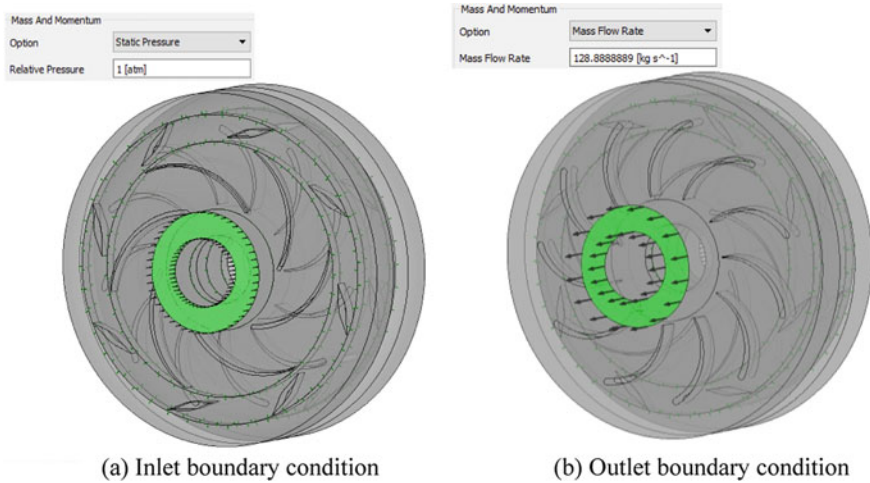
Fig. 2 Computational domain of multistage centrifugal pump

i.e. smooth walls and k–ε turbulence model is used for the simulation. The boundary condition at inlet and outlet of the pump is shown in Fig. 2.

4   Computational Parameters

For the computation of the various parameters such as head generated by the pump, power input, power output, and the efficiency of the pump, the following formulas are used.

$$\text{Head generated} = \frac{(P2 - P1)\ \text{Stan. Frame}}{\gamma} \tag{2}$$

$$\text{Input Power}\ P_{in} = \frac{2\Pi N T}{60000} \tag{3}$$

$$\text{Output Power}\ P_{\text{out}} = \frac{\gamma Q H}{1000} \tag{4}$$

$$\text{Efficiency}\ \eta = \frac{P_{\text{out}}}{P_{\text{in}}} * 100 \tag{5}$$

$$\text{Flow coefficient}\ \Psi = \frac{C_{m2}}{\sqrt{2gH}} \tag{6}$$

5 Results and Discussion

The numerical simulation has been carried out by increasing the vaned diffuser outlet heights by 10, 20, 30, and 40% of its original height (23 mm) with different rotational speed, i.e. 1450, 1600, 1750, 1900, 2200, and 2500 rpm to get various computational parameters. The variation of different parameters with different vaned diffuser outlet heights at different rotational speeds is shown in Figs. 3, 4, and 5.

From the above performance charts, it is observed that in most of the cases, the maximum head, maximum power output, and maximum efficiency are found at a 20% increment in the diffuser outlet height. In some cases, the maximum head and efficiency are found at a 30% increment, but these values are nearly equal as compared with a 20% increment. So the pump is giving the best performance at a 20% increment. Variation of head and efficiency with different rotational speeds for a 20% increment in the diffuser outlet height is shown in Fig. 6.

From the above performance Fig. 6, it is observed that as the rotational speed increases the head is also increases by a large amount, and efficiency is decreased slightly. At 1525 rpm, the pump gives the same head (67 m) and efficiency (67%),

Fig. 3 Effect of % increment at diffuser outlet height on head
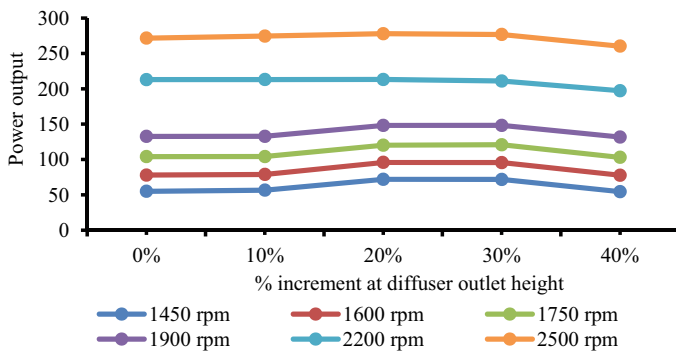
Fig. 4 Effect of % increment at diffuser outlet height on power output
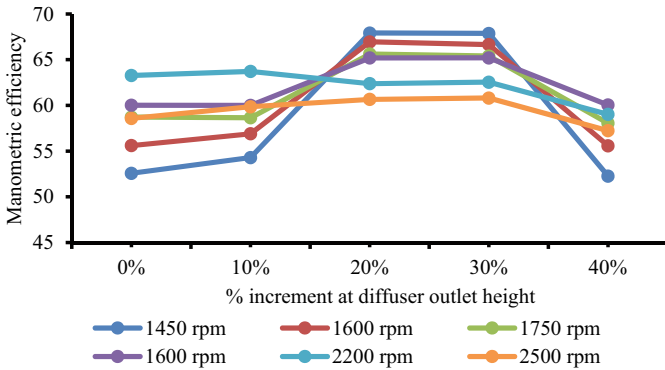
Fig. 5 Effect of % increment at diffuser outlet height on manometric efficiency
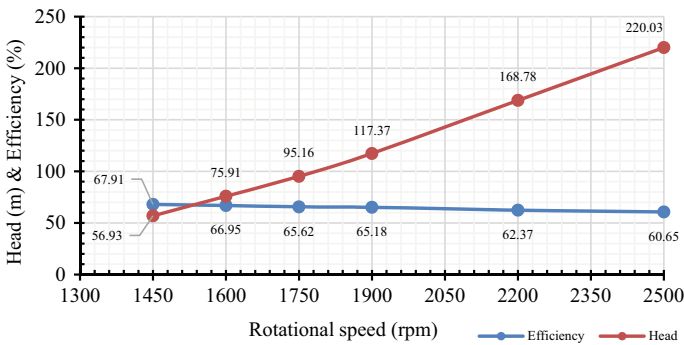
Fig. 6 Variation of head and efficiency with different rotational speed for 20% increment in the diffuser outlet height

but the head developed by the pump is too low. At 1900 rpm, the head developed by the pump is 117.37 m which is nearly two times the head developed at 1525 rpm, and the decrease in efficiency is about 1.82%. It is also observed that at 2050 rpm, the head developed by the pump is 142 m, but there is a decrease in the efficiency is about 4%. Also, the head developed at 2200 rpm is 168.78 m which is nearly two and half times the head developed at 1525 rpm, and the decrease in the efficiency is 4.63%. From the above observations, it is found that the pump gives the best head at a 20% increment in diffuser outlet height, and at 1900 rpm, but there is decrease in the efficiency is about 1.82%. The velocity streamlines and pressure contour are only drawn for a 20% increment in diffuser outlet height at 1900 rpm.
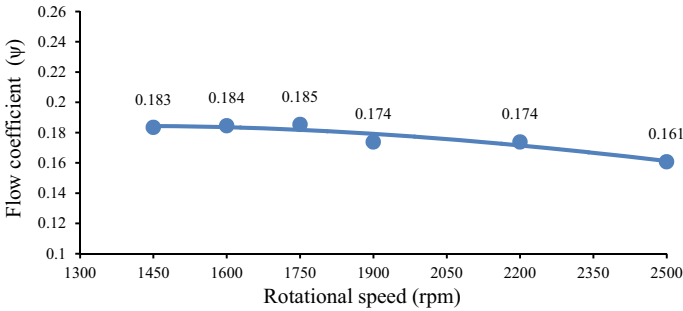
Fig. 7 Variation of flow coefficient (ψ) with different rotational speed for 20% increment in the diffuser outlet height

5.1 Variation of Flow Coefficient (ψ) with Different Rotational Speed for 20% Increment in the Diffuser Outlet Height

The flow coefficient (ψ) is the dimensionless quantity used to describe the volume flow rate. Variation of flow coefficient with different rotational speed for 20% increment in the diffuser outlet height is shown in Fig. 7. From the figure, it is observed that there is shrimpy decrement in the flow coefficient with rotational speed, because the head increases with rotational speed and flow coefficient is inversely proportional to square root of head.

5.2 Velocity Streamline for 20% Increment in Diffuser Outlet Height (27.6 mm) at 1900 rpm

From the streamline pattern, it is observed that the velocity of fluid-particle at the inlet of the pump is more than the outlet since at the suction, the pump draws the fluid at high velocity. It was also observed that the impeller is in rotating motion which forces the fluid out of domain that leads to flow fluid with the highest velocity at impeller outlet. The streamline pattern for a two-stage centrifugal pump with different views of the pump is shown in Fig. 8.

5.2.1 Comparison of Velocity Streamlines in a Diffuser for 20% Increment in Diffuser Outlet Height (27.6 mm) with 40% Increment in Diffuser Outlet Height (32.2 mm) at 1900 rpm

From Fig. 9, it is seen that at the 20% increment diffuser 1 and diffuser 2 (Figure a and b) of a two-stage pump, the spiral vortex developed is very small, but for
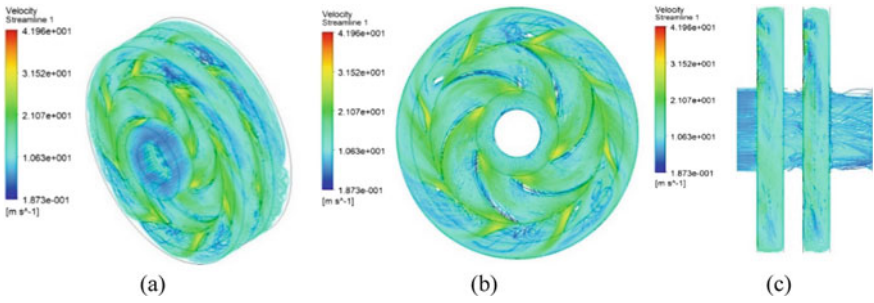
Fig. 8 **a** 3D view of pump with velocity streamline. **b** Front view pump with velocity streamline. **c** Side view of pump with velocity streamline
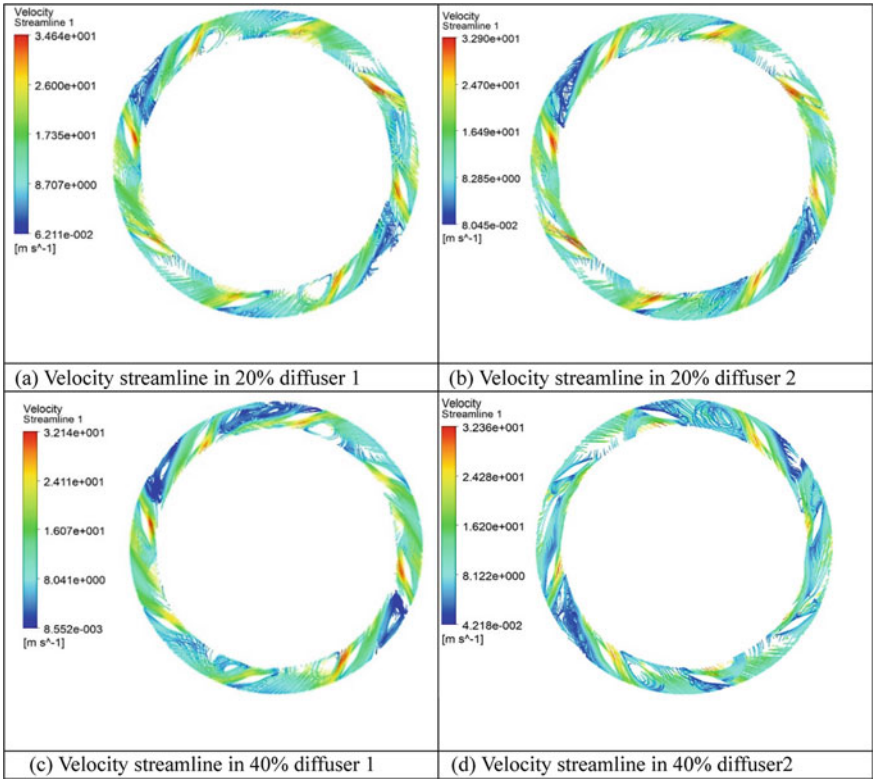
Fig. 9 Velocity streamlines in a diffuser for 20% increment in diffuser outlet height (27.6 mm) with 40% increment in diffuser outlet height (32.2 mm) at 1900 rpm

(a) 3D view of pump with pressure contour

(b) Sectional view of pump with pressure contour
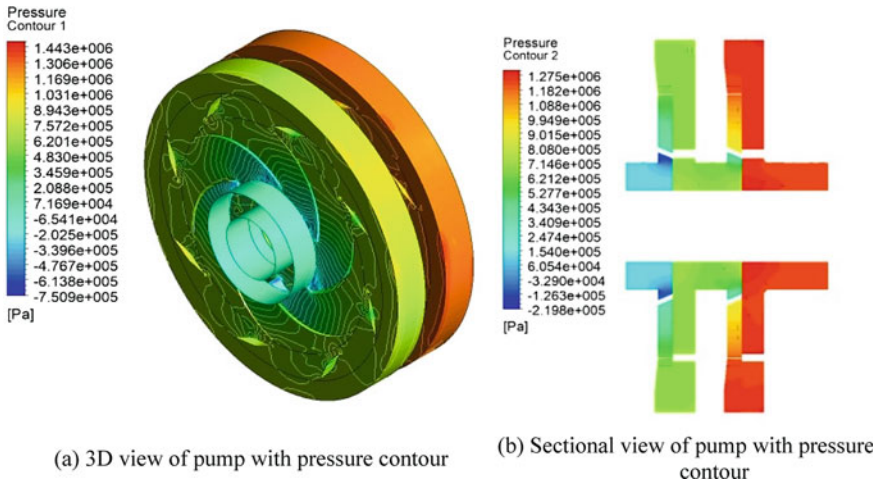
Fig. 10 Pressure distribution for 20% increment in diffuser outlet height at 1900 rpm

the 40% increment diffuser 1 and diffuser 2 (Figure c and d), the spiral vortex highly developed, therefore head developed by the pump decreases. From most of the performance charts, it is observed that the head increases up to 20% increment, it slightly decreases between 20 and 30%, and after 30%, it falls rapidly. Figure 9 shows comparison of velocity streamline in diffuser for 20% increment in diffuser outlet height (27.6 mm) with 40% increment in diffuser outlet height (32.2 mm) at 1900 rpm.

5.3 Pressure Distribution for 20% Increment in Diffuser Outlet Height at 1900 rpm

From Fig. 10, it is observed that the pressure is increasing from the inlet of the pump to the outlet. At the suction side, the pressure is nearly atmospheric, and at the discharge side, the pressure is much higher than the suction side. Pressure contour for a 20% increment in the diffuser outlet height at 1900 rpm with different views of the pump is shown in Fig. 10.

6 Conclusions

In this paper, the study of CFD flow simulation is carried out for a multistage centrifugal pump having five different vaned diffuser outlet heights with six different rotational speeds. It has been investigated that the head developed by the pump

increases as the rotational speed increases, but the efficiency of the pump decreases slightly. The following conclusions are drawn based on different vaned diffuser outlet heights with different rotational speeds.

- The velocity of the whirl at pump inlet $C_{u1} \approx 0$, which satisfies the pump theory. The return passage guide vanes deswirls the flow before entering the next stage impeller so the velocity of whirl at the inlet of next stage impeller nearly equal to zero (i.e. $C_{u2} \approx 0$).
- The multistage centrifugal pump having a different vaned diffuser outlet height with six different rotational speed is analyzed for the same mass flow rate of 128.8888889 kg/s. It is observed that the head developed by the pump increases up to a 20% increment in vaned diffuser outlet height. It slightly decreases between 20 and 30%, and after 30%, it falls rapidly because of spiral flow in the diffuser. It is observed that the pump gives the best performance at 20% increment in the diffuser outlet height.
- It is observed that as the rotational speed increases, head developed by the pump increases by a large amount, but efficiency decreases slightly. At 1525 rpm, the pump gives the same head and efficiency, i.e. 67 m and 67%, r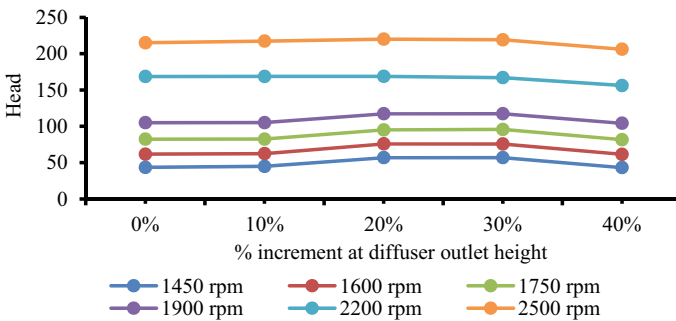espectively. At 1900 rpm, the head developed is 117.37 m which is nearly double the head developed at 1525 rpm, and a decrease in efficiency is about 1.82%. It is also observed that at 2050 rpm, the head developed by the pump is 142 m, but efficiency decreases by 4%. Also at 2200 rpm, the head developed is 168.78 m which is approximately two and a half times the head developed at 1525 rpm and the efficiency decreases by 4.63%.
- From the above observation, it is found that the pump gives the best head at a 20% increment in existing height of vaned diffuser at 1900 rpm, but there is decrease in the efficiency is about 1.82%.

The present study is useful to understand the pressure and flow variations in the multistage centrifugal pump.

References

1. Wang C, Shi W, Wang X, Jiang X, Yang Y, Li W, Zhou L (2017) Optimal design of multistage centrifugal pump based on the combined energy loss model and computational fluid dynamics. Appl Energy 187:10–26
2. Rode BR, Khare R (2021) A review on development in design of multistage centrifugal pump. Adv Comput Des 6(1):43–53
3. Zhou W, Zhao Z, Lee TS, Winoto SH (2003) Investigation of flow through centrifugal pump impellers using computational fluid dynamics. Int J Rotating Mach 9(1):49–61
4. Miyano M, Kanemoto T, Kawashima D, Wada A, Hara T, Sakoda K (2008) Return vane installed in multistage centrifugal pump. Int J Fluid Mach Syst 1(1):57–63
5. La Roche-Carrier N, Dituba Ngoma G, Ghie W (2013) Numerical investigation of a first stage of a multistage centrifugal pump: impeller, diffuser with return vanes, and casing. ISRN Mech Eng 2013

6. Zhang Q, Shi W, Xu Y, Gao X, Wang C, Lu W, Ma D (2013) A new proposed return guide vane for compact multistage centrifugal pumps. Int J Rotating Mach 2013
7. Bowade A, Parashar C (2014) A review of different blade design methods for radial flow centrifugal pump. Int J Sci Eng Res 3:24–27
8. Lai F, Zhu X, Li G, Zhu L, Wang F (2019) Numerical research on the energy loss of a single-stage centrifugal pump with different vaned diffuser outlet diameters. Energy Proc 158:5523–5528
9. Kawashima D, Kanemoto T, Sakoda K, Wada A, Hara T (2008) Matching diffuser vane with return vane installed in multistage centrifugal pump. Int J Fluid Mach Syst 1(1):86–91

Influence of Parameters on the Prediction of Dynamic Impact Factor for Railway Bridges: A Review

Kasilingam Senthil, Divyansh Tewari, Ankur Sharma, and Natraj Singh

1 Introduction

Indian Railways has a total of 147,523 bridges across the country, which are broadly classified into 3 categories based on breadth of their waterway named important bridge (>300 m), Major bridge (18 m) rest are categorized as minor bridge (around 92% bridges come into this category). 37,689 bridges in Indian railways are more than 100 years old and increase in axle load and traffic density and introduction of faster train on such bridges necessitates assessment of safety aspect of these bridges. Currently there is no difference on speed restrictions whether the locomotive moves in older bridge or new bridge such overload on the older bridge might erode its value [1]. It is of upmost importance to study the dynamics of railway because moving loads create additional response as compared to static load and ratio of live load to dead load and dynamic load is much higher for railway bridges than for similarly sized highway bridges [2]. Hence thorough study on dynamic properties of bridges should be done to define the allowable critical speed of locomotive on such bridges and ensure other parameters such as deflection, vibrations caused due to moving locomotive are within allowable limits.

The present study deals with the research conducted on the variation in impact factor caused a moving locomotive under different conditions and the importance of factors considered by various researchers. Section 2 states the classical approach conducted to understand the dynamics of bridge. Section 3 deals to understand the various research conducted to obtain expression of impact factor for different velocity

K. Senthil (✉) · D. Tewari · A. Sharma
Department of Civil Engineering, National Institute of Technology Jalandhar, Jalandhar, Punjab 144011, India
e-mail: kasilingams@nitj.ac.in

N. Singh
Bridge Workshop, Jalandhar Cant, Northern Railway, Jalandhar, Punjab 144005, India

of moving locomotive. Section 4 classifies the allowable impact factor to be used for different velocity locomotive and the importance to study the effects produced by track components. This paper will result in broadening the design of railway bridge perspective and aid with maintenance and repair of existing bridges.

2 Classical Approach of Bridge Dynamics

Dynamics of railway bridge was first studied in nineteenth century, where engineers were spilt into two opinions where some believed that passage of locomotive would create an Impact whereas others believed there will not enough time for the structure to respond to that impact of moving locomotive so to resolve the issue both analytical and experimental studies were carried by Stokes [3] and Willis [4], respectively. Analytical solution was developed using a differential equation to examine the effect of the velocity of train passing on the girder bridge under its ultimate capacity, where it was confirmed that up to a certain point deflection of the bridge increases with velocity, Willis examined the deflection or fracture caused due to a moving load on a cast iron bar through an experiment on the strength of material and concluded that the moving load imparted the higher deflection on the bar as that produced when the load was kept at rest and that increase in deflection was due to the difference in the magnitude of load and the pressure exerted on the bridge. This concluded that it was essential to study on the dynamics of moving load on railway bridge.

Extensive research on the dynamics of bridge to calculate the vibration on the bridge due to a moving locomotive subjected to a mass mounted on the spring was carried out by Inglis [5], stated that several cases for the analysis of vibration of railway bridges due to the moving load and determine the dynamic bending moment and shear forces on various points on the bridges up to 50 m span, deflection of bridge was taken as, $y = f(t) \sin\left(\pi * \frac{x}{l}\right)$. Further, Mise and Kunii [6] proposed differential equations for an 80 m span bridge to predict the dynamic deflection and critical speed at which deflection reaches its maximum value, vertical deflection of beam was considered as

$$y = \sum_{r=1}^{r=\infty} f_r(t) \sin\left(\frac{r\pi x}{l}\right)$$

Further, according to the test results by Kerr [7], the stresses on well-maintained track due to moving train is negligible when velocity of train is less than 50 km/h, whereas stresses increase noticeably when velocity of train increases.

Effects due to cyclic loading, creep, seasonal variation in older bridges causes irregularity which might introduce bouncing and pitching on the railway track and causes variation in stresses produced by wheel load of high-speed train which in turn results in higher dynamic load than static load generally dynamic wheel load is given as,

$$P_d = \emptyset \times P_s \tag{1}$$

where P_d is the dynamic wheel load, P_s is live load and $\emptyset$ is impact factor (always >1) [8].

Jain and Malla et al. [9, 10] defined dynamic magnification factor (D) as the ratio of resultant response amplitude displacement (dynamic) to static displacement. $D = \frac{x_{\text{dynamic}}}{x_{\text{static}}}$, and impact factor ($\phi$) of the bridge structure is defined as the ratio of difference between dynamic and static displacement to static displacement,

$$\phi = \frac{x_{\text{dynamic}} - x_{\text{static}}}{x_{\text{static}}} = D - 1, \tag{2}$$

Currently several standard codes (see Table 1) only consider span of the structure to evaluate dynamic impact factor, which gives conservative value for low-speed trains and underestimated value for high-speed trains as effects due to locomotive speed, surface roughness, track stiffness must also be considered for the correct evaluation.

Table 1 International prospective for impact factor calculation

S. No.	Current designing codes	Expression for impact factor
1	Bridge Rules (2014) [11]: for single track spans	$\emptyset = 1 + \text{CDA} = 1 + \left(0.15 + \frac{8}{6+L}\right)$, CDA ≤ 1
2	European standard (EN 1991–2:2003) [12]	$\emptyset = \frac{1.44}{\sqrt{L}-0.2} + 0.82$, $1.00 \leq \emptyset \leq 1.67$, for carefully maintained track
3	Bulletin of Illinois: Impact on railway bridges (1944) [13]	$\emptyset = \frac{1}{1+\frac{L^2}{20000}}$
4	AREMA MANUAL (2006) [14]	$\emptyset = 1 + \frac{0.3}{S} + 0.4 - \frac{L^2}{500}$ (for $L < 24.4$ m) $\emptyset = 1 + \frac{0.3}{S} + 0.16 - \frac{1.83}{L-0.94}$ (for $L \geq 24.4$ m) $S = $ Width of bridge
5	Iranian code (2007) [15]	$\emptyset = 1 + 0.3 - 0.005L - 0.15$ (for well-maintained track)
6	AASHTO (1996): Standard specification [16]	$\emptyset = \frac{15.24}{L+38} \leq 30\%$
7	BS 5400-2 (1978) [17, 18]	$\emptyset = 1.67$, $L \leq 3.6$ m $\emptyset = 0.82 + \frac{1.44}{\sqrt{L}-0.2}$, 3.6 m $\leq L \leq 67$ m $\emptyset = 1$, $L \geq 67$ m
8	TB10002.1-2005 (Chinese code) [19]	$\emptyset = 1 + \frac{28}{40+L}$
9	Japan Road Association (1978) [19, 20]	$\emptyset = 1 + \mu = 1 + \frac{10}{65+L} + \frac{0.52}{L^{0.2}}$, $\mu_{\max} = 0.7$

Dynamic impact factor evaluated in The Australian and New Zealand railway design manual (1974) and Bridge Code of South African Transportation Services (1983) is same as given in European standard (EN 1991–2) [21].

3 Survey on Expressions of CDA Whilst Considering Different Parameters

To attain true value of impact factor it is necessary to consider the other parameters responsible, following are such expressions given by various researchers.

3.1 O.R.E Committee/Birmann [22]

Dynamic behaviour of track was studied by measuring difference in formation, alignment (straight/curve), type of vehicle and taken into the account of ageing factor of the track. Theoretical value of dynamic impact factor was defined in terms of three dimensionless coefficients given as, $\emptyset = 1 + \alpha + \beta + \gamma$, value of α can be found from Table 2.

β is coefficient due to shift in curve dependent upon speed, super elevation deficiency and centre of gravity of vehicle. Measurements conducted by DB stated that for super elevation error of 100–130 mm, β ranges from 0.13 to 0.17; meanwhile measurement by SNCF stated for super elevation error of 150 mm, β is taken as 0.2. Both the railway companies derived expression for calculating the value of β as [8].

$$\beta = \frac{(2dh)}{g^2}, \text{ French (SNCF) formula} \tag{3}$$

$$\beta = \frac{V^2(2h + c)}{127Rg} - \frac{2ch}{g^2}, \text{ German (DB) formula} \tag{4}$$

where V = Velocity if train (Km/h); h = height of CG of vehicle (m); g = gauge width (m); d = super elevation deficiency (m); R = radius of curve (m); c = super elevation (m).

Table 2 Variation of α in different conditions

Perfectly levelled track	0
With levelling defect and very fast traffic	0.35
Curved track	< 0.18
Other cases	$\alpha* = 0.04\left(\frac{V}{100}\right)^3$

[*] Dependent on resilience of train suspension

γ is the coefficient obtained by considering speed, age factor of vehicle and maintenance condition of track.

$$\gamma = \left\{ 0.1 + 0.017 \left(\frac{V}{100} \right)^3 \right\} a_0 b_0, \tag{5}$$

where a_0 and b_0 are factors depending on the maintenance of locomotive and track. If insufficient data is available regarding super elevation of track and maintenance of track and locomotive, O.R.E has given maximum value of impact factor as

$$\phi = 1.29 + 0.04 \left(\frac{V}{100} \right)^3 \tag{6}$$

3.2 Eisenmann's Formula (1969) and Prud'Homme's (1970) [23]

Proved that distribution of dynamic load follows normal distribution (see Fig. 1). Expression adopted probabilistic approach was derived after considering train speed, track quality, contact stress and ageing of track. Coefficient of dynamic amplification given as, $C_d = 1 + t * s * \varphi$, where t depends upon certainty, s depends on condition of railway track and φ is the factor dependent upon velocity of locomotive (Table 3).

Fig. 1 Stress as a normal distribution [24]
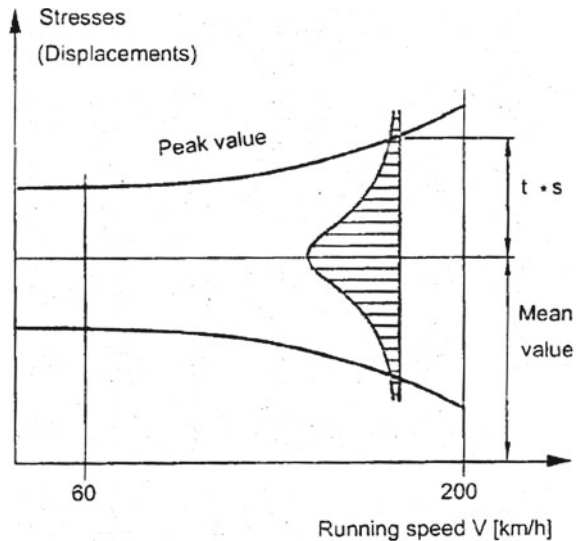
Table 3 Variation of Eisenmann's factor for different condition

Probability (%)	t	Track condition	S	Velocity (km/h)	φ
68.3	1	Very good	0.1	< 60	1
95.5	2	Good	0.2	$60 < V < 200$	$1 + \frac{V-60}{140}$
99.7	3	Poor	0.3	$200 < V < 300$ [22]	$1 + \frac{V-60}{380}$

Fig. 2 Variation in track impact factor using Prud'd Homme method and Eisenmann's method [25]
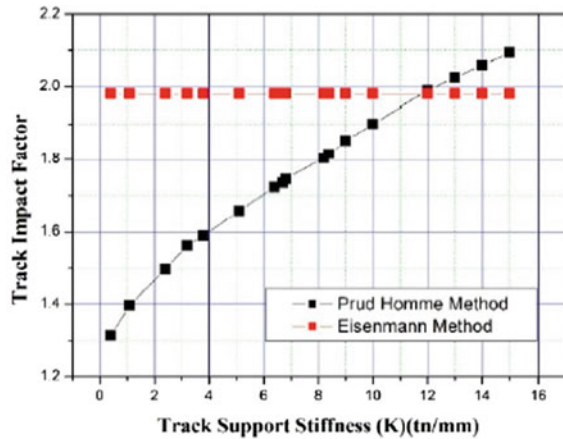
Limitation of the above expression was given by Prud'Homme's (1970) where he suggested dynamic response varies with different track types, so he developed the expression of standard deviation (σ) of dynamic load as a function of mass of train (m_{ns}), stiffness of track (K), damping of rails $\gamma(\in)$ and Velocity of train (V) [25]. As stiffness is not considered in Eisenmann's formula that might result in overdesign of the tract, see Fig. 2.

$$\sigma = 0.45 * \frac{V}{100} * b * \sqrt{m_{ns} * K * \gamma(\in)} \tag{7}$$

3.3 American Railway Engineering and Maintenance-of-Way Association (AREMA)

AREMA (former known as AREA) manual is published every year in the month of April. Expression for impact factor was first published in 1974 by Boyle [8] where the expression was only dependent on vehicle speed and wheel load given as, $\phi = 1 + 5.21 * \frac{V}{D}$, where V is speed in km/h and D is diameter of wheel (mm). Thorough field measurements using wheel impact load detector conducted by Edwards et al. [26] concluded that the above formula overestimates the impact value

Table 4 Expressions of revised impact factor for different types of rolling stocks [15]

Rail transit mode	Revised impact factor
Light	$1 + 0.0665 * \frac{\text{Speed(km/h)}}{\text{Wheeldiameter(cm)}}$
Heavy	$1 + 0.323 * \frac{\text{Speed(kmph)}}{\text{Wheeldiameter(cm)}}$
Commuter	$1 + 0.198 * \frac{\text{Speed(kmph)}}{\text{Wheeldiameter(cm)}}$

and expressions were derived by taking wheel impact load detector data (WILD) data for light, heavy and commuter rails transit systems (see Table 4).

3.4 Van Dyke et al. [27]

Dynamic load factor was determined using wheel impact load detector (WILD) on three sites, on high-speed intercity passenger transit. Wild data was taken for all the transits moving those sites for a month. Observed data underestimate the actual loading conditions as the sites were free of variation of loads due to track irregularity. However, the data retrieved represented the dynamic factor for whole North America rail transit system. The dynamic amplification factor obtained by neglecting the effect due to condition of wheel and nominal loads was given as

$$\emptyset = 1.099 + 0.00386 * V \tag{8}$$

where V is given in mph.

3.5 Dung et al. [28]

Dynamic load factor (DLF) was calculated experimentally at Cat Linh-Ha Dong line as well as simulations were done using SIMPACK software for validation considering load and speed of train, support stiffness and rail material. Experimentally regression equation obtained for DLF is given as,

$$\phi = 0.9909 + 0.004853 * V \tag{9}$$

Parametric study on DLF was carried out by varying the velocity and was concluded that 2.46% difference in DLF value was obtained when train speed varies from 0 to 80 km/h.

3.6 Other Formulas to Calculate Impact Factor

Lot of other researchers considering different factors, for different purposes and using different methods affecting the dynamics of rail bridges does research on the impact factor. Lot of them are outdated due to validation or overestimating the results, dynamic load incremental factor used in Indian railways until 1965 also known as "Indian Formula" [29] for calculating speed factor ($\phi = 1 +$ Speed factor) is given by considering modulus of track (k) in kg/cm^2 and velocity of train (V) in mph is given as

$$\text{Speed factor} = \frac{V}{18.2 * \sqrt{k}} \tag{10}$$

After 1965 Indian railways started using expression given by Schramm [29] also known as "German Formula" where impact factor was segregated for depending on the speed of train given as

$$\text{For speed up to} 100 \text{ km/h}, \quad \text{Speed factor} = \frac{V^2}{30000} \tag{11}$$

$$\text{For speed above 100 km/h}, \quad \text{Speed factor} = \frac{4.5 * V^2}{10^5} - \frac{1.5 * V^3}{10^7}, \quad V \text{ in Km/h} \tag{12}$$

In the studies conducted by Clarke [30] where he considered speed of train (V) in km/h, wheel diameter (D_w) in mm and u as the track modulus (MN/m/m)

$$\text{Impact factor } (\phi) = 1 + \frac{19.65 * V}{D_w * \sqrt{u}} \tag{13}$$

4 Results and Discussion

For optimized and most economized design it is vital to know the design wheel load with as much accuracy as possible, for that it is very essential to know more about dynamics of wheel-track interface. Comparative analysis was carried out on a carefully maintained single track considering wheel diameter as 1100 mm for broad gauge [31]. Track modulus was taken as 75 kg/cm^2 [29] and width of bridge as 5 m, Fig. 3 consist of variation of impact factor with the span of girder by considering the expressions given by various design codes (see Table 1). Figures 3 and 4 shows the variation of impact factor by changing the span of the girder and speed of the locomotive by various researchers described in Sect. 3.
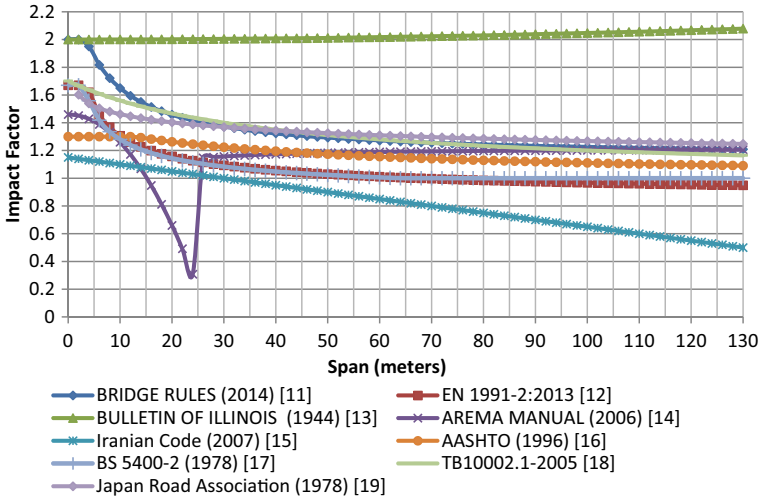
Fig. 3 Variation of dynamic impact factor with span of bridge (international perspective)
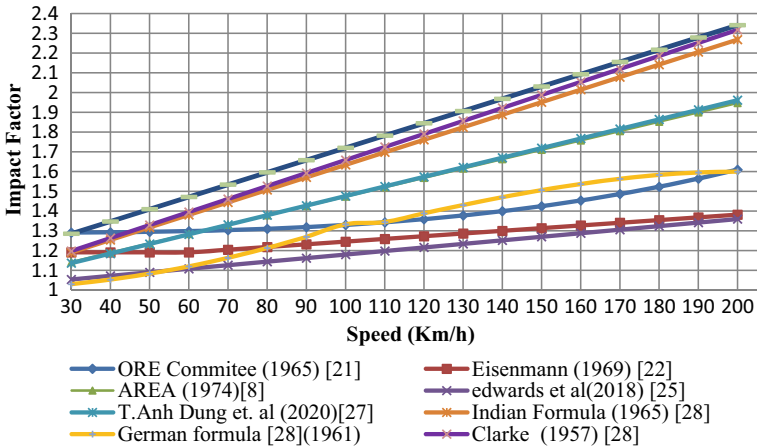
Fig. 4 Variation of impact factor with speed of locomotive

5 Conclusion

Based on detailed literature review, the following conclusions has been drawn:

- It is concluded that the classical approach underestimates the value of impact factor as variation in average values calculated for the approaches is 14.78%.
- Expression incorporating length span, velocity of locomotive and stiffness of track must be derived for different track conditions for different mode of transit until

then expression given by Dung et al. [28] and AREA (1974) resulting the most appropriate estimation for impact factor.

References

1. Ministry Of Railway (2019) Standing committee on railway. Seventeenth Lok Sabha, Lok Sabha Secretariat, New Delhi
2. Gu G, Kapoor A, Lilley DM (2008) Calculation of dynamic impact loads for railway bridges using direct integration method. Proc IMechE Part F J Rail Rapid Transit 222
3. Strokes GG (1849) Discussion of differential equation relating to breaking of railway bridges. Fellow of Pembrake College, Cambridge
4. Willis R (1849) An essay on the effect produced by causing weights to travel over elastic bar. In: Appendix to the report of the commissioners appointed to enquire into the application of Iron to railway structures
5. Inglis CE (1934) A mathematical treatise on vibrations in railway bridges, vol 203(21). Cambridge, pp xxv
6. Mise K, Kunii S (1956) a theory of forced vibrations of a railway bridge under the action of moving loads. Duart Jooro Mtcb Appl Math IX(2)
7. Kerr AD (1976) On the stress analysis of rails and ties. U.S. Department of Transportation, Washington D.C
8. Boyle NF (1980) Railway track design: a review of current practice. Australian Government Publishing Service, Canberra
9. Jain AK (2017) Dynamics of structures with Matlab applications. Pearson India Education Services Pvt. Ltd
10. Malla RB, Jacobs D, Dhakal S, Baniya S (2017) Dynamic impact factors on existing long span truss railroad bridges. Final report for Rail Safety IDEA project 25, Transport Research Board
11. Government of India Ministry of Railway (Railway Board) (2014) Bridge rules. Research Design and Standards Organisation, Lucknow
12. EN 1991–2:2003 Eurocode 1: action on structures—part 2: traffic loads on bridges. European Committee for Standardization (2003)
13. Looney CTG (1944) Impact on railway bridges, vol 42. University of Illinois Bulletin, Urbana
14. American Railway Engineering and Maintenance-of-Way Association. AREMA Manual 2006
15. Moghimi H, Ronagh HR (2008) Impact factor for a composite steel bridge using non linear dynamic simulation. Int J Impact Eng 35:1228–1243. https://doi.org/10.1016/j.ijimpeng.2007.07.003
16. Standard specification for highway bridges. American Association of State Highway and Transportation Officials, Washington DC 1996
17. B.S.5400: Part 2: 1978 (1978) Steel concrete and composite bridges: specification for loads. British Standards Institution, London
18. BS153: Part 3A: 1972 Specification for steel and girder bridges: Part 3A (loads). British Standards Institution, London
19. Youliang D, Gaoxin W (2016) Evaluation of dynamic load factors for a high speed railway truss arch bridges. Shock Vibr 15. https://doi.org/10.1155/2016/5310769
20. Standard specification for steel and composite structures, 1st edn. Japan Society of Civil Engineering 2009
21. Connor CO, Shaw PA (2000) Bridge loads an international perspective. Spon Press, London
22. Birmann F (1965–1966) Track parameter, static and dynamic. Proc Inst Mech Eng 180(3F)
23. Balmaseda L, Gallego I, Cambronero S, Rivas A (2018) Importance of vertical rail track stiffness on dynamic overloading: limitation of Eisenmann's formula. In: International congress on high speed rail: technology and long term effect, vol 5, pp 301–311

24. Esveld C (2001) Modern railway track, 2nd edn. Delft University of Technology
25. Lee J, Oh K, Park Y, Choi J (2020) Study on the applicability of dynamic factor standards by comparison of spring constant based dynamic factor of ballasted and concrete track structures. Appl Sci 10. https://doi.org/10.3390/app10238361
26. Edwards JR, Cook A, Dersch MS, Qian Y (2018) Quantification of rail transit wheel loads and development of improved dynamic and impact loading factor for design. Proc IMechE Part F J Rail Rapid Transit 1–12
27. van Dyke BJ et al (2016) Evaluation of dynamic and impact wheel load factor and their application in design processes. J Rapid Rail Transit Part F. https://doi.org/10.1177/0954409715619454
28. Dung TA, Tham MV, Quy DX, Truyen TT, Ky PV, Ha LH (2020) Numerical and experimental study of dynamic factor of the dynamic load on the urban railway. J Mech Behav Mater 29:195–202. https://doi.org/10.1515/jmbm-2020-0020
29. Chandra S, Agarwal MM (2013) Railway engineering. Oxford University Press
30. Stewart HE, Rourke TD (1988) Load factor method for dynamic track loading. J Transp Eng 114:21–39
31. Specification No. MP-0.3900.07 (2017) Specification of non contact type equipment for measurement of wheel parameters and wheel defects of broad Guage locomotives. Research Design and Standards Organisation, Lucknow

Analytical Study of Reduced Beam Section Under Cyclic Behavior

T. K. Jafla and Vishnu T. Unni

1 Introduction

RBS is usually utilized to move the plastic hinge away from the beam column junction to the neighboring side. As a result, the seismic impact on a structure is reduced since the stress concentration over the column is reduced. Furthermore, by enhancing the ductility of the beam, the use of these RBS sections can improve seismic performance. As it is not commonly utilized in India [1], several experimental investigations are still underway to bring it up to Indian standards. It is recommended for welded joints since they are more prone to premature failure [2]. A tiny crack can lead to the development of further cracks, joint failure, and severe column failure. Bolted joints give a weaker part, allowing failure to occur without inflicting significant damage to the column [2]. Furthermore, due to its complexity, establishing a large number of bolt connections is a time-consuming and labor-intensive task so that industries prefer welded connections for joints [3]. Therefore, we generally employ welded joints since they are simple and straightforward. Softening a piece of the beam flanges near the column face is one of the most promising approaches to adjust the behavior of the conventional moment frame. By reducing the area from the beam flanges near the column, the connection can be softened. This method, known as the reduced beam section method, which directs plastic hinges toward the beam span and away from the column face, hence reducing the stress concentration at the beam column interface.

T. K. Jafla (✉)
Vimal Jyothi Engineering College, Kannur 670632, India
e-mail: tkjafla@gmail.com

V. T. Unni
Structural Engineering Division, Department of Civil Engineering, Indian Institute of Technology Madras, Chennai, Tamil Nadu 600036, India
e-mail: ce20d025@smail.iitm.ac.in

2 Methodology

2.1 Literature Survey

Swati and Gaurang [1] investigated the benefits and use of RBS for Indian profiles, and researchers tested two steel moment connections with and without reduced beam section (RBS) under cyclic loads. The results were compared using experimental tests and the finite element method. They discovered that the RBS application prevented cracks at the bottom flange weld. According to the hysteresis behavior the RBS with varied voids dissipates more energy compared to other reduced sections. From the hysteresis behavior, the RBS using varied voids dissipate energy more compared to other types of reduction. Their study is quite limited and more extensive study is recommended to understand the behavior of RBS section profiles. Maleki et al. [4] studied RBS as well as double RBS and proved that double RBS connection shows a superior hysteresis behavior compared to the RBS connection.

2.2 Research Gap Identification

In many studies, double RBS is used to provide better performance against earthquake loads, no research has been done on how these RBS react when they are with different patterns of elliptical cutouts and the behavior will be studied under seismic loads.

2.3 Modeling

Beam column joint from experimental study was analyzed, and specimens are modeled based on specifications given as per AISC and FEMA codes [1]. Height of the column considered was 975 mm and length of the beam from the center of the column was 1000 mm. Other, geometrical details, Sections with 250 MPa grade were considered for this study are mentioned in Table 1. Each beam flange and Web were welded at the face of the column using filet welds [1].

Geometrical and material nonlinearity were considered. The nonlinear material properties were defined based on Table 2. The column was assumed as fixed at both

Table 1 Select members for analysis and details of the reference model for verification [1]

Member (S. No. as per IS 12778-2004)		Depth d (mm)	Web thickness tw (mm)	Flange width bf (mm)	Flange thickness tf (mm)
WPB 150	Column	162	8	154	11.5
NPB 200	Beam	200	5.6	100	8.5

Table 2 Material properties [1]

Section	*Fy*	Fu	*v*	*E* (MPa)
NPB200	330	484	0.3	2×10^5
WPB150	334	486	0.3	2×10^5

Notes Fy represents yielding stress; Fu represents ultimate strength; *v* represents Poisson's ratio; and *E* represents modulus of elasticity

the ends and at the joint beam to column element connection is configured as fully restrained.

From Fig. 1, the beam and column parts were modeled using four noded thin shell elements. Meshed model-structured quad mesh with element size 15 mm. Total number of nodes are 35,591 and are divided into 4993 elements.

The loading condition for the study is as shown in Table 3, the cyclic loading protocol with displacement amplitude was considered [1].

Fig. 1 Four noded meshing of beam column joint
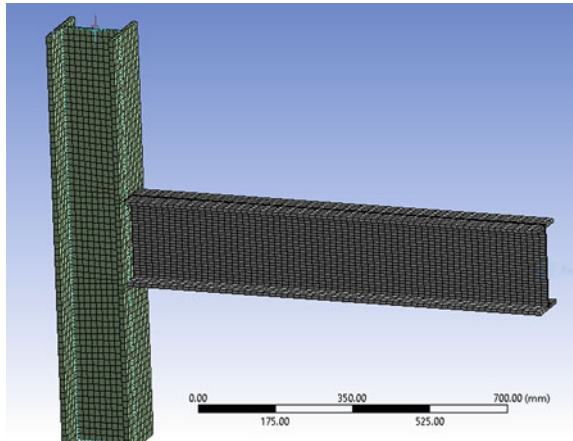
Table 3 Loading schedule [1]

Load cycles	6	6	6	4	2	2	2	2	2
Interstory drift angle (radians)	0.00375	0.05	0.0075	0.01	0.015	0.02	0.03	0.04	0.05
Beam tip displacement (mm)	± 3.75	± 5	± 7.50	± 10	± 15	± 20	± 30	± 40	± 50

3   Validation

Shows the comparison of the hysteresis curve obtained from analytical study and that of the hysteresis curve from the experimental study [1] and is found to be approximately same with a minor percentage error. It may be due to the variations in temperature as well as difference in boundary condition (Table 4). Before considering the beam column joint, one has to analytically validate it. Which means the experimental values obtained must be matched with the analytical results. By constructing the same model with same properties as given in the experimental investigations. The force–displacement hysteretic responses of the connections resulting from the experimental study are compared with those of the finite element analysis Fig. 2a and b. The von misses stress distribution for the beam column joint is as shown in Fig. 3a and b. Reasonable correlation between the analysis and experimental results [1] was observed. With cyclic displacement increasing, both specimens share the almost same shape and curve slope decreases continuously until attain the extreme limit loading. It showed that the structures remain elastic before yielding. The area of hysteretic loops gradually increased, and residual deformations were observed with the increase of displacement after yielding. Inelastic deformation occurred mainly in panel zone and beam flanges for connection so in order to resolve this RBS sections can be introduced. The percentage error can be found using the equation [5]. It may be due to the variations in controlled temperature and the minute meshing size.

$$\% \text{ Error } = \frac{(\text{Force Experimental} - \text{Force Theoretical})}{(\text{Force Experimental})} * 100 \qquad (1)$$

Table 4 Results obtained (Force in KN)

FEA	75 KN
Experimental [1]	79 KN
% of error	5%
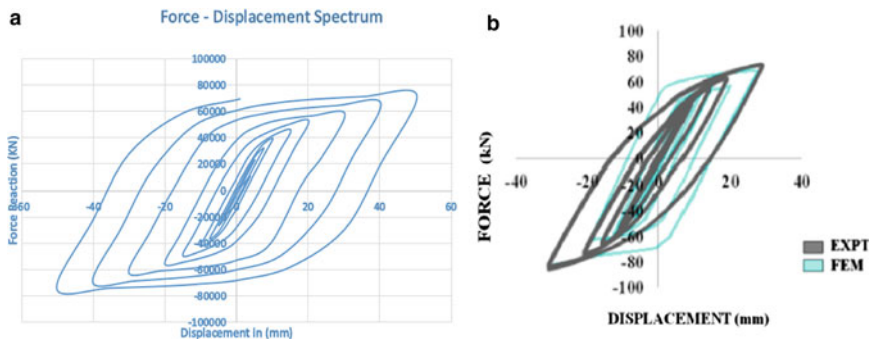
Fig. 2 Hysteretic behavior FEA (**a**) and experimental (**b**) [1]
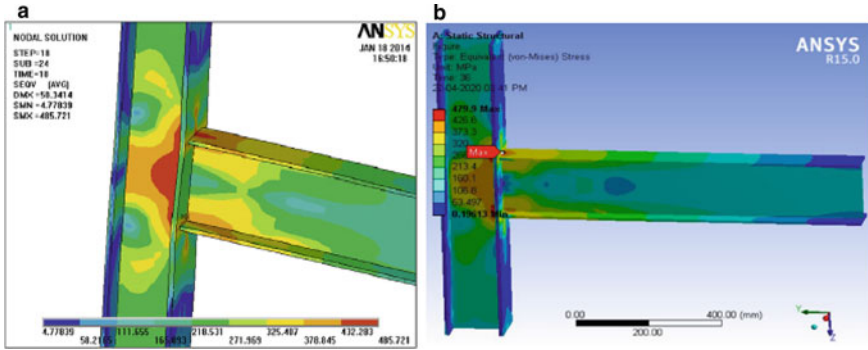
Fig. 3 **a** Von Mises stress distribution of the beam column joint at 0.02 rad (experimental study) [1] and **b** Von Mises stress distribution of the beam column joint at 0.02 rad (analytical study)

4 Result Analysis

4.1 General

An earthquake causes a succession of ground vibrations, which cause the structures to sway. As the height rises, the amount of base shear created increases. There are several strategies for reducing base shear, one of which is the RBS weakening strategy. The models are subjected to materialistic nonlinear dynamic analysis for this study. Nonlinear analysis refers to the study of a model after it reaches the proportionality limit or fulfills Hooks' law. The use of different cycles to offer a dynamic loading is used. Each cycle consists of four steps starting from zero to the maximum negative value, then to the maximum positive value and then returning back to zero [1].

4.2 Case Study 1: Comparative Study of Beams with RBS

The aim of this case study is to analyze various models of different shapes in which the RBS dimensions of these models are based on EUROCODE and FEMA 350 [6]. There are 23 models with different shapes of RBS. The models are listed in Table 5, from model R1 to R17, it is modeled under the code provisions [6]. Models R18–R23 is based on the reference [7]. On one side of the face, they employed two decreased beam sections adjacent to each other. Aims to move the plastic hinge further away from the beam column joint and to share the strain created at one RBS area with the adjacent RBS area, in order to lessen the strain developed at one RBS area. Adopting this idea in this study from models R18 to R23, RBS is increased along the length of the beam and is studied about their influence on RBS behavior. However, $a = 0.65$ bf, $b = 0.75$ db, and $c = 0.225$ bf [7] (Fig. 4).

Table 5 Various models

S. No.	Name of section	Abbreviation
1	WRBS—Without reduced beam section	R0
2	RBS—Radial cut	R1
2	RBS—Trapezoidal cut	R2
3	RBS—Rectangle small slots	R3
4	RBS—Rectangle large slots	R4
5	RBS—Staggered rectangle slots	R5
6	RBS—Double layer rectangle holes	R6
7	RBS—Single layer rectangle holes	R7
8	RBS—Double layer square holes	R8
9	RBS—Single layer circular holes	R9
10	RBS—Double layer uniform circular holes	R10
11	RBS—Double layer nonuniform circular holes	R11
12	RBS—Double layer circular holes	R12
13	RBS—Single layer triangle holes	R13
14	RBS—Double layer same point apex triangle holes	R14
15	RBS—Double layer triangle holes varying horizontally	R15
16	RBS—Double layer triangle holes	R16
17	RBS—Elliptical single slots	R17
18	RBS—Elliptical double slots	R18
19	RBS—Double-layered elliptical holes with double slots	R19
20	RBS—Double layer elliptical holes in a row	R20
21	RBS—Multiple layer elliptical holes	R21
22	RBS—Double layer elliptical holes	R22
23	RBS—Double layer large elliptical holes	R23

Fig. 4 RBS parameters for elliptical models [7]
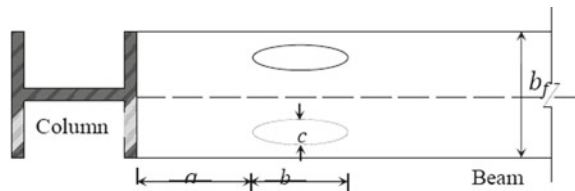
4.3 Discussion

Out of the **23** models, only **13** of them fulfilling the criteria of RBS behavior that is stress on column should be less than stress on beam. The aim of this analysis is to optimize the most efficient shape by keeping the following conditions:
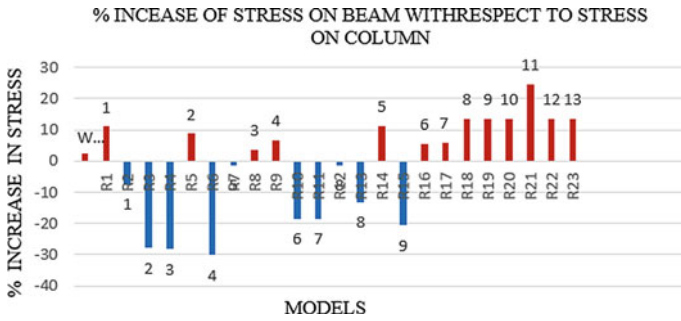
Fig. 5 % increase of stress on beam with respect to column for all the models, models [R1–R17] [6, 7], [R18–23] new models

1. To decrease the stress accumulated over the column.
2. To increase the stress developed over the beam.

The RBS behavior is mainly determined by the increase of stress on beam with respect to the stress on column.

Figure 5 shows the RBS behavior of the models based on the percentage of increase of stress on beam with respect to column.

The percentage increase on beam is calculated by:

$$\% \text{ increase} = \frac{(\text{Stress on beam} - \text{Stress on column})}{(\text{Stress on column})} * 100 \qquad (2)$$

The results are tabulated below, from 23 models, the models highlighted in red color shows RBS behavior; Blue color indicates negative values which means they are not showing RBS property. (Stress on column is higher than stress on beam) $S1$—stress on column; $S2$—stress on beam.

From Table 6, it can be noted that the values of the RBS models can never be maximum or minimum. Which means that if we consider only the load values as a parameter for defining the RBS behavior, then with the increase on load value, the RBS behavior decreases and vice versa. Figure 7 shows the load values of different RBS models on descending order of the values.

4.4 Optimized Beam Showing RBS Property

From the 13 models discussed above, by considering the load and percentage of increase of stress on beam with respect to column. R18 (RBS elliptical double slots, Fig. 8) is selected as the optimized beam section. From Fig. 6, R23 (RBS double layer large elliptical holes Fig. 9) showing much better performance of RBS property but it weakens the overall structure, as large elliptical holes are provided on the beam section; it reduces large area and increases the stress taken to its maximum as

Table 6 Tabulation of results

Tabulation of results

S. No.	Abbreviation	Deflection z-axis (mm)	Load (KN)	Time step	Cycles	$S1$	$S2$
A	WRBS	50	74.925	35	9	468.45	479.9
1	R1	50	64.636	35	9	423.34	469.9
2	R2	20	52.551	23	6	409.74	379.63
3	R3	19	52.232	19	5	535.73	386.32
4	R4	15	49.602	19	5	498.51	357.57
5	R5	15	57.389	19	5	339.03	368.51
6	R6	20	51.462	23	6	529.24	369.73
7	R7	20	53.862	23	6	357.33	352.55
8	R8	20	60.129	23	6	366.5	379.68
9	R9	20	58.597	23	6	345.4	368.22
10	R10	15	47.042	19	5	481.99	392.62
11	R11	15	45.305	19	5	457.57	373.39
12	R12	20	61.702	23	6	372.57	367.99
13	R13	14	63.456	26.7	7	411.1	356.87
14	R14	21	64.237	26.7	7	437.46	486.22
15	R15	20	65.872	23	6	443.27	351.09
16	R16	50	69.669	35	9	454.03	478.84
17	R17	50	70.724	35	9	454.07	480.25
18	R18	50	64.834	35	9	423.14	480.05
19	R19	50	63.428	35	9	423.24	480.25
20	R20	50	65.955	35	9	423.14	480.85
21	R21	50	57.812	35	9	382.97	477.53
22	R22	50	72.684	35	9	423.24	480.85
23	R23	50	55.764	35	9	327.02	480.25

well as the stress taken by the column is also lesser than other models so it cannot withstand high intensity loads. An optimal model should satisfy theoretical as well as experimental setups. Because circular and elliptical cuts have no sharp edges hence there is no stress concentration, so they exhibit more efficient RBS behavior than other form of models.

From Figs. 10 and 11, the area of maximum stress developed is shown, which is apart from the beam column joint, and hence, the welded joint is protected from failure. For R18, the stress developed over the column is comparable with model with normal beam column joint without RBS so it can be selected as the optimized RBS shape and arrangement for the beam section. Figures 12 and 13 show the response of the system to the cyclic loading applied and are almost same for both the beams. The x axis shows the displacement; whereas, the y axis shows the load. The ultimate
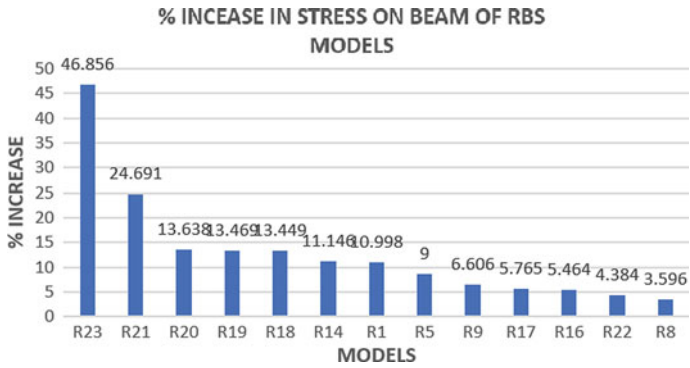
Fig. 6 Percentage increase of stress values of RBS models
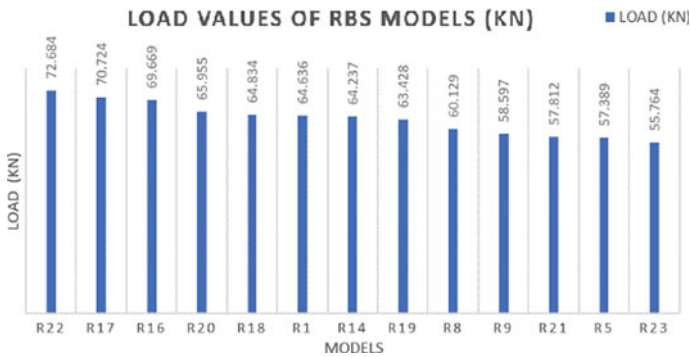
Fig. 7 Load values of RBS models

Fig. 8 RBS elliptical double slots, optimized model [R18]
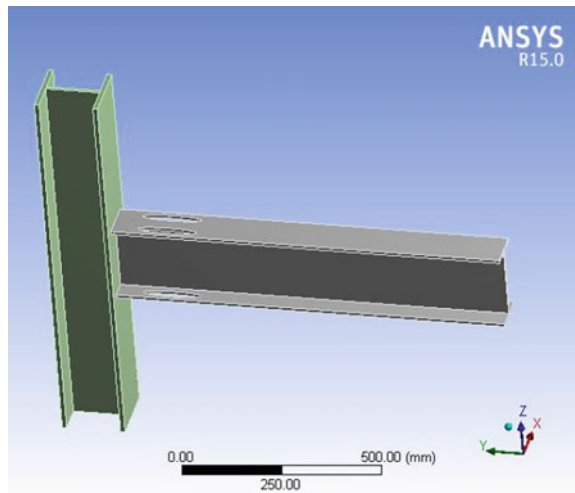
Fig. 9 RBS double layer
large elliptical holes [R23]
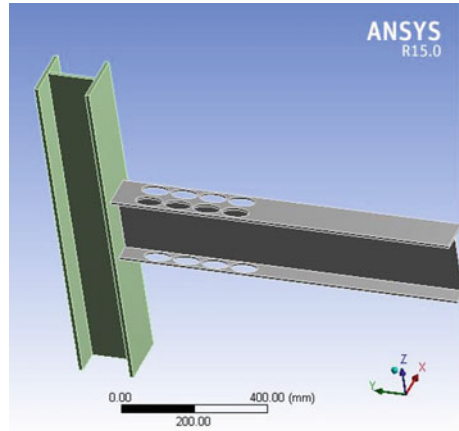
Fig. 10 Equivalent stress of
R18 (beam)
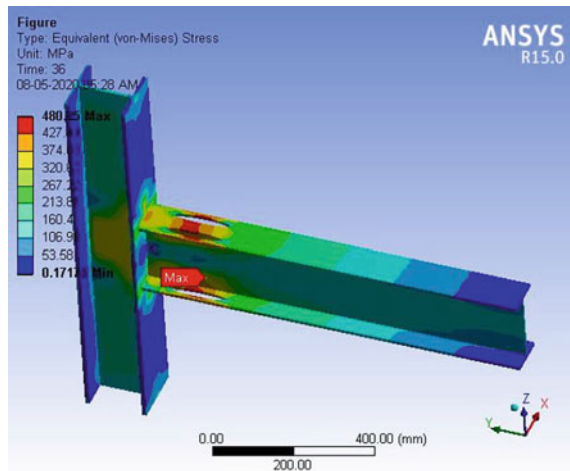
load occurred at the 36th step which approximately at the 9th cycle at 0.05 interstory
drift angle. It shows high stress values on beam and reduced stress values on column
so that the column and beam column joint are safe. As the length of RBS increases
along the beam, RBS property increases but it weakens the overall structure, it cannot
be the optimized beam, hence R18 is selected as the optimized beam.

Fig. 11 Equivalent stress of R23 (beam)
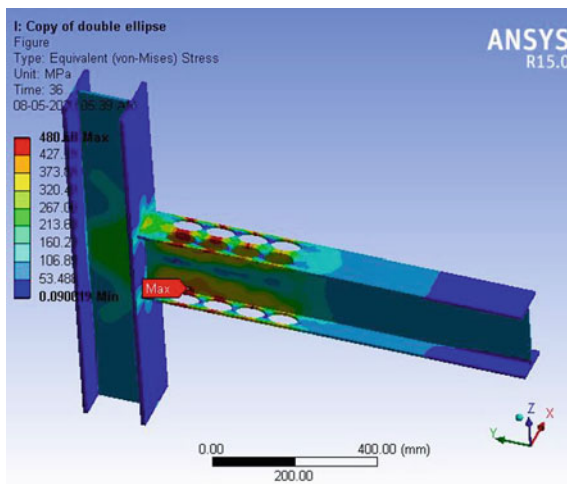
Fig. 12 Hysteresis curve [R18]
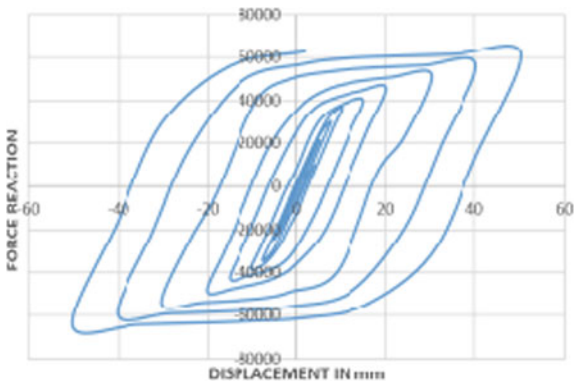
Fig. 13 Hysteresis curve [R23]
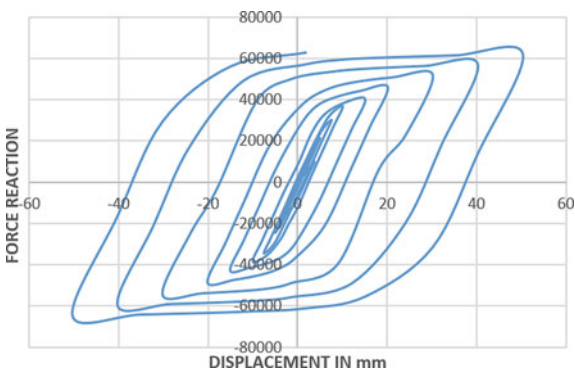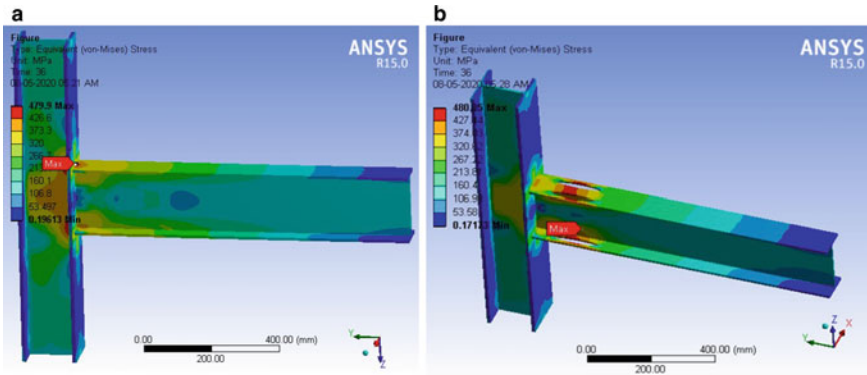
Fig. 14 **a** Stress on beam WRBS and **b** stress on beam R18

4.5 Comparison of Normal Beam Column Joint Without RBS [WRBS] and the Optimized RBS Beam Column Joint [R18]

By keeping the strength and the percentage of increase of stress on beams, as factors R18 is the optimized RBS beam section. For a normal beam column joint, the maximum stress is located at the joint (Fig. 14) hence it is more prone to fail under cyclic loads; whereas, from Fig. 14b, R18 stress is developed at the reduced area of the beam section apart from the joint. The plastic hinge is shifted from the joint to the RBS area. Hence, the joint and column is safe from failure so that the overall structure can be prevented from the failure, Here, RBS can act as a structural fuse to the seismic loads [1, 2, 6]. The column is almost free from the plastic hinge formation. From the analysis relatively, the stress developed on the column of R18 is reduced by 9.67% from the normal beam column connection without RBS. Without a large increment in the stress concentration on beam the stress in the column is reduced by RBS property. The stress on beams will be the same as that of the equivalent stress. From Fig. 15a and b the ultimate load developed in normal beam column joint without RBS is 75 KN; whereas, the ultimate load developed in the R18 is 65 KN.

Fig. 15 **a** Hysteresis curve for normal beam column joint without RBS and **b** hysteresis curve for R18
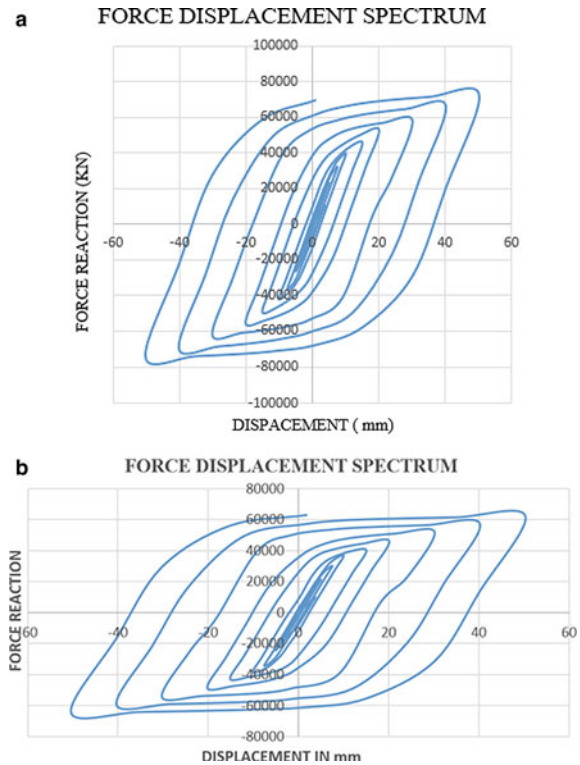
5 Conclusions

- The reduced beam section's strength can never be too high or too low, i.e., the strength of the beam column joint is directly related to the behavior of the reduced beam section.
- The shear stress and equivalent stress show clear connections with load as these values increase, and as these values increase, they have a significant impact on the increase in load values.
- As there are no sharp cutting edges in circular and elliptical cutouts which shows efficient RBS behavior than other shapes of RBS models.
- The optimized shape is RBS elliptical double slots [R18], without increasing the stress value that of normal beam column joint the position of maximum stress formed is shifted from the joint to the RBS area. Hence, the beam column connection is protected from failure.
- From the analysis relatively, the stress developed on the column of R18 is reduced by 9.67% from the normal beam column connection without RBS.
- R18 is selected as the optimized model even though RBS double layer large elliptical holes (R23) shows high RBS property, but it may weaken the overall structure.

References

1. Swati AK, Gaurang V (2014) Study of steel moment connection with and without beam section. Case Stud Struct Eng 1:26–31
2. Reshmi VB et al (2018) Analytical study of new type of reduced beam section under cyclic behavior. Int J Sci Res 9(4)
3. Carrato P (2009) Comparative study of bolted verses welded SCBF connections. https://doi.org/10.1061/41031(341)148
4. Maleki S et al (2017) Double reduced beam section connection. J Constr Steel Res 138:283–297
5. https://collegeofsanmateo.edu/physics/docs/physics250/introduction.pdf
6. Edthu JJ, Chako D (2019) Study of seismic behaviour of reduced beam sections on beam column connection under non prismatic and inclined conditions, vol 14(12). ISSN 0973-4562
7. Mohammadyan-yasouj et al (2018) Steel moment connection with elliptical reduced beam section. In: 16th European conference on earthquake engineering 18–21 June

Universal Grey Number Systems for Uncertainty Quantification

Akshay Kumar and A. S. Balu

1 Introduction

As the performance of the structure mainly depends upon the input variables. The information of the input variable is never certain, precise and complete (i.e. uncertain) [1]. The available information tends to contain various kinds of uncertainty and noise. There are two types of uncertainty parameters: aleatory uncertainty (stochastic) and epistemic uncertainty (subjective). Aleatory uncertainty is caused by intrinsic unpredictability in a physical system's or environment's attributes; whereas, epistemic uncertainty is caused by a lack of knowledge about the practical system or environment [2]. Uncertainties are usually described by probabilistic and non-probabilistic approaches. If the precise probability distribution of input parameters is available, then the probabilistic approach is adopted else non-probabilistic approach is used. As in many practical systems, a probabilistic distribution that is quite exact. Due to a lack of or insufficient data for some parameters, only their variation ranges can be provided. For uncertainty modelling and uncertainty propagation, probabilistic modelling and statistical analysis are well-established approaches [3]. The growing interest in the non-probabilistic approach developed due to the incredibility of the probabilistic approach when data is insufficient. In addition, several non-probabilistic methods have been future by many researchers in recent times, fuzzy set and possibility theory [4], probability bounds approach [5], convex models [6], interval approach [6], random set theory [7], imprecise probabilities [8], universal grey number system [9] and so on. Non-probabilistic methods can be used based

A. Kumar (✉) · A. S. Balu
Department of Civil Engineering, National Institute of Technology Karnataka, Surathkal, Karnataka 575025, India
e-mail: akshaymankal2@gmail.com

on the type of uncertainty present in the structural system. It is agreed that the non-probabilistic approach could be a more appropriate method for modelling certain non-deterministic information, leading to a more accurate depiction of bodily behaviour. The interval finite element approach has been found to be suitable for predicting the ranges of the structural system's response for such systems, whose input parameters are defined in the ranges. In the natural world, small sample sizes and poor information about uncertain systems exist commonly. Grey system approach can be used to cope with an uncertain system with only partially known information by producing, exploring and extracting valuable information from the given data [10].

2 Interval Approach

The uncertain parameter is represented by ranges or intervals with defined lower and upper limits (endpoints) in the interval method, without having a probability distribution. Therefore, the interval quantity a is represented by

$$a = [\underline{a}, \overline{a}] \tag{1}$$

where $\underline{a}$ and $\overline{a}$ represent lower limit and upper limit of the interval quantity a, respectively. In the mid-nineties, interval approach had been to describe the parameters of the engineering system. The interval approach is the best-suited method to represent the uncertain quantity, whose parameters are available in ranges. It is a straightforward and computationally efficient strategy for dealing with uncertainties whose data is supplied in ranges. For example, the thickness of a cold-form steel section is subject to a designed limit and is described as $t \pm \delta$ or in an interval form as $[t - \delta, t + \delta] = [\underline{t}, \overline{t}]$. The live load, wind load and earthquake load acting on the structural system are not known precisely but are available in the ranges. For example, if a live load ranges from 5 to 8 kN/m^2, it is featured as an interval [2, 3] kN/m^2. The load acting on the structure whose exact magnitude is unknown, or it may follow an unknown distribution with a known range. Significant bounds on the possible ranges of such numbers can be found in laboratory records, observations, statistical analysis and expert information [11]. Based on the limits of the input quantities, interval analysis provides correct bounds for structural system responses.

Real arithmetic's basic operations (addition, subtraction, multiplication and division) can be applied to intervals. The general rule for the operation over the intervals is represented by

$$a \circ b = \{a \circ b | a \in a, \ \ b \in b\} \tag{2}$$

It is simple to observe that the set of all feasible solutions for $a \in \boldsymbol{a}$, $b \in \boldsymbol{b}$ and the end limits can be computed by using a closed interval (for $\circ$ not in a denominator interval).

Table 1 Interval multiplication ab

	If $\underline{q} \geq 0$ and $\overline{q} \geq 0$	If $\underline{q} < 0 < \overline{q}$	If $\underline{q} \leq 0$ and $\overline{p} \leq 0\overline{p} \leq 0$
If $\underline{p} \geq 0$ and $\overline{p} \geq 0$	$[\underline{pq}, \overline{pq}]$	$[\overline{pq}, \overline{pq}]$	$[\overline{pq}, \underline{pq}]$
If $\underline{a} < 0 < \overline{a}$	$[\underline{pq}, \overline{pq}]$	$[\min(\overline{pq}, \overline{pq}), \max(\underline{pq}, \overline{pq})]$	$[\overline{pq}, \underline{pq}]$
If $\underline{a} \leq 0$ and $\overline{a} \leq 0$	$[\underline{pq}, \overline{pq}]$	$[\underline{pq}, \overline{pq}]$	$[\overline{pq}, \underline{pq}]$

Table 2 Interval division $p \div q\,(0 \notin q)$

	If $\underline{y} \geq 0$ and $\overline{y} \geq 0$	If $\underline{y} < 0 < \overline{y}$
If $\underline{p} \geq 0$ and $\overline{p} \geq 0$	$[\underline{p}/\overline{q}, \overline{p}/\underline{q}]$	$[\overline{p}/\overline{q}, \underline{p}/q]$
If $\underline{p} < 0 < \overline{p}$	$[\underline{p}/q, \overline{p}/\overline{q}]$	$[\overline{p}/\overline{q}, \underline{p}/q]$
If $\underline{p} \leq 0$ and $\overline{p} \leq 0$	$[\underline{p}/q, \overline{p}/\overline{q}]$	$[\overline{p}/q, \underline{p}/\overline{q}]$

$$a \circ b = [\min(a \circ b), \ \max(a \circ b)] \quad \text{for} \circ \in \{+, \ -, \ \times, \ \div\} \tag{3}$$

For addition and subtraction operation,

$$p + q = [\underline{p} + \underline{q}, \overline{p} + \overline{q}] \tag{4}$$

$$p - q = [\underline{p} - \overline{q}, \overline{p} - \underline{q}] \tag{5}$$

The result of multiplication and division is determined by the signs of a and b, as given in Tables 1 and 2 [12].

3 Grey System Theory

Grey system theory was developed to deal with systems with small samples and little information available about them. Grey system theory is also applicable to systems with unknown or partially known parameters. Grey system theory is concerned with the study of grey numbers, grey parameters, grey functions and grey relations. It includes grey number relationships between grey matrices and grey functions, as well as grey decision-making and grey optimization employing grey equations.

A grey number is a number that has clearly defined lower and upper boundaries but whose exact value or precise value is uncertain within a set of actual continuous numbers. A grey number, a, can be stated in the following way:

$$a = [\underline{a}, \ \overline{a}] = \{t \mid \underline{a} \ \leq \ t \leq \ \overline{a}\} \tag{6}$$

where t denotes the knowledge with and as the extreme left and extreme right limits of the value, respectively. As a result, a grey number is expressed as the range of possible fluctuation. In this sense, a grey number is equivalent to an interval number, and its mathematical operations are alike to those of interval number approach.

3.1 Universal Grey Number

Universal grey numbers are a sort of grey number that does not show the problem of reliance. Because of their definitions and the mathematical procedures that these numbers entail. A grey number x encompassing a set of continuous real values in the universal grey number system is expressed as

$$x = \left(\bar{x}, \left[\frac{\underline{x}}{\bar{x}}, 1 \right] \right) \tag{7}$$

3.2 UGNS Arithmetic Relations

If $|\underline{x}| \leq |\bar{x}|, \quad |\underline{y}| \leq |\bar{y}|$ with $x = [\underline{x}, \bar{x}] = \left(\bar{x}, \left[\frac{\underline{x}}{\bar{x}}, 1 \right] \right), y = [\underline{y}, \bar{y}] = \left(\bar{y}, \left[\frac{\underline{y}}{\bar{y}}, 1 \right] \right).$

(i) **Addition**

$$x + y = \left(\bar{x} + \bar{y}, \left[\frac{\underline{x} + \underline{y}}{\bar{x} + \bar{y}}, 1 \right] \right) \tag{8}$$

(ii) **Subtraction**

$$\text{if } \underline{x} - \underline{y} \leq \bar{x} - \bar{y}, \quad x - y = \left(\bar{x} - \bar{y}, \left[\frac{\underline{x} - \underline{y}}{\bar{x} - \bar{y}}, 1 \right] \right) \tag{9}$$

$$\text{if } \bar{x} - \bar{y} \leq \underline{x} - \underline{y}, \quad x - y = \left(\underline{x} - \underline{y}, \left[\frac{\bar{x} - \bar{y}}{\underline{x} - \underline{y}}, 1 \right] \right) \tag{10}$$

(iii) **Multiplication**

$$x \times y = \left(\bar{x} \times \bar{y}, \left[\frac{\underline{x} \times \underline{y}}{\bar{x} \times \bar{y}}, 1 \right] \right) \tag{11}$$

(iv) **Division**

$$\text{if } \underline{x} \times \bar{y} \leq \bar{x} \times \underline{y}, \quad \frac{x}{y} = \left(\frac{\bar{x}}{\bar{y}}, \left[\frac{\underline{x} \times \bar{y}}{\bar{x} \times \underline{y}}, 1 \right] \right) \tag{12}$$

$$\text{if } \overline{x} \times \underline{y} < \underline{x} \times \overline{y}, \quad \frac{x}{y} = \left(\frac{\underline{x}}{\underline{y}}, \left[\frac{\overline{x} \times \underline{y}}{\underline{x} \times \overline{y}}, 1 \right] \right) \tag{13}$$

3.3 Combinatorial Approach

To find the exact range for an arbitrary function f, whose parameters are expressed in interval. A combinatorial approach is used, where the method considers the lower and upper bound combination of all the parameters and evaluates the values for the each combination of the parameters.

$$f(y_1, y_2, \ldots y_n)$$

the variable y_i denoting the interval parameter. By taking into account the lower and upper limits of y_i

$$y_i = \left[\underline{y}_i, \ \overline{y}_i \right] \equiv \left[y_1^{(i)}, \ y_2^{(i)} \right] \tag{14}$$

To calculate f, various combinations of extreme left and extreme right of interval parameter for all n parameters can be utilised.

$$f_c = f\left(y_1^{(i)}, y_2^{(j)}, \ldots y_n^{(k)} \right); \quad i = 1, 2; \ j = 1, 2; \ldots, \ k = 1, 2; \ r = 1, 2, 3, \ldots, 2^n \tag{15}$$

where f_c signifies the value of f for particular combinations of extreme lower and extreme upper interval boundaries $y_1, y_2, \ldots y_n$. For linear structural problems, this method predicts the correct ranges of intervals, if n number of parameters are present in the arbitrary function, the combinational method requires 2^n analyses.

4 Numerical Example

An explicit nonlinear response function [13] in Eq. (16) is considered for solving using universal grey theory, interval and combinatorial approaches (Table 3).

$$f(x) = 16x_1^4 - 96x_1^2 + 216x_1^2 - 216x_1 - 64x_2^3 + 240x_2^2$$
$$- 300x_2 + 36x_3^2 - 84x_3 + 264 \tag{16}$$

a range of real numbers is written in the form of the universal grey number system.

Table 3 Interval multiplication xy

Approach	Response range
Interval analysis	$[-3500, 3900]$
Combinatorial	$[300, 2050]$
Universal grey number theory	$[84, 2404]$

$$x_1 = \left(3, \left[\frac{1}{3}, 1\right]\right), \quad x_2 = \left(1, \left[\frac{-1}{1}, 1\right]\right), \quad x_3 = \left(5, \left[\frac{-5}{5}, 1\right]\right), \quad \text{and } x_4 = \left(20, \left[\frac{10}{20}, 1\right]\right).$$

5 Numerical Example-2

Interval, universal grey number system and combinatorial technique are used to analyse the stepped bar. At nodes 1 and 2, axial loads are applied to the bar, i.e. $P1$ and $P2$, respectively, and the stepped bars variables are considered to be in ranges/intervals (Fig. 1).

The following percentage variation about the mean data is used in numerical computations (considering $\pm 1\%$ for A^o, $\pm 2\%$ for l^o, $\pm 3\%$ for E^o, and $\pm 4\%$ for P^o) [9].

$A_1^0 = 2$ in^2, $A_2^0 = 1$ in^2, $E_1^0 = E_2^0 = 30 \times 10^6$ psi, $l_1^0 = 0.10$ in, $l_2^0 = 0.5$ in, $P_1^0 = 0.0$ lb, and $P_2^0 = 0.100$ lb are the mean values of uncertainty parameters. Representing uncertainty parameters in the interval and universal grey form.

$$A_1 = [1.98, 2.02] = \left(2.02\left[\frac{1.98}{2.02}, 1\right]\right), \quad A_2 = [0.99, 1.01] = \left(1.01\left[\frac{0.99}{1.01}, 1\right]\right),$$

$$l_1 = [9.8, 10.2] = \left(10.2\left[\frac{9.8}{10.2}, 1\right]\right), \quad l_2 = [4.9, 5.1] = \left(5.1\left[\frac{4.9}{5.1}, 1\right]\right),$$

$$E_1 = E_2 = [29.1, 30.9] \times 10^6 = \left(30.9\left[\frac{29.1}{30.9}, 1\right]\right) \times 10^6, \quad P_1 = [0, 0] \text{ and}$$

$$P_2 = [96, 104] = \left(104\left[\frac{96}{104}, 1\right]\right),$$

Fig. 1 Stepped bar [9]
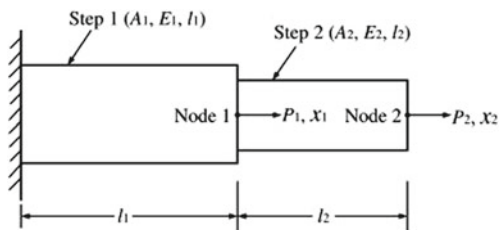
the tension load applied at point 1 and 2 and corresponding static equilibrium equations are given by

$$[K]X = P \tag{17}$$

$$X = \begin{Bmatrix} x_1 \\ x_2 \end{Bmatrix} = [K]^{-1}P \tag{18}$$

$$[K] = \begin{bmatrix} \left[\frac{A_1 E_1}{\bar{l}_1} + \frac{A_2 E_2}{\bar{l}_2}, \ \frac{\bar{A}_1 \bar{E}_1}{\bar{l}_1} + \frac{\bar{A}_2 \bar{E}_2}{\bar{l}_2} \right] & \left[-\frac{\bar{A}_2 \bar{E}_2}{\bar{l}_2}, \ -\frac{A_2 E_2}{\bar{l}_2} \right] \\ \left[-\frac{\bar{A}_2 \bar{E}_2}{\bar{l}_2}, \ -\frac{A_2 E_2}{\bar{l}_2} \right] & \left[\frac{A_2 E_2}{\bar{l}_2}, \ \frac{\bar{A}_2 \bar{E}_2}{\bar{l}_2} \right] \end{bmatrix} \tag{19}$$

The following relationship is used to calculate the axial stresses (σ_1 and σ_2) induced in the two parts of the bar (Figs. 2 and 3).

$$\begin{Bmatrix} \sigma_1 \\ \sigma_2 \end{Bmatrix} = \begin{bmatrix} \frac{E_1}{l_1} & 0 \\ -\frac{E_2}{l_2} & \frac{E_2}{l_2} \end{bmatrix} = \begin{Bmatrix} x_1 \\ x_2 \end{Bmatrix} \tag{20}$$

In the given problem, variations in uncertain variables are altered from 0.0 to 1.0 (Tables 4, 5 and 6).

Fig. 2 Variation of stress (σ_1)
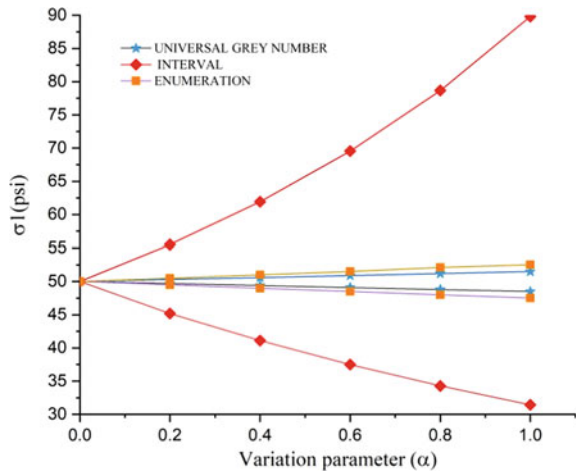
Fig. 3 Variation of stress (σ_2)
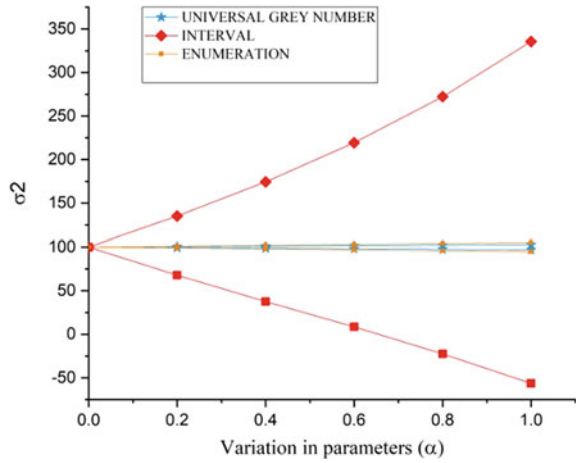
Table 4 Variation of stresses (universal grey number)

A	σ_1	σ_2
0	50	100
0.2	[49.7, 50.30]	[99.42, 100.62]
0.4	[49.40, 50.60]	[98.82, 101.20]
0.6	[49.09, 50.89]	[98.19, 101.80]
0.8	[48.80, 51.20]	[97.64, 102.40]
1	[48.50, 51.50]	[96.99, 103.02]

Table 5 Variation of stresses (interval analysis)

A	σ_1	σ_2
0	50	100
0.2	[45.20, 55.50]	[67.90, 135.07]
0.4	[41.10, 61.94]	[37.74, 174.40]
0.6	[37.50, 70.55]	[8.51, 219.37]
0.8	[34.28, 78.68]	[−22.43, 272.30]
1	[31.48, 89.90]	[−56.41, 335.64]

Table 6 Variation of stresses (enumeration method)

A	σ_1	σ_2
0	50	100
0.2	[49.50, 50.50]	[99, 101]
0.4	[49.00, 51.00]	[98, 102]
0.6	[48.50, 51.50]	[97.02, 103]
0.8	[48.00, 52.01]	[96.05, 104.03]
1	[47.56, 52.55]	[95.10, 105.08]

6 Conclusion

When compared to the interval technique for systems whose characteristics are specified as intervals or ranges, the universal grey number system (UGNS) predicts reliable results. Because, unlike the interval approach, the universal grey number theory does not disobey physical laws, UGNS is free of all the dependency problem and also delivers supportive results when compared to a combinational method.

References

1. Ranganathan R (1999) Structural reliability analysis and design. Jaico Publication House
2. Li G, Zhenzhou L, Luyi L, Ren B (2016) Aleatory and epistemic uncertainties analysis based on non-probabilistic reliability and its kriging solution. Appl Math Model 158:106–112
3. Mcnally MG (2000) Uncertainly in mechanics problems interval based approach. Environ Eng 557–566
4. Kramer W (2006) Generalized intervals and the dependency problem. PAMM Proc Appl Math Mech 6:683–684
5. Berleant DJ, Ferso S, Denver UC (2005) Combining interval and probabilistic uncertainty: foundations, algorithms, challenges—an overview. In: 4th international symposium on imprecise probabilities and their applications
6. Benhaim Y (1994) Convex models applications of uncertainty: and implications 41:139–156
7. Artstein Z (1983) Distributions of random sets and random selections. Israel J Math 46(4)
8. Walley P (1991) Statistical reasoning with imprecise probabilities. Chapman and Hall, London 27(I)
9. Rao SS, Liu XT (2017) Universal grey system theory for analysis of uncertain structural systems. AIAA J 55:3966–3979
10. Deng JL (1982) Control problems of grey systems. Syst Control Lett 1(5):288–294
11. Ferson S, Hajagos JG (2004) Arithmetic with uncertain numbers: rigorous and best possible answers. Reliab Eng Syst Saf 85:135–152
12. Neumaier A, Shen Z (1990) The Krawczyk operator and Kantorovich's theorem. J Math Anal Appl 149(2):437–443
13. Balu AS, Rao BN (2011) Explicit fuzzy analysis of systems with imprecise properties. Int J Mech Mater Des 7(4):283–289

Identification of the Domain of Significance for Bidirectional Analysis Under Seismic Excitation

Atanu Santra and Rana Roy

1 Introduction

In the event of an earthquake, a structure is subjected to three translation and three rotational components. The effect of rotational components and the vertical components is often neglected [1–4]. Hence, two orthogonal horizontal components of a ground motion may be deemed responsible for major seismic damage. Stronger vulnerability of structures due to bidirectional shaking relative to corresponding unidirectional companion is expected [5–12]. Damage histories of the past earthquakes such as the 1968 Tokachi-oki, Japan [13]; the 1971 San Fernando, USA [14, 15]; the 1994 Northridge, USA [16]; the 1995 Kobe, Japan [17] appear to reveal the same. Due to bidirectional shaking, maximum drift demand of steel frames may increase by about 46–64% with respect to unidirectional excitation [18]. Rodrigues et al. [19] noted that, for a rectangular column, bidirectional seismic loading may cause a reduction of strength by 20% in its weaker direction and 8% in stronger direction. Roy et al. [20] explored that the peak demand and cumulative demand of a bridge pier subjected to bidirectional excitations may be amplified by 4–35% and 39–70%, respectively, with respect to the unidirectional counterpart. A review has been made by Rodrigues et al. [21] covering the previous experimental studies on the structures subjected to bidirectional seismic excitation. Nigam [5] observed that for structures over a period of 1.0 s, bidirectional interaction may not bear significant effect. Pecknold [7] concluded that the impact of bidirectional shaking primarily

A. Santra (✉)
Department of Aerospace Engineering and Applied Mechanics, Indian Institute of Engineering Science and Technology, Shibpur, India
e-mail: atanu.juce@gmail.com

R. Roy
Department of Aerospace Engineering and Applied Mechanics, Indian Institute of Engineering Science and Technology, Shibpur, Howrah 711 103, India

depends primarily on the 'initial fundamental elastic period of the structure and on the amount of inelastic deformation which a single component of ground motion would produce'. It may also be noted that conducting a complete bidirectional analysis is challenging, complex, and time-consuming even today. Keeping this in view, these relatively old works motivate the authors to identify the domain in which interaction effect is imperative in terms of simple parameters, viz., elastic period of vibration (T) and amount of inelasticity measured by R.

In performance-based seismic design (PBSD), performance of a structure at different hazard levels is generally computed in terms of maximum inelastic deformation and hysteretic energy dissipation (or combination of the both parameters such as Park-Ang index, [22]). In addition to these damage measures, residual deformation of structures may also be important [23–28]. To 'avoid failure', an assessment of residual drift is inarguably important [29–34]. Hence, identifying the domain of significance for biaxial interaction has been made herein explicitly in terms of the peak, residual, and cumulative seismic demands.

To achieve this end, a single degree of freedom (SDOF) oscillator has been studied under idealized pulse-like near-fault motions that may often cause substantial damage [35]. In the present work, single-pulses and multi-pulses extracted from real pulse-like motions have been used to identify the basic trend [36, 37]. Nonlinear response history analyzes of the structures have been carried out under appropriately scaled idealized pulse, and the responses due to bidirectional and unidirectional loading have been separately computed. The present study identifying the domain of significance of interaction effect in terms of simple parameters may prove useful for practical purpose.

2 Structural Idealization and Methodology

Figure 1a presents the idealized SDOF oscillator represented by a rigid link with a lumped mass atop and a zero length spring element at the bottom of the link. Top node of the spring element coincides with the bottom node of the rigid link, whereas the bottom node of the spring element is restrained. The backbone curve of the spring is assumed to follow a tri-linear moment-rotation curve (Fig. 1b) as proposed earlier [38]. The curve comprises of a bi-linear idealized curve followed by an extension branch of zero stiffness. *Uniaxial hysteretic material* model, available in OpenSees platform [39], has been employed to simulate the tri-linear spring model. Basic structural properties have been adopted from the previous experimental study on circular bridge pier section as shown in Fig. 1c [40]. Values of moment, rotation for the tri-linear backbone curve have been obtained from the section analysis of the chosen pier (Fig. 1b).

To capture bidirectional interaction, upon choosing the tri-linear model in two principal directions, yield and ultimate strength criterion of the spring have been set to compute by Eqs. (1) and (2), respectively. The graphical form of these equations (equation of circles) has been represented in Fig. 1d in which M_{yx} and $M_{yy,}$

(a) Schematic diagram of the model

(b) Moment-Rotation curve [38]

(c) Description of bridge-pier [40]

(d) Diagram of yielding and ultimate strength criterion for bidirectional spring model
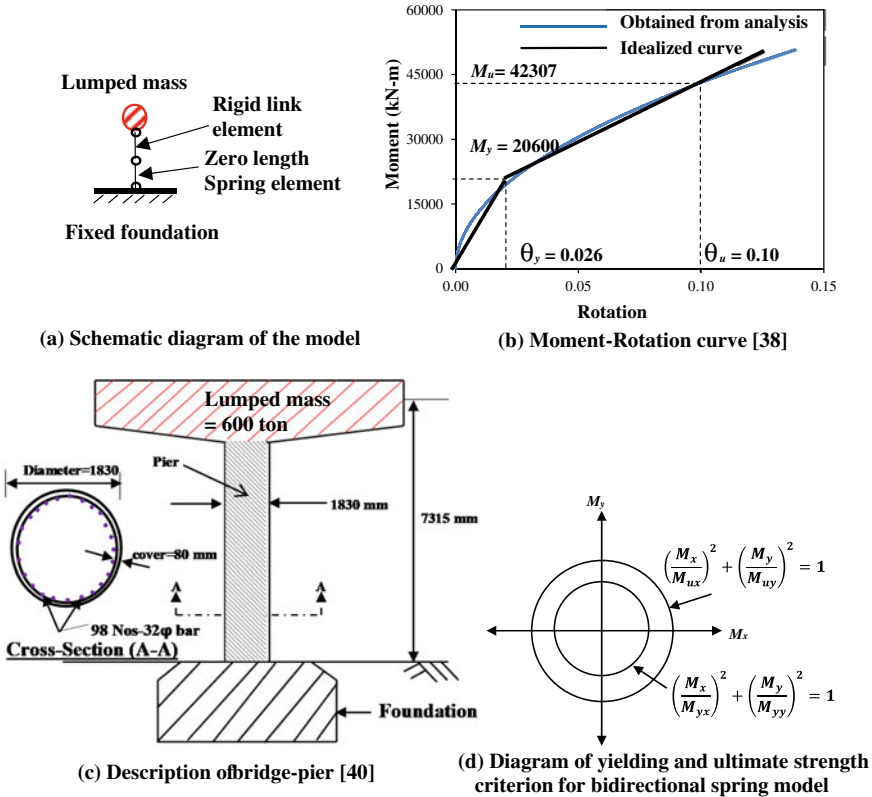
Fig. 1 Description of idealized system

respectively, representing the yield moments of the structure due to unidirectional loading in x and y directions. Further, M_{ux} and M_{uy} are ultimate moments due to unidirectional shaking in x and y directions, respectively. It may be noted that the criterion adopted for yielding or failure under bidirectional shaking represents a circular pattern. Often the actual shape may be like an ellipse; however, circular shape assumed for simplicity may be adequate for the parametric study.

$$\left(\frac{M_x}{M_{yx}}\right)^2 + \left(\frac{M_y}{M_{yy}}\right)^2 = 1 \tag{1}$$

$$\left(\frac{M_x}{M_{ux}}\right)^2 + \left(\frac{M_y}{M_{uy}}\right)^2 = 1 \tag{2}$$

Free vibration analysis is performed to compute the period of the SDOF oscillators. By changing the value of the lumped mass, different values of T such as 0.2,

1.0, 2.0, 4.0, and 8.0 s have been simulated. As the model is independent of structural parameters and material properties such as characteristic strength of concrete, reinforcement ratio, confinement factor, and axial load ratio; parametric study has easily been conducted covering values of response reduction factor (R) as 2, 3, 4, 5, 6, 7, and 8 (procedure explained in Sect. 3).

Seismic response history analyzes have been conducted in the time domain using Newmark integrator [41] and Krylov-Newton solution algorithm. Newmark parameters γ and β are chosen, respectively, as 0.5 and 0.25. Forced-based criterion (maximum no of iteration: 10 and tolerance limit: 10^{-6}) is employed to ensure convergence. While performing the analyzes, ground motions are applied (in horizontal plane) in the fixed node in the directions of principal axes of the structure, and nodal displacements of the top node in corresponding directions are noted. For unidirectional analysis, the two orthogonal horizontal components of a single motion are applied to the structure separately, and the maximum one is considered as response to unidirectional analysis for the said motion. In bidirectional analysis, two orthogonal components are simultaneously applied, and resultant response history is obtained by combining response histories in two orthogonal directions. The maximum value of response in the resultant history is considered as response to bidirectional analysis.

3   Ground Motions

Near-fault ground motions may often contain strong velocity pulses named herein as 'pulse-like ground motions' [35, 42]. Baker [36] proposed three criteria for a near-fault motion for diagnosing as pulse-like ground motion. A pulse-like motion may contain a single (single-pulse) or more multiple pulses (multi-pulse) [43]. In the present work, we have collected seven motions containing single-pulse and another set of seven motions with multi-pulse from strong-motion virtual data center (VDC) (listed in Table 1). Pulses have been extracted using the methodology based on wavelet analysis after the developments by Xia and Liu [37]. Further details in this regard are furnished in Table 1.

Continuous wavelet transformation (CWT) has been made to extract the dominating pulse signals from recorded accelerogram. To perform each CWT, optimum mother wavelet has been chosen out of fifteen available mother wavelets based on minimum cross-variance criterion [37]. CWT has been executed using Eq. (3), and the mother wavelets used in this investigation are furnished in Table 1.

$$C(l, s) = \int_{-\infty}^{+\infty} f(t) \frac{1}{\sqrt{s}} \varphi\left(\frac{t - l}{s}\right) dt \tag{3}$$

in which $f(t)$ is recorded ground motion history (variation of acceleration with time), φ is the corresponding optimum mother wavelet function, s parameter employed to

Table 1 Details of single-pulse ground motions

S. No.	Event	M_w	Single-pulse			Multi-pulse				
			Station	r (km)	W_n	Station	r (km)	1st W_n	2nd W_n	3rd W_n
1	Chi-Chi_Taiwan (9/20/1999)	7.6	CHY024	9.3	'gaus8'	CHY002	28.7	'morl'	'db6'	–
2			CHY092	22.5	'gaus3'	TCU042	24.6	'db6'	'gaus3'	–
3			CHY101	13.3	'db5'	TCU059	55.95	'gaus4'	'gaus3'	–
4			TCU029	24.5	'db6'	TCU101	1.9	'gaus3'	'db6'	–
5			TCU040	15.0	'gaus6'	TCU105	16.8	'gaus7'	'db6'	'db4'
6			TCU045	24.7	'db6'	TCU128	71.4	'gaus8'	'gaus6'	–
7			TCU046	16.5	'db5'	TCU131	26.2	'db6'	'db6'	'db6'

M_w—moment magnitude, r—closest site-to-fault-rupture distance, W_n—mother wavelet

dilate mother wavelet function, and l parameter is involved to translate it. $C_{max}(l_0, s_0)$ denotes the largest value in C, and l_0 and s_0 are corresponding coordinates.

In a typical ith iteration, dominant pulse signal p_i embedded in accelerogram S_{i-1} is extracted by applying Eq. (4), where $y_{base,i}$ is optimum mother wavelet function for the iteration. The residual signal S_i is computed by Eq. (5). The termination criteria of this iteration procedure are set such that the ratio between the cumulative square velocity of p_i and the cumulative square velocity of S_i reaches to a numerical value of 0.4 [37]. Finally, the multi-pulse signal P embedded in the original ground motion is obtained using Eq. (6).

$$p_i = y_{base,i} \frac{C_{max}\left(l_{o,i}, s_{o,i}\right)}{\sqrt{s_{o,i}}} \tag{4}$$

$$S_i = S_{i-1} - \sum_{k=1}^{k=i} p_k \tag{5}$$

$$P = \sum_{i=1}^{i=N} p_i \tag{6}$$

In case, the recorded accelerogram has only one dominant pulse signal (i.e., $N = 1$), P is considered to be single-pulse. For $N > 1$, it is termed as multi-pulse. These idealized pulses because of the simple form yet representing major characteristics of the real records have been used in the present work.

The range of ductility level used in the present investigation may be regarded as significant for practical usage. Based on the structural yield strength in advance, estimating elastic strength demand under unidirectional shaking, scale factor for each pulse of a motion is separately calculated to achieve a target R, and the minimum one has been applied to both components of the motions. Motions so scaled have been applied in both unidirectional and bidirectional analysis.

4 Unidirectional VIS-À-VIS Bidirectional Responses

Subjecting to the selected pulses, response history analysis has been carried out for each oscillator characterized by the chosen set of values for T and R. Unidirectional analysis has been performed separately applying each pulse of a record, whereas both pulses corresponding to two horizontal components of a ground motion have been employed together in bidirectional analysis. Observing the response histories, the maximum value of the displacement and the displacement upon the expiration of the pulse are noted. For unidirectional excitation, the maximum response out of the same due to two components of a specific motion is considered as peak displacement (Δ_U) and residual displacement ($\Delta_{R(U)}$), respectively. In bidirectional analysis, the displacements in the two principal directions are combined by square root of
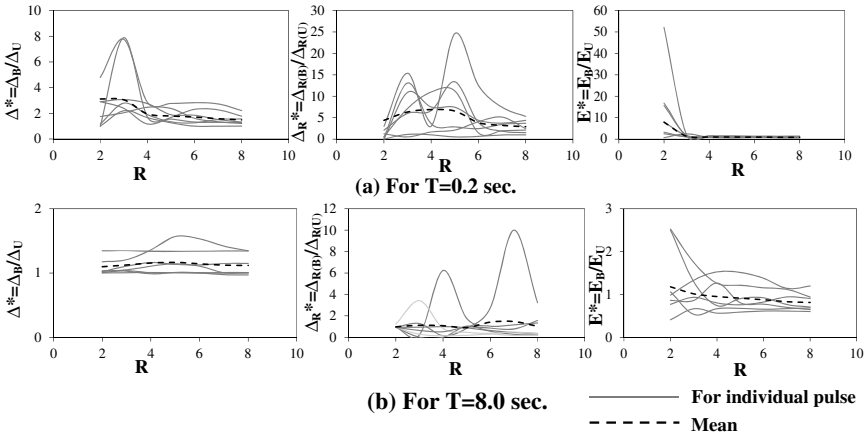
Fig. 2 Variation of amplification of bidirectional response with respect to unidirectional response due to change in R (for a fixed value of T) under single-pulse motions

sum of squares (SRSS) rule. The maximum displacement in the resultant response history is considered as peak displacement (Δ_B), and the resultant displacement at the end of the motion is taken as residual displacement ($\Delta_{R(B)}$). Further, cumulative demand has been computed by calculating the hysteretic energy dissipation (area of force–displacement curve). For unidirectional analysis, the maximum energy obtained separately from two companion components is taken as cumulative response (E_U); whereas the same due to two companion pulses applied simultaneously in two orthogonal directions are summed to determine cumulative response (E_B) under bidirectional shaking [20].

Variation of normalized peak ($\Delta^* = \Delta_B/\Delta_U$), residual ($\Delta_R^* = \Delta_{R(B)}/\Delta_{R(U)}$), and cumulative ($E^* = E_B/E_U$) responses so obtained for oscillators with different periods are plotted as a function of R. However, results for oscillators with period equal to 0.2 and 8 s are only furnished separately for single-pulse (Fig. 2) and multi-pulse motions (Fig. 3) to save space. It has been observed that, for oscillators with short periods, values of Δ^*, Δ_R^*, and E^* are well above unity indicating that the impact of bidirectional interaction may be pronounced regardless of the values of R. It may further be noted that in short period regime, the interaction effect tends to reduce with increased level of inelasticity. On the other hand, such normalized response parameters, on an average, are observed to be close to or even below unity in the long period ($T = 8.0$) for a wide range of inelasticity. Hence, it appears that the interaction effect is primarily significant for short period systems.
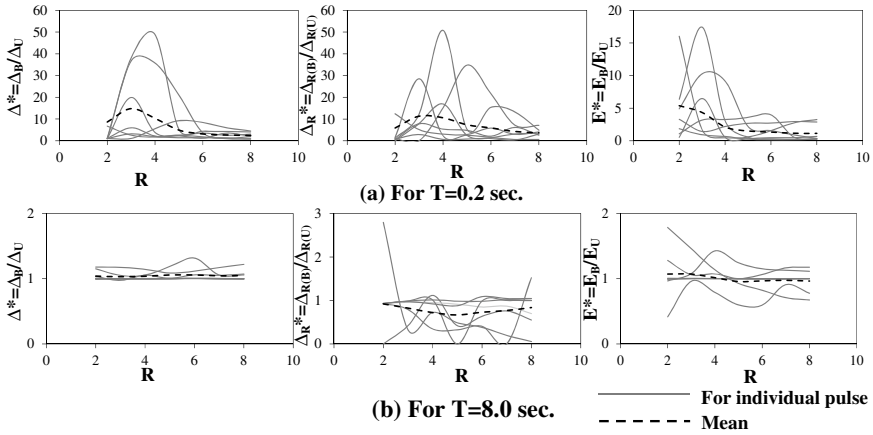
Fig. 3 Variation of amplification of bidirectional response with respect to unidirectional response due to change in R (for a fixed value of T) under multi-pulse motions

5 Regression Model

From the basic trend noted in the foregoing section, it appears useful to make an attempt to identify the domain of significance of interaction effect. To this end, nonlinear regression analyzes have been made using the results of all case studies with different values of T and R separately for single-pulse and multi-pulse motions. Bivariate regression analyzes have been conducted using the form expressed in Eqs. (7)–(9) for peak, residual, and cumulative responses, respectively; in which a, b, and c are regression constants. Levenberg–Marquardt algorithm [44] is employed in MATLAB platform and generated response surfaces are shown in Figs. 4 and 5. The values of coefficients (a, b, and c) computed in the regression analyzes are tabulated in the corresponding figures. The coefficients of determination, i.e., adjusted R^2 value (R_{adj}^2) have also been furnished in the figures. R_{adj}^2 lies between 84–88% for single-pulse and 94–97% for multi-pulse motions, and hence, the performance of the model may be considered satisfactory.

$$\Delta^* = ax R^b x T^c \tag{7}$$

$$\Delta_R^* = ax R^b x T^c \tag{8}$$

$$E^* = ax R^b x T^c \tag{9}$$

It may be interesting to observe that the value of the coefficient c is negative for all category of responses. This implies that interaction effect reduces sharply with increase of elastic period of vibration. On the other hand, comparison of the values

Coef.	
a	1.263
b	0.06131
c	-0.08303

Coef.	
a	0.7927
b	0.1435
c	-0.2622

(a) Peak disp.

(b) Residual disp.

Coef.	
a	1.013
b	0.01134
c	-0.01994

(c) Hysteretic energy
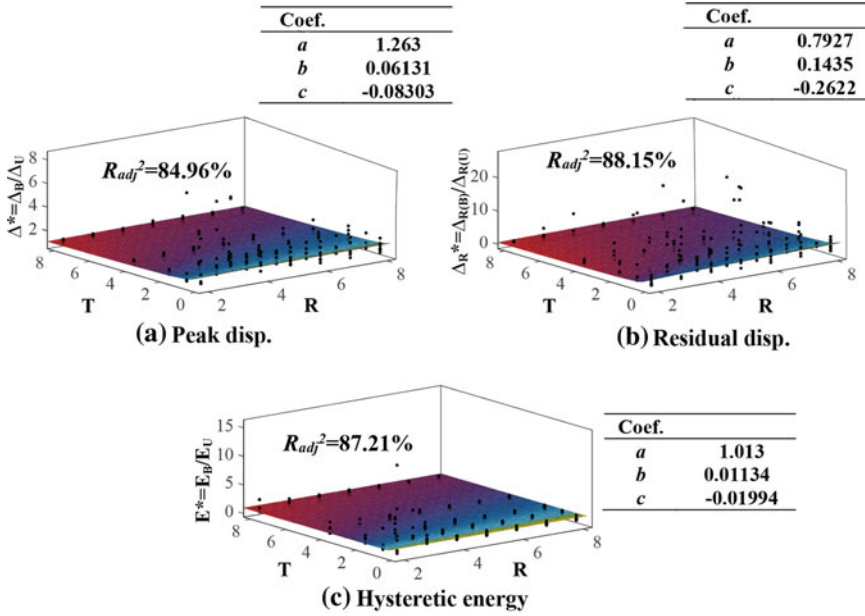
Fig. 4 Proposed regression model for amplification of responses due to bidirectional excitation over unidirectional shaking under single-pulse motions

Coef.	
a	1.035
b	0.000662
c	-0.003599

Coef.	
a	0.8368
b	0.1253
c	-0.1757

(a) Peak disp.

(b) Residual disp.

Coef.	
a	1.075
b	0.01011
c	-0.07666

(c) Hysteretic energy
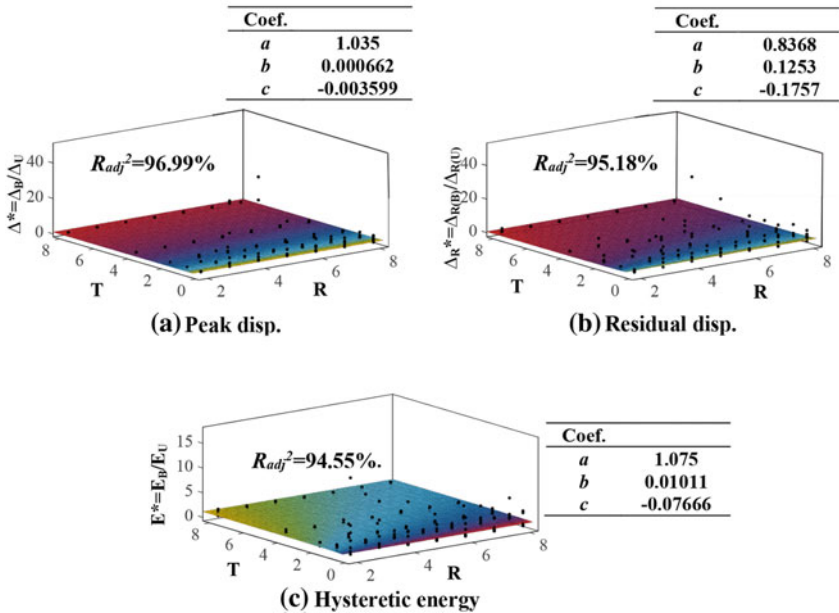
Fig. 5 Proposed regression model for amplification of responses due to bidirectional excitation over unidirectional shaking under multi-pulse motions

of *b*and *c* suggests that the bidirectional interaction effect is primarily dependent on *T* and to a lesser degree to *R*. This regression model developed using simple SDOF oscillator thus confirms the findings of Pecknold [7] and shall aid to identify the domain in which bidirectional interaction may be strongly recommended.

6 Summary and Conclusions

Past studies since 60 s identified the significance of biaxial interaction and numerous experimental and numerical studies in this area have been conducted. However, in the design contexts, performing complete bidirectional analysis is still a challenging task. Keeping this in view and motivated by a relatively old work [7], present study aims to identify the domain in which interaction effect dominates. Parametrically defined SDOF oscillators under idealized pulses extracted from real near-fault motions are studied covering a range of period of vibration and degree of inelasticity of practical significance and important response indices are studied. The following conclusions are emerged.

- Bidirectional interaction for all important response indices such as peak deformation, residual deformation, and cumulative responses may be quiet significant for short period systems.
- The difference between bidirectional and unidirectional responses of a short period system reduces with increase of inelasticity level which may be quantified through *R* factor in design.
- Interaction effect tends to decay with increase of elastic period of vibration. More precisely, regardless of the ductility level, biaxial interaction bears negligible relevance in very long period regimes.
- The proposed regression models may be employed for a preliminary assessment of the domain of significance for bidirectional analyzes.

References

1. Kubo T, Penzien J (1979) Simulation of three-dimensional strong ground motions along principal axes, San Fernando earthquake. Earthquake Eng Struct Dynam 7(3):279–294
2. Newmark NM, Hall WJ (1982) Earthquake spectra and design, Earthquake Engineering Research Institute, Okland
3. Menun C, Der Kiureghian A (1998) A replacement of the 30%, 40% and SRSS rules for multicomponent seismic analysis. Earthq Spectra 14(1):153–163
4. Beyer K, Bommer JJ (2007) Selection and scaling of real accelerogram for bi-directional loading: a review of current practice and code provisions. J Earthquake Eng 11(S1):13–45
5. Nigam NC (1967) Inelastic interactions in the dynamic response of structures, earthquake engineering research laboratory report, California Institute of Technology, Pasadena, California

6. PedillaMora R, Schnobrich WC (1974) Nonlinear response of framed structures to two-dimensional earthquake motion, Structural Engineering Series No. 408, University of Illinois at Urbana-Champaign, Urbana, Illinois
7. Pecknold D (1974) Inelastic structural response to 2D ground motion. J Eng Mech Div 100(5):949–963
8. Otani S, Cheung VWT, Lai SS (1980) Reinforced concrete columns subjected to biaxial lateral load reversals. In: Proceedings of 7th world conference on earthquake engineering, Istanbul, Turkey
9. Hisada T, Miyamura M, Kan S, Hirao Y (1988) Studies on the orthogonal effects in seismic analyses. In: Proceeding of 9th world conference on earthquake engineering, Tokyo-Kyoto, Japan
10. Hachem MM, Mahin SA, Moehle JP (2003) Performance of circular reinforced concrete bridge columns under bi-directional earthquake loading, Pacific earthquake engineering research centre, report no. PEER 2003/06, University of California, Berkeley, California, USA
11. Choi H, Saiidi M, Somerville P, El-Azazy S (2010) Experimental study of reinforced concrete bridge columns subjected to near-fault ground motions. ACI Struct J 107(1):3–12
12. Moustafa K, Sanders D, Saiidi M, El-Azazy S (2011) Seismic performance of reinforced concrete bridge bents. ACI Struct J 108(1):23–33
13. Okada T, Murakami M, Udagawa K, Nishikawa T, Osawa Y, Tanaka H (1970) Analysis of the Hachinohe library damaged by 1968 Tokachi-oki earthquake. In: Proceedings of U.S.-Japan Seminar on Earthquake engineering, Sendai, Japan
14. Selna LG, Morrill KB, Ersoy OK (1974) Earthquake response analysis of the olive view hospital psychiatric day clinic. Earthquake Eng Struct Dynam 3(1):15–32
15. Mahin, SA, Bertero VV, Chopra AK, Collins RG (1976) Response of the Olive view hospital main building during the San Fernando earthquake, Earthquake engineering research center, report no.: UCB/EERC-83/19, University of California, Berkeley
16. Celebi M (1997) Response of olive view hospital to northridge and whittier earthquakes. J Struct Eng 123(4):389–396
17. Bruneau M, Wilson JC, Tremblay R (1996) Performance of steel bridges during the 1995 Hyogo-Ken Nanbu (Kobe, Japan) earthquake. Can J Civ Eng 23(3):678–713
18. MacRae GA, Tagawa H (2001) Seismic behavior of 3D steel moment frame with biaxial columns. J Struct Eng 127(5):490–497
19. Rodrigues H, Varum H, Arêde A, Costa A (2012) Comparative efficiency analysis of different nonlinear modelling strategies to simulate the biaxial response of RC columns. Earthq Eng Eng Vib 11(4):553–566
20. Roy A, Santra A, Roy R (2018) Estimating seismic response under bi-directional shaking per uni-directional analysis: identification of preferred angle of incidence. Soil Dyn Earthq Eng 106:163–181
21. Rodrigues H, Varum H, Arêde A, Costa A (2013) Behaviour of reinforced concrete column under biaxial cyclic loading—state of the art. Int J Adv Struct Eng 5(4):1–12
22. Park YJ, Ang AHS (1985) Mechanistic seismic damage model for reinforced concrete. J Struct Eng ASCE 111(4):722–739
23. MacRae GA, Kawashima K (1997) Post-earthquake residual displacements of bilinear oscillators. Earthquake Eng Struct Dynam 26(7):701–716
24. Borzi B, Calvi G, Elnashai A, Faccioli E, Bommer J (2001) Inelastic spectra for displacement-based seismic design. Soil Dyn Earthq Eng 21(1):47–61
25. Christopoulos C, Pampanin S, Nigel Priestley MJ (2003) Performance-based seismic response of frame structures including residual deformations. Part i: single-degree of freedom systems. J Earthquake Eng 7(1):97–118
26. Quan C, Tay CJ, Huang HY (2004) 3-D deformation measurement using fringe projection and digital image correlation. Optik 115(4):164–168
27. Ruiz-García J, Miranda E (2006) Residual displacement ratios for assessment of existing structures. Earthquake Eng Struct Dynam 35(3):315–336

28. Uma SR, Pampanin S, Christopoulos C (2010) Development of probabilistic framework for performance-based seismic assessment of structures considering residual deformations. J Earthquake Eng 14(7):1092–1111
29. Phan V, Saiidi MS, Anderson J, Ghasemi H (2007) Near-fault ground motion effects on reinforced concrete bridge columns. J Struct Eng 133(7):982–989
30. Saiidi MS, Ardakani SMS (2012) An analytical study of residual displacements in RC bridge columns subjected to near-fault earthquakes. Bridge Struct 8:35–45
31. Ramirez CM, Miranda E (2012) Significance of residual drifts in building earthquake loss estimation. Earthquake Eng Struct Dynam 41(11):1477–1493
32. Shrestha B, Hao H (2015) Parametric study of seismic performance of super-elastic shape memory alloy-reinforced bridge piers. Struct Infrastruct Eng 12(9):1076–1089
33. Sultana P, Youssef MA (2016) Seismic performance of steel moment resisting frames utilizing superelastic shape memory alloys. J Constr Steel Res 125:239–251
34. Shrestha B, Li C, Hao H, Li H (2016) Performance-based seismic assessment of superelastic shape memory alloy-reinforced bridge piers considering residual deformations. J Earthquake Eng 21(7):1050–1069
35. Sengupta A, Quadery L, Sarkar S, Roy R (2016) Influence of bi-directional near-fault excitations on RC bridge piers. J Bridge Eng 21(7):04016034:1–30
36. Baker JW (2007) Quantitative classification of near-fault ground motions using wavelet analysis. Bull Seismol Soc Am 97(5):1486–1501
37. Xia C, Liu C (2020) Influence of the multi-pulse near-fault earthquake motion on the seismic risk evaluation for reinforced concrete bridge. Nat Hazards 102:759–782
38. Mazzoni S, McKenna F, Scott MH, Fenves G (2007) OpenSees command language manual, Pacific Earthquake Engineering Research Center, University of California, Berkeley
39. Wehbe N, Saiidi MS, Sanders D (1999) Seismic performance of rectangular columns with moderate confinement. ACI Struct J 96(2):248–258
40. Lehman DE, Moehle JP (2000) Seismic performance of well-confined concrete bridge columns, Pacific Earthquake Engineering Research Center, report 1998/01, University of California, Berkeley, California
41. Newmark NM (1959) A method of computation for structural dynamics. J Eng Mech Div 85(3):67–94
42. Alavi B, Krawinkler H (2001) Effects of near-fault ground motions on frame structures, blume center report 138. California, Stanford, p 301
43. Mollaioli F, Bruno S, Decanini LD (2006) Characterization of the dynamic response of structures to damaging pulse-type near-fault ground motions. Meccanica 41(1):23–46
44. Roy R, Roy A, Bhattacharya G (2020) Estimating seismic response of RC piers under unidirectional and bidirectional shaking: a mechanics-based approach. J Struct Eng 146(7):04020113:1–21

Structural Behaviour of Prestressed Concrete Hollow Core Slabs Under Elevated Temperature

T. M. Jeyashree and P. R. Kannan Rajkumar

1 Introduction

Prestressed Concrete (PC) hollow core slabs are used in various types of structural applications in recent days due to structural efficiency, high-quality control, and fast erection. Prestressed hollow core slab is used as flooring units in large-span buildings and during its service life, it can be subjected to progressive collapse and failure due to fire exposure. Many structures in the past with precast prestressed elements was subjected to structural damage during the fire. Some of the examples are Lloydstraat car park fire accident—Rotterdam 2007 (constructed partly with precast prestressed hollow concrete slabs), Don Valley Parkway bridge fire accident 2008, Deans Brook Viaduct bridge fire accident 2011, etc., Prestressed hollow core slab has degradation in strength and performance when exposed to fire due to loss of mechanical properties of concrete and prestressing steel. Study on behaviour of hollow core slab under fire is essential to identify its possible mode of failure and failure mechanism. Fire resistance design satisfying the fire failure criteria is required to ensure the safety of the hollow core slab during its service life.

Various researchers in the past conducted real-time fire tests and numerical investigation on hollow core slabs to study the behaviour under elevated temperatures [1–11]. The fire behaviour of a hollow core slab depends upon various parameters such as load ratio, aggregate type, the geometry of the slab, fire scenario, and duration. Chang et al. specifically focused on studying the effect of aspect ratio (width to length ratio) on the fire behaviour of hollow core concrete floors using finite element programme SAFIR and it is examined that the provision of side supports as

T. M. Jeyashree · P. R. Kannan Rajkumar (✉)
Department of Civil Engineering, SRM Institute of Science and Technology, Kattankulathur, Kancheepuram District, Tamil Nadu, India
e-mail: kannanrp@srmist.edu.in

an emergency beam on both sides of hollow core slab can improve the fire perfor-
mance of prestressed hollow core slab [1]. Ehab Ellobody developed a finite element
model predicting the actual behaviour of hollow core slab and a parametric study
was conducted. Significant parameters identified are load ratio and fire curve. From
this investigation, it is observed that the slabs are not subjected to shear failure and
the failure occurred due to tensile splitting [2]. It is also essential to decide the
design fire curve for fire resistance design of prestressed hollow core slab and in this
context numerical investigation was conducted by Shakya and Kodur using ASTM
E119 standard curve and ISO 834 curve [3]. Many studies focused on studying the
shear response of hollow core slab under fire and the possible failure mode of slab
identified are flexural, shear, and flexure-shear mode [4–7]. Significant parameters
affecting the behaviour of hollow core slabs under elevated temperature are identified
by various researchers but deep analysis is required to identify the critical parame-
ters for performance-based design. Hence, the present study focuses on developing
a Finite Element model for tracing the actual behaviour of hollow core slab under
fire. The Finite Element model once validated will be helpful in the execution of
the analytical investigation further to identify the critical parameters. In the present
study, the effect of varying fire curves, span/depth ratio, and boundary condition
on failure mechanism and behaviour of hollow core slab are investigated using a
validated model.

2 Finite Element Model

3-D Finite element model is developed for predicting the behaviour of prestressed
concrete hollow core slabs under elevated temperature using ABAQUS. Two models
S1 and S2 are developed as reported in experimental investigation [8, 9] for depicting
the actual behaviour of hollow core slab under elevated temperature. Modelling is
done using C3D8T: An 8-node thermally coupled brick element for concrete and
T3D2T: A 2-node 3-D thermally coupled truss for prestressing tendons. Temperature-
dependent thermal and mechanical properties of concrete are calculated as per EN:
1992-1-2:2004 [12], and the model is incorporated with these properties. The thermal
properties given are Thermal conductivity (W/mK), Coefficient of thermal expan-
sion (/°C), Specific Heat (J/kgK), and mechanical properties given are Modulus of
elasticity (MPa), Density (kg/m^3). Concrete is also defined with concrete damaged
plasticity property with maximum yield stress in compression and tension. The input
of mechanical properties for thermal analysis will be imported directly from the
defined properties of concrete according to the increment in temperature. Proper-
ties of prestressing steel, loading, and support conditions are defined as given in the
experimental procedure. Table 1 gives the detail about the material properties and
geometry used for modelling of hollow core slab.

Appropriate interaction is modelled between concrete and tendon for coupled heat
transfer and stress analysis. Prestressing tendons are subjected to stress corresponding
to 70% of the tensile strength and the stress is defined as a predefined field before

Table 1 Material properties and geometry used for modelling

Description	S1	S2
Compressive strength of concrete—28 days (N/mm^2)	75	35
Tensile strength of steel (N/mm^2)	1860	1850
Slab dimension (Width × Thickness) mm	1205 × 200	596 × 100
Length of slab (mm)	3800	2300
Diameter of tendon (mm)	12.7	4
Number of prestressing strands	7	6
Clear cover (mm)	25	20
Diameter of core (mm)	150	60

the application of load and thermal analysis. Unexposed surface and fire exposed bottom surface of the slab are provided with the Coefficient of heat transfer by Convection as 4 W/m^{2}K and 25 W/m^{2}K, respectively, for heat transfer analysis [12]. Hollow core slab is analysed using fully coupled thermal stress analysis in which the member is subjected to heat transfer and stress analysis simultaneously under a transient state. The net heat flux applied on the exposed surface is calculated as per EN: 1991-1-2 (2002) [13] and the input for the determination of heat flux is taken from the respective temperature curve of experimental studies. Both the models are subjected to an initial ambient temperature of 25 °C and this is done with defining the predefined field. The developed Finite Element model cannot depict the spalling of concrete and hence the failure criteria will be decided based on the deflection limit or maximum temperature on the unexposed surface. Figure 1 shows the loading for prestressed hollow core slab $S1$ and $S2$ used for validation.

a) Loading for Slab S1

b) Loading for Slab S2
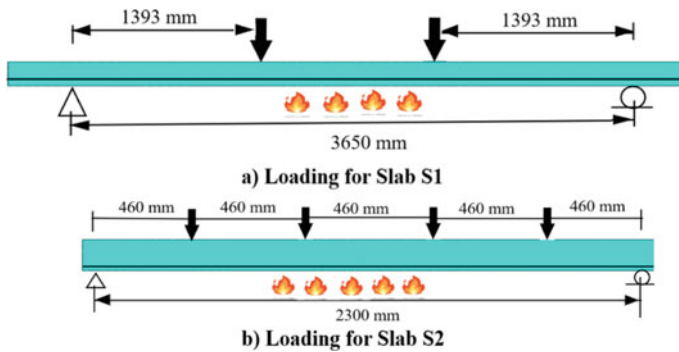
Fig. 1 Loading for hollow core slab $S1$ and $S2$

3 Validation of the Finite Element Model

The developed Finite Element model is validated by comparing the thermal response and mechanical behaviour with the experimental results [8, 9]. The coupled thermal stress analysis involves the following steps:

i. Assigning the material and thermal properties for concrete and steel
ii. Defining the maximum temperature with time incrementation
iii. Establishing the temperature curve using heat flux and surface film condition
iv. Generating temperature contour from heat transfer analysis
v. Determining the structural response by predicting deflection and failure criteria

After performing the coupled stress analysis, the temperature variation along the depth of the slab is plotted and Fig. 2 shows the temperature contour obtained from the analysis of the slab S1 after two hours of fire exposure to the standard ASTM E119 curve.

The obtained analytical results from thermal analysis and structural analysis are compared with the experimental results. As a first step, the temperature distribution along the depth of the slab has to be validated for its accuracy. Figure 3 shows the predicted temperature and measured temperature along the depth of the slab for Slab $S1$. Temperature is predicted for exposed bottom surface, and unexposed top surface. The maximum temperature measured on the exposed surface during experimental investigation is 425 °C for slab $S1$ after 110 min of fire exposure and the predicted temperature is 415 °C.

Slab $S2$ is subjected to temperature of standard curve as per ISO 834. The maximum temperature measured along the exposed bottom surface is 550 °C and the predicted temperature is 540 °C after 30 min of fire exposure. Also, the temperature progression is similar for both analytical and experimental results.

The mid-span deflection of the hollow core slabs $S1$ and $S2$ are determined from the analytical investigation. The hollow core slabs S1 and S2 are subjected to two-point loading and four-point loading with load ratio of 0.6 and 0.3, respectively, and the bottom surface of the slab are exposed to controlled fire. The comparison on deflection of the slab obtained from experimental and analytical investigation are
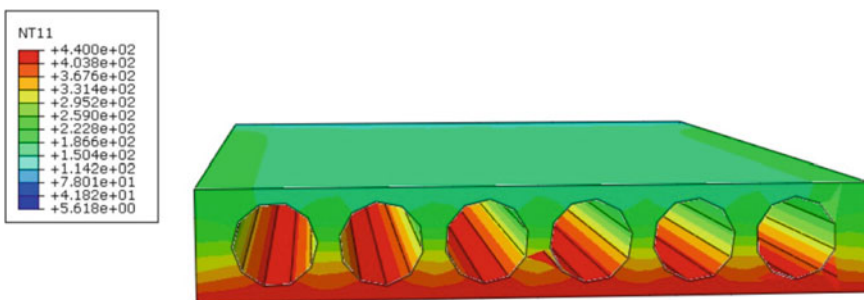
Fig. 2 Temperature contour for slab $S1$ after two hours of fire exposure
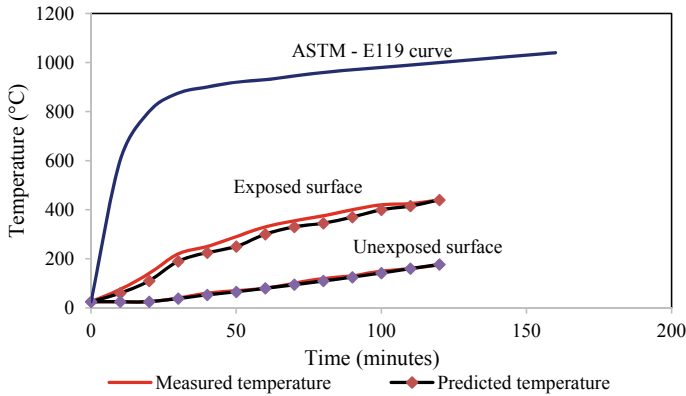
Fig. 3 Comparison of temperature obtained from analytical and experimental investigation—*S*1
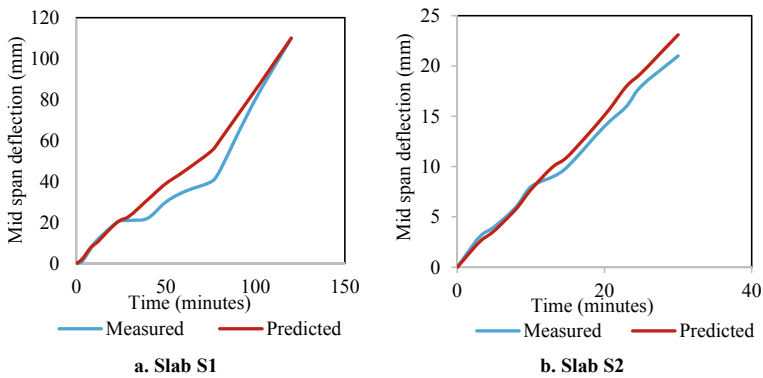
Fig. 4 **a** and **b** Comparison on mid-span deflection for Slab S1 and S2

shown in Fig. 4a, b for slab *S*1 and *S*2, respectively. For both the models, there is good agreement between experimental and analytical results. The maximum predicted deflection for slab S1 is 83 mm and from the experimental results it is 78 mm after 100 min of fire exposure. Also, for slab *S*2, the maximum predicted temperature is 23 and 21 mm from the experimental results after 30 min of fire exposure.

4 Parametric Study and Failure Criteria

Parametric study is carried out by studying the effect of different fire curve, varying span/depth ratio and boundary condition on behaviour of prestressed hollow core slab under elevated temperature. Prestressed hollow core slab is subjected to three different fire curves: Standard fire curve (ISO 834) [14], Localized fire curve and

Table 2 Geometry of slab used for parametric study

Description	P1	P2	P3
Slab dimension (Width × Thickness) mm	1205 × 200	1205 × 250	1205 × 300
Length of slab (mm)	3800	3800	3800
Diameter of tendon (mm)	12.7	12.7	12.7
Number of prestressing strands	7	10	11
Clear cover (mm)	25	25	25
Diameter of core (mm)	150	190	240

compartment fire curve [13]. The net heat flux required for thermal analysis are determined for three curves using EN: 1991-1-2 (2002) [13] Net heat flux for compartment fire curve depends upon opening factor and time factor function. Percentage of opening assumed for the compartment fire is 10%. (Area of opening $= 15.64$ m^2 and Area of building $= 154.8$ m^2).

The slab is subjected to three different fire scenario for two hours under constant load and the fire resistance is determined. 12 models are analysed in the present study with slab depth of 200, 250, 300 mm for three different fire curves with simply supported (SS) edges and fixed edges. Dimensions of model $P1$ are identical as slab $S1$. Table 2 gives the detail about geometry of slab used for parametric study. The compressive strength of concrete and tensile strength of steel is taken as 40 N/mm^2 and 1860 N/mm^2, respectively. Temperature-dependent mechanical and thermal properties of concrete are calculated and incorporated in model as per EN: 1992-1-2:2004 [12].

Hollow core slabs are analysed for three fire curves with the loading of 58 kN (equivalent to 60% of the moment capacity of the slab at room temperature) and the load ratio is 0.6. The analysed models are examined for thermal response and structural response. The structural response is determined based on the mid-span deflection curve and failure criteria. The thermal response of the slab is defined based on the obtained time—temperature curve and temperature contour.

4.1 Failure Criteria

The fire resistance and failure criteria of slab are defined based on the end point criteria as per ASTM E 119 [15] and BS 476 [16]. The heat transmission end point defined in [3] as insulation criteria and deflection criteria as given in [10] is considered for the present study to determine the fire resistance of slabs. The insulation criterion is defined based on the average temperature of the unexposed surface and the end point is defined if the temperature exceeds 139 °C (at 9 points) or 181 °C at any one point on the surface. As per the deflection criteria, the end point is defined if the maximum deflection at any fire exposure time exceeds L/30, where L is the span length of the slab (mm). The fire resistance of slab is determined based on the insulation criterion

Table 3 Summary of predicted fire resistance for various slabs

Specimen No	Fire curve	Support	Depth (mm)	Span/depth ratio	Fire resistance (minutes)	
					Deflection criterion	Insulation criterion
P1	Standard fire curve	SS	200	19	100	113
P2		SS	250	15.2	110	120
P3		SS	300	12.7	120	> 120
P4	Compartment fire	SS	200	19	90	100
P5		SS	250	15.2	105	110
P6		SS	300	12.7	115	120
P7	Localized fire curve	SS	200	19	120	120
P8		SS	250	15.2	> 120	> 120
P9		SS	300	12.7	> 120	> 120
P10	Standard fire	FIXED	200	19	110	113
P11		FIXED	250	15.2	120	120
P12		FIXED	300	12.7	> 120	> 120

and deflection criterion. Table 3 gives the summary of the predicted fire resistance for all the analysed slabs with Simply Supported (SS) edges and Fixed edges.

5 Results and Discussion

The effect of varying fire scenario, span/depth ratio and boundary condition are determined based on the results obtained from the parametric study. Comparison on structural response and thermal response for the analysed models are discussed below:

5.1 Effect of Different Fire Scenario

Based on the thermal analysis, the time–temperature curve for slabs subjected to different fire scenario are obtained at the exposed surface and unexposed surface. The comparison on temperature distribution at the unexposed and exposed surface of the slab for three fire curves are shown for slabs of span 200 mm—P1, P4 and P7 in Fig. 5. It can be observed that temperature at exposed surface is higher for compartment curve compared with localized fire curve and standard curve. The temperature is lesser for slabs subjected to localized fire curve and this can be associated to the fact that temperature induced due to this curve is lesser. Also from Table 3, it is observed that fire resistance for slabs subjected to localized fire curve is higher than the slabs
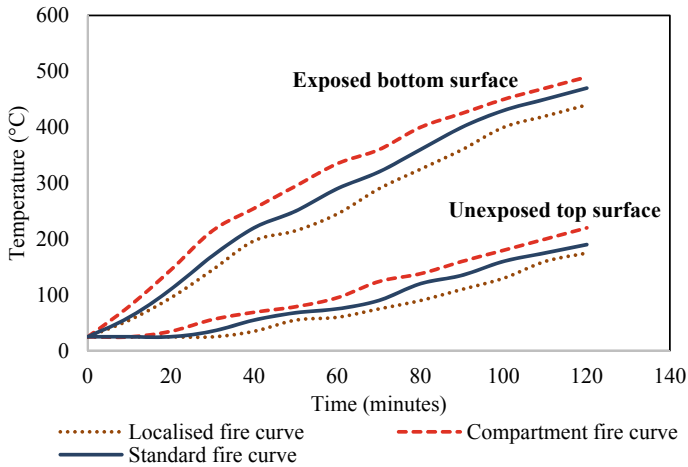
Fig. 5 Comparison on temperature distribution on slabs subjected to different fire curve

subjected to standard fire curve and compartment fire curve. The deflection is also observed to be more for slabs subjected to compartment fire curve and standard fire curve due to higher intensity of fire exposure under constant loading.

5.2 Effect of Span/Depth Ratio

To study the effect of varying depth on the response of hollow core slabs under fire exposure, the slabs are analysed with three span/depth ratio (19, 15.2, 12.7). The comparison on temperature distribution at the mid depth and unexposed surface of the slab with depth 200, 250 and 300 mm is shown in Fig. 6. It can be observed that there is similar progression of temperature distribution in all the slabs. The temperature at mid depth and unexposed surface decreases with the increase in the depth of the slab and this can be accredited to the increased thermal mass of thicker slabs.

The mid-span deflection of the slabs with varying span/depth ratio is compared and shown in Fig. 7. The deflection is found to increase with the increase in time but the progression of deflection curve is different for slabs with different thickness. The thinner slab with compartment fire has higher deflection compared to other slabs after two hours of exposure. This can be due to less stiffness and high fire exposure of thinner slab.
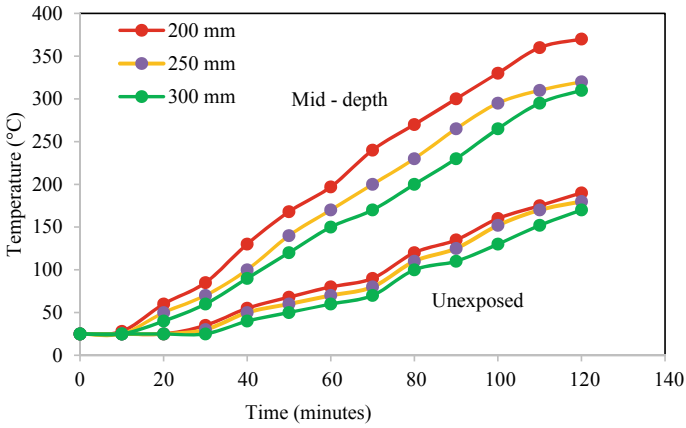
Fig. 6 Comparison on temperature distribution on slabs with varying depth

Fig. 7 Mid-span deflection for slabs with varying depth
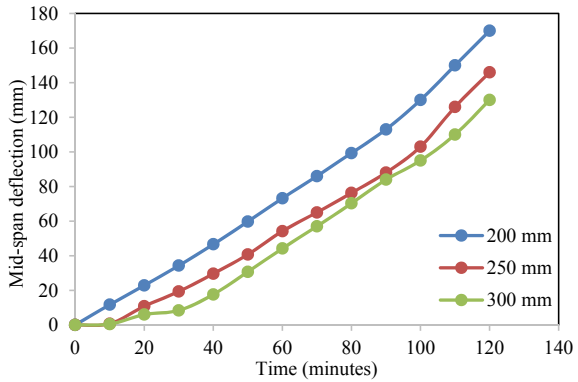
5.3 Effect of Boundary Condition

The effect of boundary condition on thermal behaviour of hollow core slab is studied by varying the support condition. 6 models are analysed with simply supported (SS) edges and fixed edges under standard fire curve to study the effect of boundary condition. From the analysis it is observed that the temperature distribution along the depth of the slab remains same and boundary condition does not have significant effect on temperature contour of hollow core slab. But the structural response is observed to be varying with the varying boundary condition and the mid-span deflection for slabs with simply supported (SS) edges are greater than that of fixed edges. The mid-span deflection for slabs with varying boundary condition is shown in Fig. 8. Also from Table 3, it is observed that fire resistance is greater than 120 min for fixed slabs as compared to those with simply supported slabs.
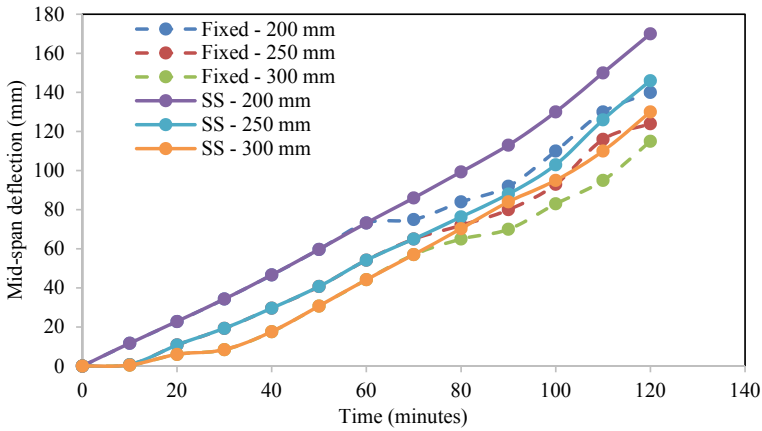
Fig. 8 Mid-span deflection for simply supported slabs and fixed slabs

6   Conclusions

From this analytical investigation, the concluding remarks highlighting the behaviour of Prestressed Concrete (PC) hollow core slab under elevated temperature are as follows:

- The proposed finite element model is used for tracing the actual behaviour of prestressed hollow core slab under elevated temperature and there is good agreement in analytical and existing experimental results. Hence, the proposed finite element model can be used for further detailed investigation on hollow core slabs and critical factors can be identified for performance-based design.
- Fire curves are found to have significant effect on hollow core slabs and compartment curve with higher intensity of fire reduces the fire resistance of hollow core slab by 10% as compared with standard curve. In addition to fire curve, ventilation provided in the building also plays a vital role in deciding the fire resistance of hollow core slab. Detailed investigation is required further to study the improvement in fire resistance with the change in ventilation area of the building.
- The fire resistance by both deflection criteria and insulation criteria is increased by 10 min with the increase in slab depth by 50 mm. Hence, span/depth ratio is also considered as significant parameter affecting the behaviour of hollow core slab subjected to elevated temperature.
- Boundary condition also plays a vital role on fire behaviour of prestressed hollow core slab. The hollow core slabs with fixed edges perform well as composed to those of slabs with simply supported edges.

References

1. Chang JJ, Moss PJ, Dhakal RP, Buchanan AH (2010) Effect of aspect ratio on fire resistance of hollow core concrete floors. Fire Technol 46:201–216
2. Ellobody E (2014) Advanced analysis of prestressed hollow core concrete slabs exposed to different fires. Adv Struct Eng 17(9):1281–1298
3. Shakya AM, Kodur VK (2014) Behaviour of prestressed concrete hollowcore slabs under standard and design fire exposure. In: Proceedings of 8th international conference on structures in fire Shanghai, China, June 11–13, 2014
4. Kodur VKR, Shakya AM (2017) Factors governing the shear response of prestressed concrete hollowcore slabs under fire conditions. Fire Saf J 88:67–88
5. Shakya AM, Kodur KR (2017) Modeling shear failure in precast prestressed concrete hollowcore slabs under fire conditions. J Struct Eng 143(9):04017093–1–04017093–14
6. de Lima Araújo D, Sales MW, Silva RP, Antunes CD, de Araújo Ferreira M (2020) Shear strength of prestressed 160 mm deep hollow core slabs. Eng Struct 218:110723–1–16
7. Nguyen HT, Tan KH (2021) Shear response of deep precast/prestressed concrete hollow core slabs subjected to fire. Eng Struct 227:111398–1–19
8. Shakya AM, Kodur VKR (2015) Response of precast prestressed concrete hollowcore slabs under fire conditions. Eng Struct 87:126–138
9. Pothisiri T, Kositsornwanee C (2015) Experimental investigation of the fire resistance of thin hollow-core concrete slabs with simple supports. Eng J 19(2):139–155
10. Torić N, Divić V, Boko I (2012) Behaviour of prestressed hollow-core concrete slab under fire—experimental study. Tech Gazette 19(4):847–856
11. Aguado JV, Albero V, Espinos A, Hospitaler A, Romero ML (2016) A 3D finite element model for predicting the fire behaviour of hollow-core slabs. Eng Struct 108:12–27
12. EN 1992–1–2 (2004) (English): Eurocode 2: design of concrete structures—part 1–2: general rules—structural fire design
13. EN 1991-1-2 (2002) (English): Eurocode 1: actions on structures—part 1–2: general actions—actions on structures exposed to fire
14. ISO 834-1 (1999) International Standard (E), fire resistance tests: elements of building construction—part 1: general requirements. International Organization for Standardization, Geneva, Switzerland
15. ASTM-E119-12 (2011) Standard test methods for fire tests of building construction and materials. Test Method, American Society for Testing and Materials, West Conshohocken, PA
16. BS 476-21 (1987) Fire tests on building materials and structure—part 21: methods for determination of the fire resistance of loadbearing elements of construction, CEN

Consequences of Sequence of Motion: Implications of Site Characteristics

Arghyadeep Banerjee and Rana Roy

1 Introduction

Due to the seismological processes, a major seismic event may often involve a number of foreshocks prior to a seismic mainshock which may follow a few aftershocks as well. Numerous evidences showing such sequence of seismic actions were found, such as, in California (Mammoth Lakes, 1980; Coalinga 1983; Whittier Narrows 1987; Northbridge 1994), Italy (Friuli 1976), Japan (Tohoku 2011), New Zealand (Christchurch 2011), among others. 2015 Nepal earthquake, a mainshock with a moment magnitude of $M_w = 7.8$, was followed by a sequence of eight aftershocks with comparable magnitudes ranging from 5.3 to 7.3. 1986 Chalfant Valley earthquake event at Zack Brothers Ranch station is observing a sequence of a foreshock with moment magnitude $M_w = 5.8$ subsequently followed by a mainshock with $M_w = 6.2$ and two aftershocks with magnitudes 5.7 and 5.4. On the other hand, seismic sequence with mainshock preceded by foreshock but followed by no aftershock can also be observed during the seismic event of Ierissos at Ierissos police station in 1983.

There is a renewed interest in assessing the effect of seismic sequences on the structural response of new and existing buildings and bridges [1]. Many researches [2–4] have been done to assess the influence of sequence of motions or multiple earthquakes on the structural response. Structural response under seismic excitation is related to ground motion characteristics which is responsible on the site effects.

A. Banerjee (✉)
Department of Aerospace Engineering and Applied Mechanics, Indian Institute of Engineering Science and Technology Shibpur, Shibpur, India
e-mail: arghyamon93@gmail.com

R. Roy
Indian Institute of Engineering Science and Technology Shibpur, Shibpur, India
e-mail: rroybec@yahoo.com

The changes in intensity, duration, and frequency contents of the accelerogram during propagation though soil deposit are commonly referred to as site effects, which have a direct impact on the response of a structure. It can be perceived that when a sequence of seismic motion propagates through sub-soil strata the soil may face nonlinearity due to strain induced by leading sequence which may change the shear modulus and damping of the soil offering for a following sequence. It leads to the fact that the site response for a mainshock event may change if it is preceded by a foreshock event in a sequential ground motion as the shear modulus and damping of the soil may undergo a change due to nonlinearity caused by the foreshock prior to the mainshock event. Similarly, this effect of sequence of ground motion may be attributed to the change of site response due to the aftershock if it is preceded by foreshock(s) and mainshock.

The effect of site characteristics on the site response is observed by choosing three different types of sand as the propagating media of the bedrock version of the sequential motion. Loose, medium, and dense sand having different soil properties are taken for the site response analysis. Sequential ground motions of different combinations (Foreshock–mainshock, mainshock–aftershock, and fore-shock–mainshock–aftershock) are collected from PEER strong ground motion database.

2   Objectives and Significance

The present paper aims to evaluate the change in ground motion parameters due to the change in sub-soil characteristics by the foreshock or aftershock that often accompany a seismic mainshock. In the routine analysis, effect of foreshocks and main-shocks is often ignored, and the seismic mainshock is only considered in assessing structural performance. Implications of such consideration and design assumptions may be confirmed from the present work for a broad range of sub-soil characteristics.

3   Site Response Analysis

Site response analysis is the process of calculating the free-field response, i.e., esti-mating the influence of soil deposit to accelerogram in the absence of structure. The changes in intensity, duration, and frequency contents of the accelerogram during propagation though soil deposit are commonly referred to as site effects. Here, one-dimensional (1D) site response analysis is adopted. We have used standard 1D site response analysis program *Deepsoil v7.0.5* [5] for this purpose. Equation of motion for vertically propagating shear waves in 1D may be expressed as

$$\rho \frac{\partial^2 u}{\partial t^2} = G \frac{\partial^2 u}{\partial z^2} + \eta \frac{\partial^3 u}{\partial z^2 \partial t} \tag{1}$$

where u is the lateral displacement of the medium, ρ is the mass density of the medium, G is the shear modulus, and η is the coefficient of viscous damping. The solution of Eq. (1) may be obtained by (a) linear time domain and frequency domain analysis, (b) nonlinear time domain analysis, and (c) equivalent nonlinear frequency domain analysis. Frequency domain analysis is done by fast Fourier transform analysis, and time domain analysis is generally done by Newmark's β method [6].

Fundamentals of site response analysis are well described in the past literature [7]. Motion history recorded at site A is taken through *deconvolution* process to the bedrock level, assumed here to exist at a depth of 30 m below ground surface to regenerate the bedrock motion (at B). *De-convolution* analysis for obtaining modified version of motion at the bedrock level is a complex inverse problem and is solved in linear frequency domain analysis. The bedrock motion is then propagated through the soil profile of interest employing *convolution* process to obtain the surface motion derivative at site C. Convolution analysis refers to the upward wave propagation analysis and is done by nonlinear time domain analysis using the Newmark-β method with average acceleration.

Time series of recorded ground motions recorded at sites under Class D and Class E soil types ($V_{s30} < 360$ m/s) only are deconvoluted to the rigid bedrock. Motions at other soil profile sites ($V_{s30} > 360$ m/s) are used as outcrop motions and used as it is during subsequent *convolution* process considering elastic half space with the site-specific properties. The original site-specific sub-soil strata is subdivided in multiple layers, while performing the deconvolution complying with the requirement that the maximum frequency ($f_{max} = V_s/4$ h, h is the layer thickness) is subjected to a minimum of 30 Hz. In the linear analysis, the maximum soil stiffness ($G_{max} = \rho V_s^2$) and a constant damping ratio (10%) are considered throughout the entire time history. Frequency independent complex shear modulus (Kramer 1996) formulation resulting in frequency independent damping formulation is used in performing frequency domain analysis. The deconvoluted bedrock motions are considered as '*within*' motion.

4 Selection of Parameters

4.1 Ground Motion Parameters

It is well known that the structural response under seismic excitation is related to the ground motion characteristics. It is important to investigate the influence of site characteristics and sequence of ground motion on the ground motion parameters. One intensity parameter, viz., peak ground acceleration (PGA) and one is frequency content, viz., T_m (Mean period) are studied in this aspect.

4.2 Soil Characterization

Homogeneous soil medium is assumed to exist over a depth of 30 m underlain by bedrock idealized as rigid half space. Three types of sand, i.e., loose, medium, and dense are chosen as the propagating media of the bedrock motion. Representative soil parameters for three types of sands are furnished in Table 1. The soil layer is discretized into 33 layers with top 6 layers of 0.5 m and next 27 layers of 1.0 m. The discretization is complying with the requirement that the maximum frequency (f_{max}) is subjected to minimum of 30 Hz for all layers. All the three types of sands are assumed to be cohesion less and having zero plasticity index (PI = 0). The target shear strength (τ_{max}) for each layer is calculated using Mohr–Coulomb failure criterion with assumed friction angle for corresponding sand type and effective vertical stress corresponding to that layer and multiplied by a factor 1.2. Thus, τ_{max} is obtained as

$$\tau_{max} = 1.2\sigma'_{v0} \tan \varphi \tag{2}$$

In absence of site-specific curves to represent dynamic soil behavior, generic modulus reduction and damping curves proposed by Darandeli [8] are used in this study. Reference curves for sand are obtained for particular values of the initial effective vertical stress (σ'_{v0}), the plasticity index (PI), the over consolidation ratio (OCR), the initial coefficient of effective lateral earth pressure (K_0), the number of loading cycle (N) in the combined resonant column and torsional shear (RCTS) test equipment and the corresponding loading frequency (f_r).

5 Performance of Model

Nonlinear behavior for 1D site response analysis is modeled by general quadratic/hyperbolic (GQ/H) model proposed by Groholski et al. [9] in this study to satisfy both the small and large-strain modeling of the backbone curve of the soil. This model obtains a limiting maximum shear stress as shear strain approaches infinity. This aspect represents its well applicability over the other models where the shear stress approaches to zero or infinity at infinite shear strain. The initial shear modulus is the maximum initial shear modulus (G_{max}) obtained as $G_{max} = \rho V_s^2$.

Table 1 Properties of different types of sand considered

S. No	Type of sand	Relative density (%)	Unit weight (γ_d) (kN/m^3)	N_{SPT}	$V_{s\,30}$ (m/s)	Angle of friction (°)	K_0	OCR
1.	Loose	15	15	6	173	30.0	0.50	1
2.	Medium	35	18	20	236	33.5	0.45	
3.	Dense	65	20	38	279	38.0	0.38	

The curve fitting parameters are selected such that the implied strength reaches a desired fraction of maximum shear strength obtained as Eq. (2) at $\gamma = 10\%$. In this paper, curve fitting is performed with the reference curve from Darandeli, as described earlier, for a shear strain range of 0.001–0.3% under the condition that the implied shear strength at $\gamma = 10\%$ reaches 95% of the target maximum shear strength, i.e., minimum strength at 10% strain is 95% of the target maximum shear strength. The choice of shear strain range for curve fitting is complying with the view that the proposed reference curves from Darandeli were based on a database that becomes sparse for shear strains beyond 0.3%, and the fitting for shear strain less than 0.001% has limited influence on G/G_{max}.

Non-Masing MRDF approach proposed by Hashash [10] is used in this study to model hysteric behavior. Non-Masing unload-reload rule which implements a reduction factor over that of the Masing [11] rule where, for initial loading, the stress–strain curve follows the backbone curve. MRDF approach provides better agreement with the damping curves at large strains. Excess pore water pressure generation is not accounted in this study, and therefore, no degradation indices are applied to the backbone and unload-reload equations. The GQ/H model curve fitting for normalized shear modulus, damping, and shear stress *vs.* shear strain with reference curves obtained from Darandeli for loose sand medium chosen at mid depths is shown in Fig. 1. Figures show well-fitting of curves within the specified range and eliminates the underestimation of implied shear strength at large strain.
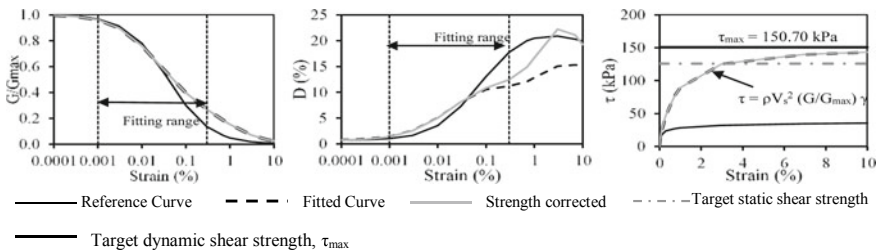
Fig. 1 Adequacy of mathematical model to represent the variation of G/G_{max}, damping (ξ in %), and shear strength (τ in kPa) with shear strain γ (%) against the selected reference companion (Darandeli 2001) for loose sand (sample plot) at mid depth of soil profile

6 Implication of Site Characteristics and Sequence of Motion on Ground Motion Parameters

6.1 Surface Derivatives

Digital recordings of two horizontal components of nine strong motions out of which two foreshock-mainshock sequential ground motions, five mainshock–aftershock sequential ground motions and two foreshock–mainshock–aftershock sequential ground motions have been collected. Original as recorded motions are deconvoluted through original site-specific soil deposit to the bedrock (for Class D and E sites; otherwise used as outcrop motion) and subsequently propagated through three different sand media of interest. Composite sequential motion is generated from as recorded foreshock–mainshock–aftershock motion by combining them assigning zero ground acceleration for a time gap of 20 s between two consecutive sequences. Individual and composite as recorded sequential acceleration history from Chalfant Valley 20/07/1986–21/07/1986, station: Zack Brothers Ranch, foreshock-mainshock-aftershock sequential ground motion, along with their bedrock versions and surface motion derivatives after propagating through loose sand (a representative case) media are furnished in Fig. 2, marking their PGA values in each sequence.

6.2 Effect on Ground Motion Parameters

Figure 3 shows the effect of site characteristics and seismic foreshock on the peak ground acceleration (PGA) and mean period (T_m) of the mainshock. The variation of PGA of mainshock with depth is furnished in (a) of each figure for three different sand media chosen, for individual ground motion components as well as the mean. The percentage change in the mean value at the surface of soil deposit from bedrock is mentioned in the figures in each case. The GM parameters of the mainshock followed by the foreshock from foreshock–mainshock sequence (e.g., PGA $_{(FS)-MS}$) is obtained at different depths, and they are normalized with that of the mainshock (e.g., PGA_{MS}) at corresponding depth. The variation of these normalized parameters of mainshock (e.g., PGA $_{(FS)-MS}$/PGA $_{MS}$) with depth is shown in (b) of each figure. The mean variation in all cases is shown along with individual records.

It can be observed from Fig. 3 that attenuation of PGA occurs during propagation of the mainshock from bedrock to the surface of the sub-soil strata. The percentage increase in PGA is the highest for dense sand which is on an average 50.2% while for medium sand 33.7% and for loose sand 19.4%. Individual records show that up to approximately 20% variation may occur in the PGA value of the mainshock if it is preceded by foreshock. The mean period also increases from bedrock version to surface derivatives, but the increase is maximum for loose sand here which is 34.7%, while for medium sand, it is 27.9% and for dense sand 9.7% on average. Foreshocks have a very small effect on the mean period of the mainshock as it can be seen that
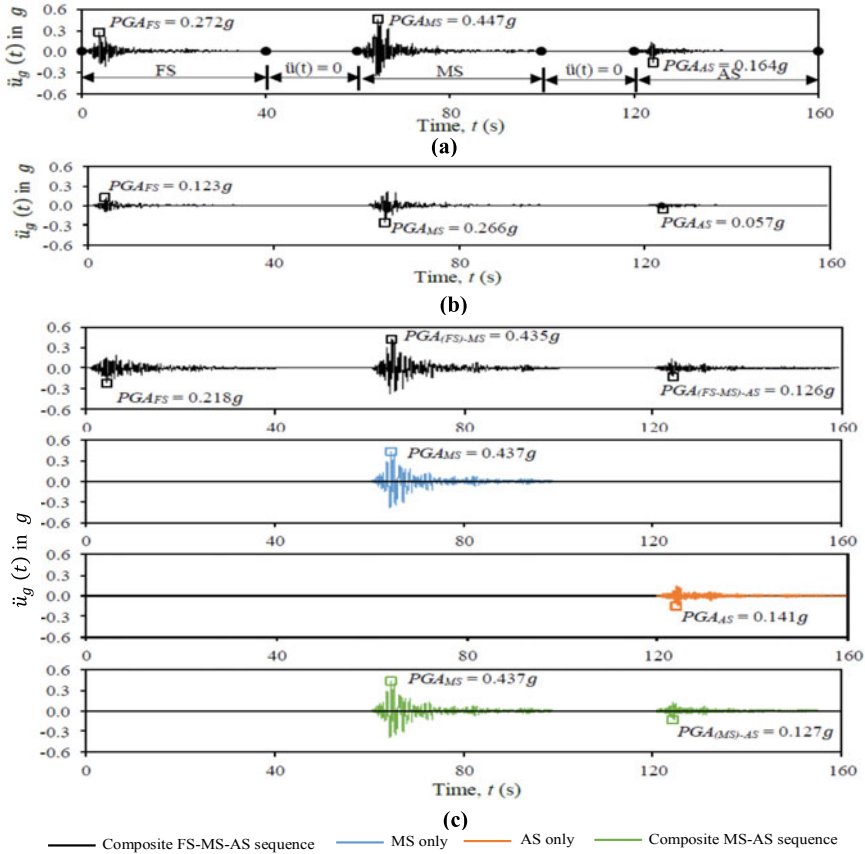
Fig. 2 Effect of site characteristics on the acceleration histories of ground motion involving FS, MS, and AS, considered alone as well as in sequence (Event: Chalfant Valley 20/07/198–6-21/07/1986, Station: Zack Brothers Ranch, Component ID: CV_ZBR_FS_I, CV_ZBR_MS_I, CV_ZBR_AS_I). **a** As recorded motion history; **b** Deconvoluted motion at bedrock level; **c** Surface derivatives of loose sand
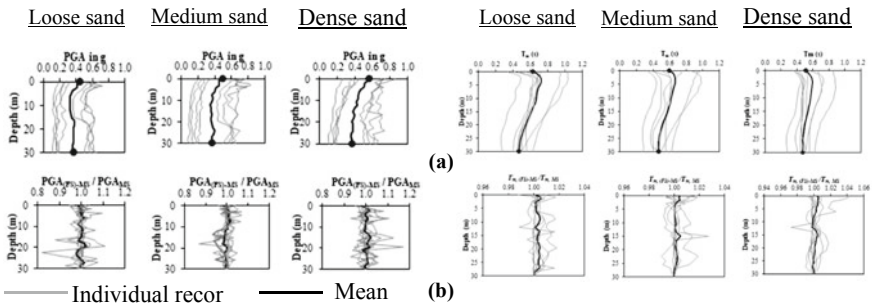
Fig. 3 Effect of site characteristics and seismic foreshock on the peak ground acceleration (PGA) and mean period (T_m) of mainshock (MS)
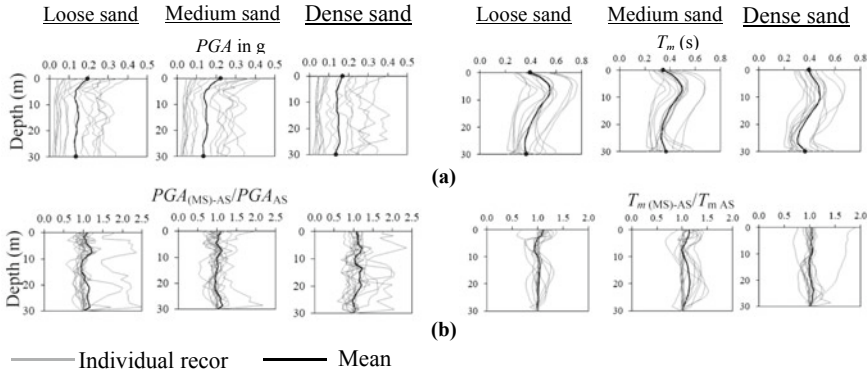
Fig. 4 Effect of site characteristics and seismic mainshock on the peak ground acceleration (PGA) and mean period (T_m) of aftershock (AS)

the maximum difference of the mean period of the mainshock if it is preceded by foreshock is about 4% for individual records. As PGA and T_m both increase as the mainshock propagates from bedrock to the surface, the energetic length scale also increases. The increase is 163.6% for the case of medium sand. On average, the L_e of the mainshock is not affected so much by the precedence of the foreshock.

The effect of sequence of motion is more significant in the mainshock–aftershock sequence. Significant change in PGA of the aftershock as preceded by mainshock can be observed in individual record. When the aftershock is preceded by a strong mainshock as we see, the PGA of the aftershock may become up to even 2.5 times the PGA if it would occur alone. On average, approximately, 10% variation may occur due to occurrence of the mainshock before the aftershock. The effect of seismic mainshock and site characteristics on the GM parameters of aftershock are furnished in Fig. 4.

7 Implication on Sub-Soil Properties

Response history in terms of shear strain history and shear stress history caused by seismic foreshock, mainshock, and aftershock is applied separately and collectively, at a depth of 15 m, for a selective case of foreshock–mainshock–aftershock sequential ground motion, east–west component of Friuli 06/05/1976, station: Tolmezzo-Diga Ambiesta, propagating through medium sand, is presented in Fig. 5. Four set of figures are presented in this respect, each set consisting of three figures representing shear strain history, shear stress ratio history and shear stress ratio versus shear strain cumulative response. Shear strain is in percentage, and shear stress ratio (τ/σ'_{v0}) is obtained as shear stress divided by the effective vertical stress at the corresponding depth. Figure 5a–d represents the response history at the selective depth
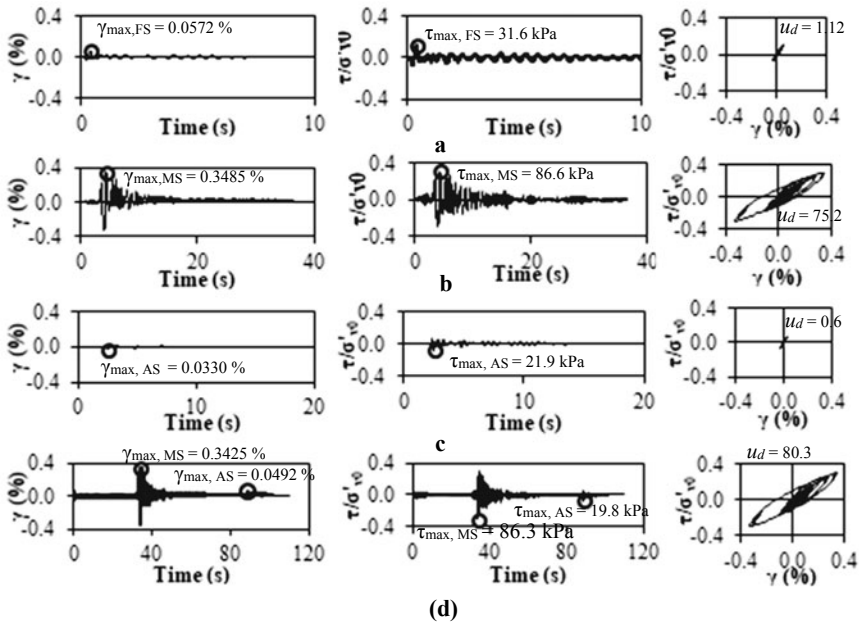
Fig. 5 Response history of soil caused by seismic foreshock, mainshock, and aftershock applied separately and collectively. **a** FS alone, **b** MS alone, **c** AS alone, **d** composite FS-MS-AS sequence. (Selected depth: 15 m, soil type: medium sand, event: Friuli, 06/05/1976, station: Tolmezzo-Diga Ambiesta, component ID: F_TDA_FS_I, F_TDA_MS_I, F_TDA_AS_I). (u_d in kN/m^2)

as foreshock alone, mainshock alone, aftershock alone, and foreshock–mainshock–aftershock combined sequence, obtained from selected event, respectively, propagate through the medium sand strata chosen. Peak shear strain occurring due to foreshock, mainshock, and aftershock is denoted as $\gamma_{max,FS}$, $\gamma_{max,MS}$, and $\gamma_{max,AS}$, respectively. In case of combined sequence, peak strain occurring at each component of sequence is marked on the strain history except for the foreshock as it remains same for any combination with it. Peak shear stresses in kPa are also marked on the stress history plots similarly, denoted by $\tau_{max,FS}$, $\tau_{max,MS}$, and $\tau_{max,AS}$. Energy dissipation per unit volume of soil, defined as energy density and denoted by u_d in units of kN/m^2, is obtained by multiplying the effective vertical stress (σ'_{v0}) by the area under shear stress ratio–shear strain hysteresis loop as given in Fig. 5.

Peak strain caused at different depths at the mid of different layers of soil profile due to propagation of sequence of motion is normalized with respect to the peak strain at the corresponding depths occurred due to propagation of mainshock only to understand the influence of sequence of motion on the characteristics of sub-soil properties. The variation of normalized peak strain with depth is shown in Fig. 6.
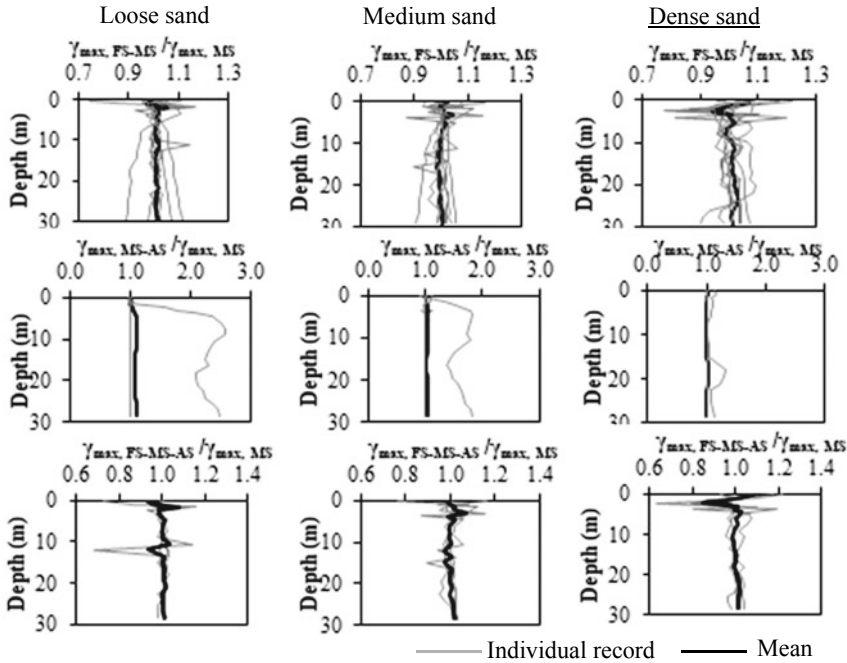
Fig. 6 Variation of peak strain with depth considering the sequence of motion

8 Conclusions

To this end, the effects of sequence of motion and site characteristics on different selected ground motion parameters as well as the influence on the sub-soil properties are evaluated. In this context, a scrutiny of the studies that explicitly account for the effects of foreshocks and aftershocks has been made. Following conclusions can be emerged from the study:

- Maximum change in the peak ground acceleration (PGA) of the mainshock due to the propagation of preceding foreshock may be around 15%. In contrast, change in soil characteristics due to the propagation of mainshock may alter the PGA of aftershock even by over 100%. Consequently, the propagation of sequence of motion, influence of one motion on the sub-soil characteristics may also lead to changes in other ground motion parameters for the motions that follow.
- The peak strain in the soil may alter by around 20% due to foreshock–mainshock sequence over that caused by corresponding mainshock alone. However, change in soil characteristics due to the propagation of mainshock may impart additional strain on the order of 100% in soil during the propagation of subsequent after-shock. It reveals that foreshocks and aftershocks may induce considerable additional energy dissipation in the sub-soil throughout the depth over that caused by mainshock.

- The changes in the sub-soil properties incurred due to the propagation of the weaker foreshocks may not significantly alter the ground motion properties of the following mainshock, whereas considerable changes in the ground motion properties of the aftershocks may occur due to changes in soil properties offered by preceding mainshock as well as foreshock–mainshock sequences. Hence, the sequence of motion must be considered in practice rather than choosing them separately in order to assess the ground motion parameters as well as to estimate the structural response.

References

1. Sarno Di L (2013) Effects of multiple earthquakes on inelastic response. J Eng Struct 56:673–381
2. Ruiz-Garcia J (2013) Discussion on effects of multiple earthquakes on inelastic structural response. J Eng Struct 58:110–111
3. Zhai CH, Wen WP, Chen Z, Li S, Xie LL (2013) Damage spectra for the mainshock-aftershock sequence-type ground motions. Soil Dyn Earthquake Eng 45:1–1
4. Hatzigeorgiou GD, Beskos DE (2009) Inelastic displacement ratios for SDOF structures, subjected to repeated earthquakes. Eng Struct 31(11):2744–2755
5. Hashash YMA, Musgrove MI, Harmon JA, Okan I, Groholski DR, Phillips CA, Park D (2017) DEEPSOIL 7.0 user manual
6. Newmark NM (1959) A method of computation for structural dynamics. J Eng Mech Div EM3:67–94
7. Kar D, Roy R (2018) Seismic behavior of RC bridge piers under bidirectional excitations: implications of site effects. J Earthquake Eng 22(2):303–331 (2018)
8. Darandeli MB (2001) Development of a new family of normalized modulus reduction and material damping curves. Ph.D. thesis, Univ. of Texas, Austin, TX
9. Groholski D, Hashash Y, Kim B, Musgrove M, Harmon J, Stewart J (2016) Simplified model for small-strain nonlinearity and strength in 1D seismic site response analysis. J Geotech Geoenviron Eng. https://doi.org/10.1061/(ASCE)GT.1943-5606,0001496,04016042
10. Phillips C, Hashash YMA (2009) Damping formulation for nonlinear 1D site response analysis. Soil Dyn Earthquake Eng 29(7):1143–1158
11. Masing G (1926) Eigenspannungen und verfestigung beim messing 2nd international congress on applied mechanics, Orell FüssliZurich, Switzerland

A Study on the Effect of Tank Shape on the Performance of Tuned Liquid Dampers

N. K. Kiran, G. Unni Kartha, and Neeraja Nair

1 Introduction

The growing popularity for high-rise structures in recent years has contributed to the evolution of vibration suppression systems viz., active, passive, and hybrid systems. Taller structures use lighter materials without much gain in structural strength and hence, attract higher vibrations due to environmental excitations like wind or earthquake loads [1]. Tuned liquid damper (TLD) is a passive vibration control device, where a liquid's (generally water) sloshing motions absorb a portion of the dynamic energy of vibration and thus control the structural vibrations under excitations. Since most structures have provisions for overhead water storage tanks, these may be utilized to act as TLD without compromising the functionality [1]. Hence, it has emerged as an effective vibration control strategy [2–4].

Research in the area led to the development of analytical model [5] and its implementation to single degree of freedom (SDOF) structure [6]. Variations in the TLD tanks in the form of baffles [7–9], nets [10], and sloped bottom [11] were found to be effective. SAP software produced reliable results to model these dampers [12, 13]. Studies on the effects on shape on response reduction have been few [1, 14, 15], especially unconventional ones. This research attempts to explore the latter.

N. K. Kiran · G. Unni Kartha (✉) · N. Nair
Department of Civil Engineering, Federal Institute of Science and Technology (FISAT),
Angamaly, Kerala 683577, India
e-mail: unnikartha@fisat.ac.in

2   Experimental Investigations

The effect of four different tank shapes (Fig. 1) in structural response reduction for a roof mounted TLD was investigated in this study. The setup consisted of a unidirectional shake table with a 1.5 m × 0.5 m sliding platform attached through a pulley system to a motor and can be used to create sinusoidal external excitation of different frequencies. A 1:10 scaled down single bay two story building frame model with story height 0.3 m was fabricated using aluminum and wood for the study. The scaling of columns is done considering stiffness of the equivalent column size. A photograph of the model is given in Fig. 2, and the model dimensions are shown in Table 1. A modal analysis was performed assuming the frame as a three degree of freedom system. The natural frequencies corresponding to the three modes were obtained as 1.03 Hz, 1.43 Hz, and 2.28 Hz. Four different tank shapes of the TLD were fabricated using acrylic. The total width and height of the tanks was kept constant for all the models. The model dimensions along with dimensions are shown in Fig. 2. Shape 1 had inward projections at ends, shape 2 outward projections, shape 3 with rectangular projections, and shape 4 with sloped bottom profile. Experimental investigations were carried out using the shake table with harmonic sinusoidal input of 0.16 g at a frequency of 1 Hz. Experiments were conducted with frequency ratios between 0.8 and 1.35 and mass ratios varying from 1 to 8%. The height of the water is adjusted to obtain the various mass and frequency ratios. The difference in the weight of the tank models was also considered for estimating the mass ratios. The response of the structure with and without TLD was measured for both free and forced vibrations. Custom made acceleration sensors with a data acquisition system were used for recording data. The sensors were placed at top and bottom stories of the model. The data were smoothed by removing the unwanted noises, and a low-pass filter was applied to remove frequencies above 5 Hz. A fast Fourier transform (FFT) was performed to obtain the frequency and magnitude of acceleration.

(a) Shape 1	(b) Shape 2
(c) Shape 3	(d) Shape 4
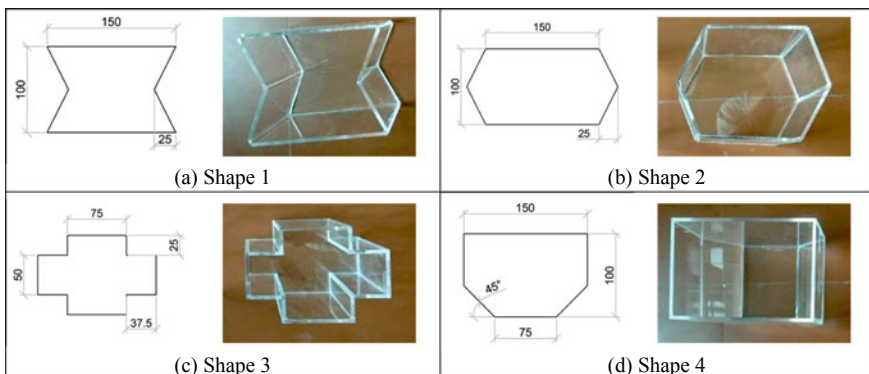
Fig. 1   TLD tank parameters

Fig. 2 Scaled model used for experiments

Table 1 Scaled model parameters

Element	Dimension (mm)	Material
Column	12×6	Aluminum
Beam	12×6	Aluminum
Slab	$300 \times 300 \times 6$	Plywood
Rectangular Tank	$150 \times 100 \times 100 \times 5$	Acrylic

3 Modeling Using SAP

A numerical model of the building and TLD was developed using SAP. Water was modeled as a linear link element according to IS 1893 (Part 2): 2014 [16]. Spring for convective mass was modeled using a linear link element whose stiffness in X and Y direction is given as $K/2$, and its degree of freedom in Z direction was set as fixed. Spring for impulsive mass was also modeled using a linear link element, but its degree of freedom was set fixed in all directions. Joint mass was assigned at the joint of the spring with values Mc and Mi in X and Y direction. Joint force was assigned at the joint of the spring with values Mc and Mi in gravity direction (Fig. 3).
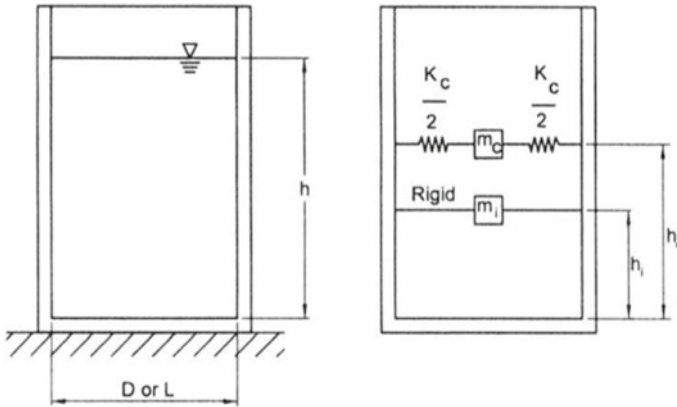
Fig. 3 Modeling liquid as per IS 1893 (Part 2): 2014

4 Results and Discussion

It was evident from the experimental investigations that the tank shapes does have an influence on the response of the structure. Maximum response reduction was obtained at resonant frequencies, i.e., frequency ratio of 1.0 as seen in Table 2. Figures 4 and 5 show the measured acceleration response of the top story and bottom story to an input motion of 0.16 g at 1 Hz different mass ratios. It was observed that the response is minimum at a mass ratio corresponding to 5% for all tank shapes. In comparison with the rectangular tank, the response of the structure obtained with tank shape 1 (with inward projections) and shape 4 (with sloped bottom profile) was lesser, and tank shape 2 (with outward projections) and shape 3 (rectangular projections) were higher in both top and bottom stories. The response reduction in percentages is shown in Figs. 6 and 7. For shape 1 and shape 4, the percentage reduction is nearly 27% at

Table 2 Comparison of experimental and simulation results (rectangular tank)

Frequency ratio	Top story acceleration (from experiment)	Top story acceleration (from SAP)	% difference
No water	1.5	1.48	1.33
0.8	1.25	1.11	11.20
0.9	1.11	1.05	5.41
1	1.10	1.04	5.45
1.1	1.15	1.10	4.35
1.2	1.31	1.19	9.16
1.3	1.31	1.26	3.82
1.35	1.40	1.28	8.57

Maximum response at top story
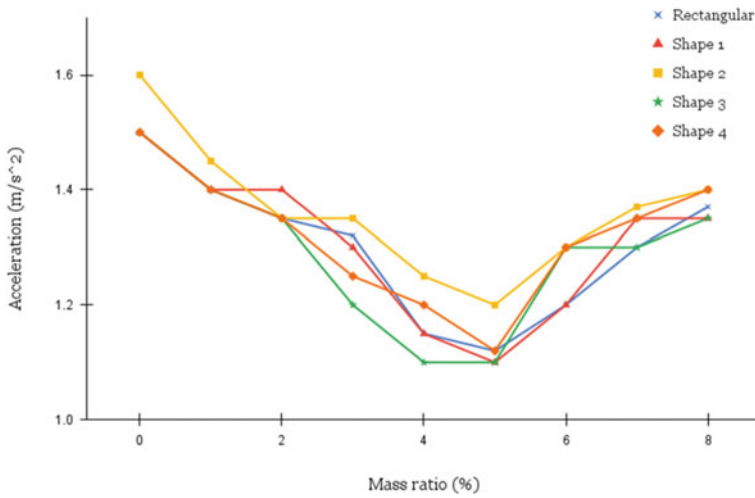
Fig. 4 Comparison of top story acceleration of various tank shapes

Maximum response at bottom story
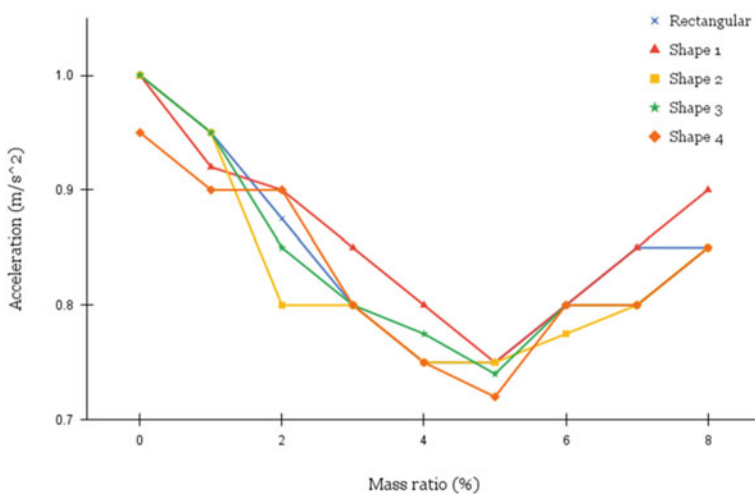
Fig. 5 Comparison of bottom story acceleration of various tank shapes

a mass ratio of 5%. The corresponding value for rectangular shape was 25.3%. For shape 2 and shape 3, the values were 25% and 24%, respectively. A similar trend is seen in the response of the bottom story. The sloshing behavior in the different tank shapes is different, and this may be the reason for the differences in the response reduction of various tank shapes.

Percentage reduction in response at top story
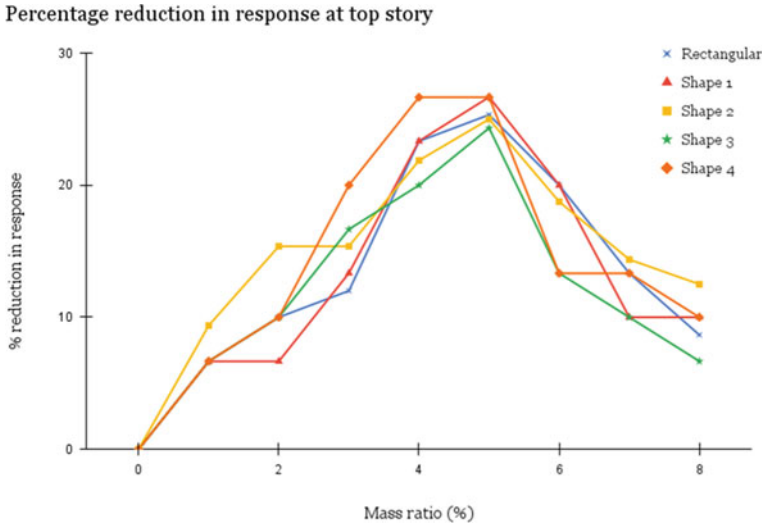
Fig. 6 Comparison of percentage reduction in acceleration of various shapes (top story)

Percentage reduction in response at bottom story
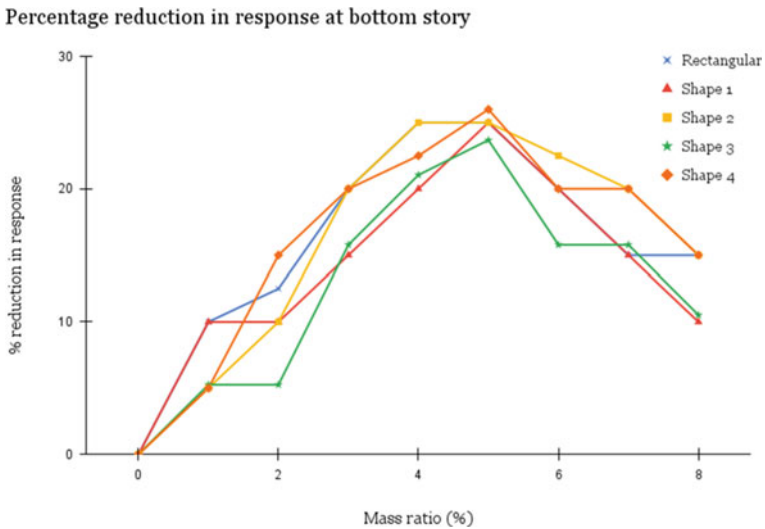
Fig. 7 Comparison of percentage reduction in acceleration of various shapes (bottom story)

5 Conclusion

The numerical and experimental analysis of scaled down structure subjected to both harmonic and recorded ground motions shows that a properly designed TLD can substantially reduce structural response.

- The performance of the TLD is observed to be effective in reducing the response of the structure when the excitation frequency ratio is near to unity, the resonant frequency.
- The response reduction is different when the tank shapes are different. This may be due to the difference in the sloshing behavior of the liquid in the tanks due to the tank shape.
- The responses predicted by SAP models were close to the experimental results.
- Sloped bottom tank was found to be more effective among the shapes evaluated as evidenced from literature [11] compared to rectangular tank.

TLDs with different tank shapes may be effectively implemented as a damping mechanism through further research. Investigations using real-time models may be conducted for determining the applicability of the findings.

References

1. Bhattacharjee E, Halder L, Sharma RP (2013) An experimental study on tuned liquid damper for mitigation of structural response. Int J Adv Struct Eng 5:3. https://doi.org/10.1186/2008-6695-5-3
2. Kareem A, Kijewski T, Tamura Y (1999) Mitigation of motions of tall buildings with specific examples of recent applications. Wind Struct 2(3):201–251
3. Fujii K, Tamura Y, Sato T, Wakahar T (1990) Wind-induced vibration of tower and practical applications of tuned sloshing damper. J Wind Eng Ind Aerodyn 33(1–2):263–272. https://doi.org/10.1016/0167-6105(90)90042-B
4. Wakahara T, Ohyama T, Fujii K (1992) Suppression of wind-induced vibration of a tall building using Tuned Liquid Damper. J Wind Eng Indus Aerodyn 43(1–3):1895–1906. https://doi.org/10.1016/0167-6105(92)90610-M
5. Sun LM, Fujino Y, Pacheco BM, Chaiseri P (1992) Modelling of tuned liquid damper (TLD). J Wind Eng Indus Aerodyn 43(1–3):1883–1894. https://doi.org/10.1016/0167-6105(92)90609-E
6. Banerji P, Murudi M, Shah AH, Popplewell N (2000) Tuned liquid dampers for controlling earthquake response of structures. Earthquake Eng Struct Dyn 29(5):587–602
7. Biswal KC, Bhattacharyya SK, Sinha PK (2003) Free-vibration analysis of liquid-filled tank with baffles. J Sound Vib 259(1):177–192. https://doi.org/10.1006/jsvi.2002.5087
8. Shang CY, Zhao JC (2008) Periods and energy dissipations of a novel TLD rectangular tank with angle-adjustable baffles. J Shanghai Jiaotong Univ (Sci) 13:139–144. https://doi.org/10.1007/s12204-008-0139-z
9. Zahrai SM, Abbasi S, Samali B, Vrcelj Z (2012) Experimental investigation of utilizing TLD with baffles in a scaled down 5-story benchmark building. J Fluids Struct 28:194–210. https://doi.org/10.1016/j.jfluidstructs.2011.08.016
10. Kaneko S, Ishikawa M (1999) Modeling of tuned liquid damper with submerged nets. ASME J Press Vessel Technol 121(3):334–343. https://doi.org/10.1115/1.2883712
11. Gardarsson S, Yeh H, Reed D (2001) Behavior of sloped-bottom tuned liquid dampers. J Eng Mech 127(3). https://doi.org/10.1061/(ASCE)0733-9399(2001)127:3(266)
12. Ras A, Boumechra N (2016) Seismic energy dissipation study of linear fluid viscous dampers in steel structure design. Alex Eng J 55(3):2821–2832. https://doi.org/10.1016/j.aej.2016.07.012
13. Prasad MLV, Mazumder EA (2016) Use of viscous damper as an energy dissipative device in steel structures. Int J Mech Prod Eng

14. Agresta A, Cavalagli N, Biscarini C, Ubertini F (2021) Effect of bottom geometry on the natural sloshing motion of water inside tanks: an experimental analysis. Appl Sci 11(2):605. https://doi.org/10.3390/app11020605
15. Tait MJ, Deng X (2008) The performance of structure-tuned liquid damper systems with different tank geometries. Struct Control Health Monit. https://doi.org/10.1002/stc.286
16. IS 1893 Part 2 (2014) Criteria for earthquake resistant design of structures. Part 2 liquid retaining tanks

Durability of Steel-Polypropylene Hybrid Fiber Concrete

Hillol Chakravarty, Sanjeev Sinha, Vavitikalva Venkataramana, and Bimal Kumar

1 Introduction

Durability of cement concrete pavements are more as compared to bituminous pavements. However, microcracks are developed which reduces the flexural strength of concrete pavements. These microcracks results due to various reasons such as shrinkage or brittleness of concrete. Fibre reinforced concrete overcome lot of such drawbacks. The type and quantity of fibre used, dispersal, geometry, orientation of fibers etc. contribute to the quality of fibre reinforced concrete [1]. Various kinds of fibers are introduced as reinforcement for cement concrete which include carbon, glass, steel and plastics such as polypropylene.

Polypropylene fibers (PF) are plastic fibers obtained from polypropylene gas, and have gained appreciation in recent times due to its low cost, toughness and high shrinkage resistance [2–6]. It is observed that with the introduction of steel fibers (SF), tensile strength of cement concrete is improved by reducing the brittleness [1, 7]. Thus, the cracks arising from both shrinkage resistance and brittleness could be overcome by using composite of SF as well as PF. Researches have been carried out to develop such composite reinforcement of SF and PFs. In one study, 0.15% PF with SF was found as optimum value; smaller length fibers effectively improved the compressive as well as split tensile strength [4]. Similar results were also obtained

H. Chakravarty (✉) · S. Sinha
Department of Civil Engineering, National Institute of Technology Patna, Patna, Bihar 800005, India
e-mail: hillol.ce@nitp.ac.in

V. Venkataramana
Town Planning Secretary, Rayachoty Municipality, Kadapa District, Andhra Pradesh 516269, India

B. Kumar
Government Engineering College, Jamui, Bihar 811313, India

for tensile strength in a different study [8]. Durability was also enhanced by the combination of PF and SF. Chloride penetration was found to decrease with usage of SF and PF [9]. In case of water absorption test, it was found to increase with increase in PF in concrete [3].

Concrete for pavement have to withstand tensile load. It has been seen that although SF and PF reinforced concrete crack at same peak tensile load as that of plain concrete, such fibre reinforced concrete does not separate and can maintain load up to large deformations [10]. SF has been seen significant usage as reinforcement for construction of pavements. Standard procedure for usage of SF has been developed for India in form of IRC SP:46–2013 because of crack control and post cracking behaviours. Along with that, such SF reinforced concrete provides improved flexural toughness, impact resistance and flexural fatigue endurance [11]. Research on PF reinforced concrete for pavement construction shows that its usage is cost effective as well as corrosion resistant [12]. Literature depicts the potential of using such hybrid mix to enhance various properties of concrete. However, limited study was observed in literature regarding durability of such concrete. This research work is conducted to determine the influence of SF and PF hybrid. Thus, the objectives of this work could be summarised as under:

1. Preparation of hybrid fibre PQC by using varying percentages of SF and PF.
2. Determination of durability of such fibre reinforced PQC.
3. Prediction of optimal dosage of combination of SF and PF.

2 Methodology

Literature suggests that implementation of hybrid fibre reinforcement leads to enhanced performance of cement concrete. Amongst various kinds of fibers and their hybrid composition, SF and PF hybrid was found to reduce cracks considerably occurring due to shrinkage and brittleness of concrete. This study is an effort to determine optimized dosage of the hybrid of SF and PF leading to improvement of durability. Pavement quality concrete (PQC) was used in the study and the grade of concrete prepared was M-40. The fibers used in the study accounted for 1% by weight of concrete mix. Amongst the total fibre used, the combinations of fibers were 1% SF, 0.80% SF and 0.20% PF, 0.70% SF and 0.30% PF, 0.60% SF and 0.40% PF. Thereafter, standard codal provisions were used to determine the rapid chloride penetration test (RCPT), water permeability test and water absorption test were used to assess the durability. The RCPT test, water permeability test and water absorption test were performed according to ASTM C1202, ASTM C577-07 and ASTM C 1585–2004 respectively. The adopted methodology for the study is presented in Fig. 1:
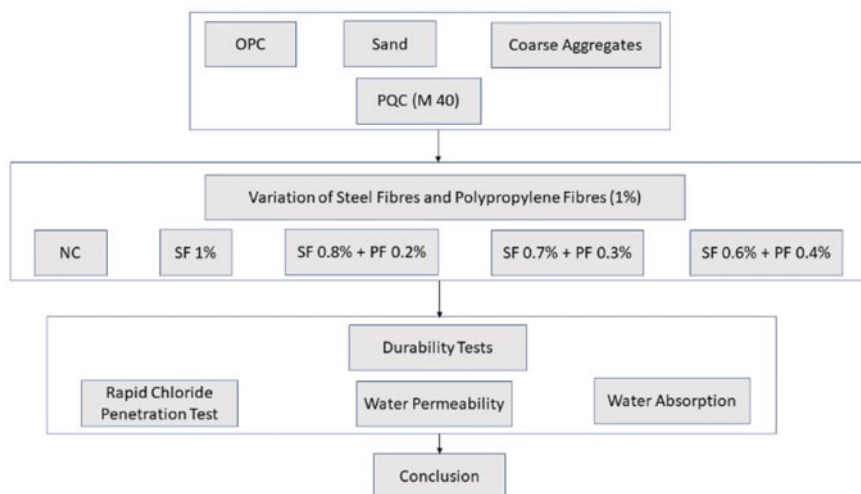
Fig. 1 Methodology for the research work

3 Materials

Ordinary Portland Cement (OPC) was used in the study to prepare the PQC. The specific gravity of the cement was determined to be 3.11 and the consistency was found to be 30%. The initial and final setting time was 140 and 255 min respectively. Sand (fine aggregates) was obtained from Sone River, Bihar. The specific gravity of sand was found to be 2.57. Coarse aggregates were obtained from Mirza Chowki, Bihar and the specific gravity was determined to be 2.79. The corresponding water absorption was determined to be 1.89% and 0.54% for fine and coarse aggregates respectively. Hooked end straight SF was obtained from Stewols India Pvt Ltd whereas PF were provided by DD solutions, India. The properties of the steel and polypropylene fibers are enlisted below under in Table 1. Mix was designed for PQC of M 40 grade as per the guidelines of IS 10262, and the different proportions of ingredients are provided in Table 2.

Table 1 Properties of fibers

Type of fiber	Length (mm)	Diameter (mm)	Aspect ratio (l/d)
Polypropylene	36	0.066	545
Steel	60	0.075	80

Table 2 Mix proportion for M40 concrete

Materials	Cement	Fine aggregates	Coarse aggregates	Water	Super plasticizer
Kg/m^3	370	660	1309	148	2.22

4 Experimentation and Results

4.1 Rapid Chloride Penetration Test (RCPT)

The test was performed in accordance with ASTM C1202. It is one of widely used test to determine the durability of cement concrete. The principle behind this test is to identify the quantity of chloride ion penetrated within cement concrete. Electrical measurements are used for that purpose by the application of 60 V DC current for 6 h on cylindrical moulds of 50 mm height and 100 mm diameter. Higher measurement of current indicates higher chloride ion penetration and decreased workability.

As can be observed from Fig. 2, the RCPT values measured at 28th day varied with varying fibre combinations. The minimum RCPT results were obtained for the combination of 0.8% SF and 0.2% PF. The result indicates that out of the different combinations used, the above-mentioned combination resulted in maximum durability. It was also observed from the RCPT results that for all the combinations of fibre reinforcement, the durability was more than normal concrete. Conductivity is influenced by the presence of steel, and hence, presence of SF has a role in the RCPT results. The results obtained are similar to the observations recorded earlier [9]. The observations can be attributed to dense structure achieved by utilizing the above-mentioned combinations upon the combined application of SF and PF.
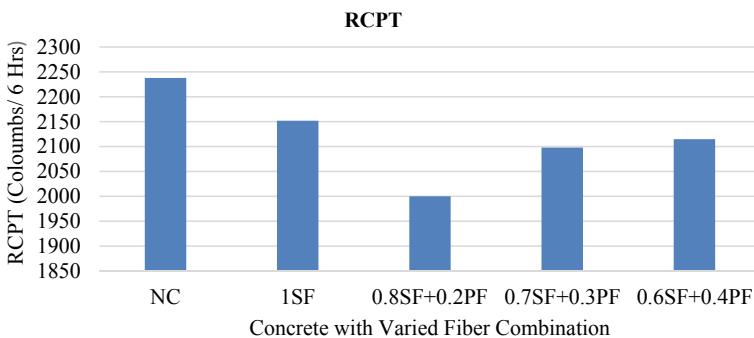
Fig. 2 RCPT Result Measured at 28th day
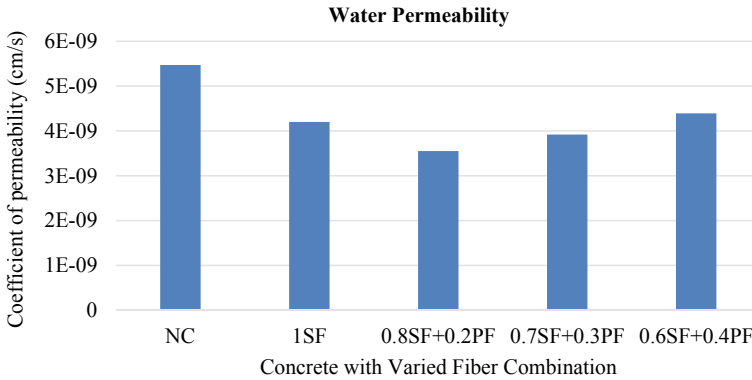
Fig. 3 Water permeability result measured at 28th day

4.2 Water Permeability Test

This test was performed in accordance with ASTM C577-07. The principle behind this test is to determine the amount of water percolated within the cement concrete under the application of pressure and identified as water permeability value.

Figure 3 indicates that permeability is most in case of normal concrete. 0.8% SF and 0.2% PF resulted in minimum value of permeability indicating increased durability. However, for all the combinations used, permeability was more than normal concrete. Although increase in PF initially resulted in more density within the matrix, however, further increase in PF increased the permeability. This can be attributed to the fibrous nature of PF which results in sufficient amount of air void within the concrete reinforcement matrix beyond a threshold application.

4.3 Water Absorption

This test is performed in accordance with ASTM C 1585–2004. It determines the amount of water ingress and absorbed within the cement concrete, and provides an estimation of the durability of cement concrete mix. The water absorption value is determined at 3 days and is reported as result.

The 3rd day water absorption was measured for all the combinations and is plotted in Fig. 4. Water absorption value was found to increase continuously for different combinations which are different from the observations in the earlier tests. However, the increase was minimal. The surface voids and anomalies imparted to the concrete due to fibre reinforcement may lead to increase in water absorption. Moreover, as percentage of fibrous PF increases, the surface porosity increases further leading to increased water absorption.
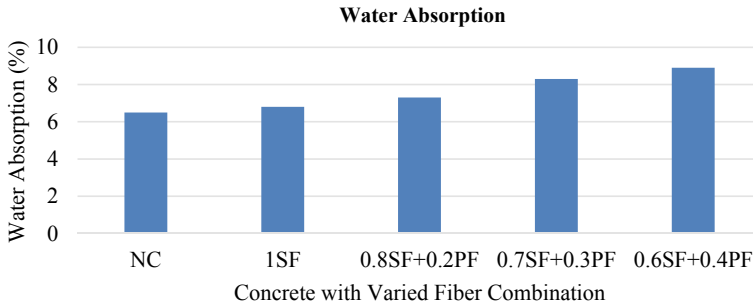
Water Absorption

Fig. 4 Water absorption result measured at 3rd day

5 Conclusion

This research was conducted to determine durability of fibre reinforced pavement quality concrete (PQC) of grade M40. For determining the durability, RCPT for 28th day aged concrete, water permeability for 28th day aged concrete and water absorption test at 3rd day aged concrete were conducted. The results obtained were inferred and conclusions are stated under:

- A total of 1% of both steel fibers (SF) and polypropylene fibers (PF) were used as reinforcement with varying combinations of SF and PF. These fibers were used as because literature suggests decrease in micro cracks which results due to shrinkage and brittleness.
- For both RCPT and water permeability, the combination of 0.8% SF and 0.2% PF yielded best results for durability amongst all the combinations used.
- With larger proportion of SF and small proportion of PF, the formation of micro-cracks is resisted. Thus, the durability of concrete increases initially. However, with increase in proportion of PF beyond a threshold limit, the porosity increases due to the fibrous nature of PF resulting in decrease in durability.
- The water absorption results observed at 3rd day continuously increased with increase in fibers content. This is due to the increased surface anomalies resulting from difficulty in providing proper surface finishes because of presence of fibers.
- The preliminary investigation indicates promising results. Further experiments with different grade of concrete, further variation in fibre reinforcement and micro study can be conducted to validate the experimental finding of the study for application purpose.

References

1. Alberti MG, Enfedaque A, Gálvez JC, Cánovas MF, Osorio IR (2014) Polyolefin fiberreinforced concrete enhanced with steel-hooked fibers in low proportions. Mater Des 60:57–65 (2014). https://doi.org/10.1016/j.matdes.2014.03.050

2. Hsie M, Tu C, Song PS (2008) Mechanical properties of polypropylene hybrid fiber reinforced concrete. Mater Sci Eng A 494(1–2):153–157. https://doi.org/10.1016/j.msea.2008.05.037

3. Söylev TA, Özturan T (2014) Durability, physical and mechanical properties of fiber reinforced concretes at low-volume fraction. Constr Build Mater 73:67–75. https://doi.org/10.1016/j.conbuildmat.2014.09.058

4. Qian CX, Stroeven P (2000) Development of hybrid polypropylene-steel fibre-reinforced concrete. Cem Concr Res 30(1):63–69. https://doi.org/10.1016/S0008.-8846(99)00202-1

5. Casanova M, Clauson C, Ebrahimpour A, Mashal M (2019) High-early strength concrete with polypropylene fibers as cost-effective alternative for field-cast connections of precast elements in accelerated bridge construction. J Mater Civ Eng 31(11):04019266. https://doi.org/10.1061/(asce)mt.1943-5533.0002927

6. Wang Y, Aslan F, Valizadeh A (2020) An investigation into the mechanical behaviour of fibre-reinforced geopolymer concrete incorporating NiTi shape memory alloy, steel and polypropylene fibers. Constr Build Mater 259:119765. https://doi.org/10.1016/j.conbuildmat.2020.119765

7. Afroughsabet V, Ozbakkaloglu T (2015) Mechanical and durability properties of high- strength concrete containing steel and polypropylene fibers. Constr Build Mater 94:73–82. https://doi.org/10.1016/j.conbuildmat.2015.06.051

8. Alwesabi EAH, Bakar BHA, Alshaikh IMH, Akil HM (2020) Experimental investigation on mechanical properties of plain and rubberised concretes with steel–polypropylene hybrid fibre. Constr Build Mater 233:117194. https://doi.org/10.1016/j.conbuildmat.2019.117194

9. Ramezanianpour AA, Esmaeili M, Ghahari SA, Najafi MH (2013) Laboratory study on the effect of polypropylene fiber on durability, and physical and mechanical characteristic of concrete for application in sleepers. Constr Build Mater 44:411–418. https://doi.org/10.1016/j.conbuildmat.2013.02.076

10. Rokade S, Pandey ND, Felix S (2014) Steel polypropylene fibre reinforced pavement quality concrete: a review. Int J Appl Eng Technol 4(4):72–78

11. Indian Road Congress (IRC) (2013) Guidelines for design and construction of fibre reinforced concrete pavements. IRC, New Delhi, India

12. Kanalli SA, Palankar R, Kumar B, Kumar P, Prakash SK (2014) Comparative study of polymer fibre reinforced concrete with conventional concrete pavement. Int J Res Eng Technol 03(01)

Uncertainty Quantification of Structures Using Belief Theory

Sushma H. Metagudda and A. S. Balu

1 Introduction

A component's or system's capability to accomplish critical duties for a specified period under specified operational conditions is defined as reliability [1]. Conventionally, reliability is determined by a probabilistic approach through failure data based on statistical methods [2]. But in real cases, physics of failure (PoF) methods are developed [3]. One disadvantage of the suggested PoF method is that it solely simulates aleatory uncertainty and ignores the impact of epistemic uncertainty. To contract with such limitations of PoF models, many reliability methods are proposed considering the effect of epistemic uncertainties; evidence theory, interval analysis theory [3], fuzzy set theory [4], and possibility theory [5] are some of the approaches that have been proposed. However, the first three theories have interval extension issues since component reliability is expressed in terms of intervals [3]. The possibility theory has unexpected results because it violates the duality axiom [3].

To address these flaws, [6] developed a new reliability matric called belief reliability, which satisfies four key axioms of uncertainty theory: normality, duality, subadditivity, and product axiom and addresses the interval extension problem. The combined contributions of design margin, aleatory uncertainty, and epistemic uncertainty are used to calculate belief reliability. Nevertheless, newly developed reliability matric cannot solve many real cases having both kinds of uncertainties, such as aleatory and epistemic uncertainties. As a result, [7] has improved belief reliability and presented a system reliability evaluation method known as chance theory,

S. H. Metagudda (✉) · A. S. Balu
Department of Civil Engineering, National Institute of Technology Karnataka, Suratkal, Karnataka 575025, India
e-mail: sushmahmetagudda.207cv012@nitk.edu.in

A. S. Balu
e-mail: asbalu@nitk.edu.in

253

which integrates probability and uncertainty theory. The reliability of system aleatory uncertainty is stated using probability theory, and epistemic uncertainty is formulated using uncertainty theory in this method. [8] To improve the effectiveness and efficiency of dealing with difficult systems, author has devised a decomposition method. The minimal cut set approach is used to determine a coherent system's belief reliability [9]. In this work, an overview of belief reliability is provided to quantify the system's uncertainty. Some essential formulas for dealing with uncertainty quantification utilizing the reliability index and belief reliability are discussed.

2 General Specifications

Some of the most often used non-probability matrices include evidence theory, interval analysis, fuzzy interval analysis, possibility theory, and uncertainty theory. An appropriate method for quantifying the influence of epistemic uncertainty should meet the duality axiom and adjust for conservatism. The former three ways provide intervals containing all possible values, and the latter two methods provide monotone measures. As a result, because it meets conservatism and duality, belief reliability utilizing uncertainty theory is considered a better matric than evidence theory, interval analysis, fuzzy theory, and possibility theory [4] (Table 1).

3 Uncertainty Theory

Portfolio selection [13], network science [14], option pricing [15], graph theory [16], and transportation [17] all use uncertainty theory, which was invented by [11] and improved by [12]. It is now used in a variety of fields, including portfolio selection [13], network science [14], option pricing [15], graph theory [16], and transportation [17]. Liu has defined reliability index and measure to evaluate system reliability index [5]. Necessary conditions for uncertainty distribution to explain uncertainty theory are presented in [9]. A quantitative measure to calculate the degree of uncertainty present in the system called entropy is defined by [6]. Uncertain random programming to handle uncertain random variables is presented in [9]. Redundant system reliability indexes have a lifetime of structure as uncertain variables are developed . Time-static and time-variant reliability indexes are established using uncertainty theory [18]. The chance theory has been utilized to derive dependability indexes when both uncertain and random variables are present [18]. An important reliability index is examined [7]. In this way, uncertainty theory is developed. Because it meets four fundamental axioms: normality, duality, subadditivity, and product axiom, uncertainty theory is an effective way for defining belief reliability.

Table 1 Comparison of reliability matrices

Non-probabilistic metrics	Reliability metric	Theory basis	Method to obtain metric	Existing problems
Metrics for PIB dependability	Evidence theory	Evidence theory	Belief and plausibility functions establish the lower and upper bounds of failure probability. Belief and plausibility functions establish the lower and upper bounds of failure probability	Metrics do not satisfy conservatism in evaluating component reliability and effectively do not consider the effect of epistemic uncertainty
	Interval analysis	Interval analysis	Range of input parameters is found by minimum and maximum failure probabilities through intervals	
	Fuzzy interval analysis	Fuzzy interval analysis	Monte Carlo simulation is used to determine the possible distribution of failure probabilities, while evidence theory is used to determine failure probability boundaries	
Monotone measure-based reliability matrices	Posbist reliability	Possibility theory	Products reliability is calculated by possibility measure	Do not satisfy duality axiom
	Belief reliability	Uncertainty theory	Design margin, aleatory uncertainty factor, and epistemic uncertainty factor are used to determine belief dependability	Research is immature

3.1 Theoretical Foundations of Uncertainty

Let τ be non-empty [8] set, £ be σ- algebra of τ and Λ be an event of £. Uncertainty theory is a branch of axiomatic mathematics concerned with the study of uncertainty. It assesses the level of belief in the occurrence of an event. Uncertainty measure, uncertainty variables, and uncertainty distribution are three important perquisites for uncertainty theory. As a result, the uncertain measure M is defined as a set of uncertainty functions defined over the interval [0, 1], complying with the following axioms:

Axiom 1 (Normality axiom). $M\{\tau\} = 1$ for universal set τ.

Axiom 2 (Duality axiom). $M\{\Lambda\} + M\{\Lambda^c\} = 1$ for any event Λ.

Axiom 3 (Subadditivity axiom). for any countable sequence of events $\Lambda_1, \Lambda_2, \ldots$.

$$M\left\{ \bigcup_{i=1}^{\infty} \Lambda_i \right\} \leq \sum_{i=1}^{\infty} M\{\Lambda_i\}$$

The triplet $(\tau, £, \Lambda)$ is referred to as uncertainty space. [7] has introduced the product axiom is the fourth axiom of uncertainty theory.

Axiom 4 (Product axiom). Let $(\tau_k, £_k, \Lambda_k)$ be uncertainty space; product measure is uncertain measure satisfying,

$$M = \left\{ \prod_{k=1}^{\infty} \Lambda_k \right\} = \bigwedge_{k=1}^{\infty} M_k = \{\Lambda_k\}$$

Here, Λ_k It is selected for arbitrarily events $k = 1, 2, \ldots n$.

4 Belief Reliability

Model-based reliability matrices that handle for both aleatory uncertainty and epistemic uncertainty are referred to as belief reliability. It is considered as an uncertain measure depending on uncertainty theory rather than probability measure [8].

4.1 Model-Based Reliability Methods

This section introduces [9] parameters related to model based reliability methods such as performance parameters and margin.

4.1.1 Performance Parameter

Failure of the system is defined when performance parameter (p) exceeds functional failure threshold (p_{th}). The system's applicable requirements are divided into three categories based on performance characteristics and available failure thresholds.

a. Smaller is better (STB) parameter: If the system fails when $p \geq p_{th}$, the STB parameter is p.
b. Larger the better (LTB) parameter: If the system fails when $p \leq p_{th,}$ the LTB parameter is p.
c. Nominal the better (NTB) parameter: If the system fails when $p \leq p_{th}$ or $p \geq p_{th,}$, NTB parameter is p.

4.1.2 Performance Margin

The performance margin (m) is a quantity that has no unit and is defined based on a deterministic model-based reliability model defined in terms of performance parameter (p) and functional threshold (p_{th}). Failure of the system is defined when $m \leq 0$.

$$m = \begin{cases} \frac{p_{th}-p}{p_{th}} & \text{if } p \text{ is STB} \\ \frac{p-p_{th}}{p_{th}} & \text{if } p \text{ is LTB} \\ \frac{p_{th}-p}{p_{th}} \text{ or } \frac{p-p_{th}}{p_{th}} & \text{if } p \text{ is NTB} \end{cases} \tag{1}$$

In model-based reliability methods, performance margin is initially based on the components' functional principles and failure mechanisms. Thus, it is evaluated by a deterministic model. While manufacturing products, values of input variables are affected by many uncertain vectors, so it is assumed that the vector of input variables is a random variable.

The structural system's performance margin is expressed in terms of

$$m = g_{m(X)} \tag{2}$$

The deterministic model used to determine the outperformance margin is denoted by $g\,m(.)$, and the vector of uncertain input variables is denoted by x.

Input variables differ from structure to structure, and depending on the parameters evaluated, variables can be random or indeterminate. To find out the reliability of random variables, probability mass function is defined in terms of probability measure R_p. Therefore, R_p is calculated using

$$R_p = \Pr\left(g_{m(X)} > 0\right) = \int \cdots \int_{g_{m(X)}>0} F_X(X) dx \tag{3}$$

4.2   Belief Reliability Definition

New reliability matrices called belief reliability are introduced by combining the contributions of design margin, irreducible uncertainty factor, and reducible uncertainty factor (Fig. 1).

4.2.1   Design Margin

When all of the input variables are set to their nominal values, the design margin describes the product's inherent reliability. It evaluates the distance between the center of the comparable performance margin distribution and the failure region's boundaries graphically, as shown in Fig. 2.

$$m_{\mathrm{d}} = g_{\mathrm{m}}(X_{\mathrm{N}}) \tag{4}$$

where X_{N} denotes nominal values of parameters.

4.2.2   Aleatory Uncertainty Factor (AUF)

AUF σ_{m} is defined based on design margin m_{d} and probabilistic reliability $Z_{R_{\mathrm{p}}}$, and it handles variations arrived from the parameters of components of the system
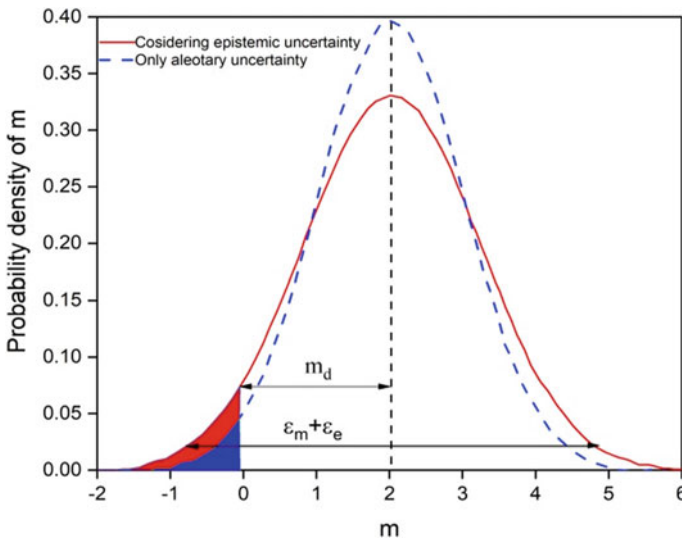
Fig. 1 Impact of epistemic uncertainty on the performance margin distribution
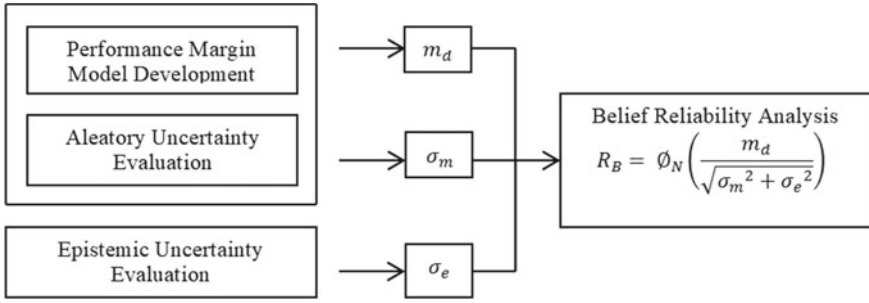
Fig. 2 Framework for evaluation of belief reliability

$$\sigma_{\mathrm{m}} = \frac{m_{\mathrm{d}}}{Z_{R_{\mathrm{p}}}} \tag{5}$$

where $Z_{R_{\mathrm{p}}}$ is calculated from inverse cumulative distribution at the value of R_p.

σ_{m} takes into account the uncertainty caused by product-to-product random fluctuations. Typically, engineering tasks such as tolerance design, environmental stress screening, and stochastic process control are used to control these random changes.

Let us present two adjustment variables, ε_{a} and ε_{e} to measure comparable performance margin to address the effect of both aleatory and epistemic uncertainties.

$$M_{\mathrm{E}} = m_{\mathrm{d}} + \varepsilon_{\mathrm{a}} + \varepsilon_{\mathrm{e}} \tag{6}$$

The amount of knowledge and information regarding system failure is directly proportional to the dispersion of uncertainty distribution.

4.2.3 Belief Reliability

Belief reliability is referred as the degree of belief that occurs, as measured by design margin, AUF, and EUF.

$$R_{\mathrm{B}} = \emptyset_{\mathrm{N}} \left(\frac{m_{\mathrm{d}}}{\sqrt{\sigma_{\mathrm{m}}^2 + \sigma_{\mathrm{e}}^2}} \right) \tag{7}$$

where $\emptyset_{\mathrm{N}}$ displays the standard normal variables' cumulative distribution.

Because $m_{\mathrm{d}} > 0$ and $\sigma_{\mathrm{e}} > 0$ are always true in practice, employing belief reliability instead of probabilistic reliability yields more conservative conclusions because belief reliability takes into account the influence of limited knowledge on reliability evaluations.

$$R_{\mathrm{B}} \leq R_{\mathrm{p}} \tag{8}$$

4.3 Evaluation of Belief Reliability

The framework for calculating system belief reliability is described. It entails calculating belief reliability by incorporating design margin, irreducible, and reducible uncertainty adjustment factors in Eq. (7).

4.3.1 Modeling of Performance Margins m_d

To obtain the value of the performance margin m, a deterministic performance margin model is constructed [10] and [11], which may be obtained by understanding the principles of function o the system and physics behind the failures of components of the system.

4.3.2 Aleatory Uncertainty Evaluation σ_m

First, m_d it is calculated according to Eq. (4), where the theoretical values of all the input variables are used. To evaluate the value of σ_m, we need to find the value of probabilistic reliability R_p. Using structural- reliability methods or Monte-Carlo simulation methods Rp is evaluated by incorporating aleatory uncertainty in model parameters according to Eq. (3). Then, the values of both R_p and m_d are included in Eq. (5) to get aleatory uncertainty factor σ_m.

4.3.3 Epistemic Uncertainty Evaluation σ_e

The epistemic uncertainty factor σ_e is derived by understanding the failure behavior of system components, which helps designers understand the system's potential failure behavior. The effectiveness of engineering-related activities is directly proportional to the state of knowledge required decreasing epistemic uncertainty and is named as y_i. Scores are given for each activity by experts on the basis of their performance criteria. Failure mode effect criticality analysis (FMECA), failure reporting analysis and corrective action system (FRACAS), reliability enhance test (RET), reliability growth test (RGT), and reliability simulation test (RST) are used to determine the failure process of elements, which are referred to as S_1, S_2…. S_n. According to FMECA, eight elements are considered, so effectiveness is defined as,

$$y_1 = \frac{1}{8} \sum_{i=1}^{8} S_i \tag{9}$$

Then, the state of knowledge regarding failure behavior is determined by using,

$$y = \sum_{i=1}^{8} \omega_i \, y_i \tag{10}$$

where ω_i is called the relative importance of respective engineering activities and $\sum_{i=1}^{n} \omega_i = 1$. Then, EUF σ_e is found out using a predefined function,

$$\sigma_e = h(y) \tag{11}$$

where σ_e determines of sharpness of epistemic uncertainty, y defines the state of knowledge, σ_e is inversely proportional to y, and $h(y)$ represents the complexity of products advised by experts,

$$h(y) = \begin{cases} \frac{1}{3\sqrt{y}} \cdot m_d & \text{for simple products} \\ \frac{1}{3y^6} \cdot m_d & \text{for complex products} \\ \frac{1}{3y^2} \cdot m_d & \text{for medium coplex products} \end{cases} \tag{12}$$

- For simple products belief reliability, i.e., R_B is a convex function, which says even for minor y, higher R_B is defined.
- For complex products belief reliability, i.e., R_B is concave function smaller, which says to define higher R_B sufficient knowledge regarding the failure behavior of the product should be collected.
- For medium complex products, R_B is defined in between concave and convex function (Fig. 3).

5 Conclusions

A new reliability metric termed belief reliability is devised to quantify the impact of epistemic uncertainty.

- The four key axioms of belief reliability are normality, duality, subadditivity, and the product axiom, which are all based on uncertainty theory.
- It incorporates design margin, aleatory uncertainty factor, and epistemic uncertainty factor contributions.
- It includes the impact of epistemic uncertainty on the effectiveness of engineering activities.
- When compared to typical probabilistic reliability matrices, belief reliability produces more conservative answers since it handles both aleatory uncertainty and epistemic.
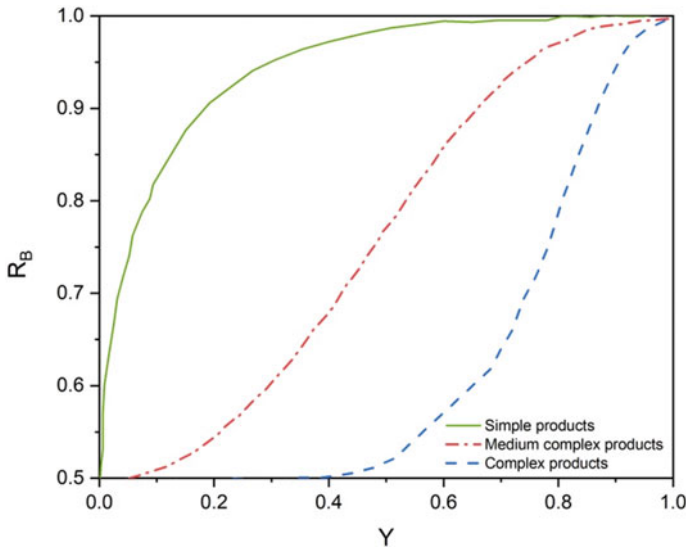
Fig. 3 Classification of R_B function based on the state of knowledge y

References

1. Zhang Q, Kang R, Wen M (2018) Belief reliability for uncertain random systems. IEEE Trans Fuzzy Syst 26:3605–3614. https://doi.org/10.1109/TFUZZ.2018.2838560
2. Der Kiureghian A (2007) Aleatory or epistemic? Does it matter?
3. Sheng Y, Ke H (2020) Reliability evaluation of uncertain k-out-of-n systems with multiple states. Reliab Eng Syst Saf 195:106696. https://doi.org/10.1016/j.ress.2019.106696
4. Kang R, Zhang Q, Zeng Z, Zio E, Li X (2016) Measuring reliability under epistemic uncertainty: review on non-probabilistic reliability metrics. Chin J Aeronaut 29:571–579. https://doi.org/10.1016/j.cja.2016.04.004
5. Wen M, Kang R (2016) Reliability analysis in uncertain random system. Fuzzy Optim Decis Mak 15:491–506. https://doi.org/10.1007/s10700-016-9235-y
6. Gao Y, Yang L, Li S, Kar S (2015) On distribution function of the diameter in uncertain graph. Inf Sci (Ny) 296:61–74. https://doi.org/10.1016/j.ins.2014.10.048
7. Barkana BD, Saricicek I, Yildirim B (2017) Performance analysis of descriptive statistical features in retinal vessel segmentation via fuzzy logic, ANN, SVM, and classifier fusion. Knowl-Based Syst 118:165–176. https://doi.org/10.1016/j.knosys.2016.11.022
8. Zeng Z, Kang R, Wen M, Zio E (2018) Uncertainty theory as a basis for belief reliability. Inf Sci (Ny) 429:26–36. https://doi.org/10.1016/j.ins.2017.10.050
9. Zeng Z, Kang R, Wen M, Zio E (2017) A model-based reliability metric considering aleatory and epistemic uncertainty. IEEE Access 5:15505–15515. https://doi.org/10.1109/ACCESS.2017.2733839
10. Zeng Z, Kang R, Chen Y (2016) Using PoF models to predict system reliability considering failure collaboration. Chin J Aeronaut 29:1294–1301. https://doi.org/10.1016/j.cja.2016.08.014
11. Zeng Z, Chen Y, Zio E, Kang R (2017) A compositional method to model dependent failure behavior based on PoF models. Chin J Aeronaut 30:1729–1739. https://doi.org/10.1016/j.cja.2017.05.009

12. Zeng Z, Kang R, Wen M, Zio E (2017) a model-based reliability metric considering aleatory and epistemic uncertainty. IEEE Access 5:15505-15515. https://doi.org/10.1109/ACCESS.2017.2733839
13. Bjerga T, Aven T, Zio E (2014) An illustration of the use of an approach for treating model uncertainties in risk assessment. Reliab Eng Syst Saf 125:46–53. https://doi.org/10.1016/j.ress.2014.01.014
14. Zhang B, Peng J, Li S (2015) Uncertain programming models for portfolio selection with uncertain returns. Int J Syst Sci 46(14):2510–2519. https://doi.org/10.1080/00207721.2013.871366
15. Han S, Peng Z, Wang S (2014) The maximum flow problem of uncertain network. Inf Sci 265:167–175. https://doi.org/10.1016/j.ins.2013.11.029
16. Gao Y, Yang L, Li S, Kar S (2015) On distribution function of the diameter in uncertain graph. Inf Sci 296:61–74. ISSN 0020-0255. https://doi.org/10.1016/j.ins.2014.10.048
17. Zhang Q, Xing H, Liu F, Ye J, Tang P (2014) Some new entropy measures for interval-valued intuitionistic fuzzy sets based on distances and their relationships with similarity and inclusion measures. Inf Sci 283:55–69. ISSN 0020-0255. https://doi.org/10.1016/j.ins.2014.06.012
18. Liu B (2010) Uncertain risk analysis and uncertain reliability analysis. J Uncertain Syst 4:163–170

Isogeometric Analysis of Composite Sandwich Plates Using Equilibrium-Based Stress Recovery Procedure

J. Chethan and G. S. Pavan

1 Introduction

Composite structures are formed by combining two or more different materials on a macroscopic scale. They are extensively adopted in aerospace, automobile, naval, space, civil, and many other engineering fields. Typically, the components of the composite materials at a microscopic level can be divided into 'fiber' and the 'matrix'. Fiber that serves as a reinforcement is embedded in a matrix, and later forms a composite material. Because of its excellent strength-to-weight ratio and rigidity, sandwich plates and composite plates are widely employed in a variety of sectors, and the ease with which the designers can tailor the required property as per the requirement. Among many failure modes of laminate, delamination is one of the most common types of failure. Prediction of delamination and other failure modes requires proper evaluation of the three-dimensional state of stress. Accordingly, many approaches have evolved based on equivalent single-layer theories (see, e.g., [1–5]) applied on different types of laminates such as functionally graded materials, composite sandwich plates, and composite laminates. It is found that equivalent single-layer theory is a better approach if the composite plates are serving as a secondary structural element. If there is a transition from secondary structural element to primary structural element, exact displacement and stresses have to be computed. In such cases, the level of accuracy offered by equivalent single-layer theory is not sufficient. It fails if the thickness is more and stress concentration or indentation occurs in a plate (see, e.g., [6]). Several theories have been presented to solve the

J. Chethan (✉) · G. S. Pavan
Department of Civil Engineering, National Institute of Technology Karnataka, Surathkal, Karnataka 575025, India
e-mail: chethanj.203st004@nitk.edu.in

G. S. Pavan
e-mail: pavan.gs@nitk.edu.in

shortcomings of equivalent single-layer theories. Layer-wise theories can be seen to compute stresses (see, e.g., [6–10]) with higher accuracy for composite laminated plates and sandwich plates. A new method of calculating the stresses that occur both in and out of plane is seen in [7].

Many developments have occurred in the framework of finite element method over the last decade. New numerical methods to solve boundary value problem have been proposed. Isogeometric analysis (IGA) proposed by Hughes et al. [11] is one among them. Isogeometric analysis primarily uses non-uniform rational B—splines (NURBS) functions. NURBS functions are a mainstream technology used by CAD systems. IGA adopts NURBS to approximate the geometry as well as the unknown field variable along with the concept of isoparametric philosophy. In comparison to the finite element method, properties of spline shape functions offer higher performance to carry out the numerical analysis. IGA has a substantial advantage over traditional numerical methods of analysis due to higher-order approximation, continuity, and simplified refinement technique.

In the previous ten years, isogeometric Galerkin formulation has been implemented over a diversified varieties of problems and is found to be very promising. IGA methods have already been adopted in problems with structure and solids [12–20], fluid mechanics [21–24], interaction of fluids and structures [22], and in medical field [25, 26].

After the successful application of isogeometric analysis, it led to the study of composite structures to compute the transverse displacement, stresses, buckling behavior, and dynamic behavior, etc., via various theories. (see, e.g., [27–31]). In a static analysis of the layer-wise approach, each interface is limited to C^0 continuity, and if a laminate seems to be a large layered structure, it entails a large number of degrees of freedom. Even this approach has high accuracy but is not completely satisfactory because of its expensive cost.

This research article discusses a two-step procedure for the static analysis of composite sandwich and laminated plates. The first step is the coarse evaluation of stresses by adopting a modified layer-wise approach (single-element approach), and the second step is associated with post-processing to recover accurate out-of-plane stresses using equilibrium equations (see, e.g., [32–35]). This procedure allows a considerable reduction in the number of degrees of freedom and hence the computation cost. Through the stress recovery procedure, it is possible to establish a precise three-dimensional stress state. The solution obtained through this technique is found to be close to the full layer-wise approach.

The following is the outline of the paper. Firstly, the adopted method of the isogeometric strategy is introduced briefly. Then, the background study of layer-wise theory and its modification adopted in this study is briefed. Later that explanation of the test case and the results obtained through coarse evaluation is discussed followed by reconstruction of transverse stresses by integrating the equations of equilibrium. Results and discussions are mentioned before drawing concluding remarks.

2 Standard IGA and Fundamentals

Isogeometric analysis is considered as cost-effective because there is no need to communicate with the CAD system again for successive refinements. IGA offers high precision since there is a new higher-order approach on the horizon by the adoption of K-refinement that outperforms classical P-refinement in terms of efficiency and robustness.

2.1 Fundamentals of B-Spline

B-spline functions of polynomial degree p are piecewise functions defined over the knot vector. In parametric space, a one-dimensional knot vector is explained as a non-decreasing set of coordinates.

$$\xi = \{\xi_1, \xi_2, \ldots, \xi_{n+p+1}\}$$

where $\xi_i \in R$ is the ith knot, i is the index, $i = 1, 2, \ldots, n + p + 1$.

ξ_i are referred to as knots. The value of knot can be recurrent at a specific point in the parametric space, and the knot multiplicity is the number of recurrent knot values at a specific knot. Generally, knot multiplicity can be represented as 'k'. An interval among two successive knots in the parametric space is expressed as a knot span that constructs an element in IGA.

The ordinate of ith B-spline basis function of polynomial degree p is expressed according to Cox—De—Boor formula and is shown below as

$$N_{i,p}(\xi) = \begin{cases} 1 \text{ if } \xi_i \leq \xi \leq \xi_{i+1} \\ 0 \text{ Otherwise} \end{cases} \tag{1}$$

$$N_{i,p}(\xi) = \frac{\xi - \xi_i}{\xi_{i+p} - \xi_i} N_{i,p-1}(\xi) + \frac{\xi_{i+p+1} - \xi}{\xi_{i+p+1} - \xi_{i+1}} N_{i+1,p-1}(\xi) \tag{2}$$

3 Background Study of Layer-wise Plate Theory

From the equilibrium of interlaminar forces, interlaminar stress present in the pth layer corresponds to interlaminar stress in the $(p + 1)$th layer. But, equivalent single-layer theory assumes displacement functions as continuous functions of thickness. Thus, in turn, results in continuous transverse strains, contrary to the equilibrium requirement. To overcome this drawback of equivalent single-layer theory, layer-wise theory assumes displacement fields to be C^0 continuous through the laminate

thickness, forcing strains to be discontinuous. This creates a possibility of transverse stresses to be continuous because the stress–strain matrix is different for each layer.

According to the equilibrium of interlaminar forces

$$
\left\{
\begin{array}{c}
\sigma_{xz} \\
\sigma_{yz} \\
\sigma_{zz}
\end{array}
\right\}^{(p)}
=
\left\{
\begin{array}{c}
\sigma_{xz} \\
\sigma_{yz} \\
\sigma_{zz}
\end{array}
\right\}^{(p+1)}
\tag{3}
$$

According to the assumption made in layer-wise theory, strains are found to be as

$$
\left\{
\begin{array}{c}
\gamma_{xz} \\
\gamma_{yz} \\
\varepsilon_{zz}
\end{array}
\right\}^{(p)}
\neq
\left\{
\begin{array}{c}
\gamma_{xz} \\
\gamma_{yz} \\
\varepsilon_{zz}
\end{array}
\right\}^{(p+1)}
\tag{4}
$$

3.1 Development of Layer-wise Plate Approach

In the layer-wise plate theory, the total displacement field expansion can be approximated as

$$
u(x, y, z, t) = \sum_{I=1}^{N}\left(\sum_{j=1}^{p} U_I^j(t)\psi_j(x, y)\right)\phi^I(z)
\tag{5}
$$

$$
v(x, y, z, t) = \sum_{I=1}^{N}\left(\sum_{j=1}^{p} V_I^j(t)\psi_j(x, y)\right)\phi^I(z)
\tag{6}
$$

$$
w(x, y, z, t) = \sum_{I=1}^{M}\left(\sum_{j=1}^{q} W_I^j(t)\varphi_j(x, y)\right)\Psi^I(z)
\tag{7}
$$

where (U_I^j, V_I^j, W_I^j) are the displacement values at Ith plane (transverse node), jth node. ϕ^I, Ψ^I are the global interpolation functions for in-plane displacement through-thickness. N, M are the number of nodes along with the depth. p, q are the number of in-plane nodes. ψ_j, φ_j are two-dimensional interpolation functions (Fig. 1).

Fig. 1 Shape functions and quadrature points in the layer-wise analysis
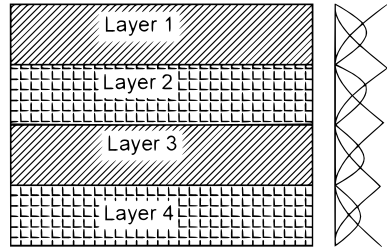
4 Single-Element Approach

In the layer-wise approach, C^0 continuity is established between the layers, and C^{-1} continuity is established at the boundaries. In this modified method of analysis, the plate is modeled as a single element across the depth. This approach helps in strongly reducing the degrees of freedom compared to the traditional layer-wise approach. Since layers must be accounted for, a unique integration rule is used, considering q-point Gauss rule on every layer. This method prior does not yield sufficiently desirable results in terms of stresses through the transverse direction, and hence, to improve the solution, it might easily be combined with a post-processor to the greater range.

The shape functions used for in-plane are the same when compared to the layer-wise theory of analysis (Fig. 2).

The same formulations mentioned in Eqs. (5)–(7) are used for the single-element approach by considering only two transverse nodes (layers, i.e., through the thickness, the top and bottom layers create a single entity.), and then, the stiffness matrix 'K' is evaluated.

Fig. 2 Shape functions and quadrature points in the single-element approach
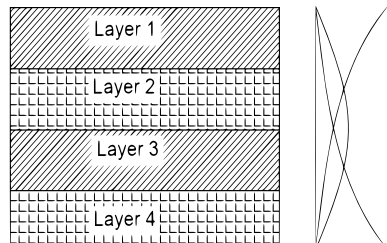
4.1 Evaluation of **k-*matrix***

K-matrix for a single-layer element is evaluated using total layer-wise displacement field expansion mentioned in Eqs. (5)–(7). An in-plane and out-of-plane shape functions of a certain degree ($p \geq 1$) are defined. K-matrix is evaluated by considering only two layers along with the thickness of the plate.

Layer-wise displacement field expansions (Eqs. (5)–(7)) are written as

$$\left\{ \begin{array}{c} u \\ v \\ w \end{array} \right\} = [N]\{d\} \tag{8}$$

where $[N]$ is defined as 'shape function matrix' which contains in-plane and out-of-plane shape functions and $\{d\}$ is defined as a 'displacement matrix'.

Equation (8) is expanded in the strain equations, and then, strains are expressed (see Eq. (9)).

$$\varepsilon = [B]\{d\} \tag{9}$$

where $[B]$ is defined as a 'strain–displacement matrix'.

The final K-matrix is obtained by using the below expression.

$$[k] = \int \int [B]^T [D][B] h |J| \mathrm{d}s \, dt \tag{10}$$

where $[D]$ is defined as a 'material coefficient matrix', h is referred to as the 'thickness of plate'. Once K-matrix is obtained, displacement, strains, and all six stress components are obtained.

5   Equilibrium-Based Stress Recovery

Among six components of stresses, the in-plane stresses are found to be more accurate. Out-of-plane stresses are inaccurate. Since interlaminar delamination is dependent upon out-of-plane components, it is better to evaluate the proper 3d state of stress. Any prediction and assessment of damage to the composite sandwich plate necessitates a precise assessment of the 3d state of stress. To improve the accuracy of the out-of-plane stresses, a new method of approach is adopted using the stress equilibrium equations [35, 36].

In a state of equilibrium,

$$\nabla.\sigma = b \tag{11}$$

where ∇ is a 'divergence operator'. From Eq. (14), out-of-lane stresses are recovered by using below expression.

$$\sigma_{i3}(X_1, X_2, X_3)$$
$$= -\int_{\overline{X_3}}^{X3} \left(\sigma_{i1,1}(X_1, X_2, \zeta) + \sigma_{i2,2}(X_1, X_2, \zeta) - b_i(X_1, X_2, \zeta)\right)$$
$$\mathrm{d}\zeta + \sigma_{i3}\left(X_1, X_2, \overline{X_3}\right) \tag{12}$$

where $\overline{X_3}$ is taken at the boundaries to fulfill the boundary conditions.

6 Numerical Test Result

The numerical test case consists of composite sandwich plate subjecting to UDL and SSL with various boundary edge conditions. The core of the composite sandwich plate is said to be transversely isotropic, and the face sheets are considered to be orthotropic. A MATLAB code is developed for the bending of sandwich plate based on first-order shear deformation theory using NURBS-based IGA.

The material properties of core are as follows:

$$E_1 = E_2 = 0.04 \times 10^6 \text{ psi}, G_{13} = G_{23} = 0.06 \times 10^6 \text{ psi},$$
$$G_{12} = 0.016 \times 10^6 \text{ psi}, \vartheta_{12} = 0.25 \tag{13}$$

The material properties of face sheets are as follows:

$$E_1 = 25E_2, E_2 = 10^6 \text{ psi}, G_{12} = G_{13} = 0.5$$
$$E_2, G_{23} = 0.5E_2, \vartheta_{12} = 0.25 \tag{14}$$

The results obtained for simply supported boundary condition subjected to sinusoidal load are shown in Table 1.

The displacement and stress contours are plotted for the present study as shown in Fig. 3

The current study's findings, i.e., central transverse displacement $\overline{w}$, in-plane stresses $\overline{\sigma_{xx}}$, $\overline{\sigma_{yy}}$, $\overline{\sigma_{xy}}$, and out-of-plane stresses $\overline{\sigma_{xz}}$, $\overline{\sigma_{yz}}$ are compared with the previous literature [6] and are found to be in good agreement. From Table 1, it can be observed that the central transverse displacement, stresses $\overline{\sigma_{yy}}, \overline{\sigma_{xy}}, \overline{\sigma_{yz}}$ of the sandwich plate reduces as the thickness of the sandwich plate decreases, whereas stresses $\overline{\sigma_{xx}}$ and $\overline{\sigma_{xz}}$ increase. In-plane stresses $\overline{\sigma_{xx}}$ and $\overline{\sigma_{yy}}$ are found to be maximum at the center of the plate; $\overline{\sigma_{xy}}$ is maximum at the corners of the plate, whereas the out-of-plane stresses are maximum at the opposite edges of the plate. Similarly, the

Table 1 Simply supported sandwich plate subjected to transverse load which is sinusoidally distributed

	$\overline{w}$	$\overline{\sigma_{xx}}$	$\overline{\sigma_{yy}}$	$\overline{\sigma_{xy}}$	$\overline{\sigma_{xz}}$	$\overline{\sigma_{yz}}$
Reddy [6]	4.7663	0.8856	0.1551	0.0901	0.1221	0.0534
Present	4.766	0.8926	0.1564	0.0908	0.123	0.0538
Reddy [6]	1.5603	1.0384	0.0792	0.0548	0.1365	0.0278
Present	1.5604	1.0466	0.0798	0.0552	0.1376	0.0296
Reddy [6]	1.0523	1.0755	0.0608	0.0462	0.1399	0.0233
Present	1.0524	1.0839	0.0613	0.0466	0.1416	0.0241
Reddy [6]	0.8851	1.0887	0.0542	0.0432	0.1412	0.0161
Present	0.8852	1.0973	0.0546	0.0435	0.1555	0.0343

$h_1 = h_3 = 0.1$ h, $h_2 = 0.8$ h $a/h = 4, 10, 20, 100$
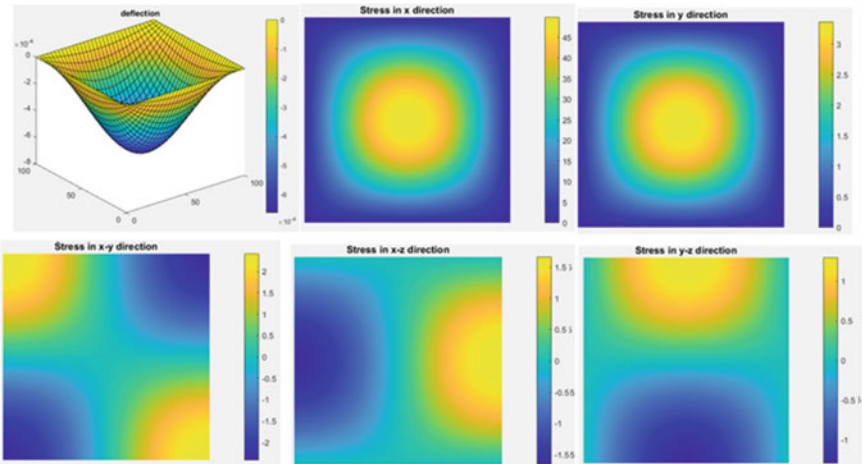
Fig. 3 Transverse displacement and stress components for a composite sandwich plate of $a/h = 10$ subjected sinusoidal load with simply supported boundary condition

same pattern of stresses and central transverse displacement is also observed for uniformly distributed loading condition.

7 Conclusions

- In this study, the authors have explored a modified layer-wise approach for the static flexural analysis of composite sandwich plate.

- The theoretical framework of the modified layer-wise approach and post-computation of transverse normal, shear stresses for composite sandwich plates is presented in this study.
- Preliminary results obtained for composite sandwich plates using FSDT ESL theory are presented in this work.
- The future scope of work includes the implementation of the proposed approach and validation of the same.
- The proposed approach is cost-effective since it reduces the number of degrees of freedom to a greater extent by adopting the single-element approach, and thus, computational costs for the evaluation of three-dimensional stresses are reduced.
- This strategy is simple to implement. Indeed, post-processing is based solely on the integration of equilibrium equations, and all essential components can be easily determined from the displacement solution.

References

1. Byun C, Kapania RK (1992) Prediction of interlaminar stresses in laminated plates using globalorthogonal interpolation polynomials. AIAA J 30:2740–2749. https://doi.org/10.2514/3.11293
2. Rolfes R, Rohwer K (1997) Improved transverse shear stresses in composite finite elements based on first order shear deformation theory. Int J Numer Methods Eng 40:51–60. https://doi.org/10.1002/(SICI)1097-0207(19970115)40:1%3c51::AID-NME49%3e3.0.CO;2-3
3. Malik M, Noor AK (2000) Accurate determination of transverse normal stresses in hybrid laminated panels subjected to electro-thermo-mechanical loadings. Int J Numer Methods Eng 47:477–495. https://doi.org/10.1002/(SICI)1097-0207(20000110/30)47:1/3%3c477::AID-NME780%3e3.0.CO;2-M
4. Auricchio F, Sacco E (2003) Refined first-order shear deformation theory models for composite laminates. J Appl Mech Trans ASME 70:381–390. https://doi.org/10.1115/1.1572901
5. Nguyen TK, Sab K, Bonnet G (2008) First-order shear deformation plate models for functionally graded materials. Compos Struct 83:25–36. https://doi.org/10.1016/j.compstruct.2007.03.004
6. Reddy JN (1993) An evaluation of equivalent-single-layer and layerwise theories of composite laminates. Compos Struct 25:21–35. https://doi.org/10.1016/0263-8223(93)90147-I
7. Carrera E (1998) Evaluation of layerwise mixed theories for laminated plates analysis. AIAA J 36:830–839. https://doi.org/10.2514/2.444
8. Roque CMC, Ferreira AJM, Jorge RMN (2005) Modelling of composite and sandwich plates by a trigonometric layerwise deformation theory and radial basis functions. Compos Part B Eng 36:559–572. https://doi.org/10.1016/j.compositesb.2005.05.003
9. Maturi DA, Ferreira AJM, Zenkour AM, Mashat DS (2014) Analysis of sandwich plates with a new layerwise formulation. Compos Part B Eng 56:484–489. https://doi.org/10.1016/j.compositesb.2013.08.086
10. Thai CH, Ferreira AJM, Abdel Wahab M, Nguyen-Xuan H (2016) A generalized layerwise higher-order shear deformation theory for laminated composite and sandwich plates based on isogeometric analysis. Acta Mech 227:1225–1250. https://doi.org/10.1007/s00707-015-1547-4
11. Hughes TJR, Cottrell JA, Bazilevs Y (2005) Isogeometric analysis: CAD, finite elements, NURBS, exact geometry and mesh refinement. Comput Methods Appl Mech Eng 194:4135–4195. https://doi.org/10.1016/j.cma.2004.10.008

12. Cottrell JA, Hughes TJR, Reali A (2007) Studies of refinement and continuity in isogeometric structural analysis. Comput Methods Appl Mech Eng 196:4160–4183. https://doi.org/10.1016/j.cma.2007.04.007

13. Elguedj T, Bazilevs Y, Calo VM, Hughes TJR (2008) over(B, -) and over(F, -) projection methods for nearly incompressible linear and non-linear elasticity and plasticity using higher-order NURBS elements. Comput Methods Appl Mech Eng 197:2732–2762. https://doi.org/10.1016/j.cma.2008.01.012

14. Lipton S, Evans JA, Bazilevs Y, Elguedj T, Hughes TJR (2010) Robustness of isogeometric structural discretizations under severe mesh distortion. Comput Methods Appl Mech Eng 199:357–373. https://doi.org/10.1016/j.cma.2009.01.022

15. Hughes TJR, Evans JA, Reali A (2014) Finite element and NURBS approximations of eigenvalue, boundary-value, and initial-value problems. Comput Methods Appl Mech Eng 272:290–320. https://doi.org/10.1016/j.cma.2013.11.012

16. Morganti S, Auricchio F, Benson DJ, Gambarin FI, Hartmann S, Hughes TJR et al (2015) Patient-specific isogeometric structural analysis of aortic valve closure. Comput Methods Appl Mech Eng 284:508–520. https://doi.org/10.1016/j.cma.2014.10.010

17. Caseiro JF, Valente RAF, Reali A, Kiendl J, Auricchio F, Alves De Sousa RJ (2014) On the assumed natural strain method to alleviate locking in solid-shell NURBS-based finite elements. Comput Mech 53:1341–53. https://doi.org/10.1007/s00466-014-0978-4

18. Reali A (2006) Of structural vibrations10:1–30

19. De Falco C, Reali A, Vázquez R (2011) GeoPDEs: a research tool for isogeometric analysis of PDEs. Adv Eng Softw 42:1020–1034. https://doi.org/10.1016/j.advengsoft.2011.06.010

20. Cottrell JA, Reali A, Bazilevs Y, Hughes TJR (2006) Isogeometric analysis of structural vibrations. Comput Methods Appl Mech Eng 195:5257–5296. https://doi.org/10.1016/j.cma.2005.09.027

21. Bazilevs Y, Hughes TJR (2008) NURBS-based isogeometric analysis for the computation of flows about rotating components. Comput Mech 43:143–150. https://doi.org/10.1007/s00466-008-0277-z

22. Bazilevs Y, Hsu M, Kiendl J, Wüchner R, Bletzinger K (2011) 3D simulation of wind turbine rotors at full scale. Part II: fluid—structure interaction modeling with composite blades. Int J Numer Methods Fluids 65:236–53. https://doi.org/10.1002/fld

23. Liu J, Gomez H, Evans JA, Hughes TJR, Landis CM (2013) Functional entropy variables: a new methodology for deriving thermodynamically consistent algorithms for complex fluids, with particular reference to the isothermal Navier-Stokes-Korteweg equations. J Comput Phys 248:47–86. https://doi.org/10.1016/j.jcp.2013.04.005

24. Akkerman I, Bazilevs Y, Calo VM, Hughes TJR, Hulshoff S (2008) The role of continuity in residual-based variational multiscale modeling of turbulence. Comput Mech 41:371–378. https://doi.org/10.1007/s00466-007-0193-7

25. Hsu MC, Kamensky D, Xu F, Kiendl J, Wang C, Wu MCH et al (2015) Dynamic and fluid–structure interaction simulations of bioprosthetic heart valves using parametric design with T-splines and Fung-type material models. Comput Mech 55:1211–1225. https://doi.org/10.1007/s00466-015-1166-x

26. Zhang Y, Bazilevs Y, Goswami S, Bajaj CL, Hughes TJR (2007) Patient-specific vascular NURBS modeling for isogeometric analysis of blood flow. Comput Methods Appl Mech Eng 196:2943–2959. https://doi.org/10.1016/j.cma.2007.02.009

27. Pavan GS, Nanjunda Rao KS (2017) Bending analysis of laminated composite plates using isogeometric collocation method. Compos Struct 176:715–728. https://doi.org/10.1016/j.compstruct.2017.04.073

28. Maurin F, Greco F, Coox L, Vandepitte D, Desmet W (2018) Isogeometric collocation for Kirchhoff-Love plates and shells. Comput Methods Appl Mech Eng 329:396–420. https://doi.org/10.1016/j.cma.2017.10.007

29. Tran LV, Kim SE (2018) Static and free vibration analyses of multilayered plates by a higher-order shear and normal deformation theory and isogeometric analysis. Thin-Walled Struct 130:622–640. https://doi.org/10.1016/j.tws.2018.06.013

30. Farzam A, Hassani B (2019) Isogeometric analysis of in-plane functionally graded porous microplates using modified couple stress theory. Aerosp Sci Technol 91:508–524. https://doi.org/10.1016/j.ast.2019.05.012

31. Auad SP, Praciano JSC, Barroso ES, Sousa JBM, Parente JE (2019) Isogeometric analysis of FGM plates. Mater Today Proc 8:738–746. https://doi.org/10.1016/j.matpr.2019.02.015

32. Dufour JE, Antolin P, Sangalli G, Auricchio F, Reali A (2018) A cost-effective isogeometric approach for composite plates based on a stress recovery procedure. Compos Part B Eng 138:12–18. https://doi.org/10.1016/j.compositesb.2017.11.026

33. Chiappa A, Groth C, Reali A, Biancolini ME (2020) A stress recovery procedure for laminated composite plates based on strong-form equilibrium enforced via the RBF Kansa method. Compos Struct 244:112292. https://doi.org/10.1016/j.compstruct.2020.112292

34. Patton A, Antolín P, Kiendl J, Reali A (2021) Efficient equilibrium-based stress recovery for isogeometric laminated curved structures. Compos Struct 272. https://doi.org/10.1016/j.compstruct.2021.113975

35. Patton A, Antolín P, Dufour JE, Kiendl J, Reali A (2021) Accurate equilibrium-based interlaminar stress recovery for isogeometric laminated composite Kirchhoff plates. Compos Struct 256:112976. https://doi.org/10.1016/j.compstruct.2020.112976

36. Patton A, Dufour JE, Antolin P, Reali A (2019) Fast and accurate elastic analysis of laminated composite plates via isogeometric collocation and an equilibrium-based stress recovery approach. Compos Struct 225:111026. https://doi.org/10.1016/j.compstruct.2019.111026

Experimental Investigations on the Uniaxial Tensile Behaviour of Carbon Textile Reinforced Geopolymer Mortar

Anjana Elsa Alexander and A. P. Shashikala

1   Introduction

Rehabilitation and retrofitting of existing structures with externally bonded fibre reinforced polymer (FRP) systems have been extensively studied in the past few decades. But the epoxy resin used in such systems is prone to degradation when subjected to high moisture, temperatures above glass transition temperature, and fire, resulting in debonding of FRP from the concrete substrate [1–3]. Hence, researchers proposed replacing the epoxy resin in FRP with an inorganic matrix like cement mortar, leading to the development of textile reinforced mortar (TRM)/concrete (TRC). But unlike polymeric matrices that present an elastic behaviour up to failure, inorganic matrices crack much before the maximum strain in textile is reached. So, proper selection of an inorganic matrix is also essential in TRM. Textile reinforced mortar is a composite material that consists of an inorganic matrix reinforced with high-strength continuous textile fabrics. These fabrics are multifilament yarns made of natural fibres such as sisal, hemp, flax, or artificial fibres such as carbon, alkali-resistant glass, aramid, basalt, PBO, and steel that are woven, non-woven, or knitted [4, 5]. Among these fibres, carbon fibre has been found to have higher modulus of elasticity, tensile strength, and resistance against chemical actions [6]. Some of the benefits of employing TRM/ TRC include increased tensile strength, pseudo-ductile behaviour, resistance to corrosion, components built with less material, longer service life, and the potential to extend the life of existing structures [5]. But its applications are limited as improved knowledge about TRMs efficiency still needs to be gained.

In this paper, the uniaxial tensile behaviour of carbon textile reinforced geopolymer mortar (CTRGM) coupon specimens is investigated experimentally. The

A. E. Alexander (✉) · A. P. Shashikala
Department of Civil Engineering, National Institute of Technology Calicut, Kozhikode, Kerala 673601, India
e-mail: anjanaelsaalexander@gmail.com

277

influence of variation in grid spacing of textile yarns and the number of textile layers on the tensile behaviour is also studied. Test procedures are done as per AC434 [7] and RILEM TC 232-TDT [8] recommendations.

2 Experimental Programme

2.1 Materials Used

For producing geopolymer mortar in CTRGM, the materials used were class F fly ash (FA), ground granulated blast-furnace slag (GGBS), fine aggregate, alkaline liquid (a blend of sodium hydroxide solution and sodium silicate solutions), and sulphonated naphthalene-based superplasticizer Conplast SP 430. The physical properties of materials used in the preparation of geopolymer mortar are given in Tables 1 and 2. The chemical composition of FA and GGBS is provided in Table 3. A trial-and-error procedure was adopted for mix proportioning geopolymer mortar as there are no standard guidelines available. Based on that, geopolymer mortar having an average 28th day compressive strength of 60 MPa was selected for the study. The mix proportion adopted for making mortar specimens was binder (70% FA and 30% GGBS) to fine aggregate weight ratio 1:3, 10 M NaOH solution, Na_2SiO_3/ NaOH ratio 2, alkaline liquid to binder ratio 0.5, superplasticizer content 2%, and water to binder ratio 7%.

Carbon strands with 12 k filaments (Fig. 1) having the properties given in Table 4 were used to make carbon textile. To hold the filaments of carbon yarn together and make the bidirectional textile, an epoxy resin was used. The epoxy (CERA-EPSA) consists of a two-part system of base and hardener that was mixed in a proportion of 3:1 by weight. The compressive strength of epoxy resin used was obtained as 75 MPa. As per the manufacturer data, the epoxy has excellent water and alkali resistance.

Table 1 Physical properties of FA, GGBS, superplasticizer

Property	FA	GGBS	Superplasticizer
Source	Mettur thermal power station	Mangalore steel industries	Fosroc chemicals
Colour	Light grey	Off white	Brown
Specific gravity	2.3	2.9	1.2

Table 2 Properties of fine aggregate

Size	Passing 2.36 mm IS sieve
Specific gravity	2.65
Water absorption	1.21%
Fineness modulus	2.65

Table 3 Chemical composition

Compounds	FA	GGBS
SiO_2	59.20	32.81
Al_2O_3	30.13	17.06
Fe_2O_3	3.65	1.60
K_2O	1.02	0.20
CaO	0.96	37.63
MgO	0.86	7.71
P_2O_5	0.38	0.04
Na_2O	0.15	0.48
SO_3	0.14	0.2
Others	3.51	2.27

Fig. 1 Carbon yarn spool
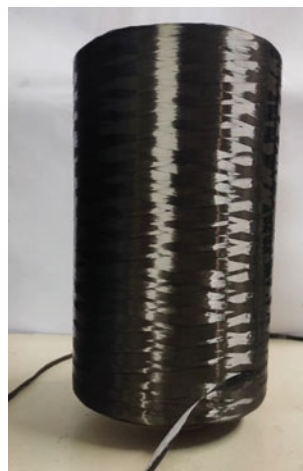
Table 4 Properties of carbon yarn (Formosa plastics)

Number of filaments	12,000
Filament diameter	7μ
Density	1.8 g/cm^3
Tensile strength of single filament	4900 MPa
Tensile modulus	250 GPa

For making the bidirectional textile, the required length of carbon yarn was cut from the spool, and a thin coat of the epoxy resin was applied over the surface of the carbon yarn. This was left for about 48 h for curing at room temperature. Then, these epoxy-coated carbon yarns were woven as bidirectional textile glued with epoxy resin to ensure sufficient bonding. Again, the textile was allowed to cure at room temperature for about 72 h. The process of making carbon textile is shown in Fig. 2.
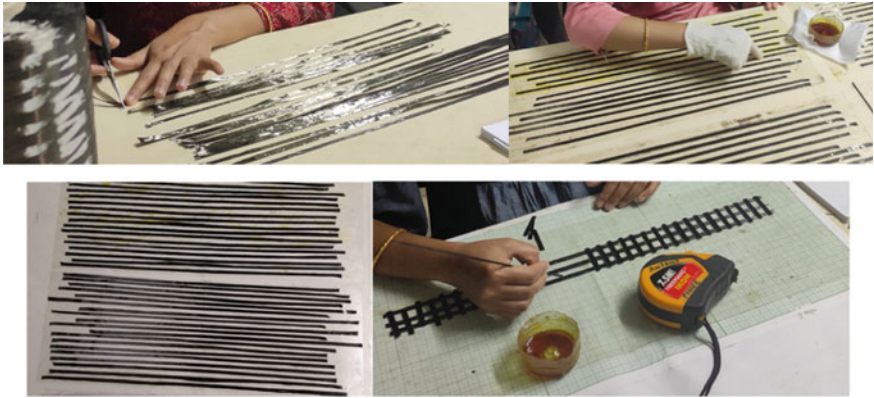
Fig. 2 Making of epoxy impregnated carbon textile

Yarns that run lengthwise (loading direction) are termed warp yarns, and that run at right angle to warp yarns is termed weft yarns.

Uniaxial tensile tests of epoxy impregnated carbon yarn Fig. 3a and carbon textile Fig. 3b were conducted to determine its tensile strength and tensile modulus as in Fig. 4. The tests were carried out using a displacement-controlled UTM with a stroke

(a)   (b)
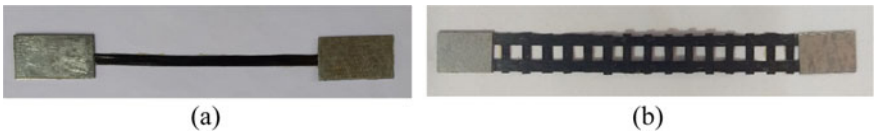
Fig. 3 Epoxy impregnated (**a**) carbon yarn and (**b**) carbon textile

Fig. 4 Tension test on
carbon yarn and textile
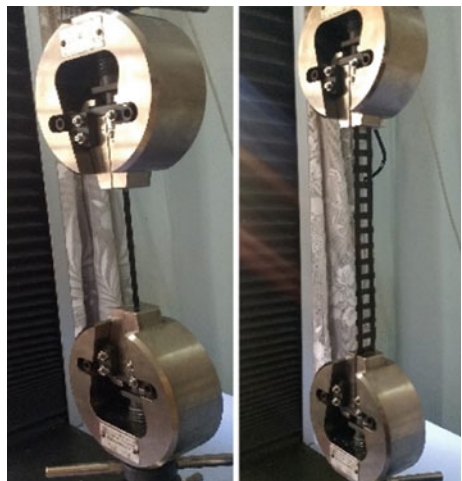
Table 5 Properties of epoxy impregnated carbon yarn and carbon textile

	Yarn	Textile
Number of warp yarn	1	2 (15 mm grid size)
Width	5 mm	10 mm
Thickness	0.1 mm	0.1 mm
Tensile strength	2978.45 MPa	2388.284 MPa
Tensile modulus	114.18 GPa	118.4 GPa

rate of 1 mm/min, according to ASTM D4018 [9]. To evenly disperse the load, end tabs were bonded to the specimens. Properties of epoxy-coated carbon yarn and textile obtained from test results are presented in Table 5.

Based on the experimental results, it was found that the carbon textiles tensile strength is less than the strength of a single yarn due to the unequal load distribution among the warp yarns. This causes some filaments to break before achieving their full efficiency. As a result, the tensile strength of the filament cannot be utilised to represent the strength of the composite. Figure 5 shows the tensile stress–strain behaviour of epoxy impregnated carbon yarn and carbon textile consisting of 12 k filaments. It can be seen that carbon yarn and textile show pseudo-ductile behaviour.
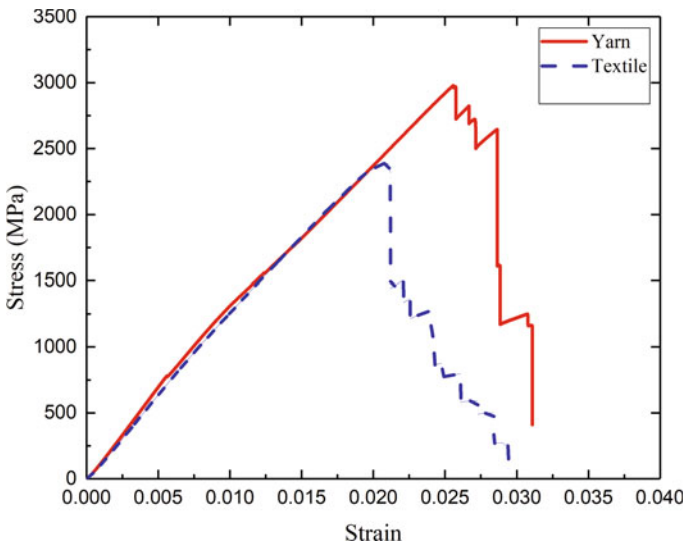
Fig. 5 Stress–strain curve of carbon yarn and textile

2.2   Test Specimens

Rectangular coupon specimens having a length of 500 mm, width 40 mm, and thickness 10 mm were made and tested under uniaxial tensile loading as per AC434 [7] and RILEM TC 232-TDT recommendation [8]. Length of the coupon includes gripping distance and gauge length. Width of the coupon consists of a minimum number of strands and the width was limited to 40 mm in the study as per the testing conditions in the laboratory. Thickness of the coupon is a function of the thickness of the mortar matrix and the number of textile layers. To distribute the load uniformly and to avoid stress concentrations at specific points, steel tabs were glued with epoxy to the gripping areas (two at each end) of the coupons. The tabs had a length of 100 mm, width 40 mm (same as the coupon), and thickness 2 mm.

Geopolymer mortar was used for casting coupons. The composite was prepared by hand layup technique. First, a thin layer of geopolymer mortar was poured up to 5 mm from the bottom of the mould, and it was vibrated. Then, the carbon textile layer(s) (1, 2, 3, 4, 5) were carefully placed above the geopolymer mortar layer and pressed into the geopolymer mortar. Again, another layer of mortar was filled up to the top of the mould and vibrated to ensure adequate bonding to the mortar layers above and below the carbon textile(s), as shown in Fig. 6. All the specimens were demoulded after 24 h and cured for 28 days at ambient conditions.

Two sets of coupons were made to study the uniaxial tensile behaviour of carbon textile reinforced geopolymer mortar by varying.

(i)   The grid spacing of textile yarns and
(ii)   The number of textile layers.

2.2.1   Grid Spacing of Textile Yarns

The maximum grid spacing of carbon textile yarns was limited to 25 mm in the study as per AC 434 [7], and the minimum size was limited to 15 mm for proper bonding of mortar layers above and below the textile layer. Coupons having grid spacing of 25 mm (T25), 20 mm (T20), and 15 mm (T15), respectively, were used in this study. As the width of coupon specimens was limited to 40 mm, T25 coupon specimens consist of 2 warp yarns and 20 weft yarns, T20 specimens consist of 2 warp yarns
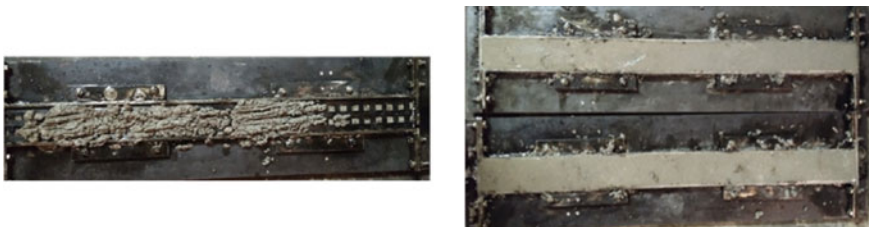
Fig. 6   Casting of TRGM tensile coupons

Fig. 7 Schematic sketch of carbon textile T15, T20, and T25
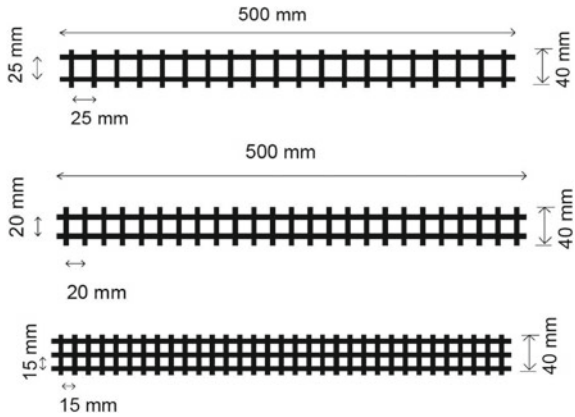
Fig. 8 Tensile coupons T15, T20, and T25
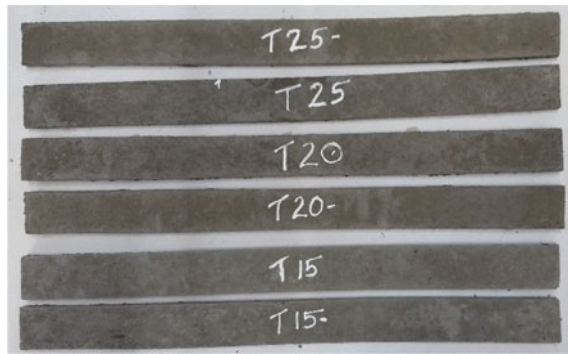
and 25 weft yarns, and T15 specimens consist of 3 warp yarns, and 33 weft yarns were used in the study as shown in Fig. 7. Figure 8 shows the tensile coupons cast.

2.2.2 Effect of Number of Textile Layers

To optimise the number of carbon textile layers, the optimum grid spacing obtained from the uniaxial tension test was used. The number of layers in coupons was varied from 1 to 5; accordingly, the coupons were designated as T1, T2, T3, T4, and T5. Figure 9 shows the carbon textile reinforcement used for the testing. However, the maximum number of textile layers was limited to four layers for a coupon thickness of 10 mm, as upon demoulding T5 specimens (five textile layers) showed severe debonding between mortar and carbon textile layers as shown in Fig. 10. So, T1, T2, T3, and T4 coupon specimens were used for the uniaxial tensile testing.

Fig. 9 Carbon textile
reinforcement T15
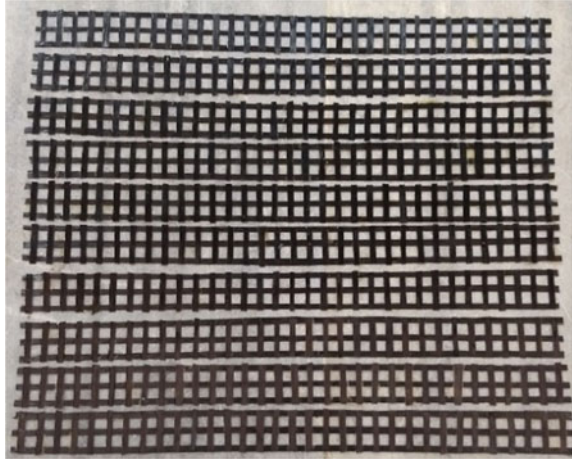
Fig. 10 Debonding of
mortar from carbon textile in
T5 specimen
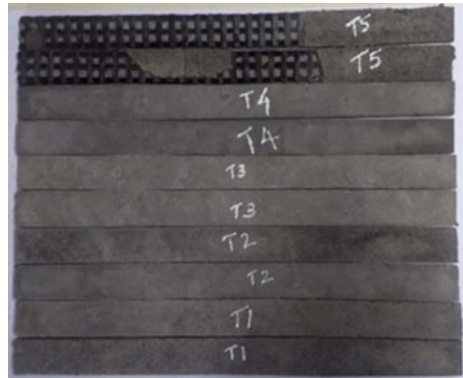
2.3 Test Set-Up and Procedure

The tests were carried out on digital universal testing equipment with 200 kN capacity
and at a loading rate of 1 kN/min, as in Fig. 11. The gripping method used for
load application is clamping grip [10]. The gauge length of coupon specimens was
300 mm. The load and corresponding displacement of the cross-heads were recorded
continuously from the machine dial. The tensile stress was calculated by dividing
the measured load by the coupon specimen's cross-sectional area (Ac). The strain
was obtained by dividing the displacement of the cross-head by the gauge length of
the specimen [7, 8].

Fig. 11 Test set-up
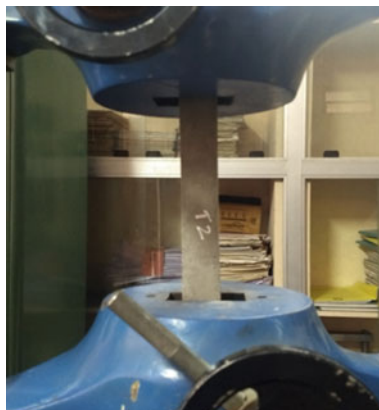
3 Results and Discussions

3.1 Failure Mode

Upon loading, tensile cracking of matrix was observed at regular spacing along the gauge length of the specimen. After the crack saturation was reached in the matrix, the crack widens, and the textile got elongated, and failure of specimen occurred by the rupture of the yarns in the textile, as shown in Fig. 12.

Fig. 12 Failure pattern of tensile coupons
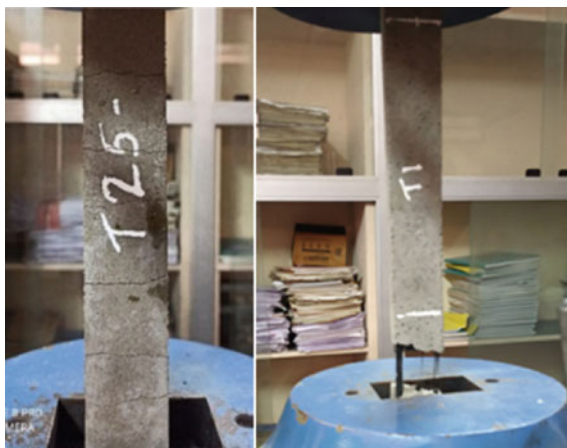
3.2 Load–Displacement Pattern

The load–displacement response (Figs. 13 and 14) is categorised by an initial linear behaviour that ended with the first matrix crack occurrence at the applied stress. The first matrix crack occurred when the tensile stress of mortar was reached, i.e. below a load of 300 N. As the cracks widen, the behaviour of the composite was mainly governed by the textile and was similar to the fibre bundle elastic modulus. Then, up to the ultimate tensile strength of its yarn, the textile reinforcement got strained. When the stress in the textile exceeded the strength of one or more warp yarns, tear in one or more yarns occurred. This can be seen by the sudden drop in load–deflection curve. The load was then redistributed to other yarns, and they continued to take up the load until its tensile strength was reached.

Table 6 shows the ultimate load and displacement values for the tensile coupons having grid spacing of 25 mm (T25), 20 mm (T20), and 15 mm (T15). It was observed that as the grid size decreases, load-carrying capacity increases due to the increased number of warp yarns to take the load. About 45% increase in tensile loading was observed for T15 specimens compared to T25 specimens. So, 15 mm grid spacing was taken as optimum in this study.

The ultimate load and displacement values for the tensile coupons based on the number of textile layers are shown in Table 7. It was observed that ultimate strength and displacement values increased non-proportional with the increase in the number of textile layers. Among the tested coupon specimens, $T4$ having four layers of carbon textile, showed an increase in tensile loading of about 146% w.r.t to $T1$
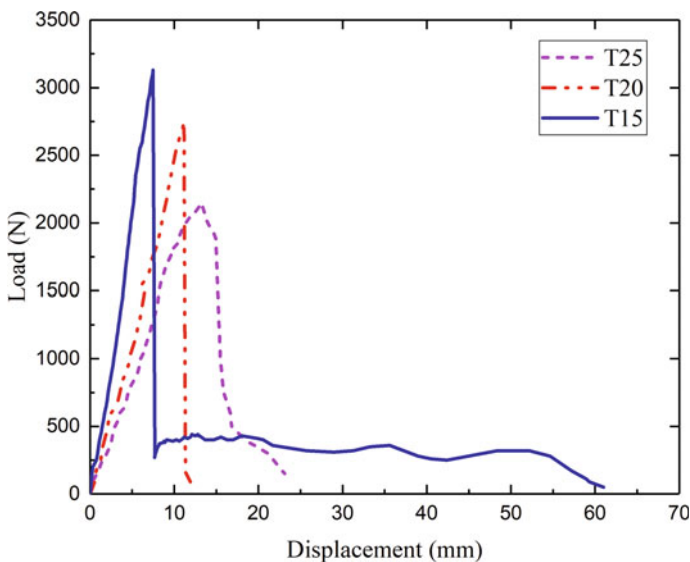
Fig. 13 Load–displacement response based on grid spacing of yarns
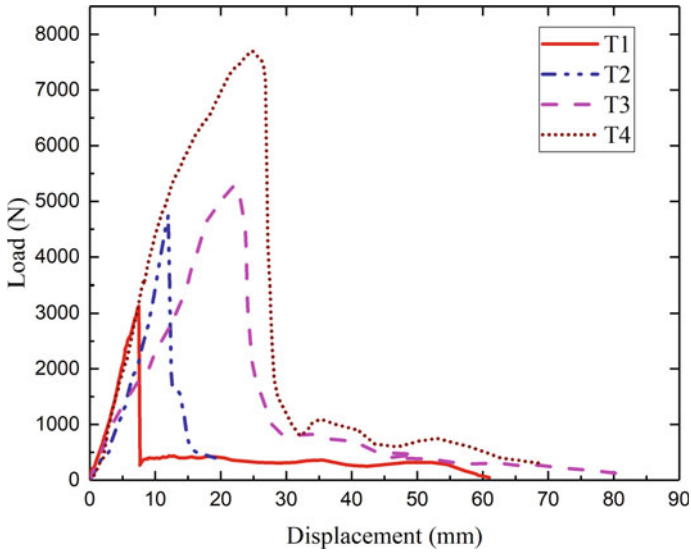
Fig. 14 Load–displacement response based on number of textile layers

Table 6 Tensile strength values of specimens based on grid spacing of yarns

Specimen ID	Number of textile layers	Load (N)	Displacement (mm)	Ultimate stress of coupon, σ_c (MPa)	Ultimate strain of coupon	Percentage increase in tensile loading (%)
T25	1	2150	13.2	5.375	0.044	0
T20	1	2750	11.16	6.875	0.0372	27.9
T15	1	3130	7.49	7.825	0.0249	45.58

Table 7 Strength values of tensile specimens based on the number of textile layers

Specimen ID	Number of textile layers	Load (N)	Displacement (mm)	Ultimate stress of coupon, σ_c (MPa)	Ultimate strain of coupon	Percentage increase in tensile loading (%)
T1	1	3130	7.49	7.825	0.0249	0
T2	2	4750	11.99	11.875	0.039	51.75
T3	3	5300	22.2	13.25	0.0735	69.33
T4	4	7700	24.84	19.25	0.0828	146

coupons because of the increased warp yarns and weft yarns. Also, ultimate stress (σ_c) calculated by considering the specimen's overall cross-sectional area (Ac) was about 19.25 MPa for $T4$ specimens ($A_c = w_s\, h_s$, where w_s is the nominal width and h_s is the nominal thickness of the coupon).

4 Conclusions

In this study, the behaviour of carbon textile reinforced geopolymer mortar under uniaxial tension was investigated experimentally. The important conclusions observed from this study are.

- Carbon textile can be used as a possible material for strengthening or reinforcing applications.
- CTRGM specimens showed a pseudo-ductile failure pattern in uniaxial tension. As indicated in literature [11], textile reinforced mortar shows a nonlinear behaviour in three stages. In the first stage, upon loading, matrix cracking occurred at regular spacing influenced by the stiffness of the geopolymer matrix. The second stage begins when the tensile strength of mortar is exceeded, then the crack widens. Finally, the third stage characterised by elastic modulus of carbon textile in which textile got elongated and failure occurred by the tensile rupture of the textile yarns.
- Coupon specimens having 15 mm grid spacing of carbon yarns (TRGM-C15) showed better performance compared to 25 mm grid spacing (TRGM-C25) and 20 mm grid spacing (TRGM-C20) specimens due to the increase in the number of warp yarns to take the tensile loading.
- Carbon textile having 15 mm grid spacing and four layers showed an improved tensile strength of about 146% compared to one layer of carbon textile reinforcement for a mortar thickness of 10 mm.

References

1. D'Antino T, Papanicolaou C (2017) Mechanical characterization of textile reinforced inorganic-matrix composites. Compos B Eng 127:78–91
2. Donnini J, Corinaldesi V (2017) Mechanical characterization of different FRCM systems for structural reinforcement. Constr Build Mater 145:565–575
3. D'antino T, Papanicolaou CC (2018) Comparison between different tensile test set-ups for the mechanical characterization of inorganic-matrix composites. Constr Build Mater 171:140–151
4. Peled A, Bentur A (2003) Fabric structure and its reinforcing efficiency in textile reinforced cement composites. Compos A Appl Sci Manuf 34(2):107–118
5. Alexander, A. E., & Shashikala, A. P. (2020). Sustainability of Construction with Textile Reinforced Concrete-A State of the Art. In *IOP Conference Series: Materials Science and Engineering* (Vol. 936, No. 1, p. 012006). IOP Publishing.
6. Peled A, Mobasher B, Bentur A (2017) Textile reinforced concrete. CRC Press

7. AC434, I. C. C (2013) Acceptance criteria for masonry and concrete strengthening using fiber-reinforced cementitious matrix (FRCM) composite systems. ICC-Evaluation Service, Whittier, CA
8. Brameshuber W, Hinzen M, Dubey A, Peled A, Mobasher B, Bentur A, Aldea C, Silva F, Hegger J, Gries T, Wastiels J (2016) Recommendation of RILEM TC 232-TDT: test methods and design of textile reinforced concrete. Mater Struct 49(12):4923–4927
9. ASTM D4018 – 17 Standard test methods for properties of continuous filament carbon and graphite fiber tows
10. Arboleda D, Carozzi FG, Nanni A, Poggi C (2016) Testing procedures for the uniaxial tensile characterization of fabric-reinforced cementitious matrix composites. J Compos Constr 20(3):04015063
11. Larrinaga P, Chastre C, Biscaia HC, San-Jose JT (2014) Experimental and numerical modeling of basalt textile reinforced mortar behavior under uniaxial tensile stress. Mater Des 55:66–74

Hydrophobic Concrete: A Review

Japneet Sidhu and Pardeep Kumar

1 Introduction

Water permeation in concrete due to its porous structure and hydrophilic nature is the major cause of physical and chemical deterioration of concrete structures leading to durability issues in concrete as the water facilitates the penetration of corrosive ion species into the concrete matrix along with it [1]. In marine environments and in the case of the deicing salt used in subzero temperatures, the water facilitates salt penetration into the concrete along with it causing not only serious damage to the rebars but also cause the ions in salts to react with the cement paste. The cycles of freezing and thawing in concrete in cold regions are also caused by water ingress into the concrete which introduces internal stresses due to ice formation in pores of concrete to an extent of inducing new cracks and causing the enlargement of the inherent microcracks in the concrete matrix. Carbonation is another major issue related to water permeation involving the transfer of CO_2 and other harmful pollutants from the atmosphere into the concrete matrix. The penetrated CO_2 reduces the pH of the pore solution in the matrix producing acidic conditions around steel rebars tending them to corrode [2].

Thus, it can be safely concluded that water ingress into concrete is the main cause of durability issues such as cracking, spalling, reinforcement corrosion, loss of cover to the embedded reinforcement, material dissolution, swelling, and expansion [3]. Inhibiting the water penetration will enable us to produce a more durable concrete with increased service life which can be done in a number of ways out of which the hydrophobic modification of concrete is increasingly becoming popular [4]. This paper aims at reviewing hydrophobic concrete. It deals with two kinds of concrete

J. Sidhu (✉) · P. Kumar
Department of Civil Engineering, National Institute of Technology, Hamirpur, Himachal Pradesh 177005, India
e-mail: japneet@nith.ac.in
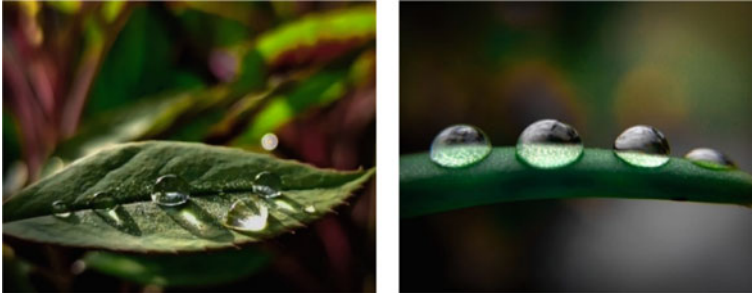
Fig. 1 Rose leaves and aloe vera leaf surface exhibiting hydrophobicity [8]

on which hydrophobic modification is carried out—the first one is the conventional cement-based concrete, and the second is a more eco-friendly alternative to conventional concrete, i.e. geopolymer concrete.

2 Hydrophobic Modification of Concrete—Overview

2.1 Concrete Durability and Biomimetics as an Inspiration

The concept of hydrophobic surfaces derived its inspiration from nature. Many plants such as the lotus leaves, taro leaves, aloe vera leaves, and rose leaves exhibit hydrophobicity [5] and self-cleaning mechanism given the name of "Lotus Effect" [6, 7] as seen in Fig. 1.

2.2 Methods Employed to Fabricate Hydrophobic Concrete

There are two methods of modifying the concrete to make it hydrophobic. The first one is by surface treatment and the second is by integral/bulk/volume hydrophobation as summarized in the Fig. 2.

2.3 Classification of Surfaces based on Water Contact Angles

Depending on water contact angle (WCA) surfaces are classified as hydrophilic, hydrophobic, over hydrophobic, and superhydrophobic as shown in Fig. 3.
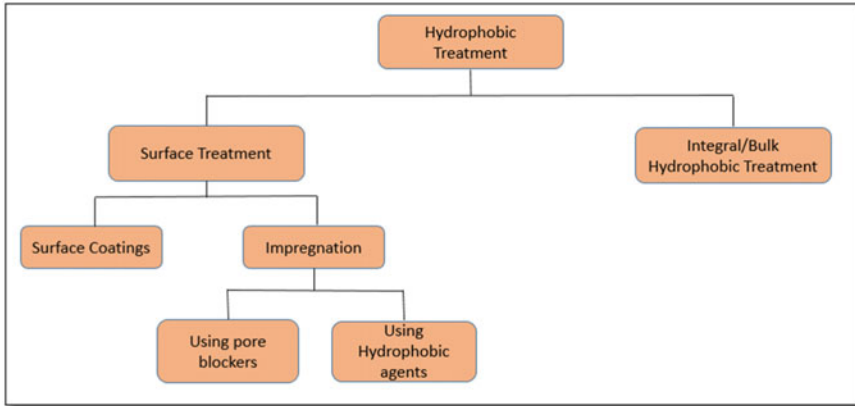
Fig. 2 Different techniques of providing hydrophobic treatment to concrete
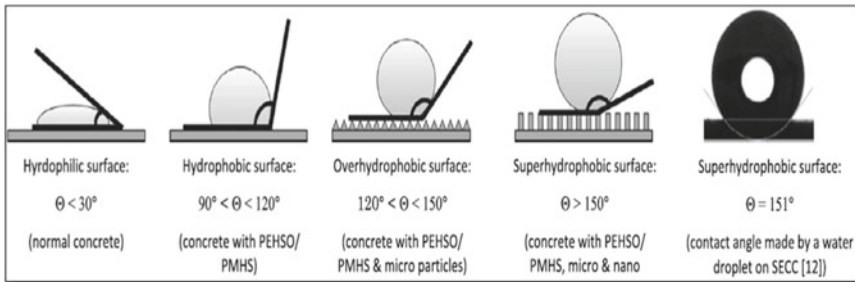
Fig. 3 Classification of surfaces based on water contact angles [9]

3 Literature Review—Hydrophobic Cement Concrete

3.1 Surface Treatment

The efficacy of hydrophobic coatings when used on concrete specimens was investigated, and it was found that silane/siloxane as a sealer yielded the best performance and was effective in reducing the rate of reinforcement corrosion [10].

In surface impregnation technique, a study was carried out in which, six different surface impregnation agents were used, four of which were silane-based hydrophobic agents, whereas the other two were based on sodium silicate pore blockers. On applying these to the concrete samples, it was reported that the pore blockers were ineffective in preventing the ingress of chloride ions into the RCC composite in marine environments. The sodium silicate impregnated samples showed just 30% reduction in water absorption compared to the untreated specimens, whereas the ones

impregnated with silanes showed a much significant reduction in water absorption which is in conjunction with the penetration depths of the impregnating agents [11].

3.2   Integral Hydrophobic Modification

A study of hydrophobic modification was carried out using natural additives comprising of linseed oil in lime mortar and lime metakaolin mortar. Linseed oil addition changes capillary surfaces from hydrophilic to hydrophobic due to non-polar nature of oil, thereby reducing water and salt ingress into the mortars. The incorporation of linseed oil in lime mortar reduces the flexural and compressive strength, but if metakaolin is added to the lime mortar, it makes up for that loss in strength. Water absorption by capillarity is reduced by around 98% and 83% when lime mortar and lime metakaolin mortar were modified by linseed oil addition, respectively, which in turn reduces the salt ingress too [12].

Integral hydrophobicity was also experimented with concrete and mortar samples by making use of industrial by-products such as flyash, amorphous carbon powder, and GGBS and these materials proved quite promising in the field of hydropho-bicity. Wong et al. made use of a superhydrophobic paper sludge ash (PSA) to prepare samples such as cement pastes admixed with hydrophobic PSA, cement pastes surface coated with hydrophobic PSA, and concretes containing admixed hydrophobic PSA. This superhydrophobic PSA was manufactured as listed in a previous research by Spathi, in which the PSA was dry milled with 4% stearic acid for 8 h which resulted in the highest water contact angle of more than 150° XRF data indicated that PSA is composed mainly of calcium alumino silicate with negligible amount of impurities [13].

An integral hydrophobic concrete as well as integral hydrophobic cement paste was manufactured by making use of waste amorphous carbon powder (ACP). The ACP modified paste samples had higher compressive strength and less porosity as compared to those without ACP. It was seen that the water absorption was reduced by up to about 23% in ACP modified cement paste. The effectiveness of adding hydrophobic ACP on reducing the rate of capillary water absorption was significant and it increased with higher ACP contents both in cement paste and concrete. The electrical resistivity of cement paste and concrete increased by up to 187% and 43% when ACP content was 15% and 20%, respectively [14]. A Table 1 indicates the highest WCA's achieved and their corresponding SA values along with the state of hydrophobicity.

Table 1 Water contact angles and sliding angles for different hydrophobic treatments

S. No.	Author (year)	Highest WCA	SA/CAH	State of hydrophobicity achieved	Treatment method
1	Facio and Mosquera (2013) [15]	150˚	7˚	Superhydrophobic	Surface treatment
2	Vivian et al. (2013) [16]	151˚	–	Superhydrophobic	Surface treatment
3	Muzenski et al. (2014) [17]	120˚–140˚	–	Overhydrophobic	Surface treatment
4	Horgnies and Chen (2014) [18]	164˚	2.5˚	Superhydrophobic	Surface treatment
5	Muzenski et al. (2015) [9]	> 120˚	–	Overhydrophobic	Surface treatment
6	Liu et al. (2017) [19]	140˚	< 5˚	Overhydrophobic	Surface treatment
7	Husni et al. (2017) [20]	152.3˚ ± 0.05˚	–	Superhydrophobic	Surface treatment
8	Barnat-Hunek et al. (2017) [21]	133.7˚	–	Overhydrophobic	Surface treatment
9	She et al. (2018) [22]	130˚ ± 4˚	27˚ ± 3˚	Overhydrophobic	Surface treatment
10	Chenxi et al. (2019) [23]	150.4˚ ± 0.3˚	8.9˚ ± 2.2˚	Superhydrophobic	Surface treatment
11	Song et al. (2019) [24]	140˚	–	Overhydrophobic	Surface treatment
12	Wang et al. (2020) [25]	> 150˚	< 10˚	Superhydrophobic	Surface treatment
13	Spathi et al. (2015) [13]	> 150˚	–	Superhydrophobic	Integral treatment
14	Grumbein et al. (2016) [26]	−90˚–110˚	–	Hydrophobic	Integral treatment
15	Song et al. (2017) [27]	158˚ ± 0.8˚	6.1˚ ± 1.2˚	Superhydrophobic	Integral treatment
16	Qu and Yu (2018) [28]	92˚	–	Hydrophobic	Integral treatment
17	Liu et al. (2018) [29]	87˚	–	Hydrophobic	Integral treatment
18	Mundo et al. (2018) [30]	> 100˚	–	Overhydrophobic	Integral treatment

(continued)

Table 1 (continued)

S. No.	Author (year)	Highest WCA	SA/CAH	State of hydrophobicity achieved	Treatment method
19	Wang et al. (2019) [31]	> 150°	< 10°	Superhydrophobic	Integral treatment
20	Dong et al. (2019) [32]	−166°	–	Superhydrophobic	Integral treatment
21	Feng et al. (2019) [33]	131.5°	81.7°	Sverhydrophobic	Integral treatment

4 Literature Review-Hydrophobicity in Different Types of Concrete

4.1 Self-compacting Concrete (SCC)

Surface hydrophobic treatment was carried out in a study on fiber reinforced SCC using siloxane resin-based commercial product and its resistance to freeze and thaw cycles was investigated. The treated specimens showed an improvement in freeze-thaw resistance because of a significant decrease in the water absorption [34].

Another study conducted on durability of SCC studied the effect of addition of a hydrophobic admixture in the form of an aqueous emulsion of butyl-ethoxy-silane in the self-compacting concrete. The admixture addition resulted in increased durability, but it lowered strength at later ages [35].

Tian et al. conducted a study to make SCC as integrally hydrophobic by making use of silane-based hydrophobic agent and waste tire rubber particles. The obtained composite exhibited hydrophobic characteristics having a WCA > 120°. The water absorption was also greatly reduced, although there was a slight reduction in the flexural and compressive strength [36].

4.2 Lightweight Concrete

A no fines concrete with recycled aggregates which is essentially a lightweight concrete was modified using a hydrophobic admixture and its effect on the no fines concrete was studied. The hydrophobic admixture was used to counteract high water absorption of recycled aggregates. The use of hydrophobic admixture resulted in a decrease in the capillary water absorption by about 70% thereby increasing the durability [37].

A hydrophobic lightweight aggregate concrete was synthesized using superhy-drophobic Ground Granulated Blast-furnace Slag (H-GGBS) made using stearic acid by ball milling process. For 15% and 20% replacements the compressive strength

is about 98% and 83% of the reference sample respectively and similar is the trend for flexural strength. The introduction of the super-hydrophobic GGBS results in an improved durability. The lightweight concrete possesses best hydrophobic performance at a 15% addition of super hydrophobic GGBS, showing a WCA of 92° [38].

Kharun et al. studied the properties of light hydrophobic concrete by making use of polymers and observed that the water absorption greatly reduced by making use of hydrophobic modification. No WCA measurements were carried out to quantify the induced hydrophobicity [39].

5 Literature Review—Hydrophobic Geopolymer Concrete

5.1 Surface Treatment

The surface modification in case of geopolymer concrete was carried out by application of a water proof layer on specimens which consisted of water, aluminium trichloride and palmitic acid dissolved in glacial acetic acid in order to yield a waterproof hydrophobic geopolymer concrete. The modified geopolymer exhibited WCAs of around 136° as compared to 36° in the unmodified ones and the modified samples absorbed 78.77% less water compared to the reference samples, thereby indicating good hydrophobic characteristics [40]. In a similar fashion, they were successful in synthesizing a waterproof fast setting geopolymer composite for repair and protection [40, 41].

Another study reported the use of silane (octyltriethoxysilane) as a surface modifying agent on a flyash-based geopolymer in an effort to inhibit efflorescence. The surface modified geopolymer exhibited a WCA of 144.1° indicating that the modification turned the surface onto hydrophobic from a hydrophilic one. A reduction in capillary absorption and diffusion of water were also reported. The mechanical strength remained unaffected due to surface modification [42]. Masek and Diblikova carried out the hydrophobic modification of geopolymer composite by using the technique of hydrophobic impregnation. The process was carried out by immersing the geopolymer composite into the hydrophobic solutions consisting of different kinds of ethoxysilanes, followed by drying. The surface of the composite was found to have turned into hydrophobic from hydrophilic one as indicated by the water contact angle and water intake measurements. The highest WCA of 123° was found to be for silanes with S_iO_2 nanoparticles [43].

5.2 Integral Hydrophobation

Zhu et al. studied the waterproofing properties of a geopolymer based on partial replacement of ultrafine fly ash by rice husk ash (RHA). It was reported that RHA led to densification of the microstructure up to 20% replacement beyond which the denseness decreases. Microstructure densification was accompanied by gel formation owing to decline in the amount of calcium hydroxide. Although the resulting geopolymer still remains hydrophilic, the WCA increased and the water absorption decreased indicating an improvement in water proof property up to 20% RHA replacement. The WCA for geopolymer with 100% flyash (reference sample) was reported as 41.16° and 45.41° on 7 days and 28 days curing, respectively, whereas 20% RHA replaced samples exhibited a WCA of 56.01° and 59.25° on the respective curing ages indicating an increase in the WCA values by 36.07% and 30.48% compared to the reference samples [44].

In another study conducted on the effect of RHA addition on the water proof property of metakaolin-based geopolymer, it was reported that the RHA addition into the geopolymer led to an enhancement in the mechanical strength and WCA owing to densification of the composite as well disruption of pore connectivity up to a 20% replacement. The WCA value of 7 day sample for 20% RHA replacement is found to be 55.2° and 28 day sample was 60° as against the reference sample (100% metakaolin) showing a WCA of 35.3° and 38° on 7 day and 28 day curing, respectively. The improvement in WCA at 20% RHA replacement was thus found to be 56.37 and 57.89% at 7 day and 28 day curing ages when compared to the reference samples [45].

The effect of superhydrophobic slag(s-slag) which was made by milling of slag with stearic acid was studied on the wetting characteristics, shrinkage and carbonation resistance of alkali-activated-slag (AAS). It was reported that a 20% application of s-slag as a partial binder resulted in a reduction of about 68% in shrinkage and around 70% in the carbonation depth whereas the WCA reported for 10%, 20% and 30% s-slag were 32°, 79°, and 81,° respectively, indicating an enhancement in the water repelling characteristics. The compressive strength decreased whereas the flexural strength was found to have increased due to a reduction in the microcracks, on the application of *s*-slag to the AAS [46].

Another study was conducted on making the bulk of a foamed hybrid geopolymer concrete as hydrophobic by making use of microbubble and microfiber modification. The microbubbles, unreacted metakaolin and gel pores imparted sufficient surface roughness on micro as well as nano scale which led to an increased the WCA to 140.9° from the unmodified samples with WCA of 112.2° which was an increase of about 25% compared to the reference hybrid geopolymer [47].

6 Conclusion

The paper examines the efficacy of hydrophobic treatment of cement concrete and mortar as well as of geopolymer concrete in preventing water penetration into its matrix resulting in an increased durability of concrete structures. The rheological, mechanical, and durability properties affected due to such modification were studied and the following conclusions can be drawn:

- Surface modification is found to be a more effective hydrophobic treatment method compared to the bulk treatment when the WCA's obtained are compared. Surface modification reported WCA's > 120° leading to attainment of over hydrophobic and super hydrophobic states. Whereas in bulk modification the WCA's vary from hydrophilic range to super hydrophobic range. However, the efficiency of the surface treatment greatly depends on its adhesiveness to the surface and mechanical robustness of the coatings against abrasion and other mechanical damages and the effective depth of penetration of the hydrophobic agents into the surface of the element.
- Integral modification is not susceptible to deterioration due to peeling/surface damage and does not require regular maintenance. Another advantage is that even after damage to the element or its cracking, the internal exposed surface of concrete/mortar still remains hydrophobic and repels water as opposed to surface treatments. But, main issue related to integral hydrophobation is that of low compressive strength due to interference of the additives with the hydration reactions of concrete and hence studies suggest their use in non-structural elements.
- For both the surface as well as bulk modification, introduction of nanoparticles lead to increased hydrophobicity and in turn increased durability in concretes and mortars as the nanoparticles help in inducing micro and nano hierarchical structures.
- Hydrophobic modification of geopolymer concrete is studied which resulted in a concrete which is not only sustainable but also durable. It also helps in lowering the carbon footprint of construction industry. WCA's up to 144° have been attained in case of geopolymer concrete making it attain over hydrophobic state. Super-hydrophobicity has yet not been reported in studies related to hydrophobicity of geopolymer concrete which makes it a possible future prospect.

References

1. Ganesh R, Ravikumar P (2016) Polymer modified mortar and concrete present status a review. IOSR J Mech Civ Eng 13:89–100. https://doi.org/10.9790/1684-13030789100
2. Tian Y, Wang P, Zhao T, Ma Z, Jin Z, Zhao H (2019) Influence of water-repellent treatment with silicon resin on properties of concrete. Adv Mater Sci Eng. https://doi.org/10.1155/2019/5743636

3. Al-tabbaa A, Paine K (2018) Biomimetic cementitious construction materials for next-generation infrastructure 171:67–76

4. Xiang T, Lv Z, Wei F, Liu J, Dong W, Li C, Zhao Y, Chen D (2019) Superhydrophobic civil engineering materials

5. Marmur A (2004) The lotus effect : superhydrophobicity and metastability, pp 3517–3519

6. Barthlott W, Neinhuis C (1997) Purity of the sacred lotus, or escape from contamination in biological surfaces. Planta 202:1–8. https://doi.org/10.1007/s004250050096

7. Feng L, Li S, Li Y, Li H, Zhang L, Zhai J, Song Y, Liu B, Jiang L, Zhu D (2002) Super-hydrophobic surfaces: from natural to artificial. Adv Mater 14:1857–1860. https://doi.org/10.1002/adma.200290020

8. Kashyap A, Freezoo momentzz photography (nd). https://instagram.com/freezoo_momentzz?utm_medium=copy_link

9. Muzenski S, Flores-Vivian I, Sobolev K (2015) Hydrophobic engineered cementitious composites for highway applications. Cem Concr Compos 57:68–74. https://doi.org/10.1016/j.cemconcomp.2014.12.009

10. Ibrahim M, Maslehuddin M, Almusallam AA (1997) Effectiveness of concrete surface treatment materials in reducing chloride-induced reinforcement corrosion 11:443–451

11. Dai J, Akira Y, Wittmann FH, Yokota H, Zhang P (2010) Cement & concrete composites water repellent surface impregnation for extension of service life of reinforced concrete structures in marine environments: the role of cracks. Cem Concr Compos 32:101–109. https://doi.org/10.1016/j.cemconcomp.2009.11.001

12. Nunes C, Slížková Z (2014) Hydrophobic lime based mortars with linseed oil: Characterization and durability assessment. Cem Concr Res 61–62:28–39. https://doi.org/10.1016/j.cemconres.2014.03.011

13. Spathi C, Young N, Heng JYY, Vandeperre LJM, Cheeseman CR (2015) A simple method for preparing super-hydrophobic powder from paper sludge ash. Mater Lett 142:80–83. https://doi.org/10.1016/j.matlet.2014.11.123

14. Shahbazi R, Korayem AH, Razmjou A, Duan WH, Wang CM, Justnes H (2020) Integrally hydrophobic cementitious composites made with waste amorphous carbon powder. Constr Build Mater 233:117238. https://doi.org/10.1016/j.conbuildmat.2019.117238

15. Facio DS, Mosquera MJ (2013) Simple strategy for producing superhydrophobic nanocomposite coatings in situ on a building substrate. ACS Appl Mater Interfaces 5:7517–7526. https://doi.org/10.1021/am401826g

16. Flores-vivian I, Hejazi V, Kozhukhova MI, Nosonovsky M, Sobolev K (2013). Self-assembling particle-siloxane coatings for superhydrophobic concrete. https://doi.org/10.1021/am404272v

17. Muzenski SW, Flores-Vivian I, Sobolev K (2014) The development of hydrophobic and super-hydrophobic cementitious composites. In: Proceeding of 4th international conference durable concrete structure ICDCS, 2014. https://doi.org/10.5703/1288284315484

18. Horgnies M, Chen JJ (2014) Superhydrophobic concrete surfaces with integrated microtexture. Cem Concr Compos 52:81–90. https://doi.org/10.1016/j.cemconcomp.2014.05.010

19. Liu P, Gao Y, Wang F, Yang J, Yu X, Zhang W, Yang L (2017) Superhydrophobic and self-cleaning behavior of Portland cement with Lotus-leaf-like microstructure. J Clean Prod. https://doi.org/10.1016/j.jclepro.2017.03.211

20. Husni H, Nazari MR, Yee HM, Rohim R, Yusuff A, Mohd Ariff MA, Ahmad NNR Leo CP, Junaidi MUM (2017) Superhydrophobic rice husk ash coating on concrete. Constr Build Mater 144:385–391. https://doi.org/10.1016/j.conbuildmat.2017.03.078

21. Barnat-Hunek D, Siddique R, Łagód G (2017) Properties of hydrophobised lightweight mortars with expanded cork. Constr Build Mater 155:15–25. https://doi.org/10.1016/j.conbuildmat.2017.08.052

22. She W, Wang X, Miao C, Zhang Q, Zhang Y, Yang J, Hong J (2018) Biomimetic super-hydrophobic surface of concrete: topographic and chemical modification assembly by direct spray. Constr Build Mater 181:347–357. https://doi.org/10.1016/j.conbuildmat.2018.06.063

23. Chenxi Z, Jian L, Lingdong C, Weiqiang L, Jing Z, Jintao Y, Jie F (2019) Dark, heat-reflective, anti-ice rain and superhydrophobic cement concrete surfaces. Constr Build Mater 220:21–28. https://doi.org/10.1016/j.conbuildmat.2019.05.188

24. Song Z, Lu Z, Lai Z (2019) Influence of hydrophobic coating on freeze-thaw cycle resistance of cement mortar 2019

25. Wang F, Xie T, Ou J, Xue M, Li W (2020) Cement based superhydrophobic coating with excellent robustness and solar re fl ective ability. J Alloys Compd 823:153702. https://doi.org/10.1016/j.jallcom.2020.153702

26. Grumbein S, Minev D, Tallawi M, Boettcher K, Prade F, Pfeiffer F, Grosse CU, Lieleg O (2016) Hydrophobic properties of biofilm-enriched hybrid mortar. Adv Mater 28:8138–8143. https://doi.org/10.1002/adma.201602123

27. Song J, Zhao D, Han Z, Xu W, Lu Y, Liu X, Liu B, Carmalt CJ, Deng X, Parkin IP (2017) Super-robust superhydrophobic concrete. J Mater Chem A. 5:14542–14550. https://doi.org/10.1039/c7ta03526h

28. Qu Z.Y, Yu Q, Ji YD, Gauvin F, Voets IK (2020) Cement and concrete research Mitigating shrinkage of alkali activated slag with biofilm 138. https://doi.org/10.1016/j.cemconres.2020.106234

29. Liu P, Feng C, Wang F, Gao Y, Yang J, Zhang W, Yang L (2018) Hydrophobic and water-resisting behavior of Portland cement incorporated by oleic acid modified fly ash. Mater Struct Constr 51. https://doi.org/10.1617/s11527-018-1161-8

30. Di Mundo R, Petrella A, Notarnicola M (2018) Surface and bulk hydrophobic cement composites by tyre rubber addition. Constr Build Mater 172:176–184. https://doi.org/10.1016/j.conbuildmat.2018.03.233

31. Wang F, Lei S, Ou J, Xue M, Li C, Li W (2019) Superhydrophobic calcium aluminate cement with super mechanical stability. Ind Eng Chem Res 58:10373–10382. https://doi.org/10.1021/acs.iecr.9b01188

32. Dong B, Wang F, Abadikhah H, Hao L, Xu X, Khan SA, Wang G, Agathopoulos S (2019) Simple fabrication of concrete with remarkable self-cleaning ability, robust superhydrophobicity, tailored porosity, and highly thermal and sound insulation. ACS Appl Mater Interfaces. https://doi.org/10.1021/acsami.9b14929

33. Feng Z, Wang F, Xie T, Ou J, Xue M, Li W (2019) Integral hydrophobic concrete without using silane. Constr Build Mater 227:116678. https://doi.org/10.1016/j.conbuildmat.2019.116678

34. Corinaldesi V, Moriconi G (2004) Durable fiber reinforced self-compacting concrete 34:249–254. https://doi.org/10.1016/j.cemconres.2003.07.005

35. Corinaldesi V (2012) Combined effect of expansive, shrinkage reducing and hydrophobic admixtures for durable self compacting concrete. Constr Build Mater 36:758–764. https://doi.org/10.1016/j.conbuildmat.2012.04.129

36. Tian L, Qiu L, Liu Y (2021) Fabrication of integrally hydrophobic self-compacting rubberized mortar with excellent waterproof ability, corrosion resistance and stable mechanical properties. Constr Build Mater 304:124684. https://doi.org/10.1016/j.conbuildmat.2021.124684

37. Tittarelli F, Carsana M, Ruello ML (2014) Effect of hydrophobic admixture and recycled aggregate on physical-mechanical properties and durability aspects of no-fines concrete. Constr Build Mater 66:30–37. https://doi.org/10.1016/j.conbuildmat.2014.05.043

38. Qu ZY, Yu QL (2018) Synthesizing super-hydrophobic ground granulated blast furnace slag to enhance the transport property of lightweight aggregate concrete 191:176–186. https://doi.org/10.1016/j.conbuildmat.2018.10.018

39. Kharun M, Ehsani A, Nasimi S, Gebre T.H, Харун М, Эхсани А, Насими Ш, Гебре ТХ (2021) Properties and behavior of light hydrophobic concrete 1 Изготовление гидрофобного полимерного легкого бетона 17:299–307. https://doi.org/10.22363/1815-5235-2021-17-3-299-307

40. Duan P, Yan C, Luo W, Zhou W (2016) A novel surface waterproof geopolymer derived from metakaolin by hydrophobic modification. Mater Lett 164:172–175. https://doi.org/10.1016/j.matlet.2015.11.006

41. Duan P, Yan C, Luo W (2016) A novel waterproof, fast setting and high early strength repair material derived from metakaolin geopolymer. Constr Build Mater 124:69–73. https://doi.org/10.1016/j.conbuildmat.2016.07.058

42. Xue X, Liu YL, Dai JG, Poon CS, Zhang WD, Zhang P (2018) Inhibiting efflorescence formation on fly ash-based geopolymer via silane surface modification. Cem Concr Compos 94:43–52. https://doi.org/10.1016/j.cemconcomp.2018.08.013
43. Mašek Z, Diblíková L (2018) Hydrophobic impregnation of geopolymer composite by ethoxysilanes. Acta Polytech 58:184–188. https://doi.org/10.14311/AP.2018.58.0184
44. Zhu H, Liang G, Xu J, Wu Q, Zhai M (2019) Influence of rice husk ash on the waterproof properties of ultrafine fly ash based geopolymer. Constr Build Mater 208:394–401. https://doi.org/10.1016/j.conbuildmat.2019.03.035
45. Liang G, Zhu H, Zhang Z, Wu Q, Du J (2019) Investigation of the waterproof property of alkali-activated metakaolin geopolymer added with rice husk ash. J Clean Prod 230:603–612. https://doi.org/10.1016/j.jclepro.2019.05.111
46. Qu ZY, Gauvin F, Wang FZ, Liu G, Brouwers HJH (2020) Effect of hydrophobicity on autogenous shrinkage and carbonation of alkali activated slag. Constr Build Mater 264. https://doi.org/10.1016/j.conbuildmat.2020.120665
47. Yan D, Ruan S, Chen S, Liu Y, Fang H, Qian X, Peng Y (2021) Microbubble-enhanced hydrophobicity of foamed hybrid geopolymer. Mater Lett 285:129054. https://doi.org/10.1016/j.matlet.2020.129054

Numerical Analysis of Geosynthetic Reinforced Soil Wall Using Fly ash as Backfill Material Under Dynamic Loading

Kunjan Saikia and Shantanu Patra

1 Introduction

Primarily due to cost savings, use of geosynthetics in retaining structures has gained massive popularity. As applications of these structures are increasing day by day, proper inspection of their behaviour under seismic loading is very important. Various investigations carried out by Ling et al. [1] after the 1999 Chi-Chi earthquake, showed that several geosynthetic reinforced soil (GRS) walls suffered medium to serious damages. They concluded that these damages were mainly due to low quality of backfill material, low connection strength, and large vertical spacing of reinforcement. Takemura and Takahashi [2] carried out a number of centrifuge tests to study the influence of various factors such as backfill density, length and spacing of the reinforcement on the dynamic response of GRS walls. Sinusoidal loading was applied to a 7.5 m high wall. They found that larger values of reinforcement tensile strains and horizontal displacements were observed in case of wall with lower density backfill material. Lee [3] developed a numerical model using FLAC, and validated it with the results of several full-scale instrumented GRS walls. Also, a study was conducted to look into the influence of properties of reinforcement, facing type as well as soil properties on the performance of these walls. They concluded that the most significant effect on reinforcement strains and facing displacements are caused due to backfill properties as well as spacing of the reinforcement.

Thermal power plants generate large quantities of fly ash which causes a lot of problems related to land scarcity for its disposal and also in terms of various environmental aspects. So, a proper effective management and utilization of fly ash is very much required. Several studies have reported usage of fly ash as a backfill material with considerable good results [4–6].

K. Saikia (✉) · S. Patra
School of Infrastructure, IIT Bhubaneswar, Argul, Odisha Khordha-752050, India
e-mail: s21ce09004@iitbbs.ac.in
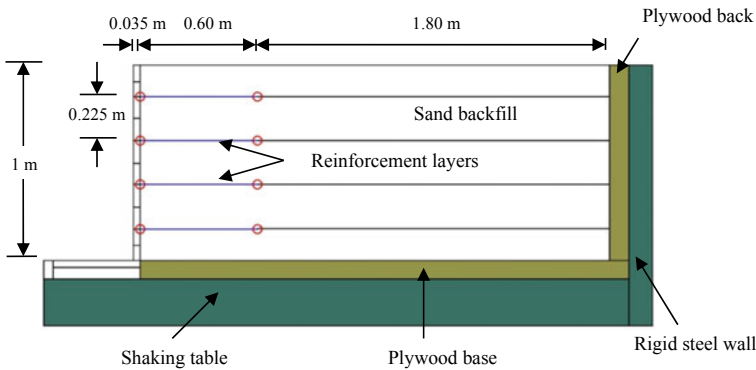
Fig. 1 Cross-section of the shake table test

This paper demonstrates the behaviour of a reinforced retaining wall backfilled with fly ash when subjected to seismic loading. At first, validation of the Abaqus model was carried out with the results of the shake table test as well as numerical analysis, reported by El Emam et al. [7]. The diagrammatic cross-section of the shake table test is depicted in Fig. 1. Then, the facing displacement at the end of the dynamic step is compared with the results of fly ash as the backfill material. And finally, the effect of stiffness of reinforcement and friction angle of fly ash on the displacement behaviour of the GRS wall was investigated by carrying out a parametric study.

2   Description of the Numerical Model

Figure 2 depicts the typical numerical model of the two dimensional, plane strain analyses performed using the Abaqus CAE software. The height of the model wall is 1 m. Soil reinforcement, made up of polyester was placed in four layers with a spacing of 0.225 m. The ratio of reinforcement length to height is taken to be 0.6.

Different steps were performed to simulate the construction of the shaking table model. To take into account the horizontal temporary supports of the facing panel, the wall was restrained in the horizontal direction during the construction step of the model. The wall supports were then released to obtain static equilibrium under gravity. And finally, the seismic loading was applied at the bottom nodes of the numerical model.

2.1   Boundary Conditions

During the static evaluation, base boundary of the model was fixed in both the horizontal as well as transverse directions. Also, the lateral peripheries were fixed only in
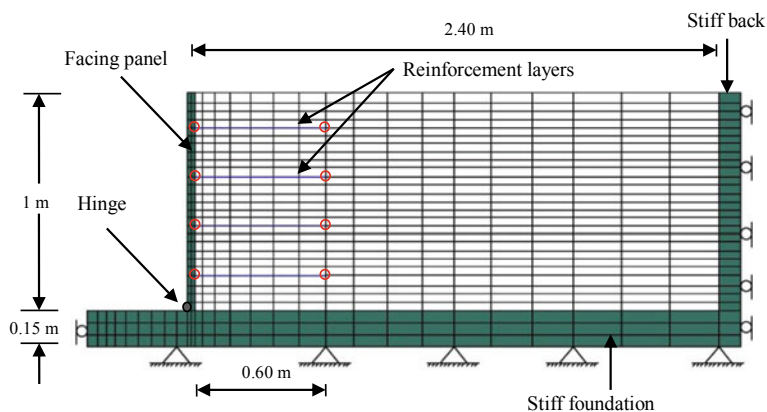
Fig. 2 Numerical model of the reinforced soil model wall with finite element mesh and boundary conditions

the horizontal directions. The boundaries were modified before start of the dynamic step. The bottom boundary was allowed to experience horizontal movements but was fixed only in the transverse direction Figure 2 shows the boundary conditions of the whole model.

2.2 Material Constitutive Model and Its Properties

The facing panel was modelled as linear elastic material with unit weight, bulk modulus, shear modulus, and Poisson's ratio as 17.2 kN/m^3, 1100 MPa, 1000 MPa, and 0.2, respectively. Four noded bilinear plane strain quadrilateral elements with reduced integration and hourglass control (CPE4R), were used for the facing panel. The shaking table (stiff foundation) and the back boundary regions (stiff back) as shown in Fig. 2 were also assigned similar material properties. To verify the numerical model, the backfill soil was first modelled as a cohesionless elastic plastic material. Mohr–Coulomb failure criterion was used and its properties are presented in Table 1 [7]. Similarly, CPE4R elements were assigned to the backfill material. To model the use of fly ash as the backfill material, Mohr–Coulomb failure criterion was used.

Table 1 Backfill soil properties

Unit weight (kN/m^3)	Peak plane strain friction angle, ϕ_{ps} (degree)	Residual friction angle, ϕ_{res} (degree)	Dilation angle, Ψ (degree)	Poisson's ratio μ	Shear Modulus G (MPa)	Bulk Modulus K (MPa)
15.7	58	46	15	0.3	7	6

Its unit weight was considered to be 19.2 kN/m3 and Poisson's ratio as 0.3. Also, friction angle of 42°, along with cohesion as 3 kPa and Young's modulus as 40 MPa was considered [8]. Beam elements of thickness 0.002 m were used to model the reinforcements. They are assigned linear-elastic perfectly plastic properties with zero compressive strength. Elastic modulus and yield strength of 45 MPa and 6.5 MPa respectively, was assigned to these elements [7]. Tie constraint was used to attach these elements to the facing wall. The soil- facing panel interface was simulated using a friction angle of 43.5° [7]. Also, a 5% damping ratio was applied to the facing wall and backfill material.

2.3   Input Base Motion

The input acceleration-time graph [7] is represented in Fig. 3. Every 5 s, the input amplitude was increased in 0.05 g base acceleration increments Fig. 3. This base acceleration was applied to each and every node of the bottom of the model.

3   Verification of the Numerical Model

For verification of the abaqus model, time histories of facing lateral displacement is compared with results of shaking table test and numerical simulation results, reported by El Emam et al. [7]. It can be seen from Fig. 4 that the results of this finite element study are in proper agreement with the compared results.
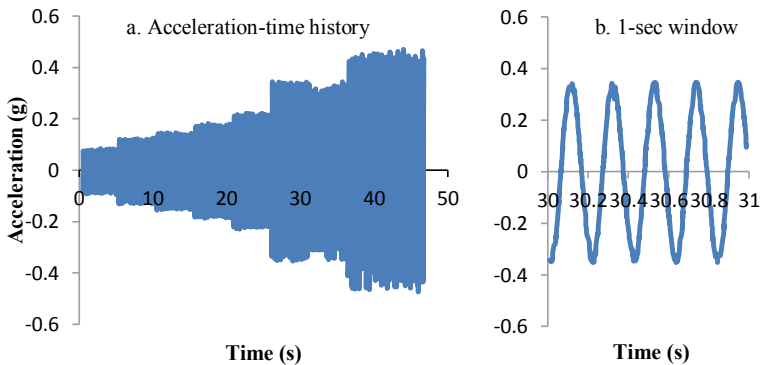
Fig. 3 Input base acceleration
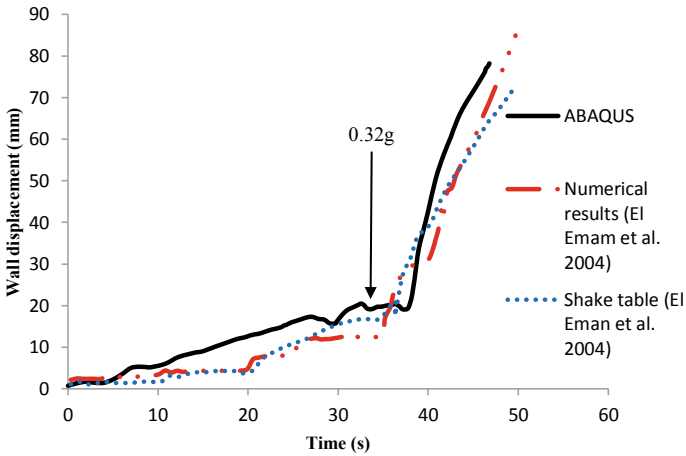
Fig. 4 Authentication of the abaqus model

4 Results

Numerical simulation results are presented in this section. Also, the parametric study results considering different factors such as angle of internal friction of fly ash, stiffness of reinforcement, and reinforcement spacing are described.

4.1 Facing Horizontal Displacement

The horizontal displacement of the facing wall at the end of seismic loading is shown in Fig. 5. A maximum facing displacement of 78.19 mm is observed using the conventional backfill material. But there was a considerable change in the maximum facing displacement on using fly ash as the backfill. The value reduced to 55.08 mm. Thus, it becomes clear that due to higher shear strength of fly ash in comparison to conventional backfill material, the maximum displacement reduces and it can be suitably utilised as a proper backfill in retaining walls.

4.2 Parametric Study

This section includes the parametric study results carried out taking into account stiffness of reinforcement and fly ash friction angle. While varying the factor of interest, the other factors were kept constant.
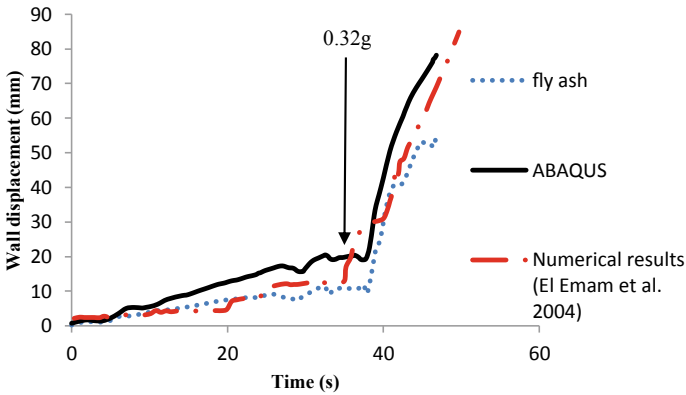
Fig. 5 Variation of lateral wall displacement with time

4.2.1 Reinforcement Stiffness

To study the impact of stiffness of reinforcement in deformation behaviour of the wall, three different values, 90 kN/m, 150 kN/m, and 300 kN/m were considered. A maximum displacement of the facing wall was observed as 55.08 mm, 51.29 mm, and 50.13 mm for stiffness values of 90 kN/m, 150 kN/m, and 300 kN/m respectively. It can be seen that though there is reduction in maximum facing displacement with increase in reinforcement stiffness, the variation is not that high. Figure 6 depicts the variation of facing displacement accompanying change in stiffness of reinforcement.
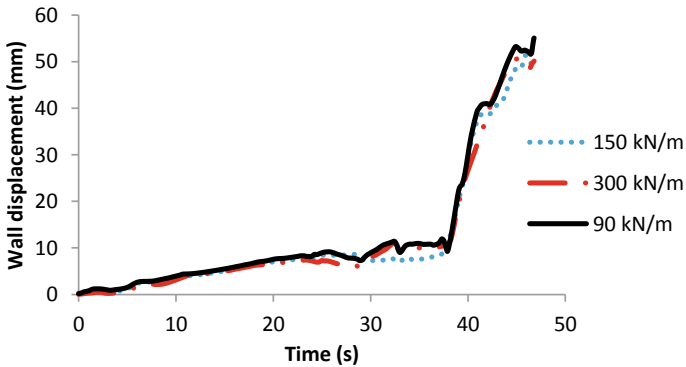
Fig. 6 Variation of lateral wall displacement with time for different values of reinforcement stiffness
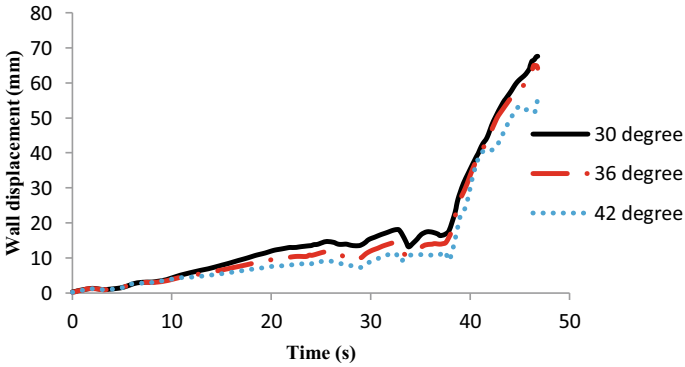
Fig. 7 Variation of lateral wall displacement with time for different values of fly ash friction angle

4.2.2 Fly Ash Friction Angle

Several studies report the variation of fly ash friction angle from 29º to 42.5º [9, 10]. This study takes into consideration three different values of friction angle, 30º, 36º, and 42º. For friction angle of 30º, the maximum wall displacement was observed as 67.57 mm. As the value of friction angle was increased to 36º and 42º, the maximum wall displacement reduced to 64.15 mm and 55.08 mm respectively. Thus, the friction angle plays a key role in the deformation behaviour of facing wall. Changes in wall displacement with friction angle are depicted in Fig. 7.

5 Conclusion

This paper presents a numerical study on deformation behaviour of GRS walls using fly ash as the backfill material. Different steps were considered in this numerical model to replicate the construction of the shaking table test. And finally, seismic loading was applied to the bottom nodes of the numerical model. Then, the numerical model was validated with the results of shake table test and numerical analysis reported by El Emam et al. [7]. And finally, to look into the deformation behaviour of the reinforced wall on variation of reinforcement stiffness and friction angle of fly ash, a parametric study was conducted.

The conclusions drawn from this study are as follows:

- The numerical model is in good agreement with the results of the shake table test and numerical analysis reported by El Emam et al. [7].
- Initially, on using uniformly graded sand as backfill, maximum facing displacement of 78.19 mm is observed. This value considerably reduced to 55.08 mm, when fly ash was used as the backfill material.

- On varying the reinforcement stiffness value as 90 kN/m, 150 kN/m, and 300 kN/m, the maximum facing displacement also reduced as 55.08 mm, 51.29 mm, and 50.13 mm respectively. Though variation in displacement is seen, the reduction is not that prominent.
- Also, it was observed that, on increasing the fly ash friction angle from 30º to 42º, the maximum facing displacement reduced from 67.57 mm to 55.08 mm. Thus, friction angle of fly ash needs to be taken into consideration on using fly ash as the backfill.

These results suggest that fly ash can be utilized as backfill material in place of conventional backfill to improve the performance of retaining walls. All the results are based on numerical modelling of reduced scale retaining wall model. Further studies on full scale model wall are very much necessary to understand their complete behaviour.

References

1. Ling HI, Leshchinsky D, Chou NNS (2001) Post-earthquake investigation on several geosynthetic-reinforced soil retaining walls and slopes during the Ji-Ji earthquake of Taiwan. Soil Dyn Earthq Eng 21:297–313
2. Takemura J, Takahashi A (2003) Centrifuge modeling of seismic performance of reinforced earth structure. In: Reinforced soil engineering: advances in research and practice, Marcel Dekker, New York, pp 417–442
3. Lee W (2000) Internal stability of analyses of geosynthetic reinforced retaining walls. Ph.D. Thesis, University of Washington, Seattle, USA
4. Joshi RC, Dunkan DM, Master HMMC (1975) New and conventional engineering uses of fly ash. J Transp Eng 101(TE4):791–806
5. Di Gioia AM, Nuzzo WL (1972) Fly ash as structural fill. J Power Div 98(1):77–92
6. Dayal U, Sinha R (1999) Design construction and monitoring of ash dyke, fly ash disposal and deposition: beyond 200 AD. Norosa Publishing House, New Delhi, India
7. El Emam M, Bathurst JR, Hatami K (2004) Numerical modelling of reinforced soil retaining walls subjected to base acceleration. In: 13th world conference on earthquake engineering Vancouver, B.C., Canada, August, pp 1–6
8. Bhatia R, Kumar A (2020) Load settlement behavior of concrete debris pile in fly ash fill. J Hazard Toxic Radioact Waste 24(3):04020006
9. Faber JH, DiGio Jr AM (1976) Use of ash in embankment construction. Transp Res Rec 593
10. Pal SK, Ghosh A (2009) Shear strength behavior of Indian fly ashes. In Indian geotechnical conference geotechnics in infrastructure development (GEOTIDE) 1:18–22

Wavelet Analysis of Near-Field Ground Motions from the Mw 7.6 1999 Chi-Chi Earthquake in Taiwan

Faisal Mehraj Wani, Mohammed Mujtaba Moid, Kanigiri Chandrakanth Reddy, Jayaprakash Vemuri, and Rajaram Chenna

1   Introduction

The 1999 Chi-Chi earthquake occurred along the Chelungpu fault, with the magnitude of 7.6 causing, heavy damage to structures in the central counties of Taichung, Nantou, and Yunlin [1, 2]. The rupture process of the Chi-Chi earthquake is more complex than the classical theory of rupture, as the rupture in Chelungpu fault is described by the jumping dislocation model [3]. This 30 s strong earthquake was the second deadliest earthquake that occurred in Taiwan since 1935 Shinchiku-Taichu earthquake. The epicenter of the earthquake was located in a town near Chi-Chi with a focal depth of 4 miles. This extreme shaking was believed to struck due to interaction between Eurasian and Philippine plate. The movement of the Philippine plate w.r.t to the Eurasian plate, is acknowledged as a key cause of seismicity in Taiwan. The strong ground motion was felt across the whole island due to its large magnitude and surface rupture. It was observed that ground motion towards the east of the fault was significantly higher than west areas. Peak ground motion exceeding 1.0 g was observed in several places across the island. The seismic energy released in the Taiwan earthquake was immense, and at least 10 times larger than the famous Kobe and Turkey earthquakes. This caused the Chi-Chi mainshock to be followed by numerous aftershocks, numbering around 10,000, with more than four being classified as "large aftershocks" of magnitude greater than 6.5, causing great damage to life and property. According to a Taiwanese official report, 2400 people lost their

F. M. Wani (✉) · M. Mujtaba Moid · K. Chandrakanth Reddy · J. Vemuri
Department of Civil Engineering, Ecole Centrale College of Engineering, Mahindra University, Hyderabad, Telangana 500043, India
e-mail: faisal20pcie006@mahindrauniversity.edu.in

R. Chenna
Department of Civil Engineering, Rajiv Gandhi Memorial College of Engineering and Technology, Kurnool, Andhra Pradesh, India

lives, 10,000 people were injured. Approximately 10,000 structures and residences were destroyed, and another 7,000 were badly damaged. Highway bridges were also severely damaged, including those built to current earthquake design requirements. At least nine bridges were destroyed, including three that were in the process of being built. Figure 1 shows the location of epicenter along with the locations where data was recorded. Response spectra of ground motions from these stations are shown in Fig. 2. The maximum values of response spectra are observed for the radial and transverse component of ground motions from the station CHY080.
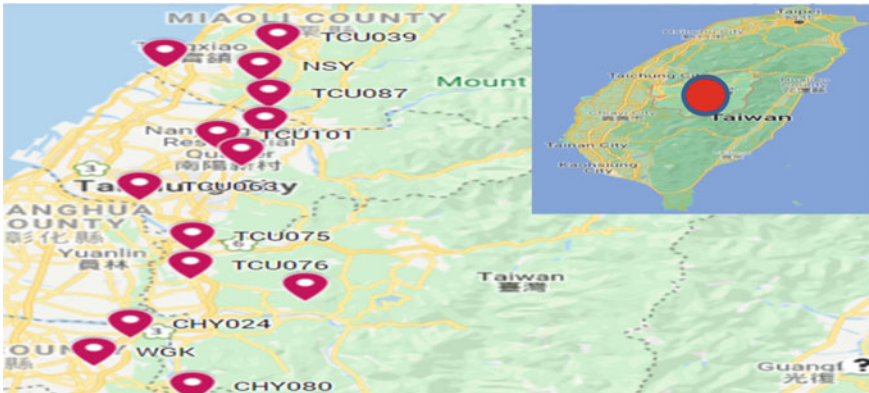
Fig. 1 Epicentre and recording stations considered in the present study
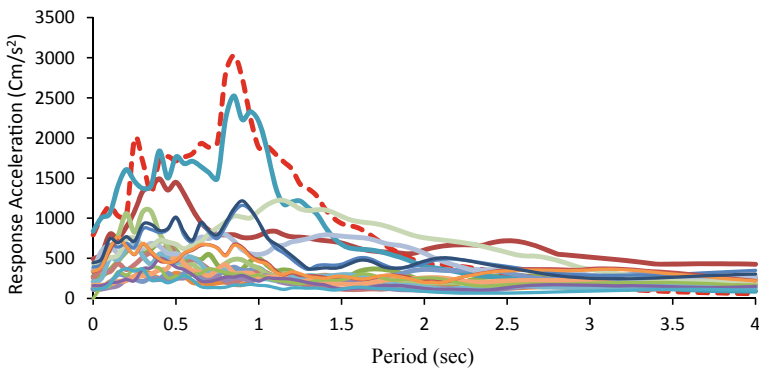
Fig. 2 Response Spectra for different ground motions (radial and transverse)

2 Damage to Structures

The strong ground motions across the island led to more than 1800 landslides, resulting in damage to structures at several locations [4]. Due to the release of high energy, numerous aftershocks shook the island, thereby causing enormous damage to structures (13 aftershocks with magnitude of less than 7). Taiwan usually follows a uniform building code similar to the US. Most of the buildings are constructed using reinforced concrete with unreinforced brick masonry partition walls. The role of the local site response like basin effect and liquefaction [5] should not be underestimated due to the presence of fertile land to the west of Chelungpu fault. One of the reasons for the toppling of medium and high rise structures was the presence of soft stories without infill. Further, the presence of a weak column with deficiencies in the steel reinforcement details contributed to the structural damage. Several schools, industrial structures, highway bridges, and, railways were damaged by the strong ground motions [6].

3 Characteristics of Ground Motions

The Chi-Chi earthquake was recorded at over 400 stations across the island providing enough data for analysis. In this paper, we selected some key stations to study the important characteristics of ground motions. Near field ground motions were taken into the consideration (less than 20 km), as they are expected to pose a predominant pulse, which affects the response of the structure. Near field ground motions are characterized by long-period pulse with high PGV, inducing a high dramatic response in the buildings. Table 1 lists the normally computed parameters of strong ground motions. The peak ground velocity (PGV) and peak ground acceleration (PGA) are determined [7] as:

$$PGA = \max|a(t)| \text{ and } PGV = \max|v(t)| \qquad (1)$$

Sustained maximum acceleration (SMA) and velocity (SMV) represent the max sustained acceleration or velocity during the three cycles [8]. The Maximum Incremental Velocity [MIV] is an important parameter that is employed in the seismic design of structures and it represents the maximum area of the acceleration graph between two zero crossings. It has been observed that ground motion scaled to the constant value of MIV results in reduced nonlinear lateral demands [9]. Further, Hancock and Bommer [2005] [10] used the maximum amplitude of motion and number of cycles to determine the Damage index (DI).

Table 1 Key characteristics of recorded ground motions

STATIONS	PGV (cm/s)	PGA (cm/s^2)	MIV (cm/s)	DI	Distance (km)	SMA (cm/s)	SMV (cm/s^2)
CHY024 (90)	50.39	276.17	79.54	1,881,582	9.3	199.1	41.57
CHY080(90)	105.547	792.81	179.34	546,615.5	3.1	467.89	75.67
CHY080(360)	93.17	836.84	168.56	399,239.8	3.1	462.65	83.89
NSY (90)	57.94	117.92	59.64	473,016.2	9.1	106.4	38.29
TCU063(360)	82.35	129.87	125.97	687,098.5	10.3	121.55	47.76
TCU075(90)	35.64	256.58	47.253	1,681,793	3.4	147.25	34.98
TCU076(90)	61.945	342.6	40.24	642,435.7	3.2	275.13	28.22
TCU087(360)	40.602	111.28	70.94	273,420.7	3.4	89.74	29.01
TCU101(90)	74.93	207.28	61.415	1,276,575	1.9	191.80	40.44
TCU128(360)	62.53	163.49	75.46	503,551.5	9.1	139.81	46.68
CHY101(90)	65.50	326.50	102.09	2,474,584	13.3	269.98	49.89
CHY101(360)	108.7	390.38	137.35	2,305,584	13.3	255.36	83.59
WGK (90)	61.12	338.55	84.33	2,385,909	13.3	272.01	37.23

4 Frequency Estimation Using FFTs

Characterization of earthquake waves is important, to identify the presence of different frequencies in the continuous stochastic seismic wave. The FFT converts the signal into the frequency domain, and is efficient when large quantities of computation are required. The Fourier transform of a time series signal is mathematically represented as:

$$F(\omega) = \int_{-\infty}^{\infty} S(t) \exp(-2\pi \text{jft}) \text{d}t \qquad (2)$$

Fourier transform of a time series signal is defined as inner product of the given signal and the basis function $\exp(-2\pi \text{jft})$, where t represents the time.

Figure 3, 4 and 5 show the derived Fourier transforms of the ground motions from the near field stations. The frequency content of the ground motions in all stations is seen to be varying from (0–40 Hz). However, this representation does not convey any information about the time sequencing, i.e. time of arrival of these frequencies.
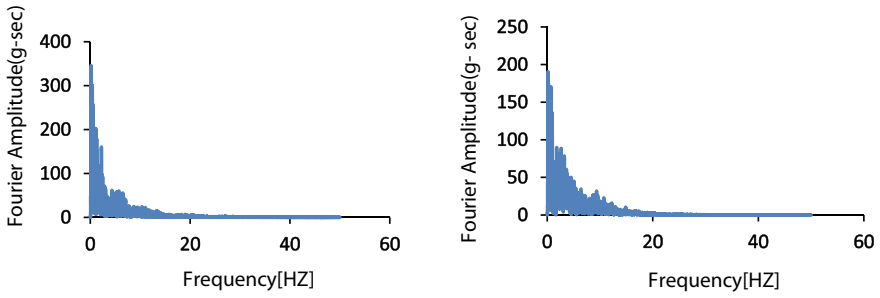
Fig. 3 FFT's of Taiwan at station: **a** NSY, **b** TCU06
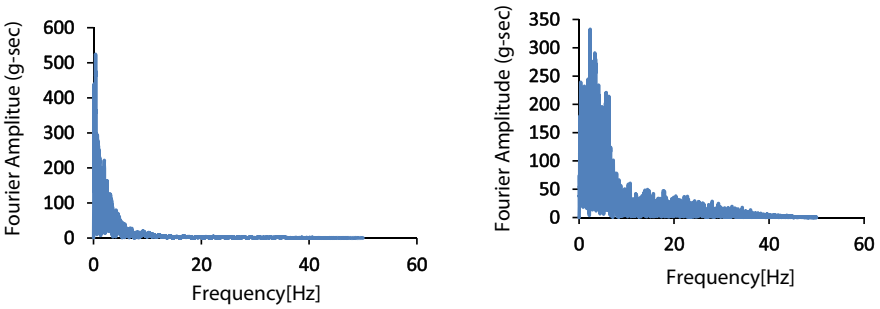
Fig. 4 FFT's of Taiwan at station: **a** TCU101, **b** TCU068
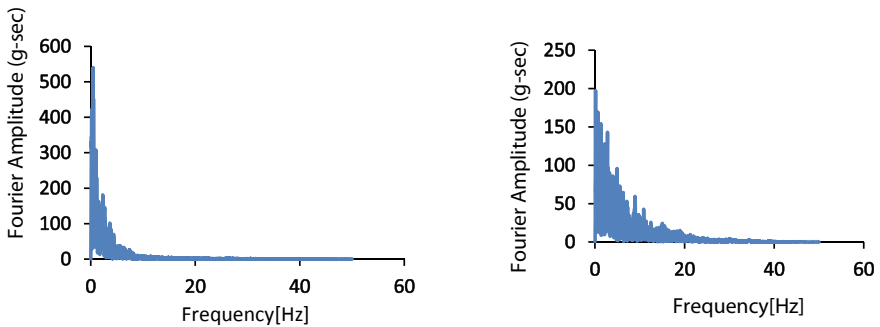
Fig. 5 FFT's of Taiwan at station: **a** TCU052, **b** TCU063

5 Continuous Wavelet Transforms of Recorded Ground Motion

In this paper, continuous wavelet transformation (CWT) is used to study the time varying frequency content, as it is known that earthquake ground motions are non-stationary, while Fourier transformation is idle for stationary signals [11]. The CWTs

are well localized in time and frequency, and are used to obtain a time–frequency analysis of any seismic wave. CWTs provide an improved representation of the damage potential of strong ground motions [12]. Mathematically, the wavelet transform of ground motion is represented by

$$F(\tau, s) = \frac{1}{\sqrt{|s|}} \int_{-\infty}^{\infty} F(t)\varphi * \left(\frac{t - \tau}{s}\right) dt \qquad (3)$$

where $\psi(t)$ is the called mother wavelet, * is the complex conjugate, $F(\tau, s)$ are CWT coefficients. Here, 'τ', and 's' are translation and dilation parameters, respectively. CWT analysis is carried out using the standard wavelet MATLAB toolbox. The continuous wavelet transforms (CWT), gives information on the time and frequency content of non-stationary data, while accounting for temporal and spectral non stationary of ground motion [13]. Since earthquake ground motion are non-stationary, they are easily represented by wavelets than sine waves. The CWT is used to analyze the changing time-period characteristics of ground motion. Analytical wavelet analysis is best suited for performing CWT analysis. The CWTs are obtained using MATLAB software using the default scaled morse wavelet along with the acceleration- time history of the original length of recorded ground motion, resulting in coefficient which are a function of wavelet scale and shift parameters. Figures 6, 7, 8 and 9 corresponds to pulse like ground motion [14]. The CWTs helps to identify the frequency distribution, time period and distribution of energy over flux. The large amplitude of the wavelet plunges for a short period of time, as shown in Figures 6, 7, 8 and 9, and the high-frequency contents attenuate more quickly. Such type of representation usually corresponds to pulse like ground motion [13] The Fig. 6a shows the CWT output in time and period, which are color-coded. The white line represents the cone of influence (COE), within which the results are accurate and reliable. It can be observed that the dominant frequency follows a different pattern at different stations. Figures 6 and 7 shows multiple dominant frequency plunge over the same period (sec) for a long duration, causing permanent damage to the structure. Sustained frequencies can be attributed to the fling step effect (large-amplitude, monotonic step in the displacement time history) at these stations. Figure 8 represents the arrival of multiple seismic waves with time periods in increasing order, i.e. the dominant frequencies arrive in the decreasing order. Figure 9 represents the arrival of dominant seismic pulses with time periods observed in the decreasing order, and that indicates that the frequencies arrive at the station in the increasing order. When a building or a structure is struck by the high amplitude seismic waves, the stiffness of the system decreases, thus increasing its natural time period (or decreasing its natural frequency) and making it more vulnerable for damage to seismic waves which exhibit arrival of high amplitude waves in increasing order of time periods (or decreasing order of frequencies).
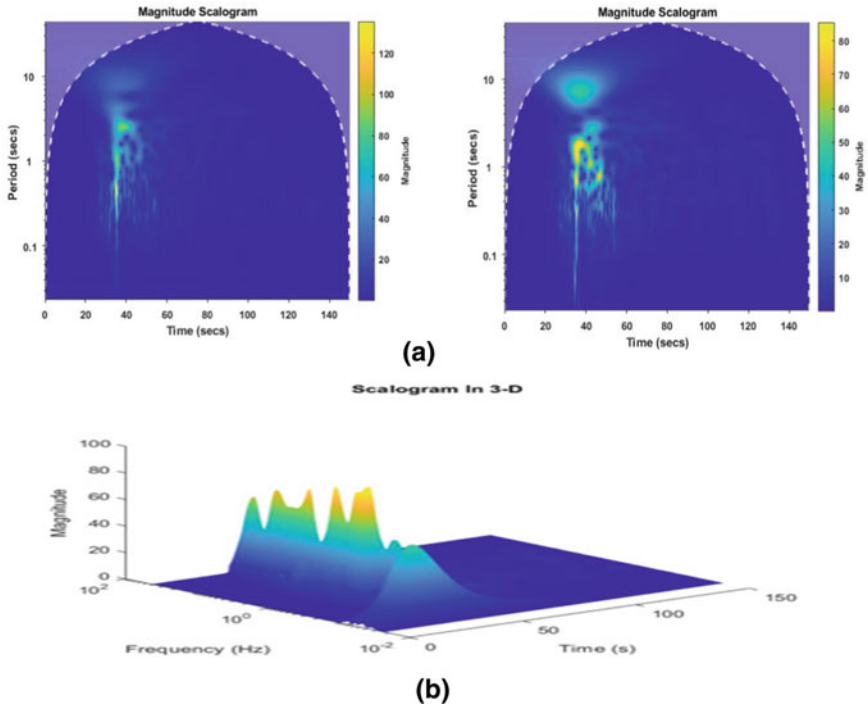
Fig. 6 CWT's of station TCU068: **a** radial, transverse **b** 3-D representation of CWT of transverse component from station TCU068
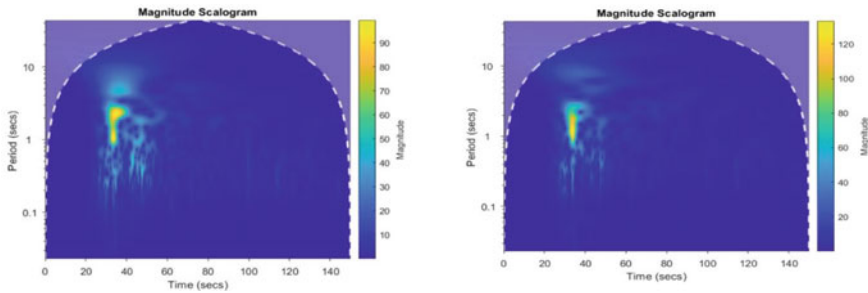
Fig. 7 CWT's of station TCU052: **a** radial, **b** transverse

6 Conclusion

Earthquake ground motions can be characterized by different parameters which are often hidden in the time domain analysis. To understand these characteristics, an attempt has been made in this paper by analyzing ground motions from the 1999 Chi-Chi earthquake, in the frequency domain using fast Fourier Transforms (FFTs)
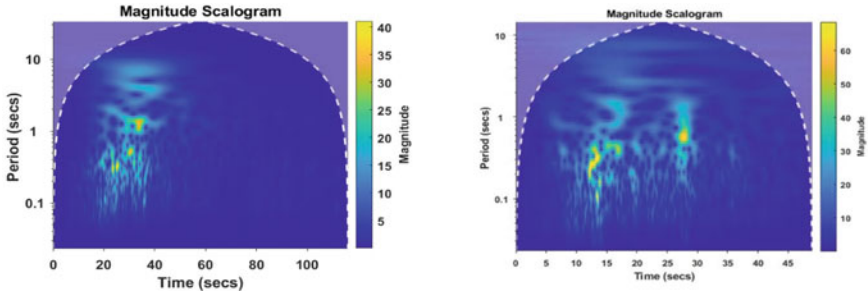
Fig. 8 CWT's of station: **a** NSY, **b** TCU101
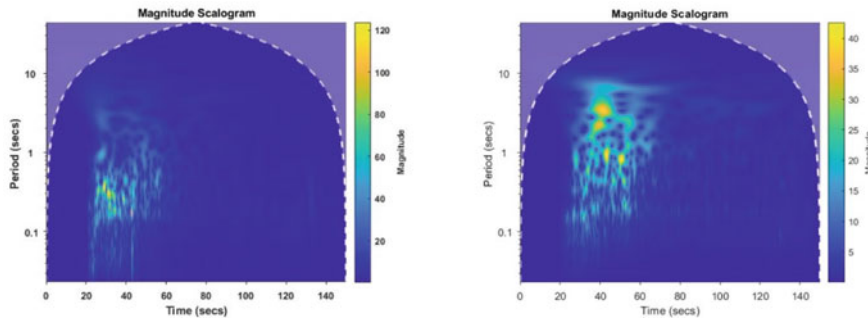
Fig. 9 CWT's of stations TC063: **a** radial, **b** transverse

and continuous wavelet transforms (CWTs). It was observed that FFTs do not efficiently represent the abrupt changes, that are often observed in seismic waves, as they are not well localized in time and frequency. The damage potential of ground motions are better represented by CWTs, which are well localized in time and frequency, thereby providing a much-improved representation of the variation in seismic damage potential. Different variety of sequences of arrivals of damaging frequencies were observed at the various near field stations, with some ground motions exhibiting high amplitude damaging frequencies recurring at multiple instants of time, while other ground motions exhibited a clear increasing or decreasing trend of the arrival of such frequencies.

References

1. Tsai KC, Hsiao CP, Bruneau M (2000) Overview of building damages in 921 Chi-Chi earthquakes. Earthq Eng Eng Seismol 2.1: 93–108
2. Hsu YT, Fu CC (2004) Seismic effect on highway bridges in Chi Chi earthquake. J Perform Constr Facil 18(1):47–53
3. Shin T-C, Teng T-L (2001) An overview of the 1999 Chi-Chi, Taiwan, earthquake. Bull Seismol

Soc Am 91(5):895–913

4. Juang C, Hsein et al. (2005) Liquefaction in the Chi-Chi earthquake-effect of fines and capping non-liquefiable layers. Soils Found 45.6:89–101

5. Kramer SL (1996) Geotechnical earthquake engineering. Prentice-Hall

6. Nuttli OW (1979) "The relation of sustained maximum ground acceleration and velocity to earthquake intensity and magnitude. Miscellaneous Paper S-71–1, Report 16, U.S. Army Corps of Engineers, Waterways Experiment Station, Vicksburg, Mississippi

7. Guaman JW (2010) Empirical ground motion relationship for maximum incremental velocity, Master's Thesis, University of Notre Dam

8. Hancock J, Bommer J (2005) The effective number of cycles of earthquake ground motion. Earthq Eng Struct Dyn 34:637–664

9. Liu SC, Fagel LW (1973) A fast Fourier transform approach to earthquake soil-structure interaction problems. In: Proceedings of the 5th world conference on earthquake engineering

10. Mallat SG (1989) A theory for multiresolution signal decomposition: the wavelet representation. IEEE Trans Pattern Anal Mach Intell 11(7):674–693

11. Gabor D (1946) Theory of communication Part 1: the analysis of information. J Inst Electr Eng Part III Radio Commun Eng 93(26):429–441

12. Ifan, MA, Mathew S, Vemuri J (2022) Wavelet analysis of far-field ground motions from the M w 7.6 2005 Kashmir Earthquake. Recent advances in earthquake engineering, Springer, Singapore, pp 11–23

13. Antoniou S, Pinho R (2004) Seismosignal: a computer program for signal processing of strong-motion data. Technical Report 4.0. 0. Pavia, Italy: SeismoSoft

14. Mangalathu S, Jeon J-S (2020) Ground motion-dependent rapid damage assessment of structures based on wavelet transform and image analysis techniques. J Struct Eng 146(11):04020230

15. Kardoutsou V, Taflampas I, Psycharis IN (2017) A new pulse indicator for classification of ground motions. Bull Seismol Soc Am 107(3):1356–1364

Comparison Study of Concrete Constitutive Models in ABAQUS for Evaluating Impact Force Under Low Velocity Impact Loading

K. Senthil and Rachit Sharma

1 Introduction

Reinforced concrete structure might get endangered in their time span to any kind of extreme loading because of impacts. Typical examples of low velocity impacts include conveyance structures exposed to vehicular crash impact; offshore structures exposed to hail impact, protective structures under air borne impacts, and civil structures exposed to debris from natural disasters [1]. In recent years, it is very important to make critical evaluations on RC structural performance and vulnerability under impact loadings. Thus, engineers are tending to numerical models to accomplish design, evaluation and critical checks for safeguarding these structures.

Experimental studies performed over a wide array of high contact velocities ranging 150–1000 m/s with steel projectiles by Hanchak et al. [2], Dancygier and Yankelevsky [3]. Past studies revealed that reinforced concrete slabs under ballistic impact resulted in localized damage to structure at impact location [4]. There were several analytical formulas accessible to predict localized effects such as perforation, penetration, scabbing and spalling of concrete [5]. Although their approaches provide good validation for local effects under ballistic impact; however, their efficiency for predicting the global response of structure is considerably less. The global response of structure can be largely affected by the local response such in case low velocity impact. Under low velocity impacts, localized shear failure are prominent modes of failure which can adversely affect the global response of the structure [6]. Because of the inability to accurately predict the global behaviour of structure, numerical models are widely used for evaluating the response of reinforced concrete structures. Several material models have been used by various software packages such

K. Senthil (✉) · R. Sharma
Department of Civil Engineering, National Institute of Technology Jalandhar, JalandharPunjab 144011, India
e-mail: urssenthil85@yahoo.co.in; kasilingams@nitj.ac.in

as ABAQUS, LS-Dyna and ANSYS; however, these material models are applicable under scenarios and governed by a particular behaviour.

Reinforced concrete under low velocity impact differs from quasi-static loadings where inertial effects and rate effects gets prominent, and enhancement is material properties are observed at high loading rates [7]. Modelling of heterogeneous models is quite complex, and most of the times a homogeneous approach is followed. Further, the testing of material under high loading rates for structural elements is quite expensive and several factors are there such which can affect the accuracy of the model over experimental results. Experimental studies under low velocity impacts were studied by several researchers [8–10] using different test setups which were further validated using finite element models. The prediction in terms of impact force was done to access the viability of structure towards low velocity impacts. Izzat et al. [11] conducted experimental investigations on impact between concrete slab and steel I-section. Excellent agreements for results of acceleration and impact velocity plots were found between experiment and numerical study performed using LS-Dyna, and steel sections were proposed for limiting the perforation of RC floor slabs because of accidental drops. For impact problems, brittle material such as concrete shows different damage mechanisms depending upon the loading path were seen as concrete flexural cracking and punching shear at the face of the impact. A material model should be able to accurately describe the material behaviour under low and high confining pressures [12].

ABAQUS offers several material models for modelling concrete behaviour. Kezmane et al. [13] employed concrete damage plasticity (CDP) model to reproduce the experimental results of reinforced concrete slabs with yielding supports; however, more sophisticated approach was highlighted for the problem. Iqbal et al. [8] studied impact response of prestressed RC plates under large mass impactor, and material model Holmquist–Johnson–Cook (HJC) was incorporated. The model was able to predict the impact force and displacement, although it was stressed that a very fine mesh was obligatory to strengthen accuracy in the model. The brittle cracking model has been used for comparison with CDP model for missile perforation, and it was found that brittle cracking model does not seem suitable to model impacts as several distorted elements were found in the simulation and there was no evidence of stress propagation through the slab [14].

The present study deals with the comparison of constitutive models available in ABAQUS to evaluate impact force under low velocity impact. To the best of author's knowledge such study was not found in the past literature, and it will be an important aspect to model the behaviour of RC structures under low velocity impact considering different material models. Section 1 contains the introduction of the problem and earlier studies pertaining to missile impact. Section 2 highlights the various models present in ABAQUS/EXPLCIT and modelling parameters taken. Section 3 constitutes experimental setup of Chen and May [1] slab and numerical modelling. Section 4 highlights the numerical result and advantages and drawbacks of different material models. Section 5 includes the references.
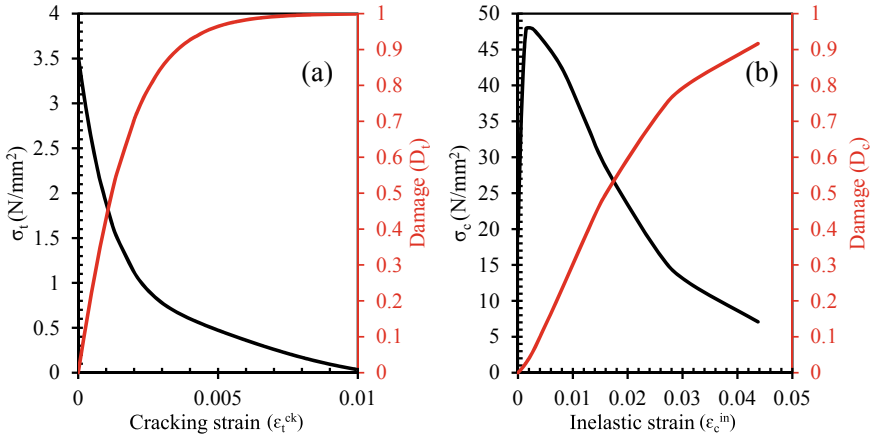
Fig. 1 Behaviour of concrete in **a** tension for brittle cracking/CDP model and **b** compression for CDP model

2 Material Models

2.1 Cracking Model for Concrete

The cracking model uses smeared crack approach for characterizing concrete discontinuities. The crack is initiated using Rankine criterion asserting that crack formation take place when max principal stress goes beyond the material tensile strength. It assumes that there is no permanent cracking strain, i.e. complete crack closure happens upon stress reversals to compressive strain. Crack formation is purely on Mode I fracture energy; however, model has also considerations for Mode II (shear softening) behaviour. The tensile stress–strain behaviour was described in Fig. 1a. The Mode II shear considerations are based on conventional opinion that shear behaviour characterized by the measure of crack opening and is defined by stating post cracking shear modulus, G_c as a fraction of uncracked shear modulus. The value for shear retention factor was taken as 0.01 for a plastic strain of 0.05. The brittle failure was introduced for element deletion by giving a value of 0.05.

2.2 Concrete Damage Plasticity Model

The concrete damage plasticity model utilizes notion of isotropic damaged elasticity in tension and compression for representing concrete inelastic behaviour. The strain hardening can be described in compression and tension as well as strain rate sensitivity, thus resembling the impact phenomenon more realistically. The model was developed by Lubliner et al. [15] and later adapted by Lee and Fenves [16] for

Table 1 Parameters of CDP model

K_c	Ψ	f_{b0}/f_{c0}	$\in$
0.67	31	1.16	0.1

dynamic and cyclic loading. The behaviour of concrete was based on the parameters given by Alfarah et al. [17] making it mesh insensitive. The uniaxial compression and tension behaviour was illustrated in Fig. 1a, b, respectively. The isotropic damage characterized by different evolutions in tension and compression were shown in Fig. 1a, b. Other constraints of CDP model were tabulated in Table 1. The parameter controls the multi axial behaviour of concrete under different confining pressures and loading conditions.

2.3 Holmquist–Johnson–Cook (HJC) Model

The model is based on elasto-viscoplastic combined with isotropic damage. The model considers the effect of strength of concrete, strain hardening and equation of state (EOS), material degradation as well as strain rate effects. The material model [18] comprises the following components: (1) deviatoric strength using pressure-shear strength relationship, (2) damage description to transit material to fractured condition and (3) an EOS for pressure-density relation together with compaction properties. The material model consists of 19 different parameters to define concrete behaviour over wide strain rates. The material parameters for EOS have been taken from the original paper [18, 19]. The material parameters have been shown in Table 2. The value of $\overline{\varepsilon}^{pl}_{f,max}$ was chosen to limit the maximum value of plastic strains based on trails. The failure strain was chosen a value of zero because hardly any projectile penetration was observed in the experiment and removal of elements from the simulation will generate negative plastic strains.

Table 2 HJC material parameter for concrete

ρ_0 (kg/m^3)	G (GPa)	A	B	N	f_c (MPa)	C	$\dot{\varepsilon}_0$
2440	14.86	0.79	1.60	0.61	48	0.007	1×10^{-3}
T (MPa)	S_{max}	P_{crush} (MPa)	μ_{crush}	P_{lock} (MPa)	μ_{lock}	D_1	D_2
4	7	16	0.001	800	0.1	0.04	1
$\overline{\varepsilon}^{pl}_{f,max}$	$\overline{\varepsilon}^{pl}_{f,min}$	FS	K_1 (GPa)	K_2 (GPa)	K_3 (GPa)		
1	0.01	0	85	-171	208		

Table 3 JH-2 material parameters for concrete

ρ_0(kg/m³)	G(GPa)	A	B	N	M	C	$\dot{\varepsilon}_0$
2440	14.86	0.79	1.65	0.0001	0.76	0.007	1×10^{-3}
T (MPa)	$\sigma_{I,\max}$	$\sigma_{f,\max}$	HEL (MPa)	P_{HEL} (MPa)	β	D_1	D_2
2.93	0.80	11.7	480.47	448.47	1	0.03	1
$\bar{\varepsilon}^{pl}_{f,\max}$	$\bar{\varepsilon}^{pl}_{f,\min}$	FS	K_1 (GPa)	K_2 (GPa)	K_3 (GPa)	1 Damage	
1	0.016	0	85	−171	208	0	

2.4 Johnson and Holmquist (JH-2) Model

The model is developed for characterizing ceramics and other brittle materials. It is intended to reproduce the mechanical response and failure behaviour of brittle materials exposed to significant strains, high pressure, and strain rates. The JH-2 model has three primary constituents (1) deviatoric strength using pressure-shear strength relationship, (2) damage description to transit material to fractured condition and (3) an EOS for pressure-density relation together with compaction properties and dilation (or bulking) effects. The material parameters have been shown in Table 3. The material parameters have been taken from original paper [18, 20]. The value of HEL was calculated from the equation proposed by Rosenberg [20] as 480.47 MPa. The value of $\sigma_{\text{HEL}} = 48$ MPa was chosen to calculate the value of P_{HEL}. The value of T was modified to 2.93 MPa in this study to increase the prediction accuracy. The 1 Damage variable was given a value zero to allow progressive damage in the model [22].

The constitutive model for rebar was isotropic elasto-plastic behaviour. The rebar yield strength was 560 MPa, and the plastic yield strength was 610 MPa. The ductile damage initiation criteria were used with value of fracture strain as 0.117 corresponding to stress triaxiality of 0.333. The rate dependency was Cowper–Symonds with the value of power and exponent as 5 and 40 [23].

3 Experimental Setup and Numerical Modelling

A sequence of well-defined drop weight tests was executed by Chen and May [1] to build a comprehensive basis for confirmation via finite element simulations. The purpose of this study was to evaluate different concrete models to calculate the structural reaction in terms of contact force. In the test setup, four 760 mm², 76 mm thick and two 2320 mm², 150 mm thick slabs were assessed under free falling weight of up to 380 kg and velocities of up to 8.7 m/s. The experimental campaign is illustrated in Fig. 2. The test data was recorded for time histories of impact force, acceleration and strain in rebar. Further, details were given in [1]. For this study, slab no. 5 in the experimental campaign with a concrete cube compressive strength of
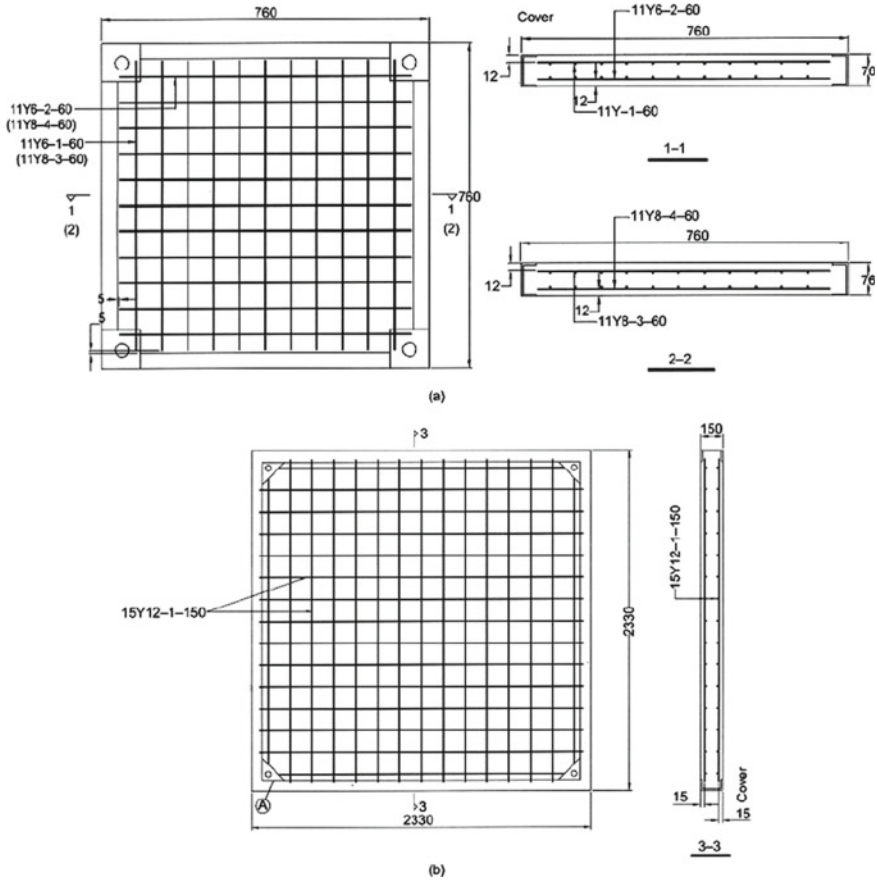
Fig. 2 Details of the slabs: **a** 760 × 760 mm slab and **b** 2330 × 2330 mm slab (All dimensions are in mm)

47.3 N/mm^2 was selected. The slab size was 2320 mm^2 with 150 mm thickness impact with a hemispherical impactor with a mass of 196.7 kg at an impacting velocity of 8.7 m/s. The recorded acceleration was filtered using Butterworth low pass filter with 2000 Hz cutting frequency.

The numerical model has Lagrangian description for the motion. The concrete slab was discretized with C3D8R elements. An aspect ratio of one was maintained for the concrete elements. One-point gauss integration and relax stiffness hourglass modes were exercised. Rebar was discretized as two node 3D truss elements. The embedded constraint was enforced to link truss elements with host elements, see Fig. 3b. The supports and impactor were modelled as discrete rigid parts with mass inertia applied to them. The impactor was given a mass of 196 kg, and a velocity of 8.7 m/s was applied to it. Kinematic surface to surface contact with finite sliding was used for interaction among the impactor and the deformable slab. The tangential
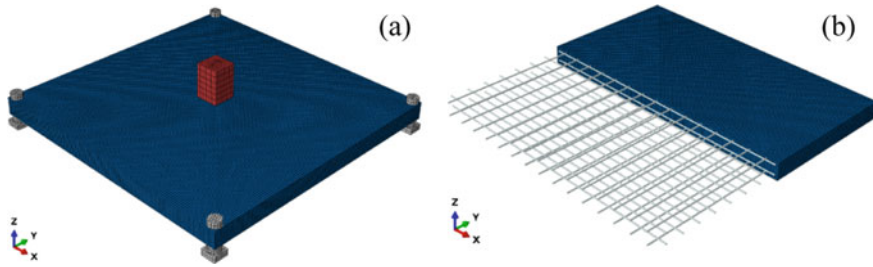
Fig. 3 Finite element model of slab no. 5, **a** assembly and **b** embedded reinforcement

behaviour was defined using Coulomb's law with a coefficient of friction as 0.3 and normal HARD behaviour was used. The supports were tied to the concrete slab such that movement was restricted in all six axes at the supports. A typical mesh model for the assembly was illustrated in Fig. 3a.

Mesh convergence study was presented to reduce mesh sensitivity in the model. A mesh size of 50, 40, 30, 25, 20 and 15 mm was used. The numerical result obtained from mesh sizes was evaluated with actual results for peak impact force and the proportion of disparity among the experimental and numerically computed results. The mesh size results were shown for 3, 4, 5, 6, 8 and 10 number of through thickness elements. The CDP model was used to verify the mesh sensitivity. The results were shown in Fig. 4. It was observed that percentage error in peak force prediction was decreased from 32.54 to 0.33% on increasing the through thickness elements from 3 to 8 and was further increasing to 3.75% for 10 through thickness elements. The reason for the same was that the behaviour of CDP model was input such that the model become mesh insensitive for a characteristic length of element as 20 mm.

Fig. 4 Mesh convergence study
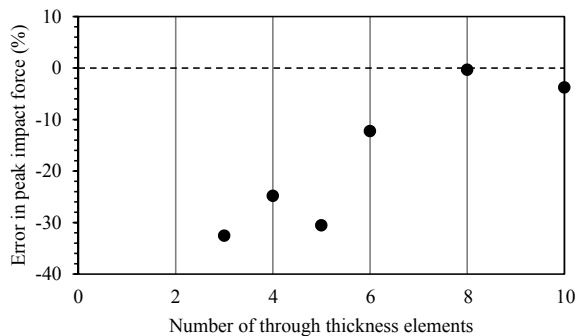
4 Results and Discussions

The models were evaluated for low velocity impact under large mass impactor. The mesh size was kept at 20 mm for all the simulations. The slab showed in experimental results as local damage occurring to the slab, while no perforation of slab occurred. The concrete smear cracking model is not accessible in ABAQUS/EXPLICIT, therefore, was not used in the study. The damage contour for the front and rear side of the slab specimen were shown in Fig. 5I-(a–d). The brittle cracking model in has no option for crack visualization. Altogether, the models were able capture the front scabbing of the RC slab. CDP model was able to accurately capture the global slab response as other model HJC and JH-2 showed highly localized damage at the front. The HJC and JH-2 material models were made for high strain rates such as under bullet impacts. Because of some limitations in HJC and JH-2 model such as tensile stiffness degradation and constant tensile hardening behaviour after peak stress, the material model is made to simulate concrete under highly localized confining pressures. The degradation at the rear side of the slab was evaluated for different material models was illustrated in Fig. 5II-(a–d). The CDP model showed best back face tensile damage pattern because of the incorporation of tensile stiffness degradation and stress reversals in the model. The HJC model because of the constant tensile function the material model shows only shear cracks and no tensile cracks. The HJC model only considers the effects of pressure-shear relationship via von Mises equivalent stress and was unable to correctly capture shear response [24]. The JH-2 model was also built with same strength function, wherein the tensile behaviour does not include stress reversals and strain rate effects.

The impact force predicted by various models is illustrated in Fig. 6. The brittle cracking model predicted peak impact force at 1477.84 kN as compared to experimental value of 582.42 kN. The model overestimated the impact force by quite a large margin. The brittle cracking model incorporates tensile stiffness degradation as well as considerations for Mode II failure using shear retention model. However, the
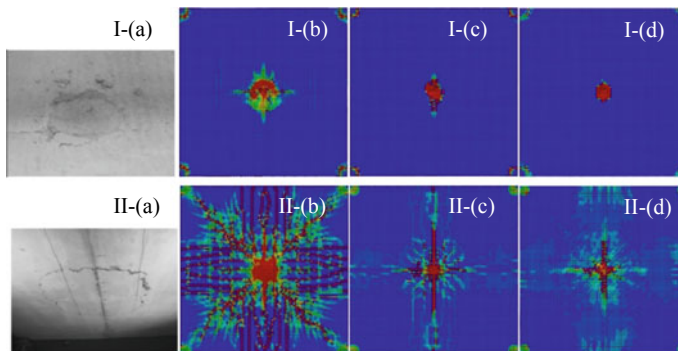
Fig. 5 Damage contours at the (I) front and (II) back face of the specimen for **a** experiment, **b** CDP model, **c** HJC model and **d** JH-2 model
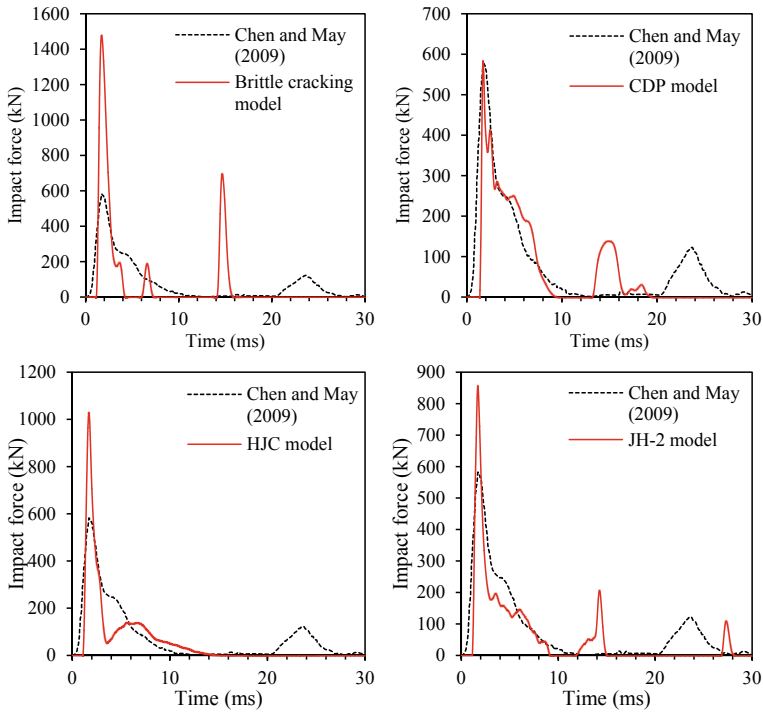
Fig. 6 Impact force prediction for different material models with experimental results

brittle cracking model considers purely elastic response for compression behaviour. Therefore, under low velocity impact where inertial forces play a major role because of absence of stiffness degradation in compression, an overestimated response was observed. The difference in peak impact force prediction can be reduced by considering a no linear compressive behaviour into the model using VUSDFLD subroutine [24]. The peak impact force predicted using CDP model was 584.348 kN with only a percentage difference of 0.33%. Good correlation was obtained for impact force–time response using CDP model. The consideration of different damage modulus for compression and tension enables the model to accurately capture the response under low velocity impact. The HJC model predicted the peak impact force at 1029.27 kN with a percentage difference of 76%. The tensile behaviour of concrete in HJC model is simply based on maximum tensile hydrostatic pressure. Also, using original HJC model strength parameters, the uniaxial compressive strength is found to overestimate by about 45% and 450% for uniaxial and biaxial compression, respectively [23]. Therefore, for accurate prediction using HJC model requires introduction of third stress invariant to differentiate the tensile and compressive meridian. Another approach was to reduce the mesh size considerably and introducing premature failure of elements can result in lower impact force generation; however, such method is not physically sound [8]. For JH-2 material model due to modifications in tensile

strength to 2.93 MPa and addition of continuous strength deterioration effects to explain descent failure in concrete material, a more precise behaviour can be obtained by refining the mesh at the impact zone. Because of large number of parameters used for describing the behaviour of HJC and JH-2 models, the testing procedures are quite expensive for accurately calibrating these models.

5 Conclusions

Based on detailed numerical study the following conclusions can be drawn:

- The brittle cracking material model is not suitable for low velocity impact because of constantly hardening compressive behaviour. The impact forces were highly overestimated. The visualization of cracks is also not possible in the model.
- The CDP model is best suited for low velocity impacts because of different stiffness degradation functions in compression and tension.
- The HJC model has pressure-shear strength function and a constant hydrostatic tensile function, therefore, modifications are required in third stress invariant and strain rate functions before it can be used for low velocity impact.
- The JH-2 model considers damage degradation when undergoing damage; however, the HEL parameters is based on net compressive strength and no consideration on tensile damage degradation was given. Also, the material model is more suited under extreme localized loadings.
- Considerable mesh refinement at the impact zone can maybe enable the HJC and JH-2 material model to accurately predict the behaviour under low velocity impact.

References

1. Chen Y, May IM (2009) Reinforced concrete members under drop-weight impacts. Proc Inst Civ Eng Struct Build 162(1):45–56. https://doi.org/10.1680/stbu.2009.162.1.45
2. Hanchak SJ, Forrestal MJ, Young ER, Ehrgott JQ (1992) Perforation of concrete slabs with 48 MPa (7 ksi) and 140 MPa (20 ksi) unconfined compressive strengths. Int J Impact Eng 12(1):1–7. https://doi.org/10.1016/0734-743X(92)90282-X
3. Dancygier AN, Yankelevsky DZ (1996) High strength concrete response to hard projectile impact. Int J Impact Eng 18(6):583–599. https://doi.org/10.1016/0734-743X(95)00063-G
4. Kasai Y, Tsubota H, Ohno T, Kogure K, Uchida T (1992) Experimental study on impact resistance of reinforced concrete slabs with thin steel plates against projectile impact. In: Proceedings of international symposium impact, pp 211–216
5. Li QM, Reid SR, Wen HM, Telford AR (2005) Local impact effects of hard missiles on concrete targets. Int J Impact Eng 32(1–4):224–284. https://doi.org/10.1016/j.ijimpeng.2005.04.005
6. Williams MS (1994) Modeling of local impact effects on plain and reinforced concrete. ACI Struct J 91(2):178–187. https://doi.org/10.14359/4603
7. Abrams DA (1917) Effect of rate of application of load on the compressive strength of concrete. Proc ASTM 17:364–365

8. Iqbal MA, Kumar V, Mittal AK (2019) Experimental and numerical studies on the drop impact resistance of prestressed concrete plates. Int J Impact Eng 123(May 2018):98–117. https://doi.org/10.1016/j.ijimpeng.2018.09.013

9. Xiao Y, Li B, Fujikake K (2016) Experimental study of reinforced concrete slabs under different loading rates. ACI Struct J 113(1):157–168. https://doi.org/10.14359/51688067

10. Senthil K, Kubba Z, Sharma R, Thakur A (2021) Experimental and numerical investigation on reinforced concrete slab under low velocity impact loading. In: IOP conference series: materials science and engineering, vol 1090, no 1, p 012090. https://doi.org/10.1088/1757-899X/1090/1/012090

11. Izatt C, May IM, Lyle J, Chen Y, Algaard W (2009) Perforation owing to impacts on reinforced concrete slabs. Proc Inst Civ Eng Struct Build 162(1):37–44. https://doi.org/10.1680/stbu.2009.162.1.37

12. Hrynyk TD, Vecchio FJ (2017) Modeling of reinforced and fiber-reinforced concrete slabs under impact loads. Am Concr Inst ACI Spec Publ 321:118–137

13. Kezmane A, Chiaia B, Kumpyak O, Maksimov V, Placidi L (2017) 3D modelling of reinforced concrete slab with yielding supports subject to impact load. Eur J Environ Civ Eng 21(7–8):988–1025. https://doi.org/10.1080/19648189.2016.1194330

14. Martin O (2010) Comparison of different constitutive models for concrete in ABAQUS/explicit for missile impact analyses. JRC Scientific and Technical Reports

15. Lubliner J, Oliver J, Oller S, Oñate E (1989) A plastic-damage model for concrete. Int J Solids Struct 25(3):299–326. https://doi.org/10.1016/0020-7683(89)90050-4

16. Lee J, Fenves GL (1998) Plastic-damage model for cyclic loading of concrete structures. J Eng Mech 124(8):892–900. https://doi.org/10.1061/(ASCE)0733-9399(1998)124:8(892)

17. Alfarah B, López-Almansa F, Oller S (2017) New methodology for calculating damage variables evolution in plastic damage model for RC structures. Eng Struct 132:70–86. https://doi.org/10.1016/j.engstruct.2016.11.022

18. Holmquist TJ, Johnson GR, Cook WH (1993) A computational constitutive model for concrete subjected to large strains, high strain rates and high pressures. J Appl Mech 78(5):051003. https://doi.org/10.1115/1.4004326

19. Lu G, Li X, Wang K (2012) A numerical study on the damage of projectile impact on concrete targets. Comput Concr 9(1):21–33. https://doi.org/10.12989/cac.2012.9.1.021

20. Oucif C, Kalyana Rama JS, Shankar Ram K, Abed F (2021) Damage modeling of ballistic penetration and impact behavior of concrete panel under low and high velocities. Def Technol 17(1):202–211. https://doi.org/10.1016/j.dt.2020.03.013

21. Rosenberg Z (1993) On the relation between the Hugoniot elastic limit and the yield strength of brittle materials. J Appl Phys 74(1):752–753. https://doi.org/10.1063/1.355247

22. Mendonça FB, Urgessa GS, Augusto AS, Rocco JAFF (2020) Experimental records from blast tests of ten reinforced concrete slabs. Civil Eng 1(2):51–74. https://doi.org/10.3390/civileng1020005

23. Børvik T, Dey S, Clausen AH (2009) Perforation resistance of five different high-strength steel plates subjected to small-arms projectiles. Int J Impact Eng 36(7):948–964. https://doi.org/10.1016/j.ijimpeng.2008.12.003

24. Polanco-Loria M, Hopperstad OS, Børvik T, Berstad T (2008) Numerical predictions of ballistic limits for concrete slabs using a modified version of the HJC concrete model. Int J Impact Eng 35(5):290–303. https://doi.org/10.1016/j.ijimpeng.2007.03.001

25. Vinlay M, Chernin L, Cotsovos DM (2014) Advanced material modelling of concrete in Abaqus. In: 9th International Concrete Conference: Environment, Efficiency and Economic Challenges for Concrete. At University of Dundee

Influence of Dry Lime Sludge on the Physico-mechanical and Microstructural Properties of Low Carbon Cementitious Composites Exposed at Elevated Temperature

Chandra Shekhar Sharma and Rajesh Kumar

1 Introduction

Globally, cement mortar has been widely used for plastering works to provide a uniform surface on brick or concrete elements of various structures [1]. The purpose of plastering is to provide a better appearance as well as a base for the paint to take [2]. Although cement plaster is not considered a part of structural elements, as it is required to meet the requirements of strength and durability as per Indian Standard Code 2250:1981. Nowadays, lime sludge has been used in mortars as a replacement material for cement and fine aggregates [3–5]. It is used in various forms in a mortar [6–9]. Exposure to elevated temperatures significantly affects the performance of masonry structures since mortar is not stable at high temperatures. Mortar heated up to 200 °C ± 5 °C does not significantly lose strength, and cement mortar can recover any strength loss through rehydration. However, in the temperature range between 250 °C ± 5 °C and 550 °C ± 5 °C, calcium hydroxide (CH) decomposes into lime and water. The C-S-H gel completely dehydrates and decomposes in the range of 600–800 °C ± 5 °C. The mechanical performance of lime sludge mortar worsens at elevated temperatures [10, 11]. The presented paper studies the effect of dry lime sludge on the physico-mechanical and microstructural properties of cement mortar exposed at elevated temperature.

C. S. Sharma · R. Kumar (✉)
Organic Building Materials (OBM) Group, CSIR-Central Building Research Institute, Roorkee, India
e-mail: rajeshkumar@cbri.res.in

Table 1 Physical characteristics of class F fly ash

Properties	Class F fly ash
Blain's fineness (m^2/kg)	489
Bulk density (kg/m^3)	2310
Bulk specific gravity	2.19
Lime reactivity index	0.82

Table 2 Chemical composition of class F fly ash

Chemical	SiO_2	Al_2O_3	Fe_2O_3	TiO_2	CaO	MgO	K_2O	Na_2O	SO_3	LOI
Content %	55	26	6.5	1.75	4.46	1.85	1.9	0.76	2.78	2

2 Materials and Composition

The raw materials used to develop CALS mortar composites are given below along with their physico-mechanical and chemical characterization:

2.1 Fly Ash

Class F fly ash was used in this study was obtained from M/s. Roza Thermal power plant district-Shahjahanpur Utter Pradesh, India. It consists pozzolanic behaviour in nature and contains less than 10% lime (CaO), which required a chemical activator such as sodium silicate to develop it as cementitious material. Physical and chemical characteristics of fly ash are given in Tables 1 and 2.

2.2 Lime Sludge

The lime sludge used in this study was procured from M/s. K.R. Paper Mill, Shahjahanpur, Utter Pradesh. The collected lime sludge was used as the fine aggregates in the lime sludge mortar. The physico-chemical properties of lime sludge waste are given in Tables 3 and 4. Calcium oxide content was observed as 74.6% which was major compound also in the lime sludge.

Table 3 Physical characteristics of raw lime sludge

Property	Value
Colour	White
Specific gravity	1.79
Water content	48%
pH	11.92
Refractivity	1.59

Table 4 Chemical composition of lime sludge

Chemical composition	Percentage (%) In lime sludge
SiO_2	6.0
Al_2O_3	3.25
Fe_2O_3	1.8
CaO	74.6
MgO	6.48
SO_3	5.54
Na_2O	2.0
P_2O_5	0.25
LOI (loss of ignition)	28

2.3 Ordinary Portland Cement (OPC)

This study used ordinary Portland cement (OPC)-43 grade for all specimens, confirming IS–8112. The physical properties of 43 grade OPC cement were, viz. standard consistency 31%, specific gravity −3.15, initial setting −90 min, final setting time −242 min, fineness −348 m^2/kg, and 28 days compressive strength 47.6 MPa. Figure 1 shows particle size distribution of PFA and cement. Mean particle size of PFA and cement was 6.11 and 19.03 μm, respectively, which shows that PFA particles are finer than OPC.

2.4 Fine Aggregate

Dark grey fine aggregate (second zone) was used in CLAS mortar for the preparation of lime sludge (CALS)-mortar mixes, confirming to IS: 383-2016. Fineness modulus was determined as 2.35. River sand consisted unit weight of 1535 kg/m^3, specific gravity of 2.63, and water absorption of 2.74%.
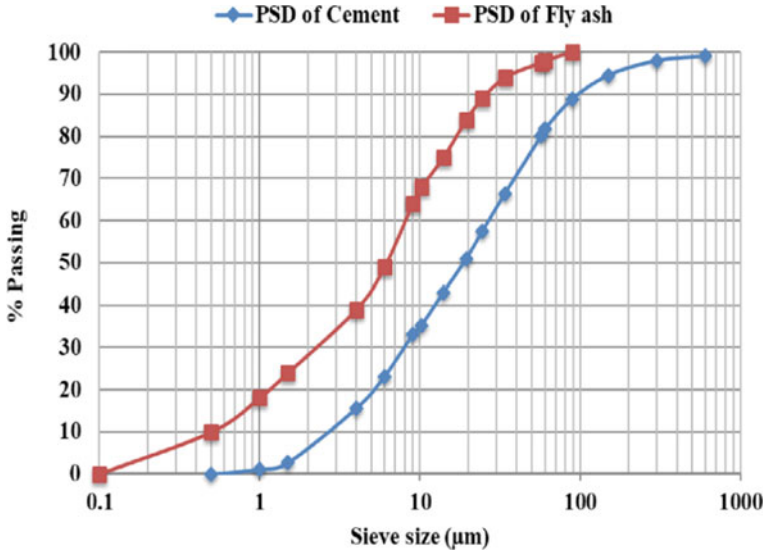
Fig. 1 Particle size distribution of OPC and class F fly ash

2.5 Chemical Activator and Admixture

As a chemical activator, to develop CALS mortar; sodium hydroxide (NaOH), and hydrogen peroxide (H_2O_2) were used. As a water reducer agent, polycarboxylated ether (PCE)-based super-plasticizer (SHALIPLAST-PEC-200) was used.

3 Experimental Programme

The mix proportion of CALS mortar mix is given in Table 5. The methodology to prepare CALS composite mortar mix is shown in Fig. 2. After weighing the raw materials, OPC was partially replaced with lime sludge in $(50 \times 50 \times 50)$ mm cubical mould specimens. The first step was the activation of lime sludge. The lime sludge and powdered NaOH (5% weight of the lime sludge) were mixed homogeneously in a high-speed planetary mortar mixer with mixing speed above 140 rpm for 20 min to the resulting mixture. Thereafter, water containing hydrogen peroxide activators (2% of lime sludge) and super-plasticizer (2% of cement) were added. Then, calculated amount of fly ash was added and mixed for another 30 min. The activated lime sludge with fly ash was mixed thoroughly with cement and fine aggregates to obtain a homogeneous mix. The lump-free mixing of material was done for about 20 min in a high-speed mortar mixer. After determining, the workability of the mortar using flow table, the fresh mortar was poured into the moulds and compacted by a vibration table machine. The curing of the mortar specimens was done for 28 days. The cured

Table 5 Mix proportion of CALS mortar mix

Raw material	Weight in %
Lime sludge	25
Cement	15
Fine crashed rock aggregate (FCA)	20
River fine sand aggregate (RFA)	20
Fly ash	15
Liquid hydrogen peroxide (H_2O_2)	2
NaOH	5
w/b ratio	0.45
Plasticizer	1
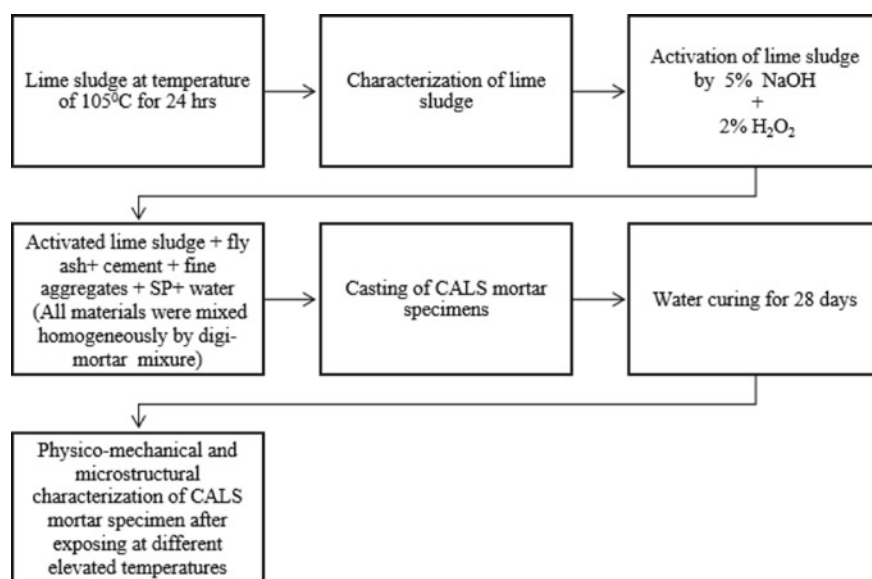
Fig. 2 Methodology to develop CALS cementitious composites

control specimens were tested for compressive strength of mortar by universal testing machine under loading rate of 140 kg/mm^2/min.

Remaining mortar test samples were subjected to the exposure of an elevated temperature of 45 °C ± 2 °C, 200 °C ± 5 °C, 400 °C ± 5 °C, 600 °C ± 5 °C, and 800 °C ± 5 °C consecutively at a heating rate of 8 °C/min, for a time duration of four hours in the programmable high-temperature furnace. After the exposure at an elevated temperature, all the mortar test sample were tested again to determine compressive strength by UTM. The consistency test of the CALS mortar was conducted using flow table and accessorise conforming to IS: 5512-1983. The test procedure was followed as per IS: code 4031 part-7. Visual analysis was done by taking images
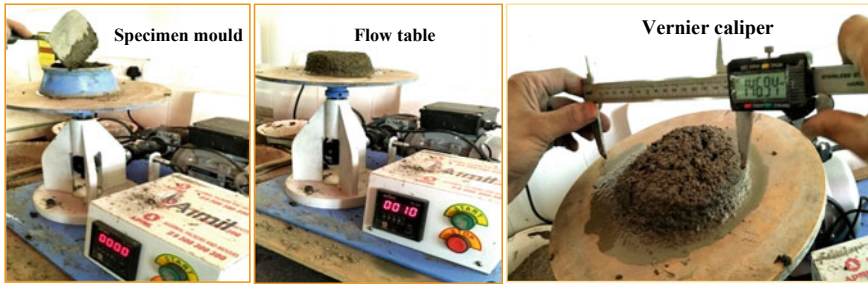
Fig. 3 Automatic flow table apparatus set up and measurement of flow using Vernier calliper

using image analyser at $20\times$ magnification. Water absorption study was conducted using electric oven, which was operated at $105\ ^\circ C \pm 5\ ^\circ C$. The weight of the CALS mortar specimens subjected to elevated temperature was determined at different temperature and fire duration. For microstructural study, SEM investigation (Carl Zeiss AG, Oberkochen, Germany) at operating voltage of 15–20 kV was done on hydrated paste samples.

4 Experimental Study

4.1 Flowability

The flow table test, as per IS 1727-1967, was conducted to determine the optimum workability for chemically activated lime sludge mortar mixes along with determination of the optimum dosage for super-plasticizer (SP) at different water to binder (w/b) ratios (Fig. 3). Polycarboxylated ether-based super-plasticizer (SHALIPLAST PCE 200) was used to reduce the water content of chemically activated lime sludge mortar [12]. It was inferred that the flowability of mortar was reduced when the content of lime sludge was increased. Minimum desirable flowability of 115 mm was recorded for the CALS mortar mix with 72% water with 2% super-plasticizer. Whereas for control mortar mix without lime sludge content, the desirable flowability of 115 mm was recorded with 42% of water.

4.2 Visual Inspection

Through visual inspection, it was observed that all the specimens did not show any noticeable change in colour or surface texture at standard temperature ($27\ ^\circ C$) to $200\ ^\circ C \pm 5\ ^\circ C$, as shown in Fig. 4. In the second stage of the test process, after heating the sample at $400\ ^\circ C$, it was found that the CALS mortar test specimen began

800⁰C±5°C	600⁰C±5°C	400⁰C±5°C	200⁰C±5°C	20⁰C
Major Cracks	Minor Cracks	Micro Cracks	No Crack	
Major Cracks	Minor Cracks	Micro Cracks	No Crack	
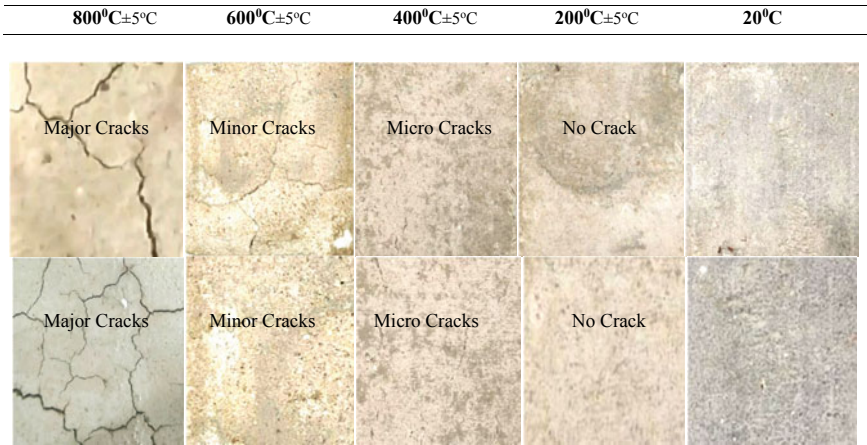
Fig. 4 Colour change and deformation of CALS mortar at elevated temperature

to lose its compression strength and micro-cracks were developed on the surface of the sample. As shown in Fig. 4, surface colour was also changed at the 600 °C ± 5 °C and CALS mortar mixture test specimen lost its 70% compression strength and gave light yellow colour. Further, at elevated temperature of 800 °C ± 5 °C as shown in Fig. 5, CALS mortar specimens lost its 85% strength, and major cracks were also developed in excessive amount. Light yellow colour of the specimen was found during the test at 800 °C ± 5 °C, as shown in Fig. 4.

Fig. 5 Exposure of CALS mortar mix at temperature of 800 °C ± 5 °C in a high-temperature furnace (Make: M/s. CarboliteGero, GmbH)

Fig. 6 Compressive strength versus different exposure temperatures
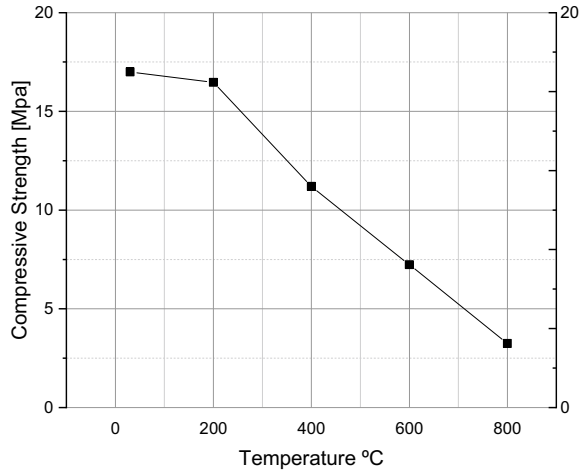
4.3 Residual Compressive Strength

Figure 6 represents the residual compressive strength of the CALS mortar at all elevated temperatures. Generally, as the temperature increases, the compressive strength decreases. Thus, the maximum compressive strength after 28 days was achieved for the CALS mortar mix as 17.05 MPa at ambient temperature of 27 °C. But further, it was decreased at 400 °C ± 5 °C (11.2 MPa), at 600 °C ± 5 °C (7.23 MPa), and finally at 800 °C ± 5 °C, the compressive strength was reached its lowest level of 3.24 MPa. Final observation was that as the elevated temperature of the sample increases, the compressive strength of the sample decreases uniformly. It was due to increase in cracks of the microstructure (with C-S-H or C-A-S-H) which caused degradation in strength continuously as exposure temperature was increased within a certain range [13].

4.4 Total Water Absorption (TWA)

The relationship between total water absorption of CALS mortar cube specimens after one hour heating at different exposure temperatures in the high-temperature electric furnace is shown in Fig. 7. The results showed that TWA was nearly constant (~5.68%) in the temperature range of 20–200 °C ± 5 °C, while TWA of the CALS mortar specimens increases gradually from 5.68% to 27.89% by increasing exposure temperature from 200 °C ± 5 °C to 800 °C ± 5 °C. Thus, the test results showed that water absorption and temperature both were proportional to each other. This was due to increase in the porosity due to microstructure degradation within mortar matrix [10, 11]. Also, open and close pores were created more as the exposure temperature was increased from 200°C to 800 °C ± 5 °C.

Fig. 7 Water absorption at different exposure temperature
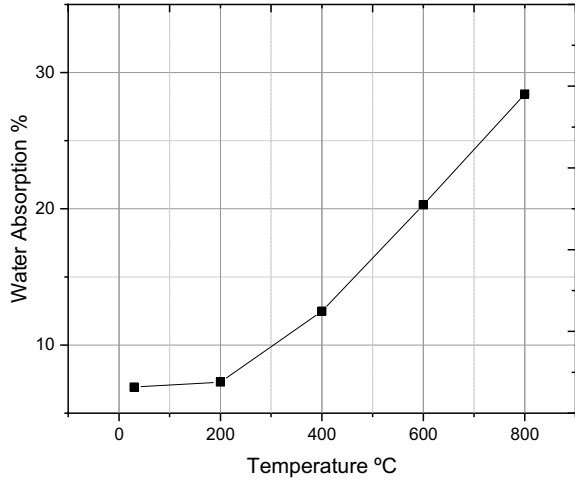
4.5 Spalling and Mass Loss

Results illustrated in Table 6 and Fig. 8 show that weight of the CALS mortar specimens subjected to elevated temperature, decreases with increases in temperature,

Table 6 Percentage weight loss of CALS mortar mixes at different temperatures

Temperature ± 5 °C	20 °C	200 °C	400 °C	600 °C	800 °C
Weight loss (%)	0	0	1.68	3.6	20.88

Fig. 8 Total weight loss
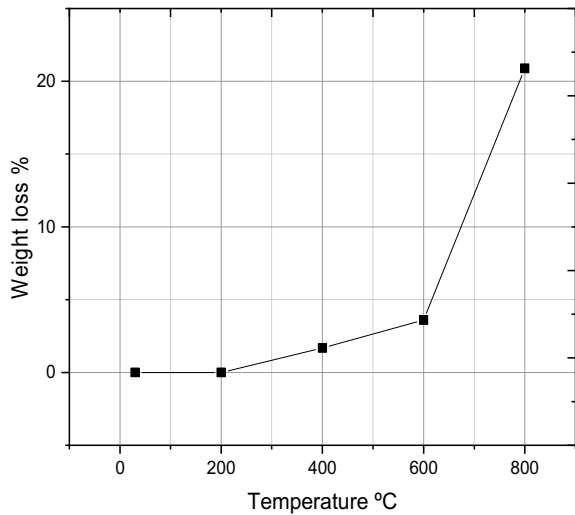
Fig. 9 Relation between
compressive strength and
water absorption at exposure
temperature from 30 to
800 °C ± 5 °C
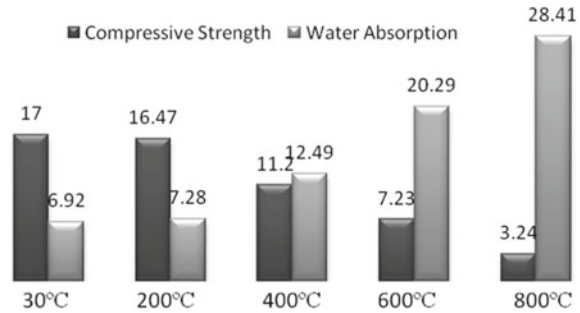
and fire duration. It was caused by the formation of air voids due to the release of
bound water from the CALS mortar matrix. The CALS mortar specimens at (200 °C
± 5 °C) showed a minimum zero percentage weight loss. Whereas, at 600 °C ±
5 °C the CALS mortar specimens lost about 1.68% of total weight and an excessive
weight loss of 20.88% at 800 °C ± 5 °C.

4.6 Relation Between Compressive Strength and Water Absorption

The loss of strength after exposure to elevated temperatures was probably due
to the decomposition of calcium hydroxide, which increases the porosity of the
CALS mortar mixture material. Moreover, the vapour pressure built into the mate-
rial develops micro-cracks due to higher exposure temperature. Consequently, the
strength of the CALS mortar material was reduced. The presented study showed that
the water absorption property and elevated temperature were linear/proportional, as
shown in Fig. 9. Overall, as the water absorption of CALS mortar composites was
increased, compressive strength was decreased by increasing exposure temperature
from 200 °C ± 5 °C to 800 °C ± 5 °C.

4.7 Relation Between Porosity and Exposure Temperature

The porosity of alternate binder (CALS composite mix) samples at different expo-
sure temperatures was measured using mercury intrusive porosimetry (MIP). The
relationship between porosity and the elevated temperature was analysed, as shown
in Fig. 10. From the figure, it can be seen that there was clear relationship between
porosity and elevated temperature. During testing, there was no significant increase
in porosity up to 200 °C ± 5 °C. This might be due to strengthening of microstructure
at higher exposure temperature up to 200 °C ± 5 °C. But the porosity of CALS mortar
mixes was increased uniformly as exposure elevated temperature was increased from

Fig. 10 Relation between porosity and temperature
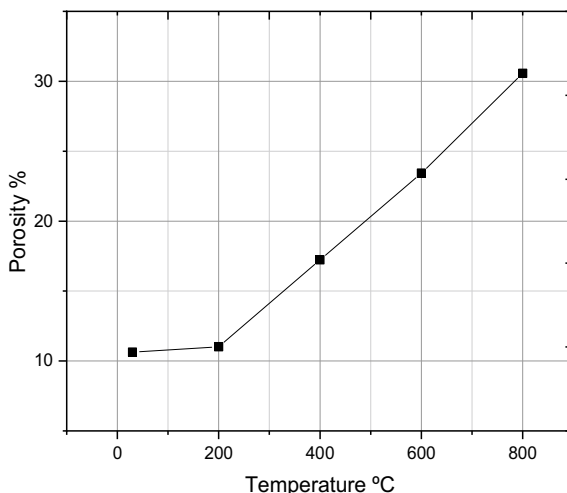
200 °C ± 5 °C to 800 °C ± 5 °C. It was caused due to creation of minor and major cracks (as discussed in Sect. 4.2), after exposing the CALS mortar specimens at higher temperature ranging from 200 °C ± 5 °C to 800 °C ± 5 °C.

4.8 Relation Between Bulk Density and Exposure Temperature

The increase of exposure temperature is accompanied with a decrease of bulk density but, with a slow rate. Table 7 represents the relation between bulk density and different phases of exposure temperature. This study shows that the ambient temperature and bulk density were inversely proportional to each other. This was due to release of free and chemically bound water from different phases (C-S-H, portlandite/CH, Ettringite, C-A-S-H, etc.) of CALS composite mix [10, 13].

Table 7 Relation between bulk density and temperature

Bulk density (g/cm^3)	Temperature (°C) ± 5 °C
1.657	30
1.643	200
1.641	400
1.532	600
1.224	800
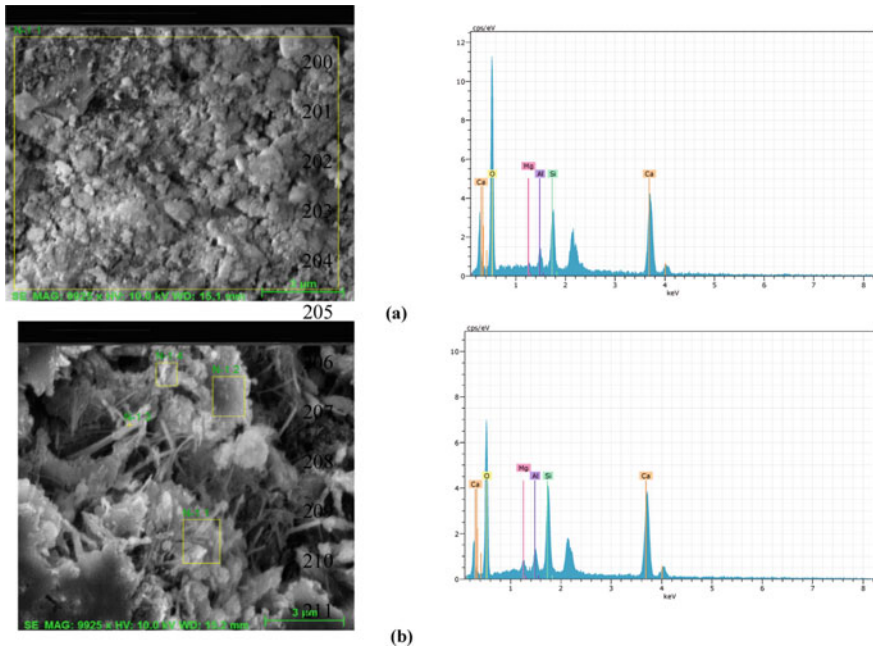
Fig. 11 Representative SEM images and corresponding EDX spectra of CALS mix at exposure temperature of **a** 100 °C ± 5 °C; **b** 800 °C ± 5 °C

4.9 Field Emission-Scanning Electron Microscopy (FE-SEM)

Figure 11a, b shows SEM images together with EDX results obtained from 28 days water cured CALS composite mix after exposing at 200 °C ± 5 °C and 800 °C ± 5 °C [14, 15]. It can be observed from Fig. 11a, b that CALS composite mix was denser at exposure temperature of 100 °C ± 5 °C as compared to exposure temperature of 800 °C ± 5 °C. This was due to the hydration of remaining cement grains at elevated temperature up to 100 °C ± 5 °C. After 100 °C, hydration products start disintegrating and releases chemical bound water and thus increase in porosity and higher water absorption as discussed in Sect. 4.6–4.8. According to the corresponding EDX spectra, the elements detected were mainly Ca, O, Al, Si, and Mg. For mix exposed to 100 °C ± 5 °C, the molar ratios of Ca to Si (Ca/Si) calculated from the weight percentages obtained from the EDX semi-quantitative chemical analyses were ranged from 1.4 to 1.61. This is in agreement with the theoretical Ca/Si ratio (1.3–2.1) [16, 17]. While for CALS mix exposed to 800 °C ± 5 °C, Ca/Si ratio was decreased in the range of 0.82–1.48, as shown in Fig. 11b.

5 Conclusions

This study was conducted to assess the properties of CALS mortar exposed to elevated temperature. The CALS mortar was exposed to different temperature levels for a certain amount of time. Then, the physico-mechanical and microscopic properties of the mortar were studied, on the basis of which the following conclusions can be drawn from the present study-

1. CALS mortar loses its physico-mechanical properties when exposed to higher elevated temperatures.
2. The compressive strength and temperature of the CALS mortar were inversely proportional to each other, i.e. the compressive strength at 400 °C temperature was decreased by 35.37%, and at 600 °C temperature compressive strength was decreased by 57.6% and finally, at 800 °C temperature, the compressive strength was decreased by 81% of the total compressive strength.
3. When the temperature gradient increases, the size of the cracks on the surface of the sample increases. Also, the colour of the surface changes as the temperature increases.
4. The water absorption and porosity properties of CALS mortar were directly proportional to each other. Whereas, both the above properties of CALS mortar are inversely proportional to the compressive strength and elevated temperature.
5. Exposure temperature ranging from 20 °C to 200 °C ± 5 °C did not affect the weight of the mortar sample. But, after each increasing the temperature by 200 °C ± 5 °C, the weight of the CALS mortar was decreased drastically.

References

1. Chen Z, Poon CS (2017) Comparative studies on the effects of sewage sludge ash and fly ash on cement hydration and properties of cement mortars. Constr Build Mater 154:791–803. https://doi.org/10.1016/j.conbuildmat.2017.08.003
2. Singh M, Garg M (2006) Reactive pozzolana from Indian clays—their use in cement mortars. Cem Concr Res 36(10):1903–1907. https://doi.org/10.1016/j.cemconres.2004.12.002
3. Vashistha P, Kumar V, Singh S, Dutt D, Tomar G, Yadav P (2019) Valorization of paper mill lime sludge via application in building construction materials: a review. Constr Build Mater 211:371–382. https://doi.org/10.1016/j.conbuildmat.2019.03.085
4. Malaiskiene J, Kizinievic O, Kizinievic V, Boris R (2018) The impact of primary sludge from paper industry on the properties of hardened cement paste and mortar. Constr Build Mater 172:553–561. https://doi.org/10.1016/j.conbuildmat.2018.04.011
5. Singh Chouhan H, Kalla P, Nagar R, Kumar Gautam P (2019) Influence of dimensional stone waste on mechanical and durability properties of mortar: a review. Constr Build Mater 227:116662. https://doi.org/10.1016/j.conbuildmat.2019.08.043

6. Alwaeli M, Gołaszewski J, Niesler M, Pizoń J, Gołaszewska M (2020) Recycle option for metallurgical sludge waste as a partial replacement for natural sand in mortars containing CSA cement to save the environment and natural resources. J Hazard Mater 398:123101. https://doi. org/10.1016/j.jhazmat.2020.123101

7. Zhang B, He P, Poon CS (2020) Optimizing the use of recycled glass materials inalkali activated cement (AAC) based mortars. J Clean Prod 255:120228. https://doi.org/10.1016/j.jclepro.2020. 120228

8. Hamood A, Khatib JM, Williams C (2017) The effectiveness of using raw sewage sludge (RSS) as a water replacement in cement mortar mixes containing unprocessed fly ash (u-FA). Constr Build Mater 147:27–34. https://doi.org/10.1016/j.conbuildmat.2017.04.159

9. Borinaga- Treviño R, Cuadrado J, Canales J, Rojí E (2021) Lime mud waste from the paper industry as a partial replacement of cement in mortars used on radiant floor heating systems. J Build Eng 41:102408. https://doi.org/10.1016/j.jobe.2021.102408

10. Mwilongo KP, Machunda RL, Jande YA (2020) Effect of elevated temperature on compressive strength and physical properties of neem seed husk ash concrete. Materials 13(5):1198. https:// doi.org/10.3390/ma13051198

11. Horszczaruk E, Sikora P, Cendrowski K, Mijowska E (2017) The effect of elevated temperature on the properties of cement mortars containing nanosilica and heavyweight aggregates. Constr Build Mater 137:420–431. https://doi.org/10.1016/j.conbuildmat.2017.02.003

12. Mobili A, Telesca A, Marroccoli M, Tittarelli F (2020) Calcium sulfoaluminate and alkali- activated fly ash cements as alternative to Portland cement: study on chemical, physical- mechanical, and durability properties of mortars with the same strength class. Constr Build Mater 246:118436. https://doi.org/10.1016/j.conbuildmat.2020.118436

13. Zhang B, He P, Poon CS (2020) Improving the high temperature mechanical properties of alkali activated cement (AAC) mortars using recycled glass as aggregates. Cement Concr Compos 112:103654. https://doi.org/10.1016/j.cemconcomp.2020.103654

14. Mymrin V, Molinetti A, Alekseev K, Avanci MA, Klitzke W, Silva DA, Ferraz FA, Iarozinski NA, Catai RE (2019) Characterization of construction materials on the base of mortar waste, activated by aluminum anodization sludge and lime production waste. Constr Build Mater 212:202–209. https://doi.org/10.1016/j.conbuildmat.2019.03.276

15. Ali Rahman Z, Mohd Saleh NM, Idris WM, Lihan T (2019) Thermal effect on mechanical characteristics of drinking water sludge brick incorporated with rice husk ash. Sains Malaysiana 48(11):2541–2549. https://doi.org/10.17576/jsm-2019-4811-24

16. Shaukat AJ, Feng H, Khitab A, Jan A (2020) Effect of admixtures on mechanical properties of cementitious mortar. Civil Eng J 6(11):2175–2187. https://doi.org/10.28991/cej-2020-030 91610

17. Yaras A (2020) Combined effects of paper mill sludge and carbonation sludge on characteristics of fired clay bricks. Constr Build Mater 249:118722. https://doi.org/10.1016/j.conbuildmat. 2020.118722

Effect of Cyclic Pressure on Sealing Behaviour of Spiral Wound Gasket in Flange Joint

N. Rino Nelson

1   Introduction

With increase in the demand for oxygen in health care application and hydrogen usage as fuel, many chemical industries have been installed. These comprises of pressure vessel for generation and piping system for transferring these gases. Gasketed flange joints are vital in pressure vessel and piping systems, acting as a common type of sealing node. They are provided with gasket interfacing element between the flange mating surfaces. These systems, in many cases are not subjected to constant load. The pressure of the internal fluid in the system varies with time due to start-up or shut down condition, varying working cycle and water hammer, in addition to surges due to uncertain conditions. In medium or high-pressure applications at elevated temperature, these systems are employed with spiral wound gaskets (SWG). It is a semi-metallic gasket with metallic spiral ring and soft filler material. The sealing behaviour of these joints, depends mainly on the compressive stress distribution in gasket under loading and unloading cycles.

The pressure fluctuations in a pipeline can occur because of fluctuations in operating pressure, temperature cycling, vibrations in pipeline, water hammer, fluctuations in fluid flow and external load. The distribution of thermal loads in the tubes causes expansion and contraction of tubes. This further causes local cyclic loading. The localized area subjected to higher temperature experiences compression, whilst the localized area subjected to lower temperature experiences tension [1]. The pressure vessel or pipeline containing gaseous hydrogen are subjected to pressure cycles which lead to fatigue loading. They are subjected to frequent fluctuation of pressure having several occasions on a day and >10,000 occasions in the

---

N. R. Nelson (✉)

Department of Mechanical Engineering, Indian Institute of Information Technology Design and Manufacturing, Kancheepuram 600127, India
e-mail: rino@iiitdm.ac.in

lifetime [2]. The gaseous hydrogen is observed to reduce the fracture resistance and fatigue behaviour of the material. The gaseous products like oxygen or hydrogen are externally compressed for proper channelling and transportation via tubes. On using reciprocating compressor for high compression ratio, it is also accompanied with considerable amount of inherent pressure fluctuations. These fluctuations usually result from forward and backward motion of the piston in the cylinder. This fluctuation may lead to ignition, explosion, or even damage of the entire system [3]. Gas-fired generators are used to balance the intermittency caused in wind generation. This causes the pressure fluctuation in the gas transmission pipelines between minimum delivery pressure and the max allowed pressure based on the material behaviour. Whenever the pressure drops below the threshold value, external compressor is used to pressurize the gaseous hydrogen which might cause large fluctuations [4]. This process can create challenges to pipelines and their reliability. Recently, American Society of Mechanical Engineers (ASME) has incorporated the methodology for accommodating the effect of hydrogen crack growth rate [5].

Water hammer also known as surge flow occurs in pipeline, with rapid change in the fluid flow causing the pressure to vary. The pressure hikes may also go to 5 to 10 times the operating pressure, in addition to high support reactions, flow reversal, bursting of pipes and leakage of joint. The sampling of pressure fluctuation data also has impact on corrosion behaviour and fatigue crack growth [6]. In order to extract the small undulations in pressure fluctuations, the experiments were performed for very small sampling interval. The procedure established using Supervisory control and data acquisition (SCADA) data generation process, misses both the minor load cycles and underload data, yielding very conservative results for liquid pipelines [7]. The effect of flow velocity and wall roughness on noise level was analysed using large eddy theory and subgrid theory [8]. The turbulency in pressure is observed to increase with increase in flow velocity and wall roughness.

In the present study, flange joint with gasket is analysed under varying internal pressure load. The effect of gasket nonlinear behaviour is modelled, including the hysteresis characteristics under loading and unloading. During assembly stage, the gasket undergoes plastic deformation, in order to get squeezed into the surface irregularities in the flange surfaces. To include this effect, the elasto-plastic behaviour of individual constituents in the gasket is considered. In operating condition, the internal pressure exerted on the inner circumference of the flange walls is of pulsating in nature under many occasions. The fluctuation in the pressure causes loading and unloading of the gasket material. Its effect on the sealing performance of the flange joint is analysed in the present work using finite element analysis. The main mode of failure is leakage through the interfacial area. The stress distribution in the gasket material is obtained and the sealing performance is predicted using the minimum residual stress retained in gasket, as recommended by ASME.

Fig. 1 Damage in pipeline
due to pressure fluctuation
[10]

2 Background

The pressure fluctuations in a pipeline can occur because of fluctuations in operating pressure, temperature cycling, vibrations in pipeline, water hammer, fluctuations in fluid flow and external load. The major contribution of pressure fluctuation will be due to the working cycle of the pressure vessel components for specific work output. In order to obtain the desired work output the pressure inside the vessel will be varied [9]. Apart from this reason, all the other causes for pressure fluctuations are undesirable. Pressure variation also occurs in long pipelines, due to thermal deformation of the component. Another major contribution comes from the water hammer (i.e.) sudden stoppage or opening of pressurized fluid causes loud banging noise. Water hammer is usually accompanied with loud noise, similar to banging a pipeline with hammer. This can be of single cycle or multiple cycle in nature, which happens when the pressurized fluid is controlled. These can cause erosion of inner walls of pipe, leakage and catastrophic failure of pipeline (Fig. 1).

3 Micromechanical Modelling of SWG

In pressure vessels and piping system, flange joints with spiral wound gasket (SWG) are used in medium and high-pressure applications. These spiral wound gasket possess high non-linearities and hysteresis during loading and unloading. Usually, in a flange joint, the gasket will be loaded during assembly stage via bolt preload and unloaded during pressurization stage via internal pressure and thermal loads from fluid. The spiral wound gasket is a semi-metallic gasket with both metallic entity and non-metallic entity. The metallic component is preformed into 'V' shape with open end of the V aligned towards the inner diameter. This preformed 'V' shape helps in spring back effect, during unloading of the gasket entity. The common metallic material used are SS 304, SS 316, Monel, etc., which have good strength and spring back effect. The non-metallic component used in SWG is usually soft and binds

Fig. 2 Individual
constituents in the
micromechanical model of
spiral wound gasket
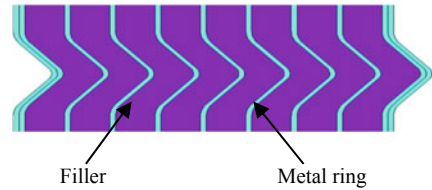
Filler   Metal ring

well with the metallic component. The common non-metallic filler material used
are graphite, Teflon and rubber based on the fluid used. Here, metal rings provide
stability and filler material provides seal ability for the gasket.

In spiral wound gasket (SWG) the minor leakage path is through the gasket internal
structure and the major leakage path is through the contact surfaces between gasket
and flange surfaces. The minor leakage path in SWG is included in the analysis by
modelling the individual components in the gasket (i.e.) metal rings and filler mate-
rials separately and establishing contacts between them. In our previous work [11],
the micromechanical model of SWG is established, considering the representative
volume element (RVE) including the metal ring and filler material is chosen based on
the volume fraction. The robustness of the model in obtaining the gasket stress along
the radial and circumferential direction is also investigated. The micromechanical
model of the spiral wound gasket used is shown in Fig. 2.

3.1   Cyclic Loading in Pipeline

In pressure vessels and pipeline, the internal fluid is pressurized to a value well
above the atmospheric condition. During operating condition, these components are
subjected to varying pressure load due to various reasons. Basically, these compo-
nents operate in cyclic nature with cyclic loading conditions, which keeps repeated
from the time of starting stage to any stoppages. The cyclic loading nature occurs
for both temperature and pressure because of working cycle, thermal expansion,
vibration and water hammer. This pressure fluctuation causes the material to expe-
rience residual effect, if the deformation enters into plastic region. In a flange joint,
the only component designed to deform plastically is gasket material for filling the
surface irregularities on sealing surfaces. Moreover, the gasket has high hysteresis
behaviour under loading and unloading the material. Since, the plastic deforma-
tion cannot be recovered upon unloading, some amount of residual or permanent
deformation will remain in the gasket, which affect the contact stress distribution.
The sealing behaviour of the flange joint is usually, defined based on the contact
stress distribution in gasket. Thus, analysing the effect of cyclic loads on gasket is
very important for designing a safe joint. The nature of pressure fluctuation [12, 13]
experienced in pressure vessel against time is shown in Fig. 3.

Fig. 3 Pressure load variation in a pipeline
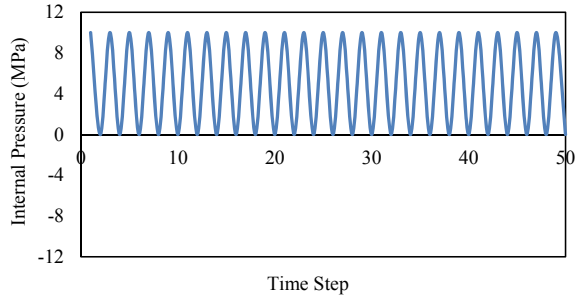
4 Methodology

The pressure fluctuations in pipelines carrying fluids with flange joints is inevitable. The performance of the flange joint, both structural integrity and the sealing performance depends the nature of loads acting on it. The sealing performance is a function of stress distribution in gasket material. The residual stress in gasket material varies based on the internal fluid pressure and its nature. During assembly stage, the gasket material gets compressed; whereas under pressurization, the gasket material gets relaxed.

Finite element analysis is carried out in flange joint with gasket, considering the individual constituents in it. The metal rings and filler tape in the SWG are modelled separately considering the individual behaviour under elastic and plastic regions. The contact stress response from the gasket is validated with the previous work of author [11]. The analysis is performed in flange joints with gasket under varying internal pressure loads and the variation in stress distribution is obtained.

5 Material Model

The flange joint is composed of weld-neck flanges, interface gasket, bolt and nut connector. The weld-neck flange is characterized using SA195 material; whereas bolt-nut connector using SA193B7 material. The flange and bolt materials are characterized considering isotropic material behaviour using Young's modulus of elasticity and Poisson's ratio. The individual entities of the gasket material, both metal rings and filler tape are characterized using elasto-plastic material behaviour. The metal rings are characterized using bilinear material model shown in Table 1. The linear elastic region is characterized using Young's modulus of elasticity and Poisson's ratio; whereas linear plastic region beyond yield stress is characterized using Tangent modulus. The filler tape is characterized using linear elastic region and nonlinear plastic region, to include the more realistic plastic behaviour. The nonlinear plastic region is characterized using unidirectional stress strain curve beyond the yield strength of the material as shown in Fig. 4.

Table 1 Material properties of joint members

	Parameters	SA195	SA193B7	SS304
Elastic property	Young's modulus (GPa)	195	203	197
	Poisson's ratio	0.3	0.3	0.29
Plastic property	Yield stress (MPa)			340
	Tangent modulus (MPa)			6850

Fig. 4 Uniaxial compressive behaviour of graphite material [11]
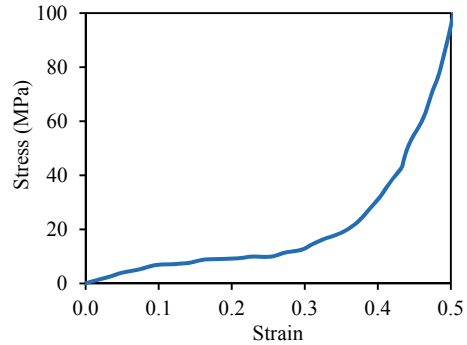
5.1　FE Model

Finite Element (FE) model of the flange joint is developed using a commercial finite element analysis (FEA) software, ANSYS v18.1. An 80 Nominal Pipe Size (NPS) 80 schedule flange joint is considered for the study. The FE model is developed with symmetric weld-neck flange, bolt-nut connector and SWG of 4.5 mm thickness. Considering the rotational symmetry, 22.5° of the flange joint is modelled with half segment of bolt region and half segment of web region. Since symmetric flange joint is considered, upper flange with half portion of the bolt in axial direction and gasket with half thickness is taken for the study.

The flange member is discretized using lower order-8 noded brick element, SOLID185; whereas bolt-nut connector using higher order-16 noded brick element, SOLID186. The pretension in the bolt is applied using PRETS179 element, by creating the master node and slave nodes along a plane. The preload applied is transferred to the slave nodes from the master node. The contact is established between flange-bolt interfaces and flange gasket interfaces. The contact is established with TARGE170 and CONTAC173 elements. In gasket, the metal rings are discretized using SOLID185 elements and filler tape using SOLID186 elements [14]. The higher order elements will be capable of capturing the discontinuity and nonlinearity in a better way (Fig. 5).

Fig. 5 FE Model of flange
joint
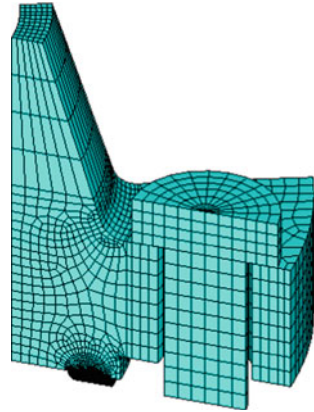
5.2 Boundary Condition

Considering the rotational and axial symmetry of the joint, symmetric boundary condition is applied on 0° and 22.5° faces of the joint including flange surface, gasket surface, bolt and nut surface. The flange joint is constrained along the axial direction by applying symmetric boundary condition in the bottom surface of the gasket.

During assembly stage, pretension is applied on the bolt shank region. The bolt pretension applied is transferred to other connected members in the joint. Upon application of pretension, the bolt is subjected to tension and other members are subjected to compression. The gasket gets compressed and fills the irregularities in the sealing surfaces. Upon application of internal pressure, the flanges are pushed away from each other. This causes relaxation in gasket and other joint members, but bolt is subjected to additional tensile load. The nature of the internal pressure load is cyclic with repeated loading.

6 Results and Discussion

Finite Element Analysis (FEA) is carried out in flange joint with gasket considering the individual constituents. The analysis is performed in two stages, namely, assembly and pressurization stage.
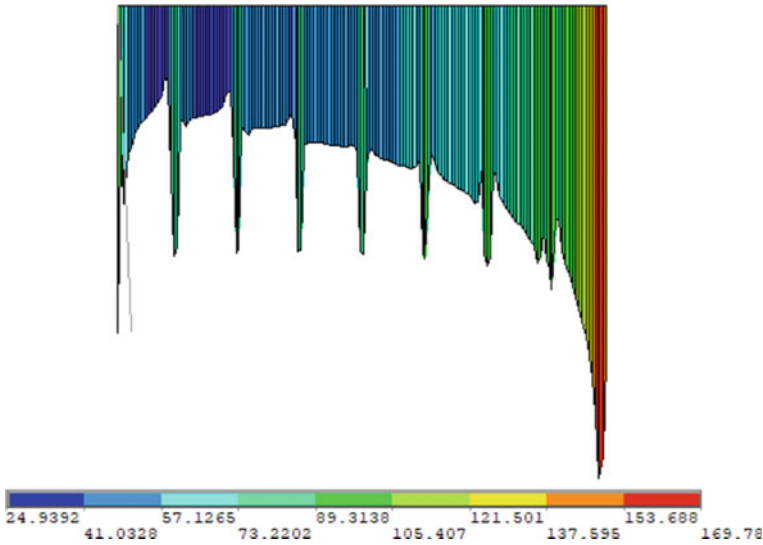
Fig. 6 Distribution of contact stress (MPa) in gasket on 0° face of flange joint under assembly stage

6.1 Assembly Stage

During assembly stage the pre-tightening torque is applied to the bolt in terms of bolt pretension. A bolt preload value of 30 kN is applied on each bolt. Upon applying the bolt preload, the bolt member gets elongated and other members of the joint gets compressed. The bolt member will be subjected to tensile stress; whereas other joint members are subjected to compressive stress. The contact gets established between the flange-bolt interface and flange gasket interfaces, so the bolt load gets transferred to the gasket. The contact stress in gasket obtained under application of bolt preload is shown in Fig. 6. The gasket contact stress varies along the radial direction from inner to outer circumference. The contact pressure is higher upon closeness towards bolt-nut connector.

6.2 Pressurization Stage

During pressurization stage, the fluid load is applied in the flange joint. The internal fluid load (i.e.) pressure is applied on the inner walls of the flange joint. The hydrostatic force components acting on the cross-sectional areas are calculated and applied on the respective areas. Upon applying the internal pressure, the flanges move away from each other. This causes increase in the bolt tensile stress and increases the bolt axial load, based on the proportion of the internal pressure load taken by the bolt.
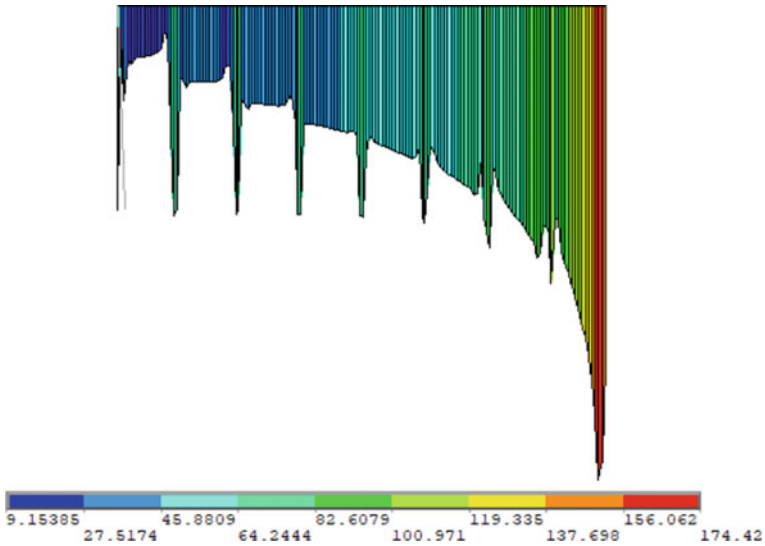
Fig. 7 Distribution of contact stress (MPa) in gasket on 0° face of flange joint under pressurization stage

Consequently, the compressive stress in the connected members reduces, resulting in reduction of gasket contact stress. Simultaneously, the compressive deformation in the gasket also reduces, leaving some part of deformation in it. The gasket contact stress distribution under internal pressure of 10 MPa is shown in Fig. 7.

6.3 Under Cyclic Internal Pressure

As discussed in Sect. 1, the pressure vessels and pipeline are subjected to fluctuating pressure during working condition. The cyclic pressure variation considered for the study is shown in Fig. 3. The analysis is done separately for assembly stage as a separate load step and pressurization stage as a separate load step. The nature of load applied is repeated loading with actual pressure applied under normal pressurization stage as maximum and 0 MPa as minimum. Upon applying the cyclic pressure loading, the gasket contact stress obtained is also of similar nature with values getting attenuated. The attenuation happens because of accumulation of plastic deformation in the gasket material under each cycle. At first cycle, the minimum gasket contact stress is 21.91 MPa, which reduces to 19.56 MPa after 50 loading cycles is shown in Fig. 8.

Fig. 8 Variation in contact stress in gasket for cyclic loading
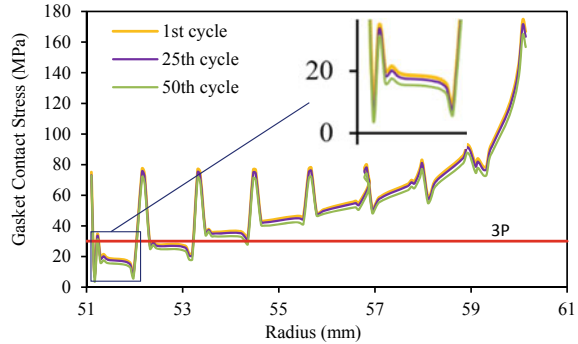
6.4 Sealing Characteristics

The sealing behaviour of the flange joint depends on the residual gasket stress in the gasket material. The minimum residual stress in gasket is provided by Eq. (1) based on internal pressure (P), defined by ASME.

$$\text{Residual Stress Line} = 3P \tag{1}$$

Under cyclic pressure loading, the ability of the flange joint to have better sealability reduces with the cycles it is subjected. Figure 8 shows the variation in sealing characteristics of flange joint subjected to repeated cyclic pressure loading after 1 cycle, 25 cycles and 50 cycles, respectively. Therefore, whilst designing the flange joint, the nature of loading should also be taken into account. The nature of loading should also be considered as an uncertainty.

7 Conclusions

The flange joint used in pressure vessel and pipeline are subjected to fluctuating pressure loading inevitably. These pressure fluctuations may be due to local thermal cycles, water hammer, vibrations and working cycles. Compared to structural integrity, the sealing characteristics of the flange joint gets affected due to fluctuating pressure.

- Due to high hysteresis, the gasket material will be subjected to both elastic and plastic deformation.
- Under cyclic pressure loading, the plastic deformation in the gasket material gets accumulated based on the cycles of operation.
- The sealing ability of the flange joint reduces with cyclic pressure loading. The nature of loading should be included to design a safe joint considering the sealability of the joint.

References

1. Pang L, Yi S, Duan L, Li W, Yang Y (2019) Thermal stress and cyclic stress analysis of a vertical water-cooled wall at a utility boiler under flexible operation. Energies 12:1170
2. Marchi C, Dedrick DE, Van Blarigan P, Somerday BP, Nibur KA, Pressure cycling of type 1 pressure vessels with gaseous hydrogen
3. Rahman M, Lee GH, Utomo TS, Jeong HM, Chung HS (2009) A Study on gas pressure fluctuation characteristics inside the snubber and pipe of hydrogen. Adv Mech Eng 2009:138708
4. Chertkov M, Fisher M, Backhaus S, Bent R, Misra S, Pressure fluctuation in natural gas networks caused by gas-electric coupling
5. Boiler and Pressure Vessel Code (2004) Section VIII, Division I. American Society of Mechanical Engineers, New York
6. Zhao J, Chen W, Chevil K, Been J, Boven GV, Keane S, Kania R (2017) Effect of pressure sampling method on pipeline integrity analysis. J Pipeline Syst Eng Pract 04017016:1–13
7. Dzierwa P (2018) New start-up curves for a 200MW steam boiler with natural circulation. MATEC Web Confer 240:05007
8. Qu D, Zhang Z, Lou J, Dai Q (2016) Numerical simulation of fluctuation pressure with liquid-filled pipes based on large eddy simulation method. Vibroeng Proc 10:2345–2533
9. Cheng S, Chenlong D, Yuemin Z, Liang D, Zhenfu L (2018) Analysis and evaluation on pressure fluctuations in air dense medium fluidized bed. Int J Min Sci Technol 28:461–467
10. Aboshoufa ME, Alkanshi AA (2016) Transient oil flow study—Waha oil pipeline. Thesis Submitted to University of Tripoli, Libiya
11. Nelson NR (2021) Effective modelling of spiral wound gasket with graphite filler in gasketed flange joint subjected to bending loads. Mater Today Proc 44(1):2199–2204
12. Sutton A, Hubert Y, Textor S, Haider S (2014) Allowable pressure cycling limits for liquid pipelines. In: 14th international pipeline conference, Canada, September 2014, V002T06A058
13. Li, Y, Yu Z, Ye Q, Yang J, Hayat S (2021) Analysis of pressure fluctuation for oil-gas two-phase flow in a horizontal pipe using the bubble number density equation. Chem Eng Commun https://doi.org/10.1080/00986445.2020.1869950
14. ANSYS 18.1, User's Manual. ANSYS Inc. Canonsburg, USA (2015)

Pushover Analysis of RC Framed Building with Various Pile Group Configurations

Prathyusha Tenepalli

1 Introduction

An earthquake is the shaking of earth surface which results in release of energy and sudden that creates seismic waves the highest intensity. Earthquake foundation design requires critical analysis of soil behaviour and soil structure interaction. We need to update our design codes which takes geometric non-linearity and material inelastic into account in evaluating seismic demand [1]. SSI is also an important factor, its effect is visible on whole structure, i.e. from superstructure, pile foundation, and site soil [2].

Structures redesign as individual components which yield or fail during earthquake. In such event, pushover analysis takes into this account along with dynamic forces by applying loads to find weak link in structure and revising model in second iteration, commonly used for retrofit analysis also useful in-case of performance-based design that rely on ductility or redundancies to resist earthquake forces. Base shear is maximum expected lateral force at base determined by combining factors like soil conditions, seismic zone, probability of significant ground motion, level of ductility and over strength, weight of structure [3].

Pile foundation as a structural element safely transfer superstructure load into deep firmer layer and provide stability. The load carrying capacity of piles results from end bearing, friction on its sides, or a combination of both. Piles can be installed as single pile or as a group of piles depending upon the loading conditions. Some important aspects to be considered whilst designing pile foundations are—type of pile, length of pile, size of pile, spacing between piles in a group, stability of the pile group, geometry of the layout, and so on. Estimating ultimate bearing capacity

P. Tenepalli (✉)
VIT University, Vellore, India
e-mail: prathyusha.shareef@gmail.com

for optimizing pile design is a complex problem, and Schectman method based on in-situ blow count (N) is considered one of reliable methods [4].

The study evaluates probabilistic seismic analyzes to define the structural seismic behaviour. Fragility analysis of an RC frame is done using Monte Carlo simulation method and analytical approximation. Both methods gave close results with each other in the analysis of symmetric structures [5, 6].

In this project, we are trying to investigate the non-linear response of RC frame with different pile group configurations, to find probability of damage by doing pushover analysis to find optimum configuration.

2 Modelling

15 storeys building having 3 × 3 bay, span of 4 × 4 m, and storey height of 3.5 m each is designed with help of SAP 2000, considering M25 grade concrete and Fe 415 HYSD bars at Chennai in accordance with Indian standard codes as shown in Fig. 1.
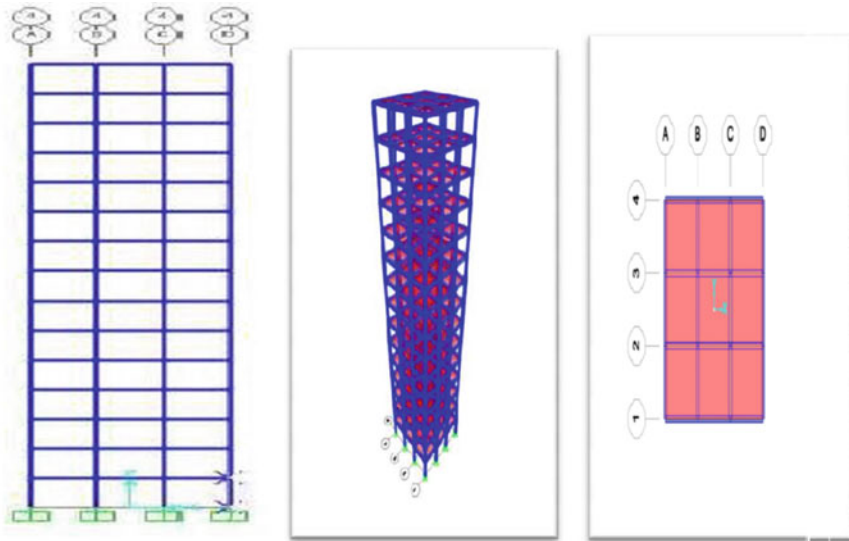
Fig. 1 2D, 3D, plan view using SAP 2000

3 Dimensions of Columns and Beams

Square column and rectangular beam are considered with heavier beam and column in bottom storey and changing dimensions for every 5 floors.

Reinforcement (<1% of area according to IS 456: 2000, longitudinal bar size-16 mm diameter).

Dimensions are not standardized, they are changed till safe, and economical model is achieved by keeping above principal intact.

Slab thickness—150 mm

Loads: Considered

- **Dead load (IS 875: part 1-1987)**

Wall load:	16.1 kN/m
Parapet load:	5.52 kN/m
Floor finish/partition load:	1.5 kN/m^2

- **Live load: 3 kN/m^2 (IS 875: part 2-1987)**
- **Seismic parameters (IS 1893: part 1-2016)**

Importance factor:	1
Response reduction factor:	5
T, Time period:	1.462

- **Wind load**

Vb (m/s):	50,
Factors:	K1 = K2 = K3 = 1

4 Storey–Drift Graph

To check the serviceability, inter-storey drift is calculated, i.e. difference in displacement of $(i + 1 - i)$ floor/storey height(= 3.5 m) for earthquake load and response spectrum load, and the values are taken from Sap 2000 and according to IS 1893:Part 2016: clause 7.11.1 for achieving limit serviceability condition, the storey drift should be less than 0.004 and as shown in Fig. 2, our design satisfies this criteria.

After checking the serviceability of design, we have designed the pile foundation for that we need type of soil versus depth, unit weight of soil, angle of friction, and cohesion values. Generally in field, N value obtained from standard penetration test is used to correlate to calculate various parameters, and the soil is classified as soft,
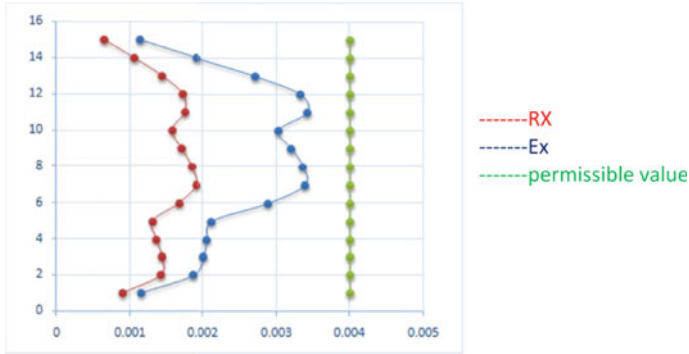
Fig. 2 Inter-storey drift versus storey height
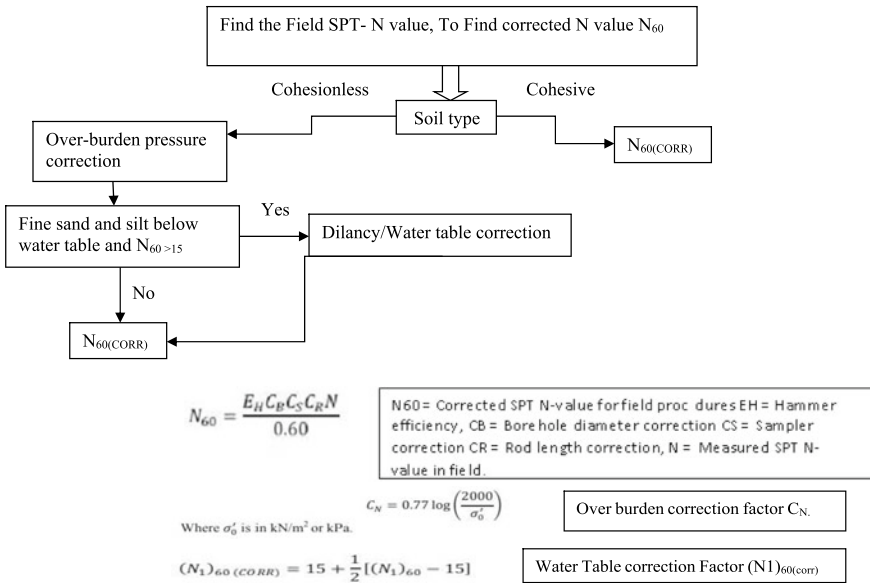
Fig. 3 Flowchart for calculating corrected N value

medium, and stiff soil based on mean N value obtained, and the parameters calculated from corrected N value (Fig. 3; Table 1) is used to calculate ultimate bearing capacity (UBC) of soil.

Table 1 Calculation for corrected *N* value

Avg depth	Category	Uncorrected	Hammer efficiency correction	Overburden pressure correction	Dilancy correction	Corrected *N* value
1.25	N-cohesive (NC)					
3.75	Cohesive (C)	13	9.75	0	0	9.75
6.75	C	15	11.25	0	0	11.25
9.75	NC	11	8.25	7.38	11.19	7.37621
11.5	NC	38	28.5	25.5	20.24	25.4815
13	NC	36	27	24.1	19.57	19.5702
15	NC	21	15.75	10.4	0	10.3553
17	NC	15	11.25	7.4	0	7.39665
19	NC	23	17.25	11.3	0	11.3415
21	C	25	18.75	0	0	18.75
22.5	NC	27	20.25	11.8	13.39	13.3928
23.5	C					
24.5	NC					
						134.664
					Average N	13.4664

Average *N* value is 13.5 so soil is classified as medium stiff soil

Design of pile foundation

- The standard penetration test has been used to correlate different soil parameters, i.e. unit weight γ, relative density Dr, angle of internal friction φ, and undrained compressive strength qu. It has also been used to estimate the ultimate pile bearing capacity
  STEPS: 1
- Collect soil profile—depth versus SPT-n value chart from a standard journal
  Reference: Evaluation of ultimate bearing capacity of pre-stressed high-strength concrete pipe pile embedded in saturated sandy soil Based on in-situ test
  By Yingjie Wei, Duli Wang, Jiawang Li, Yuxin Jie
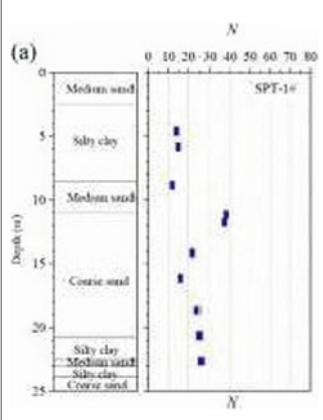
5 Finding Various Parameters Using Corrected *N* Value

To calculate ultimate bearing capacity of the pile, we need to find various parameters, and many studies have shown an empirical relationship between corrected N value and these parameters like angle of friction, unit weight, unconfined shear strength, etc.

$\phi° = 27 + 0.3(N_1)_{60}$ $q_u = 12.5N_{60}$ (kN/m^2)		
Fine-grained soil	12.5 N	Unit weight
Clay	25 N	
Silty clay	20 N	
Fine-grained soil	58 N$^{0.72}$	

After calculating UBC versus depth (Table 2), as we can see from Fig. 4 at 20 m depth UBC -1250 kN, then we need to divide total load of building take from SAP 2000 (Fig. 5) by UBC at 20 m to calculate number of piles required. As we can see from Table 3, it is 42 piles of 450 mm diameter. Similarly, we can optimize depth versus number of piles versus diameter of pile for required for various configurations of piles (Tables 4 and 5).

Table 2 Calculation of UBV versus depth

Unit weight	Angle of friction	C_U	Incremental pressure	Cumulative stress	Cumulative Eff stress at centre
8.8	29.64	0	0	0	0
18.2625	0	46.68	45.65625	45.65625	22.828125
18.4875	0	56.4	92.4375	138.09375	69.046875
8.873762095	29.66212863	0	75.42697781	213.5207278	106.7603639
9.054814567	29.71644437	0	99.60296024	313.123688	156.561844
8.995701637	29.69871049	0	107.9484196	421.0721077	210.5360538
8.9035531	29.67106593	0	124.6497434	545.7218511	272.8609255
8.8739665	29.66218995	0	141.983464	687.7053151	343.8526575
8.9134153	29.67402459	0	160.4414754	848.1467905	424.0733952
19.6125	0	105	392.25	1240.39679	620.1983952
8.9339275	29.68017825	0	196.546405	1436.943195	718.4715977
19.6125	0	0	451.0875	1888.030695	944.0153477
8.9	29.6	0	213.6	2101.630695	1050.815348

(continued)

Table 2 (continued)

Surface area of pile (cm²) surface area of	Cumulative eff stress Centre	Skin friction	QU	Skin friction 2	Cumulative	UBC
12.56	0	0	0	0	0	0
12.56	11.4140625	0	121.875	234.52032	234.52032	234.5203
17.584	34.5234375	0	140.625	396.69504	396.69504	631.2154
12.56	53.38018195	381.6007129	92.20262	0	381.6007129	1012.816
5.024	78.28092201	224.3374126	318.5182	0	224.3374126	1237.153
10.048	105.2680269	602.9204667	244.627	0	602.9204667	1840.074
10.048	136.4304628	780.5270385	129.4414	0	780.5270385	2620.601
10.048	171.9263288	983.2468978	92.45813	0	983.2468978	3603.848
10.048	212.0366976	1213.220556	141.7691	0	1213.220556	4817.068
10.048	310.0991976	0	234.375	422.016	422.016	5239.084
5.024	359.2357989	1027.98494	167.4094	0	1027.98494	6267.069
5.024	472.0076739	0		0	0	6267.069
5.024	525.4076739	1498.614557		0	0	0
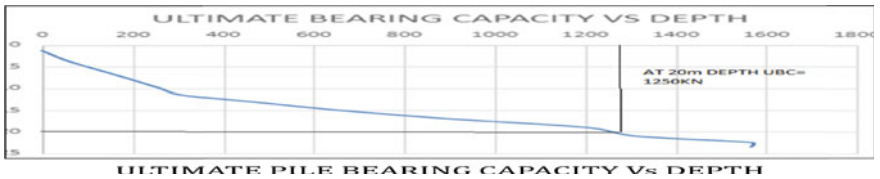
Fig. 4 UBC versus depth
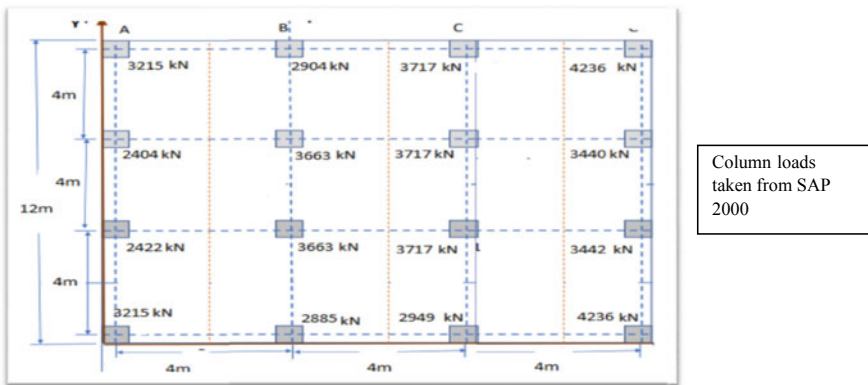
Fig. 5 Column position and loads taken from SAP 2000

Table 3 Number of piles required

F1 kN	F2 kN	F3 kN	M1 kN-m	M2 kN-m	M3 kN-m
−31.016	2.502	3215.262	7.0082	−168.3016	2.9014
−30.48	−4.255	2422.282	14.6299	−173.8518	4.8494
−32.32	−3.199	2404.137	13.4403	−182.2794	4.9901
−37.127	−8.614	3215.262	19.5251	−194.8348	2.9015
−46.334	7.278	2885.897	−5.3995	−185.7958	4.8921
−47.893	−0.674	3662.551	3.7924	−193.9497	4.5592
−50.168	−1.601	3662.551	5.1308	−202.8729	4.6032
−53.789	−9.118	2904.043	13.8271	−213.866	4.9474
−45.276	9.118	2959.013	−13.8267	−184.6042	4.8698
−48.82	1.601	3717.365	−5.1307	−195.2881	4.5592
−51.095	0.674	3717.365	−3.7925	−204.2113	4.6032
−52.731	−7.278	2940.867	5.3991	−212.6744	4.9697
−42.13	8.612	4236.432	−19.5231	−180.8165	2.9014
−46.875	3.198	3422.628	−13.4383	−193.078	4.8718
−48.715	4.257	3440.773	−14.6319	−201.5056	4.9678
−48.242	−2.501	4236.432	−7.0102	−207.3497	2.9015
		50,771.03			
		40.61			
Number of piles		42			

Table 4 Storey shear

Storey No	Storey height	Hi2	Wi	WiHi2	WiHi2/Sum	Q
15	52.5	2756.25	2346.76	6,468,257.25	0.142459075	229.0097561
14	49	2401	3047.6	7,317,287.6	0.161158405	259.0698211
13	45.5	2070.25	3047.6	6,309,293.9	0.138958013	223.3816314
12	42	1764	3047.6	5,375,966.4	0.118402094	190.3370114
11	38.5	1482.25	3047.6	4,517,305.1	0.099490648	159.935961
10	35	1225	3237.6	3,966,060	0.08734984	140.4190338
9	31.5	992.25	3237.6	3,212,508.6	0.070753371	113.7394173
8	28	784	3237.6	2,538,278.4	0.055903898	89.86818161
7	24.5	600.25	3237.6	1,943,369.4	0.042801422	68.80532654
6	21	441	3237.6	1,427,781.6	0.031445943	50.55085216

(continued)

Table 4 (continued)

Storey No	Storey height	Hi2	Wi	WiHi2	WiHi2/Sum	Q
5	17.5	306.25	3455.6	1,058,277.5	0.02330786	37.46849619
4	14	196	3455.6	677,297.6	0.01491703	23.97983756
3	10.5	110.25	3455.6	380,979.9	0.00839083	13.48865863
2	7	49	3455.6	169,324.4	0.003729258	5.994959391
1	3.5	12.25	3455.6	42,331.1	0.000932314	1.498739848
				45,404,318.75		

Table 5 Pile design details

Grid	Length of pile	Dia of pile	Spacing	L/D	Total BC	FOS
3 × 3	20	1	3	20	58,701.672	1.128878308
3 × 3	20	1	5	20	58,701.672	1.128878308
3 × 3	20	1	7	20	58,701.672	1.128878308
3 × 3	15	1.6	4.8	9.375	52,831.5048	1.015990477
3 × 3	15	1.6	8	9.375	52,831.5048	1.015990477
3 × 3	15	1.6	11.2	9.375	52,831.5048	1.015990477
3 × 3	22.5	0.8	2.4	28.125	59,435.4429	1.142989287
3 × 3	25	0.6	3	41.66667	55,032.8175	1.058323413
3 × 3	25	0.6	4.2	41.66667	55,032.8175	1.058323413
4 × 4	20	0.55	3	36.36364	57,397.1904	1.103792123
4 × 4	20	0.6	5	33.33333	62,615.1168	1.204136862
4 × 4	20	0.6	7	33.33333	62,615.1168	1.204136862
4 × 4	15	0.9	2.7	16.66667	52,831.5048	1.015990477
4 × 4	15	0.9	4.5	16.66667	52,831.5048	1.015990477
4 × 4	15	0.9	6.3	16.66667	52,831.5048	1.015990477
4 × 4	22.5	0.55	1.65	40.90909	72,643.3191	1.396986906
4 × 4	25	0.5	2.5	50	81,530.1	1.567886538
4 × 4	25	0.5	3.5	50	81,530.1	1.567886538
5 × 5	20	0.45	3	44.44444	73,377.09	1.411097885
5 × 5	20	0.45	5	44.44444	73,377.09	1.411097885
5 × 5	20	0.45	7	44.44444	73,377.09	1.411097885
5 × 5	15	0.6	1.8	25	55,032.8175	1.058323413
5 × 5	15	0.6	3	25	55,032.8175	1.058323413
5 × 5	15	0.6	4.2	25	55,032.8175	1.058323413
5 × 5	22.5	0.45	1.35	50	92,867.8795	1.78592076
5 × 5	25	0.45	2.25	55.55556	114,651.703	2.204840445
5 × 5	25	0.45	3.15	55.55556	114,651.703	2.204840445

6   Raft Design

- Maximum dimensions of raft calculated 20 × 20 m
- Depth of raft calculated is 1.75 m it is calculated as per standard procedure.

Base Shear Calculations

- $W = 52233.098$ kN
- $A_h = ((Z/2) \times (Sa/g) \times (I/R)) = 0.033$
- $V_b = W \times A_h = 1607.54$ kN

After calculating various parameters like soil profile raft depth, pile location, and its properties, base shear values all these are entered into Plaxis 3D simulation (Fig. 6).

Steps:

- Enter soil profile and properties.
- Give the dimension of beams and columns and various loads acting at each level.
- Give the location, thickness and properties of raft.
- Enter pile location, i.e. co-ordinates.
- Apply base shear such that the value at end x–x grid is twice the middle grid.
- Run the simulation for various parameters like spacing of piles (3D, 5D, 7D), grid variation (3 × 3, 4 × 4, 5 × 5), and length variation keeping other parameters constant. And draw M-stage versus deflection graph for each parameter (Figs. 7, 8 and 9).

PLAXIS MODELLING

FRONT VIEW OF STRUCTURE   3-D VIEW OF STRUCTURE
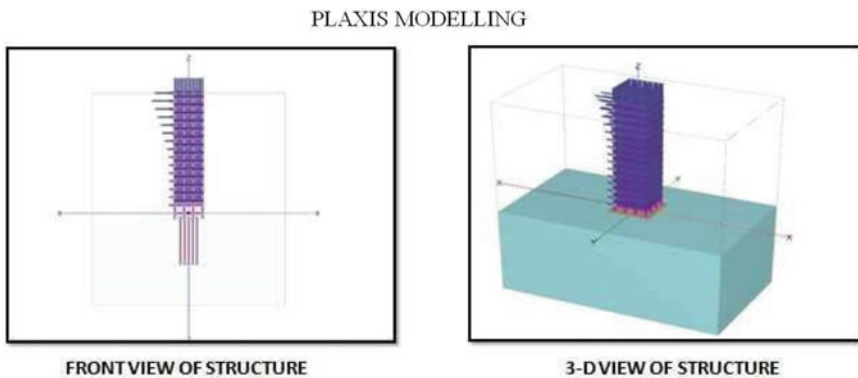
Fig. 6 Plaxis simulation
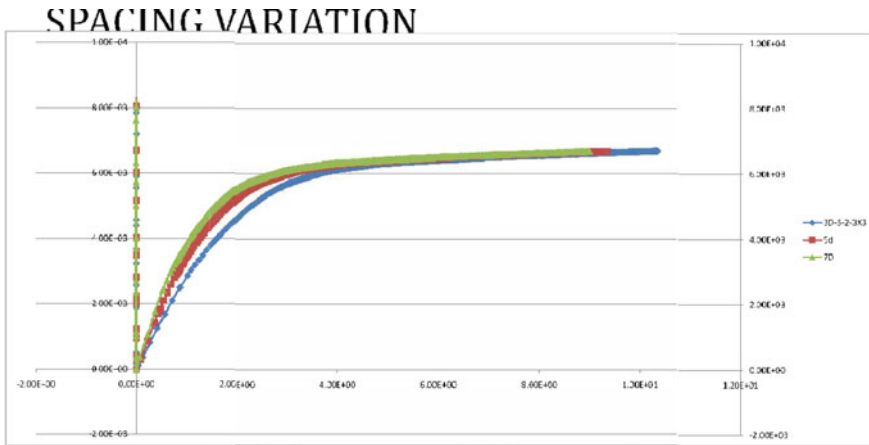
Fig. 7 M-stage versus deflection for various spacing 3×3 grids
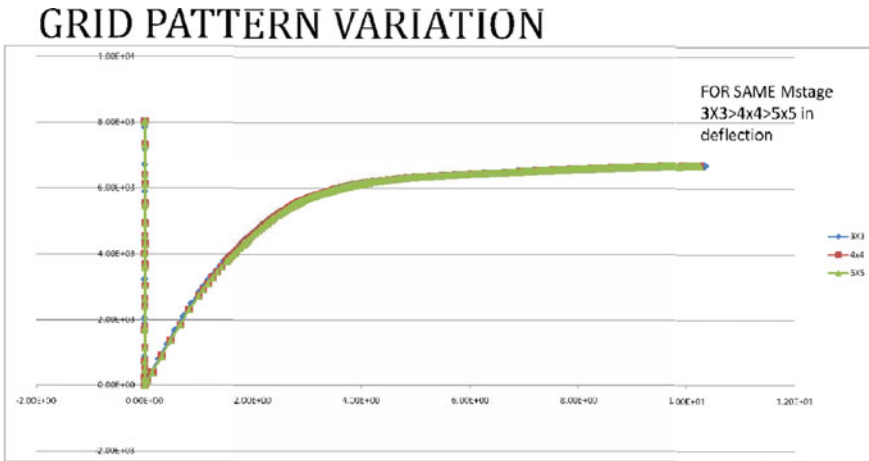
Fig. 8 M-stage versus deflection for various grid pattern with same spacing
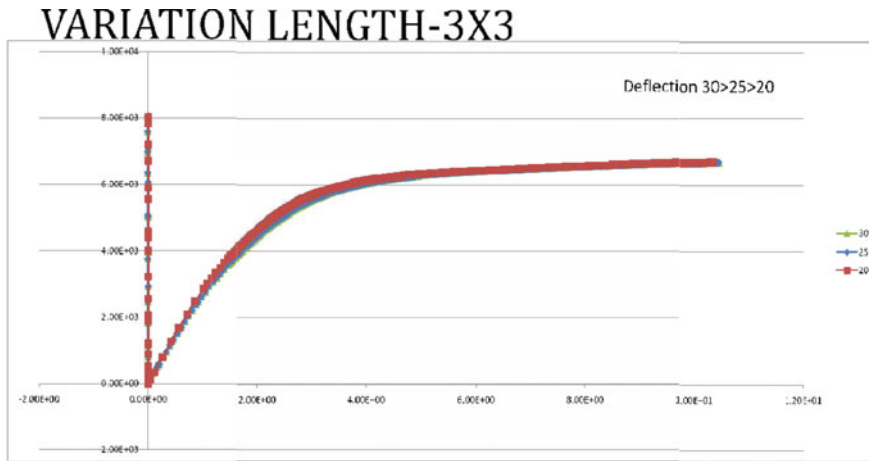
Fig. 9 M-stage versus deflection graph for various length same grid pattern

7 Conclusion

- After pushover analysis of various models, we can conclude that
- *For varying spacing*: *Eventhough 7D shown more stability for higher base shear value it has deflected less compared to 5D and 5D performed better than 3D.*
- *For varying grid pattern: Showed less variation for same base shear 5×5 showed less deflection $> 4 \times 4 > 3 \times 3$ pattern*
- *For varying L/D ratio: For Same base shear value L/D ratio 30 showed less deflection compared to 25 > 20*

The models are under further examination…. This study should be further extended to even higher raised buildings as variation observed for 15 storey is very less.

References

1. Pinho R. Using pushover analysis for assessment of buildings and bridges. In: Pecker A (ed) Advanced earthquake engineering analysis
2. Sun L, Xie W (2019) Experimental assessment of soil–structure interaction efects on a super long-span cable-stayed-bridge with pile group foundations. Bull Earthq Eng 17:3169–3196
3. Ali Khan M (2013) Seismic design for buildings. Earthq Resist Struct. https://doi.org/10.1016/B978-1-85617-501-2.00010-9
4. Qiua D, Chenb J, Xub Q (2020) Improved pushover analysis for underground large-scale frame structures based on structural dynamic responses Tunnel Undergr Sp Technol 103(2020):103405
5. Ansari M, Nazari M, Panah A (2021) Influence of foundation flexibility on seismic fragility of reinforced concrete high-rise buildings. Soil Dyn Eng Earthq 142(2021):1065
6. Korkmaz KA (2008) Evaluation of seismic fragility analyses. In: The 14th World Conference on Earthquake Engineering October 12–17, 2008, Beijing, China

Monitoring Loading Effects of Construction Steel Structure Using Piezo Transducer for Electromechanical Impedance Techniques

Lukesh Parida and Sumedha Moharana

1 Introduction

The application of piezoelectric smart materials in damage detection techniques is a relatively new and promising innovation in the field of structural health monitoring (SHM) in civil and mechanical infrastructure. The invent of smart materials possess the ability to assess the condition of structures and relay the information about its load and strain usage and any damage (if occurred) target specific areas for inspection. The implementation of piezoelectric material like Lead Zirconate Titanate (PZT) in SHM became more efficient with the advancement of electromechanical impedance (EMI) techniques. Piezoelectric materials are commonly used in structural dynamics applications because they are light weight, long term stability, low cost, and come in a variety of sizes and shapes. Bhalla and Soh [1] derived the following expressions for the bonded/embedded PZT patch's coupled complex admittance signature

$$\overline{Y} = G + Bj = 4\omega j \frac{l^2}{h} \left[\overline{\varepsilon_{33}^T} - \frac{2\,d_{31}^2\,\overline{Y^E}}{(1-\mu)} + \frac{2\,d_{31}^2\,\overline{Y^E}}{(1-\mu)} \left(\frac{Z_{a,\text{eff}}}{Z_{S,\text{eff}} + Z_{a,\text{eff}}} \right) \overline{T} \right] \quad (1)$$

where G and B are the conductance and susceptance, l, w, and h are the dimensions of the PZT patch, μ poisons ratio, and $\overline{\varepsilon_{33}^T}$ complex electrical permittivity, k is wave number, and $Z_{a,\text{eff}}$ and $Z_{S,\text{eff}}$ denote effective impedance of PZT patch and structure, respectively. $\overline{Y^E}$ and $\overline{\varepsilon_{33}^T}$ are the complex young's modulus of elasticity and complex electrical permittivity, respectively. $d31$ piezo electric strain coefficient, T is the complex tangent ratio equal to $\frac{\tan kl}{kl}$, and ω is angular frequency of excitation.

L. Parida (✉) · S. Moharana

Department of Civil Engineering, Shiv Nadar University, Uttar Pradesh, Dadri 201314, India

e-mail: lp617@snu.edu.in

The EMI technique utilizes a small PZT patch attached to the host structure to impart a harmonic force on the structure by applying an electric field (AC voltage signal) across the patch. The structural response comprises of peaks and valleys in "admittance versus frequency" plot, which is known as the electromechanical (EM) "admittance signature." If damage occurs in the structure, its mechanical impedance will change, which will modify the admittance signature, thereby providing indication of the damage [2, 3]. This equation couples the mechanical impedance of the structure with the electrical admittance which means that any damage to the structure (change of $Z_{s,eff}$) will reflect itself as change in.

From the past studies, many researchers have demonstrated the usage of PZT transducers for detecting incipient damage in structures using high frequency excitations [4–6]. PZT sensors were employed to determine the location and severity level of damage [7]. Many researchers also found the suitability of EMI techniques for various structural applications and incipient damage detection. Impedance-based structural health monitoring gained much popularity among researchers to determine the damage detection, localization, and quantification of concrete, composite and steel structures, where most of the studies utilized PZT patch directly attached to host structure only [8–12]. On the other hand, the brittleness of the PZT patch makes attaching the patch to surfaces with complex geometrics difficult. Furthermore, direct bonding the PZT patch to the structures surface may not be viable if the structure is constantly under impact load or is exposed to high temperature environment and may not be easily accessible. To address these issues, Na and Lee [13] proposed metal wire-based electromechanical impedance (MWBEMI) approaches, in which PZT patch is not directly attached to the structures surface but instead functions from the end of a steel wire that is attached to the structure.

This paper aims to explore non-bonded and reusable piezo configuration in depth through experimental investigations. Naskar and Bhalla [14] only studied MWBEMI approach to successfully identify and localize the two-dimensional structure. This article utilizes multi piezo configuration-based EMI techniques to determine better sensing of *loading and it's consequences* in construction steel sample using tensile test. Three different locations of PZT sensor, i.e., surface bonded, metal wire-based and clamped arrangements is used for HYSD bar of 12 mm to monitor the load action through tensile pull test. Statistical damage metrics (RMSD) are used for better quantification of signature. The prime focus of the current study is to address non-bonded and reusable configuration because of non-assessed and deformed surface of reinforced bar.

2 Materials and Experiments

In this investigations, tensile pull test was conducted for construction steel rebar to assess the loading effects using non-bonded and reusable piezo configuration. The experimental steel rebar has a diameter of 12 mm and a length of 300 mm HYSD bar according to IS 432-1982. After fabrication of test specimen, three different

Table 1 Properties of PZT patch (PI ceramic, 2014)

Property	Unit	Value
Size of PZT patch	m^2	0.010×0.010
Thickness	M	3.000×10^{-4}
Piezoelectric strain coefficient, d_{31}	m/V	-2.100×10^{-10}
Electric permittivity, ε_{33}^T	Farad/m	2.124×10^{-8}
Young's modulus, Y^E	N/m^2	6.667×10^{10}
Dielectric loss factor, δ		0.0224
Mechanical loss factor, η		0.0325
Poison's ratio, μ		0.3000

arrangements of PZT patches were bonded to it. In this studies, The PZT patches (PIC 151) were utilized for evaluating the employability of multiple piezo sensors for monitoring the tensile loading of steel bar through UTM machine. The detailed properties of PZT patch were reported in Table 1. Firstly, an aluminum strip with a length of 30 mm, a width of 10 mm, and a thickness of 1 mm was directly attached to steel rebar, and PZT patches were bonded to strip using epoxy adhesive with clamp tightened at two ends (refer Fig. 1a). A square cut was made in the center of the PZT, and epoxy adhesive was used to attach the PZT to the rebar (refer Fig. 1b). A metal wire with a length of 500 mm, a width of 10 mm, and a thickness of 1 mm was directly attached to 12 mm diameter steel rebar, and PZT patches bonded to foil ends with high strength epoxy adhesive (refer Fig. 1c). Electrical wires were soldered to the PZT electrodes with care after applying the epoxy adhesive and allowing it to cure for about 24 h. *The piezo-impedance signatures were recorded through impedance analyzer with excitation voltage of 1Vrms and frequency swept from 30 to 300 kHz with 100substeps.* The schematic diagram of total system is shown in Fig. 2. As a protective measure, the PZT patch was then coated with a thin coating of epoxy adhesive. Tensile force action is imposed using universal testing machine (UTM). Conductance signatures were obtained via a connection between the impedance analyzer for all three piezo configurations. RMSD index was calculated

(a)   (b)   (c)
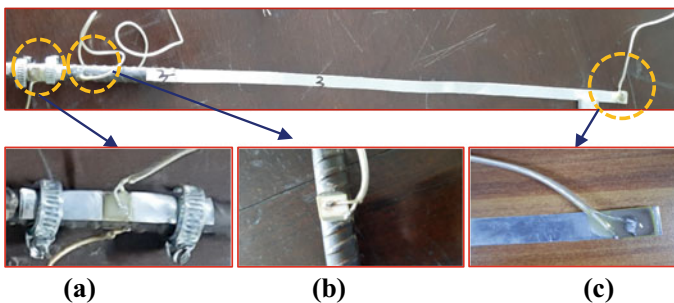
Fig. 1 Specimen with PZT attached for (**a**) clamped, (**b**) surface bonded, and (**c**) metal wire
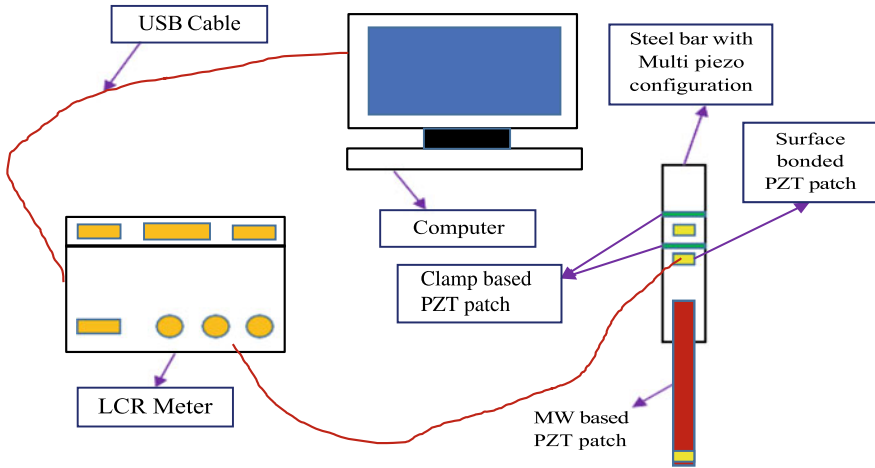
Fig. 2 Schematic diagram of total system

for each tensile load cases and all the lab-sized samples and compared with the baseline signatures. The following section will cover the sensor readings and their quantifications.

3 Results and Discussions

3.1 Sensor Stabilization

The structural deterioration of infrastructure systems may take long time, and it may affect the system's lifespan and reliability. As a result, it is vital to assure sensor stabilization under the same structural health situation. So far sensor stabilization of multi piezo configuration of steel sample is needed to attain the baseline signature required EMI technique. Hence, three different lab-sized instruments with PZT patch have used for acquiring conductance signatures, typically recorded over a finite period time while ensuring a sensor reading and good repeatability. In the same fashion, baseline signature was obtained for three different piezo sensor location (surface bonded, metal wire based, clamped) for the 30–300 kHz frequency range at 27 °C without any structural loading in steel.

The signatures recorded from surface bonded, metal wire-based and clamp-based PZT patches for day 1, day 7, and day 21 are compared in Figs. 3, 4 and 5, respectively. Different days reading are mentioned to signify the bond curing and good sensor bonding quality of proposed experimental approach.

From the above results, it can be seen that all signatures for surface bonded, clamp and metal wire-based PZT patch are coinciding with baseline signature with
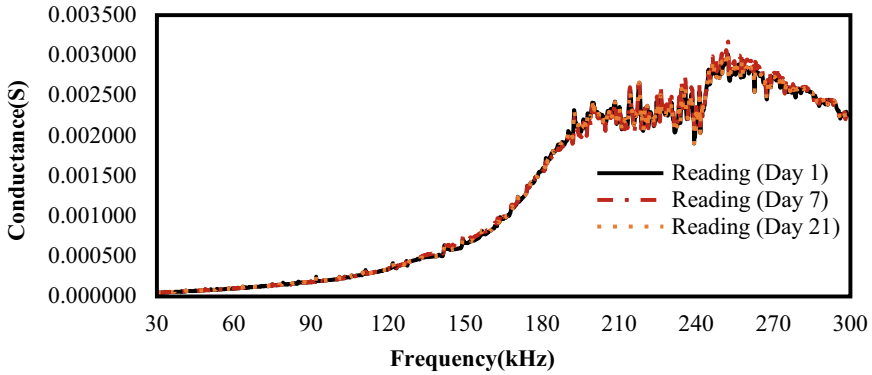
Fig. 3 Sensor stabilization for surface-bonded PZT patch
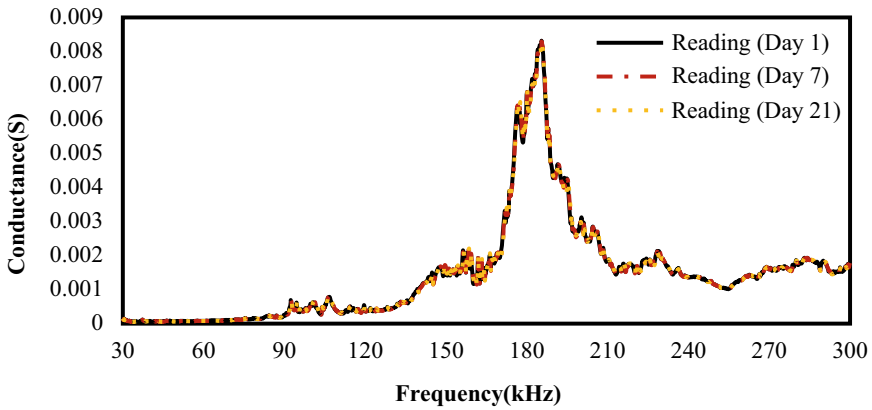
Fig. 4 Sensor stabilization for clamp-based PZT patch
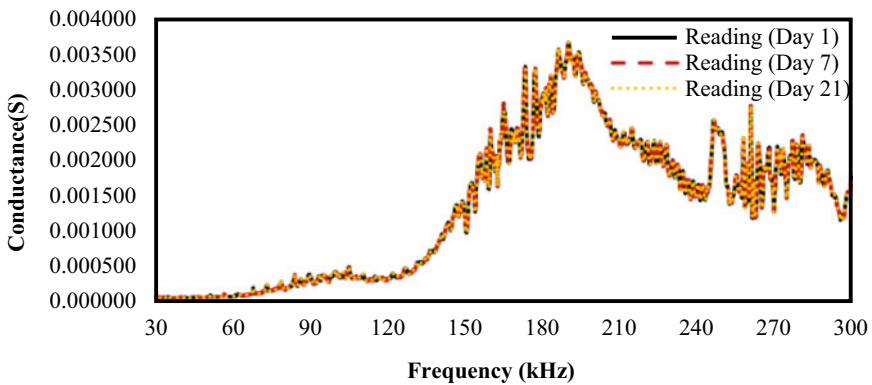
Fig. 5 Sensor stabilization for metal wire-based PZT patch

a repetitive manner. It shows the bond is cured, and all sensor signals are quite stabilized over time. So it is considered as the baseline signatures for the structure.

3.2 Effect of Tensile Strength of Steel Rebar

Mostly concrete and steel are being only one of the most suitable and composite material for new age civil infrastructure construction. In steel concrete composite structure, the ultimate tensile stress is taken care by the steel rebar only but while being embedded, one has to look out anchorage pull dominated with overall shear tensile forces, caused initial dimensional crack, i.e., splitting. Here, the author is limiting the sensor reading for lower strength range (i.e., 0–30 kN). The reason behind for selecting the load is to simulate the anchorage-based shear tensile in HYSD bar, and the main objective of this study is to evaluate the sensor efficiency for the multiple piezo location to detect the shear tensile pull on constructional steel. The overall load deformation graph of lab-sized sample has shown in Fig. 6.

The conductance signatures were acquired for tensile pull on lab sizes steel bars instrumented with sensors for three loading cases, i.e., 9, 18, and 27 kN. The initial load ranges are chosen to evaluate the piezo sensor efficiency toward the detection of incipient force traction on steel bar. The piezo coupled signatures are plotted in Figs. 7, 8, and 9 for the surface bonded, clamped, and metal wire based, respectively. All the sensors are equally participated and the behavioral signature pattern to indicate the tensile force action in steel sample, the conductance peak shifting toward leftward and with the increase of load the frequency is shifting toward left (Fig. 7). For other two configurations though conductance variation is not much prominent but the overall trend (i.e., decrement of frequency and piezo resonance peak) is quite
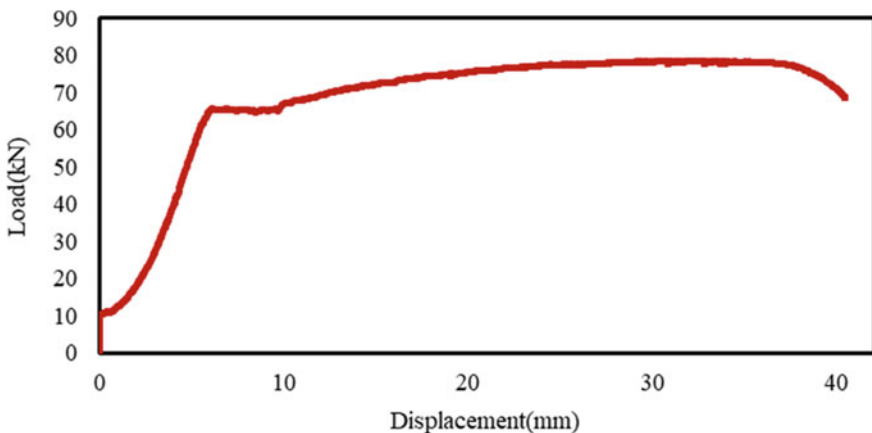
Fig. 6 Load versus displacement curve of lab-sized steel sample
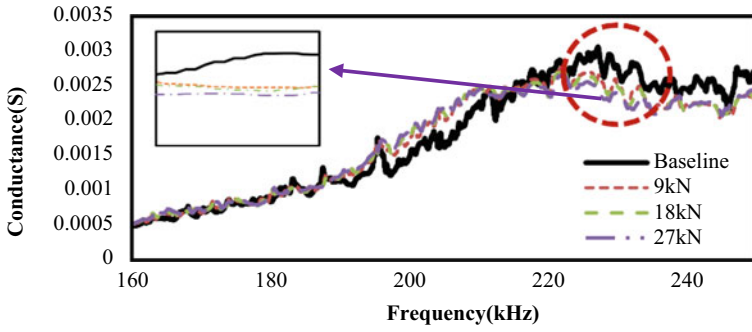
Fig. 7 Effect of tensile pull load on surface-bonded PZT patch
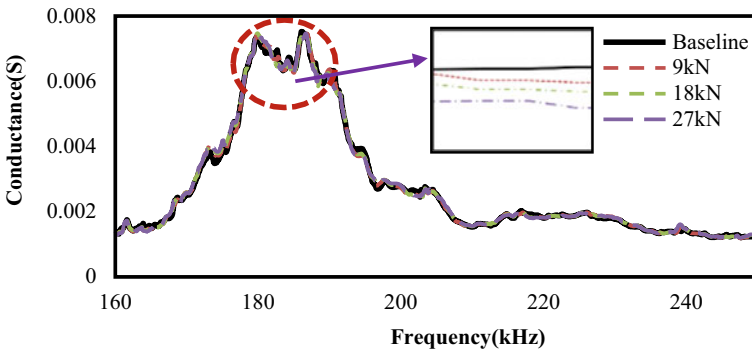
Fig. 8 Effect of tensile pull load on clamp-based PZT patch
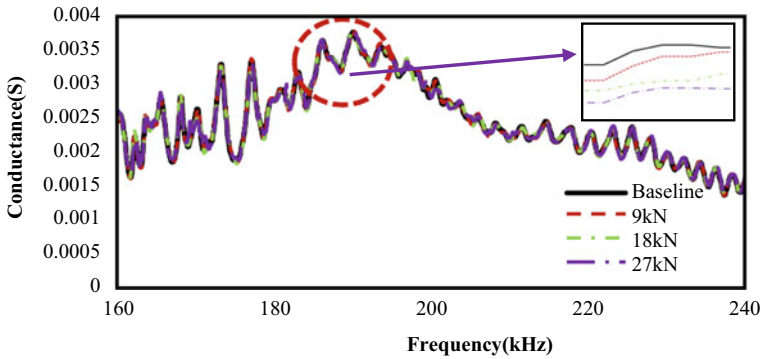
Fig. 9 Effect of tensile pull load on metal wire-based PZT patch

evident from the Figs. 8 and 9. Looking for the efficiency of three different piezo locations, we found that clamp and metal wire-based EMI techniques are quite feasible for the ribbed and complex surface of the steel bars, for reusable and non-bonded configuration.

The root mean square deviation (RMSD) index is used to quantify changes in signature due to damage. RMSD index for piezo coupled structure can be expressed as Giurgiutiu and Rogers [15, 16].

$$\text{RMSD (\%)} = \sqrt{\frac{\sum_{j=1}^{N} (G_j^1 - G_j^0)^2}{\sum_{j=1}^{N} (G_j^0)^2}} \tag{2}$$

where G_j^1 is the conductance signatures obtained for various load cases.

G_j^0 is the conductance signatures obtained for baseline signatures.

The RMSD value for all configurations for lab-sized steel samples are shown in Figs. 10, 11, and 12, respectively.

From the RMSD values, it is clearly evident that clamped and metal wired-based techniques are less sensitive (see Figs. 11 and 12) compared to that of surface-bonded case (see Fig. 10). However, it follows same trend like surface-bonded PZT arrangements to detect the loading effects and corresponding structural changes with respect to baseline signatures. Although metal wire and clamp-based PZT has lower sensitivity, but it can be utilized in situations where a standard EMI method is not possible, especially in case of complex structural geometry and inaccessible portion of bridge structure.
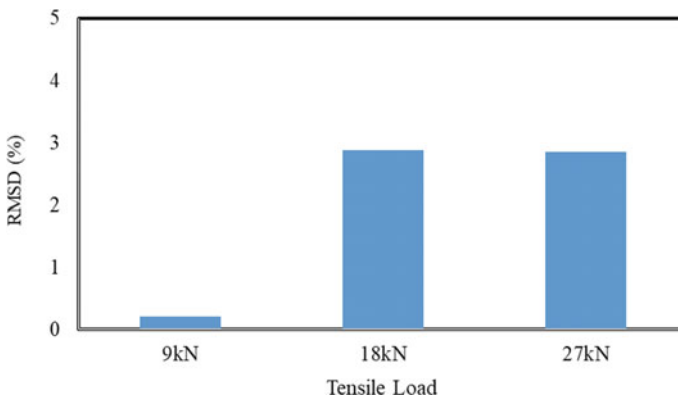
Fig. 10 RMSD values for rebar-bonded PZT patch for tensile load
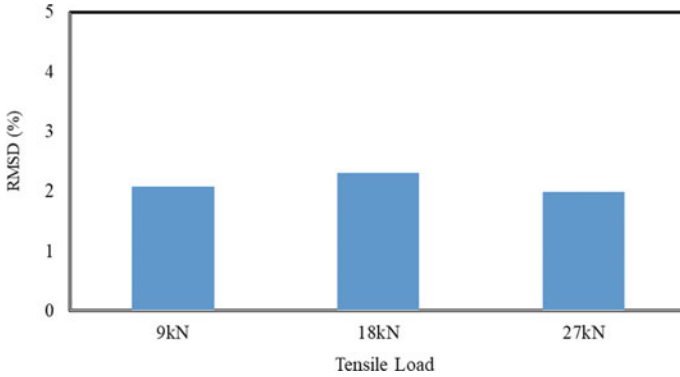
Fig. 11 RMSD values for clamped PZT patch for tensile load
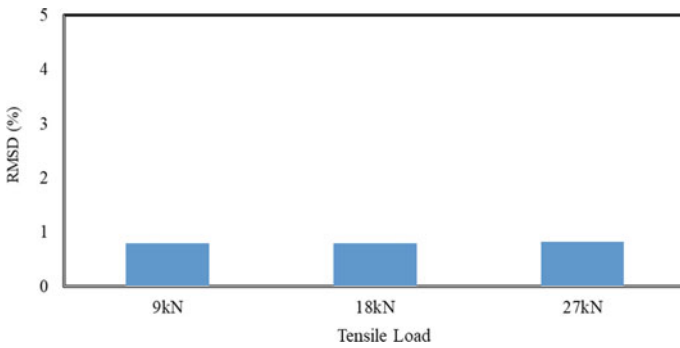
Fig. 12 RMSD values for metal wire-bonded PZT patch for tensile load

4 Conclusions

This current study mainly focuses to evaluate the multiple piezo configuration toward tensile loading of HYSD construction steel bar. It proposes the reusable and non-bonded piezo configuration for curved surface of steel bar subjected to load cases while embedded in concrete for shear tensile to stimulate the anchorage bond behavior. The lab-sized steel samples instrumented with the PZT patches are loaded with tensile pull and conductance signature were acquired. From signatures, it can be found that EMI signatures for three different configurations are capable to detect the tensile pulling (for lower load range). Also, through RMSD quantification, it has been seen that the reusable and non-bonded configuration has ability to detect the internal structural resistance changes against tensile fully successfully. This study may further explored, and its implication can be used for the cases where complex civil infrastructure component which are not assessable or direct assessment of structure is prohibited.

References

1. Bhalla S, Kiong Soh C (2003) Structural impedance based damage diagnosis by piezo-transducers. Earthquake Eng Struct Dynam 32(12):1897–1916
2. Moharana S, Bhalla S (2012) Numerical investigations of shear lag effect on PZT-structure interaction: review and application. Current Sci 685–696
3. Yang JW, Zhu HP, Yu J, Wang DS (2013) Experimental study on monitoring steel beam local corrosion based on EMI technique. In: Applied mechanics and materials, vol 273, pp 623–627. Trans Tech Publications Ltd.
4. Tawie R, Lee HK (2010) Piezoelectric-based non-destructive monitoring of hydration of reinforced concrete as an indicator of bond development at the steel–concrete interface. Cem Concr Res 40(12):1697–1703
5. Fan S, Zhao S, Qi B, Kong Q (2018) Damage evaluation of concrete column under impact load using a piezoelectric-based EMI technique. Sensors 18(5):1591
6. Park SH, Yi JH, Yun CB, Roh YR (2004) Impedance-based damage detection for civil infrastructures. KSCE J Civ Eng 8(4):425–433
7. Divsholi BS, Yang Y (2008) Application of PZT sensors for detection of damage severity and location in concrete. In: *Smart structures, devices, and systems IV*, vol 7268, p 726813. International Society for Optics and Photonics
8. Na WS, Park KT (2017) A cost-effective impedance-based structural health monitoring technique for steel structures by monitoring multiple areas. J Intell Mater Syst Struct 28(2):154–162
9. Li W, Liu T, Wang J, Zou D, Gao S (2019) Finite-element analysis of an electromechanical impedance–based corrosion sensor with experimental verification. J Aerosp Eng 32(3):04019012
10. Kim JW, Lee C, Park S, Koh KT (2013) Real-time strength development monitoring for concrete structures using wired and wireless electro-mechanical impedance techniques. KSCE J Civ Eng 17(6):1432–1436
11. Na S, Lee HK (2012) A technique for improving the damage detection ability of the electro-mechanical impedance method on concrete structures. Smart Mater Struct 21(8):085024
12. Zhu H, Luo H, Ai D, Wang C (2016) Mechanical impedance-based technique for steel structural corrosion damage detection. Measurement 88:353–359
13. Na S, Lee HK (2013) Steel wire electromechanical impedance method using a piezoelectric material for composite structures with complex surfaces. Compos Struct 98:79–84
14. Naskar S, Bhalla S (2016) Metal-wire-based twin one-dimensional orthogonal array configuration of PZT patches for damage assessment of two-dimensional structures. J Intell Mater Syst Struct 27(11):1440–1460
15. Giurgiutiu V, Rogers CA (1998) Recent advancements in the electro-mechanical (E/M) impedance method for structural health monitoring and NDE. In: Proceedings of SPIE conference on smart structures and integrated systems, San Diego, California, March, SPIE, vol 3329, pp 536–547
16. Li W, Liu T, Zou D, Wang J, Yi TH (2019) PZT based smart corrosion coupon using electromechanical impedance. Mech Syst Signal Process 129:455–469

Benefit Cost Analysis of 3D Printed Concrete Building

Najeeb Manhanpally and Suman Saha

1 Introduction

To have a safe shelter is considered amongst the primary need of human beings. Throughout the history of mankind, we have been in constant search for better building materials, which allow us to build stronger but cheaper houses. Invention of cement and concrete has revolutionised the construction industry. With an annual production of 10 million tons, concrete is the most widely consumed resource material after water [1]. Due to increased rate of construction all over the world, construction industry is now facing shortage of materials leading to high material cost. Also, the construction world is now facing a shortage of labour. Both increased material and labour cost are causing high expenditures in building construction [2]. Even today in the modern times of automation in every field, construction industry is still based on the labour-intensive construction practices. This has forced the construction industry not to taste the benefit of less cost which many other industries are already getting. There is an urgent demand for transforming and upgrading the practices in construction industry with different construction automation technology [2].

Cement-based additive manufacturing, which is often referred to as 3D concrete printing, has been under research and development for the past decade [3, 4]. In 3D printed concrete (3DPC), use conventional moulds like formworks are avoided by precisely placing and setting of concrete material printed in sequential layers under an automated process. 3D printing technology is an intelligent technology which

N. Manhanpally (✉) · S. Saha
Department of Civil Engineering, National Institute of Technology Calicut, Kozhikode, Kerala 673601, India
e-mail: najeeb_p200033ce@nitc.ac.in

S. Saha
Department of Civil Engineering, National Institute of Technology Durgapur, Durgapur, West Bengal, India

is making great impacts in the fields of manufacturing. This technology allows to prepare complex-shaped parts with ease according to the imagination of the user. The use of 3D printing technology in the construction industry is gaining more and more interest in recent years. In comparison with conventional labour-intensive construction practices, 3D printing technology in manufacturing allows faster construction with lesser labour consumption and thus leading to lower cost. Since no formworks are required in this method, it allows design liberalisation and low resource consumption [5]. The 3D printing construction market is projected to grow about 250% between 2019 and 2024. The market for 3D printed structures is growing at a fast-paced rate due to the high demand for complex-shape structures in the building and infrastructure sectors. 3D printing is considered as an important tool for the third industrial revolution [2].

The development of 3D printing in construction industry started with the introduction of contour crafting by Khoshnevis in the mid-1990s [4]. Contour crafting was based on the fused deposition modelling of additive manufacturing method [5]. There are different approaches to 3D printing in construction industry, namely contour crafting, smart dynamic casting and extrusion-based printing. Amongst these techniques, extrusion-based printing is the most accepted one [6]. In extrusion-based printing, extruded concrete filament is deposited onto one another in sequential layers. The extrusion of continuous filament through a small nozzle is done with help of nozzle mounted on gantry [3]. Due to its layered structure, 3DPC cannot be considered as a homogenous structure [7].

The primary concerns for a consumer to adopt a new technology are the cost incurred and benefits associated with the technology. Anybody will be hesitant to adopt relatively new technique if the cost is associated with it is higher than the traditional method, even if there are benefits over the old method. Only, a few studies have been conducted on the cost analysis of 3D printed concrete. Most of the studies were focussed on comparison of 3DPC to the traditional concrete. But, the 3DPC is essentially replacing the masonry construction. In this study, a cost comparison of 3DPC with masonry construction is done in order to understand its benefits over the conventional construction method.

2 Literature Review

2.1 Materials Used for 3D Printing

From the literature, materials used for preparing 3DPC are mainly cement and aggregates. The material selection for 3DPC is highly dependent on the fresh properties required for the printing or extrusion of the material. Supplementary cementitious materials, admixtures and fibres are added to enhance and meet the requirements of 3DPC.

Most researches have used cement as primary binder used in 3DPC. In order to be able to smoothly extrude the material, cement requirement of 3DPC is very high, which increases the cost of the material [5]. Also, increased cement content will also adversely affect the sustainability factor of 3DPC due to the carbon dioxide emission during the manufacturing of cement [5]. Based on the life cycle analysis, the environmental impact as well as the pollutant emission caused by 3DPC was found to be more than those of conventional concrete [2]. Supplementary cementitious materials like fly ash, limestone filler and blast furnace slag are used to partially replace cement and hence make 3DPC more environmental friendly [5]. Geopolymers are also used as an alternative binder material in 3DPC [8]. The addition of nano-clay decreased the flowability, setting time and improved the buildability of 3D printing materials [9].

Even though it is called as concrete, most of the 3DPC are mortars without coarse aggregate [10]. Maximum size of aggregates typically used in 3DPC is less than 2 mm [11]. 3D printing mortar mixed with continuous-graded sand is shown to have better buildability than the gap-graded mortar [9]. The main constraint in using coarse aggregate for 3DPC is the difficulty in printing due to small nozzle size and often use of conventional rotor pumps. Rahul et al. [11] conducted studies on 3DPC by incorporating lightweight coarse aggregates with a maximum size of 10 mm by using piston pump-based system, and the sand replacement ratio reached up to 10%. Replacing natural fine aggregates with recycled sand in 3D printed construction will improve the cost-effectiveness and sustainability of 3DPC [9]. By adding sodium gluconate, 100% recycled sand gives longer printability and higher green strength than those of 100% natural sand [12].

Adding admixtures to 3DPC can enhance the printable as well as strength characteristics. Chemical admixtures such as superplasticizers, viscosity-modifying agents, setting retarders and accelerators can improve the fresh as well as hardened properties of concrete. It also improves the flow properties required for smooth extrusion. Addition of superplasticizer has become an inevitable part of 3D printable concrete due to its capability of successful extrusion [5]. Once laid the concrete needs to be hardened before the deposition of next layer, where setting accelerators play a significant role. Since 3DPC is rich in cement content, adding shrinkage reducing agents can reduce the occurrence of shrinkage cracks in 3DPC. Viscosity-modifying agents (VMAs) are used in 3DPC to enhance the viscosity, cohesion and shape stability of concrete. Additions of nano-clay improves the robustness of the 3DPC mixture by decreasing the flowability and setting time and hence improving the buildability of 3D printing materials [13]. The addition of hydroxypropyl methylcellulose shall enhance the yield stress, viscosity and shape retention of 3DPC [5]. Studies conducted by Rahul et al. [14] indicated the combine use of polycarboxylic ether-based superplasticizer in liquid form and hydroxypropyl methylcellulose (HPMC) as a viscosity-modifying admixture in the powder form gives good results when added to 3DPC.

Concrete is susceptible to the occurrence of cracks due to its weak tensile nature compared to compressive strength. This is further visible in 3DPC due to its rich cement further contributing to shrinkage cracks. Addition of reinforcement to 3DPC is the best solution to overcome this problem. However, due to layer by layer printing

of 3DPC, incorporation of reinforcement is one of the primary challenges regarding 3DPC. This drawback of 3DPC is usually overcome by constructing compression-only structures. Integration of vertical reinforcement in 3DPC is achieved either by introducing reinforcement post-printing or by introducing reinforcement in line with printing [1]. Addition of fibres to the mix can enhance the flexural properties of 3DPC and reduce the development of cracks. Organic fibres like poly propylene fibre, polyethylene fibre, polyvinyl alcohol fibre, basalt fibre, carbon fibre and glass fibre have been used in 3DPC [5]. Using steel fibres as a reinforced material in additive manufacturing of concrete technology isn't recommended [8].

2.2 Properties of 3D Printed Concrete

2.2.1 Fresh Properties

The particular challenge in achieving suitable mix for 3DPC remains the printability, extrudability and buildability of 3DPC which is closely related to the fresh properties and rheological parameters. Pumpability of printable concrete is described as the ease with the concrete mix is transported from pump to extrusion through nozzle [3]. Printability is usually examined by deformation of freshly printed layers. Extrudability can be defined as the ease to extrude the mix through a nozzle as continuous filament without considerable deformation [3]. 3DPC should be a homogeneous material and able to be extruded continuously without any blockage, cracking and segregation. The ability of the material to retain its shape under the self-weight and the load of concrete from above layers is called buildability. The most direct way to assess buildability is to compare the maximum height or number of layers that can be built with the same printing setup [15]. The thickness of 3DPC layer is generally set to be varied from 1 to 10 cm to limit the initial gravity stress to control the deformation whilst printing consequent layers [3]. Yield stress and viscosity are usually used to assess the extrudability and buildability of 3DPC. Adequate extrudability and buildability are usually achieved when the material yield stress is within certain range of 1.5–2.5 kPa [9].

2.2.2 Mechanical Properties

Mechanical properties at the early stage as well as hardened state are very important for the 3DPC. The early age mechanical properties influence the printability and buildability of 3DPC. There should be only a slow increase in the green strength of concrete at the early stage to aid the printability, but the concrete should attain enough strength before the subsequent layer is printed to achieve the required buildability. Hence, there should be a rapid development in the compressive strength of 3DPC [5].

The major problem for 3DPC in achieving adequate mechanical properties is the interlayer bond strength and the resulting anisotropy [5]. 3DPC element cannot be considered as homogenous material due to its layered structure with more porous and weaker interfaces [6]. Recent studies show that up to a 36% reduction in flexural strength is obtained for 3D printed samples due to the effect of the interlayer bond [16]. Also, the increased print speed decreases the bond strength. Different studies have been done to increase the interlayer bond strength. Hosseini et al. [17] used to glue the two layers together with a new polymer consisting of black carbon and sulphur (SBC), and results showed significant improvement.

The tensile bond strength can depend on the print parameters such as time gap between two successive layers, print speed and the height from which the nozzle is depositing the layer [18, 19]. The compressive strength and the flexural strength of 3DPC and cast concrete were enhanced with the decrease of cement to aggregate ratio values when incorporating coarse aggregate into the concrete [10].

2.2.3 Durability of 3D Printed Concrete

Since the studies on 3DPC is in its early stage, most studies are focussing on mix design and early age characteristics [5]. Even though durability is an important aspect for considering the long-term performance of 3DPC, studies on durability of 3DPC are limited. Freeze–thaw cycle, carbonation, chloride penetration, alkali aggregate reaction are the major environmental problems affecting the durability of any concrete. The weak interlayer bonding decreases the durability of 3DPC [20]. As 3DPC is rich in cement content, the chances for occurrences of shrinkage cracks are also high. Chances for occurrence of plastic shrinkage and dry shrinkage are increased in 3DPC, as the concrete surface is exposed directly after laying since no formwork being used [5].

2.3 Benefits of 3D Printed Concrete

The major advantage of 3DPC is attributed to the introduction automation in construction industry. The labour-intensive construction industry is facing huge delays in project due to the shortage of labours. As the 3DPC uses very less labours, the shortage of labours can be addressed. Due to automatic operation and no need of formwork, 3D printing has distinctive advantages over traditional construction practices, contributing to higher construction efficiency, reduced labour and reduced wastage production [21]. As reduced labour is required for 3DPC-based construction, associated injuries to labour at site are also reduced.

The buildings constructed are mainly box-shaped structures due to the limitation of materials used and formworks. Formwork is one of the most important aspect in construction where extra care is required to reduce the wastage in construction industry. As formwork is mainly made from wooden materials, it also attributes to the

increased environmental impact of construction. With 3DPC building, formworks are less required. Also, there is design flexibility to construct complex-shaped structures using 3DPC.

3 Methodology

The benefits of 3DPC are associated with reduced labour, freeform construction and freedom of design complexity. But, when it comes to a consumer, the primary concern is regarding the cost of construction. Only, a few studies were found regarding cost analysis of 3DPC. Many of the studies are focussed on comparison of 3DPC with conventional concrete construction. However, due to the poor tensile characteristics, 3DPC is primarily replacing wall masonry in building construction.

The purpose of this study is to analyse the economic impact of 3D printing technology in building construction and to compare it with traditional masonry construction. The capital cost of 3D printed system can be regarded as fixed assessment in similar to previous asset investment in traditional construction [2]. It is very difficult to assess the cost associated with investment in pre-construction stage. Therefore, in this study, the direct costs associated with the construction are only considered. All other works such as plumbing, electrification, wood works and finish works are done similar in both construction methods; the cost incurred for these are not considered in this study.

The cost of materials and analysis of rates in this study is primarily adopted based on the Delhi Schedule of Rates 2018 and Delhi Analysis of Rates 2019, published by Central Public Works Department of India.

3.1 Materials and Scenarios

For studying the cost comparison of 3DPC wall with traditional brick masonry, a hypothetical single-storey house with an area of 56.73 m^2 (610 ft^2) was taken (see Fig. 1). For the brick masonry wall, brick work with common burnt clay F.P.S. (non-modular) bricks of class designation 7.5 in cement mortar 1:4 was taken (see Fig. 2a). The criteria for 3D printed wall were taken based on India's first 3D printed full-scale structure constructed by a research group in IIT Madras [6]. 3D printed wall module is taken as a hollow structure with two horizontal layers forming the perimeter and interconnecting layers at every 50 cm (see Fig. 2b). The width of layer was taken as 30 mm. Reinforcement was inserted with concrete infilling of grade M20, through cavities provided at corners. Total width of both wall is taken as 20 cm.

Mixture proportion for 3DPC is adopted based on the concrete formulation developed by Rahul et al. [11] for large-scale 3D printer system. The mixture formulation is given in Table 1.
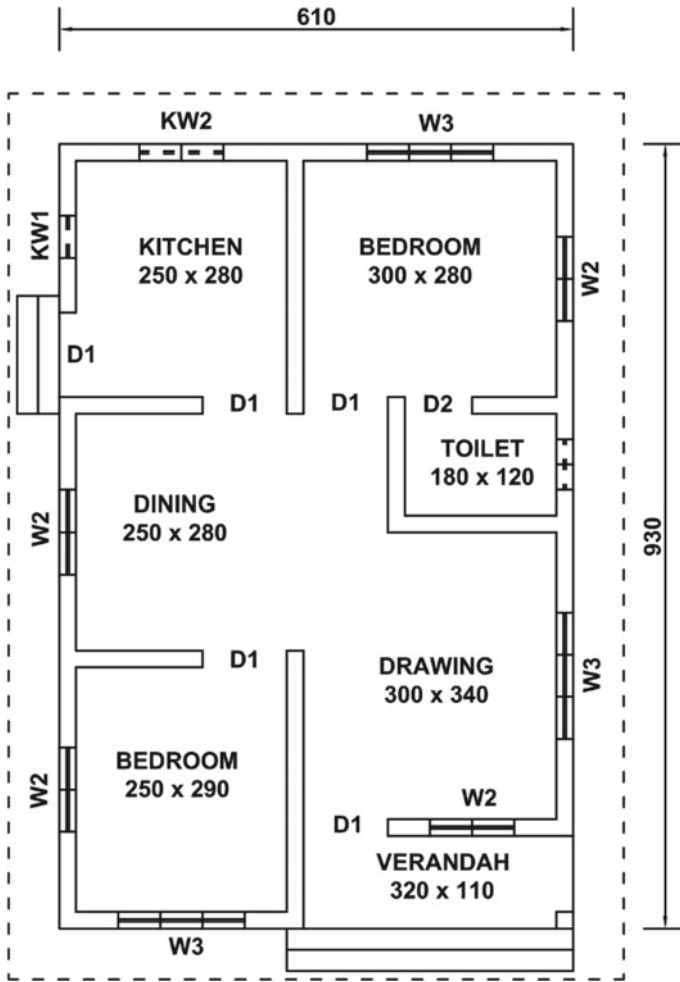
Fig. 1 Plan for hypothetical single-storey building

(a) Model of Brick Masonry wall   (b) Model of 3D printed wall
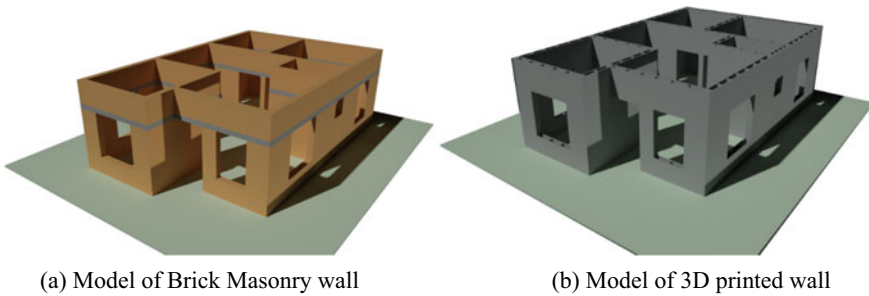
Fig. 2 3D models of walls considered for the study

Table 1 Ingredients considered for 1 m³ 3DPC mix (Rahul et al. [11])

Material	Quantity (kg)
Cement	660
Class F fly ash	165
Sand (max. size 2 mm)	1237
Water	264
Superplasticizer (polycarboxylate ether based)	0.66
Methylcellulose	2.06

3.2 Economic Analysis

To understand the difference in cost of materials for 3DPC, the materials required for unit quantity of brick masonry, normal concrete of grade M20 and 3DPC was calculated, and a cost comparison was done. The quantities of different ingredients required for brick masonry and M20 concrete were calculated based on Delhi Analysis of Rates 2019. The unit rate of materials was referenced from Delhi Schedule of Rates 2018. The cost of methylcellulose is not available in the referenced material; hence, it was taken based on the market rate at the time of study. The cost comparison for 1m³ of brick masonry, M20 concrete and 3DPC is listed in Table 2.

To examine the economic benefit of 3DPC building, the cost incurred for materials and labour at construction stage was analysed with normal brick masonry construction. The quantity of materials, labours, formwork, etc. required for each item of work was taken according to the Delhi Analysis of Rates 2019. As the common practice, a reinforced cement concrete lintel beam is provided throughout the masonry at lintel level for the brick masonry construction. Since it is considered that the 3DPC use reduced labour as the process is automated, the labour required for 3DPC was assumed as 2 skilled labours for handling the raw materials and an operator to operate

Table 2 Cost comparison of 1 m³ brick masonry, M20 concrete and 3D printed wall

	Brick masonry (₹)	M20 concrete (₹)	3D printed concrete (₹)
Bricks	2388.36	–	–
Portland cement	558.43	2021.90	5147.98
Coarse aggregates	–	1235.70	–
Sand	448.99	617.85	1922.34
Fly ash	–	–	53.88
Super plasticizer	–	–	72.60
Methyl cellulose	–	–	721.00
Total	3395.79	3866.45	7917.80

Table 3 Cost of construction for brick masonry and 3D printed wall

	Brick masonry (₹)	3D printed concrete wall (₹)
Materials	74,409.98	73,399.65
Formwork	4690.39	–
Labour	68,163.55	14,721.45
Others (sundries, rent, etc.)	930.08	139.02
Total	148,194.00	88,260.12

the machine. The cost of construction calculated for both 3DPC wall and normal brick masonry wall is listed in Table 3.

4 Results and Discussion

The cost comparison for unit quantity of materials for 3DPC, brick masonry and M20 concrete is highlighted in Fig. 3. According to the statistics given in Table 2 and Fig. 3, the cost of materials for unit quantity in case of 3DPC is much higher than that of brick masonry and M20 concrete. The rate per unit quantity of 3D printed concrete is more than twice the cost of brick masonry and normal concrete. Increased cement content in the 3DPC is the main reason for the significantly higher cost. The cost of additives also adds to the cost.

Even though 3DPC is termed as concrete, it is not replacing the normal grade concrete in the construction due to the poor-strength characteristics of 3DPC when compared with normal concrete. The 3DPC is mainly used for the construction of
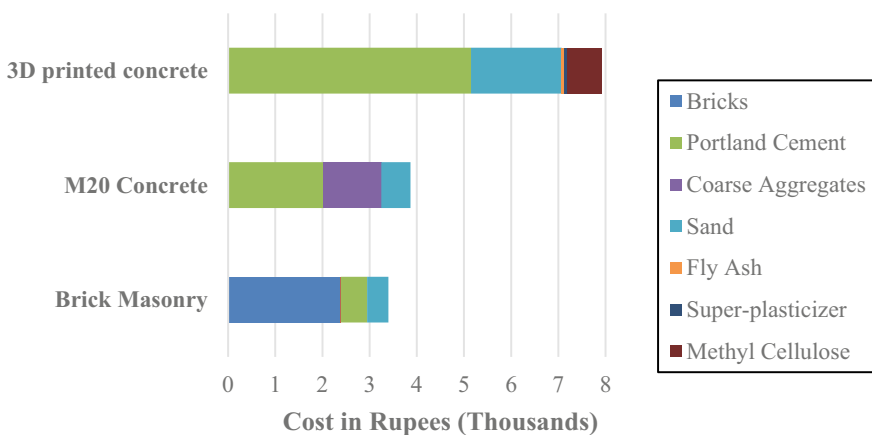
Fig. 3 Cost comparison chart for 1m^3 of brick masonry, M20 concrete and 3DPC

a wall in a building construction. The contribution of the building materials, labour and formwork towards the cost of construction for 3DPC wall and brick masonry wall is represented in Fig. 4a, b. It is understood that the major contributor to the total cost of construction in case of 3DPC is the cost of materials. Whereas, for brick masonry, the cost of labour is almost as important as cost of materials.

Figure 5 highlights the proportion of total cost of building materials, formwork costs and labour costs. The cost of constructing 3D printed wall is 40% lesser than that of brick masonry wall. The cost of 3DPC is much less than that of brick masonry construction. From Fig. 5, it is understood that the cost of materials is almost the same for both methods of construction even though the cost for unit quantity of 3DPC is much higher than brick masonry. This is mainly because of the material saving in the 3DPC wall because of its unique hollow structure. The difference making factor in the total cost is the reduced labour consumption for 3DPC. The profound economic advantage of 3DPC will be further evident in complex-shaped structures.

(a) 3D printed concrete wall   (b) Brick masonry wall
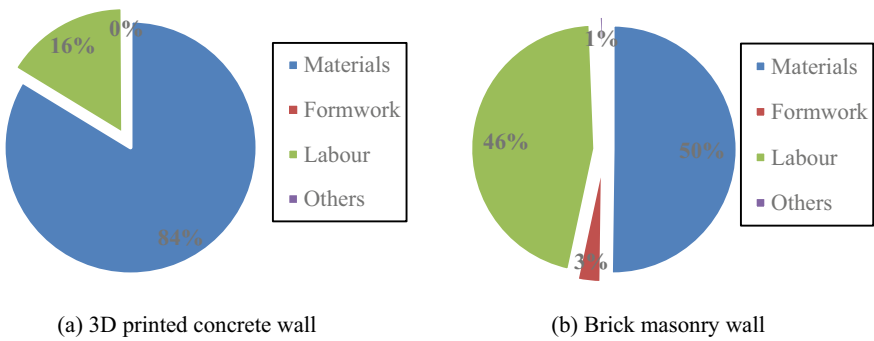
Fig. 4 Percentage contribution of materials, labour and formwork to total cost
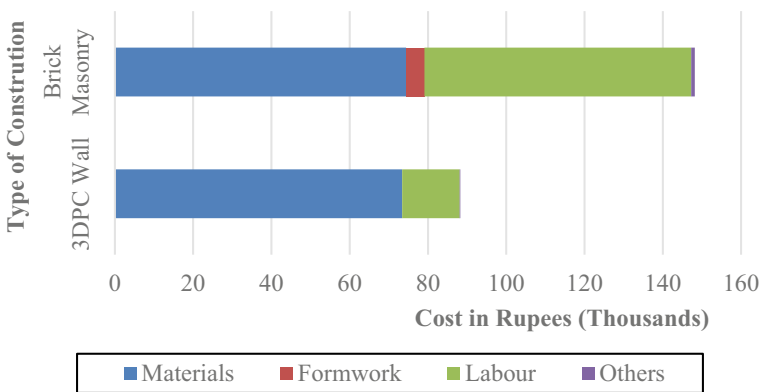
Fig. 5 Analysis of total construction cost

The cost of materials for 3DPC can be further brought down by reducing the cement content, as it is the major cost-deciding factor for cost of 3DPC. Also, the increased cement content can contribute to the shrinkage cracks and reduce the durability. With the significant cost advantage of 3DPC, as identified in this study, it is reasonable to believe that as the 3D printing technology matures through researches by reducing the cement content, adding coarse aggregate to the mix, the economic benefit can be made much higher.

5 Conclusions

3DPC is a recent development in the construction industry. It is rapidly gaining interest amongst researchers and industry due to its reduced labour consumption and form-free construction. This is mainly because of the very slim chance for occurrence of errors and wastage with 3DPC as the operation will be computer controlled. Also, there is freedom of design complexity with the 3DPC.

This study employed the analysis of economic benefit of 3DPC over traditional construction practice by doing a cost comparison. Based on the study, we arrived following conclusion;

- The rate per unit quantity of materials for 3DPC is more than twice the cost for brick masonry and normal concrete due to the increased cement content in 3DPC.
- The cost of materials and labour for constructing 3D printed wall is 40% less than constructing a brick masonry due to the unique structure of 3DPC wall and reduced labour consumption.
- The 3DPC has significant economic advantage over traditional construction practices, even if the cost of materials for unit quantity is higher than other items of works.
- The increased speed of construction and early completion of the project can help the consumer to overcome the unnecessary expenses like variation in cost of materials involved with delays in constructions.
- The material cost for 3DPC can be further reduced with further technological and material improvement.

References

1. Mohan MK, Rahul AV, De Schutter G, Van Tittelboom K (2021) Extrusion-based concrete 3D printing from a material perspective: a state-of-the-art review. Cem Concr Compos 115(June 2020):103855. https://doi.org/10.1016/j.cemconcomp.2020.103855
2. Han Y, Yang Z, Ding T, Xiao J (2021) Environmental and economic assessment on 3D printed buildings with recycled concrete. J Clean Prod 278:123884. https://doi.org/10.1016/j.jclepro.2020.123884

3. Buswell RA, Leal de Silva WR, Jones SZ, Dirrenberger J (2018) 3D printing using concrete extrusion: a roadmap for research. Cem Concr Res 112(October 2017):37–49. https://doi.org/10.1016/j.cemconres.2018.05.006

4. Bos F, Wolfs R, Ahmed Z, Salet T (2016) Additive manufacturing of concrete in construction: potentials and challenges of 3D concrete printing. Virtual Phys Prototyp 11(3):209–225. https://doi.org/10.1080/17452759.2016.1209867

5. Hou S, Duan Z, Xiao J, Ye J (2021) A review of 3D printed concrete: performance requirements, testing measurements and mix design. Constr Build Mater 273:121745. https://doi.org/10.1016/j.conbuildmat.2020.121745

6. Bhattacherjee S, Rahul AV, Santhanam M (2020) 3D printing—progress worldwide. Indian Concr J 94(9):8–25

7. De Schutter G, Lesage K, Mechtcherine V, Nerella VN, Habert G, Agusti-Juan I (2018) Vision of 3D printing with concrete—technical, economic and environmental potentials. Cem Concr Res 112(June):25–36. https://doi.org/10.1016/j.cemconres.2018.06.001

8. Al-Qutaifi S, Nazari A, Bagheri A (2018) Mechanical properties of layered geopolymer structures applicable in concrete 3D-printing. Constr Build Mater 176:690–699. https://doi.org/10.1016/j.conbuildmat.2018.04.195

9. Xiao J et al (2021) Large-scale 3D printing concrete technology: Current status and future opportunities. Cem Concr Compos 122(April):104115. https://doi.org/10.1016/j.cemconcomp.2021.104115

10. Chen Y, Zhang Y, Pang B, Liu Z, Liu G (2021) Extrusion-based 3D printing concrete with coarse aggregate: printability and direction-dependent mechanical performance. Constr Build Mater 296:123624. https://doi.org/10.1016/j.conbuildmat.2021.123624

11. Rahul AV, Santhanam M (2020) Evaluating the printability of concretes containing lightweight coarse aggregates. Cem Concr Compos 109(September 2019):103570. https://doi.org/10.1016/j.cemconcomp.2020.103570

12. Zou S, Xiao J, Ding T, Duan Z, Zhang Q (2021) Printability and advantages of 3D printing mortar with 100% recycled sand. Constr Build Mater 273:121699. https://doi.org/10.1016/j.conbuildmat.2020.121699

13. Rahul AV, Santhanam M, Meena H, Ghani Z (2019) 3D printable concrete: mixture design and test methods. Cem Concr Compos 97:13–23. https://doi.org/10.1016/j.cemconcomp.2018.12.014

14. Rahul AV, Santhanam M, Meena H, Ghani Z (2019) Mechanical characterization of 3D printable concrete. Constr Build Mater 227:116710. https://doi.org/10.1016/j.conbuildmat.2019.116710

15. Bos FP, Kruger PJ, Lucas SS, van Zijl GPAG (2021) Juxtaposing fresh material characterisation methods for buildability assessment of 3D printable cementitious mortars. Cem Concr Compos 120(April):104024. https://doi.org/10.1016/j.cemconcomp.2021.104024

16. Le TT et al (2012) Hardened properties of high-performance printing concrete. Cem Concr Res 42(3):558–566. https://doi.org/10.1016/j.cemconres.2011.12.003

17. Hosseini E, Zakertabrizi M, Korayem AH, Xu G (2019) A novel method to enhance the interlayer bonding of 3D printing concrete: an experimental and computational investigation. Cem Concr Compos 99(January):112–119. https://doi.org/10.1016/j.cemconcomp.2019.03.008

18. Tay YWD, Ting GHA, Qian Y, Panda B, He L, Tan MJ (2019) Time gap effect on bond strength of 3D-printed concrete. Virtual Phys Prototyp 14(1):104–113. https://doi.org/10.1080/17452759.2018.1500420

19. Tay YWD, Panda B, Paul SC, Noor Mohamed NA, Tan MJ, Leong KF (2017) 3D printing trends in building and construction industry: a review. Virtual Phys Prototyp 12(3):261–276. https://doi.org/10.1080/17452759.2017.1326724

20. Kruger J, du Plessis A, van Zijl G (2021) An investigation into the porosity of extrusion-based 3D printed concrete. Addit Manuf 37(November 2020):101740. https://doi.org/10.1016/j.addma.2020.101740

21. Lu B et al (2019) A systematical review of 3D printable cementitious materials. Constr Build Mater 207:477–490. https://doi.org/10.1016/j.conbuildmat.2019.02.144

Seismic Behaviour of RC Building with Multiple Soft Storey Considering Different Soil Conditions

Mohammadsaheb Mujawar and Tejas D. Doshi

1 Introduction

Reinforced concrete-framed (RC) structures are the inventions over the load-bearing structures in recent decades. In the earlier days, load-bearing buildings were designed only for gravity loads. Lateral loads such as seismic loads and wind loads were neglected. During earthquake, such type of building tends to collapse first. Nowadays, RC-framed structures are designed for gravity loads as well as seismic loads. RC-framed structure has beam, column and slab as a primary elements. Load transfer pattern will be as follows: slab transfers load to beam; beam transfers load to column; column transfers load to foundation, and foundation transfers load to sub-soil. Hence, designing each structural element as a safe member is very much important. Earthquakes are the most disastrous and most unpredictable things ever which acts laterally to the building, and type of soil is also important factor to be considered during designing structural elements.

In recent times, reinforced concrete frame structures have an exceptional characteristic, i.e. particular storey is kept as open storey for the parking or for some commercial purpose. Such type of buildings is known as soft storey (SS) or weak storey or building on slits. Specially, ground storey (GF) is kept as open for parking purpose, and it is termed as open-ground storey (OGS) in civil engineeringterminology. Bujade and Dahat [1] in this paper seismic analysis is done on RC framed high rise building with multiple-soft storey at different levels. Soft storeys are placed at 13th storey and 25th storey with shear wall. Conclusion is given as, soft storey has to be constructed with struts in both direction or to provide shear wall to the full height. Pavithra and Prakash [2] in this paper research is carried out on soft-storey at discrete levels in multi-storey RC frame building. Storey shear, displacement and

M. Mujawar (✉) · T. D. Doshi
KLE Dr. M.S. Sheshgiri College of Engineering and Technology, Belagavi, India
e-mail: mmmujawar.07@gmail.com

storey drift are obtained by considering response spectrum method. At the end it is concluded that Lateral drift value decreases as the location of soft storey shifts upper. Kiran et al. [3] this paper explores seismic analysis of soft storey in multiple storey building using different structural arrangements. Paper concludes, as to a greater extent shear wall can reduce soft storey effect in the building. Cholekar and Yasin Mudalgi [4] study shows that analysis of soft storey of RC building is carried out. It is concluded that soft storey structures exhibit less safe behaviour than regular structures. Joshi et al. [5] in this study, soft storey in RC building is done by considering 3 types of building plans. 20 load cases and 15 soft storey cases are considered. Infill is ignored and height of floor varies with floors. With this research it is concluded that for all type of buildings, shear force and moments are maximum when the first storey is soft storey. Uttamraj and Mythill [6] in this thesis, analysis of soft storey in zone-IV is done by applying finite element method. Behaviour of soft storey under seismic and wind load are considered. General conclusion is given as soft storey will be having very substantial effect on structural behaviour of building. Chowdhury et al. [7] study shows that 9 storied RC frame building are modelled with finite element software ETABS. Equivalent static method is approached considering seismic load and wind load as per Bangladesh national building code, BNBC-1993. Researchers concluded that by increasing the modulus of elasticity of masonry infill lateral displacement can be reduced. Providing shear wall at corners is the best approach to reduce the soft storey irregularity. Increasing column stiffness than beam stiffness is also effective technique to reduce soft storey irregularity effect. Hejazil et al. [8] in this paper soft storey present at base level of high rise building subjected to earthquake are studied. Bracing are used in various arrangements in order to reduce the effect at the soft stories. It is concluded by the researchers that soft storey present at ground floor perform poorly during strong earthquake and it is also found that position and number of bracings acts as an important factor. Bracing reduces horizontal and vertical movements as well.

2 Objectives of the Study

- To investigate seismic behaviour of building with soft storeys at different floor levels.
- To analyse seismic behaviour of RC building including and excluding soft storey in different soil conditions.
- To compare performance of RC building with and without SS using response spectrum method (RSM).
- Results in terms of axial force, storey drift, storey displacement, axial force, bending moment and time period are examined.

3 Methodology and Model Analysis

As per IS 1893 (part 1): 2002 (clause 7.8.2, page no 25), dynamic analysis can be done by two methods.

1. Response spectrum method.
2. Time history method.

In both the above-mentioned methods, designed base shear (V_b) and base shear (V^1_b—which is derived and calculated using fundamental period) are compared. When V_b is less than V^1_b, all response parameters like storey shear, member forces, storey shear, displacement and base reactions are multiplied with V^1_b/V_b.

The response spectrum explains interactivity between structural system and ground acceleration, by providing an envelope of different ground motion records. For seismic analysis, design spectrum is given as Fig. 2, IS 1893 (part 1) 2002 [9]. Response spectrum for different soil condition is given as per IS 1893 (part 1) 2002 [9].

G + 7 RC frame structure is modelled in ETABS software, and analysis is done by RSM.

To complete the present study, following methodology is adopted.

- Review of the available literature studies and brief study of the Indian design code provisions for earthquake resisting structures.
- Building parameters and seismic parameters are fixed confirming to design code of standards.
- G + 7 RC frame structures with and without soft storey are modelling.

3.1 Structural Configuration

The present study is carried on following models.

Model type	Model description	Soil type
Type A	Building with no soft storey	Hard soil
		Medium soil
		Soft soil
Type B	Building with soft storey at GF	Hard soil
		Medium soil
		Soft soil
Type C	Building with soft storey at GF and first floor	Hard soil
		Medium soil
		Soft soil
Type D	Building with soft storey at GF and top floor	Hard soil

(continued)

(continued)

Model type	Model description	Soil type
		Medium soil
		Soft soil

3.2 Model Configuration

The data used to prepare the models are as shown in Table 1.

3.3 Seismic Parameters

The seismic parameters considered for different types of models are given in Table 2 and considered for analysis confirming to IS 1893: 2002.

The Soil types considered for different types of models are hard, medium and soft soil. Values as per IS1893: 2002 considered are 0.16, 0.24 and 0.36 whilst drafting the model using ETABS software.

Table 1 Model detail

Plan dimensions	20 m × 15 m
Storey type	3D RC strcture
Number of floors	G + 7
Height of building	24 m
Depth of footing	2 m
Height of each storey	3 m
Height of parapet	1 m
Slab panel	5 m × 5 m
Seismic zone (Z)	III
Number of floors	G + 7
Concrete grade	M25
Steel grade	Fe 500
Concrete density	25 kN/m^3
Brick infill wall Density	19 kN/m^3

Table 2 Seismic parameters

Seismic zone	Structure type	Response factor	Damping ratio	Importance factor
III	OMRF	3	5%	1
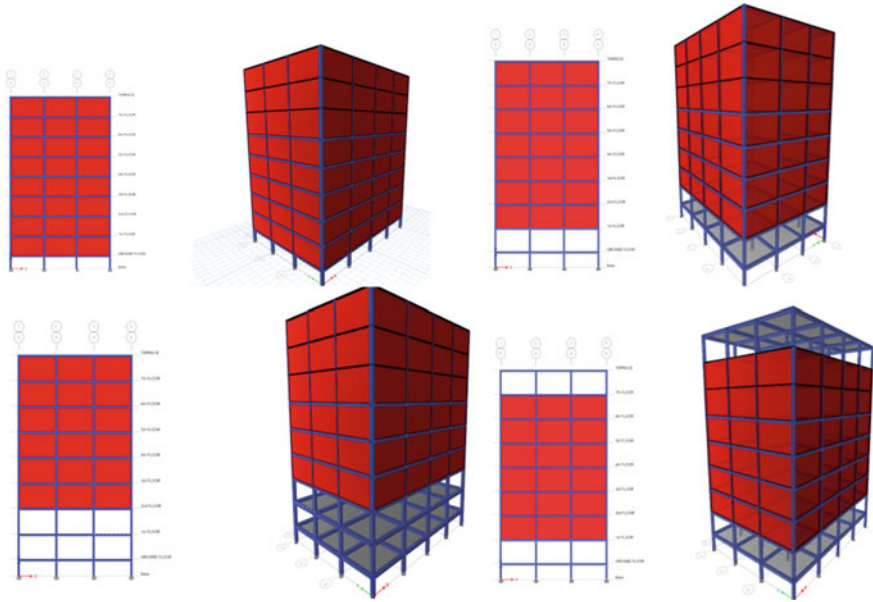
Fig. 1 Elevation and isometric view of all four models

3.4 Model Details

The elevation and isometric views of different types of RC buildings modelled in ETABS software are shown in Fig. 1.

4 Results and Discussions

Following are the results generated after analysing models and are compared using charts, and parameters like displacement, bending moment, storey drift, axial force, time period and base shear are discussed.

4.1 Displacement

By referring to Fig. 2, it is observed that max displacement of infill wall building (Type A) is less compared to other buildings with soft storey combination (Type B, C and D). Max displacement will be higher in soft soil compared to hard and medium soil condition. Displacement of building with no soft storey (Type A) is 82.42% less compared to building with soft storey (Type D) due to presence of infill

Maximum Displacement

	HARD	MEDIUM	SOFT
TYPE A	30.38	32.64	32.95
TYPE B	173.93	179.47	184.23
TYPE C	343.1	351.1	357.99
TYPE D	172.81	178.58	183.54

Type of soils

Fig. 2 Max displacement

walls. Displacement is maximum for a building with consecutive soft storeys (Type C) compared to other type (A, B and D) of building.

4.2 Drift

By referring to Fig. 3, it is observed that max drift is less for type A building compared to type B, C and D building. Max drift will be higher in soft soil compared to hard and medium soil condition.

Maximum Drift

	HARD	MEDIUM	SOFT
TYPE A	26.47	28.37	28.626
TYPE B	114.98	118.63	121.78
TYPE C	167.26	171.09	174.39
TYPE D	108.75	112.26	115.28

Type of soils

Fig. 3 Max drift

Base shear

	HARD	MEDIUM	SOFT
TYPE A	1652.75	2247.74	2329.33
TYPE B	608.18	827.13	1015.66
TYPE C	397.25	540.26	663.41
TYPE D	584.76	795.28	976.55

Type of soils
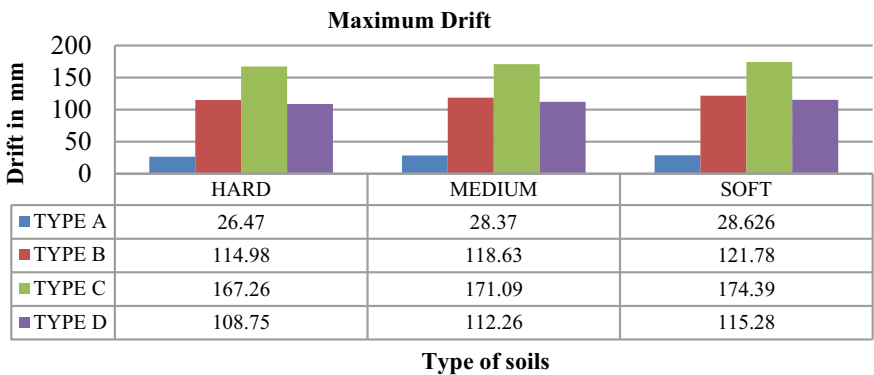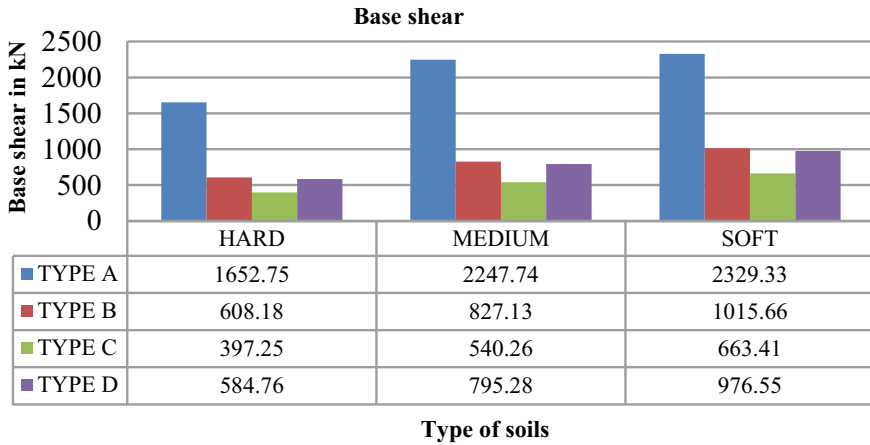
Fig. 4 Maximum base shear

Drift of building with no soft storey (Type A) is 84.17% less compared to building with soft storey (Type C). Drift is maximum for a building with consecutive soft storeys (Type C) compared to other type (A, B and D) of building.

4.3 Base Shear

By referring to Fig. 4, it is observed max base shear is maximum for type A building compared to type B, C and D building. Max base shear will be higher in soft soil compared to hard and medium soil condition. Base shear of building with no soft storey (Type A) is 75.96% more compared to building with soft storey (Type C). Base shear is minimum for a building with consecutive soft storeys (Type C) compared to other type (A, B and D) of building.

4.4 Axial Force

By referring to Fig. 5, it is observed max axial force is maximum for type A building compared to type B, C and D building.

Max axial force will be higher in soft soil compared to hard and medium soil condition. Axial force of building with no soft storey (Type A) is 15.86% more compared to building with soft storey (Type C). Axial force is minimum for a building with consecutive soft storeys (Type C) compared to other type (A, B and D) of building.

Axial force

	HARD	MEDIUM	SOFT
■ TYPE A	4425.02	4584.39	4619.4
■ TYPE B	3978.85	4028.62	4071.47
■ TYPE C	3704.75	3738.19	3766.98
■ TYPE D	3723.02	3775.88	3821.4

Type of soils
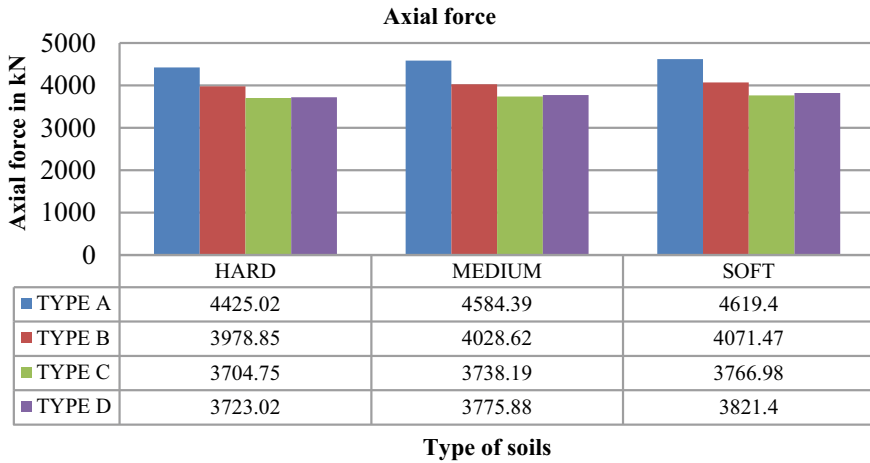
Fig. 5 Maximum axial force

4.5 *Maximum Bending Moment*

By referring to Fig. 6, it is observed max bending moment is less for type A building compared to type B, C and D building. Max bending moment will be higher in soft soil compared to hard and medium soil condition. Bending moment of building with no soft storey (Type A) is 92.57% less compared to building with soft storey (Type C). Bending moment is maximum for a building with consecutive soft storeys (Type C) compared to other type (A, B and D) of building.
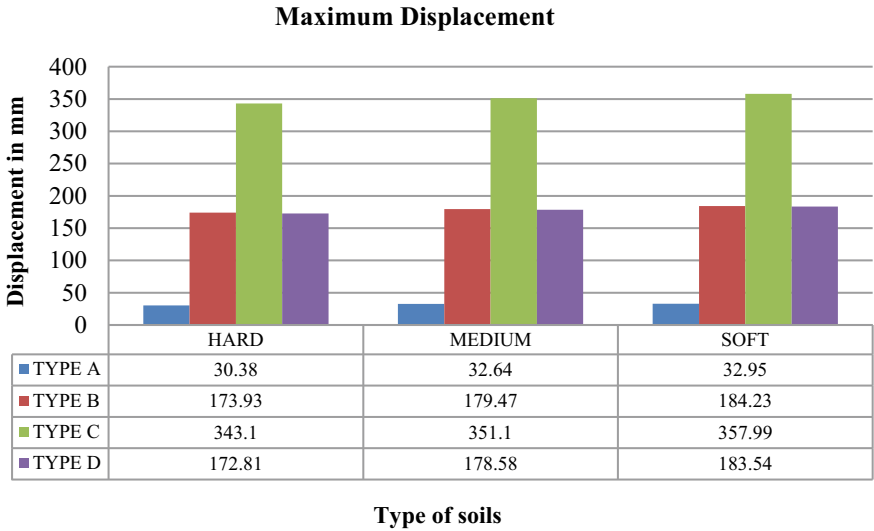
Max. Bending moment

	HARD	MEDIUM	SOFT
■ TYPE A	57.01	57.01	57.01
■ TYPE B	620.21	638.79	654.78
■ TYPE C	768.20	785.68	800.73
■ TYPE D	586.20	606.48	621.86

Types of soils
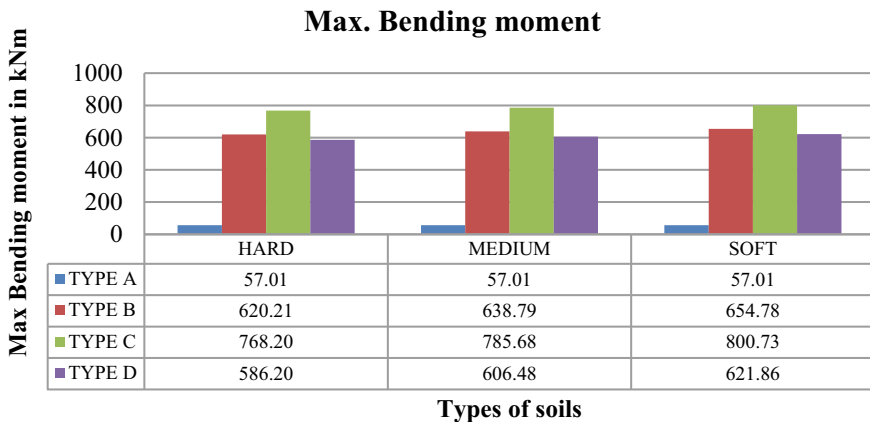
Fig. 6 Max bending moment
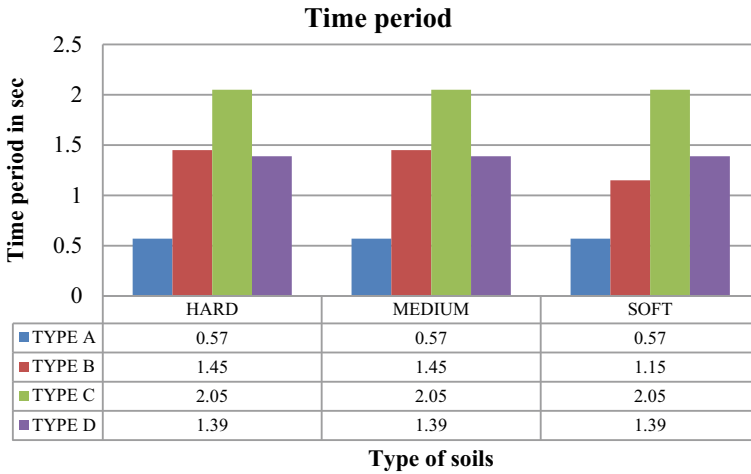
Fig. 7 Time period

4.6 Time Period

By referring to Fig. 7, it is observed time period is maximum for type C with consecutive SS building compared to type A, B and D buildings. Time period increases with addition of SS in a building. Time period of RC building with and without SS does not change with respect to soil condition.

5 Conclusions

In this study, four different models with and without soft storey are analysed. After analysing, conclusions are made as follows:

- Based on the results, it is concluded that soft storey structures exhibit less safe behaviour in all aspects compared to other regular buildings. It is due to the mass concentration at the floor next to soft storey, which results in failure of structure.
- RC frame building with soft storeys at ground floor and top floor combination is safe compared to building with other all combination of soft storeys.
- Building with soft storey in hard and medium soil condition is more effective compared to soft soil condition.
- At the location of soft storey, column demands higher displacement, drift and bending moment.
- Base shear is minimum for building with soft storeys compared to regular building because of reduction in infill wall weight.
- Axial force is maximum for regular building compared to buildings with soft storey.

- Displacement, drift and bending moment are maximum in soft storey buildings compared to regular building irrespective of soil conditions.
- Base shear and axial force are maximum in regular building compared to soft storey buildings irrespective of soil conditions.

References

1. Bujade S, Dahat I (2020) Seismic analysis of RC high rised structural building with multiple soft storey at various level and its optimization. Int J Res Appl Sci Eng Technol (IJRASET) 8(VII)
2. Pavithra R, Prakash TM (2018) Study of behaviour of the storey ay different location in multi-story building. Int J Eng Res Technol (IJERT) 7(6)
3. Kiran S, Ramtekkar GD, Titiksh A (2017) Comparative study for mitigating the soft storey effect in multi storey building using different structural arrangements. Int J Civil EngTechnol (IJCIET) 8(3)
4. Cholekar SB, Yasin Mudalgi Md (2014) Behaviour assessment of soft storey RC structure under seismic loading. IUP J Struct Eng
5. Joshi G, Pathak KK, Akhtar S (2013) Seismic analysis of soft storey buildings considering structural and geometrical parameters. Today's Idea Tomorrow's Technol 1(2)
6. Uttamraj S, Mythill K (2014) Analysis of soft storey for multi story building in zone-4. Int J Res Appl Sci Eng Technol (IJRASET) 1(I)
7. Chowdhury SR, Hassan W, Zaber SI, Modal R, Sirajee MN (2013) Preventing soft storey irregularity in RC frame building. In: International Conference on Engineering Research, Innovation and Education (ICERIE)
8. Hejazi F, Jilani S, Noorani J, Chieng CY, Jaafar MS, Abang Ali AA (2011) Effect of soft storey on structural response of high rise building. In: IOP conference series materials science and engineering
9. IS: 1893-2002 (2002) Indian standard criteria for earthquake resistant design of structures Part-I General provisions and buildings, (Fifth revision). Bureau of Indian standards, New Delhi

Investigate the Effect of Floating Column and Composite Transfer Beam Under the Influence of Seismic Forces

Amit A. Kaloji, Nikhil A. Jambhale, and Tejas D. Doshi

1 Introduction

A multi-storey framed building column is the important structural member, which transfers load from the superstructure to the base of the foundation and carries compressive loads. When it comes to the topic of floating column, these members are similar to the normal reinforced concrete columns, but it does not rest on the base of the foundation. It rests on the girder of the building and the girder transfers the load to the supporting column and these columns transfer the load to the base of the foundation. With the rapid growth in the urban population and construction industry residential and commercial multi-storey buildings with the ground floor as column-free space or at the entrance of the building as column-free space for larger entrance areas as an aesthetic appearance as per architectural requirement. In most of the commercial buildings, basement or ground floor has parking requirements with column-free space for the vehicle movements with no obstructions are interrupted.

In the past decades, reinforced cement concrete structures are popular due to their ease of availability and better results in short period, these results are only good for low to medium height buildings for high rise buildings reinforced cement concrete increases the dead weight of the structure and which increases the cost of the construction. In the present era of developing countries using steel–concrete composite as the best alternative to the normal RC structure, because of its high durability, high stiffness, reduced dead weights and section sizes.

A. A. Kaloji (✉) · N. A. Jambhale · T. D. Doshi
Department of Civil Engineering, KLE Dr. M. S. Sheshgiri College of Engineering and Technology, Belagavi, Karnataka 590008, India
e-mail: amitkaloji728@gmail.com

The present study investigates the effect of the floating column on different building elements and especially on girder which floating column is resting, as the floating column rests on the girder the bending moment results are high due to huge vertical load on the beam, as the bending moment increases the depth of the normal RC beam also increases and which will increase in the cost of the construction and reduction in the building height. To solve the problem and to reduce bending moments in the beam, steel–concrete composite beams in the base of the floating column can be used. This will help to decrease the depth of the beam at the entrance or on the floors.

2 Literature Survey

Umesh Rajendra Tubachi [1] G + 30 high rise building is considered for analysis, and analysis is done by static, dynamic and wind analysis method. Bending moment, shear force and storey drift are having lesser values for composite materials as compared to RC structures [1].

Gujar [2] Study shows vertical irregularity in the loads and sequence analysis. Floating columns are provided at the different corners of the plan and checked for results. Models considered in this paper are Case 1. Floating column at mid first floor, Case 2. Floating column at corner [2].

Satyanarayana [3] Study shows each type of frame is analysed separately by equivalent static method and response spectrum method using ETABS. The results are differentiated in terms of base shear, storey deflections and storey drifts. Analysis is done by equivalent static analysis and response spectrum method [3].

Rahman Naveed [4] Study shows the behaviour of multi-storey buildings with floating columns under earthquake excitations. Linear time history analysis is carried out for the multi-storey buildings under different earthquake loading. In this project, the frames have been analysed by using ETABS, which uses stiffness method for analysis of structure [4].

Deeksitha [5] The main objective of this study is to analyse the G + 5 storey building with floating columns at different locations and also to check the storey displacement, storey drift and storey shear for floating columns at various locations. To find, whether the structure is safe or unsafe with floating column when built in seismically active areas [5].

Abhinay [6] Study shows G + 15 building is analysed by equivalent static method, and building is compared for different seismic conditions and soil conditions. Three cases are considered in this research, (1) normal building without floating column, (2) building with floating column and (3) building with floating column and with changed dimensions in frames [6].

Birje [7] G + 10, G + 20, G + 30 building is considered for analysis, and analysis is done by static method and response spectrum method. From this paper, it concludes that composite is better than RC because of composite structure having less dead weight which reduces the cost of construction [7].

3 Objectives of the Study

- To study the performance of the floating column by linear static analysis.
- To study and evaluate the performance of the structure by using the composite structure and conventional RC structures.
- To study the structural response of the following parameters like lateral displacement, base shear, natural period, storey drift, bending moment of transfer beam and weight of structure.

4 Methodology and Model Analysis

- Study the available papers and Indian design codes for earthquake-resistant structures.
- Modelling of G + 10 RC and composite structure using ETABS 2018.
- Adding data from the plan and codal provisions as per IS 1893–2002.
- Using equivalent (linear) static method analysis is carried out and output results are obtained.
- Comparison of results with normal RC structure and composite structures.

4.1 Model Configuration

Model 0 Normal building without floating column.

Model 1 Building with floating columns at centre of exterior frame.

Model 2 Building with floating columns at intermediate of exterior frame.

Model 3 Building with floating columns at corners of exterior frame.
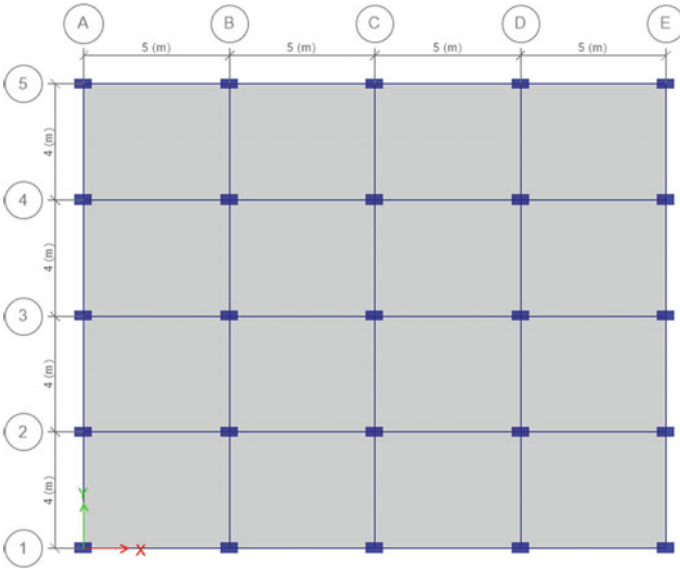
Fig. 1 Typical plan of model 0

4.2 Model Details

Building with RC frame showing floating column provided at different positions in plan and elevation (Figs. 1, 2, 3, 4, 5, 6, 7 and 8).

4.3 Structural Configuration

The data used for building models are as follows (Tables 1 and 2).

4.4 Section Properties

See Tables 3 and 4.
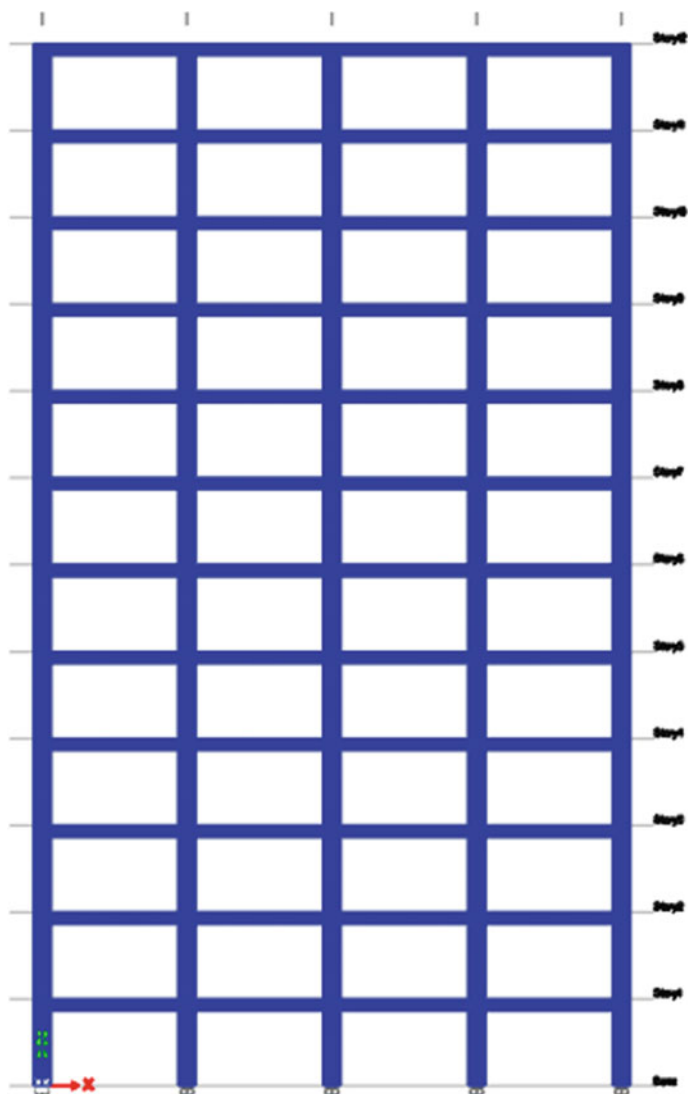
Fig. 2 Elevation of model 0

5 Results and Discussion

5.1 Lateral Displacement

Results from Fig. 9, Model 1 shows RC building with floating column has 20.74% increased values than normal RC building. RC building with floating column transfer
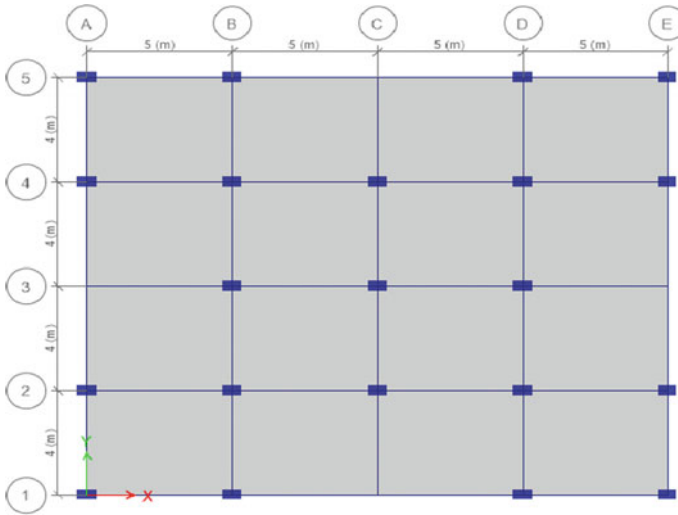
Fig. 3 Typical plan of model 1

beam as composite has 18.66% increased values than normal RC building. Results from Fig. 9, Model 2 shows RC building with floating column has 7.65% increased values than normal building. RC building with floating column transfer beam as composite has 7.43% decreased values than normal building.

Results from Fig. 9, Model 3 shows RC building with floating column has 39.18% increased values than normal building. RC building with floating column transfer beam as composite has 32.77% increased values than normal building. In all three models, displacement values are different according to their position of floating column and displacement values are minimum at the base and maximum at the top storey of the building.

5.2 Base Shear

Results from Fig. 10, Model 1 shows RC building with floating column at centre is 12.89% decreased values than normal building and floating column with composite transfer beam has 28.53% decreased values than normal building. Results from Fig. 10, Model 2 shows RC building with floating column at intermediate is 12.12% increased values than normal building and floating column with composite transfer beam has 15.53% increased values than normal building. Results from Fig. 10, Model 3 shows RC building with floating column at centre is 20.83% decreased values than normal building and floating column with composite transfer beam has 24.73% decreased values than normal building. Present study results show building without floating column having higher base shear, because of stiffness of the structure. Due
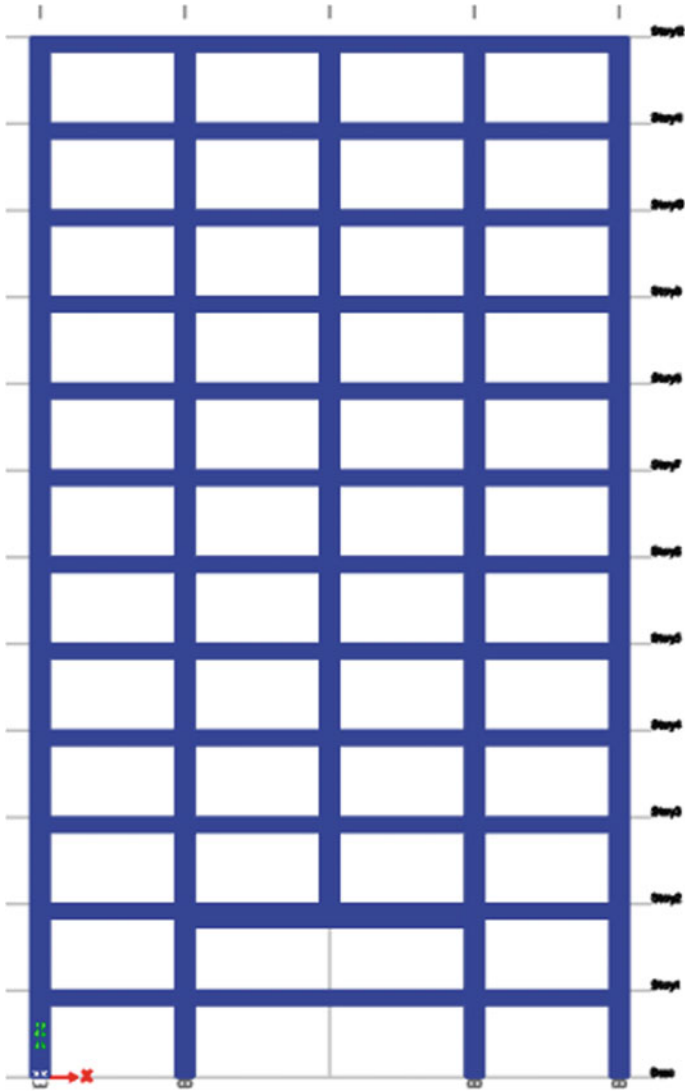
Fig. 4 Elevation of model 1

to introduction of floating column in the structure stiffness of the structure reduces. It will lead to decrease in the base shear of the structure.
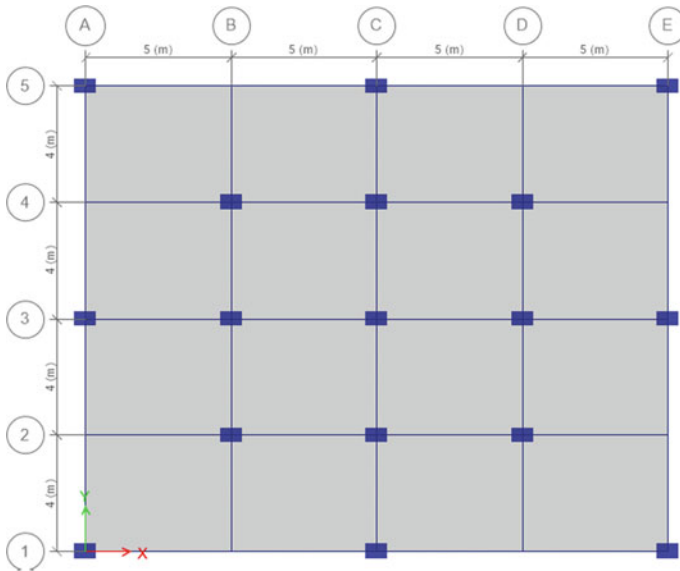
Fig. 5 Typical plan of model 2

5.3 Natural Time Period

Results from Fig. 11, Model 1 shows building with floating column has 18.28% increased values than normal building and floating column building with transfer beam as composite has 27.41% increased values than normal building. Results from Fig. 11, Model 2 shows building with floating column has 8.33% increased values than normal building and floating column building with transfer beam as composite has 4.02% increased values than normal building. Results from Fig. 11, Model 3 shows building with floating column has 35% increased values than normal building and floating column building with transfer beam as composite has 27.04% increased values than normal building. Present study results show building models with floating column having more time period than normal RC buildings. Presence of floating column in the structure affects the natural time period.

5.4 Storey Drift

Results from Fig. 12, Model 1 shows building with floating column has 29.83% increased values than normal building and floating column building with composite transfer beam has 38.38% increased values than normal building. Results from Fig. 12, Model 2 shows building with floating column has 25.05% increased values than normal building and floating column building with composite transfer beam has
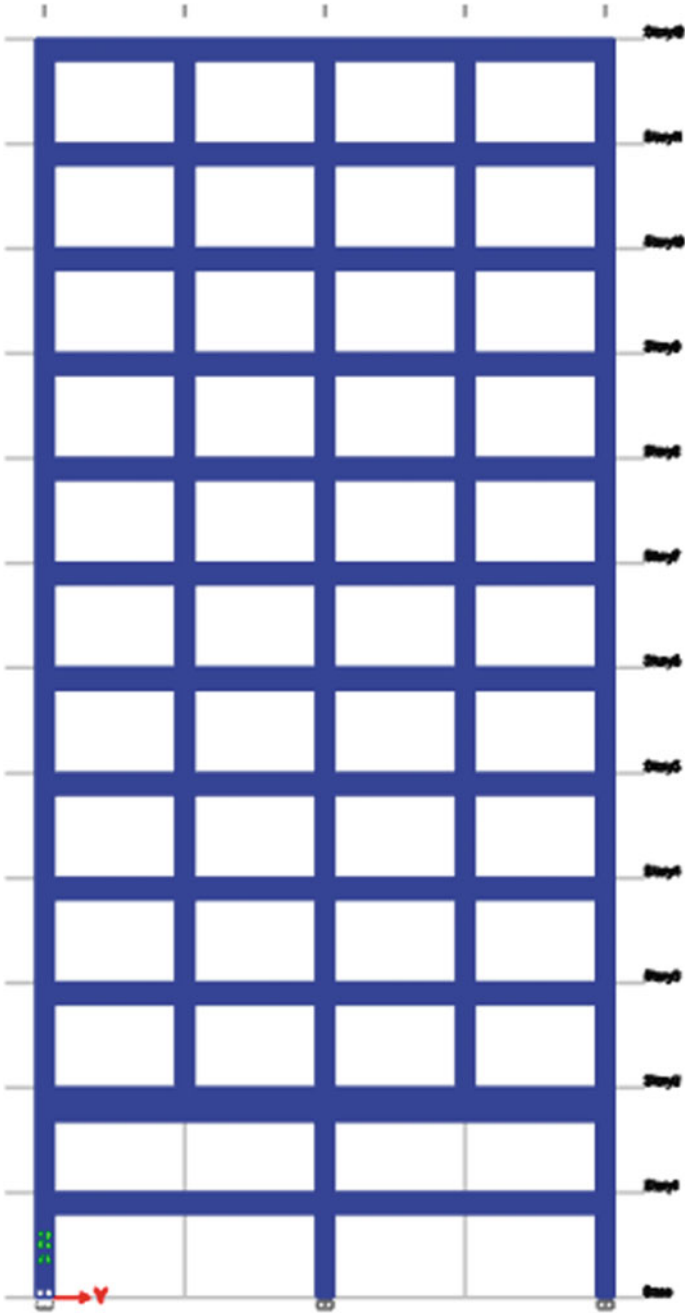
Fig. 6 Elevation of model 2
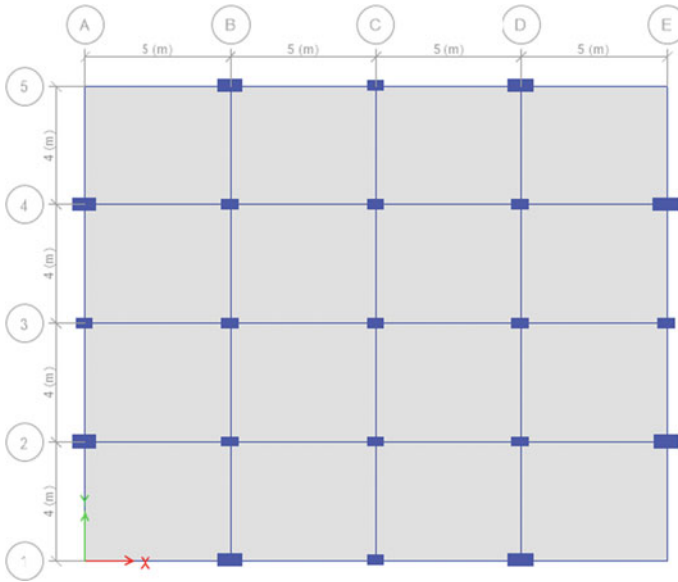
Fig. 7 Typical plan of model 3

12.41% increased values than normal building. Results from Fig. 12, Model 3 shows building with floating column has 49.86% increased values than normal building and floating column building with composite transfer beam has 45.63% increased values than normal building. Present study results show building with floating column at centre and corner of exterior frame having more storey drift than at the intermediate of exterior frame of the structure.

5.5   Bending Moment of Transfer Beam

Results from Fig. 13, Model 1 shows building with floating column with RC transfer beam has 41.17% higher bending moment than composite transfer beam using load combination 1.5 (DL + EQX). Results from Fig. 13, Model 2 shows building with floating column with RC transfer beam has 69.10% higher bending moment than composite transfer beam. Results from Fig. 13, Model 3 shows building with floating column with RC transfer beam has 45.46% higher bending moment than composite transfer beam. Present study results show building with composite transfer beam decrease the bending moment of the beam as compared to normal RC transfer beam. Steel–concrete composite beam decreases the section size, due to decrease in the bending moment of transfer beam.
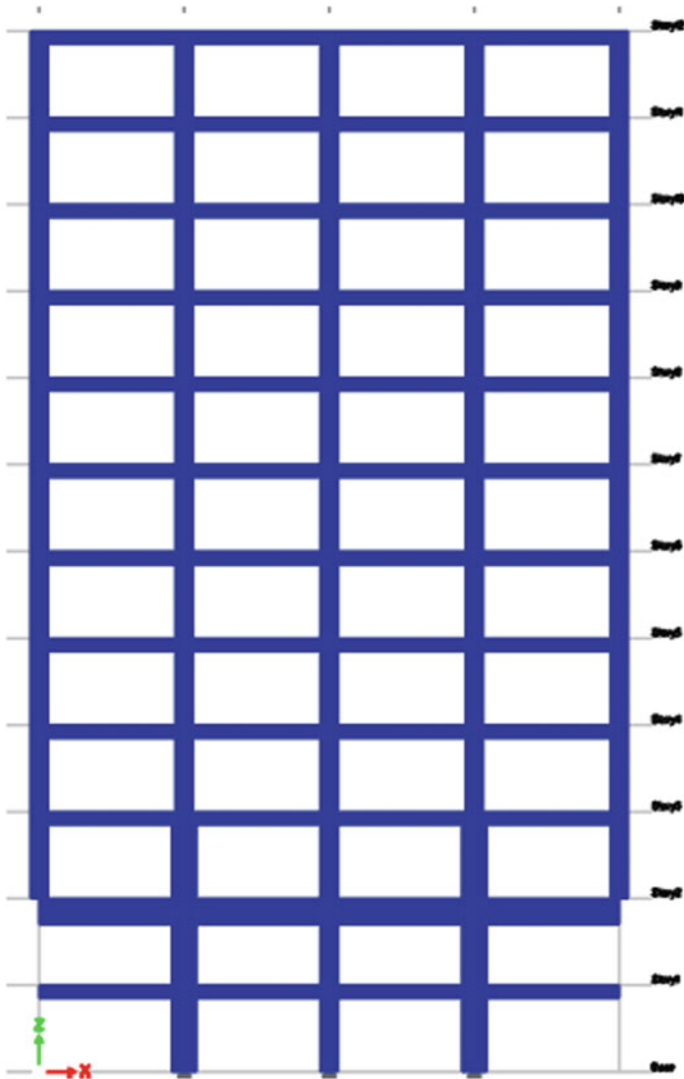
Fig. 8 Elevation of model 3

5.6　*Weight of Structure*

In all models, RC building with floating column has more weight than composite transfer beam. But there is not much difference in the values of the weight, because we just changed the transfer beam material, wherever floating column is provided (Fig. 14).

Table 1 Building data for analysis

Floor plan size	20 m × 16 m
Foundation depth	3.0 m
Storey height	3.0 m
Height of parapet	1.0 m
Wall thickness	0.23 m
Partition wall	0.15 m
Thickness of slab	0.12 m
Seismic zone type	III
Importance factor	1
Response reduction factor	3
Soil type	Medium soil
Damping ratio	5%
Grade of concrete	M25

Table 2 Loads as per IS 875 Part 1 and 2 [8]

Type of load	Total load
Dead load	
Wall load	12.55 kN/m
Partition wall	8.10 kN/m
Parapet wall	4.80 kN/m
Live load	
Floor live load	3.0 kN/m^2
Roof live load	1.5 kN/m^2

Table 3 Section properties of RC and composite sections

	Model 0	Model 1	Model 2	Model 3
Section	RC	RC + FC	RC + FC	RC + FC
Beam (mm)	300 × 500	300 × 500	300 × 600	300 × 450
Column (mm)	400 × 500	400 × 650	500 × 750	350 × 600
Transfer beam (RC) (mm)	–	400 × 700	500 × 950	450 × 900
Section	–	COMP + FC	COMP + FC	COMP + FC
Transfer beam (Comp) (mm)	–	300 × 600	400 × 500	400 × 600
I Section	–	ISHB 350	ISHB 450	ISHB 450

Table 4 Details of composite section and I section properties as per IS 800:2007 [9]

	Model 1	Model 2	Model 3
Section	ISHB 350	ISHB 450	ISHB 450
Details of composite section			

DISPLACEMENT

	MODEL 1	MODEL 2	MODEL 3
REGULAR BUILDING	41.00	41.00	41.00
RC+FLOATING COLUMN	51.73	44.39	67.41
RC+COMPOSITE FLOATING COLUMN	50.41	37.95	60.99
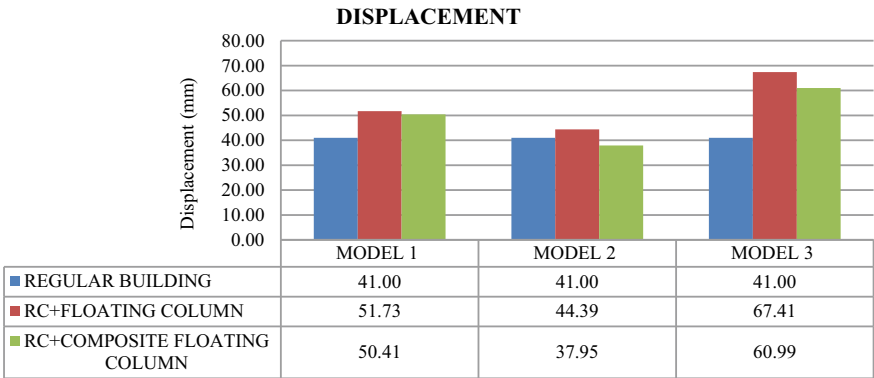
Fig. 9 Maximum lateral displacement of different type of models

BASE SHEAR

	MODEL 1	MODEL 2	MODEL 3
REGULAR BUILDING	1419.00	1419.00	1419.00
RC+FLOATING COLUMN	1235.95	1614.83	1123.42
RC+COMPOSITE FLOATING COLUMN	1014.04	1680.03	1067.99

Fig. 10 Base shear of different type of models

NATURAL TIME PERIOD

	MODEL 1	MODEL 2	MODEL 3
■ REGULAR BUILDING	1.43	1.43	1.43
■ RC+FLOATING COLUMN	1.75	1.56	2.2
■ RC+COMPOSITE FLOATING COLUMN	1.97	1.49	1.96
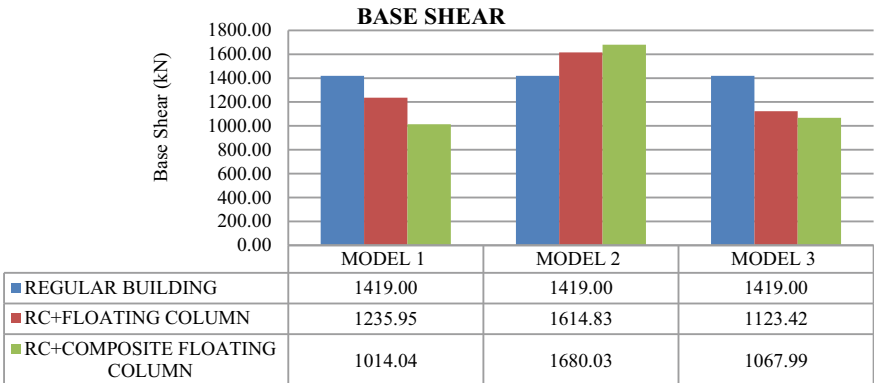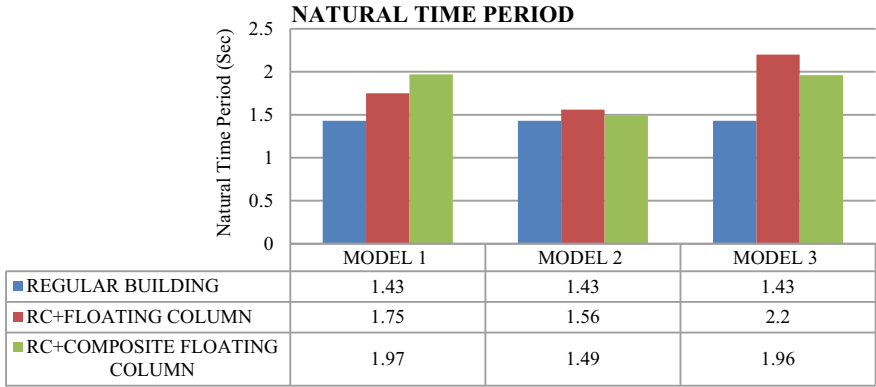
Fig. 11 Natural time period of different types of models

STOREY DRIFT

	MODEL 1	MODEL 2	MODEL 3
■ REGULAR BUILDING	0.000374	0.000374	0.000374
■ RC+FLOATING COLUMN	0.000533	0.000499	0.000746
■ RC+COMPOSITE FLOATING COLUMN	0.000607	0.0006	0.000688

Fig. 12 Storey drift of different types of models

BENDING MOMENT

	MODEL 1	MODEL 2	MODEL 3
■ REGULAR BUILDING	106	106	106
■ RC+FLOATING COLUMN	1246	1767	1476
■ RC+COMPOSITE FLOATING COLUMN	402	546	805

Fig. 13 Bending moment of transfer beam

WEIGHT OF STRUCTURE

	MODEL 1	MODEL 2	MODEL 3
■ REGULAR BUILDING	56104	56104	56104
■ RC+FLOATING COLUMN	59533	63400	58365
■ RC+COMPOSITE FLOATING COLUMN	54995	62811	57980

Fig. 14 Weight of structure

6 Conclusions

- Lateral displacement values are higher for buildings with floating column. Buildings with floating column in the centre and corners of exterior frame are subjected to more displacement than intermediate floating columns. All displacement values are within IS code 1893-2002.
- Building with floating column and transfer beam as RC will result in higher values of base shear compared to floating column with composite transfer beam building, but when compared to normal RC building, the values of base shear are higher, because of stiffness of the structure is more.
- Fundamental natural period from codebook IS 1893-2002 is depending on height and length of the structure. Building with higher time period has low frequency of vibration, hence RC structure having less time period and building with floating columns have high time period, because of introduction of floating column in the structure increases the time period.
- Storey displacement for floating column buildings is higher as compared to normal building, similarly storey drift will also have higher values than RC structure, because of floating column structure subjected decreased stiffness. Floating column at centre and corners shows increased drift values than at intermediate floating columns.
- Bending moments in transfer beam of composite section shown the best results than transfer beam of RC, because of reduction in the moments of the transfer beam, it decreases the section size, self-weight of that beam and increase in floor to floor height.
- In this study, building with floating column and composite transfer beam overall results are good, but in weight of structure results do not vary much because in building we just replaced transfer beam as composite section.

References

1. Umesh Rajendra Tubachi M (2019) Analysis of steel concrete composite structure and its comparison with RC structure. IJESC
2. Gujar A, Jadhav HS (2019) Performance of multi-storey RC structure with floating column. Int Res Eng Technol
3. Satyanarayana A, Sowjanya P (2019) Comparative seismic and design of multi-storey building using RC, Steel and composite structures by ETABS. Int J Profes Eng Stud
4. Rahman Naveed FU, Abdul Khadeer Md, Afroz M, Khan MH, Najeeb Ur Rahman Md, Rajkumar Singh B (2018) Analysis of multi-storey building with floating column. Int J Innov Technol 6(1)
5. Deeksitha R, Sureshchandra HS (2017) Analysis of multistorey building with and without floating column. Int J Eng Res Technol (IJERT) 6(6)
6. Abhinay Y, Sudarshan Rao H, Ghorpade VG (2017) Comparison of seismic analysis of a floating column building and a normal building. Int J Mater Sci 12
7. Birje MM (2014) Comparative study on structural parameter of RC and composite building. IISTE
8. IS 875 (part 1 and part 2) (1987) Code of Practice for design loads for buildings and structures. Bureau of Indian Standards, New Delhi, India
9. IS 800:2007, Indian standard code of practice for general construction in steel. Bureau of Indian Standards, New Delhi, India

Response Control of Base-Isolated Structures Using Tuned-Mass Dampers—A Numerical Study

M. Azeem, A. S. Sajith, and P. V. Indira

1 Introduction

A base isolation system is a technique of earthquake protection that separates the structure (superstructure) from the foundation (substructure). It is an effective method of earthquake protection because it restricts plastic deformation to easily replaceable and affordable components, leaving the remainder of the structure elastic and thereby significantly reducing transmitted ground motion energy. In earthquake-prone areas, seismic base isolation has been widely used in passive vibration control of civil engineering projects to avoid or minimize damage caused by the shaking ground. The base-isolated system (BIS) absorbs the majority of the earthquake-induced displacement demand by providing flexibility at the structure's base [1]. This has a substantial impact on the design and construction processes of the base-isolated (BI) structure since BIS must be developed to tolerate significant displacements. The design engineer employs large isolators and costly flexible utility connections (such as waterworks, gas fittings and electrical conduits) to allow for the necessary displacements while keeping a sufficient separation distance between buildings to avoid collision of nearby structures [2].

These factors inspired the development of a number of hybrid control systems aimed at increasing the earthquake resistance of BI buildings or simply minimizing the displacement demand of the BIS. However, while extra damping may minimize the BIS's significant displacements, it will increase inter-storey drifts and floor accelerations in the superstructure [3]. The purpose of this research is to investigate a passive control strategy for base-isolated structure in order to preserve the benefits of the system while also ensuring its safety and integrity. This serves purpose of a hybrid technique which combines the concept of isolation and absorption.

M. Azeem (✉) · A. S. Sajith · P. V. Indira
Department of Civil Engineering, NIT Calicut, Calicut, Kerala, India
e-mail: azeem_p190019ce@nitc.ac.in

Recent studies have looked into the use of passive control systems for controlling the seismic response of base-isolated constructions. For the most part, these investigations have looked at how well the classical tuned-mass damper (TMD) coupled to the base isolation sub-system controls vibration and noise levels [4, 5]. There have been several techniques to optimizing the design of these systems for both base excitation [5, 6] and wind loading [7]. When low damping isolators are utilized, the TMD has been found to be quite successful, reducing the displacement demand on the base isolation sub-system while still conserving tiny inter-storey drifts in the main structure [8]. Long stroke lengths, however, make TMD implementation difficult in real-world applications due to the large amount of area they require. The viability and cost effectiveness of this hybrid control technique may be hindered in practical implementations due to economic factors if such an additional mass is not allocated an architectural function (e.g. a parking space and a utilities room). It is anticipated that, as a result of this study, a few easy approaches for minimizing displacement demand base-isolated structures will be provided.

The present investigation aims to review and compare different hybrid passive control strategies incorporated with TMDs and BISs. Further, this study intends to provide an insight into the limiting design and seismic performance parameters of relevant passive hybrid systems. In first phase of the present investigation, the response of a fixed-base structure is compared with that of base-isolated (BI) structure. The need for development of a feasible technique for reducing the base displacement of the isolation system is discussed. A simple and efficient TMD in the form of vertical cantilever with a tip mass is used along with base-isolated system to enhance the performance of the structure. The analysis of the BI + TMD structure is done by modelling in SAP2000. The response of this structure to both harmonic and earthquake ground motions is studied. The combined system is found to show better control than a simple BI structure. In another attempt, an optimally designed TMD (TMDopt) presented by Tsai [4] was used to model a BI + TMDopt structure. The numerical procedure was repeated for this structure as well.

2   Structural Modelling and Analysis

The modelling and analyses of the structure are done in the finite element analysis software SAP2000. Using elastic/linear analyses, this study examined the performance of a five-storey moment resistant frame structure subjected to severe earthquake stresses. SAP2000 was used to model the structural systems detailed in the following sections. The study comprised a fixed-base model (without base isolators (BIs) and tuned-mass dampers (TMDs)), whereas the remaining models contained BIs, TMDs, and an optimally designed TMD (TMDopt) for each scenario. A five-storey two-dimensional concrete frame serves as the simulation's fixed foundation model. With a floor height of 3.6 m and concrete grade M25, the columns are (300 × 300) mm in size and the beams are (200 × 300) mm in size. The fixed-base structure's

Table 1 Parameters of base-isolated structures

Time period (s)	Damping ratio	Horizontal stiffness (N/m)	Vertical stiffness (N/m)
2	0.05	54,331	17,803,211
3	0.05	24,147	14,003,745

natural period (T) and natural frequency (ω) were determined using modal analysis in SAP2000; $T = 0.55952$ s and $\omega = 11.228$ rad/s.

2.1 Design of Base Isolation Systems

As per Union Building Code 97 (UBC 97), base isolation system parameters for the structure were calculated. For base isolators, rubber isolation property available SAP2000 was used. The upper structure will operate as a rigid body as a result of the flexible layer being introduced between the foundation and the superstructure. Period-shifting is made possible by the use of isolators with high vertical rigidity but low horizontal stiffness. Two fundamental isolated models were examined: one with a time period of two seconds and the other with a time period of three seconds. A base floor beam with a dimension of (200 × 300) mm was incorporated. The beams, columns and isolated structure as a whole weigh 2752.42 kg, 8257.26 kg and 11,009.68 kg, respectively. The system is designed so that there is adequate seismic isolation in place so that the structure will not be damaged by lateral seismic motion [1, 9] (Table 1).

2.2 Design of Tuned-Mass Dampers

The tuned-mass damper (TMD) is technically a conventional dynamic vibration absorber (DVA), which is an auxiliary vibrating element connected to a primary vibration system in order to mitigate the primary system's vibration. Tuned-mass dampers' ability to reduce seismic response is directly influenced by the parameters they are configured with. Tuning frequencies and damping ratios were calculated using the isolated base structure as the principal structure. The base isolation system's inherent frequency is often lower than the dominating frequency range of earthquakes. This is one of the advantages of using a tuned-mass damper in base-isolated buildings. The isolated structure's natural frequency was derived using SAP2000 in accordance with the design of the TMD. When examining the parameters of tuned-mass dampers, the principal structure is typically simplified to a main mass with a natural frequency of ω_p and a damping ratio of ζ_p. The mass of tuned-mass dampers is stated in terms of the mass ratio γ, that is, the damper mass divided by the main mass. The

Table 2 Parameters of tuned-mass dampers in combined systems

Period of BI structure (s)	Combined system	Damping ratio of TMD	Length of the vertical cantilever (m)
2	BI + TMD	0.0200	0.989
	BI + TMDopt	0.1435	1.050
3	BI + TMD	0.0200	1.295
	BI + TMDopt	0.1435	1.376

tuning frequency ratio, f, is used to determine the stiffness of tuned-mass damper. It is defined as the ratio of the damper's natural frequency to the primary structure's frequency. The tuned-mass damper's damping ratio is represented by ζ_s [10].

An appropriate mass ratio of 5% is chosen for the TMD. The parameters of the TMD are fixed so that the condition $k - m\omega_p^2 = 0$ is satisfied, where ω_p is the natural frequency of the base-isolated structure, m is the mass of the TMD and k is the stiffness required for TMD. In our study, a vertical cantilever with tip mass is used as TMD. So, the length of the TMD leg can be obtained by using the stiffness equation of cantilever beam. Steel flat of cross section (100×10) mm was used for the vertical cantilever. Mass at the tip of the cantilever was obtained as 550.48 kg.

To make the optimally designed tuned-mass damper (TMDopt) [4], Tsai and Lin [10] calculated the tuning frequency and damping ratio as (Table 2)

$$f = \left(\frac{\sqrt{1 - 0.5\gamma}}{1 + \gamma} + \sqrt{1 - 2\xi_p^2} - 1\sqrt{\gamma} - 0.426\gamma \right)\sqrt{\gamma}\xi_p$$
$$- \left(3.730 - 16.903\sqrt{\gamma} + 20.496\gamma\right)\sqrt{\gamma}\xi_p^2 \tag{1}$$

$$\xi_s = \sqrt{\frac{3\gamma}{8(1 + \gamma)(1 - 0.5\gamma)}} + \left(0.151\xi_p - 0.170\xi_p^2\right) + \left(0.163\xi_p + 4.980\xi_p^2\right)\gamma \tag{2}$$

Increased damping can be achieved practically by connecting a TMD via a dashpot to the ground. It could be a low cost, high-convenience solution to the problem of TMD-based vibration suppression. A schematic representation of a five-storey base-isolated structure equipped with vertical cantilever having a tip mass as TMD is shown in Fig. 1.

2.3 Input Excitation Frequencies

A linear dynamic analysis was conducted in SAP2000. The building models were excited under a sinusoidal loading with a forcing frequency equal to the fundamental

Fig. 1 Vertical cantilever with tip mass as TMD on BI structure
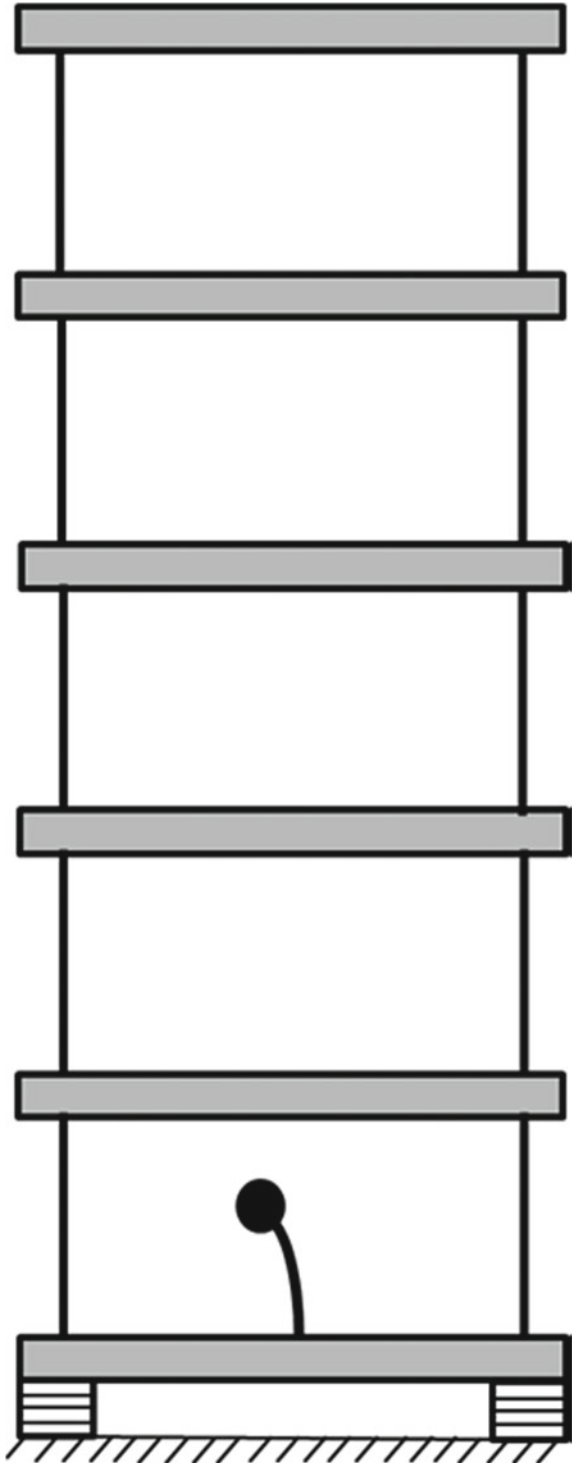
Table 3 Time histories used and their characteristics

Event	Elcentro	Imperial valley	Loma prieta	Landers	Kobe
Max accel (g)	0.28	0.59	0.37	0.25	0.28
Predominant period (s)	0.46	0.42	0.54	0.68	0.48

frequency of the fixed-base structure, i.e. 11.228 rad/s, and with acceleration amplitude of 0.3 g at the base. The base-isolated structures were also subjected to the same forcing frequency. Later, these structures were subjected to real earthquake excitations. Time histories with predominant period comparable to natural period of fixed-base structure were chosen. The earthquake data was collected from the PEER Ground Motion Database—PEER Center (Table 3).

3 Time History Analysis and Comparisons

The dynamic performance of the aforementioned models in the time domain is examined in this section. While it is widely established that seismic isolators are extremely sensitive to the bidirectional character of ground motion, the purpose of this paper is to examine structural control systems that incorporate TMD. The structure's simplified two-dimensional schematization has been limited to this primary objective.

3.1 Dynamic response of fixed-base and BI structures

For fixed-base structures, resonance conditions prevail and amplitude picks up to a time of five seconds (in transient state) and then slowly reaches steady state. Since the natural period of isolated structure is different from that of the forcing harmonic excitation, its amplitude decreased in comparison with the fixed-base case (Figs. 2 and 3).

Earthquake motion can be recorded in terms of ground displacement, velocity or acceleration. Almost all modern earthquakes are documented in the "PEER Ground Motion Database". The natural period of the fixed-base structure was found to be 0.55952 s. Elcentro, Imperial Valley, Loma Prieta, Landers, and Kobe were identified as the five most significant modern earthquakes from the PEER Database. It was decided to use data from a single station for each earthquake since the primary period of that station was closest to the natural period of the fixed-base structure (Figs. 4 and 5).
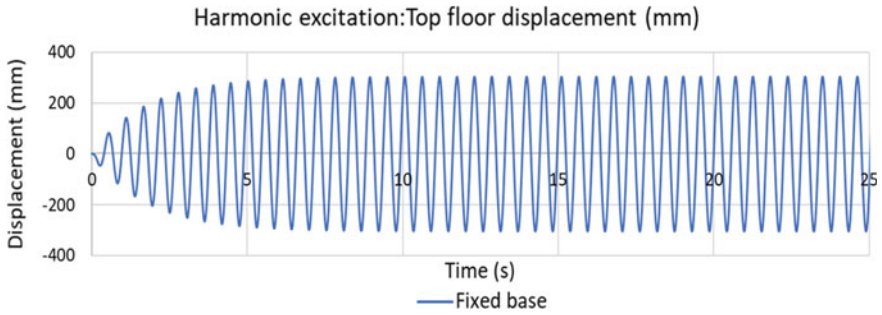
Fig. 2 Displacement response under harmonic excitation for fixed-base model
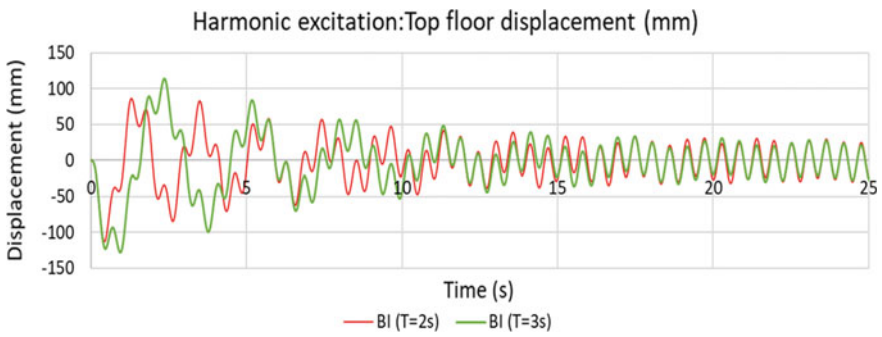
Fig. 3 Displacement response under harmonic excitation for base-isolated models
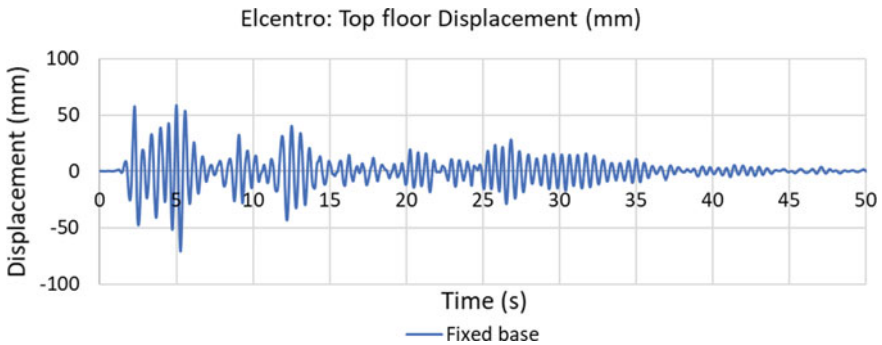
Fig. 4 Displacement response under Elcentro ground motion for fixed-base model

3.2   *Dynamic Response of BI, BI + TMD, BI + TMDopt*

See Figs. 6 and 7.
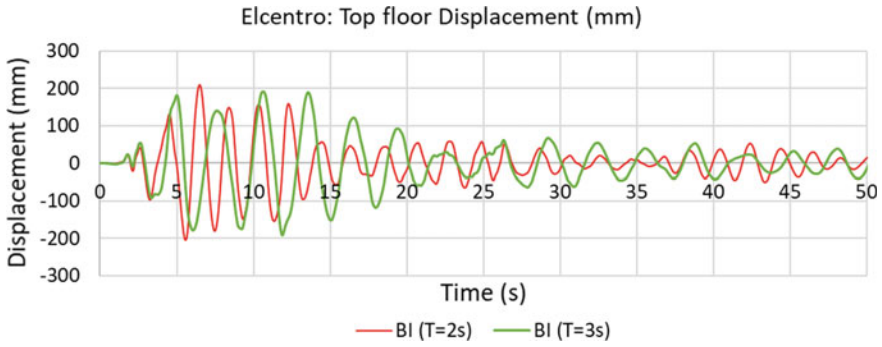
Fig. 5 Displacement response under Elcentro ground motion for base-isolated models
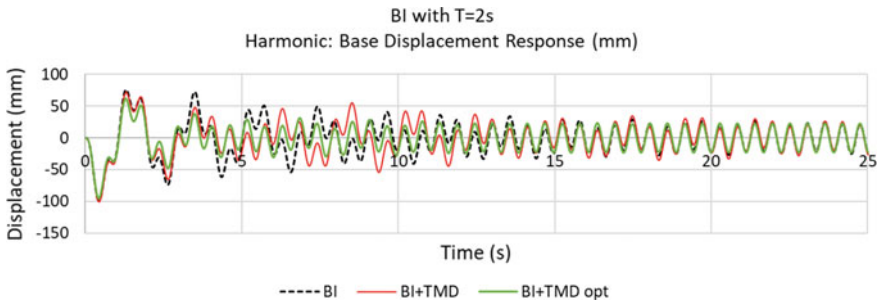
Fig. 6 Base floor displacement for BI ($T = 2$ s) hybrid cases
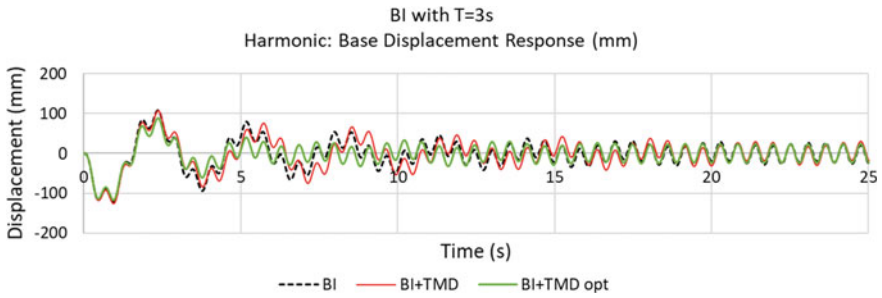
Fig. 7 Base floor displacement for BI ($T = 3$ s) hybrid cases

3.3 *Response Comparison of BI, BI + TMD, BI + TMDopt*

See Figs. 8, 9, 10 and 11.
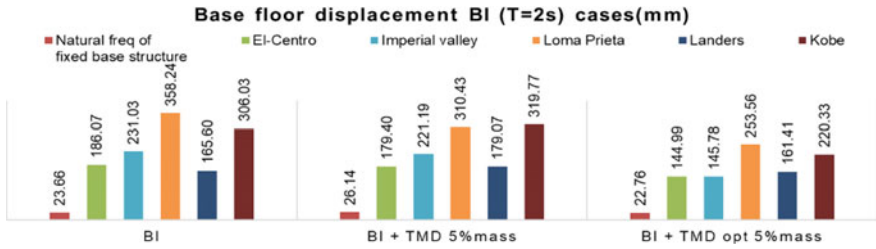
Fig. 8 Base floor displacement for BI ($T = 2$ s) cases
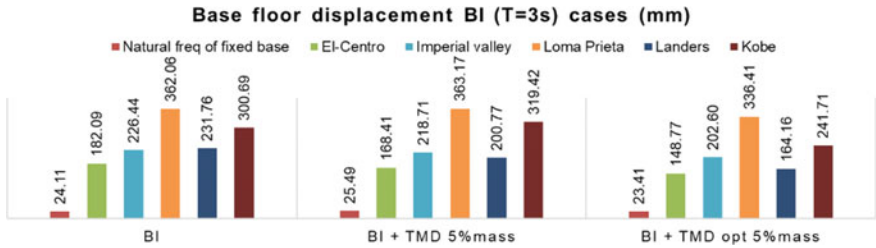
Fig. 9 Base floor displacement for BI ($T = 3$ s) cases
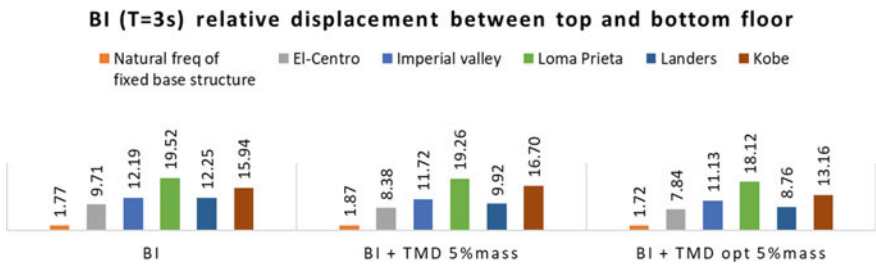
Fig. 10 Relative displacement between base and top floor for BI ($T = 2$ s) cases
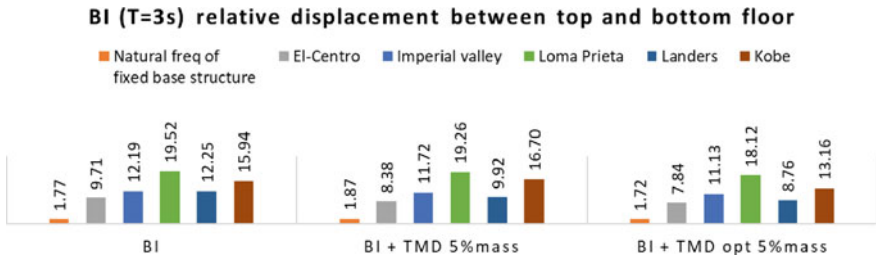
Fig. 11 Relative displacement between base and top floor for BI ($T = 3$ s) cases

4   Conclusions

This study examines the response control of a base-isolated structure equipped with a TMD at the isolation level with the intention of reducing the large lateral displacements at the base. Two TMDs are investigated, (i) a conventional TMD and (ii) an optimally designed TMD (TMDopt). Here, the TMDs are modelled as vertical cantilever with tip mass. The effectiveness of these in lowering the dynamic response of base-isolated structures is compared to the response of an uncontrolled base-isolated structure. The following are some important observations.

- The input earthquake motions have a significant impact on the response of base-isolated structures with tuned-mass dampers.
- Base-isolated structure equipped with optimally designed TMD (TMDopt) as suggested by Tsai et.al is showing better response reduction than the one equipped with a conventional TMD.
- Reduced seismic response at the base in base-isolated structures could be achieved by using the optimal tuning frequency and damping ratio of a tuned-mass damper as a design guideline.
- The numerical studies indicate that the optimally designed TMD reduces the base displacement by about 40% in the case of isolated buildings under the Imperial Valley and Loma Prieta earthquakes.
- Since the tuned-mass damper is dependent on the primary structure's motion to react, it has a little impact on the structural response during the first 5–10 s of the excitation. This could differ according on the type of input stimulation used.

References

1. Farzad Naeim JMK (2000) Design of seismic isolated structures: from theory to practice
2. De Domenico D, Ricciardi G (2018) An enhanced base isolation system equipped with optimal tuned mass damper inerter (TMDI). Earthq Eng Struct Dyn 1169–1192. https://doi.org/10.1002/eqe.3011
3. De Domenico D, Ricciardi G (2018) Improving the dynamic performance of base—isolated structures via tuned mass damper and inerter devices : a comparative study. Struct Control Heal Monit 1–24. https://doi.org/10.1002/stc.2234
4. Tsai HC (1995) The effect of tuned-mass dampers on the seismic response of base-isolated structures. Int J Solids Struct 32(8–9):1195–1210. https://doi.org/10.1016/0020-7683(94)00150-U
5. Yang JN, Danielians A, Liu SC (1991) Aseismic hybrid control systems for building structures. J Eng Mech 117(4):836–853
6. Taniguchi T, Der Kiureghian A, Melkumyan M (2008) Effect of tuned mass damper on displacement demand of base-isolated structures 30(12):3478–3488. https://doi.org/10.1016/j.engstruct.2008.05.027
7. Kareem A (1997) Modelling of base-isolated buildings with passive dampers under winds. J Wind Eng Ind Aerodyn 72(1–3):323–333. https://doi.org/10.1016/S0167-6105(97)00232-8
8. Xiang P, Nishitani A (2013) Optimum design for more effective tuned mass damper system and its application to base-isolated buildings 98–114 (2014). https://doi.org/10.1002/stc.1556

9. Kelly JM (1993) Earthquake-resistant design with rubber
10. Tsai HC, Lin GC (1993) Optimum tuned-mass dampers for minimizing steady-state response of support-excited and damped systems. Earthq Eng Struct Dyn 22(11):957–973. https://doi.org/10.1002/eqe.4290221104

Response of Dynamic Wind Load on High-Rise Building Supported on Raft and Piled Raft Foundation Using Different Outrigger System

Kiran A. Mayacharya, Tejas D. Doshi, and V. D. Gundakalle

1 Introduction

Nowadays, cities are having scarcity of land which has resulted in the increase land rates in the last few decades. The rapid increase in the growth of urban population has resulted in reduced availability of shelter [1]. It is a modern-day problem which requires modern-day solution, that is constructing a high-rise building. Nearly all buildings residential, public and government buildings are constructed as tall buildings in order to maximize the capacity and functionality in provided land space [2].

Recent developments in the construction sector have showed advancement in the tall buildings to reduce factors like displacement and drift of the building for the maximum comfort of the occupants. As we know, lateral loads are the governing factor for the tall buildings. So, in order to reduce the problems caused by the lateral loads, there are several types of structural systems used, and those are moment resisting frames, bundled tube structure, tube-in-tube structure, frames with shear core, etc. [2, 3]. However, out of different types of lateral load resisting systems used, outrigger and belt truss system give significant improvement in the displacement control of the structure [3].

The structural engineers have achieved so much in the long run from moment frames to ultra-efficient braced framed structure. The creation of architecturally and structurally innovative buildings has been possible because of the recent advancement in the finite element method along with the structural software's recent developments [4]. The perfect balancing between understanding of behaviour of structure and then

K. A. Mayacharya (✉) · T. D. Doshi · V. D. Gundakalle
Department of Civil Engineering, KLE Dr. M. S. Sheshgiri College of Engineering and
Technology, Belagavi, Karnataka 590008, India
e-mail: kiranam96@gmail.com

depending on computing tools might help in changing the way the buildings will be designed and constructed [5].

The control of the displacement of building at highest floor and the base moments in tall buildings is of main concerns in the structural design of high-rise structures. This problem of the structures can be solved by increasing the stiffness of the building. Along with the lateral loads, gravity and other loads of the buildings are to be kept in mind for the construction of the building. Also with the strength, serviceability and aesthetics the building should also be economical. So, considering all these factors, best way to improve building performance is providing the outriggers and belt truss system [6]. Dynamic behaviour of the building is usually due to wind and seismic forces. But for the forces, the criteria for design are different. In wind load, there is gradual increase in force from bottom of the structure to the top and throughout the whole building. Seismic forces impact on the foundation creating severe movements and vibration in the building. Seismic loads are generally displacement type loading and wind loads are force type loading [7]. Diagrid structural system is adopted in tall buildings due to its structural efficiency and flexibility in architectural planning. Compared to closely spaced vertical columns in framed tube, diagrid structure consists of inclined columns on the exterior surface of building. Due to inclined columns lateral loads are resisted by axial action of the diagonal compared to bending of vertical columns in framed tube structure. Diagrid structures generally do not require core because lateral shear can be carried by the diagonals on the periphery of building [8]. An interactive design method that takes into account the coupling between the stiffness of the superstructure, the piled raft and the soil has been proposed for analyzing the response of building structure. Special attention is given to consideration of interaction between the superstructure and the piled raft. It can be effectively used to perform the design of a superstructure-piled raft foundation system [9]. The new trend towards constructing taller buildings makes modern tall buildings be increasingly susceptible to wind excitations. Therefore, a combined aerodynamic control, including the shape optimization of the cross section (passive aerodynamic control) and air suction (active aerodynamic control), is put forward to achieve a more considerable reduction of the wind-induced responses of a tall building with square cross-section, so as to improve its wind-resistance performance. The results show that the combined aerodynamic control is very effective in reducing the along-wind and across-wind responses at most cases, however, it can sometimes be unfavorable to the torsional responses [10]. The study is to evaluate the capability of the proposed numerical method by comparing its output with case study data. The raft-soil and pile interaction problem outside the verified case is to be understood by running a series of the parametric studies. The interaction mechanism of raft-soil and pile under seismic and vertical load is based on inertia and kinematic interaction indicated through the analysis [11].

2   Objectives of the Study

- Generation of 3D model in STAAD.Pro with different types of outrigger systems and different types of support conditions.
- To study the response of tall buildings using raft and piled raft foundations in different soil strata.
- To know the behaviour of tall buildings with different types of outriggers and belt truss system.
- To study the response of the structure in terms of displacement, drift, base moments and axial forces for different structural models in various soil strata.

3   Methodology and Model Analysis

To complete the present study, following methodology is adopted

- First literature review for related subject was done and then Indian standard design codes provisions for lateral loads.
- Different parameters like structural plan, etc., and wind parameters are fixed with respect to design code.
- Modelling of 40 storey RC framed structure with different types of outriggers for raft and piled raft foundation was carried out in STAAD.Pro software.
- The frame of the structure used is rectangular and symmetric, and the wind load applied on the structure is calculated according to the IS 875 part-3 code provision.

3.1   Structural Configuration

The different types of structures considered for analysis are given below:

- Building with conventional outrigger system with raft foundation.
- Building with virtual outrigger system with raft foundation.
- Building with offset outrigger system with raft foundation.
- Building with conventional outrigger system with piled raft foundation.
- Building with virtual outrigger system with piled raft foundation.
- Building with offset outrigger system with piled raft foundation.

Modelling details of the 40 storey RC frame building, sectional properties elements and different material properties used in the building are given in Table 1.

The models prepared are having eight numbers of bays in X direction and five number of bays in Z direction. Columns are spaced at 5 m centre to centre in both directions.

Table 1 Example of construction of a table

Plan area	40 m × 25 m
Number of storeys	40
Height of each storey	4 m
Column size	1.5 m × 1.5 m
Beam size	0.3 m × 0.75 m
Core wall thickness	0.45 m
Outrigger beam size	0.3 m × 4 m
Belt truss section	Double angle section of ISA 200 × 200 × 25
Steel grade	Fe 500
Concrete grade	M40
Raft thickness	3.5 m
Pile diameter	0.8 m
Pile length	40 m
Piles per column	9 numbers

Table 2 Loads applied on the model

Dead load	
Wall load	14.95 kN/m
Parapet wall load	4.60 kN/m
Slab and floor finish load	4.75 kN/m^2
Live load	
Floor live load	3.0 kN/m^2
Roof live load	1.5 kN/m^2

3.2 Model Configuration

The configuration used to prepare the models is as given in Table 1.

3.3 Load and Load Combinations

The applied loads on the models are mentioned in Table 2, and load combinations for wind analysis are adopted confirming to IS 875 part-3.

3.4 Wind and Soil Parameters

The wind parameters considered for different models are given in Table 3 and considered for analysis confirming to IS 875 part-3. The soil parameters and coefficients

Table 3 Wind parameters

Wind zone	5
Basic wind speed	50 m/s
Terrain category	3
Structure life	50 years
Class of structure	Not required

Table 4 Modulus of subgrade reaction of different soil

Soil type	Stiff	Very stiff	Hard
Subgrade modulus (kN/m^3)	27,000	54,000	108,000

Table 5 Coefficients of soil springs for piles

Soil type	Pile diameter (m)	Soil layer depth (m)	Subgrade modulus (kN/m^3)	Vertical spring constant (kN/m)	Horizontal spring constant (kN/m)
Stiff	1.2	2	27,000	37,800	1890
Very stiff	1.2	2	54,000	75,600	3780
Hard	1.2	2	108,000	151,200	7560

of soil springs for piles considered for different models are given in Tables 4 and 5, respectively.

3.5 Model Details

The structural plan and isometric view with different types of outriggers are shown in Figs. 1 and 2, respectively.

4 Results and Discussion

The results are obtained and recorded from wind load analysis from STAAD.Pro software and are given in the form of charts below and comparison is done.
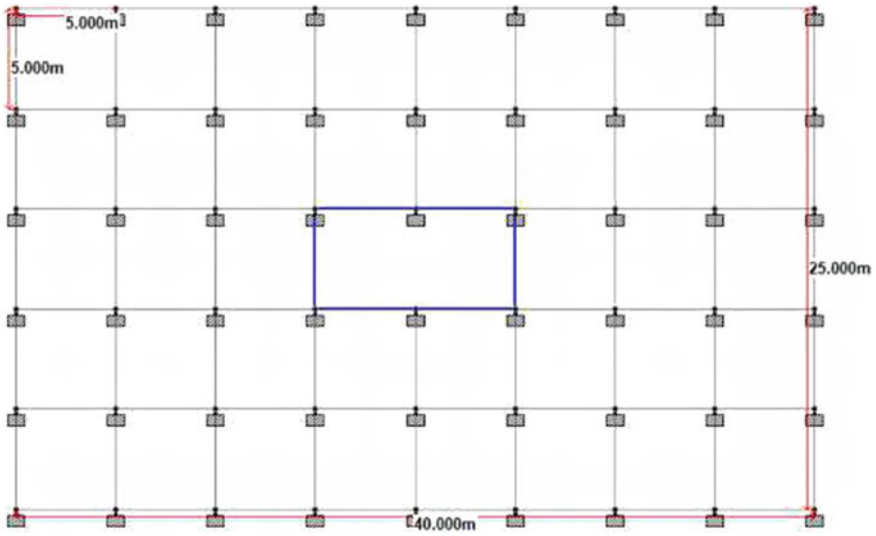
Fig. 1 Structural plan
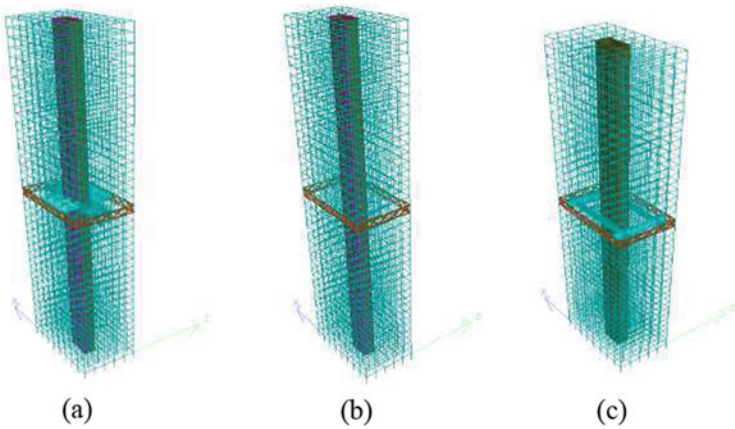
Fig. 2 Isometric view of building with **a** Conventional outrigger **b** virtual outrigger **c** offset outrigger

4.1 For Raft Foundation

4.1.1 Displacement

From Fig. 3, the results obtained indicate that reduction in top storey displacement in hard soil is more when the conventional outrigger is used in the structure. The displacement reduction increased for conventional outrigger by 0.6% and 2.8% more

Fig. 3 Top storey
displacement for different
types of outriggers in various
soil strata with raft
foundation

Top displacement (mm)

Conventional Outrigger: 604.03, 554.11, 528.96
Offset Outrigger: 607.28, 557.27, 532.161
Virtual Outrigger: 619.21, 569.27, 544.19

Type of outrigger

■ Stiff ■ Very Stiff ■ Hard
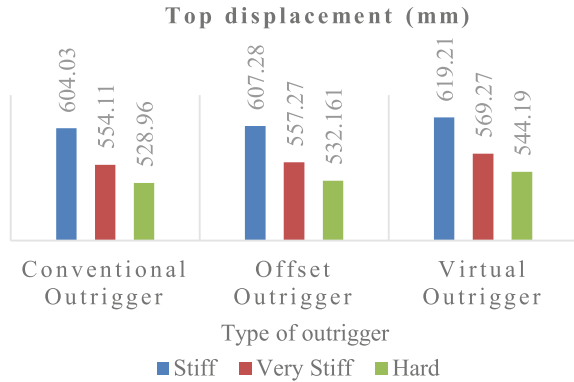
than offset and virtual outrigger for hard soil, by 0.56% and 2.66% in very stiff soil, and by 0.53% and 2.45% in stiff soil. For all configurations, the outrigger location was fixed at 0.5H of the building. The reduction in displacement for conventional outrigger system is more because the horizontal beam (outrigger) is connected to the central shear wall and other columns which provide increased stiffness to the structure.

4.1.2 Storey Drift

The reduction in displacement for conventional outrigger system is more because the horizontal beam (outrigger) is connected to the central shear wall and other columns, which provides increased stiffness to the structure. From results, it is observed that, drift is less for conventional outrigger positioned at 0.5H, so the drift of structure for conventional outrigger in different soils is given in Fig. 4. From Fig. 4, it is figured out that providing conventional outrigger to structure reduces more drift for hard soil as compared to very stiff and stiff soil.

Fig. 4 Storey drift at each
storey for structure with
conventional outrigger in
various soil strata with raft
foundation

Storey Drift in mm for Raft Foundation

STOREY

——For Hard Soil ——For Very Stiff Soil ——For stiff soil

Fig. 5 Moments at base of the structure for different outriggers in various soil strata with raft foundation

4.1.3 Bending Moment

From Fig. 5, it is evident that moments at base are decreased by 9.44% and 19.8%, 9.54% and 19.99%, 9.55% and 20.02% for hard strata compared to that of stiff strata soil for the conventional outrigger, offset outrigger and virtual outrigger provided at fixed position of 0.5H for raft foundation. The bending moment is least in the virtual outrigger system as members are less in the virtual outrigger system which results in reduced loading on the structure.

4.1.4 Axial Force

From Fig. 6, it is observed that axial forces induced are least for virtual outriggers compared to offset and conventional outrigger. The axial forces at base decreased by 3.957% and 4.46%, 3.93% and 5.36%, 3.94% and 5.49% for very stiff strata and hard strata compared to that of stiff strata soil for the conventional outrigger, offset outrigger and virtual outrigger provided at fixed position of 0.5H of building for raft

Fig. 6 Axial forces at the base of the structure for different outriggers in various soil strata with raft foundation
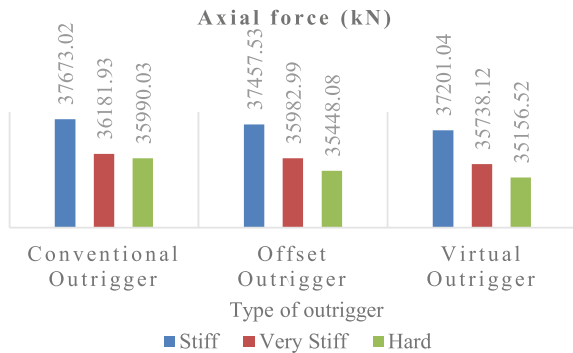
Fig. 7 Top storey displacement for different types of outriggers in various soil strata with piled raft foundation

Top Displacement (mm)
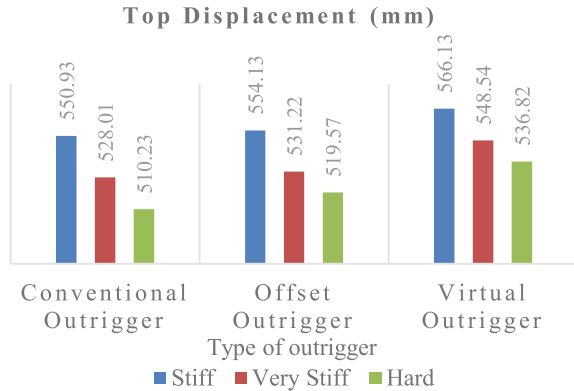
foundation. It is due to the less number of members used in the virtual outrigger system that the axial force is reduced compared to other outrigger systems.

4.2 For Piled Raft Foundation

4.2.1 Displacement

From Fig. 7, in piled raft system, least displacement is observed in conventional outrigger with position of outrigger fixed at 0.5H of the building. The displacement reduction increased for conventional outrigger by 0.58% and 2.68% more than offset and virtual outrigger for stiff soil, by 0.60% and 3.74% in very stiff soil and by 1.79% and 4.95% in hard soil. The reduction in displacement for conventional outrigger system is more because the horizontal beam (outrigger) is connected to the central shear wall and other columns, which provides increased stiffness to the structure.

4.2.2 Storey Drift

From Fig. 8, the decrease in drift for conventional outrigger system in hard soil is more as compared to stiff and very stiff soil. It is evident that the storey drift is reduced when piled raft foundation is used as compared to the raft foundation. The reduction in the storey drift of the structure with piled raft foundation is 2.5% compared to raft foundation.

4.2.3 Bending Moment

From Fig. 9, it is evident that moments at base are decreased by 7.17% and 13.24%, 7.21% and 13.31%, 7.81% and 13.79% for very stiff strata and hard strata compared

Storey Drift for Piled Raft Foundation
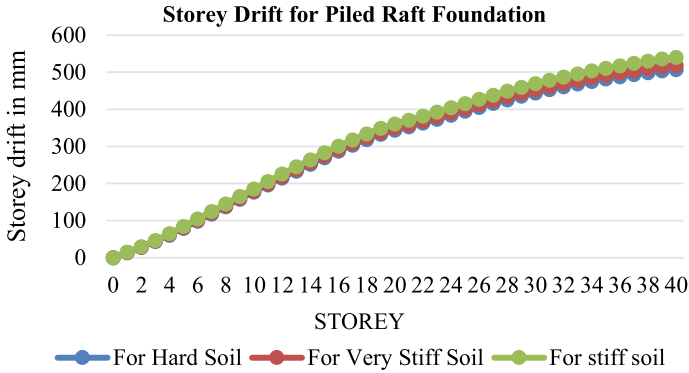
Fig. 8 Storey drift at each storey for structure with conventional outrigger in various soil strata with piled raft foundation
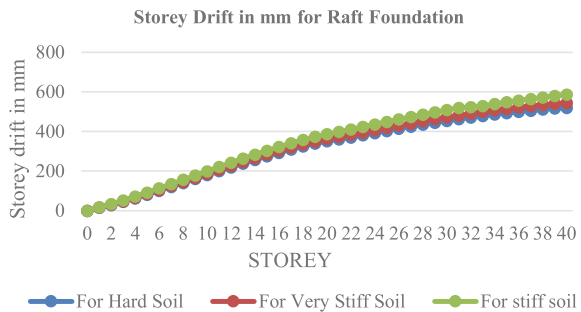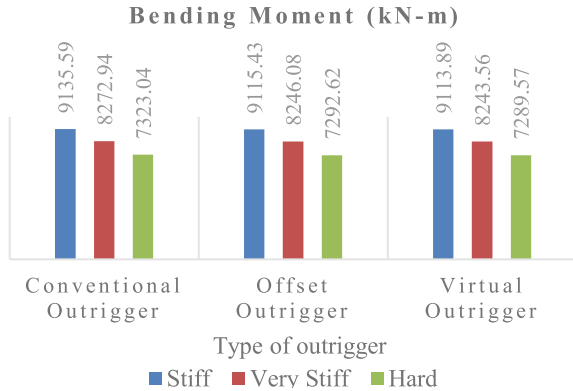
Fig. 9 Moments at base of the structure for different outriggers in various soil strata with piled raft foundation
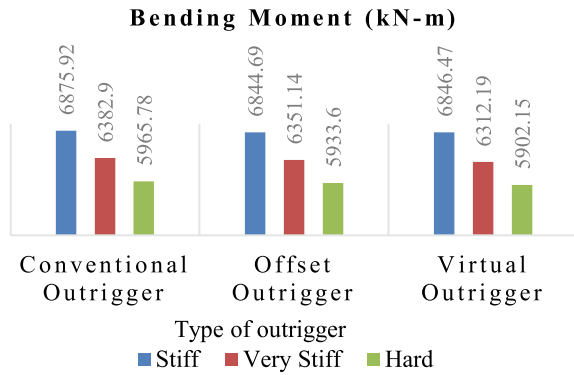
to that of stiff strata soil for the conventional outrigger, offset outrigger and virtual outrigger provided at fixed position of 0.5H of the building for piled raft foundation. The bending moment is least in the virtual outrigger system as members are less in the virtual outrigger system which results in reduced loading on the structure.

4.2.4 Axial Forces

From Fig. 10, it is observed that axial forces induced are least for virtual outriggers compared to offset and conventional outrigger system for piled raft foundation. The axial forces at base decreased by 0.25% and 0.64%, 0.69% and 1.06%, 0.34 and 1.83% for very stiff strata and hard strata compared to that of stiff strata soil for the conventional outrigger, offset outrigger and virtual outrigger provided at fixed position of 0.5H for raft foundation. It is due to the less number of members used in the virtual outrigger system that the axial force is reduced compared to other outrigger systems.

Fig. 10 Axial forces at the base of the structure for different outriggers in various soil strata with piled raft foundation
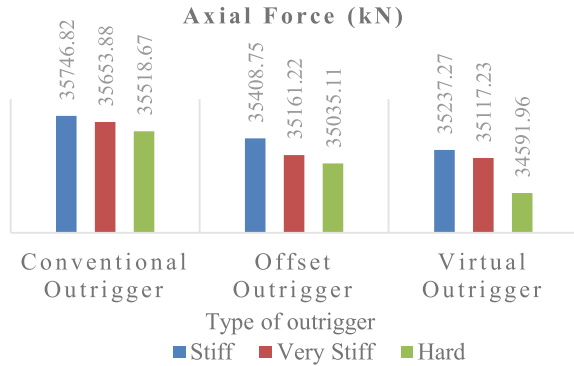
5 Conclusions

This project deals with finding best type of outrigger system with dynamic effects caused due to wind forces for raft and piled raft foundation. These effects are also studied for different soil strata.

- Conventional outrigger system gives reduced displacement and drift as compared to offset outrigger system and virtual outrigger system. As the lateral load coming on the structure is distributed uniformly to all the columns in the conventional outrigger system, it reduces displacement by more margin.
- Bending moment for the structure with virtual outrigger is least out of the three considered types of outriggers. Axial force induced at the structure base is least in the virtual outrigger system as compared to other outrigger systems. This is because of the less number of members in the virtual outrigger which results in reduced self-weight of the building and in turn reduces axial force and bending moment compared to other two outrigger system.
- Top storey displacement and storey drift reduces by 2.38% for piled raft foundation in comparison with raft foundation. Axial forces and bending moment at the structure base reduces for piled raft foundation as compared to raft foundation for all soil conditions considered as the piled raft counter acts the axial force coming from the above structure and distributes uniformly to the ground.
- It can be concluded that the piled raft system is better for the stability of tall buildings, while there is not much difference between the performance of the three outrigger systems considered with respect to the lateral loads applied. So, it can be said that all the outrigger system is good but the important factor being reduction in displacement of structure at top the conventional outrigger system is the better system to be provided in the tall structures.

References

1. Paulos HG, Chow H, Small JC (2011) Piled raft foundation for tall buildings. Geotech Eng J SEAGS AGSSEA 42(2)
2. Kamath K, Divya N, Rao A (2012) A study on static and dynamic behaviour of outrigger structural system for tall buildings. Bonfring Int J Ind Eng Manage Sci 2(4)
3. Simantini BM, Manjunath M (2015) An analysis of outrigger belt truss system in high-rise buildings. IUP J Struct Eng 08(3):16–24
4. Nandeesh M, Devi S (2017) Dynamic performance analysis of outrigger and outrigger with belt truss system in composite high-rise building. Int Res J Eng Technol 4(11)
5. Sundar RS, Gore NG (2017) A study on tall RC structure with outrigger system subjected to seismic and wind loading. Int J Eng Res Technol 6(2)
6. Khade RB, Kulkarni PM (2019) Effect of wind load on structural performance of dimensionally regular and irregular high-rise buildings with different outrigger systems. Int J Eng Manage Res 9(4)
7. Amoussou CPD, Lei H, Alhaddad W, Halabi Y (2021) Simplified modelling and analysis method of skyscrapers with outrigger system. Structures 33. https://doi.org/10.1016/j.istruc.2021.04.096
8. Jani K, Patel PV (2013) Analysis and design of diagrid structural system for high rise steel buildings. Proc Eng 51:92–100
9. Ko J, Cho J, Jeong S (2017) Nonlinear 3D interactive analysis of superstructure and piled raft foundation. Eng Struct 143:204–218
10. Zheng C, Xie Y, Khan M, Wu Y, Liu J (2018) Wind-induced responses of tall buildings under combined aerodynamic control. Eng Struct 175:86–100
11. El-Attar A (2019) Dynamic analysis of combined piled raft system. Ain Shams Eng J. https://doi.org/10.1016/j.asej.2020.12.014

Effect of Vertical-Stepped Geometric Irregularity on the Seismic Performance of Buildings

Aditi Parashar, Saurabh Kumar Sharma, Bikram Paul, and Kushal Ghosh

1 Introduction

Severe damages in buildings are caused due to earthquakes. So, it is very necessary to keep in mind the changes in structural behaviour due to seismic effects and one should adopt the necessary assumptions before design. To perform well in an earthquake, a building should possess four main attributes: simple and regular configuration, adequate lateral strength, stiffness and ductility.

But in recent times, functional and aesthetic requirements govern the architectural nature of structures which lead to irregular structures. These are useful in urban areas, where buildings are closely spaced and provide adequate sunlight and ventilation for bottom storey. Irregularities of a building can be characterised into two types: (a) plan irregularities and (b) vertical irregularities.

Irregularity type and description according to IS 1893 (Part-1): 2016 are stiffness irregularity (classified as soft storey and extreme soft storey), mass irregularity, vertical geometric irregularity, in-plane discontinuity in vertical elements resisting lateral force and strength irregularity (Weak storey) (Fig. 1).

A type of vertical geometric irregularity is the use of staggered reductions in the floor area of multi-storied structures along the height resulting in a change of mass, strength and stiffness. This type of building is generally referred to as a setback building.

Setback ratio is defined as the ratio of horizontal distance between the edge of building and extreme end of setback (A), to the maximum horizontal plan dimension of building (L).

A. Parashar · S. K. Sharma · B. Paul · K. Ghosh (✉)
Department of Civil Engineering, National Institute of Technology Sikkim, Barfung block, Ravangla, South Sikkim, India
e-mail: kushal@nitsikkim.ac.in
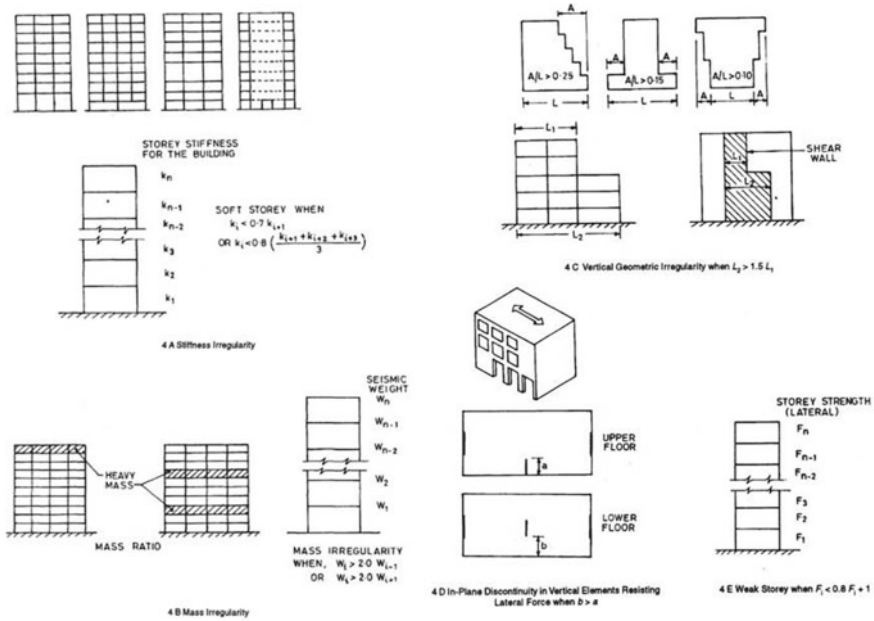
Fig. 1 Vertical irregularities (IS 1893 (Part-1): 2016 [1])

The behaviour of these buildings under seismic loads is different from regular structures. An effort has been made in this study to understand the effect of the setback distance on the structural behaviour of buildings.

2 Review of Previous Studies on Vertical Irregularity

Several research studies are there with regard to effects of irregularities on seismic performance of a building [2–13]. Based on the published data available, the following points were noted. The definition of setback building proposed in design codes is not appropriate [14]. Drift demand increases with increase in height [15]. For setback structures, ductility demand is higher as compared to regular structures [16]. Concentration of damage was seen to occur near vicinity of setbacks [17]. Time period decreases with increase in stepping irregularity [18]. Clear definitions of irregularities are provided in codes [19]. Mass irregularity shows least seismic response, but the effect of strength irregularity is larger as compared to the of stiffness irregularity [20]. Formulas of design code were modified using modification factor [1].

3 Methodology

In the present work, seismic response of frames having different configurations is obtained numerically using STAAD Pro. software. The major inputs are geometry of the frame including dimensions of storeys, beams and columns, seismic zone, soil type, reduction factor, importance factor, damping ratio and earthquake data as well as different loads such as dead load, live load, earthquake load and wind load. Damping ratio of 5% is assumed for damping. The results are structural response in the form of maximum displacement in x and z direction and base shear. In order to validate the results, response obtained for the structures graphs is plotted, and equations are obtained and then checked for other structures with offsets, whether it satisfies the curve equation. For both validation and subsequent analysis, same methodology is adopted.

3.1 Equivalence Static Method of Analysis

For this study, total nine (G + 14) frames with different setback ratios (0.25, 0.3125, 0.375, 0.4375, 0.5, 0.5625, 0.625, 0.6875 and 0.75) are modelled using STAAD Pro (Figs. 2, 3, and 4). Software. Model is done as per IS 1893 (Part-1) 2016, IS 875 (Part 3) 2015 and IS 456 2000. All models have floor height at each level of 3 m except ground floor which has floor height 3.6 m. Total height of each model is 45.6 m. The buildings have fifteen bays in x and z directions, each bay of 3 m wide. Columns are assumed to be rigid/fixed at base of the foundation level (Tables 1 and 2).

Table 1 Description of developed RC setback frame models

S. No.	Parameter	Remarks
1	Type of structure	Residential
2	Number of storeys	15
3	Floor height	3 m
4	Total height of building	45.6 m
5	Column size	600 mm × 600 mm
6	Beam size	250 mm × 600 mm
7	Slab thickness	100 mm
8	Masonry wall thickness	250 mm
9	Soil type	Type ll-medium soil
10	Damping ratio	5%
11	Seismic zone	IV
12	Response reduction factor	5
13	Importance factor	12

Table 2 Setback ratios

S. No.	Model identity (Setback ratio)
1	SI (0.25)
2	S2 (0.3125)
3	S3 (0.375)
4	S4 (0.4375)
5	S5 (0.5)
6	S6 (0.5625)
7	S7 (0.625)
8	S8 (0.6875)
9	S9 (0.75)

3.1.1 Models

See Figs. 2, 3 and 4.

3.1.2 Results and Conclusion of Equivalent Static Method Analysis

Figure 5 shows resultant displacement of X and Z direction for irregular-stepped building increases with increase in setback. The storey drift is also seen to be generally increase with increasing setbacks. This can be attributed to the fact that non-uniform distribution of stiffness has a negative effect on the seismic performance of a building.

Figure 6 shows storey drift versus setback curve for irregular-stepped building, and that drift is increasing with increase in setback ratio. This can be attributed to the fact that as setback ratio increases, the building becomes more irregular, and hence, the drift demands are more. It also justifies the displacement result attributing the fact that non-uniform distribution of stiffness has a negative effect on the seismic performance of a building.

Figure 7 shows a base shear curve which is a another very important parameter whilst doing seismic analysis as Vb depends on horizontal seismic coefficient and vertical loads. Also, as per IS code 1893 (Part-1): 2016, the horizontal seismic coefficient depends on factors like seismic zone (Z), importance factor (I), response reduction factor (R) and design acceleration coefficient (Sa/g), and all these factors after analysis are observed to be constant throughout. Therefore, base shear is governed by vertical load (that consists of dead load + 25% live load) which is decreasing with increasing offsets. Hence, base shear also decreases with increase in offsets (Fig. 8).
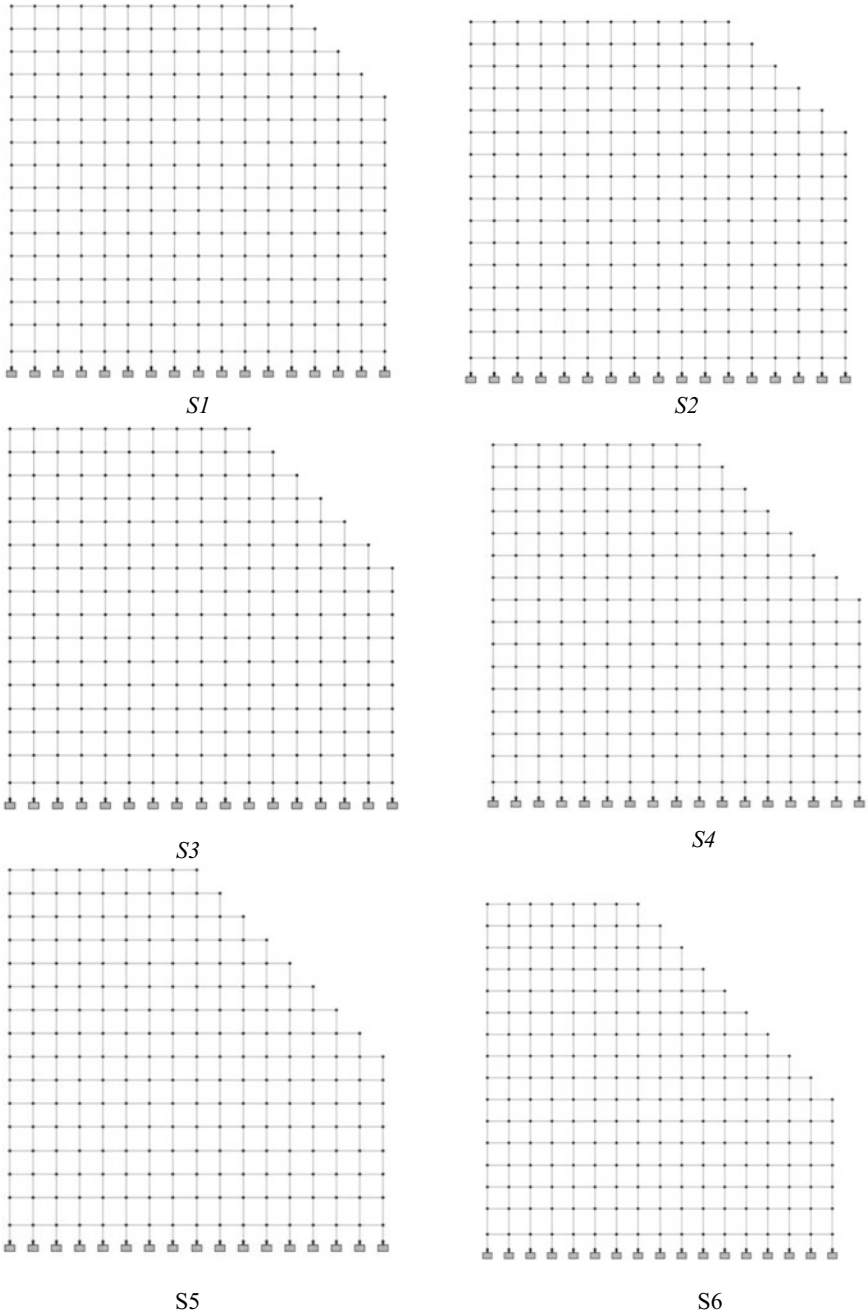
Fig. 2 Sectional elevations of structures with various setback distances
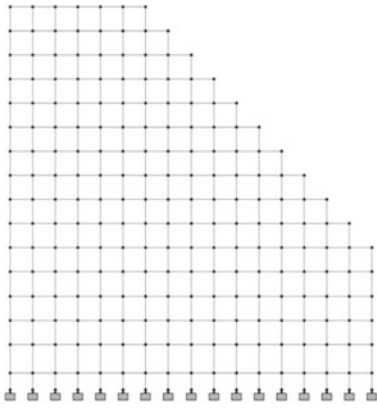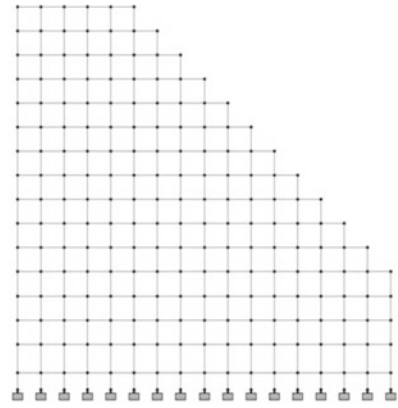
S7   S8
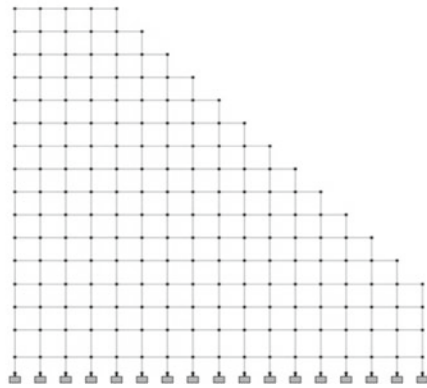
S9

Fig. 2 (continued)

3.2 Dynamic Analysis

Figure 9 shows resultant deflection in X and Z direction up to the certain value of setback ratio; the displacement increases with increase in the setback ratio but beyond that point shows a significant and continuous decrease in deflection value with increasing setbacks.

Figure 10 shows the value of base shear decreases with the increase in the setback ratio.
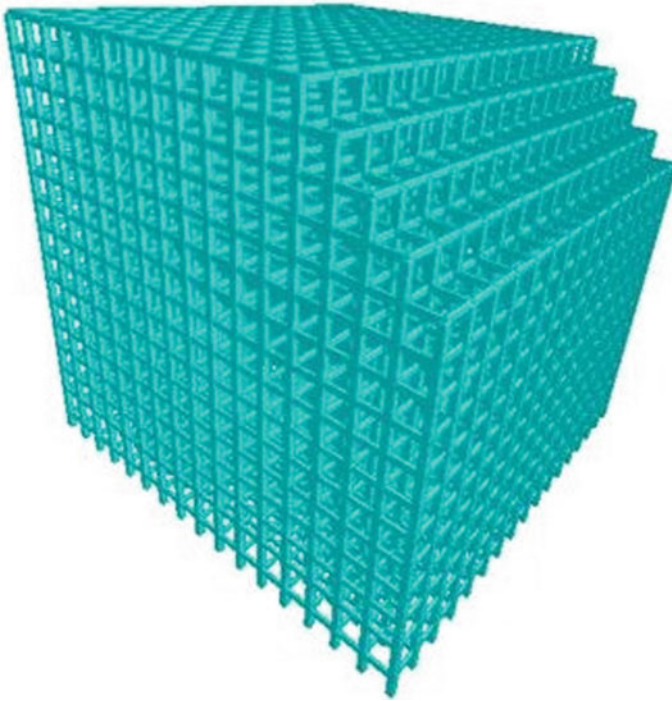
Fig. 3 3D rendered view
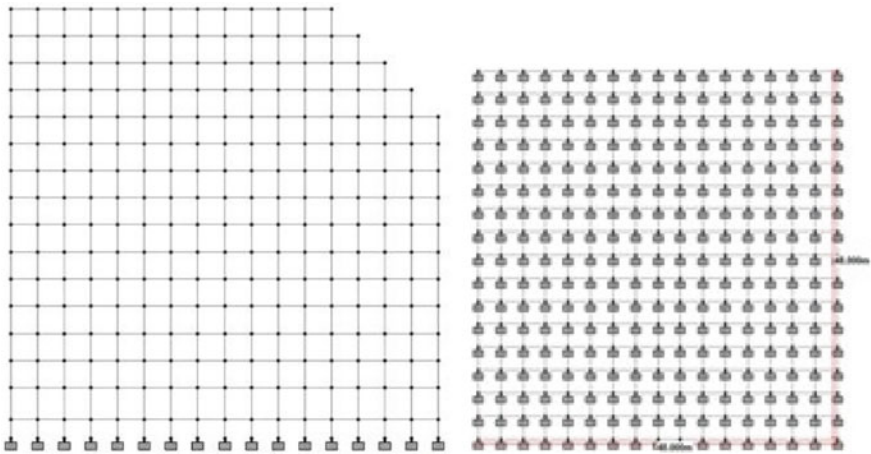
Fig. 4 Front elevation: model S1 and plan

Displacement (R)

$y = 20.817x + 48.938$

Fig. 5 Resultant deflection of X and Z direction

Storey Drift

$y = 0.0205x^4 - 0.0474x^3 + 0.04x^2 - 0.0137x + 0.0029$
$R^2 = 0.9963$
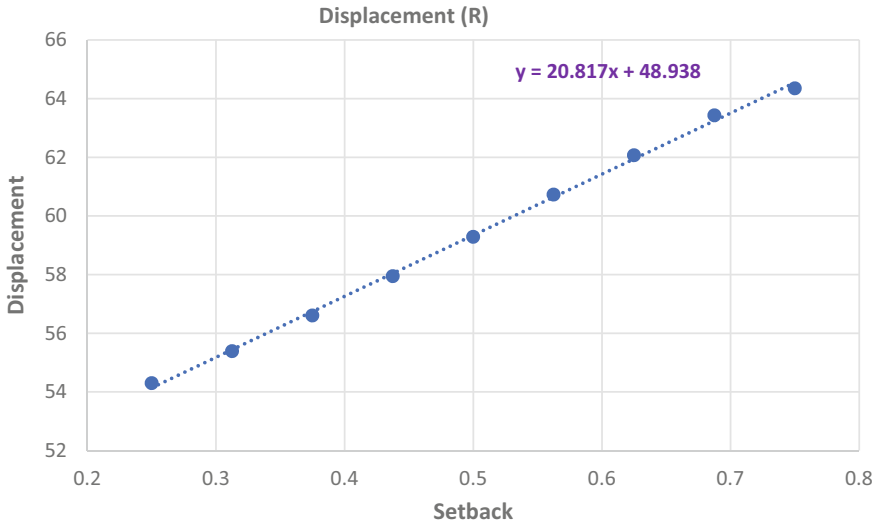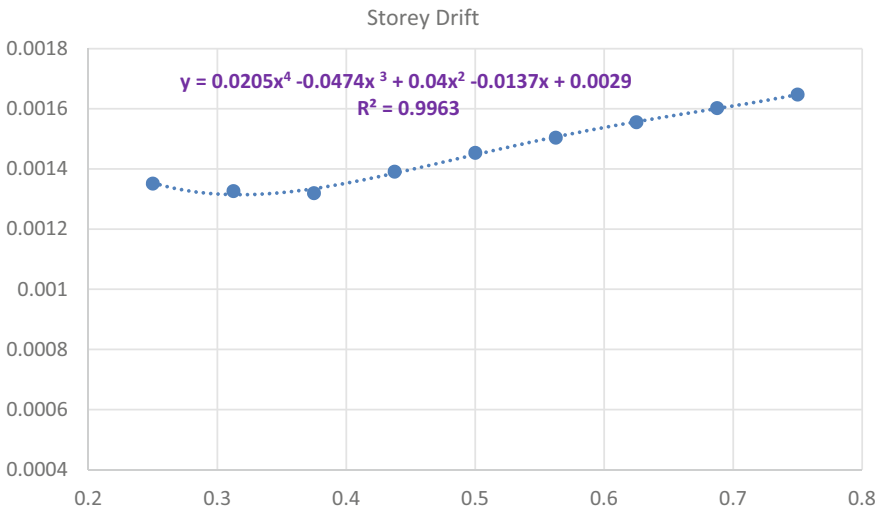
Fig. 6 Storey drift versus setback curve

4   Conclusions

- Multi-storey frames with irregularities and their structural behaviour are studied. The results show that irregularities significantly affect the structural response of a building against seismic forces. In all cases, response change is observed for
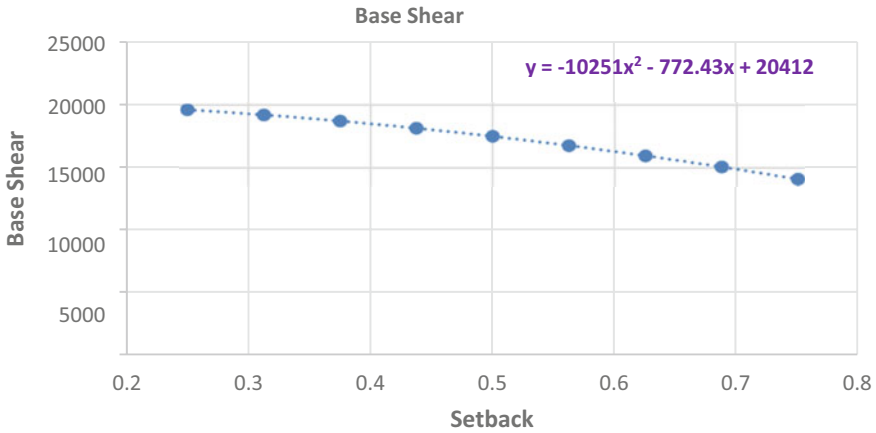
Fig. 7 Effect of setback on base shear
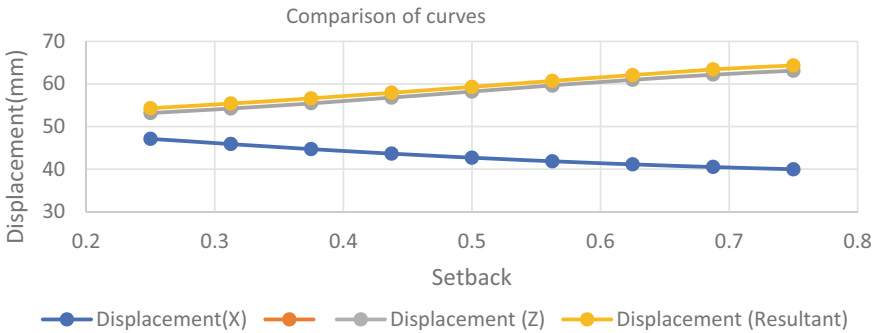
Fig. 8 Comparison of displacements along different directions

frames having irregularities in form of different offsets with respect to the regular configuration.

- For Irregular Stepped Buildings:

  (a) Resultant displacement as seen from equivalent static method increases with increase in setbacks as due to non-uniformity of stiffness and also decrease in mass (Fig. 5).

  (b) Attributing to above-mentioned point, drift curve (Fig. 6) is also plotted showing general increase in drift with increasing setbacks. All these results are in sync with the early published works [15–17].

  (c) Base shear in accordance to equivalent static method as well as dynamic analysis shows the same trend, i.e. increasing with decrease in setback (Figs. 7 and 10).
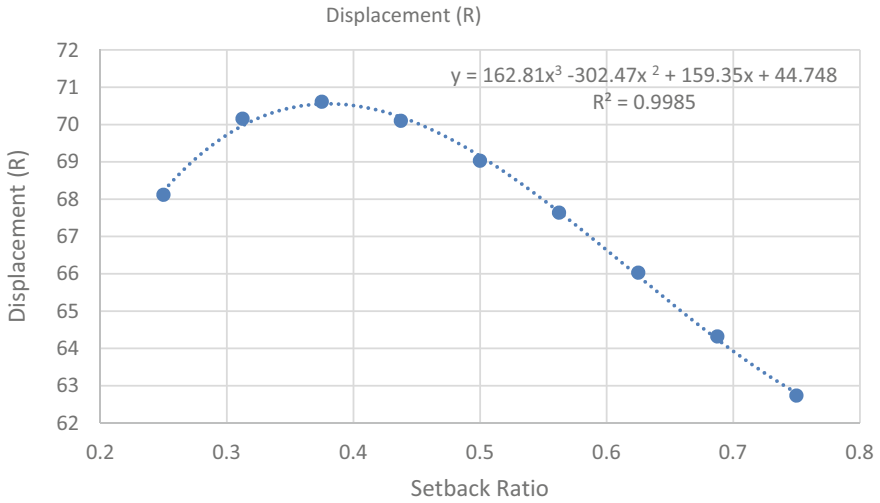
Fig. 9 Resultant deflection of X and Z direction (dynamic analysis)
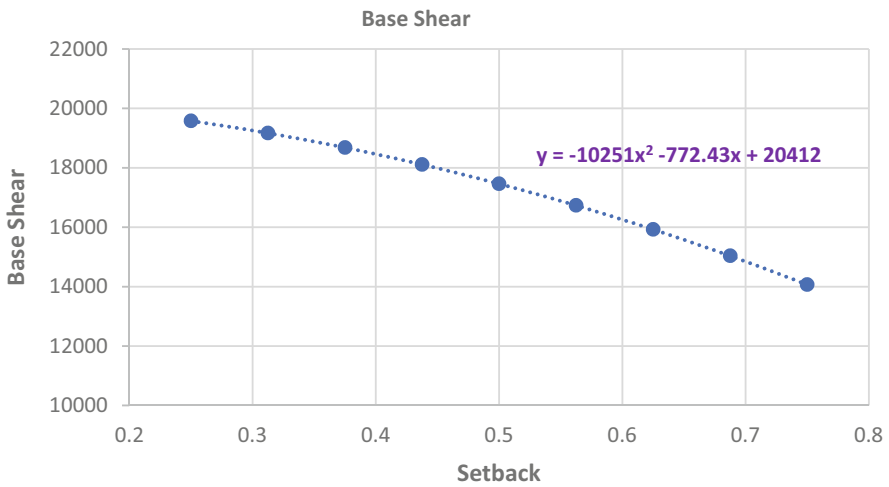
Fig. 10 Base shear

(d) Studies and formulas that are suggested in this study are not universally valid and limited to specific plan, floor height, total height, seismic zone, cross-section of members, etc.

References

1. Sarkar P, Prasad AM, Menon D (2010) Vertical geometric irregularity in stepped building frames. Eng Struct 32(8):2175–2182
2. Michalis F, Dimitrios V, Manolis P (2006) Evaluation of the influence of vertical irregularities on the seismic performance of a nine-storey steel frame. Earthq Eng Struct Dyn 35(12):1489–1509
3. Wang J, Dai K, Yin Y, Tesfamariam S (2018) Seismic performance-based design and risk analysis of thermal power plant building with consideration of vertical and mass irregularities. Eng Struct 164:141–154
4. Tremblay R, Poncet L (2005) Seismic performance of concentrically braced steel frames in multi-story buildings with mass irregularity. J Struct Eng 131(9):1363–1375
5. Ahmed MMM, Raheem SEA, Ahmed MM, Shafy AGAA (2016) Irregularity effects on the seismic performance of L-shaped multi-story buildings. JES J Eng Sci 44(5):513–536
6. Cui JL, Chey M-H, Kim SI (2016) Seismic performance of urban structures with various horizontal irregularities using equivalent static analysis. J Convergenc Soc SMB 6(1):25–32
7. Yakut A (2004) Preliminary seismic performance assessment procedure for existing RC buildings. Eng Struct 26(10):1447–1461
8. Rajeev P, Tesfamariam S (2012) Seismic fragilities for reinforced concrete buildings with consideration of irregularities. Struct Saf 39:1–13
9. Pirizadeh M, Shakib H (2013) Probabilistic seismic performance evaluation of non-geometric vertically irregular steel buildings. J Constr Steel Res 82:88–98
10. D'Ambrisi A, De Stefano M, Tanganelli M, Viti S (2013) The effect of common irregularities on the seismic performance of existing RC framed buildings. In: Seismic behaviour and design of irregular and complex civil structures. Springer, Dordrecht, pp 47–58
11. Homaei F, Shakib H, Soltani M (2017) Probabilistic seismic performance evaluation of vertically irregular steel building considering soil–structure interaction. Int J Civ Eng 15(4):611–625
12. Mohsenian V, Nikkhoo A (2019) A study on the effects of vertical mass irregularity on seismic performance of tunnel-form structural system. Adv Concr Construct 7(3):131–141
13. Khanal B, Chaulagain H (2020) Seismic elastic performance of L-shaped building frames through plan irregularities. Structures 27:22–36
14. Shahrooz BM, Moehle JP (1990) Seismic response and design of setback buildings. J Struct Eng ASCE 116(5):1423–1439
15. Humar JL, Wright EW (1977) Earthquake response of steel-framed multi-storey buildings with set-backs. Earthq Eng Struct Dyn 5(1):15–39
16. Aranda GR (1984) Ductility demands for R/C frames irregular in elevation. In: Proceedings of the eighth world conference on earthquake engineering, San Francisco, U.S.A., vol 4, pp 559–566
17. Moehle JP (1984) Seismic response of vertically irregular structures. J Struct Eng 110(9):2002–2014
18. Young KC (2011) An investigation of the fundamental period of vibration of irregular steel structures, Thesis for Master of Science in the Graduate School of The Ohio State University
19. BIS (2016) IS 1893 (Part 1)-2016: Indian standard criteria for earthquake resistant design of structures, part 1—general provisions and buildings (sixth revision). Bureau of Indian Standards, New Delhi
20. Al-Ali AAK, Krawinkler H (1998) Effects of vertical irregularities on seismic behavior of building structures. Report No. 130, The John A. Blume Earthquake Engineering Center, Department of Civil and Environmental Engineering, Stanford University, Stanford, U.S.A.

Investigate the Effect of Isolation System for RC Structure Under Seismic Forces

Faisal Ahmad, Nikhil A. Jambhale, and Tejas D. Doshi

1 Introduction

The performance of multi-storey structure under the seismic loadings depends upon the effects of earthquake ground motion eliminated by the structure. The motion of ground makes buildings to collapse and undergo landslides, as well as having many effects. Many techniques have been developed to reduce the effect of earthquake forces such as shear wall and isolation system. The isolation system is one of the most prominent vibration resist techniques. To protect the structure against earthquake forces, these are placed at substructure and superstructures. These isolators act as energy absorber of seismic energy and reduce transmission of above storeys. Seismic isolation generally uses for low and medium rise buildings, only for new propose structure having large plan area. Usually, base isolation system divides the structure from its foundation. This results to reduce the interstorey drift and effective displacement of the floors of base isolated structures which helps to reduce the damage of the structure and also helps to increase the life of structure.

Shear wall is the wall used to fill the empty space created by beams and columns. The presence of shear wall helps to increase the stability of the structures specially in the seismic prone areas. Shear walls are constructed using concrete and steel bars. These are also known as structural walls. Mainly, shear walls are adopted in seismic areas because these help to increase the stiffness of the structure, reduce the beam and column sizes which results in light weight.

F. Ahmad (✉) · N. A. Jambhale · T. D. Doshi
Department of Civil Engineering, KLE Dr. M. S. Sheshgiri College of Engineering and Technology, Belagavi, Karnataka 590008, India
e-mail: khanfaisal0505@gmail.com

1.1 Concept of Base Isolation

In this system, building is isolated from the ground in a such a way that only small portion of seismic motion transferred to the building. During an earthquake, fixed base building which is built directly on ground will move and sustain damage as a result, but base isolated buildings which are built away from ground will not move. So, the solution to the problem is to used layer generally between super structure and foundation, which is more flexible than the other structural elements and will be able to transmit the vertical loads when it is under go lateral displacement without any critical damages.

1.2 Concept of Storey Isolation

Base isolation techniques upgrade storey isolation technique. To overcome the disadvantages that are due to base isolation technique as discussed above, storey isolation technique is developed. The same technique performs as the same as that which is of base isolation but the difference is in the selected isolation interface for the structure in order to reduced seismic energy transmission. When there is change of the stiffness of structure from every floor to floor or where floor behaves as weak floor, this floor is selected as isolation interface. Below the column, the isolators are installed where these isolators are designed for axial load.

1.3 Types of Isolators

- Lead rubber bearing.
- Flat sliding bearing.
- Friction pendulum bearing system.
- Laminated rubber bearing.
- High-damper rubber bearing.

1.3.1 Lead Rubber Bearing

Lead rubber is the best example of elastomeric bearing having a perforated hole which is used to insert lead plugs. It produces more stiffness and damping for gravity as well as lateral loadings as compared to elastomeric bearing. As it contains rubbers, it helps to absorb energy. In the elastomeric bearing, interlocking of steel plates takes place and it leads to shear deformation when lead is undergoing laterally deformation.

2 Literature Survey

In this paper, G + 2, G + 4, G + 6, G + 8 building is modelled in zone *V* and analysed by response spectrum method. It is concluded that model with base isolation increases natural period, reduces base shear, and increases of displacement. Finally, it is concluded that after providing base isolation system, it increases structural stability against earthquake (Jitendra et al. [1]).

In this research, G + 10, G + 15 structures with and without isolator are modelled in ETAB software. It is concluded that time period of structure increases two times when base isolation provided to fixed base structure. After using base isolator, lateral seismic load, storey shear, column force, and moment are reduced (Sahoo et al. [2]).

In this study, G + 3, G + 20, and storey RC frame building are modelled. It is concluded that base isolation is the better method for earthquake resistant design. Use of these base isolator increases time period. Vertical irregular base isolated has more time period than plan irregular base isolator (Balachandran and Abraham [3]).

In this thesis G + 10, multi-storey building with and without base isolator a studied building dimension of size 18 m × 21.5 m with each storey height of 3.5 m is considered. It is concluded that for base isolated building as height of building increases, displacement decreases. And for fixed base building displacement as height of building increases, displacement increases (Santosh and Mahesh [4]).

This research was carried out to analyse base isolated building in seismic prone areas. The comparison in carried out between two different symmetrical G + 6, RC frames having same structural properties. Conclusion said that the existence of LRB helps to increase model displacement in each storey which is important in the structural flexibility point of view. Increased natural period affects to reduce earthquake forces whilst shaking (Ambasta et al. [5]). The isolators minimize the lateral load imposed on the structure and in accordance to that it also tend to reduce the size of the building components. The (G+15) RCC building is considered for the case study. It is modeled in SAP2000 software and analyzed for fixed base, bracing and Isolator. The non-linear time intervals analysis is carried out by considering El-Centro time history ground acceleration data. It is concluded that effectiveness of isolation technology can be perceptible when it is compared to the results obtained from the analysis of non-isolated buildings [6].

3 Objectives of the Study

- To study the effect of base isolation system for fixed base structure under the influence of seismic forces using ETABS.
- To investigate the performance of fixed base structure with shear wall and base isolation system under the influence of seismic forces.
- To examine the optimum position of base isolation system for structure with and without shear wall.

4   Methodology and Model Analysis

- A literature survey is carried out on seismic behaviour of multi-storey RC building with and without isolation.
- Modelling of G + 9 RC structure using ETABS 2018.
- Structure plan, member dimensions, seismic parameters, and material properties are considered.
- The isolator is designed by uniform building code (UBC) 97, and the analytical part is carried out as per the IS 1893:2002.
- The building model is analysed by response spectrum method according to IS 1893:2002 using ETABS software [7].

4.1   Design of Lead Rubber Bearing

The design of lead rubber bearing is carried out by referring to design code of standards UBC 97, Volume II [8] (Table 1).

Max load on column, (W)	6529.53 kN
Shear modulus, (G)	0.7 N/mm^2
Time period	1.009 s
Seismic zone, (Z)	0.36
Source type of seismic	B
Near source factor, (Na)	1
Near source Factor, (Nv)	1
Earthquake response coefficient, (M_m)	1.5
Soil type	Sd
Seismic coefficient, (C_v)	0.54
Response reduction factor, (R)	0.85
Structural system above isolation interface, (R_i)	2
Effective damping ratio	5%

Table 1   Input values for software

Rotational inertia	0.023	kN/m
For U$_1$ effective stiffness	9,414,101.15	kN/m
For U$_2$ & U$_3$ effective stiffness	94,141.01	kN/m
For U$_2$ & U$_3$ effective damping	0.05	%
For U$_2$ & U$_3$ distance from end J	0.0065	m
For U$_2$ & U$_3$ stiffness	867,475.22	kN/m
For U$_2$ & U$_3$ stiffness	567.57	kN

Damping coefficient	1
Design disablement, (D_d)	$(gCvT_d/4Pi2B_d) = 0.1353$ m
Effective stiffness, (K_{eff})	$(W/g) * (2Pi/T_d)2 = 25{,}810.13$ kN/m
Energy dissipated per cycle, (W_d)	$2 * Pi * K_{eff}*D_d2*\beta_{eff} = 148.43$ kN/m
Force at design displacement or characteristic strength, (Q)	$Wd/4D_d = 274.26$ kN
Pre-yield in rubber, (K_2)	$K_{eff}-Q/D_d = 23{,}783.07$ kN/m
Post-yield stiffness ratio for rubber, (n)	$K_2/K_1 = 0.1$
Yield displacement, (D_y)	$Q/(K_1-K_2) = 0.00128$ m
Recalculation of force Q to (Q_R)	$Wd/4(D_D-D_y) = 276.88$ kN/m
Yield strength of LRB	10 MPa
Area of lead plug, (A)	$Q_R/(10*103) = 0.027$ m^2
Diameter of lead plug (d)	$sqrt(4*A/Pi) = 0.185$ m
Recalc of rubber stiffness K_{eff} to $K_{eff}(R)$	$K_{eff}-Q_R/D_D = 23{,}763.71$ kN/m
Max shear strain of rubber, Υ	100%
Thickness of rubber, (t_r)	$D_d/\Upsilon = 0.135$ m
Area of bearing, (A_{LRB})	$K_{eff}*t_r/G = 0.459$ m
Bearing dia, (D_{LRB})	$sqrt(4*A/Pi) = 0.764$ m^2
Horizontal time period consider	2 s
Horizontal frequency, (f_h)	0.5 Hz
Vertical frequency, (f_v)	10 Hz
Shape factor, s	$f_v/(2.4*f_h) = 8.33$
Single layer rubber, (t)	$Ø_{LRB}/(4*S) = 31.21$ mm
No. of rubber layers, (N)	$T_r/t = 23$
Provide single layer of rubber	38 mm
Thick of shim plates	3 mm
No. of shim layers, (n)	22
End plate thickness in between 19 and 38 mm	30 mm
Total height of LRB, (h)	660 mm
Bulk modulus (K)	2000 MPa
Horizontal stiffness, (K_H)	$G*A_{LRB}/t = 2374.72$ kN/m
Vertical stiffness, (K_V)	191,765.45 kN/m
Cover from lead to end plate	38 mm
Bonded diameter,	0.76 mm
Moment of inertia (I)	$Pi*B4/64 = 0.163$ m
Yield strength, (F_y)	$Q + K_2*D_y = 304.67$ kN/m

4.2 Structural Configuration

The present study is conducted on the following models as shown in table below (Table 2).

Table 2 Models considered for analysis

Model I	Fixed base structure
Model II	Base isolation structure
Model III	Fixed base with shear wall structure
Model IV	Base isolation with shear wall structure
Model V	Storey isolation with fixed base structure
Model VI	Storey isolation with shear wall structure

4.3 Model Configuration

The data used for building models are as Tables 3 and 4.

4.4 Model Details

G + 9 RC frame building with and without base isolator is modelled (Figs. 1, 2, 3, 4, 5, 6, and 7).

Table 3 Building data for analysis

Floor plan size	20 m × 16 m
Number of floors	G + 9
Storey height	3.0 m
Seismic zone	V
Type of soil	Hard
Column size	550 mm × 550 mm
Thickness of slab	150 mm
Concrete grade	M30
Steel grade	Fe 500
Concerte density	25 kN/m^3
Importance factor	1
Response reduction factor	3
Density of masonry wall	20 kN/m^2

Table 4 Loads as per IS 875 part 1 and 2

Type of load	Total load
Dead load	
Wall load	12.55 kN/m
Partition wall	8.10 kN/m
Parapet wall	4.80 kN/m
Live load	
Floor live load	3.0 kN/m^2
Roof live load	1.5 kN/m^2
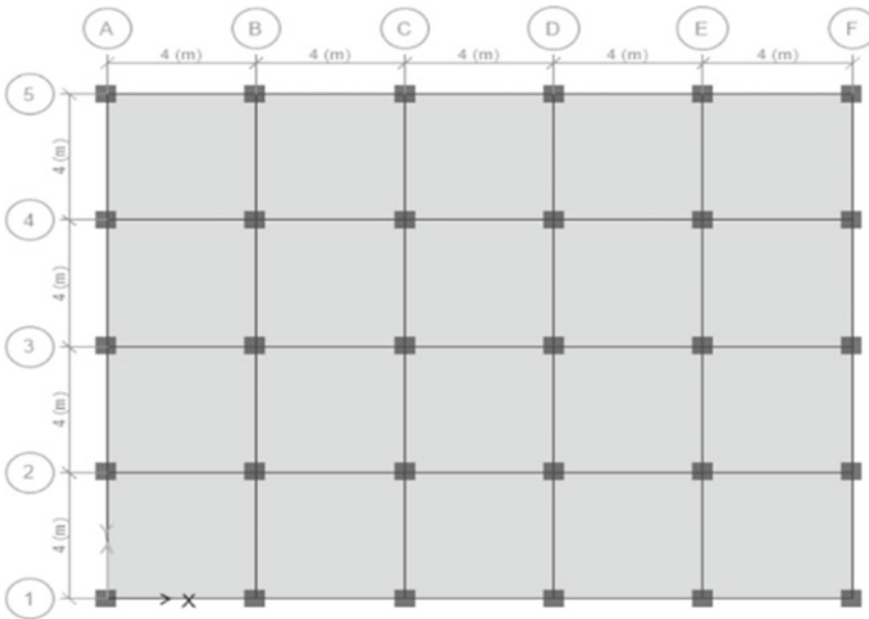
Fig. 1 Plan of RC frame building with and without base isolators

5 Results and Discussion

5.1 Lateral Displacement

Results from above table show that the displacement reduces for the structure with model VI when compared to other models. Displacement for model VI was decreased by 89.45% compared model I. Storey isolation with shear wall structure has less displacement because of optimum location of isolator and presence of shear wall load (Fig. 8).
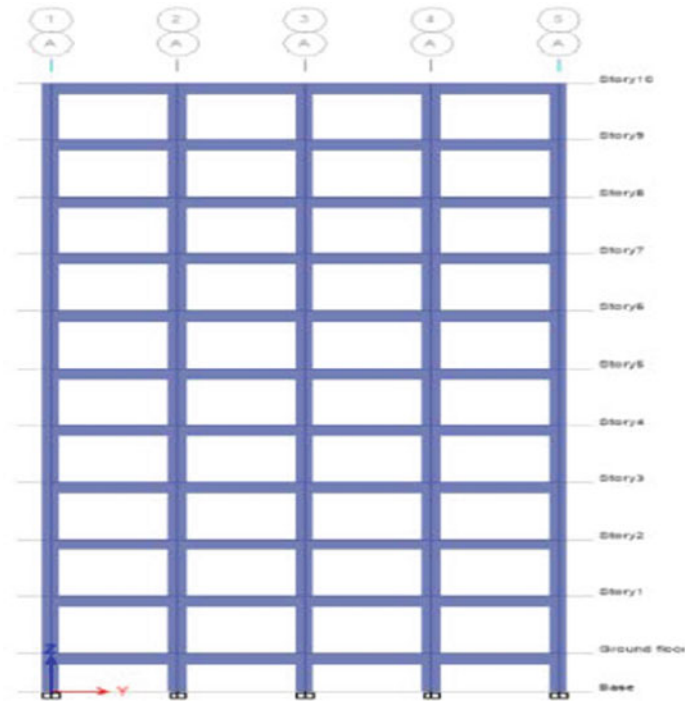
Fig. 2 Elevation of fixed base structure

5.2 *Storey Drift*

It is observed from Fig. 9 that storey drift is decreased for the Model VI as compared to Model I, because in model 6, the isolator is provided at 7th floor. The storey drift of model VI decreased by 59.83% compared to model I.

5.3 *Base Shear*

Results from Fig. 10 depict that the base shear is higher for Model VI as compared to remaining other models. The base shear of model VI increased by 64.90% compared to Model I.

5.4 *Time Period*

Results from Fig. 11 show that the model 6 has the lowest time period compared
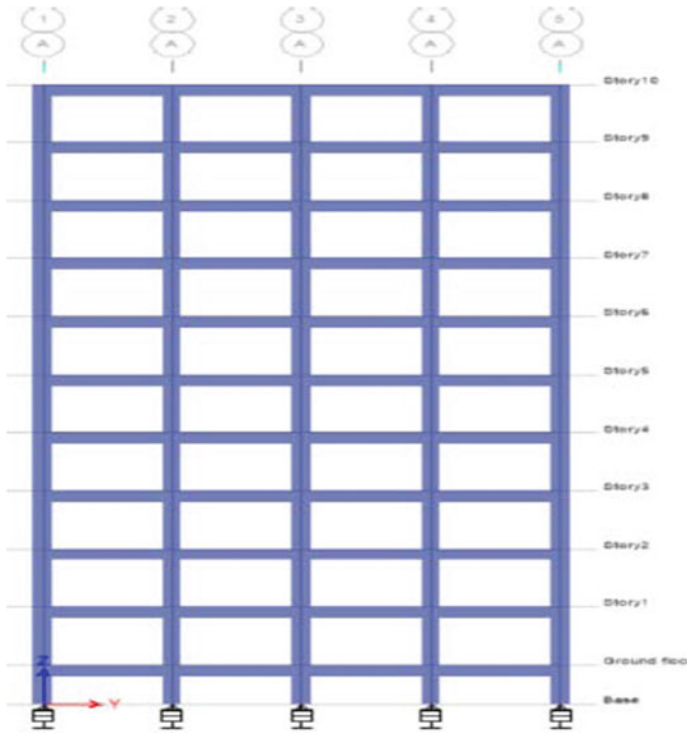
Fig. 3 Elevation of base isolation structure

to others models. The time period of Model VI decreased by 79.04% compared to Model I because of shear wall and storey isolation system in Model VI.

5.5 Maximum Bending Moment

Results from Fig. 12 show that the Model VI has the lowest bending moment compared to other models. The bending moment decreased by 75.06% due to addition of shear wall in the structure.

5.6 Axial Forces

Figure 13 shows that the Model IV has more axial force compare to other models because of addition of shear wall. The axial force of Model VI decreased by 73.07% compared to Model IV.
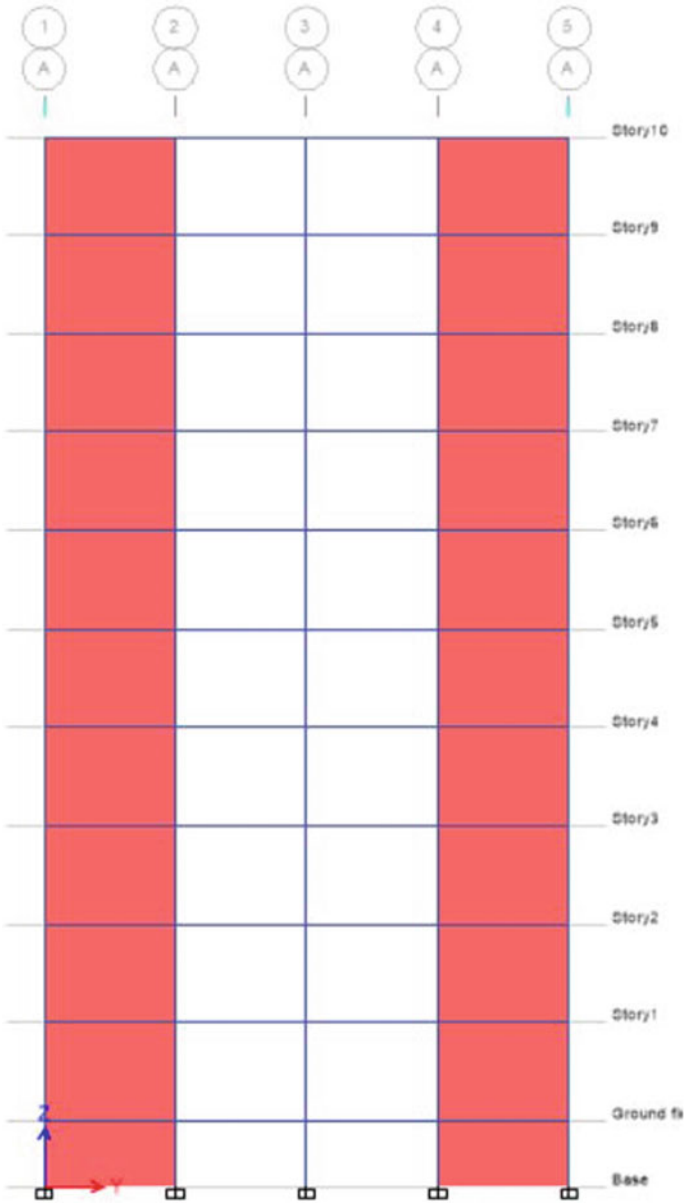
Fig. 4 Elevation of fixed base with shear wall structure
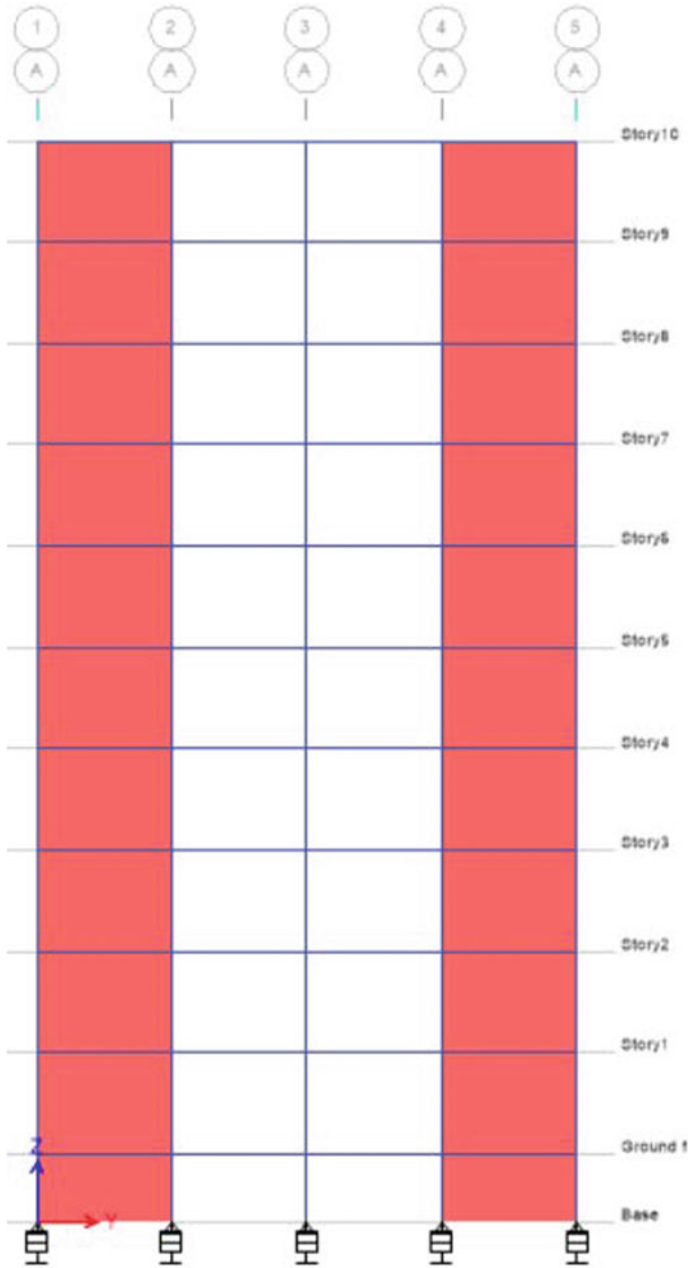
Fig. 5 Elevation of base isolation with shear wall structure
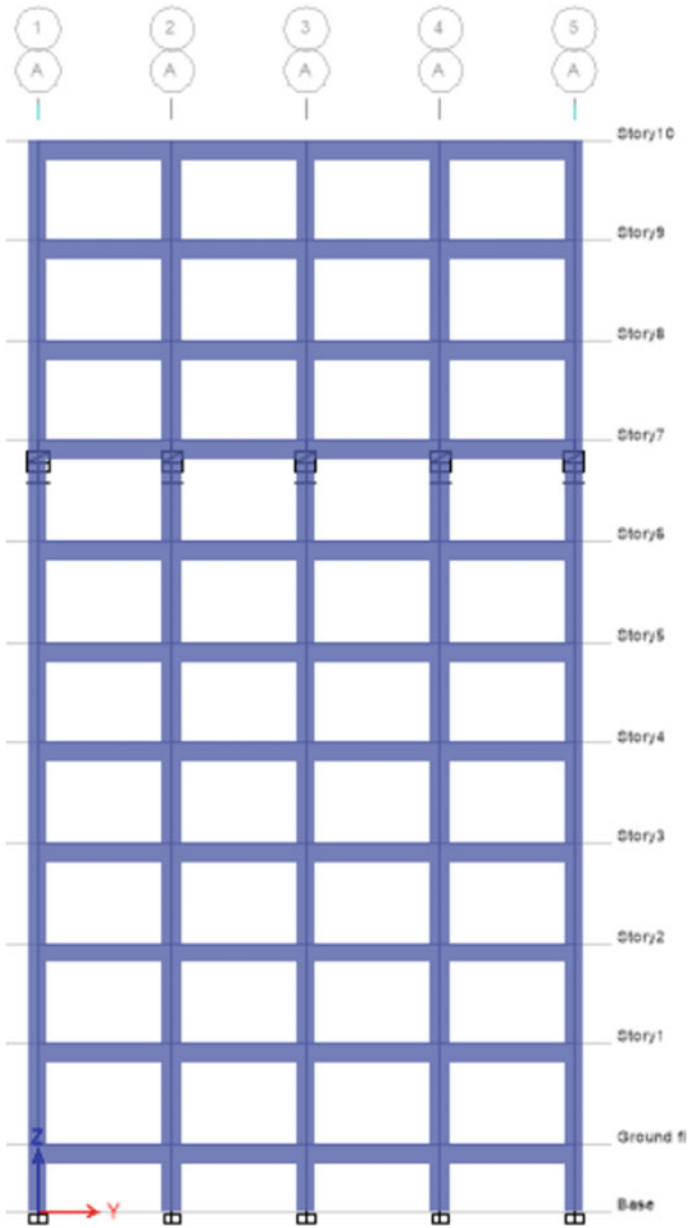
Fig. 6 Elevation of storey isolation with fixed base structure

Fig. 7 Elevation of storey isolation with shear wall structure

Displacement

	10	9	8	7	6	5	4	3	2	1	GF	Base
Model I	76.61	74.13	70.14	64.68	57.96	50.18	41.55	32.22	22.36	12.21	2.85	0
Model II	82.19	79.81	75.99	70.7	64.35	56.91	48.64	39.69	30.18	20.18	9.32	0
Model III	48.52	43.98	39.11	33.94	28.54	23.02	17.55	12.33	7.61	3.68	0.9	0
Model IV	48.65	44.12	39.25	34.09	28.69	23.18	17.72	12.5	7.77	3.84	1.06	0
Model V	29.07	26.26	20.75	14.67	14.63	14.9	13.93	11.78	8.72	5.01	1.22	0
Model VI	8.08	7.08	5.92	4.84	4.61	4.22	3.6	2.8	1.91	1.02	0.28	0
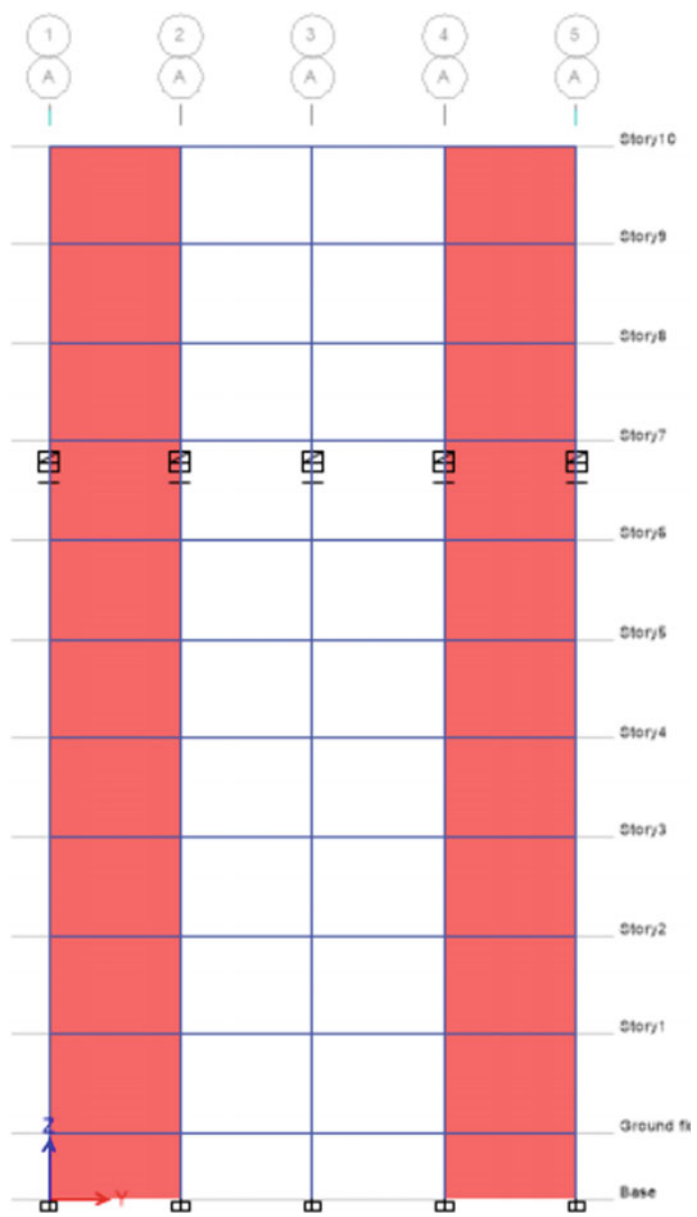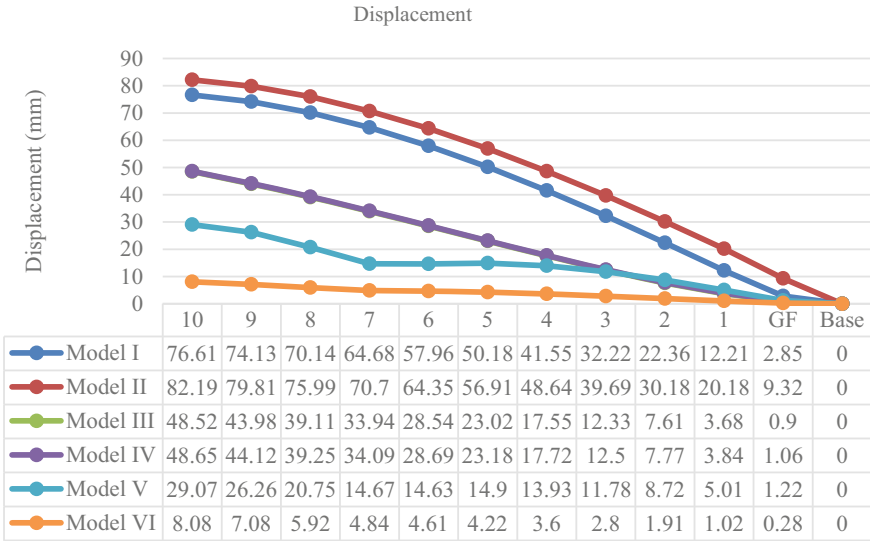
Fig. 8 Storey displacement of diff type of models

Storey drift

	10	9	8	7	6	5	4	3	2	1	GF	Base
Model I	0.82	1.33	1.82	2.24	2.59	2.87	3.11	3.28	3.38	3.12	1.42	0
Model II	0.79	1.27	1.74	2.14	2.47	2.75	2.98	3.16	3.33	3.61	4.66	0
Model III	1.51	1.62	1.72	1.8	1.83	1.82	1.74	1.57	1.3	0.92	0.45	0
Model IV	1.51	1.62	1.72	1.79	1.83	1.82	1.73	1.57	1.31	0.92	0.53	0
Model V	0.94	1.83	2.02	0.01	0.08	0.32	0.71	1.02	1.23	1.26	0.61	0
Model VI	0.33	0.38	0.35	0.07	0.13	0.2	0.26	0.29	0.29	0.24	0.14	0
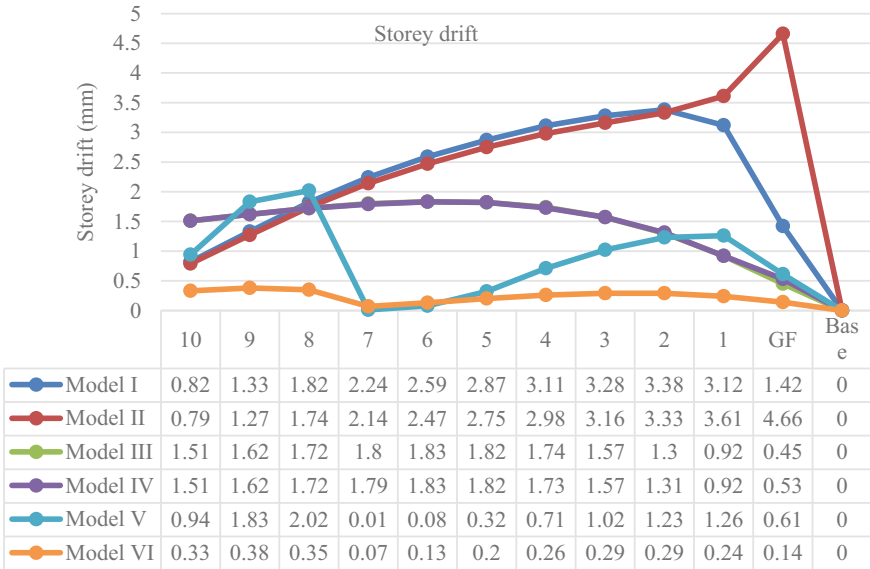
Fig. 9 Storey drift of different type of models
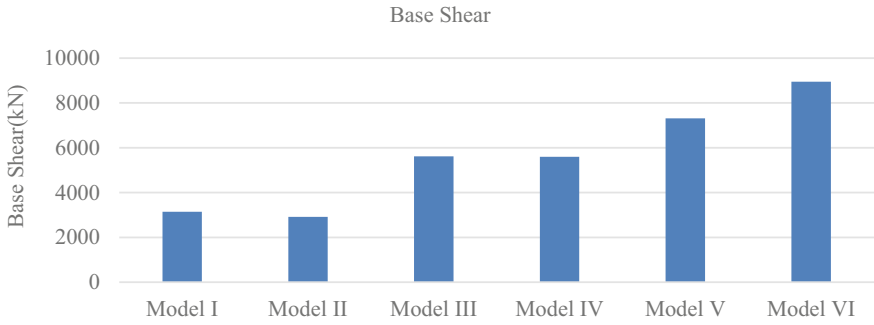
Fig. 10 Max base shear of different type of models
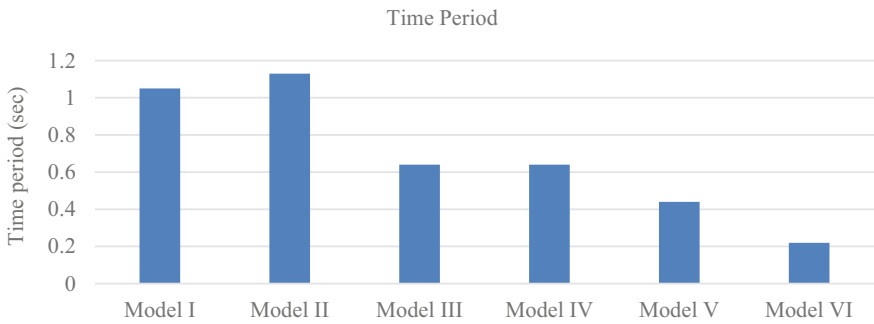
Fig. 11 Time period of different types of models
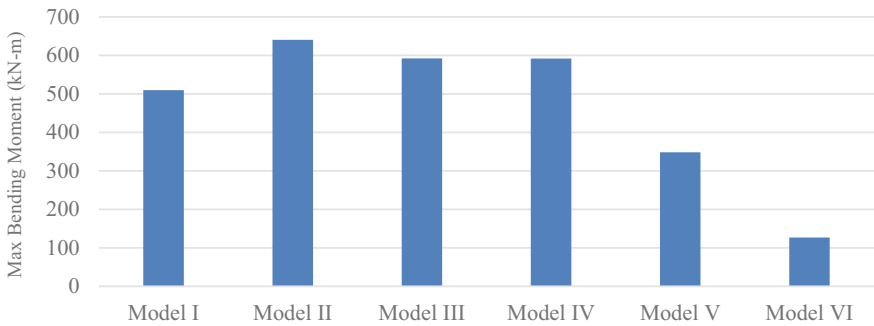
Fig. 12 Max bending moment of different types of models
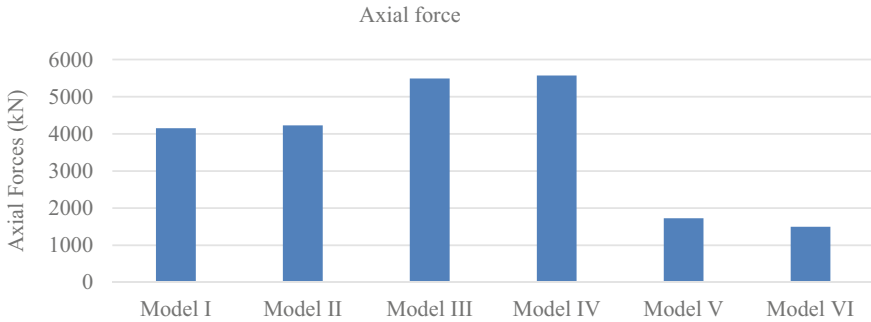
Axial force

Fig. 13 Axial forces of different types of models

6 Conclusions

In general, it is concluded that isolation system provided for structure under seismic force with shear wall and isolator provided at optimum position gives safe behaviour in all aspects.

- It is concluded that storey isolation building with shear wall has less displacement compare to other regular buildings.
- Structure with base isolation system has more storey drift when compared to storey isolation system building with structural components like shear walls.
- Base shear of building increases when structural components like shear walls are provided.
- Combination of shear wall and storey isolation at optimum position leads to minimum bending moment.
- Building with shear wall and isolation at base gives maximum axial force.
- Structure with base isolation without structural element such as shear wall has more time period compared to other models.
- Seismic isolation building is superior to non-isolation building.
- In general, it is concluded that isolation system provided for structure under seismic force with shear wall and isolator provided at optimum position gives safe behaviour in all aspects.

References

1. Jitendra T et al (2018) Study of base isolated building. Int Res J Eng Technol (IRJET) 05(11)
2. Sahoo DN et al (2018) Base isolation of residential building using lead rubber bearing technique. Int J Eng Res Technol (IJERT) 7(05)
3. Balachandran B, Abraham S (2018) Effect of base isolation in multi-storeyed RC building. Int Organ Sci Res (IOSR) 08(6)

4. Santosh K, Mahesh Y (2017) Deflection analysis of multi storey building G+10, in various seismic zones with and without isolation using ETABS. IOSR J Mech Civ Eng (IOSR-JMCE) 14(2)
5. Ambasta S et al (2018) Analyse of the base isolated building (lead rubber bearing) in ETABS. Int Res J Eng Technol (IRJET) 05(01)
6. Thorat VR, Talikoti RS (2014) Base isolation in seismic structural design. Int J Eng Res Technol (IJERT) 3(7)
7. IS 1893:2002 For Earthquake resistant design of structures, Bureau of Indian Standard, New Criterion
8. Uniform Building Code 1997 Volume 2 ATC 40 Seismic evaluation and retrofit of concrete buildings

Enhancement of Lateral Stability of High-Rise Structures Adopting Effective Lateral Load Resisting Systems

L. Meghashree and Y. K. Guruprasad

1 Introduction

Lateral load effects are dominant in high-rise structures when they are subjected to either seismic or wind loads. The lateral stability of the structure decreases with increase in the height of the structure. There is a necessity in the design to ensure that the high-rise structures are laterally stable. Some of the lateral load resisting systems to enhance the lateral stability of such high-rise structures are shear wall system, steel bracing systems, diagrids. Hence, high-rise structures should be structurally stable to resist lateral loads that originate due to earthquakes or wind so as to avoid catastrophic failure. Ahamad and Pratap [1] analysed a G + 20 multistoreyed building for storey displacements, storey drifts, base shear and torsional irregularity for all the seismic zones of India. Their results concluded that the shear walls placed symmetrically enhances the lateral stability of the structures when compared to structures without shear walls. Karthik Reddy [2] worked on G + 15 storied building subjected to seismic and wind loads. A comparative study between the concrete and steel bracings was carried out, and their results showed that *X* bracings are more efficient to reduce the inter-storey drifts. Guleria [3] worked on structural response for different plan configurations. The obtained results such as maximum bending moment, shear force and maximum storey displacement showed that the structure with asymmetrical plan configuration undergoes maximum storey displacement compared to the structure having asymmetrical plan. Tirkey and Ramesh Kumar [4] worked on the

L. Meghashree
MTech Student, Structural Engineering, Department of Civil Engineering, Ramaiah Institute of Technology, Bangalore, Karnataka 560054, India

Y. K. Guruprasad (✉)
Associate Professor, Department of Civil Engineering, Ramaiah Institute of Technology, Bangalore, Karnataka 560054, India
e-mail: guruprasadyk.civil.iisc@gmail.com

comparative analysis of conventional high-rise structure and diagrid structure for the load combinations of earthquake using ETABS. The obtained results showed that the diagrids reduce the structural elements, and it is efficient in decreasing the maximum storey displacements, storey drift and base shear compared to conventional structure and acts as efficient lateral load resisting system. It is understood from the literature that the stability of high-rise structures are to be well accounted for in the design to effectively resist lateral loads. This work aims at enhancing the lateral stability of two 60-storey high-rise structures having symmetry and asymmetry in plan along with storey stiffness irregularity, by adopting a selected set of additional lateral load resisting systems, individually applied on both of the 60-storey high-rise structures subjected to strong earthquake and wind loads as a case study. The lateral load resisting systems adopted and applied individually on the two 60-storey high-rise structures are shear walls, X bracing, V bracing and diagrids. Comparison of the structural responses of both the 60-storey high-rise structures having symmetry and asymmetry in plan, with different lateral load resisting systems applied individually on them, has been recorded to identify the most effective lateral load resisting system.

2 Lateral Stability Analysis of High-Rise Structures Having Plan and Stiffness Irregularity Strengthened with Different Lateral Load Resisting Systems Subjected to Earthquake and Wind Loads

Two high-rise structures, one with asymmetry in plan and another with symmetry in plan, are modelled in ETABS. In both cases of high-rise structures that have symmetricity and asymmetricity in plan, there exists storey stiffness irregularity at the 15th floor, where a couple of bays have columns connecting to two-storey heights without an intermediate floor slab. Both the structures (asymmetric and symmetric in plan) are analysed for earthquake and wind load combinations, without adopting any lateral load resisting systems (shown in Figs. 1 and 5). Both the structures (asymmetric and symmetric in plan) are also analysed for earthquake, and wind load combinations are provided with lateral load resisting systems such as: shear walls (shown in Figs. 2 and 6), X bracings (shown in Figs. 4 and 8), V bracings (shown in

Fig. 1 Plan of an asymmetrical structure without any lateral load resisting systems
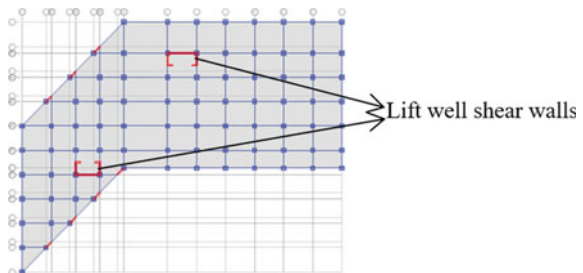
Figs. 3 and 7) and diagrids (shown in Figs. 9 and 10), applied individually on each structure, respectively. Response spectrum method has been adopted to analyse the structural models as per IS 1893:2016 (Part 1) [5] for earthquakes for the following data—damping ratio: 0.05, seismic zone: *V*, seismic zone factor, *Z*: 0.36, importance factor: 1.5, soil type: II, and response reduction factor: 5. The wind load analysis has been carried out to analyse the structural models as per IS 875:2015 (Part 3) [6] for the following data—wind speed: 50 m/s, terrain category: 2, importance factor: 1.3, risk coefficient factor (*k*1): 1.08, topography (*k*3): 1, windward coefficient, (C_p): 0.7 and leeward coefficient, (C_p): 0.7. The typical details of the symmetrical and asymmetrical 60-storey high-rise structures are—height of the structure: 181 m, structure designed for commercial occupancy, floor to floor height: 3 m, size of floor beams (both directions): (250 × 500) mm, size of composite columns: (900 × 900) mm with steel I section ISMB 500 encased within, thickness of the slab: 200 mm, grade of concrete adopted for RC beams and columns: M60, grade of concrete adopted for RC slabs and shear walls in lift wells: M40, live load: 5 kN/m^2, floor finish: 1 kN/m^2 and wall load: 15 kN/m.

Fig. 2 Isometric view of an asymmetrical structure retrofitted with additional shear walls

Additional shear walls
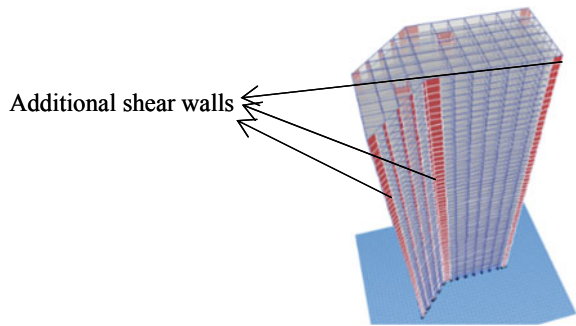
Fig. 3 Isometric view of an asymmetrical structure retrofitted with *V* bracings
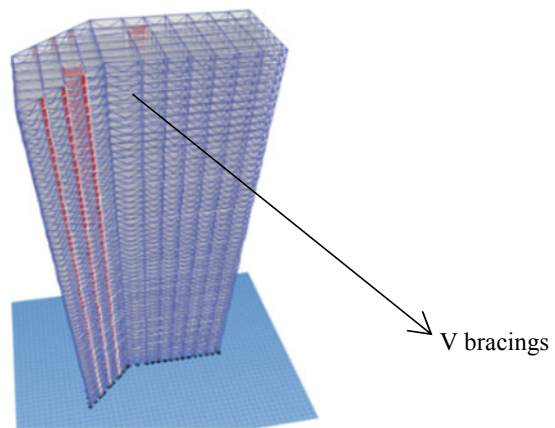
V bracings

Fig. 4 Isometric view of an asymmetrical structure retrofitted with *X* bracings
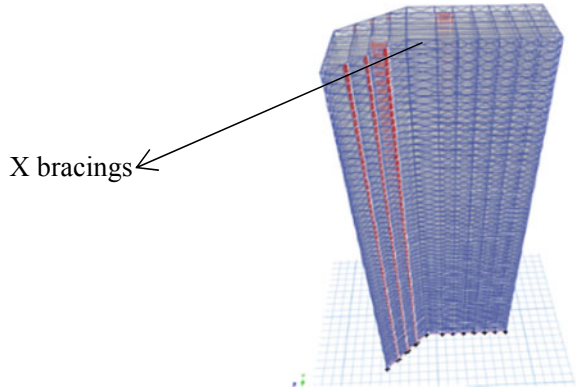
X bracings

Fig. 5 Plan of a symmetric structure without any lateral load resisting systems
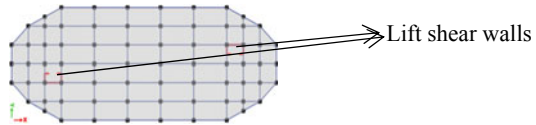
Lift shear walls

Fig. 6 Isometric view of symmetric structure retrofitted with shear walls

Additional shear walls
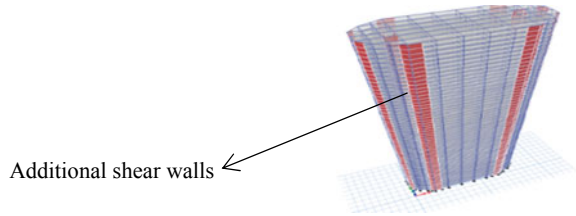
Fig. 7 Isometric view of symmetric structure retrofitted with *V* bracings

V bracings
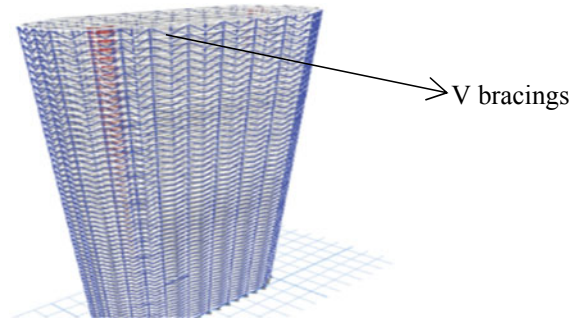
2.1 Shear Walls Adopted as Lateral Load Resisting System

The grade of concrete used in shear wall [7] is M40, and the shear wall has a thickness of 250 mm without boundary elements.

Fig. 8 Isometric view of symmetric structure retrofitted with *X* bracings
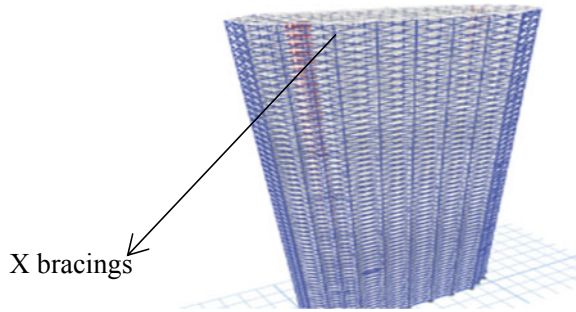
X bracings

Fig. 9 Isometric view of asymmetric structure retrofitted with diagrids

Diagrids
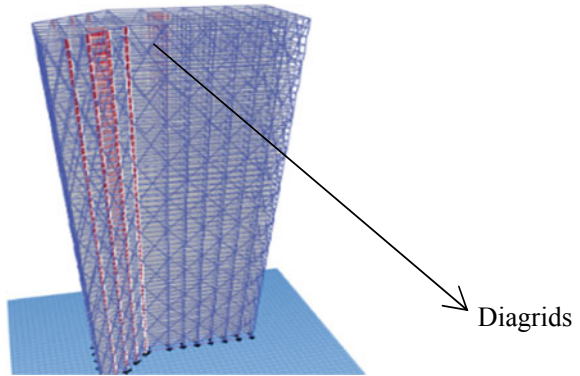
Fig. 10 Isometric view of symmetric structure retrofitted with diagrids
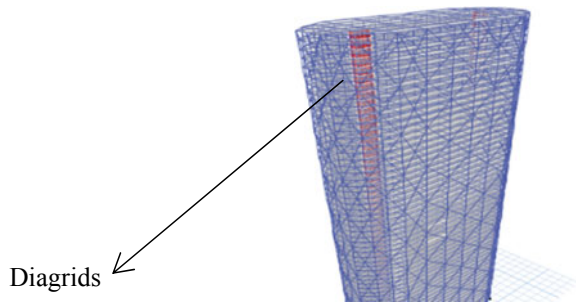
Diagrids

2.2 Steel Bracings Adopted as Lateral Load Resisting System

Channel section—ISMC300 [8] corresponding to Fe 345 grade of steel has been adopted for both '*X*' and '*V*' bracings (as shown in Figs. 3, 4, 7 and 8).

2.3 *Diagrid Adopted as Lateral Load Resisting System*

Steel pipe section having an outer diameter equal to 450 mm and thickness of 25 mm corresponding to Fe 345 grade of steel is used as diagrids [9–11] in the analysis (as shown in Figs. 9 and 10).

3 Results and Discussion

A comparative analysis is carried out between the two structures (that have symmetry and asymmetry in plan) without any additional lateral load resisting system and with additional lateral load resisting systems, namely additional shear walls, *X* bracings, *V* bracings and diagrids [9–11] applied individually on each structure to obtain maximum storey displacements and maximum storey drifts. The results are obtained for the critical load combination (Envelope). The load combinations adopted in the analysis are as follows:

1. $1.5(DL + LL)$
2. $1.2(DL + LL \pm (Eqx \pm 0.3EQy))$ and $1.2(DL + LL \pm (Eqy \pm 0.3Eqx))$
3. $1.5(DL \pm (Eqx \pm 0.3EQy))$ and $1.5(DL \pm (Eqy \pm 0.3Eqx))$
4. $0.9DL \pm 1.5(Eqx \pm 0.3EQy)$ and $0.9DL \pm 1.5(Eqy \pm 0.3Eqx)$
5. $1.5(DL \pm WLx)$
6. $1.5(DL \pm WLy)$
7. $0.9DL \pm 1.5WLx$
8. $0.9DL \pm 1.5WLy$

where DL-dead load, LL-live load, Eq-earthquake load in *x* and *y* in plan, WL-wind load in *x* and *y* in plan

Figures 11 and 12 show the maximum storey displacements of the asymmetric structure for the critical load combination (Envelope) for earthquake in global x and y directions, respectively. Figures 13 and 14 show the maximum storey displacements of the asymmetric structure for wind load in global *x* and *y* directions, respectively.

Figure 15a and b show the maximum storey drifts of asymmetric structure for the
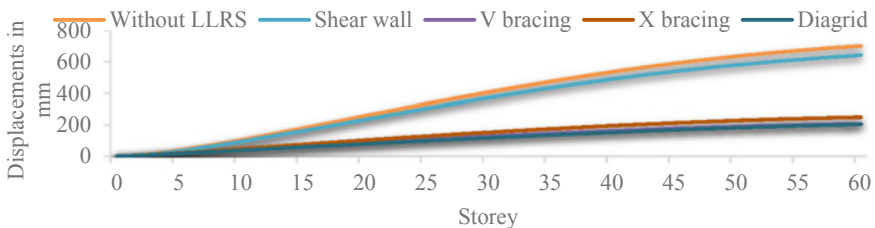
Fig. 11 Storey displacement of the asymmetric structure for EQ in *x* direction (Without LLRS-without lateral load resisting system)
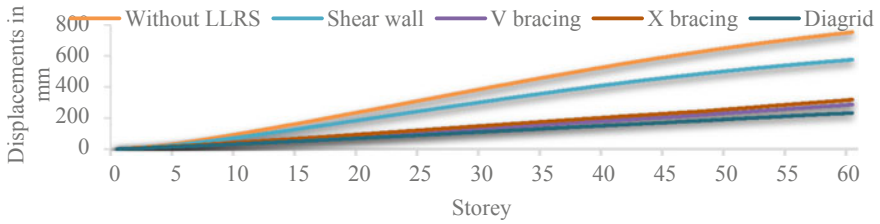
Fig. 12 Storey displacement of the asymmetric structure for EQ in *y* direction (Without LLRS-without lateral load resisting system)
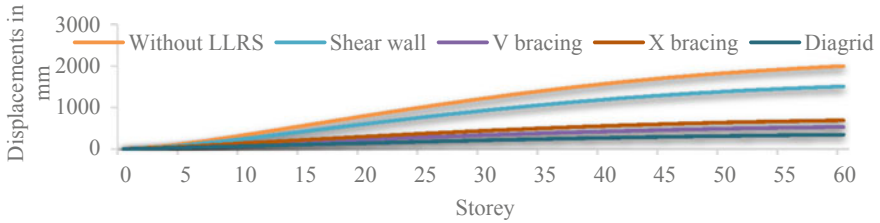
Fig. 13 Storey displacement of the asymmetric structure for WL in *x* direction (Without LLRS-without lateral load resisting system)
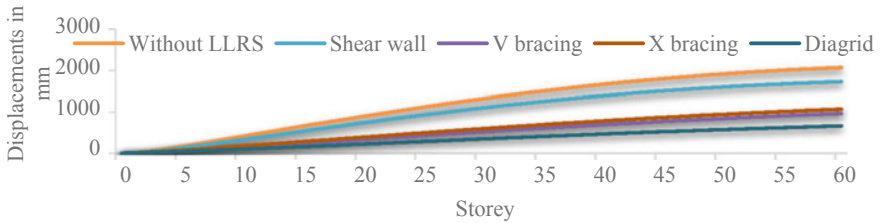
Fig. 14 Storey displacement of the asymmetric structure for WL in *y* direction (Without LLRS-without lateral load resisting system)
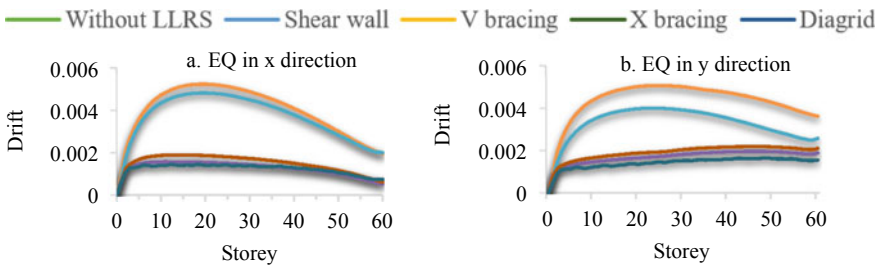
Fig. 15 Storey drift of the asymmetric structure for: **a** EQ in *x* direction and **b** EQ in *y* direction (Without LLRS-without lateral load resisting system)

critical load combinations of earthquake in global *x* and *y* directions, respectively. Figure 16a and b show the maximum storey drifts of asymmetric structure for wind load in global *x* and *y* directions, respectively.

Figures 17 and 18 show the maximum storey displacements of symmetric structure for the critical load combinations of earthquake in global *x* and *y* directions, respectively. Figures 19 and 20 show the maximum storey displacements of symmetric structure for wind load in global *x* and *y* directions, respectively.

From Fig. 18, it is observed that the storey displacements of the symmetric structure subjected to wind loads are comparatively less in global *y* direction when
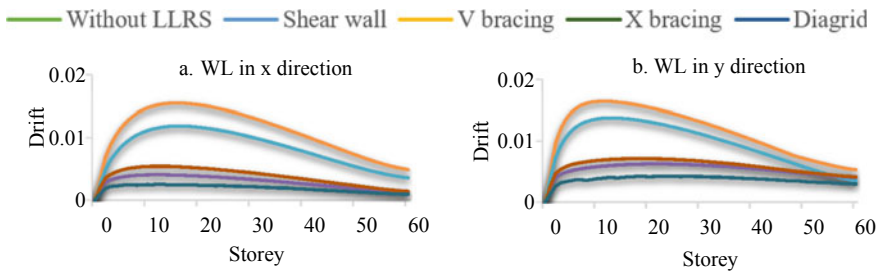
Fig. 16 Storey drift of the asymmetric structure for: **a** WL in *x* direction and **b** WL in *y* direction (Without LLRS-without lateral load resisting system)
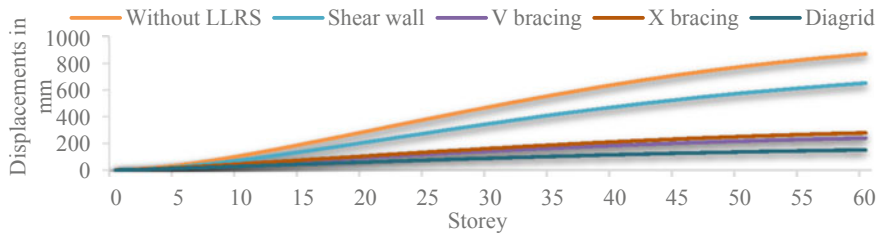
Fig. 17 Storey displacement of the symmetric structure for EQ in *x* direction (Without LLRS-without lateral load resisting system)
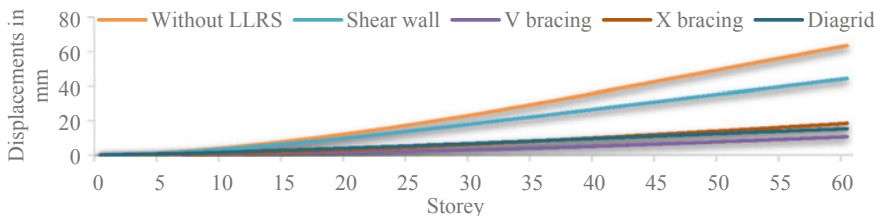
Fig. 18 Storey displacement of the symmetric structure for EQ in *y* direction (Without LLRS-without lateral load resisting system)
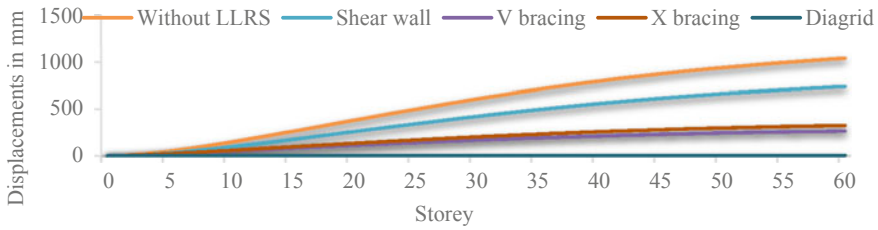
Fig. 19 Storey displacement of the symmetric structure for WL in *x* direction (Without LLRS-without lateral load resisting system)
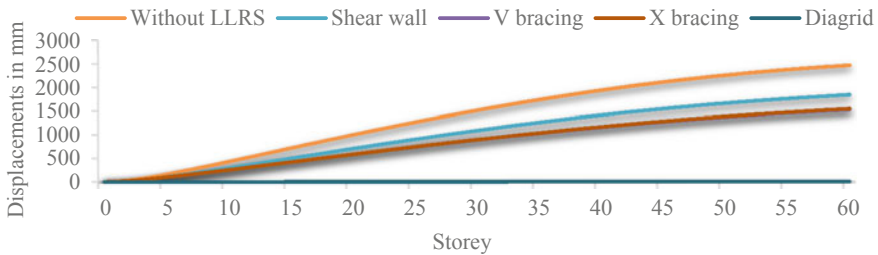
Fig. 20 Storey displacement of the symmetric structure for WL in *y* direction (Without LLRS-without lateral load resisting system)

compared to the storey displacements in global *x* direction for all additional lateral load systems applied individually in the structures.

Figures 21a and b show the maximum storey drifts of the symmetric structure for the critical load combination for earthquake in global *x* and *y* directions. Figures 22a and b show the maximum storey drifts of the symmetric structure for wind load in global *x* and *y* directions, respectively.

To identify the most effective lateral load resisting system, the percentage decrease in storey displacements of the asymmetric and symmetric structures is calculated and is shown in Fig. 23a and b, respectively. The percentage decrease in storey drifts of
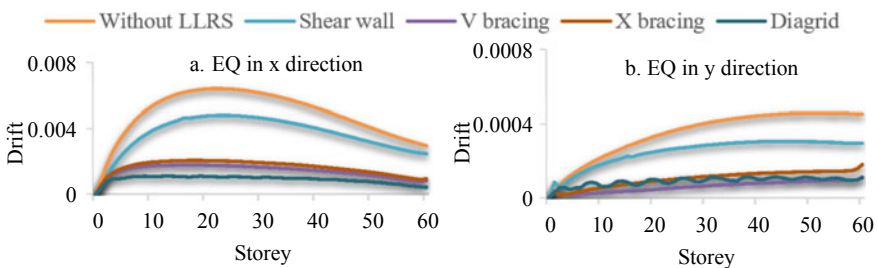
Fig. 21 Storey drift of the symmetric structure for: **a** EQ in *x* direction and **b** *y* direction (Without LLRS-without lateral load resisting system)
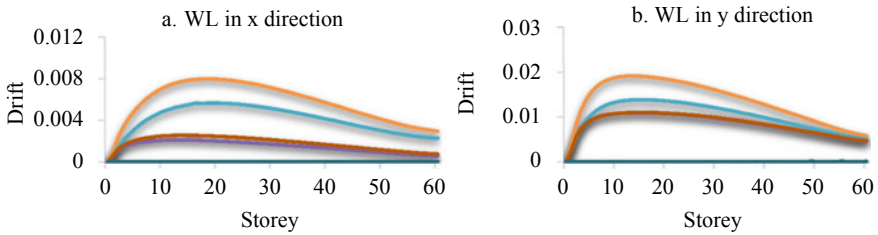
Fig. 22 Storey drift of the symmetric structure for: **a** WL in *x* direction and **b** WL *y* direction (Without LLRS-without lateral load resisting system)
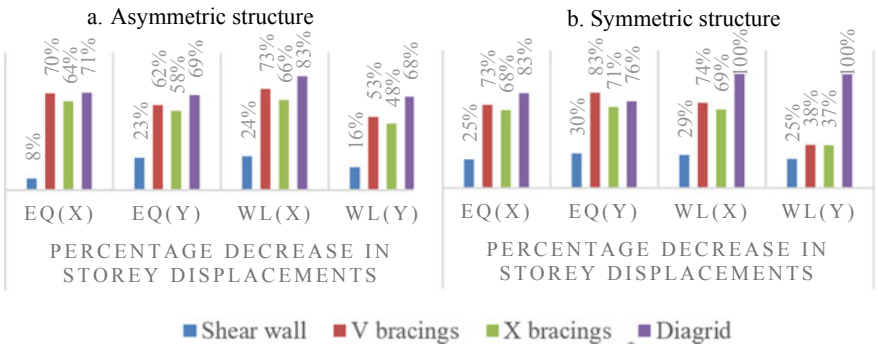
Fig. 23 Percentage decrease in displacements of: **a** Asymmetric and **b** symmetric structure

the asymmetric and symmetric structures is shown in Fig. 24a and b, respectively.

It is observed from the results that the top storey displacement of the asymmetric and symmetric structures for earthquake in *x* and *y* directions is 701.84 mm, 751.58 mm and 871.3 mm, 63.567 mm, respectively. The top storey displacements of
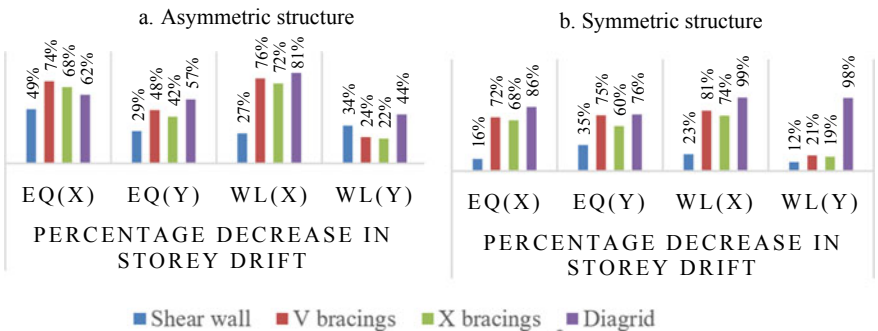
Fig. 24 Percentage decrease in storey drift of: **a** Asymmetric and **b** symmetric structures
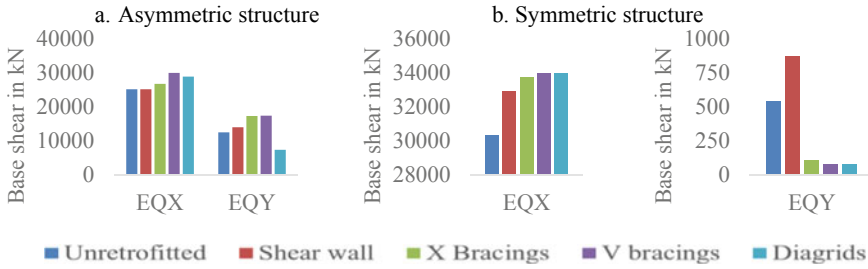
Fig. 25 Base shear (in kN) of: **a** Asymmetric structure **b** symmetric structure

the asymmetric and symmetric structures in case of wind loads in *x* and *y* directions are 2002.7 mm, 2076.4 mm and 1042.3 mm, 2474.5 mm, respectively.

After application of the shear walls as an additional lateral load resisting system in the asymmetric and symmetric structures, there has been a reduction in the top storey displacement by 8.45% and 25.12% for earthquake loads and 24.5% and 28.9% for wind loads, respectively.

When *V* bracings are applied as an additional lateral load resisting system in the asymmetric and symmetric structures, there has been a reduction in the top storey displacement by 70.4% and 72.6% for earthquake loads and 73.5% and 74.5% for wind loads, respectively. When *X* bracings have been applied as an additional lateral load resisting system in the asymmetric and symmetric structures, there has been a reduction in the top storey displacement by 64.5% and 68.1% for earthquake loads and 65.5% and 68.6% for wind loads in, respectively. In the case of diagrids that are applied as an additional lateral load resisting system in the asymmetric and symmetric structures, there has been a reduction in the top storey displacement by 70.9% and 82.7% for earthquake loads and 82.7% and 99.5% for wind loads, respectively. Figure 25 shows the base shear of the asymmetric and symmetric structures with different lateral load resisting systems installed individually in the structure. It is observed that the structure with *X* bracings, *V* bracings and diagrids was found to make the structure comparatively stiffer, making the structure to attract a higher value of base shear.

4 Conclusion

1. The results showed that the symmetrical and asymmetrical structures that were not provided with any lateral load resisting systems were found to have a comparatively larger storey displacements and storey drifts for the critical load combinations (envelope) for earthquake and wind loads individually, when compared to the symmetrical and asymmetrical structures that were provided with different lateral load resisting systems, namely shear wall, steel bracings (*X* and *V*) and diagrids.

2. From Fig. 23, it is inferred that for the asymmetrical structure, the lateral storey displacement at the 60th storey (top storey) was reduced by: 15.75% (on an average for EQ in x and y directions) and 30.22% (on an average for WL in x and y directions) when the structure is applied with shear walls. When the structure is applied with V bracings, the lateral storey displacement at the 60th storey is reduced by 66.11% (on an average for EQ in x and y directions) and 63.38% (on an average for WL in x and y directions). When the structure is applied with X bracings, the lateral storey displacement at the 60th storey is reduced by 61.09% (on an average for EQ in x and y directions) and 56.93% (on an average for WL in x and y directions). When the structure is applied diagrids, the lateral storey displacement at the 60th storey reduced by and 69.97% (on an average for EQ in x and y directions) and 75.36% (on an average for WL in x and y directions).

3. From Fig. 25, the structure with X bracings, V bracings and diagrids was found to make the structure comparatively stiffer, making the structure to attract a higher value of base shear.

4. It is observed from the results of the present work, the diagrids have been found to be an effective lateral load resisting system, to resist both earthquake and wind loads when compared to the other lateral load resisting systems when applied to high-rise structures that have asymmetry in plan and storey stiffness irregularity.

References

1. Ahamad SA, Pratap KV (2020) Dynamic analysis of G + 20 multi storied building by using shear walls in various locations for different seismic zones by using Etabs. Mater Today: Proc 43, Part 2, 1043–1048
2. Karthik Reddy KSK (2015) A comparative study on behaviour of multi-storeyed building with different types and arrangements of bracing systems. Int J Sci Technol Eng 2(2):135–149
3. Guleria A (2014) Structural analysis of a multi-storied building using ETABS for different plan configurations. Int J Eng Res Technol 3(5):1481–1485
4. Tirkey N, Ramesh Kumar GB (2020) Analysis on the diagrid structure with the conventional building frame using ETABS. In: International conference on materials engineering and characterization 2019, vol 22 (Part: 3), pp 514–518
5. IS 1893: 2016 (Part 1), Criteria for earthquake resistant design of structures, Bureau of Indian Standards, India
6. IS 875: 2015 (Part 3), Wind loads on buildings and structures, Bureau of Indian Standards, India
7. IS 456: 2000, Plain and reinforced concrete—code of practice, Bureau of Indian Standards, India
8. IS 800:2007, General construction in steel—code of practice, Bureau of Indian Standards, India
9. Shah MI, Mevada SV, Patel VB (2016) Comparative study of diagrid structures with conventional frame structures. Int J Eng Res Appl 6(5), (Part-2), 22–29

10. Kalaria DR, Agrawal VV, Patel VB (2019) Parametric study of diagrid structures subjected to seismic forces. J Emerg Technol Innov Res (JETIR) 6(4):146–153
11. Panchal NB, Patel VR (2014) Diagrid structural system: strategies to reduce lateral forces on high-rise buildings. Int J Res Eng Technol 3(4):374–378

Retrofitting of RC Footings Subjected to Settlement Due to Earthquake

Nadeem Bilagi and Y. K. Guruprasad

1 Introduction

To prevent a building from damage caused due to disaster during earthquakes, the existing structurally deficit members of a building must be upgraded to carry new loads and to improve its performance under existing loads. Seismic retrofitting is one of the most studied and researched area, seismic retrofitting is retrofitting for the structures which are vulnerable to failure and damage due to seismic load, over past three decades, numerous moderate to severe earthquakes have occurred around the world. Retrofitting and repair of a structure is carried out after condition assessment of the building, this will determine if a building needs to be retrofitted or to be demolished and built back again. If a structure has undergone damage due to an earthquake or has to be built to resist earthquake forces in future, the structure has to retrofit. There are different methods of retrofitting a structure depending upon the type of damage or degree of damage. Some of the retrofitting methods are RC jacketing, mild steel jacketing, wrapping with fibre reinforced polymers. Outcome of the retrofitting process are, increase in lateral strength and stiffness of structure, increase in ductility of member, thereby avoiding brittle failure of members, earthquake resistant structure.

Ranjan and Dhiman [1] conducted a case study on an existing building situated in Patna, Bihar. They used STAAD PRO software to design and analyse the building was initially designed to be built up to 4 storey in approximately 2000 ft^2. There are

N. Bilagi
Mtech Student, Structural Engineering, Department of Civil Engineering, Ramaiah Institute of Technology, Bangalore 560054, India

Y. K. Guruprasad (✉)
Associate Professor, Department of Civil Engineering, Ramaiah Institute of Technology, Bangalore 560054, India
e-mail: guruprasadyk.civil.iisc@gmail.com

22 live pile foundations that are 9 m deep in the soil and 9 dead pile foundations which are 7 m deep in the soil. The building has 31 tie beams of dimension 300 mm × 300 mm. Later it was needed to raise the building to 6 floors (adding two more floors), designing was done as per code and analysed using STAAD PRO V8i software.

They retrofitted the building using three different methods in software and did cost analysis, the different methods of retrofitting used were RC jacketing, fibre reinforced concrete and steel fibre reinforced concrete. The outcome of their work was that in RC jacketing, the damaged members were jacketed using new concrete, in RC jacketing method the moment carrying capacity, shear strength capacity and axial load carrying capacity of members increased. FRP jacketing enhanced the performance of concrete and was a bit costlier compared to both RC jacketing and SFRC jacketing.

Kaliyaperumal and Sengupta [2] conducted an experiment on three specimen, in which first was for slant shear test to study the bond between old concrete and new concrete, the second specimen was used to study the strength of column and the third specimen was a beam-column-joint-assembly to study the ductility and energy dissipation. Analytical investigations were used to predict the experimental results. Incremental nonlinear method was adopted to predict the lateral loads versus displacement behaviour for a retrofitted structure. Outcome of the author's work was that the moment carrying capacity of the retrofitted column specimens were comparatively more than the existing columns. The retrofitted beam-column-joint-assembly specimens showed substantial increase in the lateral strength, ductility and energy dissipation.

Cotor et al. [3] carried out an experimental study that was conducted on possibilities of adding a new floor in an existing building, and the primary focus was to study the soil structure interaction below individual footing. The analysis was performed according to Romanian code P100-3/2008 and Eurocode 7, using finite element software. The outcome of the study was after adding a strip beam in existing isolated footing resulted in reduction of rotation of the footing. It the increased rigidity and moment carrying capacity of the footing was also increased.

It is observed from the literature that retrofitting of RC members adopting various methods such as RC jacketing, FRP and SFRP have been carried out. It is also observed from the existing studies, for retrofitting isolated RC footings, the parameters considered were loads acting on the footings. Therefore, there is a necessity to carry out studies towards determination of settlement of footings after application of retrofitting of footings.

The objective of the present study is to enhance the load carrying capacity and reduce the settlement of existing RC isolated footings, that are deficient in load carrying capacity due to erroneous structural design, by adopting section enlargement method (RC jacketing) as one case and introducing new steel columns founded on slab bases as a second case, to improve the stability of the structure.

2 Retrofitting of RC Footings Having Deficiency in Load Carrying Capacity Due to Erroneous Structural Design Subjected to Seismic Loads

In the present work, a five storey RC building for office use is considered as a case study and is modelled and analysed in SAP2000, along with the footings founded on the soil in three-dimension. The isolated footings initially provided in the building are deficient in load carrying capacity due to erroneous design, with respect to comparatively lower size of the footings thus provided. The five storey RC office building with its foundation resting on soil media is subjected to seismic loads adopting response spectrum method. Changes in the settlement in deficiently designed footings are recorded. RC jacketing method has been adopted to retrofit the distressed footings as well as new structural steel columns (I section) founded on slab base foundation have been separately introduced in between existing RC columns and footings to reduce the possible settlements. The study is purely based on horizontal ground motion; effect of vertical ground acceleration is not considered. Retrofitting of the footings in this study is a practical attempt to increase the footing area and depth by section enlargement method (RC jacketing), to reduce the settlement of existing footings that are under designed to restore the overall stability of the structure.

2.1 Details of Reinforced Concrete Office Building

Number of storeys	5
Floor height	3.5 m
Size of RC columns	0.3 m × 0.3 m
Size of RC beams	0.3 m × 0.45 m
Size of RC footings (deficiently designed)	1.5 m × 1.5 m × 0.6 m

Concrete having a characteristic compressive strength of 30 N/mm^2 has been adopted for beams, columns and slabs. Yield strength of steel that has been adopted for steel reinforcement in all RC structural members is 415 N/mm^2.

Three soil layers are considered in the study, and the soil layers are modelled as solid elements. The properties of soil layers I, II and III are shown in Tables 1, 2 and 3, respectively.

Table 1 Properties of soil layer

Details	Properties of soil layer		
	Layer I Medium sand	Layer II Medium clay	Layer III Hard rock
Unit weight	18 kN/m^3	16 kN/m^3	30 kN/m^3
Modulus of elasticity	25,000 kN/m^2	35,000 kN/m^2	45,000 kN/m^2
Poisons ratio	0.3	0.25	0.3
Thickness of soil layer	3 m	4 m	3 m

Table 2 Comparison of settlement of RC footing for different load combinations and retrofit cases

S. No.	Gravity load DL + LL UR	Load combination for seismic load: envelop				The maximum permissible settlement for multi-storeyed RC building as per IS 1904:1986 is 60 mm
		UR	R1	R2	R3	
Vertical settlement (mm)	52.83	117.23	65.3	42	24.23	

DL dead loads; *LL* live loads; *UR* unreinforced case of footing size 1.5 m × 1.5 m × 0.6 m
R1: Reinforced case 1 of footing size 2 m × 2 m × 0.9 m; R2: Reinforced case 2 of footing size 2.5 m × 2.5 m × 1 m; R3: Reinforced case 3 of footing size 2.5 m × 2.5 m × 1 m with inclusion of steel columns

2.2 Load Combinations

The loads applied on the building are dead load, floor finish of 1 kN/m^2 and live load of 5 kN/m^2 as per IS 875 part 1 1987 [4] and IS 875 Part 2 1987 [5], respectively.

Response spectrum method is adopted for applying earthquake loads as per IS 1893 Part 1 2016 [6]. The parameters considered for the seismic analysis are as per response spectrum method is shown below

Damping ratio: 0.05
Seismic zone: IV
Seismic zone factor: 0.24
Importance factor: 1.0
Soil type: II.
Response reduction factor: 3.

Load combinations as per IS 1893 (part 1) 2016 is given below

1.2(DL + LL ± (EQx ± 0.3Ely))
1.2(DL + LL ± (EQy ± 0.3ELx))
1.5(DL + LL ± (EQx ± 0.3Ely))
1.5(DL + LL ± (EQy ± 0.3ELx))
0.9*DL ± 1.5(EQx ± 0.3Ely))

Table 3 Time period of vibration for different cases of retrofit

Mode number		1	2	3	4	5	6	7	8	9	10	11	12
Time period (s)	Un-retrofitted	1.344	1.337	0.536	0.514	0.471	0.433	0.430	0.428	0.252	0.186	0.170	0.097
	Retrofit 1	1.356	1.336	0.536	0.514	0.472	0.433	0.430	0.427	0.252	0.186	0.170	0.098
	Retrofit 2	1.326	1.301	0.536	0.514	0.471	0.433	0.430	0.427	0.252	0.186	0.170	0.099
	Retrofit 3	1.218	0.897	0.881	0.570	0.570	0.569	0.569	0.543	0.543	0.542	0.542	0.536

0.9*DL $\pm$ 1.5(EQy + 0.3ELx))

The envelope of all the 24 load combinations was considered in the analysis to study the results.

Three-dimensional view of the structure along with the deficiently designed isolated footings that is having size 1.5 m $\times$ 1.5 m $\times$ 0.6 m and founded on soil layer I is shown in Fig. 1. Figure 2a, b shows the 2D model of the same structure in X–Z plane and in Y–Z plane, respectively.

The retrofitting of the deficiently designed RC footing has been carried out adopting section enlargement method/RC jacketing. The existing RC footing size was increased in size and thickness by section enlargement method to 2 m $\times$ 2 m $\times$ 0.9 m as the first RC footing retrofit case study and the existing RC footing size was increased to 2.5 m $\times$ 2.5 m $\times$ 1 m as the second retrofit case study to observe the reduction in settlement of the footings in two separate analyses that were carried out. The section enlargement method/RC jacketing [7–9] of the existing RC footing is carried out by, providing new steel rebars (Fe415) having 12 mm diameter provided in both directions that are welded to the existing reinforcement of the footing, and thereafter, the concrete is placed to the required new size of the footings as mentioned above. Figure 3a shows the 3D model of the structure whose isolated footings are

Fig. 1 Three-dimensional view of the structure showing deficiently designed isolated footings (1.5 m $\times$ 1.5 m $\times$ 0.6 m) founded on soil layer I
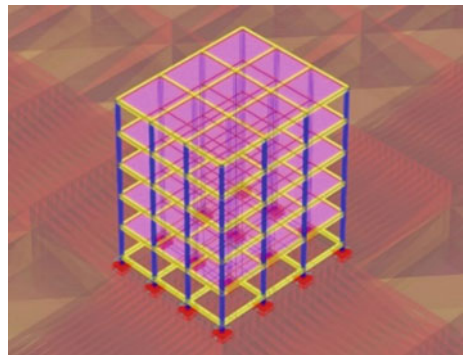
Fig. 2 Two-dimensional view of the structure founded on the soil in **a** X–Z plane **b** Y–Z plane

Steel columns-
ISMB300
supported on slab
base foundation

(c)
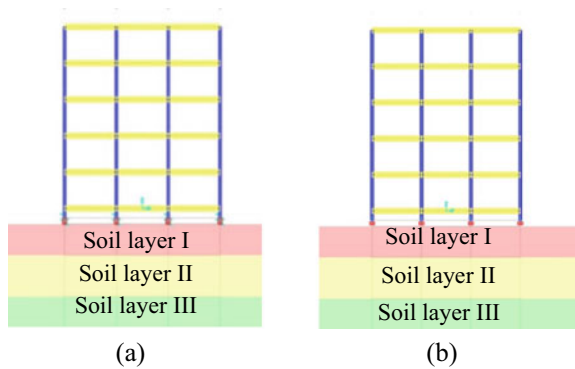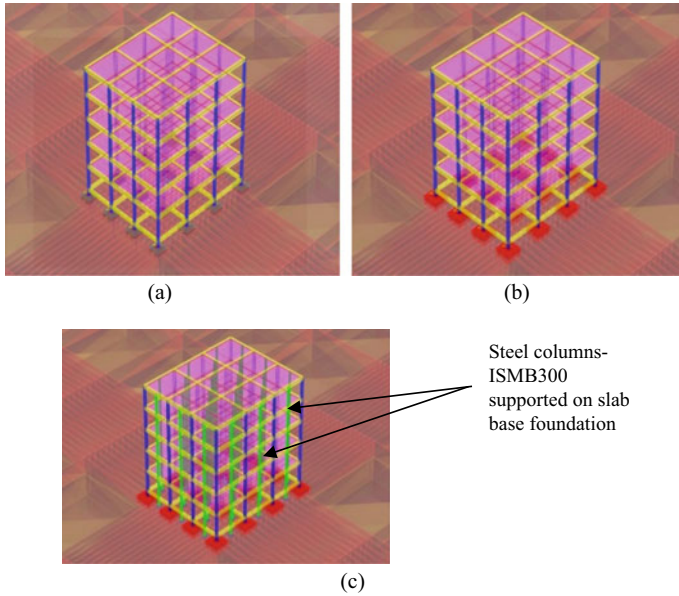
Fig. 3 Three-dimensional view of the structure showing the retrofitted isolated footings **a** (2 m × 2 m × 0.9 m) founded on soil layer I as per the first case of retrofit study, **b** (2.5 m × 2.5 m × 1 m) founded on soil layer I as per the second case study and **c** three-dimensional model of the structure with isolated RC footings retrofitted to a size of 2.5 m × 2.5 m × 1 m adopting RC jacketing [7–9] along with introduction of new structural steel columns (ISMB300) supported on slab base foundation, provided between existing RC columns

retrofitted to an increased size of 2 m × 2 m × 0.9 m to study the possible reduction in settlement, as a first case study. Figure 3b shows the 3D model of the structure whose isolated footings are retrofitted as a second case study to an increased size of 2.5 m × 2.5 m × 1 m to study the possible reduction in settlement, as a second case study.

The building is separately modelled as a third case study, where the existing RC footings are retrofitted to a size of 2.5 m × 2.5 m × 1 m adopting RC jacketing along with introduction of new structural steel columns (ISMB300) supported on slab base foundation, provided between existing RC columns, as a measure to further reduce the possible settlements taking place. The steel columns thus introduced are welded to the reinforcement of the floor beams above and below with the help of insert steel plates, after removal of the concrete cover. The properties of steel column supported on slab base is mentioned below

Structural steel column: ISMB300
Grade of steel: Fe345
Base plate size: 400 mm × 600 mm × 20 mm, Fe345 grade steel fixed on M40 grade concrete. Steel insert plate size of 325 mm × 325 mm × 10 mm are welded the structural steel columns and to the exposed reinforcement of the floor beams.

Figure 3c shows the 3D model of the structure with isolated RC footings retrofitted to a size of 2.5 m × 2.5 m × 1 m adopting RC jacketing along with introduction of new structural steel columns (ISMB300) supported on slab base foundation, provided between existing RC columns.

3 Results and Discussion

It is observed that after carrying out the analysis, the settlements in the isolated footings are recorded, and all the footings are retrofitted by section enlargement method/RC jacketing. Before retrofit, size of the existing footings was 1.5 m × 1.5 m × 0.6 m. The average maximum vertical settlement of one of the isolated footing (1.5 m × 1.5 m × 0.6 m) before retrofit is found to be 117.23 mm as indicated and shown in Fig. 4.

As a first case study of retrofitting of the isolated footings by section enlargement method, the footing sizes were enlarged to 2 m × 2 m × 0.9 m as shown in Fig. 5a, by increasing the length by 500 mm on each side in *x* and *y* directions, and increasing

Fig. 4 Settlement in deficiently designed isolated footings (1.5 m × 1.5 m × 0.6 m) before retrofitting

(a)

(b)
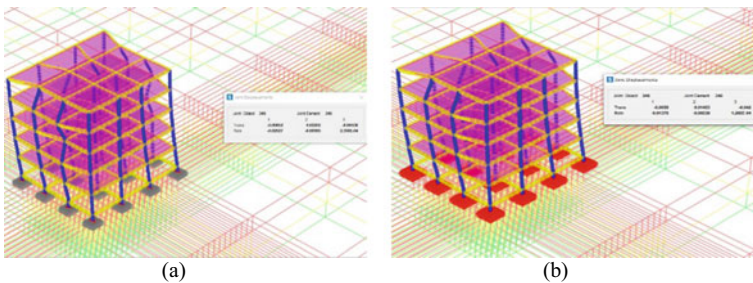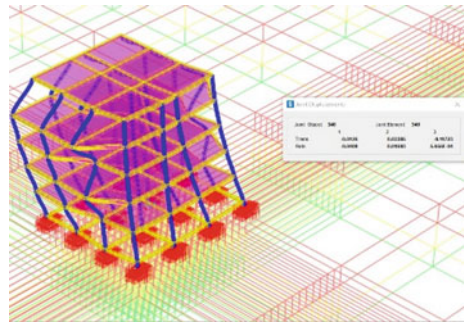
Fig. 5 Reduction in settlement in isolated footings **a** in the first case study of retrofitting of the isolated footings by section enlargement method—footing sizes enlarged to 2 m × 2 m × 0.9 m and **b** in the second case study of retrofitting of the isolated footings by section enlargement method—footing sizes enlarged to 2.5 m × 2.5 m × 1 m

the depth of the footings by 300 mm, when compared to the un-retrofitted footing sizes. The average settlement in one of the footing was observed to have reduced to 65.3 mm from 117.23 mm (average settlement in un-retrofitted footings). The total reduction in the settlement of the footings in this case was observed to be 79.52%.

In the second case study of retrofitting, the footing sizes were increased to 2.5 m × 2.5 m × 1 m, such that, increasing the length by 1000 mm on each side in x and y directions, and increasing the depth of footings by 400 mm, when compared to the un-retrofitted footing sizes. It was observed that in the second case study of retrofitting, the settlement reduced to a value of 42 mm from 117.23 mm (average settlement in un-retrofitted footings), as shown in Fig. 5b. The total reduction in the settlement of the footings in this case was observed to be 179.2%. The reduction in the settlement of the retrofitted footings corresponding to the first and second case study is due to the increased area and depth of the footings adopting RC jacketing.

Figure 6 shows the settlement in existing RC footings that are retrofitted adopting RC jacketing to a size of 2.5 m × 2.5 m × 1 m along with inclusion of new steel structural columns (ISMB300) supported on slab base foundation provided between existing RC columns. After provision of steel columns supported on slab base in between existing RC columns, the settlement in the existing retrofitted RC footings was observed to be 24.23 mm in the vertical direction when compared to 117.23 mm (average settlement in un-retrofitted footings). The total percentage reduction in settlement in the existing RC footings after providing new steel columns supported on slab base in between existing RC columns is 383.82%. The reduction in the settlement is predominantly due to the distribution of the loads to the newly introduced steel columns that is transferred to the slab base foundation.

It is observed from the results for case of only gravity loads (dead load and live load) under service load conditions, the maximum average settlement has been found to be 52.83 mm in vertical direction. The maximum average settlement under the footing was found to be 117.23 mm in the case when seismic loads were applied. Table 2 shows the comparison of maximum average vertical settlement under service load and earthquake load for different retrofit cases.
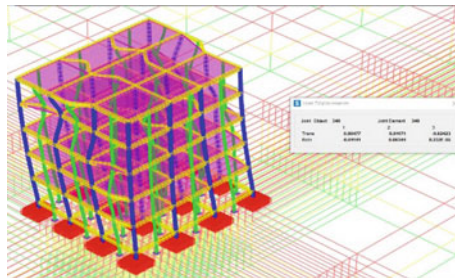
Fig. 6 Reduction in the average settlement in existing RC footings that are retrofitted adopting RC jacketing to a size of 2.5 m × 2.5 m × 1 m along with inclusion of new steel structural columns (ISMB300) supported on slab base foundation provided between existing RC columns
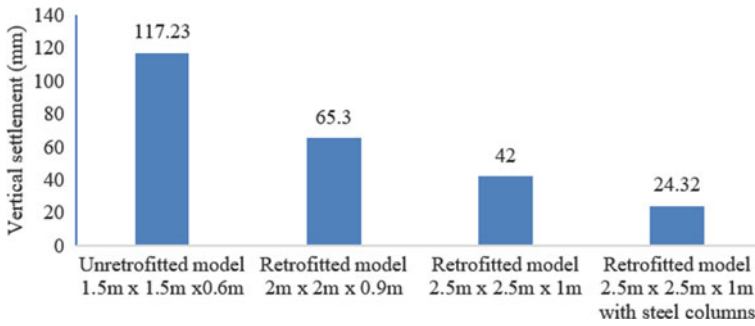
Fig. 7 Maximum average vertical settlement in isolated footings for different retrofit cases

Figure 7 shows the graphical representation of maximum average vertical settlement of isolated RC footing for different retrofit cases.

Modal analysis for all the retrofit cases have been carried out, and the time period of vibration corresponding to 12 modes have been presented in Table 3. Figures 8, 9, 10 and 11 show the mode shapes typically for mode 1, mode 10 and mode 12 for different retrofit cases.

An average settlement of 117.23 mm has been observed in the isolated footings having a size 1.5 m × 1.5 m × 0.6 m before retrofitting. By applying section enlargement method as a retrofit strategy, the size of the deficiently designed isolated footings was increased to 2 m × 2 m × 0.9 m as the first case study. The average settlement in the first case of retrofitted footings (2 m × 2 m × 0.9 m) was found to be 65.3 mm. Further, the deficiently designed RC isolated footings were retrofitted adopting section enlargement method by increasing the size of the footings to 2.5 m × 2.5 m × 1 m as a second case study. The average settlement in the second case study of retrofitted isolated footings (2.5 m × 2.5 m × 1 m) was found to be 42 mm. Further, in a third case study, when the existing RC footings are retrofitted to a size
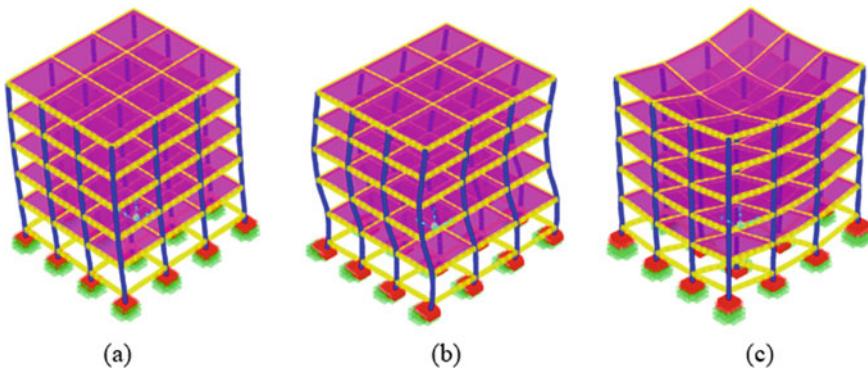
Fig. 8 Mode shape 1 (**a**) mode shape 10, (**b**) mode shape 12 and (**c**) for un-retrofitted case of footing size 1.5 m × 1.5 m × 0.6 m
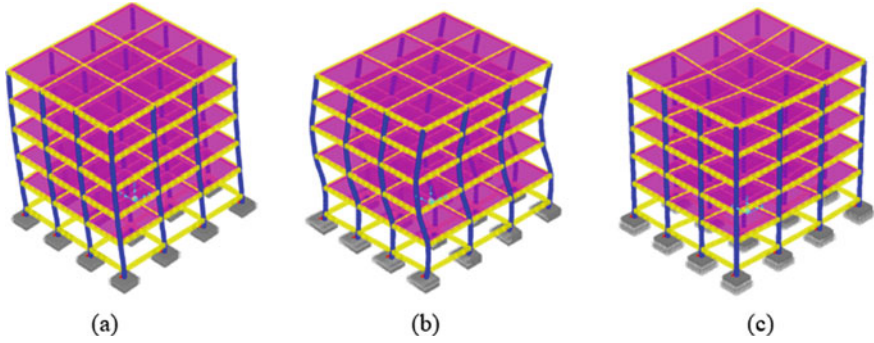
Fig. 9 Mode shape 1 (**a**) mode shape 10 (**b**) mode shape 12 and (**c**) for retrofitted case 1 of footing size 2 m × 2 m × 0.9 m
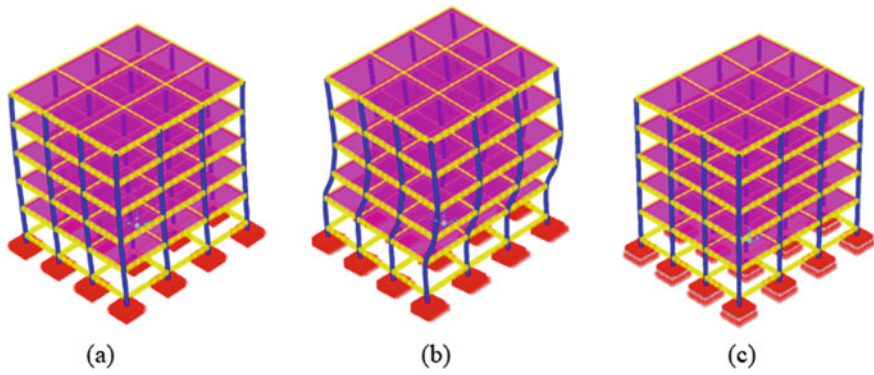
Fig. 10 Mode shape 1 (**a**) mode shape 10 (**b**) mode shape 12 and (**c**) for retrofitted case 2 of footing size 2.5 m × 2.5 m × 1 m
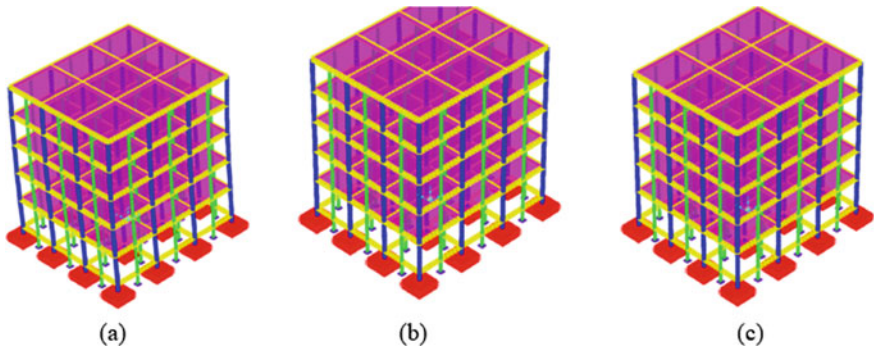
Fig. 11 Mode shape 1 (**a**) mode shape 10 (**b**) mode shape 12 and (**c**) for retrofitted case 3 of footing size 2.5 m × 2.5 m × 1 m with newly introduced steel column supported on slab base

of 2.5 m × 2.5 m × 1 m adopting RC jacketing method along with inclusion of new steel structural columns (ISMB300) supported on slab base foundation, provided between existing RC, the average vertical settlement in the existing RC footings was observed to be 24.32 mm. Therefore, it is observed that by increasing the footing size to 2 m × 2 m × 0.9 m in the first case study of retrofit, there is reduction in the settlement by 79.52% and when the footing size was increased to 2.5 m × 2.5 m × 1 m in the second case study of retrofit the reduction in settlement was found to be 179.52%. It has also been observed from the results, the reduction in settlement when the existing RC footing are retrofitted using RC jacketing along with new structural steel columns supported on slab base are introduced in between existing RC columns, the settlement was found to have reduced up to 383.82%. It is learnt from the results of the study that when the base spans are comparatively large and a comparatively larger settlement has taken place in existing RC footings, inclusion of new structural steel columns supported on slab base foundations at the central bay spans in between the existing RC columns along with RC jacketing of existing footings helps to reduce any future settlements effectively and restores the stability of structure. In cases, where the settlement in existing RC footings due to erroneous design or comparatively weak soil conditions locally present around existing footings, the RC jacketing or section enlargement method of retrofit itself is effective in preventing any further settlements.

4 Conclusion

The following are the main conclusions that are drawn out of the present work,

- It is observed that there is significant decrease in settlement as the size of isolated footings is increased due to application of retrofitting adopting section enlargement method for the footings.
- The average settlement of isolated RC footings in this study has been found to have reduced to 42 mm from a value of 117.23 mm when isolated footings are retrofitted adopting section enlargement method, therefore, causing a percentage decrease in vertical settlement of 179.2%.
- Further, the vertical settlement decreased to 24.23 mm when the structure is retrofitted with inclusion of new steel columns sections-ISMB300, therefore, reducing the settlement by 73.338%.
- The overall settlement is reduced by 383.82% when the structure is retrofitted adopting section enlargement method and adding extra new steel columns in between existing RC columns.
- Inclusion of new structural steel columns supported on slab base foundations at the central bay spans in between the existing RC columns along with RC jacketing of existing footings helps to reduce any future settlements effectively and restores the stability of structure.

References

1. Ranjan P, Dhinam P (2016) Retrofitting of columns of an existing building by RC, FRP, SFRC jacketing techniques. J Mech Civ Eng (IOSR-JMCE) e-ISSN: 2278-1684, p-ISSN: 2320–334X, pp 40–46
2. Kaliyaperumal G, Sengupta AK (2009) Seismic retrofit of columns in buildings for flexure using concrete jacket. ISET J Earthq Technol 46(2):77–107
3. Cotor A, Lungu I, Olteanu-Donţov I (2019) Retrofitting individual foundation in building rehabilitation. The Bulletin of the Polytechnic Institute of Jassy, Construction. Architecture Section, Volumul 65 (69), Numărul 3., pp 1–12
4. IS 875-Part 1 (1987) Dead loads—code of practice for design loads (other than earthquake) for building and structures. Bureau of Indian Standards, New Delhi
5. IS 875-Part 2 (1987) Live loads—code of practice for design loads (other than earthquake) for building and structures. Bureau of Indian Standards, New Delhi
6. IS 1893-Part1 (2016) Criteria for earthquake resistant design of structures. Bureau of Indian Standards, New Delhi
7. IS 456(2000) Plain and reinforced concrete—code of practice. Bureau of Indian Standards, New Delhi
8. IS 15988 (2013) Seismic evaluation and strengthening of existing reinforced concrete buildings—guidelines. Bureau of Indian Standards, New Delhi
9. Chandrakar J, Singh AK (2017) Study of various local and global seismic retrofitting strategies—a review. Int J Eng Res Technol (IJERT), 6(06):824–831

Combined Use of Fine and Coarse Recycled Concrete Aggregates in Concrete for Sustainable Development: A Review

Anasuya Sahu, Sanjay Kumar, and A. K. L. Srivastava

1 Introduction

With the massive increase in population and heavy industrialisation in urban areas, the rate of production of concrete gradually increases as well as deploying of natural resources which creates serious environmental issue. As we know that construction industry requires huge amount of cement, natural aggregates (NAs) and water as basic materials for the manufacture of concrete. In 2014, the world production of cement was about 4.3 billion tonnes [1]. Likewise, the construction sector utilises an estimated 48 billion metric tonnes of aggregates per year around the world [2] and it is expected to rise up to 66.3 billion tonnes by 2022 (World Bank Annual report, 2012) which leads to huge depletion of NA. Figure 1 describes the comparative sketch of worldwide production of aggregate among which Asia and Pacific were found to be the highest consumption rates [3]. As a result, aggregates which account for about 55–80% of total concrete volume have a significant impact on the environment and the long-term viability of structures. On the other hand, due to rapid growth of industrialisation and urbanisation, large amounts of debris are produced from construction and demolition (C&D) waste which creates disposal problem due to scarcity of land, environmental pollution, heavy transportation cost, and environmental imbalance. As a result of the gradual depletion of natural resources and increased awareness of sustainable waste management across developed and emerging economies, C&D trash in civil engineering projects is becoming increasingly important. According to the World Bank's annual report (2012), the global build up of C&D waste is almost 1.3 billion tonnes per year. Furthermore, by 2025, the annual build up of C&D waste is predicted to reach 2.2 billion tonnes.

A. Sahu (✉) · S. Kumar · A. K. L. Srivastava

Department of Civil Engineering, National Institute of Technology, Jamshedpur, Jharkhand 831014, India

e-mail: anasuyasahu1980@gmail.com

Fig. 1 Consumption rate of aggregates in worldwide [3]
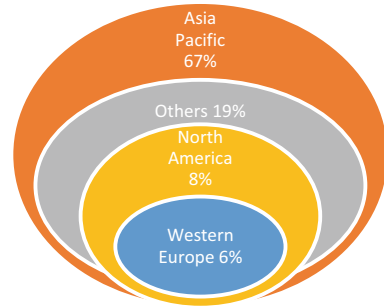
The above-mentioned environmental issues, such as the depletion of natural resources and the accumulation of C&D wastes, can be addressed simultaneously by using these wastes as raw material substitutes in the production of concrete. In this context, the usage of recycled concrete aggregate (RCA) derived from the crushing and sieving of C&D wastes could be a part of the solution because it provides an alternative aggregate to NAs. By turning these waste materials into aggregate (RCA) to be utilised in concrete production while lowering the consumption of raw materials, the reuse of these waste materials will undoubtedly contribute to the achievement of sustainable development goal.

1.1 Recycled Concrete Aggregate

Recycled aggregate (RA) is extracted mainly by crushing and recycling of the waste obtained from construction and demolition of the concrete structures and other construction detritus. During extraction, RAs are consisting of brick aggregate, concrete aggregate and mixed aggregates. Among these, RCA is the most widely used RA in construction today, and organisations in several countries have produced specifications [4]. The main purpose of using RCA in construction sector is to make a greener and sustainable concrete. The distinguish feature of RCA and NA is attached old mortar which is adhered to the NA existing at the core. With increasing nominal aggregate size, the percent of adhering mortar decreases [5].

The RCA is consisting of coarse recycled concrete aggregate (CRCA) and fine RCA (FRCA). The CRCA is a small concrete component made up of old coarse aggregate, mortar and interfacial transition zone (ITZ) as shown in Fig. 2. Whereas the FRCA (<5 mm) is formed by crushing and sieving bits of old waste concrete mortar. Like coarse RCA, fine RCA can also be used in production of concrete to minimise the acute shortage of river sand as well as the major environmental issues. It has been observed that concrete built with CRCA exhibits qualities similar to concrete manufactured with NAs [6]. Whereas the use of FRCA in concrete production requires caution due to its higher water absorption tendency than NA, which might negatively affect the qualities of concrete. Many researchers review that [7, 8]

Fig. 2 Physical
Characteristics of RCA

New ITZ

Porous adhered mortar

Old ITZ

Cracks in aggregate
due to processing
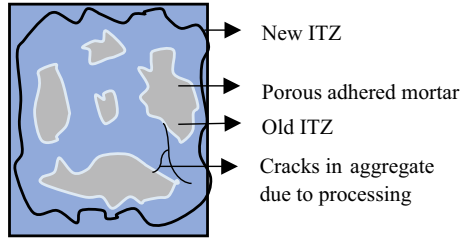
the strength of concrete decreases by using FRCA as it contains old mortar which makes the concrete porous and less dense. Though limited research has been done on FRCA, recent research [9–11] has observed that if the RCA mix is adjusted to compensate for the water absorbed by FRA during mixing, basic mechanical properties can be equal to those of normal aggregate concrete. It has also been observed that [12–14] the combined use of CRCA and FRCA can produce more sustainable concrete as compared to the use of CRCA and FRCA alone because combined use does not required sieving to separate fractions, and all of the recycled material produced is used, which means no new by-waste is generated. The usage of RCA in construction sector as a structural material may prove to be a viable cost option, environmental awareness, as well as waste minimization in bulk resources. The present review focussed on the combined use of coarse and fine RCA, their properties and analyses the viability of their application in construction industry towards the sustainable development.

2 Characterisation of FRCA and CRCA

RCA is made by crushing of discarded concrete into aggregate size particles using mechanically powered equipment. Due to crushing action, it consists of two basic material phases: adhering mortar and natural coarse aggregate phase. These two phases are separated by a thin interface known as old ITZ. The properties of CRCA and FRCA are greatly influenced by an interface (old ITZ) present in between the aggregate and attached mortar. The amount of attached mortar indicates the original concrete's strength properties, the efficiency of the crushing technique, crushing method and the particle size of RCA. As compared to NA, RCA has higher water absorption, lesser density, lesser specific gravity, high-moisture content and poor particle size distribution. These properties of RCA containing CRCA and FRCA can affect the workability, strength, durability, setting and hardening, shrinkage and creep of concrete. Water absorption (WA) and density of the aggregate are considered as the main parameter in mix design of concrete. It was observed that for coarse and fine fractions, the water absorption of RCA is 3–12% greater than that of NA [15, 16]. It was also observed by Juan and Gutiérrez [17] that WA and Particle size of RCA is varying inversely. He studied that the WA capacity of FRCA is more than that
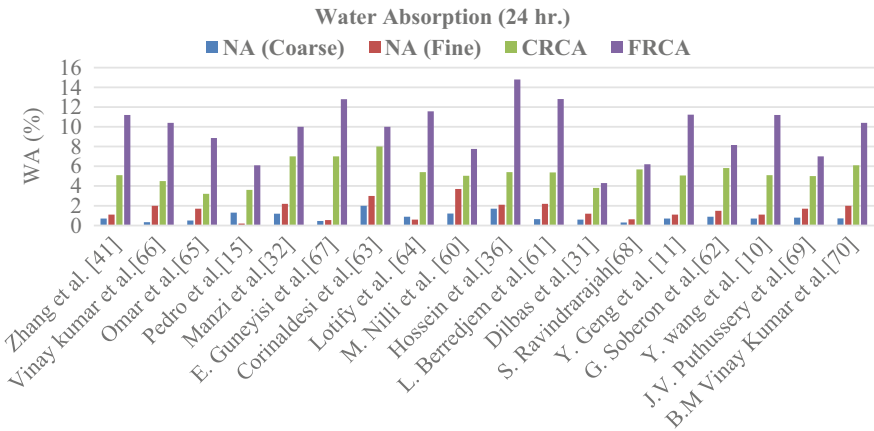
Fig. 3 Water absorption and SSD density of natural aggregates and RCA (FRCA & CRCA) from literature

of CRCA due to the greater specific surface area so larger is the amount of adhered mortar. This is due to the recycling methods applied, where the use of multiple processing stages increases the amount of paste accumulated in the fine fraction whilst decreasing the attached mortar content in the coarse aggregates [18]. The aggregate quality is generally determined by its SSD and must be considered along with the WA during the mixing and stirring process of concrete [19]. For example, D. Pedro et al. [14] obtained the WA value of 6.9% for FRCA, whereas the value was 3.6% for CRCA. Wang et al. [9] reported that the WA value of FRCA is 6.8% more than that of CRCA.

There is a greatest difference between RCA (CRCA & FRCA) and NA has been observed from water absorption (WA) as demonstrated in Fig. 3. From various literatures which have adverse impact on the concrete mix design. These differences are mainly due to the lower density and high porosity of the attached mortar in the RCA.

The mechanical and chemical properties of RCA are considered essential considerations in aggregate research. The review shows the mechanical strength of RCA is higher than that of parent aggregates because of the attached mortar. According to Suryavanshi et al. [20], for 20–10 mm and 10–4.75 mm sized aggregates, crushing strength of RCA was found to be much higher (33 and 45%) as compared to NAs. Durability of RCA is generally determined by its chemical properties (amount of sulphate and chloride exist). According to Nagataki et al. [21], the sulphate losses for RCA vary between 29.1 and 49% depending on the source, whereas the value for coarse NA was 9.1 and 2.6% for fine NA. The research work revealed that when higher degree of crushing was applied to RCAs, their performance enhanced dramatically. Another critical chemical property is chloride content, as high levels of chloride can cause reinforcement steel to corrode quickly. Debieb et al. [22] suggested that if the aggregate contains an excessive amount of chloride, it can be removed by pouring the aggregate in water. However, based on the literature, the properties of RCAs were

found to be highly dependent on the aggregate source, the age and the nature of the concrete from which it is derived. But, these properties of RCA can be enhanced by adopting suitable mixing approaches and treatment methods.

3 Fresh Properties

Fresh state includes workability and density of concrete mix. These qualities are greatly influenced by a number of parameters, aggregate size, moisture content, water absorption and aggregate shape and texture [22]. Due to high porosity, RCA attains low workability than the NA. It has also been observed that with increasing in RCA replacement, the workability of RCA reduces and also have a greater loss in slump as compared to the natural concrete aggregate [23]. When coarse RCA is utilised in a dry environment, the workability of the concrete is severely impeded, depending on the amount of RCA used. Similarly, adding up to 20% fine RCA into the concrete mix has been shown to have no significant influence on its workability. However, increasing the fine RCA content causes a significant reduction in workability [22]. The use of RFA was shown to have just a little effect on wet density in compared to natural concrete aggregate.

However, the workability of RCA can be enhanced by using chemical admixtures or superplasticizers (SPs) as suggested by many researchers. It was observed that, by using high-performance SPs for concrete mixes with a 25 and 100% replacement of coarse RCA increases slump by around 7.31% and 25.80%, respectively [24]. D. Pedro et al. [14] observed that with the addition of SPs, the workability of concrete with 50% coarse and 50% fine RCA is same as that of concrete with NAs. The workability problem of RCA can be overcome economically by adopting low-cost methods such as pre-soaking aggregates for general construction. However, SPs and other admixtures are advised for high strength requirements.

4 Hardened Properties

4.1 Compressive Strength

Compressive strength is one of the major important qualities of concrete that affects its strength, durability and performance. Many factors influenced the qualities of RCA, including the water-binder ratio, the replacement level of RCA, the properties of adhering mortar and the properties of the admixtures used and the mixing method. It was observed that the strength of concrete decreased by using fine RCA, [8] as the old mortar in fine RCA making concrete more porous and less dense. However, according to Silva [6], the replacement levels up to 30% coarse RCA or 20% fine RCA have less effect on the strength development of concrete; however, with the increasing

of replacement level of RCA, strength gradually decreases. Some literatures also suggests that in an average 20–30% strength loss occurs in concrete by incorporating 100% coarse RCA or 50% fine RCA to NA. Pedro et al. [14] studied the compressive strength of concrete including both coarse and fine RCAs, and observed that concrete having both coarse and fine RCAs at the same time may reach equal performance to regular concrete. Hassan et al. [25] replaced both fine and coarse aggregates with varying percentage (50 and 100%) of fine and coarse RCA and found that the compressive strength was decreased about (48.1 and 39.88%) from which he concluded that strength of RCA may greatly be influenced by the RCA content and properties. The review shows that though RCA minimises concrete's compressive strength due to increased water absorption by aggregates and a weak residual mortar layer, it is not impossible to make stronger concrete than normal concrete if the parent concrete is stronger than the condition where recycled aggregate concrete (RAC) is used [25].

The strength of RCA basically depends upon the strength of parent concrete. The study shows that higher-grade concrete made with RCA has less compressive strength as compared to control concrete. Pedro et al. [14] performed the experiments on high-performance concrete (M70) by using fine and coarse RCA (25/25, 50/50 and 100/100%) as a replacement of NAs. He observed that the compressive strength values decrease to 5.1%, 12.1% and 16%, respectively, as compared to the reference concrete. The obtained loss is may be due to the mortar fraction in the RCA. Thus, it was concluded that achieving target strength becomes more challenging with increasing target strength. Compressive strength of RCA may be improved by using admixtures, increasing the cement content [55, 61], employing plasticizers and mixing procedures [26–28]. According to Dilbas et al. [29], the compressive strength increased by 11.4%, 5%, 3.2% and 14%, respectively, with the addition of silica fume 5–100% NA, FRCA, CRCA and both. Manzi et al. [30] replaced the NA with RCA (both fine and coarse) by adding acrylic-based SP to achieve compressive strength of 30 Mpa and observed that the strength was increased about 27% higher than the reference concrete. According to Tam et al. [26] the maximum replacement level of RCA is to be 25–40% by adopting two-stage mixing approach (TSMA). Figure 4 depicts the effect of the RCA replacement ratio (both coarse and fine) on the strength of concrete. The plot shows that there is marginal decrease in strength with 50% replacement made with FRCA and CRCA. But, the compressive strength of concrete made with RCA (FRCA + FRCA) is comparatively less than that of control concrete with fully replacement (100%). However, the reduction in strength is not significant, and RA could be used in regular structures that do not require a lot of strength.

4.2 Split Tensile Strength

Split strength is the common indirect technique to determine the strength of concrete. The split tensile strength of RCA exhibits similar behaviour to compressive strength
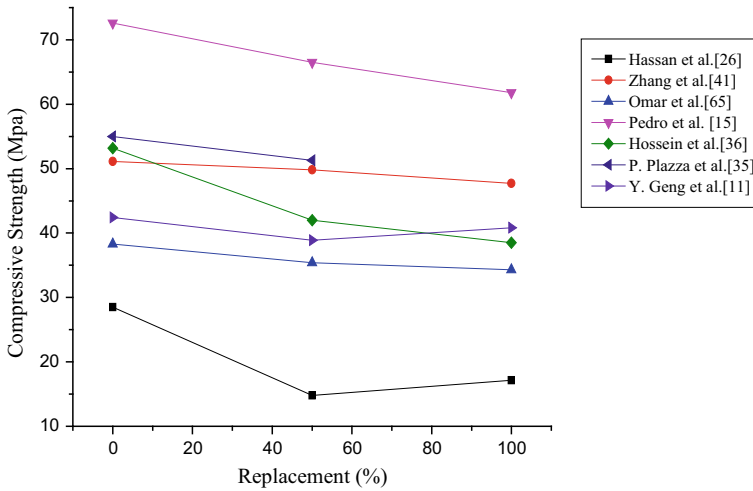
Fig. 4 Compressive strength of RAC from various literature studies

as it is affected by a number of variables, including RCA replacement, w/c ratio, mixing procedures, cement type and quality of RCA. The increased tensile strength of RAC is attributed to the WA capacity of adhering mortar, which creates a proper bonding between aggregate and matrix [27]. According to M. Nedeljkovi´c et al. [26] tensile strength of RAC was reduced to 10.2%, 10.8%, 17.8% and 33%, respectively, when the fine aggregate is replaced by FRCA (10%, 30%, 50% and 100% replacement ratio, respectively). Similarly, when RCA made with both FRCA and CRCA the tensile strength was 20% lower than the conventional concrete [31, 32]. Plaza et al. [33] observed that simultaneous use of both fine (50%) and coarse (100%) fraction of RCA gave lower strength than the reference, having losses up to 14.13%. However, the negative effects of RCA substitution can be overcome by addition of SPs and using mineral admixtures. Hossein et al. [34] reported that by using polycarboxylate-based SPs the strength increased to 10–29% relative to control mix with the replacement of 25% coarse RCA. Whereas the strength increased to 4% and 22%, respectively, with 50% replacement of fine RCA as well as both fine and coarse RCA. Figure 5 shows the effect of split tensile strength with various RCA replacement remarked by several researchers. It shows that the replacement ratio increases the tensile strength of concrete made with RCA decreases as compare to the control concrete. This literature review not only identifies the different aspects that may influence the tensile strength of concrete produced from RCA but it also gives a clear image of the parameters that may affect it, allowing them to be modified as needed.
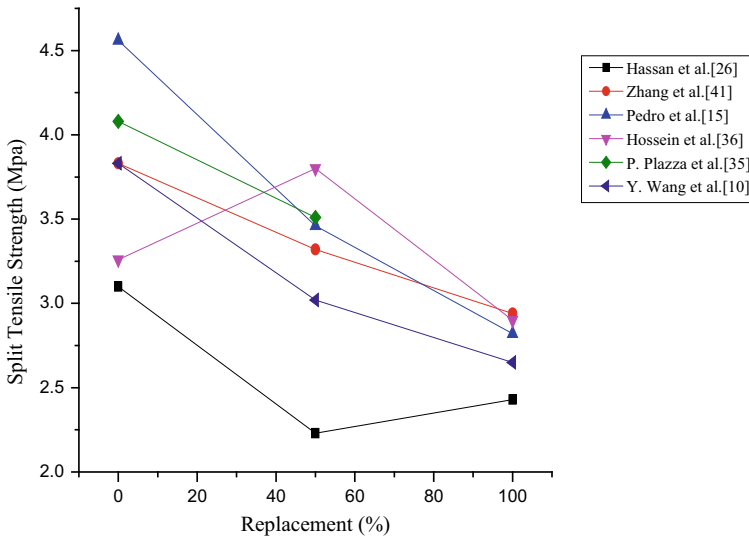
Fig. 5 Split Tensile strength of RAC from various literature studies

4.3 Flexural Strength

Another aspect affecting concrete's structural performance is its flexural strength. It is determined by the RCA replacement ratio, aggregate moisture content, concrete curing time, water-binder ratio and among other factors. Literature shows that flexural strength of RCA has been decreased when the replacement ratio increases [23, 35, 36]. It has been observed that concrete made with the replacement of 25% and 50%, RCA had 6–13% lower than the conventional concrete. When 100% RCA was utilised to make RAC, the flexural strength was reduced by 26% compared to standard concrete [36]. This is mainly due to the weak interfacial bond between the old adhered mortar covering RCA and the new mortar. Hassan et al. [25] replaced fine and coarse RCA (50 and 100%)) combinedly by NA and observed that the strength was decreased (43 and 33%) with the increase of replacement ratio as compared to the traditional concrete. Manzi et al. [30] used an acrylic-based SP and observed that by replacing 20, 30 and 60% RCA (both fine & coarse) with NCA leads to reduction of flexural strength by 9.3%, 23% and 25%, respectively. The real flexural strength, on the other hand, decreases when the water to cement ratio rises. The strength of RAC was improved by using RCA with a reduced water absorption capacity [37]. Figure 6 depicts the influence of various % of RCA replacement on the flexural strength of RAC which shows that as the replacement percentage increases, the strength of modulus of rupture remain decreases.

Fig. 6 Flexural strength of RAC from various literature studies
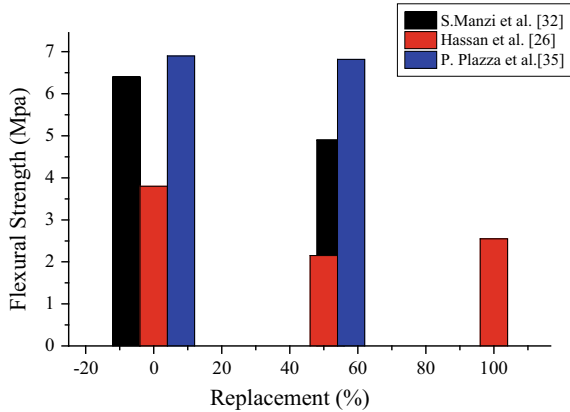
4.4 Modulus of Elasticity

Incorporation of RCA has been shown to reduce modulus of elasticity [38]. In fact, the aggregate modulus of elasticity has been identified as an important factor which affects the modulus of elasticity of concrete with RCA. As RCA is more susceptible to deformation than raw aggregate, the aggregates' weakness reduces the Young's modulus for concrete when RCA is used. According to Kou et al. [38], with the 50% replacement ratio of coarse RCA, the elasticity modulus decreased by 12.6%, whereas with the 100% replacement ratio it is decreased by 25.2%. Zhang et al. [39] determined the effect of elastic modulus by incorporating CRCA, FRCA and combination of both into the concrete mix with the replacement ratio 0%, 50% and 100%, respectively. He observed that the elastic modulus is decreased by 10.8% and 22% at 50% and 100% replacement of CRCA as compared to conventional concrete, whereas it is decreased by 2.07% and 14% at same % of replacement of FRCA. Similarly, the elastic modulus is also decreased up to 24% by replacing both CRCA and FRCA (50 and 100%) than the control mix. So, it is concluded that the FRCA had a minor influence on the elastic modulus of the resulting concrete than CRCA. Figure 7 shows the difference of elasticity modulus of RAC with various replacement % of RCA. The graph shows that the elasticity modulus decreases as the RCA replacement % increases. However, it should be noted that, up to 50% replacement ratio, the influence of FRCA and CRCA was less significant in comparison to normal concrete.
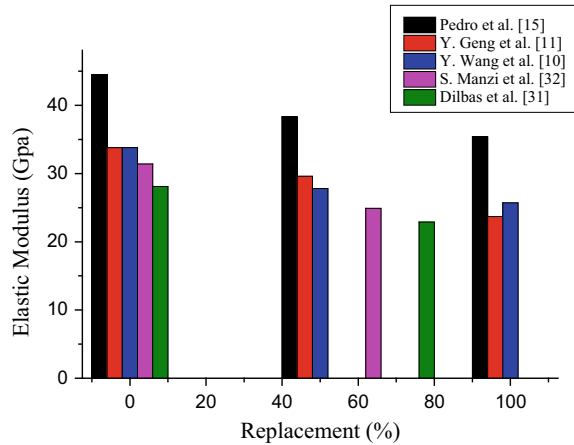
5 Techniques for Improving Properties of Recycled Concrete Aggregate

Recycled aggregate exhibits inferior quality compared to the NA as it has possessed high porosity, low density, increased WA rate and micro features in parent mortar and at the ITZs. On the other hand, due to repeated recycling process RA became weaker [40] than first-generation RA [41]. As a result, the RCA generated from RA has inferior characteristics than the NA [42] which lowers the compressive strength, tensile strength and flexural strength of recycled concrete as compared to the natural concrete. Therefore, it becomes necessary to improve the qualities of RCA in order to make it widely applicable and usable in the production of recycled concrete. The review provides a Comparative analysis of different methods utilized, their impact on fresh hardened properties, durability and their environmental impact which has summarised in tabular form (Table 1).

6 Conclusions

- According to the study, the water absorption of both FRCA and CRCA is lesser as compared to the conventional aggregates due to the old attached mortar which can be reduced by adopting proper treatment method to RCA.
- The literatures recommended that the compressive strength of concrete made with RCA (FRCA + CRCA) for replacement ratios of up to 50% is comparable to that of fresh aggregate concrete.
- The review shows that the replacement level of RCA increases the corresponding tensile strength, flexural strength and modulus of elasticity decreases. However,

for replacement up to 50%, the influence of FRCA and CRCA was less significant in comparison to normal concrete.

- The study shows that though in some cases the performance of concrete made with both CRCA and FRCA is poor by using various chemical and mineral admixtures, adopting suitable treatment method or mixing method the properties of RCA can be improved. As a result, the potential for using RCA in various construction fields is peak, particularly in terms of ecological sustainability.
- The paper explains how the properties of RCA can be enhanced by applying a proper treatment technique to the RCA and adding a suitable percentage of admixtures to the fresh RAC mix. However, a proper treatment method and strategy for mix design is still in process.
- The literature proposed the different treatment methods for coarse RCA only. So, it is required to establish a proper treatment method for fine RCA also.
- Another important area for future research is modification of ITZ in long run, which affects the properties of RCA. So, the study of microstructure and behaviour of RCA in long term may be the key factor for future research.
- Both coarse and fine RCA derived from C&D waste may be recommended as a suitable construction material in future, and these RCA may be referred to as a

Table 1 Treatment method for enhancing RCA properties

Methods	Applications	Advantages
Addition of mineral admixtures [43, 44]	used as admixtures (Fly ash (FA), silica fume (SF) ground granulated blast furnace slag (GGBFS), etc.) as well as pozzolana slurry for coating the aggregate surface	1. Improving durability properties of RCA by using fly ash. 2. Mechanical and density properties were improved
Emulsion of polymer [45]	Applied the solution of polyvinyl alcohol (PVA) 6–12% with water to the RCA which is placed in a desiccator with a vacuum pump and allowed to soak for 24 h	1. Reduced the water absorption capacity of RCA. 2. Bond strength of cement paste and aggregate phase can be improved.
Carbonation [46]	CO_2 is injected into the RCA at a constant level up to 5 bar and kept (with 100% concentration of CO_2) for 7 days	1. The WA of RCA is reduced to 22% and specific gravity increased to 0.8%.
Cement slurry coating [47]	Applied a thin film of cement paste (0.16–0.23 mm) around the aggregate grain (4 mm-8 mm fraction) in a laboratory granulator (45 cm dia) and rotated in a drum for 5 min. with a desired w/c ratio (0.25–0.5)	1. Porosity of RCA was reduced to 55% which lowers the water absorption. 2. Increased the compressive strength up to 12% as compared to the untreated RCA.

Table 1 (continued)

Methods	Applications	Advantages
Self-healing techniques [48, 49]	The approach is based on calcium carbonate bio deposition by bacteria termed 'Sporosarcina pasteurii,' which attract calcium ions ($Ca2 +$) and create calcite ($CaCO_3$) from a liquid culture medium obtained from urea, Urease (urea amidohydrolase) and Urease (urea amidohydrolase)	1. Reduced the porosity and moisture absorption of RCA inside as the bacteria can easily enter into the micro-pores due to its small size. Enhanced the mechanical properties of treated RCA as compared to the untreated RCA.
Methods	Applications	Advantages
Industrial applicable mixing method [50]	Incorporating nano materials like nano silica and micro $CaCo_3$ in the strengthening surface coating slurry and mixing with water for 120 s. The untreated recycled aggregate is then immersed in the slurry for 45 min. Removed the soaked aggregate and placed on the screen for removing extra nano slurries present on RA	1. Particles of binder are densely packed which increase the strength 2. Improved the proper hydration of cementitious materials 3. Improved the mechanical properties at long term
Mechanical grinding [51]	Removed the weak mortar attached in RCA by using Los Angeles abrasion machine with 12 steel spheres at 300 rpm for 5 min	WA reduced to 32.3% whereas 3.5% increment of specific gravity than the untreated aggregate
Acid treatment [52, 53]	Used different types of acids like sulfuric acid (H_2SO_4), hydrochloric acid (HCl), phosphoric acid (H_3PO_4) and acetic acid (CH_3COOH) (strong to medium concentration) to remove the attached mortar. In this method, RCA was pre-soaked in acidic solution	1. WA of treated RA reduced to 36.7% and specific gravity is increased to 5.4% as compared to the untreated RCA 2. Enhanced the mechanical properties (crushing value and impact value of RCA increased to 6% and 7% respectively).
Thermo-chemical treatment [55, 56]	The samples were first soaked in water for 24 h and then being heated in a muffle furnace with HCL (0.1 M, 0.4 M & 0.7 M) at a constant thermal load for 120 min	This method was applied on recycled fine aggregate, and the results showed that combining a 300 °C heat load with chemical treatment is the most efficient technique to extract cement paste when compared to other options

(continued)

Table 1 (continued)

Methods	Applications	Advantages
Two-stage mixing approach (TSMA) [26]	The mixing process is split into two sections, each of which is fully reliant on the addition of water to the concrete mix at separate times	1. The compressive strength of RAC was increased by up to 21.90% for a 20% substitution of NA by RCA after 28 days of curing. 2. Improve durability. This is most likely due to an improvement in the aggregate surface interface.

basic material for economic construction. As a result, the chances of substantial use of C&D waste in the construction industries are more by gathering existing awareness, allowing for future research and the development of practical guidelines that are acceptable to industries.

References

1. Agenda 21: the Rio Declaration on Environment and Development, the Statement of Forest Principles, the United Nations Framework Convention on Climate Change and the United Nations Convention on Biological Diversity, United Nations Conference on Environment and Development (UNCED), Rio de Janeiro, Brazil, 3 to 14 June 1992, section II (Conservation and management of resources for development), see A/CONF.151/26 (Vol. II)
2. Mohammed SI, Najim KB (2020) Mechanical strength, flexural behavior and fracture energy of Recycled Concrete Aggregate self-compacting concrete. Structures 23:34–43
3. Yehia S et al (2015) Strength and durability evaluation of recycled aggregate concrete. Int J Concr Struct Mater 9(2):219–239
4. EN-12620 (2002) Aggregates for Concrete, Comité European de Normalisation (CEN), Brussels (Belgium), 56
5. Hansen TC, Henrik N (1983) Strength of recycled concrete made from crushed concrete coarse aggregate. Concr Int 5(1):79–83
6. Silvaa RV, de Brito J, Dhir RK (2015) The influence of the use of recycled aggregates on the compressive strength of concrete: a review. Eur J Environ Civ Eng 19(7):825–849
7. Khatib JM (2005) Properties of concrete incorporating fine recycled aggregate. Cem Concr Res 35:763–769
8. Evangelista L, de Brito J (2007) Mechanical behaviour of concrete made with fine recycled concrete aggregates. Cem Concr Compos 29:397–401
9. Wang Y, Zhang H, Geng Y, Wang Q, Zhang S (2019) Prediction of the elastic modulus and the splitting tensile strength of concrete incorporating both fine and coarse recycled aggregate. Constr Build Mater 215:332–346
10. Geng Y, Zhao M, Yang H, Wang Y (2019) Creep model of concrete with recycled coarse and fine aggregates that accounts for creep development trend difference between recycled and natural aggregate concrete. Cem Concr Compos 103:303–317
11. Pereira P, Evangelista L, de Brito J (2012) The effect of superplasticisers on the workability and compressive strength of concrete made with fine recycled concrete aggregates. Constr Build Mater 28(1):722–729

12. Kou SC, Poon CS (2009) Properties of self-compacting concrete prepared with coarse and fine recycled concrete aggregates. Cem Concr Compos 31:622–627
13. Tangchirapat W, Rattanashotinunt C, Buranasing R, Jaturapitakkul C (2013) Influence of fly ash on slump loss and strength of concrete fully incorporating recycled concrete aggregates. J Mater Civ Eng 25:243–251
14. Pedro D, de Brito J, Evangelista L (2017) Structural concrete with simultaneous incorporation of fine and coarse recycled concrete aggregates: mechanical, durability and long-term properties. Constr Build Mater 154:294–309
15. Martín-Morales M, Zamorano M, Ruiz-Moyano A, Valverde-Espinosa I (2011) Characterization of RAs construction and demolition waste for concrete production following the Spanish Structural Concrete Code EHE-08. Constr Build Mater 25(2):742–748
16. Katz A (2003) Properties of concrete made with RA from partially hydrated old concrete. Cem Concr Res 33:703–711
17. Juan M, Gutiérrez P (2009) Study on the influence of attached mortar content on properties of recycled concrete aggregate. Constr Build Mater 23(2):872–877
18. Nagataki S, Lida K (2001) Recycling of demolished concrete. In: Fifth CANMET/ACI international conference on recent advances in concrete technology, Singapore, Canada Centre for Mineral and Energy Technology (CANMET) of Natural Resources Canada, American Concrete Institute, pp 1–20
19. Agrela F, Sánchez de Juan M, Ayuso J, Geraldes VL, Jiménez JR (2011) Limiting properties in the characterisation of mixed recycled aggregates for use in the manufacture of concrete. Constr Build Mater 25(10):3950–3955
20. Suryawanshi SR, Singh B, Bhargava P (2015) Characterization of RAC. In: Matsagar V (ed) Advances in structural engineering: materials, vol 3. Springer, New Delhi, pp 1813–1822
21. Nagatakia S, Gokceb A, Saekic T, Hisada M (2004) Assessment of recycling process induced damage sensitivity of recycled concrete aggregates. Cem Concr Res 34(6):965–971
22. Debieb F, Courard L, Kenai S, Degeimbre R (2009) Roller compacted concrete with contaminated RAs. Constr Build Mater 23(11):3382–3387
23. Malešev M, Radonjanin V, Marinković S (2010) Recycled concrete as aggregate for structural concrete production. Sustainability 2(5):1204–1225
24. Zhu YG, Kou SC, Poon CS, Dai JG, Li QY (2013) Influence of silane-based water repellent on the durability properties of RAC. Cem Concr Compos 35(1):32–38
25. Hassan RY, Faroun GA, Mohammed SK (2021) Mechanical properties of concrete made with coarse and fine recycled aggregates. Mater Today: Proc
26. Tam VW, Gao XF, Tam CM (2005) Microstructural analysis of RAC produced from two-stage mixing approach. Cem Concr Res 35(6):1195–1203
27. Tam VW, Gao XF, Tam CM (2006) Comparing performance of modified two-stage mixing approach for producing RAC. Mag Concr Res 58(7):477–484
28. Tam VW, Tam CM (2007) Assessment of durability of RAC produced by two-stage mixing approach. J Mater Sci 42(10):3592–3602
29. Dilbas H, Simsek M, Çakır Ö (2014) An investigation on mechanical and physical properties of recycled aggregate concrete (RAC) with and without silica fume. Constr Build Mater 61:50–59
30. Manzi S, Mazzotti C, Bignozzi MC (2013) Short and long-term behavior of structural concrete with recycled concrete aggregate. Cem Concr Compos 37(2013):312–318
31. Sri R, Tam CT (1985) Properties of concrete made with crushed concrete as coarse aggregate. Mag Concr Res 37(130):29–38
32. Gerardu JJA, Hendriks CF (1985) Recycling of road pavement materials in the Netherlands. Rijkswaterstaat, Dienst Weg- en Waterbouwkunde
33. Plaza P, Sáez del Bosque IF, Frías M, Sánchez de Rojas MI, Medina C (2021) Use of recycled coarse and fine aggregates in structural eco-concretes. Physical and mechanical properties and CO_2 emissions. Const Build Mater 285:122926
34. Sasanipour H, Aslani F (2020) Durability properties evaluation of self-compacting concrete prepared with waste fine and coarse recycled concrete aggregate. Const Build Mater 236:117–540

35. Nixon PJ (1978) Recycled concrete as an aggregate for concrete—a review. Matér Constr 11(5):371–378
36. Bairagi NK, Ravande K, Pareek VK (1993) Behaviour of concrete with different proportions of natural and RAs. Resour Conserv Recycl 9(1–2):109–126
37. Yang KH, Chung HS, Ashour AF (2008) Influence of type and replacement level of RAs on concrete properties. ACI Mater J 105:289
38. Kou SC, Poon CS (2013) Long-term mechanical and durability properties of RAC prepared with the incorporation of fly ash. Cem Concr Compos 37:12–19
39. Zhang H, Wang Y, Lehman DE, Geng Y, Kuder K (2020) Time-dependent drying shrinkage model for concrete with coarse and fine recycled aggregate. Cem Concr Compos 105:103426
40. Thomas C, de Brito J, Gil V, Sainz-Aja JA, Cimentada A (2018) Multiple recycled aggregate properties analysed by X-ray microtomography. Constr Build Mater 166:171–180
41. Thomas C, de Brito J, Cimentada A, Sainz-Aja JA (2020) Macro- and micro properties of multi-recycled aggregate concrete. J Cleaner Prod 245:118843
42. Kou SC, Poon CS, Agrela F (2011) Comparisons of natural and RACs prepared with the addition of different mineral admixtures. Cem Concr Compos 33:788–795
43. Li X (2008) Recycling and reuse of waste concrete in China: part I. Material behaviour of recycled aggregate concrete. Resour Conserv Recycl 53(1–2):36–44
44. Mansor AM, Hamed A, Borg RP (2016) Effect of silica fume on high performance concrete strength. In: Conference paper (PDF available) March 2016 with 243 reads conference: SBE
45. Kou SC, Poon CS (2010) Properties of concrete prepared with PVA-impregnated recycled concrete aggregates. Cem Concr Compos 32:649–654
46. Xuan D, Zhan B, Poon CS (2016) Assessment of mechanical properties of concrete incorporating carbonated recycled concrete aggregates. Cem Concr Compos 65:67–74
47. Martirena F, Castaño T, Alujas A, Orozco-morales R, Martinez L, Linsel S (2016) Improving quality of coarse recycled aggregates through cement coating. J Sustain Cem Mater 6(1):69–84
48. Grabiec AM, Klama J, Zawal D, Krupa D (2012) Modification of recycled concrete aggregate by calcium carbonate biodeposition. Constr Build Mater 34:145–150
49. Charpe AU, Latkar MV (2020) Effect of biocementation using soil bacteria to augment the mechanical properties of cementitious materials. Mater Today Proc 21:1218–1222
50. Yue Y, Zhou Y, Xing F, Gong G, Hu B, Guo M (2020) An industrial applicable method to improve the properties of recycled aggregate concrete by incorporating nano-silica and micro-CaCO3. J Cl Prod 259:120920
51. Pandurangan K, Dayanithy A, Om Prakash S (2016) Influence of treatment methods on the bond strength of recycled aggregate concrete. Constr Build Mater 120:212–221
52. Ismail S, Ramli M (2013) Engineering properties of treated recycled concrete aggregate (RCA) for structural applications. Constr Build Mater 44:464–476
53. Wang L, Wang J, Qian X, Chen P, Xu Y, Guo J (2017) An environmentally friendly method to improve the quality of recycled concrete aggregates. Constr Build Mater 144:432–441
54. Al-bayati HKA, Das PK, Tighe SL, Baaj H (2016) Evaluation of various treatment methods for enhancing the physical and morphological properties of coarse recycled concrete aggregate. Constr Build Mater 112:284–298
55. Kumar GS, Minocha AK (2017) Studies on thermo-chemical treatment of recycled concrete fine aggregates for use in concrete. J Mater Cycles Waste Manage 20(1):469–480
56. Tam VW, Tam CM (2008) Diversifying two-stage mixing approach (TSMA) for RAC: TSMAs and TSMAsc. Constr Build Mater 22(10):2068–2077
57. Nili M, Sasanipour H, Aslani F (2019) The effect of fine and coarse recycled aggregates on fresh and mechanical properties of self-compacting concrete. Materials (Basel) 12:1–14
58. Berredjem L, Arabi N, Molez L (2020) Mechanical and durability properties of concrete based on recycled coarse and fine aggregates produced from demolished concrete. Constr Build Mater 246:118421
59. Gómez-Soberón JMV (2002) Porosity of recycled concrete with substitution of recycled concrete aggregate: an experimental study. Cem Concr Res 32(8):1301–1311

60. Corinaldesi V, Moriconi G (2009) Influence of mineral additions on the performance of 100% RAC. Constr Build Mater 23(8):2869–2876
61. Lotfy A, Al-Fayez M (2015) Performance evaluation of structural concrete using controlled quality coarse and fine recycled concrete aggregate. Cem Concr Compos 61:36–43
62. Djelloul OK, Menadi B, Wardeh G, Kenai S (2018) Performance of self-compacting concrete made with coarse and fine recycled concrete aggregates and ground granulated blast-furnace slag. Adv Concr Constr 6(2):103–121
63. Kumar BMV, Ananthan H, Balaji KVA (2017) Experimental studies on utilization of coarse and finer fractions of recycled concrete aggregates in self compacting concrete mixes. J Build Eng 9:100–108
64. Güneyisi E, Gesoglu M, Algın Z, Yazıcı H (2016) Rheological and fresh properties of self-compacting concretes containing coarse and fine recycled concrete aggregates. Const Build Mater 113:622–630
65. Sri Ravindrarajah R, Loo YH, Tam CT (1987) Recycled concrete as fine and coarse aggregates in concrete. Mag Concr Res 39(141):214–220
66. Puthussery JV, Kumar R, Garg A (2016) Evaluation of recycled concrete aggregates for their suitability in construction activities: an experimental study. Waste Manage 60:270–276
67. Vinay Kumar BM, Ananthan H, Balaji KVA (2018) Experimental studies on utilization of recycled coarse and fine aggregates in high performance concrete mixes. Alexandria Engg J 57:1749–1759

Restoration of Vertical and Lateral Stability of a Distressed RC Structure Adopting RC Jacketing and Composite Structural Members

Rakesh A. Patil and Y. K. Guruprasad

1 Introduction

A structure during its life span is subjected to various types of loads such as dead load, live load, earthquake, wind and loads induced due to fire. The loss of strength, stiffness and stability of a structure leads towards the failure of the structure. Loss of stiffness and load carrying capacity in a structural component (beams, columns or slabs) is predominately due to damage taken place in a structural component due to the over-stressed condition because of the applied loads. Failure of such over-stressed structural members leads towards partial or total collapse of the structure. Based on the amount of distress taken place in the over-stressed structural members, suitable retrofitting methods can be applied to such distressed structural members to restore them, when the damage is within repairable range.

Retrofitting is a technique through which the strength and load carrying capacity is restored and enhanced. This technique is mainly adopted to restore and enhance the strength and load carrying capacity of old or distressed structures. Structures damaged in the event of an earthquake are retrofitted to improve with stiffness, load carrying capacity and stability for further use when the damage is within repairable limits. Seismic retrofitting of structures is carried out at global and local levels. The cost for retrofitting is about 20 to 30% of the total construction cost.

Alaee and Karihaloo [1] developed a technique using the CARDIFRC strip bonding system which helps in improving the flexural and shear behaviour. As well

R. A. Patil · Y. K. Guruprasad (✉)
MTech Student, Structural Engineering, Department of Civil Engineering, Ramaiah Institute of Technology, Bangalore 580054, India
e-mail: guruprasadyk.civil.iisc@gmail.com

Y. K. Guruprasad
Associate Professor, Department of Civil Engineering, Ramaiah Institute of Technology, Bangalore 560054, India

517

as the serviceability of damaged concrete beams. It does not suffer from the drawbacks of the existing techniques. This technique does not mismatch in the properties between the concrete and the repair material.

The moment resistance and load-deflection response of the beams retrofitted using this technique can be predicted analytically. Providing that the strain hardening and tension softening. Research is currently being undertaken to study the fatigue, shrinkage and creep properties of CARDIFRC.

Bencardino and Condello [2] studied the structural performance of an innovative eco-friendly solution for RC members with deteriorated cover concrete. The beams strengthened with IRS-SRGM failed by concrete crushing and slippage at UHTSS-matrix interface. Whereas the beams strengthened with EB-SRGM failed by brittle end debonding. RC beams strengthened with one layer of SRGM system had an increase of the ultimate load from 16 to 30% after application.

Georgios and Dimos [3] studied three different seismic retrofit approaches in this paper. Reinforced concrete jacketing and concrete covered steel caging are two local retrofit approaches that help in upgrading structural performance. The installation of adequate steel bracings seems to be often necessary in overly under designed buildings. RC jacketing increased the load carrying capacity of column by 30%.

Lavorato and Nuti [4] carried out research studies on the seismic behaviour of repaired and seismically upgraded reinforced concrete bridges that were severely damaged after an earthquake. Pseudo-dynamic tests were performed on these bridges by means of in-house test apparatus. Complete comparison is made in design of bridge by Italian code and Euro code.

Based on the review of the literature, it is observed that the assessment of seismic damage in RC columns [5] and adopting and applying suitable retrofitting modalities on to such distressed RC columns helps in restoring the overall stability of the structure. It is also observed from the literature that application of a particular type of retrofitting based on the degree of damage that has taken place in the distressed columns need attention. This work mainly focuses on strengthening of RC columns that have undergone distress due to an over-stressed condition on account of earthquake [6] loads. Such over-stressed RC columns in this work are retrofitted adopting, RC jacketing and replacing excessively damaged over-stressed RC columns with composite column sections having structural steel sections encased in the concrete core of the columns. The uniqueness of this work is that the structural designer has the practical option of being selective on retrofitting, by adopting a particular optimum thickness of the RC jacket for a particular degree of damage by RC jacketing method or replacement of the RC column adopting composite column section when the degree of damage is beyond a certain degree of damage. In case the degree of damage of a particular column is more than 60%, then that particular column member is replaced with a composite column section. The RC jacketing method is preferred when the degree of damage ranges from 25 to 45%. Different thickness of RC jacket has been adopted in the present study to arrive at an optimum thickness of the RC jacket that is effective in restoring the strength and stiffness of the existing distressed RC columns, whose damage levels are within repairable limits. By adopting an optimum thickness of the RC jacket for retrofit, one is optimizing from the economy

point of view after priorly satisfying the structural safety. Composite columns having different sized structural steel sections encased in concrete are adopted in the present study, to arrive at an optimum composite section of the column, that is applied as a replacement to the existing RC column whose damage is beyond repairable limits. Using these optimization in retrofitting methods, the probability of reconstruction of the RC building is greatly avoided. The retrofitting adopted in the present work saves up to 65 to 70% of the actual total cost of the building to be newly constructed.

2 Retrofitting of Overstressed RC Columns in a Commercial Building Subjected to Earthquakes

A five storey RC commercial building is considered as case study in this work and is subjected to earthquake loading in ETABS. Response spectrum method has been adopted for analysing the commercial building for earthquake loading. The load cases considered in the analysis of the commercial building are dead load (DL), live load (LL) and earthquake load (EQ) in x and y directions in plan, respectively.

2.1 Details of Commercial Building

Size of the Commercial building	32 m × 28 m
Spacing of columns in x direction in plan	8 m
Spacing of column in y direction in plan	7 m
Size of column	350 mm × 700 mm
Size of beam = along x direction: $B1$	300 mm × 570 mm
Size of beam= along y direction: $B2$	300 mm × 500 mm
Thickness of slab	150 mm
Grade of Concrete (column, beam and slab)	M30
Shear wall thickness for lift wells (M40)	200 mm
Response Reduction factor	3
Earthquake Zone	5
Importance factor	1.5
Soil type	2

Fig. 1 Plan of five storey
commercial building
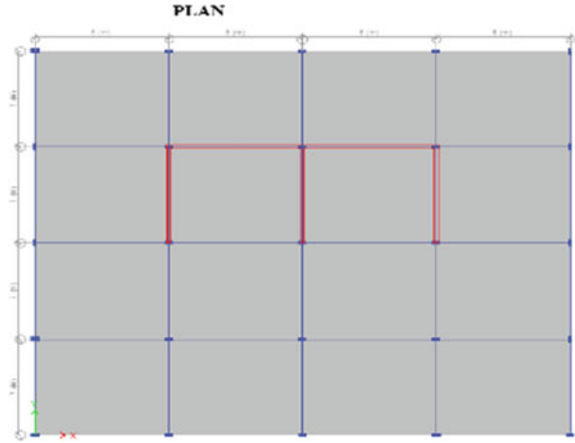
Magnitudes of Gravity Loads considered for analysis

Live load on floor (IS 875 Part 2)	5 kN/m² [8]
Dead load of Tile flooring (IS 875 Part 1)	1 kN/m² [7]
Wall load (IS 875 Part 1)	11 kN/m

2.1.1 Seismic Load Combinations Considered in the Analysis as Per IS Code 1893 (Part-1) 2016 [6]

(1) $1.2(DL + LL \pm (EQx \pm 0.3EQy))$
(2) $1.2(DL + LL \pm (EQy \pm 0.3EQx))$
(3) $1.5(DL + LL \pm (EQx \pm 0.3EQy))$
(4) $1.5(DL + LL \pm (EQy \pm 0.3EQx))$
(5) $0.9(DL + LL \pm (EQx \pm 0.3EQy))$
(6) $0.9(DL + LL \pm (EQy \pm 0.3EQx))$

The plan view of the five storey commercial building is shown in Fig. 1. The over-stressed columns C17, C20 and C23 identified in the structure when subjected to seismic load combinations are shown in Fig. 2.

2.2 Retrofitting the RC Structure by Adopting RC Jacketing

In this method, the columns that are over stressed are retrofitted adopting RC jacketing. Different RC jacket [9] thickness (100 mm, 125 mm, 150 mm and 200 mm) are applied individually on to over-stressed RC columns that have been identified in the structure to determine the optimum RC jacket thickness. The RC columns C17,

Failure of RC
columns in the commercial
building due to over stress

Overstressed Columns
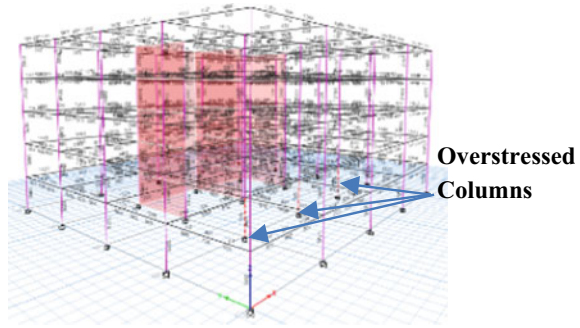
C20 and C23 that are retrofitted individually with RC jacket having the following thicknesses: 100 mm, 125 mm, 150 mm and 200 mm, respectively. The results of retrofitting of over-stressed RC columns adopting RC jacket having different thicknesses are shown in Table 1.

Figure 3 shows the typical cross sectional details of addition of a 100 mm thick RC jacket around one of the over-stressed RC column.

Table 1 Shear force, bending moment and torsion in the RC columns retrofitted adopting RC jackets having different thicknesses

Column No.	RC column retrofitted with RC jacket having different thicknesses (mm)	Bending moment (kN-m)		Shear force (kN)	Torsion (kN-m)
		At support	At span	At support	
C17	100	813.42	397.55	347.44	17.05
	125	980.54	494.05	403.91	21.27
	150	1163.69	612.93	463.56	26.42
	200	1570.17	868.46	590.8	35.87
	100	797.97	401.03	327.09	17.13
	125	964.07	507.7	381.23	21.38
	150	1146.72	614.64	438.56	26.56
	200	1553.66	860.92	563	36.08
C23	100	790.67	411.08	317.58	17.13
	125	956.28	510.58	370.56	21.38
	150	1138.82	631.73	427.35	26.55
	200	1546.71	893.31	550.75	36.05

Fig. 3 Typical cross section
showing retrofitting of RC
columns adopting $t = $
100 mm thick RC jacketing

18 numbers of
16 mm dia bars

10 numbers of
16 mm dia bars

Lateral ties of 8 mm
dia at 200 mm c/c

All dimensions are in mm
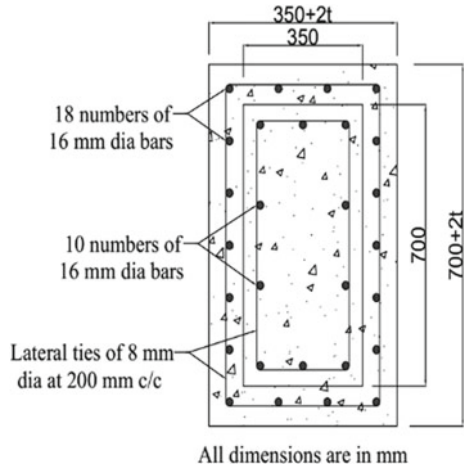
2.3 Retrofitting by Replacement of the Over-Stressed RC Columns by Composite Column Section Encased ISMB Column Sections

The columns C17, C20 and C23 that are over stressed are replaced by composite column sections as a second case of retrofitting [10] to study the reduction in storey displacements and improvement in the stability of the overall structure.

The composite column sections consist of an I section that is encased with lateral ties of 8 mm diameter at 200 mm spacing with 10 numbers of longitudinal rebars having diameter of 16 mm all embedded in M30 grade concrete.

A typical cross section of the composite column section with ISMB200 encased inside it is shown in Fig. 4.

Fig. 4 Typical cross section
of composite
column—ISMB200 encased
column section

Lateral ties of 8 mm
dia at 200 mm c/c

ISMB200

10 numbers of
16 mm dia bars

All dimensions are in mm
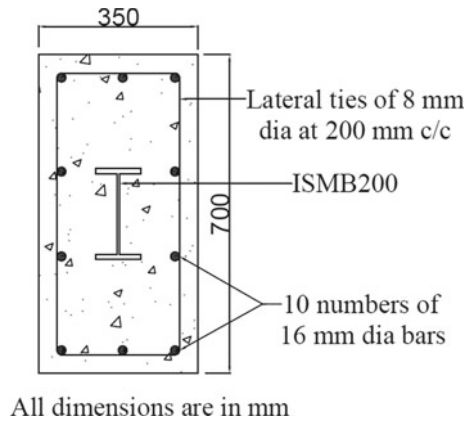
3   Results and Discussion

Lateral displacement of each storey is shown in Fig. 5 before retrofitting. The results are obtained in ETABS for envelope load combination.

Lateral displacement of the building verses number of storeys when the over-stressed RC columns C17, C20 and C23 are retrofitted adopting an RC jacket thickness of 100 mm, 125 mm, 150 mm and 200 mm are shown in Figs. 6, 7, 8 and 9, respectively.
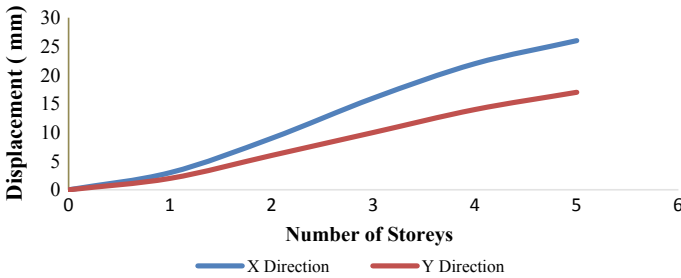
Fig. 5   Displacement of RC structure before application of retrofitting
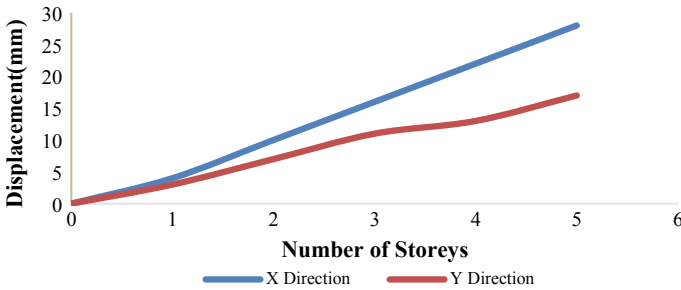
Fig. 6   Displacement of RC structure after adopting RC jacketing of 100 mm thickness
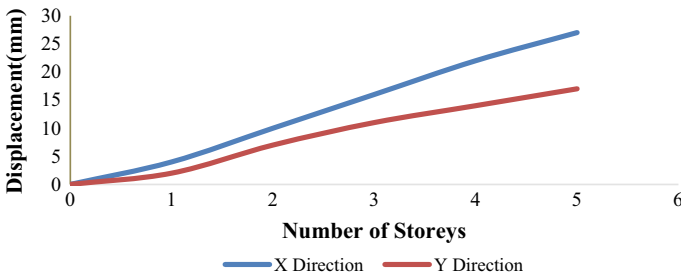
Fig. 7   Displacement of RC structure after applying RC jacketing of 125 mm thickness
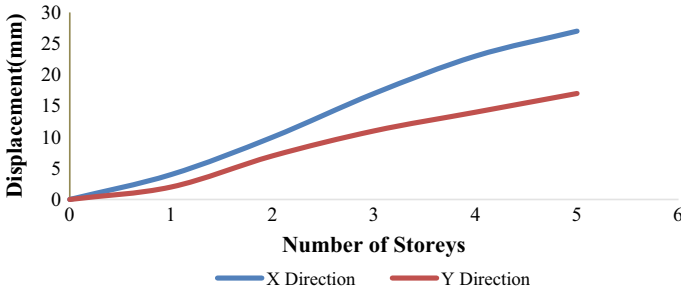
Fig. 8 Displacement of RC structure after application of RC jacketing 150 mm thickness
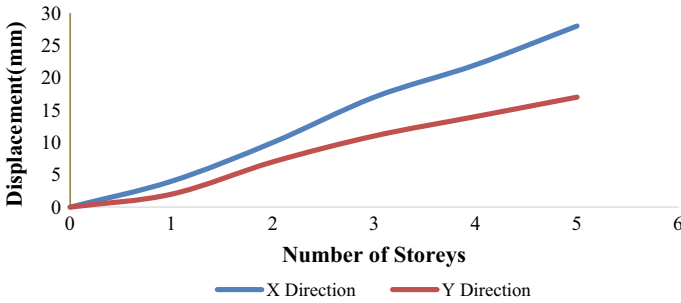
Fig. 9 Displacement of RC structure after applying RC jacketing of 200 mm thickness

The shear force, bending moment and torsion developed in the retrofitted RC columns C17, C20 and C23 for different thicknesses of the RC jacket applied individually on the RC columns are given in Table 1.

Lateral displacement of each storey after replacing the overstressed RC columns C17, C20 and C23 with composite column sections encased with ISMB200, ISMB250 and ISMB300 is shown in Figs. 10, 11 and 12, respectively.
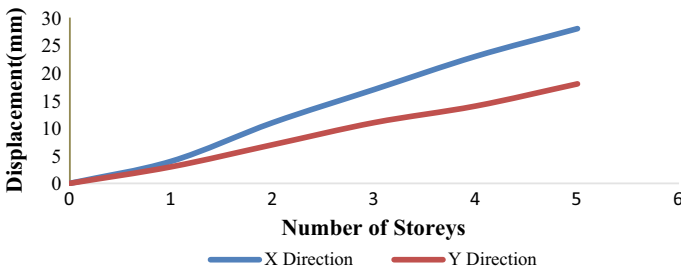
Fig. 10 Lateral displacement of each storey after replacing the over-stressed RC columns C17, C20 and C23 with composite column sections encased with ISMB200
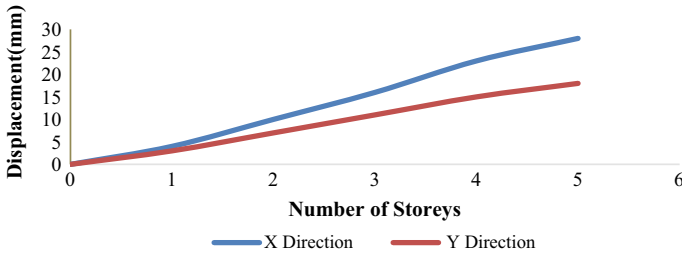
Fig. 11 Lateral displacement of each storey after replacing the over-stressed RC columns C17, C20 and C23 with composite column sections encased with ISMB250 section
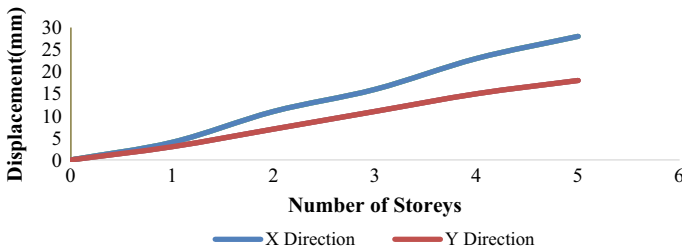
Fig. 12 Lateral displacement of each storey after replacing the over-stressed RC columns C17, C20 and C23 with composite column sections encased with ISMB300 section

The shear force, bending moment and torsion developed in the composite columns that have been provided as a replacement of over-stressed RC columns C17, C20 and C23 having different ISMB sections encased in the composite column sections applied individually in the structure is shown in Table 2.

By observing the results shown in Table 3, it is found that the top storey lateral displacement of the RC structure decreases with increase in thickness of the RC jacket. The RC structure without retrofitting undergoes a maximum lateral displacement of 29 mm along the *X* direction. The structure which is retrofitted with RC jacketing having a jacket thickness of 125 mm and 200 mm undergoes a maximum lateral displacement of 26 mm along the *X* direction when subjected to earthquake loading.

By observing the results shown in Table 4, it is found that the top storey lateral displacement of the RC structure decreased with increase in the size of the ISMB steel section that is encased in the composite column section. The RC structure without retrofitting undergoes a maximum lateral displacement of 29 mm along the *X* direction. The structure which is provided with composite columns as a replacement of the over-stressed RC columns was found to have a minimum lateral displacement of 23 mm along the *X* direction when subjected to earthquake loading for both ISMB250 and ISMB300 steel section that are embedded in the column section.

Table 2 The shear force, bending moment and torsion developed in the composite columns that have been provided as a replacement of over-stressed RC columns C17, C20 and C23 having different ISMB sections encased in the composite column sections applied individually in the structure

Column No.	Encased RC column with different ISMB sections	Bending moment (kN-m)		Shear force (kN)	Torsion (kN-m)
		At support	At span	At support	
C17	200	317.48	127.32	157.83	4.51
	250	323.18	129.81	160.54	4.52
	300	329.85	132.01	163.52	4.52
C20	200	309.96	129.25	148.79	4.53
	250	315.06	131.82	151.04	4.53
	300	321.44	134.99	153.69	4.54
C23	200	307.07	132.32	145.65	4.53
	250	312.2	136.23	147.7	4.54
	300	318.44	138.32	150.2	4.54

Table 3 Top storey displacement of RC structure retrofitted by using RC jacketing

	RC jacketing 100		RC jacketing 125		RC jacketing 150		RC jacketing 200	
	Direction		Direction		Direction		Direction	
	X	Y	X	Y	X	Y	X	Y
Displacement of top storey no. 5 (mm)	28	17	26	16	27	17	26	14

Table 4 Top storey displacement of RC structure without retrofitted and with application of encased ISMB

	Without retrofitting		ISMB200		ISMB250		ISMB300	
	Direction		Direction		Direction		Direction	
	X	Y	X	Y	X	Y	X	Y
Displacement of top storey no. 5 (mm)	29	17	28	18	23	14	23	11

It observed from results in Table 3 that when the retrofitting is carried out adopting RC jacketing to restore the over-stressed RC columns C17, C20 and C23 the RC jacket having thickness of 125 mm was found to be the optimum thickness to be provided for retrofitting of the columns. By observing the results presented in Table 4, the composite columns that are provided as replacement of over-stressed RC columns C17, C20 and C23 having ISMB250 steel section embedded was found to be the optimum composite column section as a restoration measure. It may be noted that

both RC jacketing method of retrofitting and replacement of over-stressed columns using composite section are structurally effective in restoring the distressed structure in the present work. It may be noted, from a construction and cost point of view an RC jacket having a thickness of 125 mm is found to be a comparatively an effective retrofit solution in the present study.

4 Conclusions

- It is observed from the results in the case of retrofitting adopting RC jacketing method, to restore over-stressed RC columns C17, C20 and C23, an RC jacket having a thickness of 125 mm is structurally and economically effective when compared to larger RC jacket thicknesses (150 mm and 200 mm) in the present study.
- It is observed from the results in the case of replacing over-stressed RC columns C17, C20 and C23, with composite columns with ISMB steel section embedded in the composite column sections, a composite column section having ISMB250 steel section embedded was found to be the optimum composite column section for restoration purpose.
- It may be noted that both RC jacketing method of retrofitting and replacement of over-stressed columns using composite section are structurally effective in restoring the distressed structure in the present work. It may be further noted that from a construction and cost point of view an RC jacket having a thickness of 125 mm is found to be a comparatively an effective retrofit solution in the present study.
- Retrofitting in terms of replacement of RC columns that are severely over stressed or damaged adopting composite column sections is preferred, when the degree of damage in the column is very high (damage > 65 to 75%).

References

1. Alaee FJ, Karihaloo BL (1990) Retrofitting of reinforced concrete beams with CARDIFRC. J Compo Constr 7(3):174–186
2. Bencardino F, Condello A (2016) Innovation solution to retrofit RC member. Construc & Build Mater 117:171–181
3. Georgios, Dimos (2006) Seismic retrofit schemes for RC structures and local–global consequences. Prog Struct Eng Mater 8:1–15
4. Lavorato D, Nuti C (2015) Pseudo dynamic tests on reinforced concrete bridges repaired and retrofitting after seismic damage. J Eng Struct 1–12
5. IS 456(2000) Plain and reinforced concrete—code of practice. Bureau of Indian Standards, New Delhi
6. IS 1893-Part1 (2016) Criteria for earthquake resistant design of structures. Bureau of Indian Standards, New Delhi

7. IS 875-Part 1 (1987) Dead loads—code of practice for design loads (other than earthquake) for building and structures. Bureau of Indian Standards, New Delhi
8. IS 875-Part 2 (1987 Reaffirmed 2008) Live loads—code of practice for design loads (other than earthquake) for building and structures. Bureau of Indian Standards, New Delhi
9. Karayannis CG, Challoris C, Sirkells GM (2008) Local retrofit of exterior RC beam—column joints using thin RC jackets—An experimental Study. Earthq Eng Struct Dyn 37(5):727–746
10. Antonopoulos CP, Trianafillou TC (2003) Experimental investigation of FRP—strengthened RC beam column joints. J Compos Constr 7(1):39–49

Experimental and Numerical Studies on the Effect of Built-In Gradient on Rigid Pavements

Priya Grace Itti Eipe, M. Nazeer, and Reebu Zachariah Koshy

1 Introduction

Rigid pavements have become an intrinsic part of transportation systems all over the world due to the specific advantages they offer over flexible pavements. They can withstand heavy traffic loads, provide a good riding surface, do not require frequent maintenance and are easy to construct. However the high initial construction cost can be a disadvantage. By ensuring a long service life, rigid pavements can be made cost effective, economic and hence a sustainable option.

Extensive research is being carried out to study the various causes of pavement deterioration and the different methods that can be adopted to prevent or delay them. In this context it has been seen that apart from the stresses generated in the pavement due to the various traffic loads, temperature and moisture gradients that develop in the pavement slab can also lead to the generation of additional stresses that can get added on to the existing stresses in the pavement slab, ultimately resulting in critical stress levels that can cause deterioration of the pavement. These temperature and moisture gradients on the other hand depend on the climatic conditions that exist at the the time of construction of the pavement. This in turn largely depends on the geographic location of the pavement system. Hence, region specific studies could

P. G. I. Eipe (✉)
Department of Civil Engineering, Mahaguru Institute of Technology, Kayamkulam, Kerala 690503, India
e-mail: priyaittieipe@gmail.com

M. Nazeer
Department of Civil Engineering, TKM College of Engineering, Kollam, Kerala 691005, India

R. Z. Koshy
Department of Civil Engineering, Saintgits College of Engineering, Kottayam, Kerala 686532, India

help in adoptng better design and construction techniques for the longevity of the pavement system.

Such a study is being attempted here on slab specimens constructed under the climatic conditions of Kerala in India. Kerala has a tropical *climate* whereas large pavement studies have been seen to be conducted in countries of temperate climatic zones. Hence such a study conducted in Kerala would give an insight into the actual temperature and moisture gradients that develop in the pavement slabs.

2   Temperature Stresses

Concrete pavement slabs when exposed to atmospheric conditions may develop a temperature and/or moisture gradient in the pavement slab depth since the slab top is directly exposed to the atmosphere whereas the slab bottom is in contact with the sub grade and hence not influenced by the atmospheric conditions directly. The pavement slab may then undergo deflections called curling due to the temperature gradient and warping due to the moisture gradient. These deflections may then generate stresses in the slab.

In a tropical region like India, due to the intense solar radiation during the daytime, positive temperature differentials exist in the slab due to which the slab corners curl downwards since the slab expands more on the top when compared to the bottom. Since this curling is resisted by the self-weight of the slab, it will exert stresses of opposite nature. That is, compressive stresses at the top of the slab and tensile stresses at the bottom of the slab. During night time, the negative temperature differential between the top and bottom of the slab results in upward curling of the concrete slab since the slab expands more at the bottom when compared to the top. This curling of the slab is resisted by its self-weight and restraining condition provided by the sub grade support. Hence tensile stresses are exerted at the top of the slab and compressive stresses are exerted at the bottom of the slab.

Moisture gradients generally result in upward warping since the exposed surface of the slab is more prone to drying out resulting in the top of the slab contracting more than the bottom.

3   Built-In Temperature Gradients

Temperature and moisture gradients that develop in concrete slabs can be transient or permanent, where transient gradients are due to the seasonal changes to which the slabs are subjected whereas permanent gradients are due to atmospheric conditions the slab is exposed to during the setting of slab. Permanent gradients are also known as built-in temperature gradients.

Temperature gradients that exist during the construction of a pavement slab do not result in any deflection in the slab since the slab remains flat due to the plastic

stage of the concrete. However when the slab hardens enough to withstand strain the temperature gradient that exists at that particular moment gets captured in the pavement slab and is known as the built-in temperature gradient. The slab remains flat at this built-in temperature gradient and curls at any other temperature gradient. It can be seen that this built-in temperature gradient results in the building up of a permanent curl in the slab. The built-in temperature gradient of a slab plays a significant role since this gradient has to be added algebraically to the actual temperature differential existing at any time in the slab for the correct evaluation of stresses in the slab. A proper evaluation of the stresses thus results in a proper design of the pavement slab thus increasing its life span.

4 Literature Review

Literature review was carried out for the experimental and numerical investigations to be carried out.

4.1 Experimental Analysis

Armaghani et al. [1] studied the temperatures in a pavement slab and the corresponding horizontal and vertical displacements in the pavement slab, so as to obtain a proper insight into the response of the pavement slab to temperature. Helpful conclusions were arrived at in the study. Siddique [2] studied the curling in a pavement slab when subjected to temperature differentials across the slab thickness. Correlations between the magnitude of the differential and the curling were established. Jeong and Zollinger [3] conducted a study on the temperature, moisture and creep effects on a pavement slab under different curing conditions. It was seen that the method of curing had an impact on the slab behaviour. Vandenbossche and Asbahan [4] conducted a study on the effects of temperature and moisture gradients on slab curvatures for JPCPs. A comparison using the measured and default built-in temperature gradients was also carried out and it was seen that the MEPDG default value was suitable for restrained slabs. Nassiri and Vandenbossche [5] proposed a method to estimate built-in temperature gradients for JPCPs in Pennsylvania. A temperature model was also suggested on the basis of this study.

4.2 Numerical Analysis

Maitra et al. [6] developed a finite element model to estimate the critical stresses that may develop in a concrete pavement due to the combined effect of wheel load and positive temperature gradient. A generalized equation was also suggested in the

study for this purpose. Westergaard [7] conducted a mathematical analysis and developed a method by which stresses in a round concrete slab could be computed. This method was then applied for the stress calculations and design of concrete pavement slabs. Belletti et al. [8] arrived at a nonlinear finite element method by which proper modeling of Fibre Reinforced Concrete could be carried out. A comparison between the behaviour of concrete when reinforced by either steel fibres or steel bars or a combination of both was also done. Belletti et al. [9] conducted a numerical analysis in which the development of primary and secondary cracks in steel fibre reinforced concrete slabs was simulated. The numerical results were validated on comparison with the experimental results. Maitra et al. [10] examined the load transfer efficiency of a pavement joint under varying parameters and a 3-D finite element model was developed for this purpose. The individual and group action of dowel bars was also looked into and relationships between the two were established. Joseph et al. [11] adopted a modeling technique for conducting a numerical nonlinear static analysis of concrete pavements and showed that the results of the numerical analysis and that of Westergaard's method had close similarity. Elsaigh et al. [12, 13] conducted research and presented a material model and a slab model to determine the tensile stress–strain responses of SFRC slabs which was then used in the nonlinear finite element analysis of the slabs. The load displacement response of these slabs was also studied. The calculated results compared well with the experimental observations. Koshy et al. [14] studied and compared the performance and efficiency of PCC and SFRC pavements by conducting a nonlinear static analysis. It was seen that the ultimate load carrying capacity and joint efficiency for the SFRC slabs was significantly better. Mackiewicz [15] considered additional features regarding the interaction between the dowels and concrete whilst conducting a finite element analysis of pavement slabs and arrived at empirical equations and relationships that would be helpful in pavement slab design.

5 Experimental Investigations

To study the effect of built-in temperature gradients, an experimental analysis was conducted on beam specimens used to simulate the pavement slab and subjected to exposed atmospheric conditions. The beam specimens were cast of size 0.15 m × 0.15 m × 1.0 m. One set of beams were cast in the morning and another set was cast in the afternoon. The temperature gradients in the beams were calculated on an hourly basis by measuring the temperature at the various depths in the beam hourly. The temperatures were measured using thermocouples embedded at the required depths in the concrete specimens. After the hardening of the beams the deflections of the beam were also measured. For the measurement of deflections dial gauges were mounted on the beam at one-third of the length of the beam specimens and measurements were taken. Fibre reinforced concrete beam specimens were also used for the experiments along with the plain cement concrete specimens to study whether fibre reinforced

concrete had any influence on the built-in temperature gradient and deflection of the beams. For this purpose polypropylene and coir fibres were used.

6　Numerical Investigations

The beam specimens were modeled in ANSYS using SOLID185 element. Measured temperatures across the depth of the specimen were applied on the model at nodes corresponding to that depth. The input parameters required for analysis were Modulus of elasticity, Poisson's ratio, coefficient of thermal expansion, reference temperature and density of concrete.

7　Results and Discussion

The results of the experimental analysis conducted on the various specimens made of PCC and FRC are represented in graphical form. The numerical analysis carried out can be seen to validate the experimental results.

A sample plot of the deflected shape and the stress variation of the PCC specimen as obtained by the numerical analysis is given in Fig. 1.

The temperatures along the depth of the PCC, Synthetic FRC and Coir FRC specimens cast in the morning, measured on an hourly basis on day 1, the day of casting, are given in Fig. 2.

The day 1 temperatures can be seen to be influenced by the heat of hydration of concrete apart from the external atmospheric temperature. The mid-depth temperatures are seen to increase for each hourly measurement for both PCC and coir FRC specimens. In the case of synthetic FRC, the mid-depth temperatures are seen to decrease for the early hours of the day. For both the FRC specimens, the mid-depth and bottom temperatures are seen to be spread over a wider range of temperature with the bottom temperatures mostly lower than the top. Coir FRC specimens are seen to have lowest top temperatures throughout the day.

The temperature variation along the depth of the PCC, Synthetic FRC and Coir FRC specimens cast in the morning, on day 2, the next day of casting, are given in Fig. 3.

The day 2 temperatures depend mainly on the ambient temperature. The recorded ambient temperature for day 2 is seen to be lower than that for day 1. Also since the heat of hydration is less at this stage there is not much heat generation from within the concrete specimens. As a result the temperatures at the top, mid-depth and bottom of the specimens are lower than that of day 1 and are almost within the same range. Synthetic FRC specimens show a wider range for mid-depth and bottom temperatures. Coir FRC specimens are seen to have lowest top, middle and bottom temperatures throughout the day.
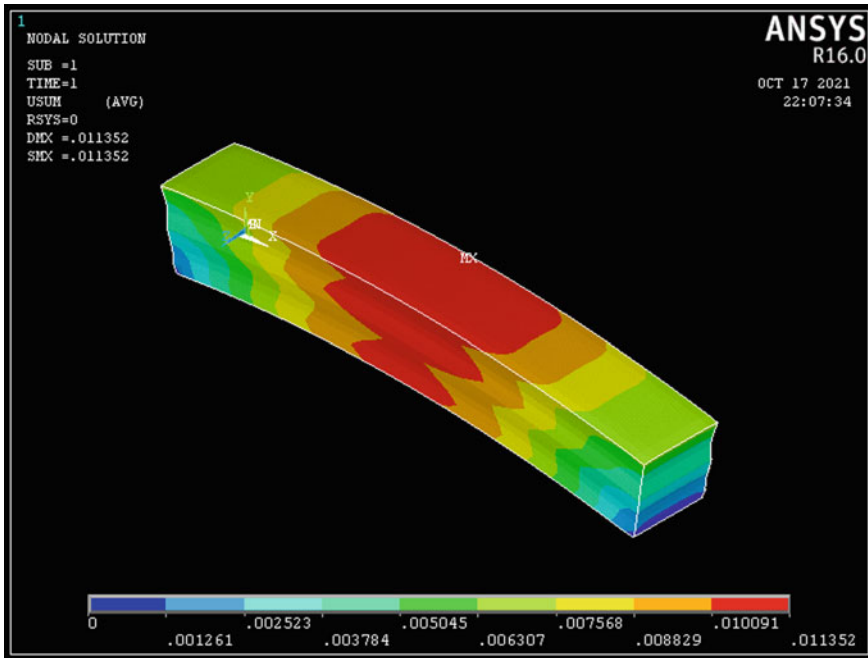
Fig. 1 ANSYS plot of deflected shape and stress variation of the PCC specimen

The temperature variation along the depth of the PCC, Synthetic FRC and Coir FRC specimens cast in the afternoon, on day 1, the day of casting, are given in Fig. 4.

As seen earlier, the day 1 temperatures are influenced by the heat of hydration of concrete. However since the specimens were cast in the afternoon, with the heat of hydration yet to peak and the declining ambient temperature, the measured temperatures are much lesser than those for the morning specimens. The mid-depth and bottom temperatures are higher than the top temperatures for all specimens. Synthetic FRC specimens have lower temperatures at all depths.

The temperature variation along the depth of the PCC, Synthetic FRC and Coir FRC specimens cast in the afternoon, on day 2, the next day of casting, are given in Fig. 5.

For the afternoon specimens, the day 2 temperatures are influenced to a certain extent by the heat of hydration. The ambient temperature also contributes towards the temperatures. The ambient temperature for day 2 is lower than that for day 1 as seen earlier. However the combined effect of heat of hydration and ambient temperature leads to higher temperatures along the depth of the specimens. The temperatures at the top are seen to be higher than those at the mid-depth and bottom of the specimens. FRC specimens show a wider range of temperature at the mid-depth and the bottom with synthetic FRC specimens showing least temperatures at the bottom.

The temperature gradients in the PCC, Synthetic FRC and Coir FRC specimens cast in the morning and afternoon, on day 1 and day 2, are given in Fig. 6.
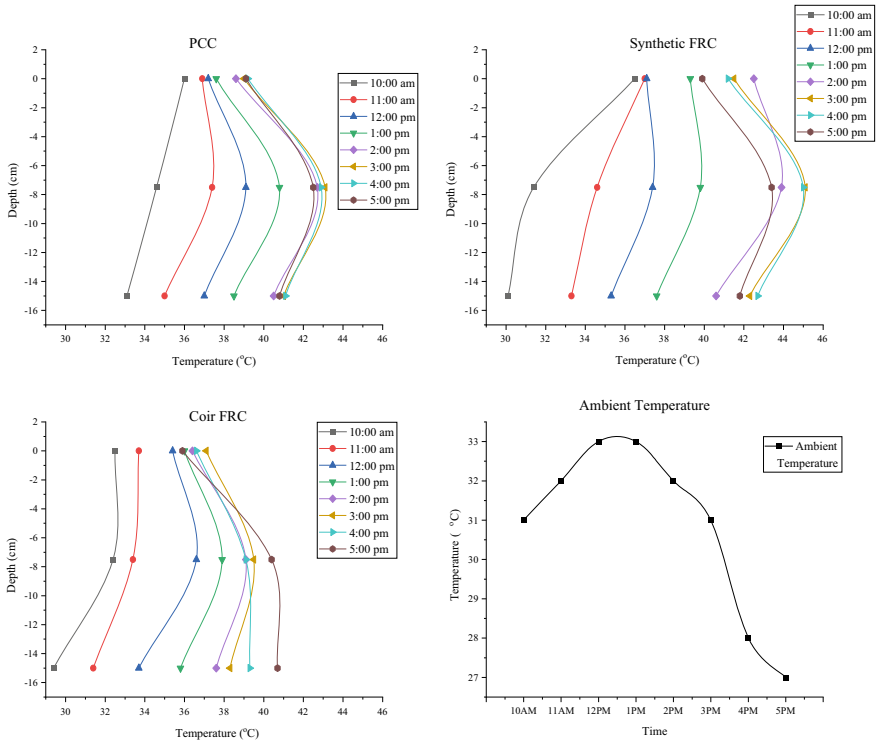
Fig. 2 Temperature variation for morning specimens (day 1)

The temperature gradients in the morning specimens on day 1 and day 2 as well as in the afternoon specimens for day 2 are positive for the morning hours and negative towards the evening. In the case of afternoon specimens, on day 1 due to higher bottom temperatures the temperature gradients are predominantly negative. In the case of morning specimens on day 1 and afternoon specimens on day 2, when heat of hydration is generated and internal body temperatures are high, the FRC specimens are seen to have greater gradient magnitudes than PCC specimens since the temperatures are dissipated to a lower range at the bottom of the specimens. For morning specimens on day 2 and afternoon specimens on day 1 when the temperatures are mainly dependent on the ambient temperature, the FRC specimens are seen to have smaller gradient magnitudes than PCC specimens since the top temperatures are not carried much into the depth of the specimen.

It can be seen that late morning/afternoon construction of pavements can lead to negative temperature gradients being captured in the pavement slab.

When the temperatures in the pavement slab are mainly dependent on the ambient temperature, the FRC specimens are seen to have smaller gradient magnitudes than PCC specimens since the top temperatures are not carried much into the depth of the specimen.
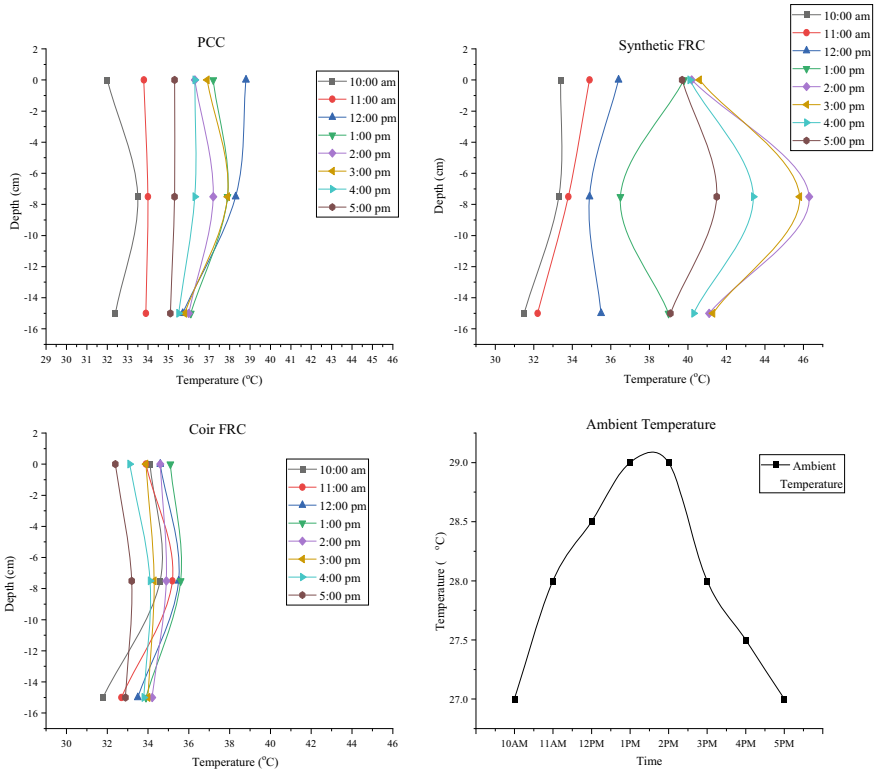
Fig. 3 Temperature variation for morning specimens (day 2)

The deflections of the specimens cast in the morning and measured on day 2 are shown in Fig. 7.

The deflections measured during the day time show that the PCC specimens have maximum deflections during the afternoon hours whereas the FRC specimens have maximum deflection during the evening hours.

The deflections of the specimens cast in the afternoon and measured on day 2 are shown in Fig. 8.

Similar to the morning specimens, the deflections of the afternoon specimens measured during the day time show that the PCC specimens have maximum deflections during the afternoon and the FRC specimens have maximum deflection during the evening hours.

In both the cases of deflection measurements it can be seen that FRC specimens have a delayed maximum deflection occurring towards the evening.

Future scope for conducting further studies in the field of pavement construction in Kerala may include studies held during the monsoon season of Kerala. Late night or early morning studies can also be carried out for both the summer and monsoon climates in Kerala.
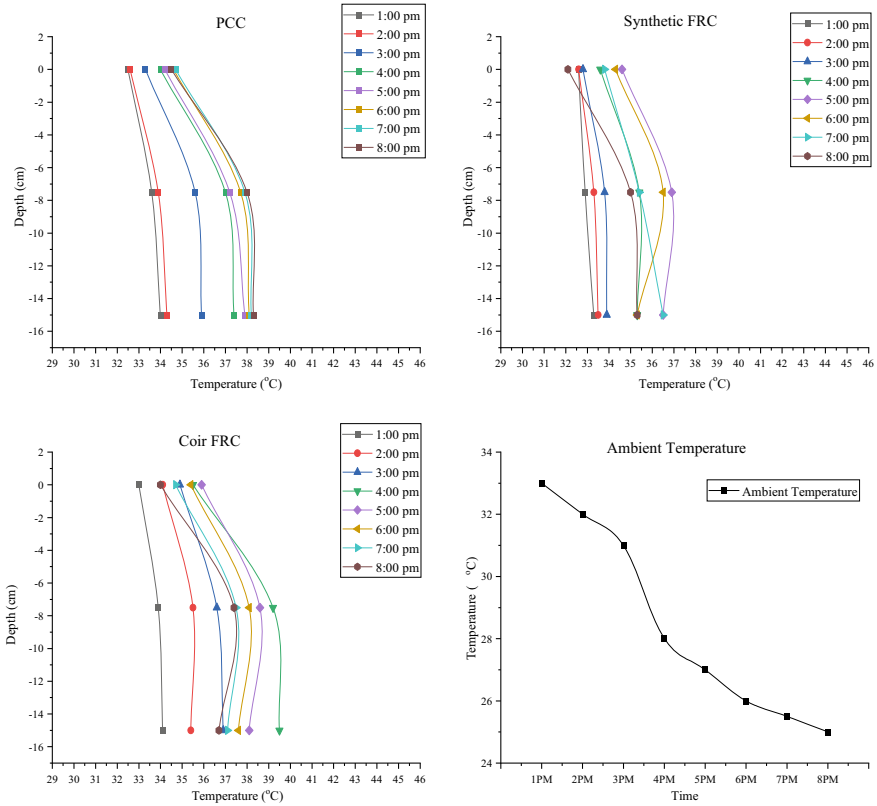
Fig. 4 Temperature variation for afternoon specimens (day 1)

8   Conclusions

After conducting this study it was seen that:

- During the summers in Kerala, the hot conditions that exist during the day time can result in high positive built-in temperature gradients in the pavement slabs cast in the late night/early morning hours. However casting the pavement slabs during the daytime i.e. late morning/afternoon/early evening can prevent such a build up of heat and result in negative built-in gradients of lesser magnitude.
- For FRC specimens, the mid-depth and bottom temperatures are seen to be spread over a wider range of temperature with the bottom temperatures mostly lower than the top. FRC specimens are also seen to have smaller gradient magnitudes than PCC specimens when subjected to any given ambient temperature.
- The experimental and numerical results are within comparable range and hence can be validated.
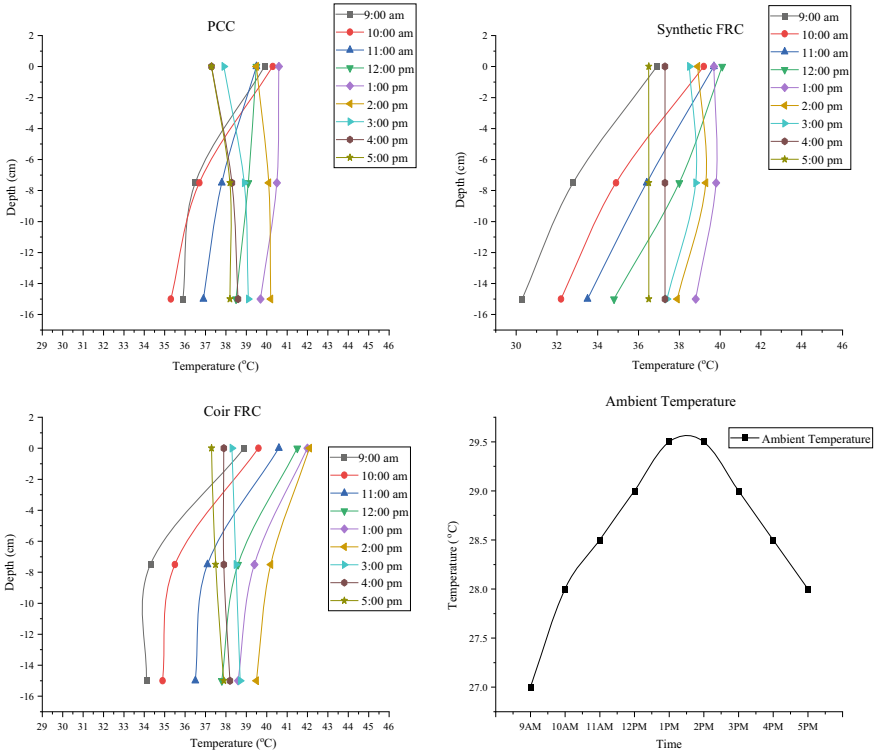
Fig. 5 Temperature variation for afternoon specimens (day2)
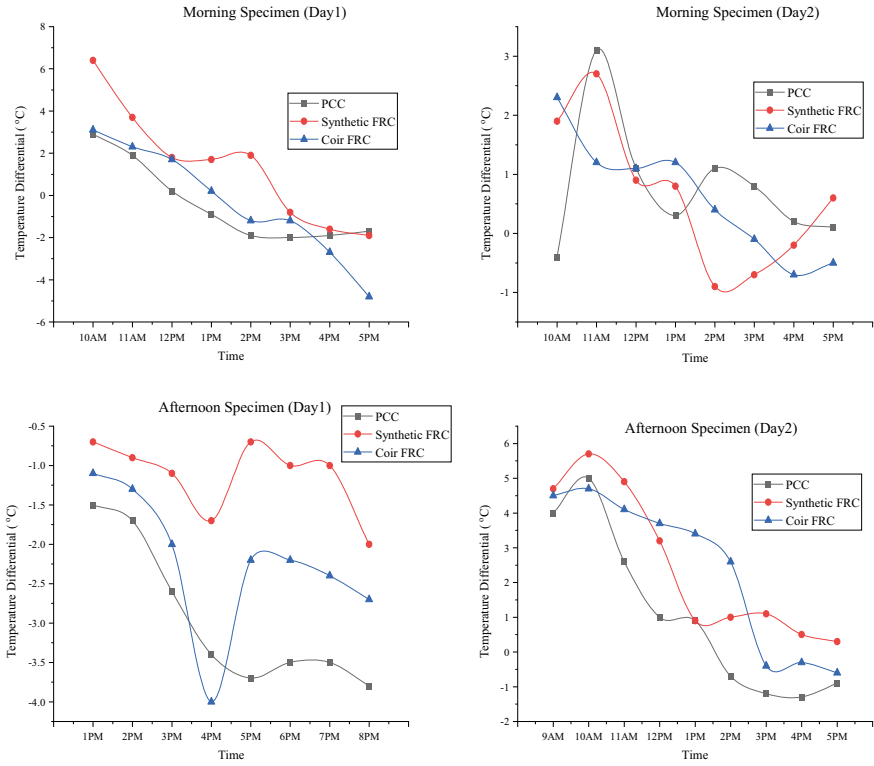
Fig. 6 Temperature gradients in the morning and afternoon specimens
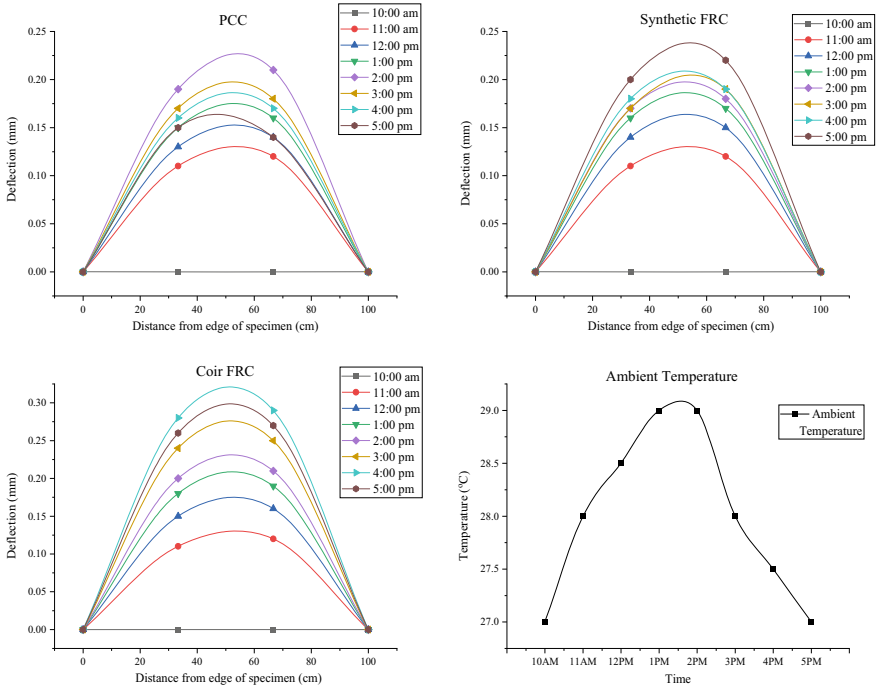
Fig. 7 Deflections in the morning specimens (day 2)
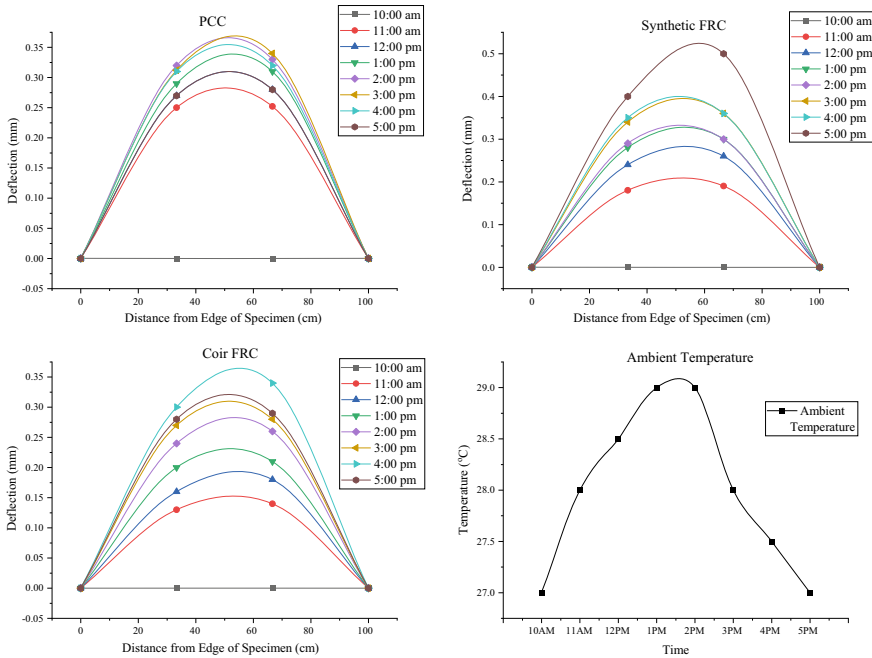
Fig. 8 Deflections in the afternoon specimens (day 2)

References

1. Armaghani JM, Larsen TJ, Smith LL (1987) Temperature response of concrete pavements. Transp Res Rec 1121:23–33
2. Siddique ZQ (2005) Temperature and curling measurements on concrete pavement. In: Proceedings of the mid-continent transportation research symposium, Ames, Iowa
3. Jeong JH, Zollinger D (2004) Early-age curling and warping behaviour: insights from a fully instrumented test-slab system. Transp Res Rec 1896(1):66–74
4. Vandenbossche JM, Asbahan RE (2011) Effects of temperature and moisture gradients on slab deformation for jointed plain concrete pavements. J Transp Rec 137(8):563–570
5. Nassiri S, Vandenbossche JM (2012) Establishing built-in temperature gradient for jointed plain concrete pavements in Pennsylvania. Int J Pavement Res Technol 5(4):245–256
6. Maitra SR, Reddy KS, Ramachandra LS (2013) Estimation of critical stress in jointed concrete pavement. In: 2nd conference of transportation research group of India (2nd CTRG). Soc Behav Sci 104(11):208–217
7. Westergaard HM (1926) Stresses in concrete pavements computed by theoretical analysis. Public Roads 7(2):25–35
8. Belletti B, Bernardi P, Meda A, Plizzari G (2004) A NLFM method for the prediction of slabs on grade behaviour. In: Digital repository, Convegno IGF XVII Bologna
9. Belletti B, Cerioni R, Meda A, Plizzari G (2008) Design aspects on steel fiber-reinforced concrete pavements. J Mater Civ Eng © ASCE 20(9):599–607
10. Maitra S, Reddy K, Ramachandra L (2009) Load transfer characteristics of dowel bar system in jointed concrete pavement. J Transp Eng 135(11):813–821

11. Joseph A, Koshy RZ, Nair SS (2011) Numerical modeling of rigid pavements using finite element method. In: Proceedings of international conference on advances in materials and techniques for infrastructure development, NIT Calicut T031
12. Elsaigh WA, Robberts JM, Kearsley EP (2011) Modeling the behavior of steel-fiber reinforced concrete ground slabs. I: development of material model. J Transp Eng © ASCE 137(12):882–888
13. Elsaigh WA, Robberts JM, Kearsley EP (2011) Modeling the behavior of steel-fiber reinforced concrete ground slabs. II: development of slab model. J Transp Eng © ASCE 137(12):889–896
14. Koshy RZ, Joseph A, Nair SS (2013) Steel fibre reinforced concrete pavement slabs with contraction joints. In: Proceedings of international conference on advances in civil, structural and environmental engineering—Zurich, pp 130–33. ISBN 978-981-07-7965-8
15. Mackiewicz P (2015) Finite-element analysis of stress concentration around dowel bars in jointed plain concrete pavement. J Transp Eng 141(6):06015001

Improving Resistance Towards Progressive Collapse of RC Structures Subjected to Seismic Loads

C. K. Mohamed Saqlain and Y. K. Guruprasad

1 Introduction

Earthquakes cause destruction and loss of lives due to partial or total collapse of buildings when they occur. A seismic resistant design will help in saving lives and minimising major structural damages in the event of an earthquake. Hence, it is important to design the structures to be resistant towards seismic loads. In the event of an earthquake, reversal of stresses occurs in the structure. RC frame structures with plan irregularity face severe shear in columns due to torsion taking place. The collapse of the structure in the event of an earthquake is initiated due to formation of plastic hinges in critically stressed zones in the structural members. Progressive collapse is an event where damage in a portion of an RC structure causes further failure of other structural members that are located near the zone of damage. Petrone et al. [1] studied modelling of RC frame buildings for progressive collapse analysis. Time history analysis was carried out for sudden failure of a column. Simulations were done mimicking extreme events via column-removal scenarios. By using a RC frame building model and considering constitutive modelling of materials, gravity loads were discussed with the goal of achieving consistent models that can be used in collapse scenarios. These collapses involved successive loss of loadbearing columns at lower level of the structure. An energy-based approach for identifying the proximity to collapse of regular multi-storey buildings was proposed. Nethercot [2] studied the design of building structures to improve their resistance to progressive

C. K. Mohamed Saqlain · Y. K. Guruprasad (✉)
MTech Student, Structural Engineering, Department of Civil Engineering, Ramaiah Institute of Technology, Bangalore 560054, India
e-mail: guruprasadyk.civil.iisc@gmail.com

Y. K. Guruprasad
Associate Professor, Department of Civil Engineering, Ramaiah Institute of Technology, Bangalore 560054, India

543

collapse. The critical columns were identified and removed to initiate the progressive collapse. Then, the controlling mechanics involving progressive collapse of multi-storey steel and composite structures were studied. The pseudo-static floor responses were recorded for critical column-removal scenarios. From the results obtained, it is concluded that the combination of moment capacity, rotational stiffness and deformation capacity controls the resistance of the structure in case of sudden column removal. Also, methods of balancing these characteristics were discussed to ensure optimal performance.

It is observed from the literature that behaviour of buildings with respect to progressive collapse [4–9] when subjected to earthquakes needs attention. In this paper, progressive collapse in the event of an earthquake [10] in an RC-framed [11] hospital building having nine floors has been carried out. The hospital building considered in the present study has been deficiently designed for earthquake resistance; therefore, the strengthening and retrofit measures have been adopted in the present study to restore the stability of the hospital building for future earthquakes.

Nonlinear pushover analysis of the nine-storey hospital building has been performed in ETABS, and the formation of plastic hinges in the building is studied. The building is further strengthened using global and local retrofitting methods in the zones where formation of plastic hinges in the structural members has occurred. RC shear walls and structural steel bracings are used as global retrofitting to strengthen and stiffen the portions in the hospital building where plastic hinges formations have taken place. RC jacketing has been applied as a local retrofitting method on structural members where plastic hinges are formed to strengthen such damaged structural members locally. The storey displacements of the building are recorded after performing a nonlinear pushover analysis on the retrofitted structure to arrive at an effective and optimised retrofitting solution to improve the seismic resistance of the structure.

2 Nonlinear Pushover Analysis and Retrofitting of Nine-Storey Hospital Building

A nine-storey RC frame hospital building is modelled in ETABS. The typical floor plan of the hospital building is shown in Fig. 1. The isometric view of the RC frame building is shown in Fig. 2.

2.1 Details of the Hospital Building

The details of the hospital building and loading considered are shown in Table 1.

Live loads are considered as per IS875 (Part 2) [3].

Fig. 1 Typical floor plan of the hospital building (dimensions in metres)
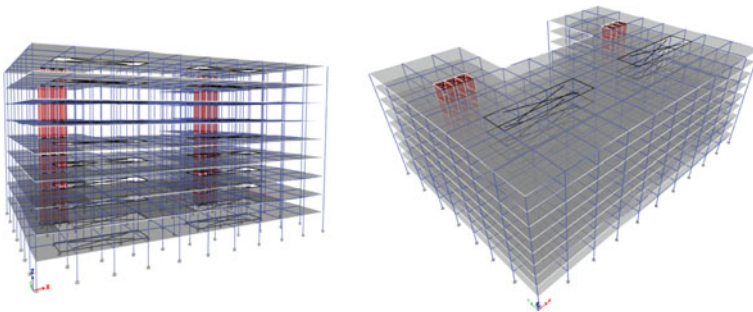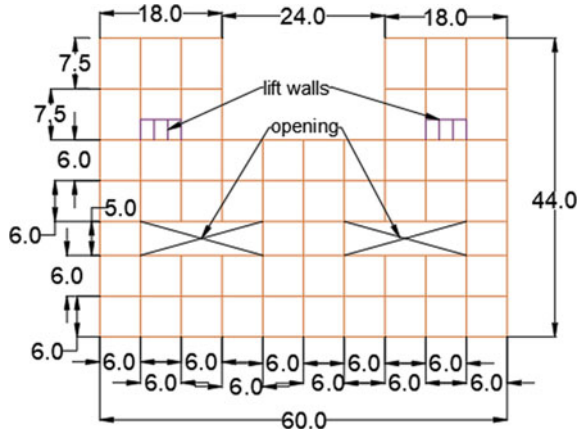
Fig. 2 Isometric view of nine-storey hospital building

Table 1 Details of hospital building and loading

No. of storeyes	Nine
Floor height	3 m
Live load	4.5 kN/m^2
Floor finishes	1 kN/m^2

The building model is restrained by fixed supports at ground level. The hospital building is located in seismic zone V. The hospital building rests on medium soil.

2.2 Details of Structural Elements Present in the Hospital Building

The dimensions of structural members present in the hospital building and concrete the grades adopted in the structural elements are shown in Table 2.

Table 2 Details of structural elements present in the hospital building

Beams	Dimensions	300×700 mm
	Grade of concrete	M40
Columns	Dimensions	550×550 mm
	Grade of concrete	M45
Slabs	Thickness	170 mm
	Grade of concrete	M40
Lift walls	Thickness	170 mm
	Grade of concrete	M40

Fe500 grade steel is adopted for reinforcing steel throughout.

2.3 Enhancing the Lateral Stability of the Hospital Building Adopting Global and Local Retrofitting Methods

Three types of retrofitting methods at global and local levels have been applied individually on the hospital building to restore its strength and stability to resist earthquake loading.

1. Structural steel bracings are introduced into the portions of the hospital building as a global retrofit measure, where more number of plastic hinges have developed in the structural members.
2. Concrete shear walls are introduced into the portions of the hospital building as a global retrofit measure, where more number of plastic hinges have developed in the structural members leading towards instability of the structure.
3. RC jacketing method as a local retrofit measure has been applied onto a particular number of identified beams and columns, in whom plastic hinges have developed.

2.3.1 Structural Steel Bracings Introduced into the Hospital Building as a Global Retrofit Measure

ISMC 300 is used as a section for *X* bracings that are introduced into the portions of the hospital building, where more number of plastic hinges have developed in the structural members—in RC beams and RC columns are shown in Fig. 3.

2.3.2 Reinforced Concrete Shear Walls Introduced into the Hospital Building as a Global Retrofit Measure

RC shear walls that are 170 mm thick and made up of M40 grade concrete and Fe500 grade steel are introduced into the portions of the hospital building, where
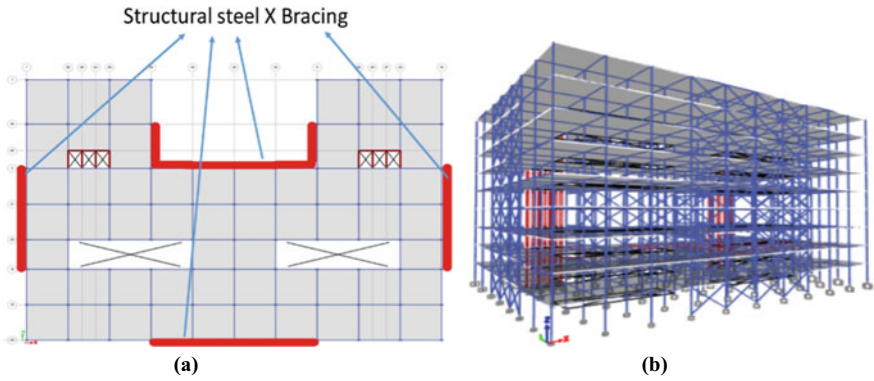
Fig. 3 Hospital building retrofitted globally with *X* bracings where plastic hinges have developed in structural members due to earthquake loading: **a** plan and **b** isometric view
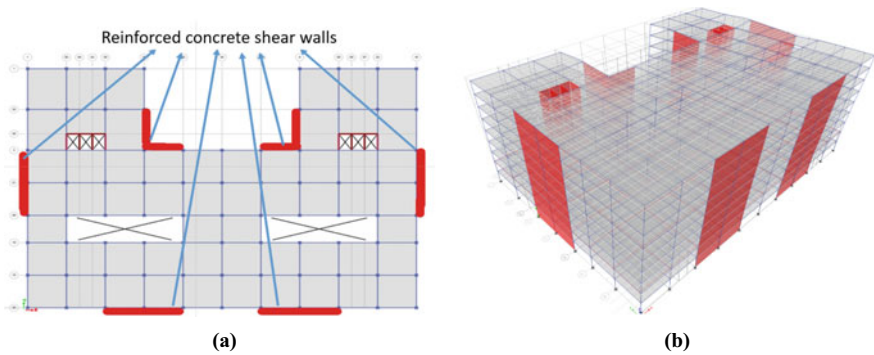
Fig. 4 Hospital building retrofitted globally with reinforced concrete shear walls where plastic hinges have developed in structural members due to earthquake loading: **a** plan and **b** isometric view

more number of plastic hinges have developed in the structural members—in RC beams and RC columns are shown in Fig. 4.

2.3.3 Reinforced Concrete Jacketing Introduced into the Hospital Building on Distressed Structural Members as a Local Retrofit Measure

RC jacketing that is 125 mm thick and made of M55 grade concrete and Fe500 grade steel is introduced into the portions of the hospital building, where more number of plastic hinges have developed in a particular in RC beams and RC columns as shown in Fig. 5.

(a)   **(b)**
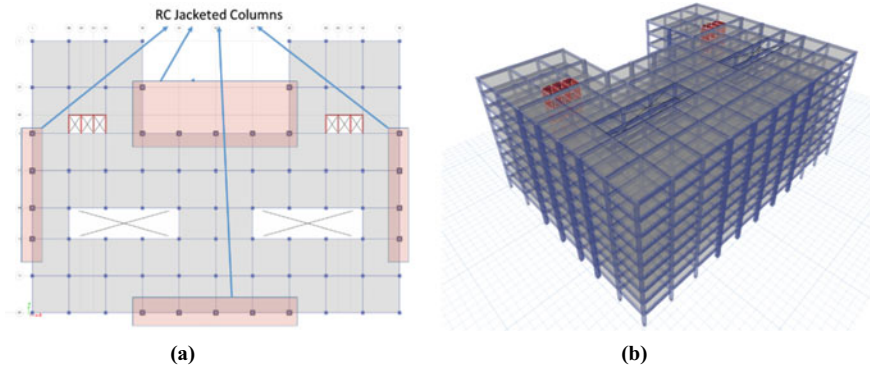
Fig. 5 Hospital building retrofitted locally with reinforced concrete jacketing introduced into the hospital building on distressed structural members due to earthquake loading: **a** plan and **b** isometric view

In the RC jacket applied, 25-mm-diameter rebars are used as longitudinal reinforcements, and 10-mm-diameter rebars are adopted for stirrups in beams and lateral ties in columns at 200 mm centre to centre spacing.

3 Results and Discussion

Nonlinear pushover analysis is carried out on the hospital building without any form of retrofit and also with global and local retrofits applied onto the hospital building. The maximum storey displacements and the formation of plastic hinges in the hospital building are recorded whilst carrying out the nonlinear pushover analysis.

3.1 *Storey Displacements in X Direction*

The maximum storey displacements in X direction of the hospital building with and without global and local retrofits when subjected to nonlinear pushover analysis are shown in Fig. 6.

The top-storey displacements are found to be 148.1 mm, 84.5 mm, 111.3 mm and 80.0 mm in X direction for the hospital building without retrofit, with bracings-global retrofit, with shear walls-global retrofit and with RC jacketing-local retrofit, respectively.
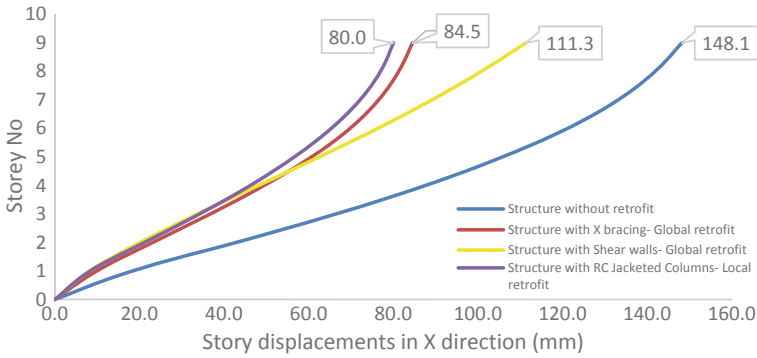
Fig. 6 Maximum storey displacements taking place in the hospital along *X* direction with and without global and local retrofit when subjected to nonlinear pushover analysis

3.2 Storey Displacements in Y Direction

The maximum storey displacements in *Y* direction of the hospital building with and without global and local retrofits when subjected to nonlinear pushover analysis are shown in Fig. 7.

The top-storey displacements are found to be 112.9 mm, 81.8 mm, 37.8 mm and 105.9 mm in *Y* direction for the hospital building without retrofit, with bracings-global retrofit, with shear walls-global retrofit and with RC jacketing-local retrofit, respectively.

The stiffness of the building is increased by the addition of all the three types of retrofitting methods (global and local) adopted in the present study, that is, RC jacketing of existing columns, shear walls and *X* bracings, respectively. The average
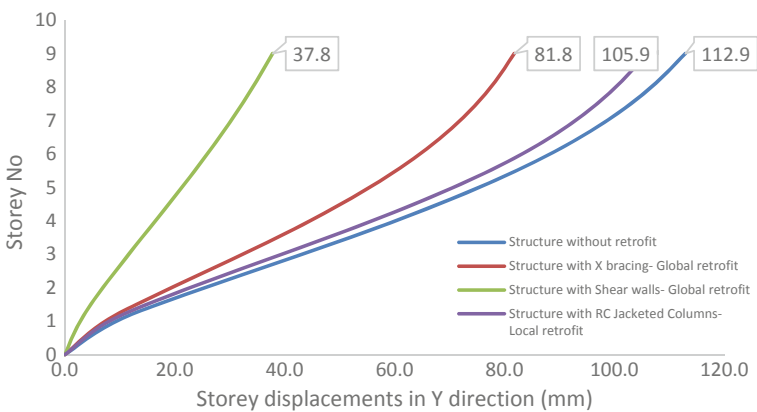
Fig. 7 Maximum storey displacements taking place in the hospital along *Y* direction with and without global and local retrofit when subjected to nonlinear pushover analysis

number of plastic hinges formed in the structural members present in the hospital building ranges from 30 to 40, when the structure was subjected to nonlinear pushover analysis without any form of retrofit. Due to the increased stiffness by all the three types of retrofitting methods adopted in the present work, there is a reduction in the number of plastic hinges formed in the frame members when the hospital building is subjected to a nonlinear pushover analysis. It is observed that the inclusion of shear wall and X bracing in the hospital building as a global retrofit measure reduced the number of plastic hinges formed by about 65% and 40%, respectively, when subjected to nonlinear pushover analysis.

The reduction in the number of plastic hinges is attributed to the reduction in the top-storey displacements of the hospital building, thereby improving the stability of the structure.

When shear walls and X bracings are applied in the hospital building as global retrofit methods, there was a reduction of 45.7 and 35.3% in the average top-storey displacements. There was a reduction in the average top-storey displacement of about 26%, when the distressed RC columns in the structure were retrofitted with an RC jacket having a thickness of 125 mm.

4 Conclusions

- When shear walls were applied as a first global retrofit method in the hospital building that is subjected to seismic loads considered in this work, a reduction of about 45.7% in the average top-storey displacement was reported. When the hospital building was globally retrofitted using the second method of retrofit, namely X bracings, the average top storey displacements reduced by 35.3%. When RC jacketing has a thickness of 125 mm was applied as a local retrofit measure on the existing RC columns present in the hospital building, a reduction of about 26.1% was observed in the top-storey displacement.
- It is inferred from the results, addition of shear walls results in a larger reduction in the number of plastic hinges formed in the frame members by about 65%. Whereas, addition of bracings helped in reduction of plastic hinges formed in the structural members by about 40%. Addition of RC jacketing helped in locally strengthening the distressed RC columns, by improving the lateral stiffness of the columns. The improved lateral stiffness of the columns helped to reduce the overall average top-storey displacements along with restoring the lateral stability of the structure.

References

1. Petrone F, Shan L, Kunnath SK (2016) Modeling of RC frame buildings for progressive collapse analysis. Int J Concr Struct Mater 10:1–13
2. Nethercot DA (2011) Design of building structures to improve their resistance to progressive collapse. Proc Eng 14:1-13O
3. IS 875 (Part 2) (1987, Reaffirmed 2008) Code of practice for design loads (other than earthquake) for building and structures-imposed loads. Bureau of Indian Standards, New Delhi
4. Tsai M-H, Huang T-C (2011) Progressive collapse analysis of an RC building with exterior non-structural walls. Proc Eng 14:377–384
5. Mohan Kumar S, Jeyanthi R (2016) Progressive collapse analysis of a multistorey RCC building using pushover analysis. Int J Eng Res Technol 05:747–750
6. Sunamy SL, Binu P, Girija K (2014) Progressive collapse analysis of a reinforced concrete frame building. Int J Civ Eng Technol 12:93–98
7. Raghavendra C, Pradeep AR (2014) Progressive collapse analysis of reinforced concrete framed structure. Int J Civ Struct Eng Res 1:143–149
8. Helmy H, Mourad S (2003) Computer aided assessment of progressive collapse of reinforced concrete structures according to GSA code. J Perform Constr Facil 529–539
9. Bracci JM, Kunnath SK, Reinhorn AM (1997) Seismic performance and retrofit evaluation of reinforced concrete structures. J Struct Eng 123(1):3–10
10. IS 1893-Part 1 (2016) Criteria for earthquake resistant design of structures. Bureau of Indian Standards, New Delhi
11. IS 456(2000) Plain and reinforced concrete—code of practice. Bureau of Indian Standards, New Delhi

Improved Blast Resistance of Existing Industrial Building Adopting Global and Local Retrofit Strategies

Pratiksha U. Dodamani and Y. K. Guruprasad

1 Introduction

The recent explosion in Beirut caused by the detonation of tones of ammonium nitrate (also used to make explosives) and similar accidental blasts in various petrochemical industries, gas storage structures, warehouses, small-scale manufacturing industries such as incense stick manufacturing units and fireworks (cracker) factories, that store and handle hazardous explosive materials, raises concern about the safety of such industrial building and their surrounding buildings against failure due to blast. Such internal explosions have been common phenomena these days leading to structural failure of the existing building and surrounding buildings causing complete/partial collapse of structure as well as increased human deaths and injuries. To reduce the casualties, the buildings subjected to blasts need to be restored to overcome the collapse in accidental explosions.

Turgut et al. [1] carried out an in situ investigation on an LPG explosion in the basement of the building and reported the aftermath of an explosion. The damage in the structural members and the behaviour of the building in the event of an explosion were explained. Column and shear wall failures and various damage in the surrounding building were reported. They suggested that buildings in the event of internal explosions should possess solid frame and has to be designed to avoid dangerous fragments. This is achieved by providing a strong blast curtain/wall in the middle of the building,

P. U. Dodamani · Y. K. Guruprasad (✉)
MTech Student, Structural Engineering, Department of Civil Engineering, Ramaiah Institute of Technology, Bangalore 560054, India
e-mail: guruprasadyk.civil.iisc@gmail.com

Y. K. Guruprasad
Associate Professor, Department of Civil Engineering, Ramaiah Institute of Technology, Bangalore 560054, India

such that the turbulent flow of the blast wave is withheld and the wave is directed out from the blast portion of the building.

Rizwan et al. [2] estimated the variation of blast load parameters for a twenty-storey building, compared the responses of the RC structure with shear wall and the RC structure with bracings. The building is modelled in ETABS to obtain the storey displacements for various standoff distances. It is observed from the results obtained by the authors that, by increasing the blast load and by decreasing the standoff distance, there is rapid increase in displacement and storey drift. Hence, the response depends on the standoff distances and magnitude of blast load. The maximum displacement for two different models with different standoff distances is evaluated.

Milner et al. [3] carried out computational analysis with a higher degree of refinement and produced results that were realistic with respect to structural damage and fatality. The authors reduced the extent of conservatism observed in the results and reduced the amount of mitigation measures that were costly and not necessary. A pre-engineered metal building was considered by the authors as a case study to assess the effect of different loads adopting sophistication in the analysis. The authors have also considered FEM and CFD as tools to study the structure's behaviour.

Ngo et al. [4] have considered the explosive air blast loading on the structure where RC column subjected to blast loading is considered. The increase in ultimate lateral displacements at failure is recorded for both high-strength and low-strength columns. Progressive collapse was performed. The various types of failures of slab lifting up beams and column failure are explained.

The above literature looks at buildings subjected to external blast loading that occurs in commercial/tall buildings. The objective of the current study is to enhance the blast resistance of an existing industrial building to prevent it from partial or complete collapse in the event of a blast caused due to an accidental internal chemical explosion. In the present work, a four-storey industrial building is analysed for internal explosion and suitable retrofit techniques such as providing X-bracing, shear wall and CFRP wrap are suggested to restore the strength and stability of the structure in the event of an internal blast.

In the present study, an existing four-storey industrial RC building subjected to blast loading (internal blast) is analysed using a nonlinear finite element analysis procedure. The RC industrial building considered in the study is a real-life case study, wherein the probable failure of the structure due to an accidental internal chemical explosion has to be prevented in a certain portion of the building where the possibility of industrial chemicals and the manufacturing unit is placed that can be subjected to blast when they are accidentally exposed to higher temperature in the event of fire.

The four-storey industrial building considered in the present study is analysed for a positive overpressure with respect to time (blast pressure time history) and is evaluated as the pressure generated by an equivalent trinitrotoluene (TNT) as per IS4991 [5], European Commission Joint Research Centre (JRC) technical reports [6, 7] and "Explosive Shocks in Air" [8]. The blast is considered to be incident on one portion of the RC building [9], and the possible types of failures in the building

are analysed in ETABS, and the response is checked for displacements in structural members and displacements at different storey levels. The deformation patterns of the structural members due to the blast loading such as, the deflection in slab (at the point of detonation), deformations in beams and columns, are noted.

Thereby, retrofitting techniques such as: inclusion of new RC shear walls, providing bracings and adopting CFRP wrapping on structural members are considered in the present study, to enhance the blast-resistant capacity of the industrial building so that the possible collapse of the structure due to future accidental internal explosion can be mitigated.

2 Global and Local Retrofit Strategies Applied to Improve the Blast Resistance of an Industrial Building Subjected to an Internal Chemical Blast

Case study: A four-storey industrial building is considered to be analysed for the blast pressure so as to prevent probable collapse due to an internal chemical explosion. The pressure due to blast is applied in the manufacturing unit where the chemicals placed. Figure 1 shows the time history of the wave pressure due to blast. The positive portion of the overpressure is considered for the analysis.
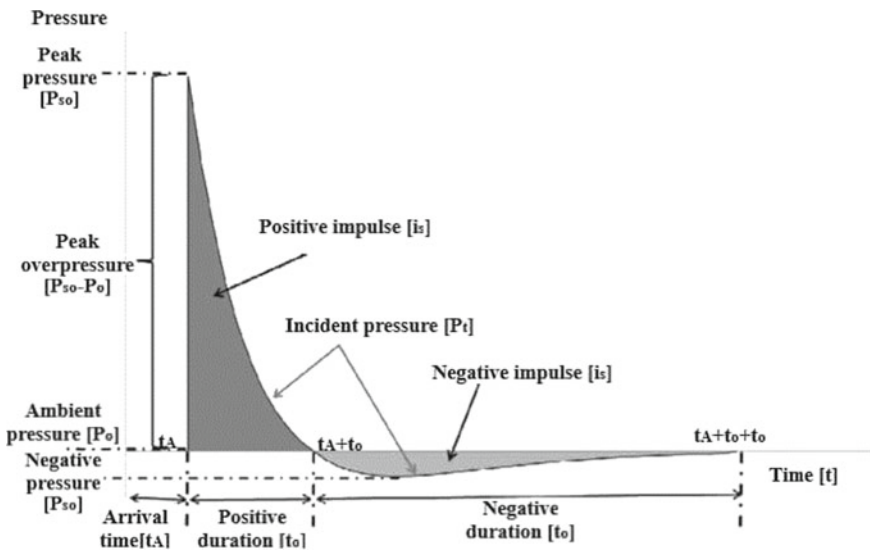
Fig. 1 Time history of the wave pressure due to blast [6]

2.1 Preliminary Data

- A four-storey industrial building has been considered.
- Slab panel having a thickness of 200 mm, shear wall having a thickness of 250 mm, beams having the dimensions 300 × 450 mm, columns having the dimensions 300 × 500 mm, M30 grade concrete and Fe500 grade steel adopted for rebars in beams, columns, slabs and shear walls. Fe345 grade adopted for structural steel.
- X-Bracing—ISMC300, considered for bracing.
- CFRP details: mass per unit volume—1800 kg/m^3, thickness—1.5 mm (including epoxy).
- Dimensions of the building in plan: 54 m × 18 m.
- Dead loads—self-weight of structural elements, floor finishes; live loads—(4.5 kN/m^2) as per IS 875 part 2.
- The shear walls provided around the blast area and X-bracings are adopted in the analysis on the basis of lateral displacements, to improve and restore the stability of the structure due to blast.

2.2 Details of Four Storey RC Industrial Building

The following models of the RC industrial building are adopted in the analysis; the typical structural floor plan of the industrial building is shown in Fig. 2. The structural models considered in the present work are shown in Fig. 3. The RC industrial building that has the lift wall only is shown in Fig. 3a. Figure 3b shows the RC industrial building with a pseudo-wall to apply overpressure. After the initial analysis, various local and global retrofit techniques were applied and analysed. Figure 3c shows model with X-bracings for the bays around the manufacturing unit; Fig. 3d shows the model with shear wall around manufacturing unit. The structural members such as beams and columns around the blast compartment were wrapped with CFRP of 1.5 mm thickness. Figure 3e shows the typical cross-sectional details of the structural member (RC beam) retrofitted using CFRP wrap.
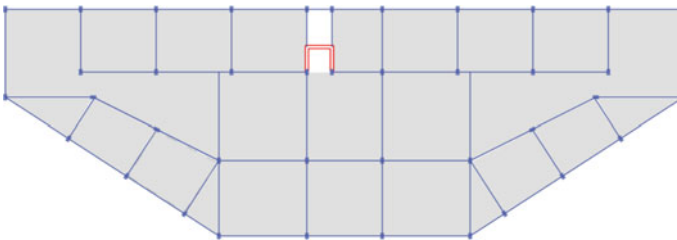
Fig. 2 Typical floor plan of the structural layout of the industrial building

(a) RC industrial building

(b) RC structure with a pseudo wall

(c) Model with X bracings

(d) Model with shear wall

1.5mm CFRP

300X500 Column

(e) Typical cross sectional details of an RC
beam retrofitted using CFRP wrap
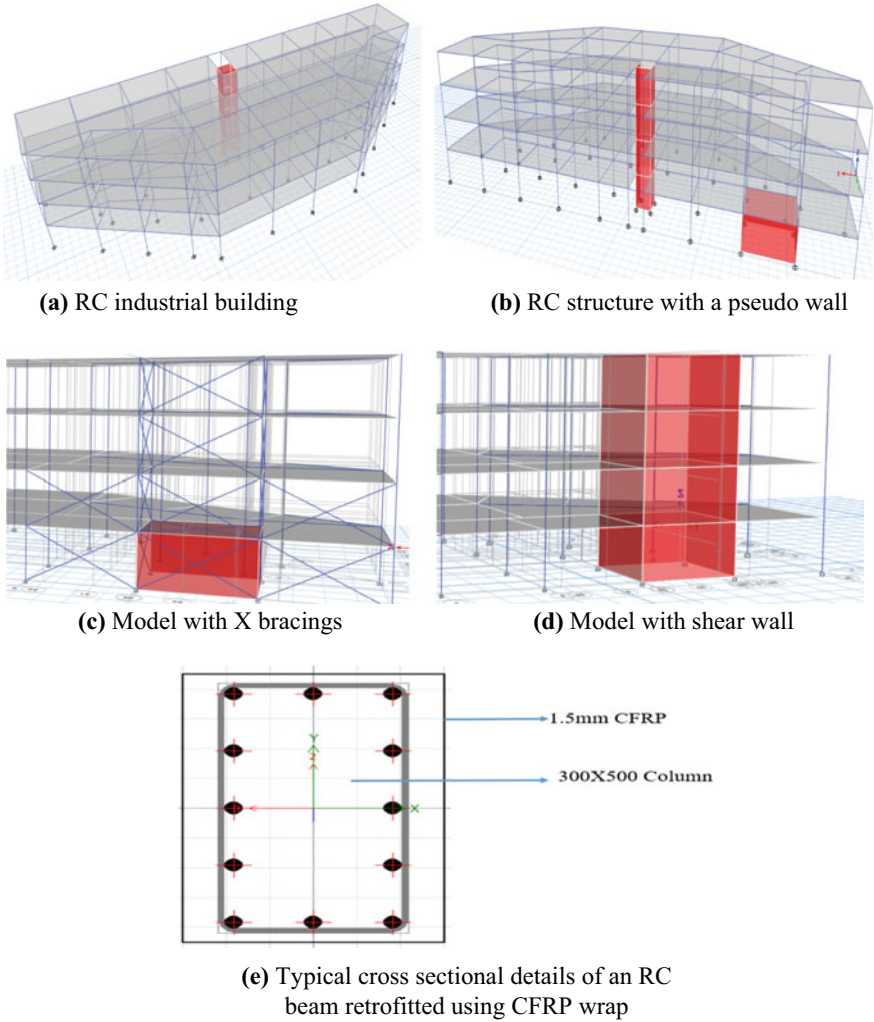
Fig. 3 Structural models and details adopted in the present study, **a** RC industrial building, **b** RC structure with a pseudo-wall, **c** model with *X*-bracings, **d** model with shear wall, **e** typical cross-sectional details of an RC beam retrofitted using CFRP wrap

2.3 Details of Blast Pressure Application

In the present case for the analysis of the industrial building under the blast, an equivalent TNT explosive charge is considered at the centre of the manufacturing unit, leading to an accidental internal explosion. Blast pressure is applied to the particular

Table 1 Blast pressure calculations

Parameter	Symbol	Value
Scaled distance	Z	0.43 m/kg$^{1/3}$
Equivalent TNT charge	W	100 kg TNT
Peak overpressure	P_o	5196 kN/m^2
Positive-phase duration	T_d	0.48 ms
Ambient atmospheric pressure	P_a	101.325 kN/m^2

compartment which is a manufacturing unit. Overpressure is applied perpendicularly on pseudo-walls on all four sides of the manufacturing unit and slab as blast overpressure time history. Sections 2.4 and 2.5 present the procedure of calculations.

2.4 Blast Pressure Calculations

The calculations of the pressure due to blast given by Kinney and Graham [8] are formulated which is based on chemical type explosions. It is described by Eqs. (1), (2) and (3).

$$Z = R/\left(W^{1/3}\right) \tag{1}$$

$$P_o = P_a \times 808 \left[1 + (Z/4.5)^2\right]/\left\{\left[1 + (Z/0.048)^2\right]\right.$$
$$\left.\left[1 + (Z/0.32)^2\right]\left[1 + (Z/1.35)^2\right]\right\}^{0.5} \tag{2}$$

$$t_d/W^{1/3} = 980\left[1 + (Z/0.54)^{10}\right]/\left[1 + (Z/0.02)^3\right]$$
$$\left[1 + (Z/0.74)^6\right]\left\{\left[1 + (Z/6.9)^2\right]^{0.5}\right\} \tag{3}$$

where Z $\left(\text{m/kg}^{1/3}\right)$ is the scaled distance.

P_o is the peak overpressure.

P_a is the ambient pressure.

t_d is the duration of positive phase overpressure.

The parameters corresponding to the pressure due to blast is presented in Table 1. Table 2 presents the gravity loads adopted in the analysis.

2.5 Blast Pressure Application

The time history function considered in the analysis is shown in Fig. 4. The blast

Table 2 Gravity loads considered in analysis as per IS 875 parts I and II [10, 11]

Type of load	
Beam load/load from walls	14 kN/m
Live load	4.5 kN/m²
Roof live load	1 kN/m²

Fig. 4 Time history function considered in the analysis
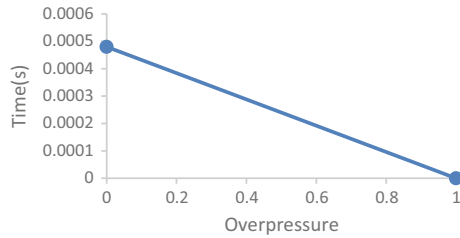
Fig. 5 Deflection in slab above the manufacturing unit
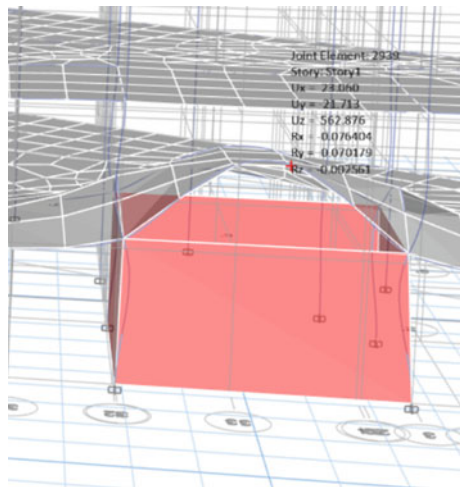
pressure values evaluated in Sect. 2.4 is applied to the manufacturing unit in the perpendicular direction (pseudo-walls on all four sides of the manufacturing unit and slab) so that the pressure due to blast acts for a time duration of 0.48 ms. Figure 5 shows the deflection in slab above the manufacturing unit which is 562.876 mm in an upward direction due to blast for an existing building.

3 Results and Discussion

1. The deformation in the industrial structure subjected to the pressure due to blast is shown in Fig. 6.
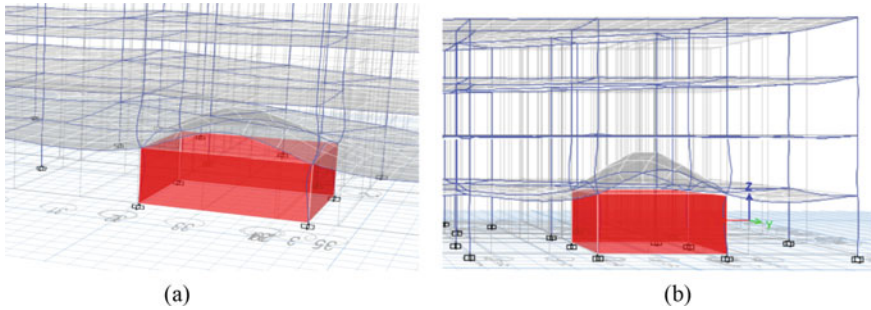
Fig. 6 Deformation in the industrial structure subjected to the pressure due to blast

2. The maximum storey displacements at different storey levels in the existing industrial building subjected to blast loading and retrofitted with *X*-bracings in the manufacturing compartment and surrounding bays, shear walls introduced as global retrofit around the manufacturing unit and applying local retrofit adopting CFRP wrapped around the structural elements present in the bays surrounding the manufacturing unit are shown in Table 3 in the *x*-direction and Table 4 in *y*-direction.

3. Figure 7 shows the maximum storey displacement in *x*- and *y*-direction for the combination of DL + LL + Blast and maximum deflection in slab just above the manufacturing unit (For 4 cases (a) existing building, (b) building retrofitted with bracing in and around the manufacturing unit, (c) retrofitted with shear wall of 250 mm thickness around manufacturing unit (d) retrofitted with CFRP wrapped beams and columns, respectively.

4. The slab panel in the portion where the blast has taken place deflects in the upward direction by 562.876 mm for the existing building, after retrofitting the deflection of slab for the cases (b), (c) and (d) were 499.758, 228.700 and 497.084, respectively. Suggesting that the shear wall reduces the deflection in the slab of the blast compartment.

Table 3 Maximum storey displacements (mm) in the *x*-direction

Maximum storey displacement (mm) in *x*-direction

Storey	Height (m)	No retrofit	Retrofit applied	Retrofit applied	Retrofit applied
		Existing industrial building	Bracing	Shear wall	CFRP wrap
Storey 4	12	6.293	8.168	7.851	5.992
Storey 3	9	4.729	5.081	6.122	4.562
Storey 2	6	4.093	3.857	3.874	3.902
Storey 1	3	73.039	47.075	4.827	62.509
Base	0	0	0	0	0

Table 4 Maximum storey displacements (mm) in the *y*-direction

Storey	Height (m)	No retrofit	Retrofit applied	Retrofit applied	Retrofit applied
		Existing industrial building	Bracing	Shear wall	CFRP wrap
Storey 4	12	14.007	19.738	15.635	14.41
Storey 3	9	7.025	11.985	12.099	7.863
Storey 2	6	5.914	4.765	6.943	3.687
Storey 1	3	44.446	29.344	7.25	38.186
Base	0	0	0	0	0
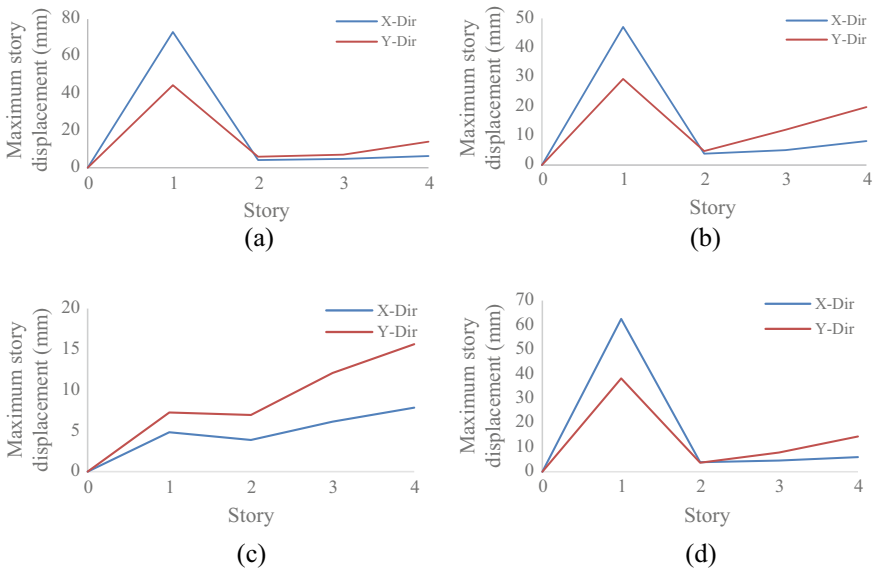
Fig. 7 Maximum storey displacements, **a** maximum storey displacement of an existing industrial building, **b** maximum storey displacement of the industrial building retrofitted with bracing, **c** maximum storey displacement of the industrial building retrofitted with shear wall, **d** maximum storey displacement of the industrial building retrofitted with CFRP wrapped beams and columns

5. From the analysis, we can infer that the storey displacement at the first storey is maximum at the blast and which is reduced after the retrofit. The maximum storey displacement of an industrial building with CFRP is highest followed by bracing and shear wall; hence, the shear wall provision around the blast compartment drastically reduces the displacement in the first storey in both *x*- and *y*-direction, but there is a slight increase of displacement in the last storey.

6. Based on the results obtained for the blast-damaged industrial building, structural retrofits such as *X*-bracing, shear walls and CFRP were used as stiffening measures in the structural models. The incorporation of shear walls, CFRP and *X*-bracings provided better stability to the industrial building under blast, as evidenced by the results, which shows that providing combinations of different retrofit methods has reduced the lateral displacements in the structure.

4   Conclusions

- As per the analytical results obtained, the inclusion of individual structural elements: shear wall, CFRP and *X*-bracings around the manufacturing unit has reduced the magnitude of displacements in the building by increasing the stiffness and stability in the event of blast.
- The first-storey displacements are reduced by 35.55% and 33.9% in *x*- and *y*-direction, respectively, in the industrial building with bracings only (global retrofit).
- The first-storey displacements are reduced by 93.39% and 83.68% in *x*- and *y*-direction, respectively, in the industrial building with the shear wall (global retrofit).
- The first-storey displacements are reduced by 14.41% and 14.08% in *x*- and *y*-direction, respectively, in the industrial building with CFRP (local retrofit).
- Hence, the energy dissipated is thus absorbed by the shear wall and hence resulting in efficient retrofit when subjected to blast.
- The deflection in the roof slab of the manufacturing unit present at the first storey is reduced by: 153.12 mm for the building retrofitted with bracing, by 334.176 mm for the building retrofitted with shear wall and by 65.792 mm for the building retrofitted with CFRP wrapping.
- Based on these conclusions, an optimum combination of bracing, shear wall and CFRP can be chosen and provided to lower displacements in the structure and hence prevent the partial or complete collapse of the industrial building.

References

1. Turgut P, Arif Gurel M, Kadir Pekgokgoz R (2013) LPG explosion damage of a reinforced concrete building: a case study in Sanliurfa, Turkey. Eng Fail Anal 32:220–235
2. Rizwan Q, Raghu Prasad BK, Amarnath K (2017) Structural analysis of blast resistant buildings. Int J Res & Develop Technol 8(3):173–178
3. Milner D, Wesevich J, Nikodym L, Nasri V, Lawver D, Mould J (2018) Improved blast capacity of pre-engineered metal buildings using coupled CFD and FEA modelling. J Loss Prev Process Ind S0950-4230(18)30094-9, JLPP 3793
4. Ngo T, Mendis P, Gupta A, Ramsay J (2007) Blast loading and blast effects on structures—an overview. EJSE Electron J Struct Eng (1):6–91

5. IS 4991(1968): Criteria for blast resistant design of structures for explosions above ground. Bureau of Indian Standards, New Delhi
6. Karlos V, Solomos G (2013) Calculation of blast loads for application to structural components. European Commission Joint Research Centre Institute for the Protection and Security of the Citizen, Luxembourg, Publications Office of the European Union
7. Kevin C, van Doormaal A, Haberacker C, Hüsken G, Larcher M, Saarenheimo A, Solomos G, Stolz A, Thamie L, Valsamos G (2013) Resistance of structures to explosion effects: review report of testing methods. European Commission Joint Research Centre Institute for the Protection and Security of the Citizen. ISSN 1831-9424, ISBN 978-92-79-35104-4
8. Kinney GF, Graham KJ (1985) Explosive shocks in air, 2nd edn. Springer, Berlin. ISBN 978-3-642-86684-5 and 82-1
9. IS 456 (2000) Plain and reinforced concrete—code of practice. Bureau of Indian Standards, New Delhi
10. IS 875-Part 1 (1987) Dead loads—code of practice for design loads (other than earthquake) for building and structures. Bureau of Indian Standards, New Delhi
11. IS 875-Part 2 (1987) Live loads—code of practice for design loads (other than earthquake) for building and structures. Bureau of Indian Standards, New Delhi

Investigations with Blast Wave Simulators

Kaviarasu Kannan, Shyam Sundar, and Alagappan Ponnalagu

1 Introduction

Shock tubes are widely used in several engineering disciplines such as aerospace, chemical, and biomedical engineering. And, there are several types of shock tubes such as explosive driven, compressed gas, and oxyacetylene driven shock tubes. Recently, there has been increasing focus on developing compressive gas-driven shock tubes capable of producing Friedlander type pressure–time profile. These shock tubes are widely preferred over free field explosion experiments since they are cost-effective, safe, and repeatable. A detailed review of various shock tubes used for blast-related research can be found in the recent study by Sundar and Ponnalagu [1]. Several experimental, numerical, and analytical studies investigated the effect of different shock tube parameters on Friedlander profile formation in shock tubes [2–4]. And, there are some novel blast wave simulator (BWS) facilities [5–7] available in several research institutes. Even with several advancements, the literature lacks preliminary guidelines and suggestions for the design of blast wave simulators. So, our main objective is to provide detailed guidelines for the design of blast wave simulators. This study is part of that main objective, which investigates the role of the driver length in the design of blast wave simulators. Also, the experimental results of this study will serve as a validation data set for numerical models. A demonstration is shown with the numerical model developed in ABAQUS/Explicit (a commercial FEA solver). Also, the developed model can be further improved and used for parametric studies in the design of blast wave simulators.

K. Kannan (✉) · S. Sundar · A. Ponnalagu
Department of Civil Engineering, Indian Institute of Technology Madras, Chennai, Tamil Nadu 600036, India
e-mail: ce19d023@smail.iitm.ac.in
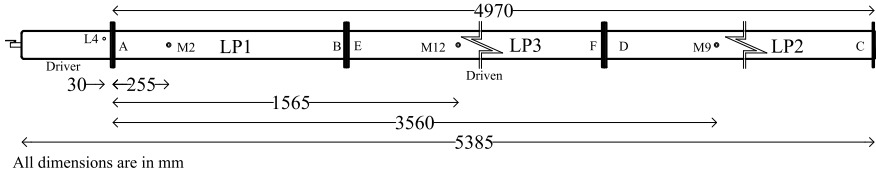
Fig. 1 Schematic of blastwave simulator

Fig. 2 Driver sections (HP1, HP2, HP3, and HP4)

2   Experimental Investigation

2.1   Shock Tube

The schematic view of the blastwave stimulator used in this study is shown in Fig. 1. It consists of a 5000 mm long driven section and four reconfigurable driver sections (HP1, HP2, HP3, and HP4) of length 50 mm, 100 mm, 200 mm, and 400 mm, respectively (refer to Fig. 1). The cross-section of the blastwave simulator is 93 mm x 93 mm. The pressure is measured at probe locations M1 to M14. But for the sake of brevity, only results from the probe locations M2, M12 and M9 are presented in this study. In our experiments, two 80 GSM thick butter sheets are used as a diaphragm, and compressed air is used for pressurizing the driver section.

2.2   Instrumentation

Burst pressure is measured using a piezo-resistive type pressure transducer (Kulite XCQ-093-17BARA) at a location, L1, 30 mm from the diaphragm. The analog data

Fig. 3 Experimental setup

Table 1 Experimental design

Driver length	Open-end			Closed-end	
	Trial 1	Trial 2	Trial 3	Trial 1	Trial 2
HP1 50 mm	✓	✓	✓	✗	✗
HP2 100 mm	✓	✓	✓	✓	✓
HP3 200 mm	✓	✓	✓	✗	✗
HP4 400 mm	✓	✓	✓	✗	✗

from the transducer is conditioned and acquired using a data acquisition system (HBM quantumX). Driven pressure is measured using piezoelectric type pressure transducers (PCB 11). The analog data from the transducers are conditioned using a signal conditioner (PCB 483C) and acquired using a data acquisition system (PCI card). The data acquisition systems are controlled using catman and LabVIEW software. The experimental setup with instrumentation is shown in Fig. 3.

Details of experiments carried out in this study are shown in Table 1. The investigation is repeated thrice for all driver configurations to verify consistency in the pressure–time profile.

3 Numerical Analysis

Numerical simulation of the one-dimensional shock wave propagation is carried out using the commercial finite element package ABAQUS. Experimental burst pressure values are converted into density using the ideal gas equation and inputted as an initial condition for the numerical model. The total simulation time is 50 ms with time stepping 0.005 ms. A mesh size of 1mm is chosen after verifying mesh convergence. Velocity perpendicular to the shock tube walls is assumed to be zero. Viscous effects are not considered in our numerical model. The numerical model geometry, mesh, and boundary conditions are shown in Fig. 4 (geometry and mesh are not to scale).
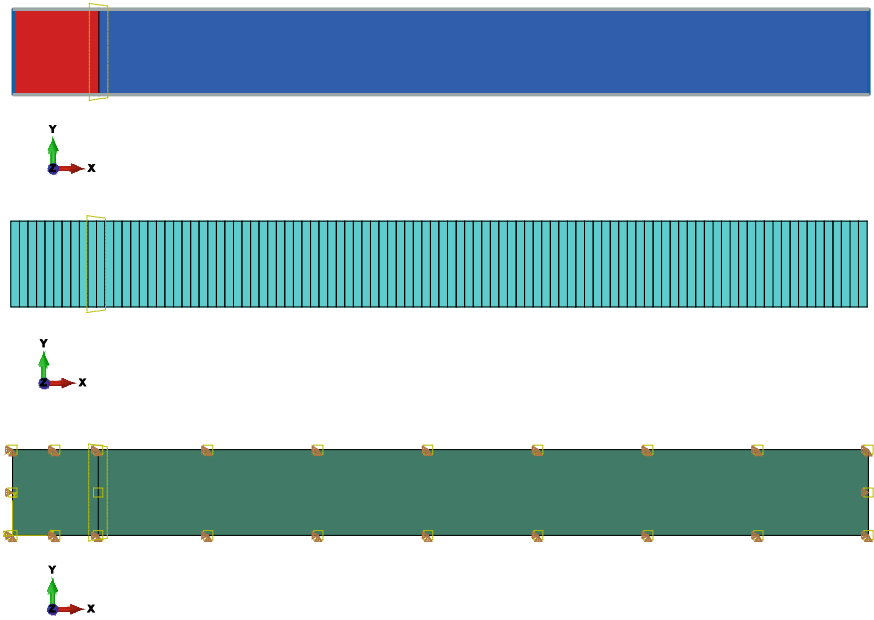
Fig. 4 Finite element model of shock tube

4 Results and Discussion

The burst pressure for various trails is shown in Table 2. The variation in burst pressure values between trials is due to the randomness in the diaphragm opening process.

The pressure–time plot at probe locations (M2, M12, and M9) for different driver configurations are shown in Figs. 5, 6, 7, and 8. All the figures show that pressure–time plots for different trials are consistent, confirming repeatability in our experiments. Also, we can see that in the HP1 case, the typical Friedlander profile is attained in the first probe location, M2. In other cases (HP2 and HP3), Friedlander profile formation occurred at later probe locations M12 and M9, respectively. But for the HP4 case, there was only a flat-top profile at all the probe locations. This observation shows that Friedlander profile formation distance depends upon the driver length.

Table 2 Experimentally recorded burst pressure, bar

Driver/trial	Trial 1	Trial 2	Trial 3	% variation of range	Mean
HP1	2.324	2.420	2.391	3.960	2.3785
HP2	2.429	2.336	2.284	5.950	2.3497
HP3	2.738	2.723	2.878	5.400	2.7798
HP4	2.867	2.868	3.009	4.700	2.9145

Table 3 Comparison of experimental and numerical results

Driver	Sensor location	Positive peak overpressure (P_{so}^+)			Positive phase duration (t_d^+)		
		Exp (bar)	Num (bar)	% variation	Exp (ms)	Num (ms)	% variation
HP1	M2	1.591	1.520	4.475	0.720	0.620	13.889
	M12	1.450	1.350	6.909	1.400	1.180	15.714
	M9	1.276	1.240	2.814	2.040	1.750	14.216
HP2	M2	1.696	1.550	8.586	1.020	1.180	13.559
	M12	1.613	1.530	5.118	1.840	1.810	1.630
	M9	1.385	1.360	1.798	2.720	2.590	4.779
HP3	M2	1.669	1.630	2.334	1.560	2.420	35.537
	M12	1.636	1.630	0.384	2.550	3.140	18.790
	M9	1.517	1.590	4.609	3.490	4.250	17.882
HP4	M2	1.646	1.670	1.414	3.100	4.880	36.475
	M12	1.677	1.670	0.422	4.090	5.660	27.739
	M9	1.582	1.670	5.269	5.100	5.610	22.844
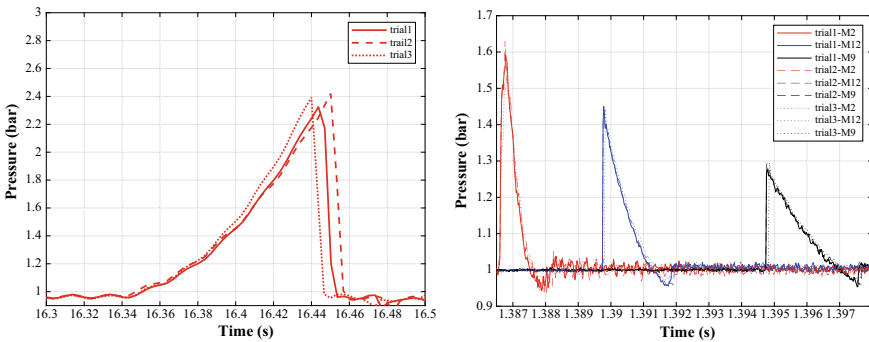
Fig. 5 Pressure time profile at the driver and driven section for HP1 case

So with a shorter driver length, we can achieve Friedlander profile at shorter driven lengths. A comparison of experimental pressure–time profiles at locations M2, M12, and M9 for various driver lengths is shown in Fig. 9. It is evident that decreasing the driver length causes a decrease in the recorded peak overpressure values. The peak overpressure value decreases along the length of the shock tube in all driver configurations. The amount of reduction of peak overpressure was significant, which is 53.85% between M2 and M9 in the HP1 case and 11.76% variation between the M2 and M9 locations in the HP4 case.

A comparison of pressure-time profiles for open and closed-end configurations for the HP3 driver case is shown in Fig. 10. It is evident from the figure that both
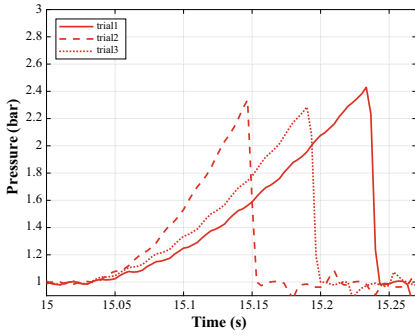
Fig. 6 Pressure time profile at the driver and driven section for HP2 case
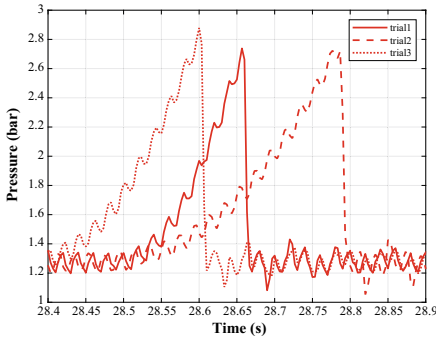
Fig. 7 Pressure time profile at the driver and driven section for HP3 case
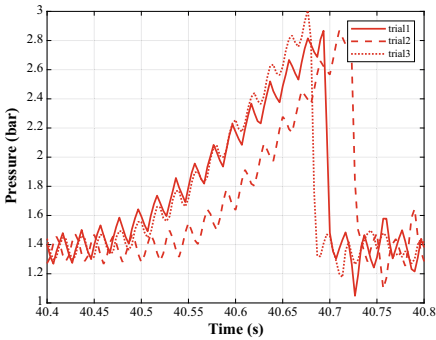
Fig. 8 Pressure time profile at the driver and driven section for HP4 case
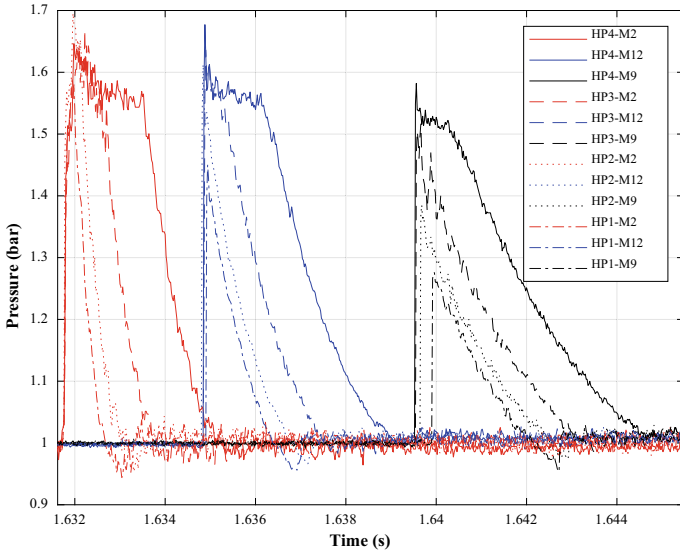
Fig. 9 Comparison of pressure–time profile for different driver configurations (HP1, HP2, HP3, and HP4)
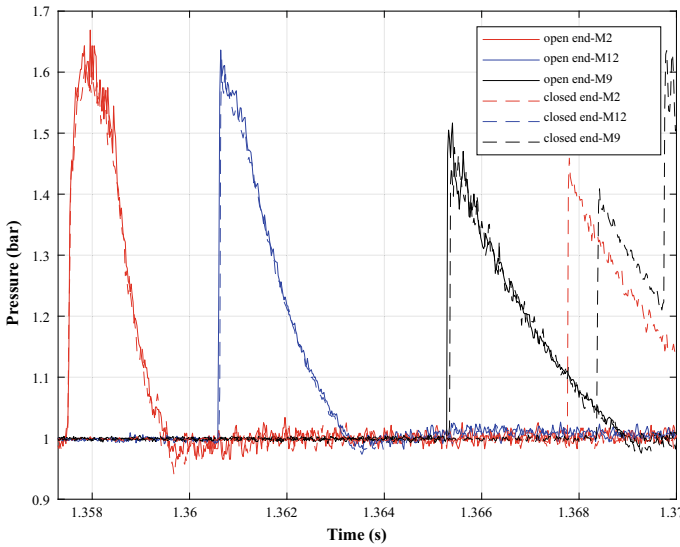
Fig. 10 Comparison of pressure–time profile for open and closed-end configurations

open and closed configurations produced similar pressure-time profiles in the positive phase. Modeling an open-end shock tube is computationally costly since it involves modeling the ambient air domain surrounding the shock tube. So with the above supporting evidence, an open-end shock tube can be numerically modeled as a closed-end shock tube if the focus is only on the positive phase of the primary shock. In this study, numerical simulations are performed with a closed-end configuration and compared with the experimental results of the open-end configuration.
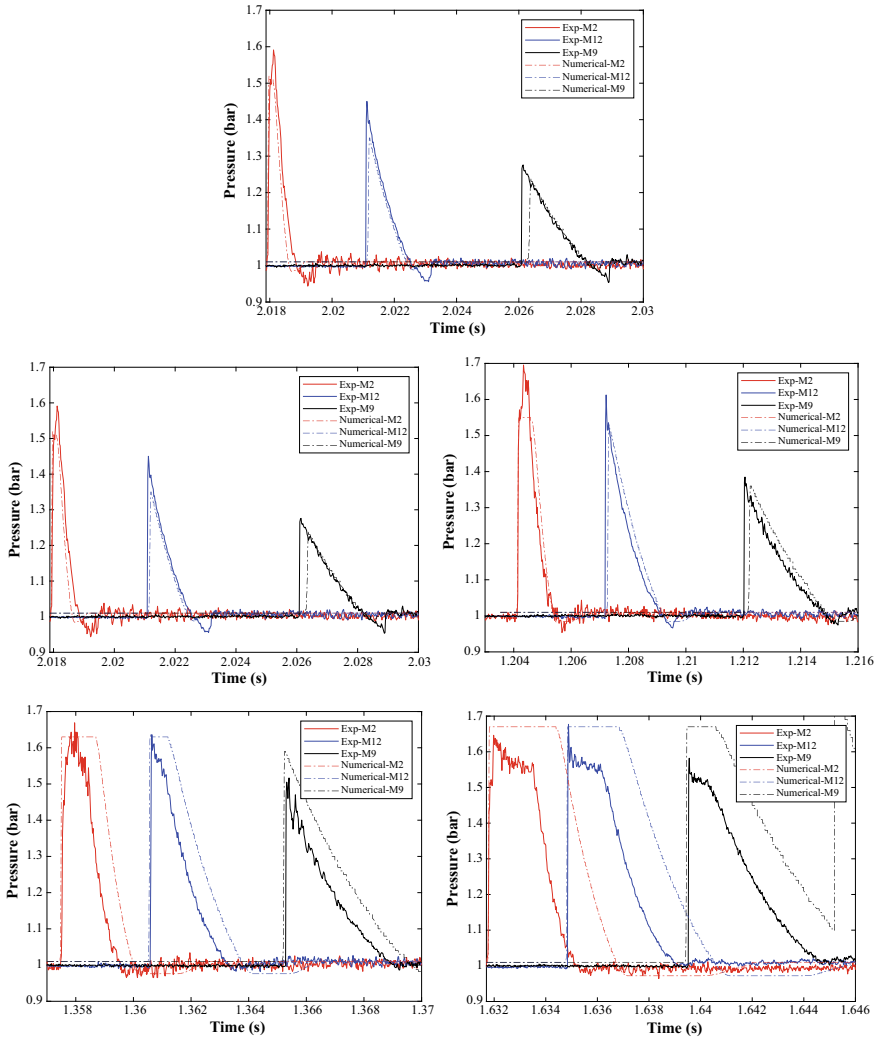
Fig. 11 a Comparison of experimental and numerical pressure–time profile for HP1 case. **b** Comparison of experimental and numerical pressure–time profile for HP1, HP2, HP3, HP4 case

Comparison of peak over-pressure and positive phase duration values at sensor locations M2, M12, and M9 for various driver lengths are shown in Table 3. The maximum variation in peak overpressure values between experimental and numerical results is less than 10%. The difference can be due to uncertainty associated with the diaphragm opening process and the viscous effects. The maximum positive phase duration value variation for HP1 and HP2 cases is less than 16%. But significant variations are observed in the positive phase duration values for HP3 and HP4 cases. In future studies,we will further improve the numerical model for accurate predictions.

A comparison of numerical and experimental pressure–time profiles at locations M2, M12, and M9 for different driver case are shown in Fig. 11a. The numerical pressure–time profile well matches the experimental results in the positive phase for the HP1 case. The variations between the experimental and numerical results for the cases HP2, HP3 and HP4 are due to the idealizations in the numerical model, which can be further reduced by considering viscous effects and the diaphragm rupture process. An experimentally observed negative phase is not found in the numerical results due to the closed-end assumption in the numerical model.

5 Conclusions

In this study, we experimentally observed that the driver length of the shock tube is a significant parameter that influences the peak overpressure, positive phase duration and Friedlander profile formation distance. Increasing the driver length causes an increase in positive phase duration and Friedlander profile formation distance. The above results suggest that in the design of blast wave simulators, the driver lengths need to be short so that we can effectively reduce the overall length of the shock tube. Also, the numerical model developed in this study is capable of predicting the experimentally measured shock wave parameters with reasonable accuracy.

References

1. Sundar S, Ponnalagu A (2021) Biomechanical analysis of head subjected to blast waves and the role of combat protective headgear under blast loading: a review. J Biomech Eng 143(10):1–18
2. Sundaramurthy A, Chandra N (2014) A parametric approach to shape field relevant blast wave profiles in compressed gas-driven shock tube. Front Neurol 5(253):10
3. Kumar R, Nedungadi A (2020) Using gas-driven shock tubes to produce blast wave signatures. Front Neurol 11:1–9
4. Tasissa AF, Hautefeuille M, Fitek JH, Radovitzky RA (2016) On the formation of Friedlander waves in a compressed-gas-driven shock tube. Proc R Soc A Math Phys Eng Sci 472(2186)

5. Kochavi E et al (2020) Design and construction of an in-laboratory novel blast wave simulator. Exp Mech 60(8):1149–1159
6. Obed Samuelraj I, Jagadeesh G (2019) Laboratory simulation of explosions using conical shock tubes. In: 31st international symposium on shock waves 1, pp 135–142
7. Remennikov A, Uy B, Chan E, Ritzel D (2019) The Australian national facility for physical blast simulation. In: Coal operators conference, pp 337–344
8. Blanc L, Schunck T, Eckenfels D (2021) Sacrificial cladding with brittle materials for blast protection. Materials (Basel) 14(14)

Variability in the Compressive Strength of Paving Blocks Using Waste Plastic

Jyoti Prakash Giri, Monalisa Priyadarshini, and Ruchismita Mahakhud

1 Introduction

India is a developing country where the pollution is increasing exponentially every year and the use of plastic products like plastic bags, water bottles, various plastic utensils, etc., also increased. The dumping of such waste not only pollutes the environment but also effects directly and indirectly on both humans and animals. Hence, it is critical to properly dispose of this plastic garbage in accordance with our government's standards. Hence, one of the possibilities of proper utilization of these wastes is in paver block as primary motive to minimize the pollutants and reduce the usage of natural resources. It was noted from the past research that the plastic waste can be a replacement of cement which provides economic and environmental benefits [1–8]. Keeping view on the above-mentioned points, here, a sincere effort is made to reuse the plastic in the manufacturing process of paver blocks. These blocks can be replacing with the traditional paving blocks and can be used where much loading is found on the floor like parking place. In this attempt, the solid waste quarry dust, fly ash, and low-density polyethylene (LDP) have used in different proportion with an aim to improve the mechanical properties like compressive strength and water absorption, compared to conventional cement paver blocks.

J. P. Giri
Department of Civil Engineering, GITAM University, Bengaluru, Karnataka 561203, India
e-mail: jyotiprakash.nitr@gmail.com

M. Priyadarshini (✉) · R. Mahakhud
Department of Civil Engineering, Government College of Engineering Kalahandi, Bhawanipatna, Odisha 766002, India
e-mail: monalisa@gcekbpatna.ac.in

R. Mahakhud
e-mail: ruchirgt23@gmail.com

2   Materials and Methodology

In this experimental study, the paver blocks are prepared with different waste materials like plastic bags, fly ash as well as with conventional materials like quarry dust and sand. The details methodology of this research work is given in Fig. 1. The waste plastic generated from the milk packets, covers, plastic bags is collected from the surrounding locality as shown in Fig. 2. Fine aggregate that consists of natural sand (Fig. 3) collected from the local river. Fly ash (FA) collected from the thermal power plant and cement collected from the local market. Dry quarry dust is accumulated from local stone crushing unit that sieved by 4.75 mm sieve before use. The details of the material specific gravity considered in the study are summarized in Table 1.
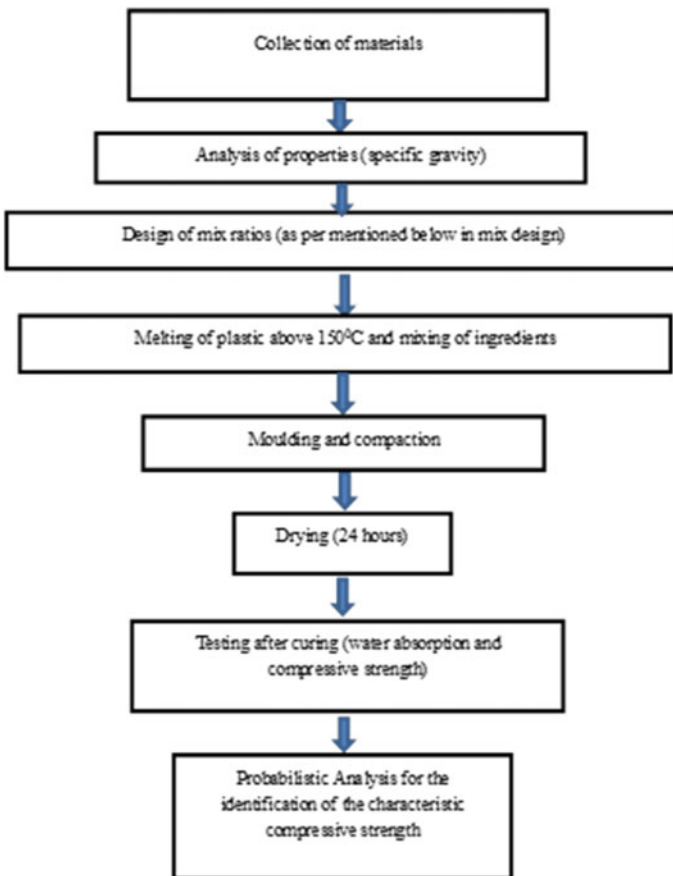
Fig. 1 Flowchat of the experimental methodology

Fig. 2 Material used for preparing paving block

Fig. 3 Melting process of waste plastic

Table 1 Specific gravity of materials

Material	Specific gravity
Sand	2.67
Fly ash	2.19
Cement	3.14
Quarry dust	2.68

3 Preparation of Paving Block

In this study, the mix of the different compositions followed based upon trial-and-error method. Based on the trial-and-error, first mixture is prepared with waste plastic, fly ash, and sand whereas second one is waste plastic, fly ash, and quarry dust. The third mixture consists of cement, fly ash, and sand. The details of proportions for the mixtures are presented in Tables 2, 3, and 4, respectively. The percentage of the individual material is taken by weight of the total mix.

Table 2 Type 1 PFS blocks

Proportions name	Plastic (%)	Fly ash (%)	Sand (%)
B-1	80	–	20
B-2	50	30	20
B-3	50	40	10

Table 3 Type 2 PFQ blocks

Proportions name	Plastic (%)	Fly ash (%)	Quarry dust (%)
PB-1	25	25	50
PB-2	30	25	45
PB-3	35	25	40

Table 4 Type 3 cement blocks

Proportions name	Cement (%)	Fly ash (%)	Sand (%)
CB-1	70	30	0
CB-2	60	30	10
CB-3	50	30	20

After fixing the proportions, the plastic wastes are heated in a metal container (Fig. 3) at a temperature of above the melting point of plastic to confirm the homogeneous mixture with other ingredients. Further, the metal paving block mould is cleaned and applied oil inside it followed by transferring the plastic mixture into it (Fig. 4). Then, the blocks are allowed to cool for 24 h in room temperature so that they set to hard in nature. After 24 h, the paver block is removed from the moulds (Fig. 5).

Fig. 4 Paver block placing and compaction in mould

Fig. 5 Paver block after removing from mould

4 Results and Discussion

4.1 Water Absorption

After 24 h of hardening, the block is removed from the mould and kept in the water for 24 h, before that the weight of the block is noted as w_1. After 24 h, the block is taken out from the water and dried in air then again weighted (noted as w_2). The water absorption is calculated using Eq. 1 and for all the mixture types are shown in Fig. 6.

$$\text{Water absorption } (\%) = \left(\left(w_2 - w_1 \middle/ w_1\right)\right) * 100 \tag{1}$$

From Fig. 6, it is observed that block prepared with waste plastic, fly ash, and sand offering better performance in the water absorption quality as compared to other two considerations. In PFQ and cement block, the percentage of the plastic content is less compared to PFS case. In general, plastic is having antipathy to water, which leads to less absorption of water in PFS paving block.

4.2 Compressive Strength

The compressive strength for all the nonconventional blocks is presented in Fig. 7. From Fig. 7, it is observed that the block compacted with waste plastic, fly ash, and quarry dust resulting higher compressive strength compared to PFS and conventional cement block. The highest strength observed for the PB-2 block as 50 MPa and 14 MPa for CB-3. The highest compressive strength gained by PFQ blocks may be due to the fine aggregate content available in the quarry dust.

(a) PFS blocks

(b) PFQ blocks
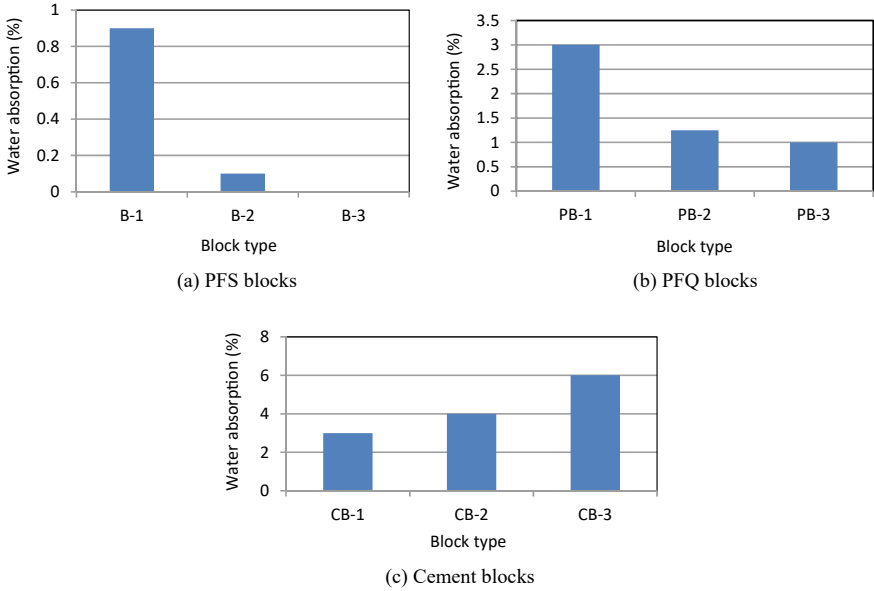
(c) Cement blocks

Fig. 6 Water absorption of PFS, PFQ, and cement blocks

(a) PFS blocks

(b) PFQ blocks
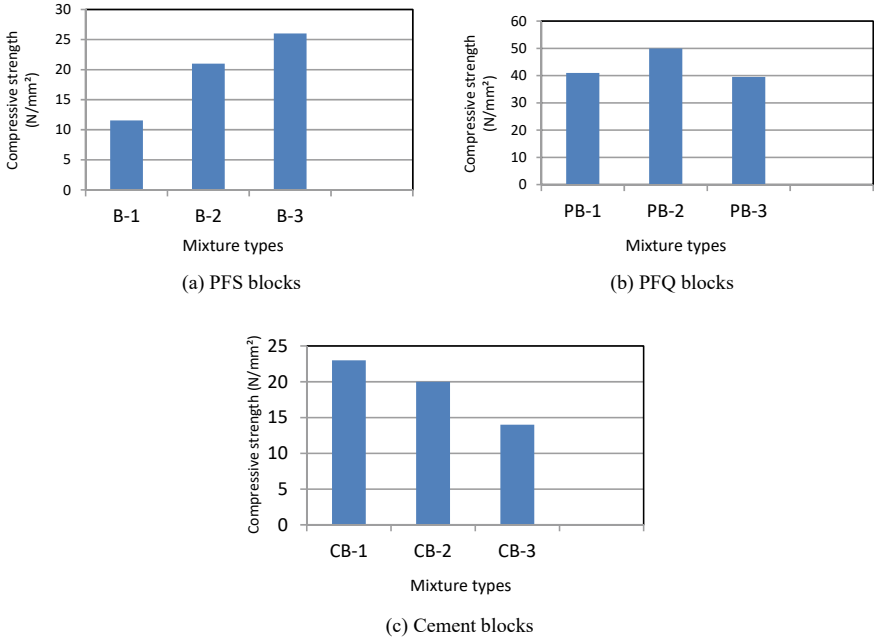
(c) Cement blocks

Fig. 7 Compressive strength of PFS, PFQ, and cement blocks

5 Probabilistic Analysis

The uncertainty, which arises in real-world engineering situations, may be solving with an appropriate probabilistic model according to Ang and Tang [9]. Basically, the normal distribution is the most extensively used distribution in statistics and is also applicable to a wide range of events in civil engineering applications [10, 11].

The normal distribution function is defined by

$$f(x) = \frac{1}{\sigma\sqrt{2\pi}} \exp\left[-\frac{1}{2}\left\{\frac{(x-\mu)}{\sigma}\right\}^2\right]$$

(2)

where μ and σ are represented as the mean and standard deviation.

The empirical rule in statistics is often referred to as the three-sigma rule or the rule for determine the proportion of values that fall within certain distances from the mean. The data in a normal distribution are converted to a standard score in normal distribution, and the empirical rule describes the percentage of the data which fall within a specific numbers. The standard deviations (σ) and the mean (μ) derived from the experimental which resulted to a bell-shaped curve. The probability of randomly obtaining a score is valuated from a normal distribution using empirical rule. From Fig. 8, it can predict that at 95% of probability level, the values fall within the two standard deviations from the mean (-2 and $+2$). Fifty numbers of samples were tested in laboratory, and the compressive strength value was monitored with a required curing period. From the recorded strength values, the statistical parameters as mean and standard deviation values are evaluated, and the obtained characteristic compressive strength is shown in Table 5.

Fig. 8 Normal distribution curve [9]
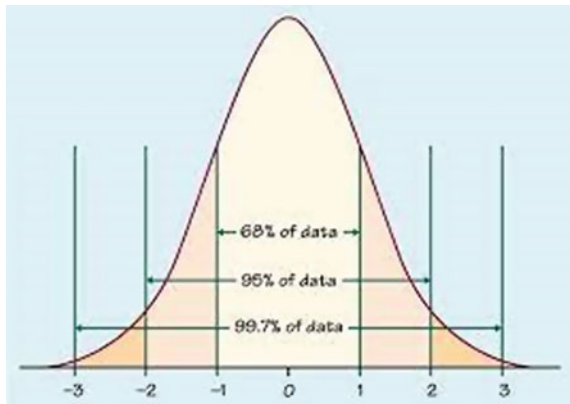
Table 5 At 95% probability level, the measured characteristic compressive strength of different paving blocks

Proportions name	Mean (μ)	Standard deviation (σ)	Characteristic compressive strength (in MPa)
B-1	11.55	0.702	12.28
B-2	21.01	0.75	21.85
B-3	26.5	0.695	27.49
PB-1	40.2	0.65	40.85
PB-2	50.71	0.691	51.39
PB-3	39.45	0.75	40.25
CB-1	23.4	0.71	24.11
CB-2	20.41	0.605	21.0
CB-3	14.72	0.65	15.36

6   Conclusions

The present study utilized the waste plastic as a replacement for cement to produce paving blocks. The experimental results showed that the PFS block offering less water absorption capacity compared to PFQ and cement as the percentage of plastic content is up to 50% in PFS. Whereas, in compressive strength characteristic, the block prepared with PFQ is higher followed by PFS and cement block. This same thing also confirmed through probability analysis at 95% confidence level. Overall, from this investigation, it is concluded that the paving blocks prepared with different waste materials satisfying the requirement for a sustainable and economical paver block to some extend as the cost of the collection and processing of the waste materials are minimal compared to conventional resources. These blocks can be utilized for serving as parking or shoulder materials. However, further more extension research is required to recommend this block for field use.

References

1. Agyeman S, Obeng-Ahenkora NK, Assiamah S, Twumasi G (2019) Exploiting recycled plastic waste as an alternative binder for paving blocks production. Case Stud Constr Mater 11:e00246
2. Harini BR, Elangovan P (2015) Experimental study on flexural behaviour of hybrid fibre reinforced concrete with elastomeric pads. Bonfring Int J Ind Eng Manage Sci 5(2):67–72
3. Kodua J (2015) Influence of recycled waste high density polyethylene plastic aggregate on the physico-chemical and mechanical properties of concrete. MPhil Thesis, Kwame Nkrumah University of Science and Technology, Ghana
4. Jnr AK, Yunana D, Kamsouloum P, Webster M, Wilson DC, Cheeseman C (2018) Recycling waste plastics in developing countries: use of low-density polyethylene water sachets to form plastic bonded sand blocks. Waste Manage 80:112–118

5. Sharma P, Batra RK (2016) Cement concrete paver blocks for rural roads. In: Proceedings international conference on futuristic trends in engineering, science, humanities, and technology (Gwalior)
6. Meng Y, Ling TC, Mo KH (2018) Recycling of wastes for value-added applications in concrete blocks: an overview. Resour Conserv Recycl 138:298–312
7. Ghuge J, Surale S, Patil BM, Bhutekar SB (2019) Utilization of waste plastic in manufacturing of paver blocks system. Int Res J Eng Technol 6(04):1967–1970
8. Banerjee T, Srivastava RK, Hung YT (2014) Chapter 17: plastics waste management in India: an integrated solid waste management approach. In: Handbook of environment and waste management: land and groundwater pollution control, pp 1029–1060
9. Ang AHS, Tang WH (2007) Probability concepts in engineering. Emphasis on applications to civil and environmental engineering, 2nd edn. Wiley, New York
10. Priyadarshini M, Patnaik M, Giri JP (2018) A probabilistic approach for identification of compressive strength of fly ash bricks. Innov Infrastruct Solutions 3(1):56
11. Priyadarshini M, Giri JP, Patnaik M (2021) Variability in the compressive strength of non-conventional bricks containing agro and industrial waste. Case Stud Constr Mater 14:e00506

The Overview and Application of Generalised Beam Theory in Buckling Analysis of Thin-Walled Structures

Aparna Baburaj and Vijaya Vengadesh Kumar Jeyapragasam

1 Introduction

Structural steel members are broadly classified as hot rolled and cold-formed steel members based on the manufacturing process. Cold-formed steel members are formed by cold rolling or pressing to obtain steel with thickness less than 10 mm which contributes to the high strength-to-weight ratio [1]. Due to this desirable aspect, thin-walled (cold-formed) steel members have lately found widespread use in the construction industry. But the slenderness of the section also makes the members more susceptible to local/distortional buckling. As a consequence, analysing the structural behavioural response of thin-walled members is critical. Finite element method (FEM) and finite strip method (FSM) are the two most commonly used methods for studying the buckling behaviour and ultimate strength of cold-formed steel sections, however, it does not provide the modal participation in failure.

The most practical approach to obtain elastic buckling solutions eliminating this drawback is using generalised beam theory (GBT). Professor Schardt and his colleagues at the Technical University of Darmstadt in Germany were the first to develop the theory. It permits the isolation of deformation modes of buckling in the analysis, unlike most other alternatives. GBT is perceived as an extension of Vlasov's classical beam theory in Schardt's research work, which was documented in German and published as a book "*Verallgemeinerte Technische Biegetheorie*" (VTB) in 1989 [2], still serving as a primary source for the theory's conception. Later, after almost three decades, Professor Davies was the one who conducted

A. Baburaj (✉) · V. V. K. Jeyapragasam
Department of Civil Engineering, National Institute of Technology Karnataka, Suratkal, Karnataka 575025, India
e-mail: ab.203st002@nitk.edu.in

V. V. K. Jeyapragasam
e-mail: vj@nitk.edu.in

studies based on Schardt's work and brought the concepts of GBT to the English-speaking research community through his publications [3–5]. Professors Camotim and Silvestre, together with their research team, have thoroughly investigated the scope of this theory's application and have subsequently published all of their findings in over 100 journal publications. Their initial work dealt with developing fundamental first- and second-order GBT formulations for orthotropic materials [6, 7]. Finite element formulations for solving eigenvalue problems associated with GBT equations were proposed and evaluated in the article presenting the analysis of pultruded FRP-lipped channel members [8]. GBT's scope was expanded to encompass the analysis of nonlinear elastic materials such as stainless steel and aluminium members under uniform compression, by introducing appropriate modifications to incorporate instantaneous elastic moduli [9]. The bifurcation analysis of stainless steel and aluminium assuming general loading conditions was then carried out using these derived formulations [10]. Cross-sectional analysis is established later for arbitrarily "branched" open cross sections using GBT formulations [11]. Bebiano collaborated with Silvestre and Camotim to expand GBT to members subjected to non-uniform bending [12]. He was a key member of Professor Camotim's research group at the University of Lisbon in developing the GBTUL software, which can do both buckling and vibration analysis. In his thesis, he confides through GBT formulas for buckling and dynamic response of thin-walled members in detail [13] and has made many publications in this regard [14–16]. A new approach for the cross-sectional analysis of GBT which ranks the deformation modes according to their priority [17, 18] enables one to allow the member to buckle in a particular buckling mode of interest for a better understanding of the structural response of thin-walled members. Further application of GBT includes buckling analysis of members with variable cross section, tubular and conical shells [19–22].

This paper aims to give a brief overview of the concepts involved in GBT buckling analysis that is both (i) cross-sectional and (ii) member analyses and later the review of available literature on GBT for one to get a consolidated knowledge about the theory and its applications.

2 Literature Review

The generalised beam theory was first studied by Professor Schardt and his colleagues at the University of Darmstadt in Germany. He conceived this theory as an extension of folded plate theory and Vlasov's theory of thin-walled sections. However, since all of his publications were documented in German, there was very little information available to the rest of the research world. But later Davies and Leach explored Schardt's research and brought his remarkable invention of GBT to the world's attention through their first two publications on first and second-order generalised beam theory [4, 5]. The articles show the equivalence of the fundamentals of GBT with the classical theories to analyse thin-walled members and demonstrate its application using an illustration done manually on lipped angle section. GBT is an attempt

in unifying the conventional theories to extend it to higher modes of deformations in cross-sectional levels like distortion applying the knowledge of basic structural mechanics. Since Davies's publications [4, 5] still remain as the primary source for fundamentals of GBT, explanations are done first based on them.

The four classical beam theories that deal with loading conditions, namely axial extension, major and minor principle axis bending and torsion (refer Fig. 1) form the basis for generalised beam theory [5]. Axial extension is the deformation of a member parallel to its axis which can be described using rod theory, Euler beam bending theory gives the expression for bending about major and minor axis and Vlasov's torsion theory is employed for torsion case. Equations (1–4), respectively presents the basic conventional equations that form the essence of GBT.

$$EAu'' = -q_x; \quad N = EAu' \tag{1}$$

$$EI_y w'''' = -q_x; \quad M_y = -EI_y w'' \tag{2}$$

$$EI_z v'''' = q_y; \quad M_z = -EI_z v'' \tag{3}$$

$$EC_w \theta'''' - GI_T \theta'' = m_x; \quad B = -EC_w \theta'' \tag{4}$$
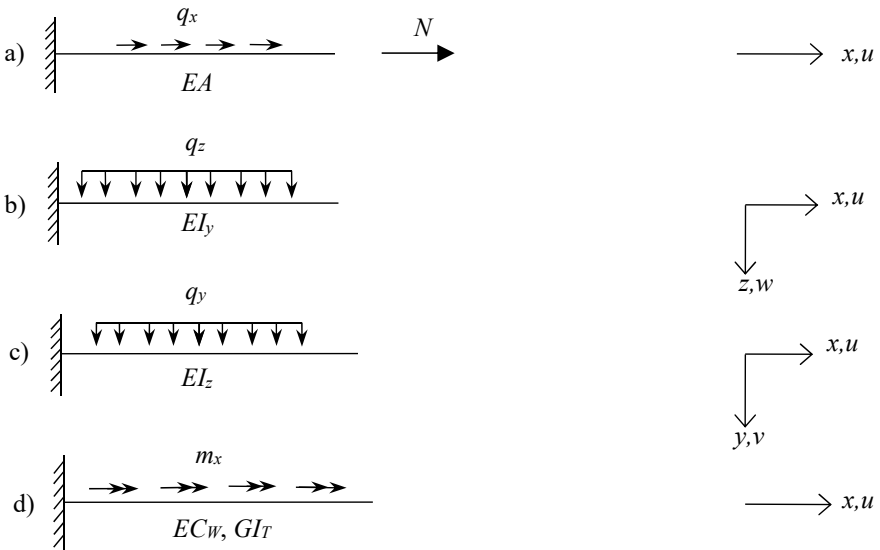
Fig. 1 **a** Axial extension **b** major axis bending **c** minor axis bending **d** torsion

where E, G, A, I_y, I_z, C_w and I_T are the modulus of elasticity, modulus of rigidity, area of cross section, moment of inertia about major and minor axis, warping constant and torsion constant, respectively.

Four fundamental modes of deformation are thus introduced which are referred to as "rigid body modes" since they do not involve any distortion at the cross-sectional level. The total number of deformation modes involved in the analysis is calculated as equal to the number of natural nodes of cross section which are defined at the ends or junctions of wall/plate elements. So, for a cross section having five natural nodes, number of deformation modes will be five: the first four representing the rigid body modes and the fifth mode being the distortional one as shown in Fig. 2. Each of these modes is associated with a warping function, corresponding cross-sectional displacements, section properties and distortional bending stress for modes 5 and above. Among these, the warping function ($^k u$, where k denotes deformation mode) is a novel feature of GBT related to the distribution of axial strain over the cross section. The warping functions can be directly calculated for the fundamental modes since for the first mode (axial extension) it is the uniform axial strain distribution, i.e. $^1 u = -1$; for second and third bending modes, the functions are the linear distribution of strain about major and minor principal axes, and for fourth mode (torsion), the warping function is the distribution of axial strain due to bi-moment known as the sectorial coordinate. The function values for higher modes can be calculated by utilising the orthogonality condition of warping functions.

The fundamental equation of GBT derived using the principal of virtual work is given by,

$$E^k C^k V - G^k D^k V'' + {}^k B^k V = {}^k q \tag{5}$$

where $E = $ Young's modulus; $G = $ shear modulus; $^k C, {}^k D, {}^k B = $ section properties of kth mode; $^k V = $ generalised deformation in mode k; $^k q = $ distributed load applicable to mode.

The analogy between conventional theories and generalised beam theory can now be established by comparing Eqs. (1–4) and Eq. (5), refer to Table 1.

Here, C represents the stiffness with regard to the direct stress, D represents the stiffness with regard to shear stress due to twisting and B represents the stiffness concerning transverse bending stress. The section properties can be determined utilising the equivalence of GBT with the conventional theories.

Using GBT to analyse thin-walled members entails primarily two steps: first, calculating all cross-sectional parameters such as warping function, set of displacements, and section properties and second, solving the GBT fundamental equation for each mode. The author describes three methods for solving the GBT fundamental equation: (i) An explicit solution may be achieved by noting the similarity of the GBT equation with the basic beam equation of elastic foundation. (ii) Using the finite difference approach, the values of deflection and stress at mid-span are obtained by dividing the span into 6 slices and solving 14 simultaneous equations.

(a) Cross - section with five nodes

1. Axial Stress

2. Bending

3. Bending

4. Torsion

Displaced Shape   Warping Function

(b) Rigid body modes (k=1... 4)

Displaced Shape   Warping Function

(c) Cross - section distortion mode (k=5)
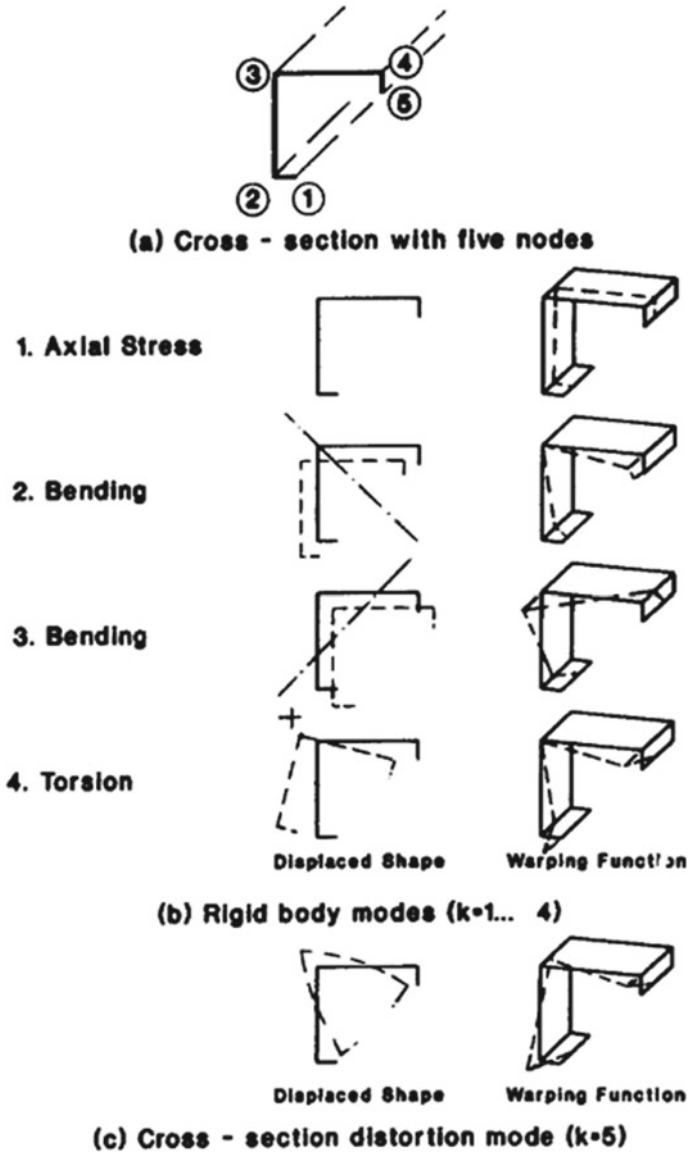
Fig. 2 Typical displaced shape and warping functions [5]

(iii) The problem may be treated as a simple two-element finite element model with four degrees of freedom and solved.

In practical cases, such as lateral-torsional buckling of a beam or an axially loaded compression member, the response of a cold-formed steel structure is mostly nonlinear. The second-order terms introduced in the fundamental second-order GBT

Table 1 Example of construction of a table

Deformation mode	Conventional theory			Generalised beam theory		
1	A			^{1}C		
2	I_{XX}			^{2}C		
3	I_{YY}			^{3}C		
4	Γ	J		^{4}C	^{4}D	
5	^{5}C	^{5}D	^{5}B	^{k}C	^{k}D	^{k}B

equation Eq. (6) account for this consequence of geometric nonlinearity [4], and the analysis is done to obtain the critical buckling load.

$$E^{k}C^{k}V'''' - G^{k}D^{k}V'' + {}^{k}B^{k}V + \sum_{i}\sum_{j} {}^{ijk}\kappa \left({}^{i}W^{i}V' \right)' = {}^{k}q \qquad (6)$$

where

^{i}W is the warping stress resultant in the ith mode and $^{ijk}\kappa$ is the second-order term that accounts for all the interactions between in-plane stresses in the faces and out-of-plane deformations. The third term in Eq. (6) can be inferred as the deviation force resulting from axial stresses and deformation of the members. The expression for axial stress (σ_x) in the cross section resulting from the m warping stress resultants ^{i}W is given by Eq. (7).

$$\sigma_x = -\sum_{i}^{m} \frac{{}^{i}W^{i}u}{{}^{i}C} \qquad (7)$$

Second-order GBT equation for the bifurcation case is easy to solve since the load causing deformation is zero which makes the right-hand side of Eq. (6) null. In the case of axial load or uniform bending moment, explicit equations are obtained which can be directly solved, but for other varying load conditions one has to resort to numerical analysis methods, the most effective being the finite difference method. GBT allows modal decomposition to study the effect of either an individual mode or a combination of more than one mode by considering the interaction between modes of deformation. Davies and Leach have thereby established the power and versatility of GBT for buckling analysis of isotropic cold-formed sections, clearing the door for future studies to investigate the efficacy of utilising GBT.

Silvestre and Camotim accomplished a significant breakthrough in GBT research in 2002 by formulating the derivation of the fundamental GBT equation as well as the boundary conditions for members with orthotropic materialistic property. The basic assumptions and kinematic relation are the same as in the isotropic case, with the constitutive relationship differing because of orthotropy.
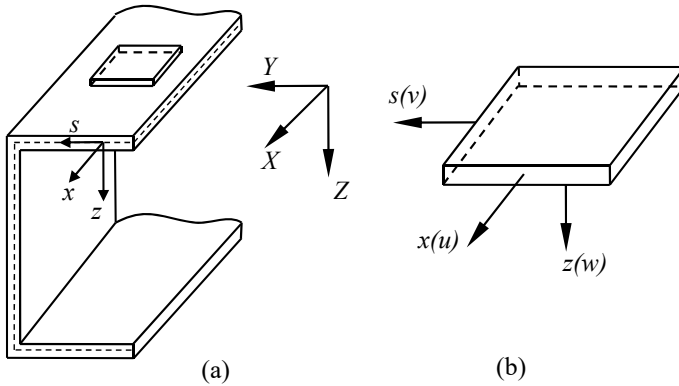
Fig. 3 **a** Prismatic thin-wall member with arbitrary cross-section **b** Wall(plate) element

2.1 Assumptions

Consider an arbitrary open cross section as shown in Fig. 3 with global coordinate system represented by *X–Y–Z* and along each wall a local coordinate system *x–s–z* is chosen where *x* is along global *X* axis, *s* along the direction of wall mid-plane and *z* along the thickness direction of the wall. The basic assumptions employed for formulating kinematic relations of GBT is based on Kirchhoff-Love hypothesis which are,

(i)   Straight line fibres which are initially normal to the middle surface remain straight and normal to the middle surface even after deformation ($\varepsilon_{zz} = \gamma_{xz} = \gamma_{sz} = 0$).

(ii) Out of plane normal and shear stresses are negligibly small compared to the in-plane shear stresses of the plate and hence can be neglected ($\sigma_{zz} = \tau_{xz} = \tau_{sz} = 0$).

Vlasov's theory provides the basis for the next set of assumptions:

(iii) Transverse extensions, that is mid-plane fibres parallel to *x* and *s* axes, remain perpendicular to each other even after deformation ($\gamma_{xs} = 0$).

(iv) Shear strains are neglected ($\varepsilon_{ss} = 0$).

2.2 Kinematic Relations

Displacement components u_x, u_y, u_z considering the assumptions of GBT as mentioned above are given by Eq. (8).

$$u_x(x, s, z) = u(x, s) - zw_{,x}(x, s);$$
$$u_y(x, s, z) = v(x, s) - zw_{,s}(x, s);$$

$$u_z(x, s, z) = u(x, s) - zw_{,x}(x, s) \tag{8}$$

$u(x, s)$ and $v(x, s)$ are the mid-plane displacement field (i.e. ($z = 0$) and $(.)_{,x}$ represents $\partial/\partial x$. These displacement fields can be suitably expressed as the product of two separate functions [6]; (i) a function of s which represents the mid-line cross-sectional displacement value and (ii) an arbitrary function of x defined along the member length for each deformation mode k, refer Eq. (9), ($1 \le k \le N_d$), where n is number of wall segments and N_d denotes number of nodes).

$$
\begin{aligned}
u_k(x, s) &= u_k(s) \cdot \varphi_{k,x}(x) \\
v_k(x, s) &= v_k(s) \cdot \varphi_k(x) \\
w_k(x, s) &= w_k(s) \cdot \varphi_k(x)
\end{aligned}
\tag{9}
$$

With this, one can arrive at the strain–displacement relation incorporating the assumptions and kinematic relations given by Eq. (8), (the linear strain components can be expressed as the sum of membrane $(.)^M$ and flexural $(.)^F$ strain components).

$$
\begin{aligned}
\varepsilon_{xx}^L &= \varepsilon_{xx}^{L \cdot M} + \varepsilon_{xx}^{L \cdot F} = u_{,x} - zw_{,xx} \\
\varepsilon_{ss}^L &= \varepsilon_{ss}^{L \cdot M} + \varepsilon_{ss}^{L \cdot F} = 0 - zw_{,ss} \\
\gamma_{xs}^L &= \gamma_{xs}^{L \cdot M} + \gamma_{xs}^{L \cdot F} = 0 - 2zw_{,xs}
\end{aligned}
\tag{10}
$$

The assumptions in the second-order analysis are the same as in the first, with the exception that nonlinear strain components must be included to account for the effects of geometric nonlinearity (refer Eq. (11)). Thus, along with the membrane, longitudinal extension (ε_{xx}^M) one has to consider the second-order terms associated with mid-plane transverse displacement components (v and w) [7].

$$
\begin{aligned}
\varepsilon_{xx}^{NL \cdot M} &= \frac{v_{,x}^2 + w_{,x}^2}{2} \\
\therefore \varepsilon_{xx}^M &= \varepsilon_{xx}^{L \cdot M} + \varepsilon_{xx}^{NL \cdot M} = u_{,x} + \frac{v_{,x}^2 + w_{,x}^2}{2}
\end{aligned}
\tag{11}
$$

Later, Bebiano et al. [12] investigated at the effects of non-uniform axial force or bending, which results in longitudinal normal stress gradients and shear stress due to varying bending moment. Equation (12) represents the membrane nonlinear shear strain component,

$$\gamma_{xx}^{NL} \equiv \gamma_{xs}^{NL \cdot M} = w_{,x}w_{,s} + v_{,x}v_{,s} \tag{12}$$

2.3 Constitutive Relation

The constitutive relationship, which is dependent on the material characteristics, relates the stress and strain components. For linear isotropic materials, the relationship is expressed in Eq. (13) while for composite material composition one can refer [7] for the constitutive relationship expression.

$$\sigma = \sigma^M + \sigma^F = \begin{Bmatrix} \sigma_{xx} \\ \sigma_{ss} \\ \tau_{xs} \end{Bmatrix}^M + \begin{Bmatrix} \sigma_{xx} \\ \sigma_{ss} \\ \tau_{xs} \end{Bmatrix}^F = H^M \varepsilon^M + H^F \varepsilon^F \tag{13}$$

where H^M and H^F (Eq. (14)) are the linear elastic constitutive relation [18]. This expression is more versatile since it could incorporate the influence of transverse extension if it is chosen to be included during the analysis.

$$H^M = \begin{bmatrix} \frac{\alpha E}{1-\nu^2} & \frac{\nu E}{1-\nu^2} & 0 \\ \frac{\nu E}{1-\nu^2} & \frac{E}{1-\nu^2} & 0 \\ 0 & 0 & G \end{bmatrix} \quad and \quad H^F = \begin{bmatrix} \frac{E}{1-\nu^2} & \frac{\nu E}{1-\nu^2} & 0 \\ \frac{\nu E}{1-\nu^2} & \frac{E}{1-\nu^2} & 0 \\ 0 & 0 & G \end{bmatrix} \tag{14}$$

Here, ν, E, and G are the material Poisson's ratio, modulus of elasticity and modulus of rigidity, respectively, and α is a factor whose value is (i) $\alpha = 1$ (i.e., $H^M = H^F$) if transverse extensions are considered ($\varepsilon_{ss}^M \neq 0$) and (ii) $\alpha = 1 - \nu^2$ if transverse extensions are excluded ($\varepsilon_{ss}^M = 0$).

2.4 Principle of Virtual Work

The GBT fundamental equation is derived by means of the principle of virtual work which is given by, $\delta V = \delta U + \delta \prod = 0$, where δV is the total potential energy of the member, δU the virtual work done by internal forces (refer Eq. 15) and, $\delta \prod$ the virtual work related to external loads (refer Eq. 16).

$$\delta U = \int_L \int_b \int_t (\sigma_{xx} \delta \varepsilon_{xx} + \sigma_{xx} \delta \varepsilon_{xx} + \sigma_{xs} \delta \gamma_{xs}) \mathrm{d}z \mathrm{d}s \mathrm{d}x = \delta U_{xx} + \delta U_{ss} + \delta U_{xs}$$

$$\tag{15}$$

Considering an applied force $q(x, s)$ which is decomposed into three components q_x, q_s, q_z and the virtual work done by the external load ($\delta \prod$) is obtained by adding these load components associated with displacements δu, δv and δw, respectively. Therefore, $\delta \prod$ becomes,

$$\delta \prod = - \int\limits_{L} \int\limits_{b} (q_x \delta u + q_s \delta v + q_z \delta w) \, ds \, dx \tag{16}$$

2.5 Fundamental GBT Equations and Boundary Condition

2.5.1 Linear (Static) Analysis

For the isotropic static (geometrically linear) analysis, Eq. (17) reads the GBT equilibrium equation and boundary condition (Eq. 18) derived using principle of virtual work. Similarly, for members showing orthotropy, GBT equilibrium equation is formulated by Silvestre and Camotim [7], taking care of the modified constitutive relation.

$$EC_{ik}\varphi_{k,xxxx} - GD_{ik}\varphi_{k,xx} + B_{ik}\varphi_k = q_i - q_{x,x.i} \tag{17}$$

$$\left(-EC_{ik}\varphi_{k,xxxx} + G\left(D_{ik}^I - D_{ik}^{II}\right)\varphi_{k,x} - \int\limits_{b} q_x u_i ds\right)\delta = 0;$$

$$\left[\left(EC_{ik}\varphi_{k,xx} + GD_{ik}^{II}\varphi_k\right)\delta\varphi_{i,x}\right]_0^L = 0 \tag{18}$$

2.5.2 Buckling (Nonlinear) Analysis

For buckling analysis using GBT second-order effects due to nonlinearity of the applied loads which was briefly described in [4] is now closely studied to arrive at equation of equilibrium and boundary condition (Eqs. (19–20)) [7, 8, 13].

$$EC_{ik}\varphi_{k,xxxx} - GD_{ik}\varphi_{k,xx} + B_{ik}\varphi_k + W_j X_{jik}^\sigma \varphi_{k,xx} = 0 \tag{19}$$

$$\left[W_j^\tau - W_j X_{jik}^\sigma \varphi_{k,x}\right]\delta\varphi_i\big|_0^L = 0 \quad W_i^\sigma \delta\varphi_{i,x}\big|_0^L = 0 \tag{20}$$

where W_j represents the associated normal (W_i^σ) and shear (W_j^τ) stress resultants, C_{ik}, D_{ik} and B_{ik} display the stiffness and X_{jik} the geometric stiffness matrices developed from the integration of cross-sectional displacements leading to Eqs. (21–25).

$$C_{ik} = \int\limits_{s} t u_i u_k ds + \frac{1}{12(1 - v^2)} \int\limits_{s} t^3 w_i w_k ds \tag{21}$$

$$B_{ik} = \frac{E}{12\left(1 - v^2\right)} \int_s t^3 w_{i,ss} w_{k,ss} \, \mathrm{d}s \tag{22}$$

$$D_{ik} = D_{ik}^I - \left(D_{ik}^I + D_{ik}^{II}\right) = \frac{1}{3} \int_s t^3 w_{i,s} w_{k,s} \, \mathrm{d}s$$

$$- \frac{vE}{12G\left(1 - v^2\right)} \int_s t^3 \left(w_i w_{k,ss} + w_k w_{i,ss}\right) \mathrm{d}s \tag{23}$$

$$X_{jik} = \int_s \frac{t u_j}{C_{jj}} (v_i v_k + w_i w_k) \mathrm{d}s \tag{24}$$

$$W_i^\sigma = E C_{ik} \varphi_{k,xx} + D_{ik}^{II} \varphi_k \quad W_i^\tau = -W_{i,x}^\sigma + G D_{ik}^I \varphi_{k,x} \tag{25}$$

2.6 Cross-Sectional Analysis

Static or buckling analysis of thin-walled members usually comprises two basic steps: (i) cross-sectional analysis and (ii) member analysis. The first one deals with finding the warping and flexural displacements to determine the modal properties and GBT matrices. The second step entails constructing the GBT equilibrium and boundary conditions, as well as solving Eqs. (17, 19) using the suitable technique. More emphasis should be placed on the cross-sectional analysis, a detailed report of which is made by researchers Schardt [2], Davies and Leach [5], Silvestre and Camotim [6] for open unbranched cross sections. While for "branched" open cross section, due to the presence of branching nodes, warping functions are to be chosen appropriately and displacement method is used to find out the flexural shape functions [11]. Goncalves et al. [17] and Bebiano et al. [18] established novel methodologies particularly for cross-sectional analysis to arrange deformation modes in a hierarchical manner with a proper knowledge of their structural/mechanical characteristics. Nedelcu [19] devised an analytical approach for performing cross-sectional analysis on members with varying cross sections.

2.7 Member Analysis

Once the cross-sectional analysis is performed, the member analysis is quite explicit since it involves only the common operations of solving a structural analysis problem. The results from cross-sectional analysis, material properties, length of member and applied loads are used to form the GBT equilibrium equation (Eqs. 17, 19) which is a fourth-order differential equation. For each mode of deformation, this equation is

solved, which helps in the assessment of modal participation in buckling. In effect the user can choose a set of deformation modes and solve the related set of equilibrium equations. In the first place, finite differences or finite element method was the common methods used to solve the set of differential equation by Schardt [2], Davies and Leach [5] and Silvestre and Camotim [6, 7] based on the complexity of boundary condition. Silvestre and Camotim [8] were the first to develop a general finite element formulation for solving first/second-order GBT equilibrium equations with arbitrary boundary conditions and applied loads. To approximate the amplitude function $\varphi_k(x)$, Hermitean polynomials are being used, which could then be substituted into the variational form of Eqs. (17 or 19) and integrated to produce the finite element matrix equation, Eqs. (26–27) (refer [8, 13] for detailed derivation).

$$[K]\{d\} = \{f\} \tag{26}$$

$$([K] + \lambda[G])\{d\} = \{0\} \tag{27}$$

Equation (26) shows the matrix form of equilibrium equation of first-order static analysis and Eq. (27) the eigenvalue system of equations for buckling analysis where $[K]$ is the stiffness and $[G]$ is the geometric stiffness matrix and λ denotes the eigenvalue. The solution of Eq. (27) gives the buckling loads and the corresponding buckling modes $\{d_b\}$ eigenvectors.

2.8 Modal Participation

GBT provides a method to find the participation of each modes of deformation in the buckling behaviour in terms of modal participation factor (P_i) [13]. The expression for modal participation factor for ith mode is read as Eq. (28). The cumulative P_k versus L modal participation graphs give a fair idea of how the nature and characteristics of the deformed configuration mode fluctuate with member length.

$$P_i = \frac{\int_L |\varphi(x)| \mathrm{d}x}{\sum_{k=1}^{N_d} \int_L |\varphi_k(x)| \mathrm{d}x} \times 100\% \tag{28}$$

3 Application of GBT

The design of members prone to buckling is critical because the buckling load is depending on its mode shape. The geometry of the cross section also significantly influences the buckling behaviour. For example, the buckling behaviour of open section is entirely different than the closed sections in which open section has

lower torsional rigidity and results in torsionally weaker section. These open section compression members have the tendency to undergo the coupled flexural–torsional buckling when the centroid of the cross section does not coincide with the shear centre of the section. Such a mono-symmetric compression member may buckle in lower load than the flexural buckling capacity about the asymmetry axis of the cross section. Therefore, appropriate buckling load which is the minimum of flexural–torsional buckling and flexural buckling about minor axis has to be considered in the design of member.

Since the global (rigid body) buckling mode is possible for cold-formed and hot-rolled sections, care must be taken while designing the hot-rolled compression member using the IS: 800-2007. At present, there is no information available in IS 800-2007 to design a mono-symmetric compression member which may fail in flexural–torsional buckling. However, the mono-symmetric sections such as angle, tee and channel sections are widely used as truss members and main compression members. Although few guidelines are available in IS: 800-2007 for designing the angle section, it is not explicitly discussing about flexural–torsional buckling. Moreover, the angle section's local buckling is very similar to the torsional mode which will have different post-buckling strength. In such conditions, the thorough knowledge of buckling and its modal participations is inevitable to any design engineer. The mono-symmetric compression member design is dealt in Eurocode by considering the minimum elastic critical buckling load while determining the non-dimensional slenderness ratio of the section. The determination of flexural–torsional buckling load for various mono-symmetric and asymmetric sections is mostly in research level and hence the engineers experience the difficulties in its capacity estimation. The calculations involved in flexural–torsional critical buckling load require the details about warping constant which needs knowledge about sectorial coordinates and hence make it cumbersome. For the practical design, the GBTUL software can be used by the design engineer which is available at free of cost. This software is capable of including any geometrical shape like open with (I section) and without element branches (C, L and T sections), closed (Circular/rectangular hollow sections) or combined (Trapezoidal section with multiple cells and extended top flange) in the analysis. It also provides the option to consider different loading and boundary conditions and provides the geometrical properties and accurate critical buckling load with its mode participation to identify the failure mode. With the aid of generalised beam theory, the design engineer can safely design the members subject to compression, bending, torsion or its combined action. Figure 4 represents the buckling curve for a simply supported ISMC 200 section carrying axial compression.

It should be noted that, the flanges of ISMC have unsymmetric decreasing tapering from web to tip, which cannot be modelled in GBTUL and hence idealised as prismatic flange with centreline dimensions. However, the geometrical properties are not deviating more than 2% for the section and therefore the results are considered to be accurate. From Fig. 4, the elastic critical buckling load for a particular column length can be considered to determine its non-dimensional slenderness ratio and further its axial capacity.

Fig. 4 Buckling load versus
simply supported column
length curve
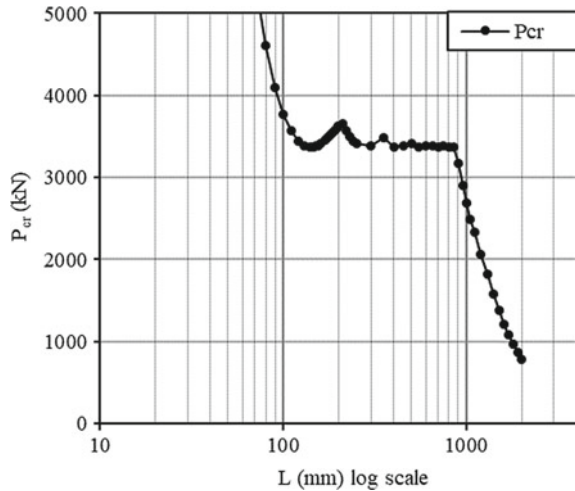
4   Conclusion

In this article, the basic theory behind the generalised beam theory and its evaluation are detailed. The systematic advancement of this theory is presented in detail. The practical application of this theory is demonstrated for ISMC 200 compression member. With the advantage of GBT, the designer can determine the geometrical and buckling characteristics of any member susceptible to buckling. The procedure is straightforward in GBTUL software and can be extended for any support and loading conditions. Therefore, the chances of estimating the accurate geometrical properties and buckling load values are extremely high. The care must be taken when the geometrical properties are used to find the extreme stress values in cross section because the extreme bending stress will occur at the extreme fibres but not at the centreline of flanges/web. The same procedure is readily applicable to vibration problems which is mathematically equivalent to buckling problems.

References

1. 13 Thin-walled metal construction (2004)
2. Schardt R (1989) Verallgemeinerte technische biegetheorie. https://doi.org/10.1007/978-3-642-52330-4
3. Davies JM, Jiang C (1996) Design of thin-walled beams for distortional buckling. In: International specialty conference on cold-formed steel structures, pp 141–153.
4. Davies JM, Leach P, Heinz D (1994) Second-order generalised beam theory. J Constr Steel Res 31:221–241. https://doi.org/10.1016/0143-974X(94)90011-6
5. Davies JM, Leach P (1994) First-order generalised beam theory. J Constr Steel Res 31:187–220. https://doi.org/10.1016/0143-974X(94)90010-8

6. Silvestre N, Camotim D (2002) First-order generalised beam theory for arbitrary orthotropic materials. Thin-Walled Struct 40. https://doi.org/10.1016/S0263-8231(02)00026-5
7. Silvestre N, Camotim D (2002) Second-order generalised beam theory for arbitrary orthotropic materials. Thin-Walled Struct 40:791–820. https://doi.org/10.1016/S0263-8231(02)00026-5
8. Silvestre N, Camotim D (2003) GBT buckling analysis of pultruded FRP lipped channel members. Comput Struct 81:1889–1904. https://doi.org/10.1016/S0045-7949(03)00209-8
9. Gonçalves R, Camotim D (2004) GBT local and global buckling analysis of aluminium and stainless steel columns. Comput Struct 82:1473–1484. https://doi.org/10.1016/j.compstruc.2004.03.043
10. Gonçalves R, Camotim D (2007) Thin-walled member plastic bifurcation analysis using generalised beam theory. Adv Eng Softw 38:637–646. https://doi.org/10.1016/j.advengsoft.2006.08.027
11. Dinis PB, Camotim D, Silvestre N (2006) GBT formulation to analyse the buckling behaviour of thin-walled members with arbitrarily "branched" open cross-sections. Thin-Walled Struct 44. https://doi.org/10.1016/j.tws.2005.09.005
12. Bebiano R, Silvestre N, Camotim D (2007) GBT formulation to analyze the buckling behavior of thin-walled members subjected to non-uniform bending 7:23–54
13. Bebiano R (2010) Stability and dynamics of thin-walled members—application of generalised beam theory
14. Bebiano R, Silvestre N, Camotim D (2008) GBTUL—a code for the buckling analysis of cold-formed steel members. In: 19th international specialty conference on cold-formed steel structures, pp 61–79
15. Bebiano R, Camotim D, Gonçalves R (2018) GBTUL 2.0—a second-generation code for the GBT-based buckling and vibration analysis of thin-walled members. Thin-Walled Struct 124:235–257. https://doi.org/10.1016/j.tws.2017.12.002
16. Bebiano R, Camotim D, Silvestre N (2013) Dynamic analysis of thin-walled members using generalised beam theory (GBT). Thin-Walled Struct 72:188–205. https://doi.org/10.1016/j.tws.2013.07.004
17. Gonçalves R, Ritto-Corrêa M, Camotim D (2010) A new approach to the calculation of cross-section deformation modes in the framework of generalized beam theory. Comput Mech 46:759–781. https://doi.org/10.1007/s00466-010-0512-2
18. Bebiano R, Gonçalves R, Camotim D (2015) A cross-section analysis procedure to rationalise and automate the performance of GBT-based structural analyses. Thin-Walled Struct 92:29–47. https://doi.org/10.1016/j.tws.2015.02.017
19. Nedelcu M (2010) GBT formulation to analyse the behaviour of thin-walled members with variable cross-section. Thin-Walled Struct 48:629–638. https://doi.org/10.1016/j.tws.2010.03.001
20. Nedelcu M (2011) GBT formulation to analyse the buckling behaviour of isotropic conical shells. Thin-Walled Struct 49:812–818. https://doi.org/10.1016/j.tws.2011.02.006
21. Abambres M, Camotim D, Silvestre N (2020) Non-linear GBT analysis of tubular thin-walled metal members. To cite this version : HAL Id: hal-02450451, pp 0–15
22. Muresan AA, Nedelcu M, Gonçalves R (2019) GBT-based FE formulation to analyse the buckling behaviour of isotropic conical shells with circular cross-section. Thin-Walled Struct 134:84–101. https://doi.org/10.1016/j.tws.2018.07.032

Durability Properties of Geopolymer Concrete from Fly Ash and GGBS

T. Srividya and P. R. Kannan Rajkumar

1 Introduction

Geopolymers are amorphous natured inorganic polymeric structures with better mechanical properties than OPC concrete [1]. Durability can be termed as the measure of concrete's resistance for deterioration due to weathering, chemical attack and abrasion. Deteriorations can be controlled by permeability of concrete in the aggressive environment, since attack due to chloride and sulphates are governed by the transportation of fluid in concrete [2]. Like CS, durability needs to be studied at 28 days and sometimes 56 and 90 days for the long term performance of concrete in a service environment [3]. Unlike OPC concrete, GPC has no transition zone which makes it more durable leading to less or no shrinkage [4–6]. Concentrations of acid and exposure time affects the deterioration [7]. Experimental studies on the long term characteristics of low calcium FA-based GPC showed an outstanding performance under sulphate exposure. Being subjected to sulphate exposure for a period of 365 days, there were no appreciable strength and mass loss found. Significantly better performance was found on immersion in sulphuric acid than that of OPC concrete [8, 9]. Exposure of FA-based GPC specimens under 2% sulphuric acid, there was an increase in mass along with damages in the surface of specimens. But over a period of time, loss in mass was observed. In acidic medium, geopolymer (GP) materials were found to be more resistant than OPC [10]. Studies on the durability performance of FA-GLSS (granulated lead smelter slag)-based GPC for a period of 270 days were carried out under diverse alkaline conditions: 5% NaCl (sodium chloride), 5% Na_2SO_4 (sodium sulphate), 5% Na_2SO_4 with 5% $MgSO_4$ (magnesium sulphate) and 3% H_2SO_4 (sulphuric acid) of 10 N. Parameters like water absorption, sorptivity,

T. Srividya (✉) · P. R. Kannan Rajkumar
Department of Civil Engineering, SRM Institute of Science and Technology, Kattankulathur, Tamil Nadu, India
e-mail: st1899@srmist.edu.in

porosity, weight loss and CS under wetting–drying and heating–cooling cycles were also investigated. Under the range of considered exposure, durability performance of GPC was found to be superior to that of OPC concrete [11]. Durability performance of GGBS-based GP mortar was compared with OPC under oven curing (CO) at 75 °C for 1 day, air curing (CA) for 28 days and water curing (CW). For the activation of GGBS, sodium metasilicate of sodium concentration 4%, 8% and 12% has been used. At elevated temperature, under CW condition 4% Na showed better results. In the abrasion test, both CA and CW curing gave good results for 8% and 12% Na [12]. Authors have given a brief review on the durability performance like resistance to sulphate and acid of FA and GGBS-based GP specimens. It was inferred that GP specimens resisted well after exposure to alkaline and acidic environmental conditions [13].

As geopolymer technology is a new technique under limelight over a period of two decades, limited data are existing on the long term performance of FA-GGBS blend GPC. High early strength under ambient curing can be achieved by inclusion of GGBS in FA-based GPC. Since FA-based GPC requires heat curing because of the higher concentration of silicon dioxide. The significance of this research article is to bring deeper knowledge about the durability performance like resistance to sulphate and acid, chloride resistance, water penetration, etc., of FA-GGBS-based GPC with binder ratio (FA: GGBS) of 4:1 (GPC 1) and 1:1 (GPC 2).

2 Experimental Investigation

2.1 Materials Used

In this Investigation, Class F FA was procured from Ennore power plant, India. The fineness of FA was found to be $330 \, m^3/kg$ (Blaine) with specific gravity of 2.2. GGBS was purchased from JSW (India) of specific gravity 2.85. The chemical composition of the FA and GGBS as determined from EDXRF is listed in Table 1.

Table 1 Chemical composition of FA and GGBS

Component (%)	Flyash (%)	GGBS (%)
Silicon dioxide (SiO_2)	55.00	36.74
Iron oxide (Fe_2O_3)	10.17	0.4
Aluminium oxide (Al_2O_3)	26.00	10.78
Calcium oxide (CaO)	2.09	43.34
Magnesium oxide (MgO)	0.80	3.21
Sulphur trioxide (SO_3)	–	0.5
Na_2O	0.4	0.18
K_2O	1.65	0.17
Loss on ignition (LOI)	3.89	0.6

Table 2 GPC mix proportion

Mix ID	FA (kg/m^3)	GGBS (kg/m^3)	M sand (kg/m^3)	CA (kg/m^3)	NaOH (kg/m^3)	Na$_2$SiO$_3$ (kg/m^3)	Comp strength (MPa)
GPC 1	336	84	630	1050	70	140	44.07
GPC 2	210	210	630	1050	70	140	45.4

In addition to Fe$_2$O$_3$, FA comprises approximately 80% of SiO$_2$ and Al$_2$O$_3$, less than 5% of CaO and fragments of other oxides. GGBS has a higher content of CaO which is responsible for the early setting time of GGBS-based GPC. Commercially available Na$_2$SiO$_3$ solution of silica modulus-Ms (SiO$_2$/Na$_2$O) 2.0 and NaOH lye of 48% concentration in liquid form were used to prepare the alkali activator solution (AAS).

2.2 Mix Proportion of GPC

Based on literature studies and past experience, mix proportion of GPC mixes was arrived. GPC mixes were prepared by blending of FA and GGBS in varying proportion of 80:20 and 50:50 along with M sand, coarse aggregate and alkali activators. They were designated as GPC 1 and GPC 2. The ultimate goal was to achieve CS of 40 N/mm^2. The mix proportion of GPC mixes was listed in Table 2. In a 100 L pan mixer, dry ingredients were added and allowed to mix for 2 min. Alkali activators used for GPC was combination of NaOH solution, Na$_2$SiO$_3$ solution and water. The alkaline liquid to binder ratio was 0.55. Premixed activator solution was prepared 24 h prior to casting and added to the blend. Fresh concrete was poured into cube and cylinder moulds. Specimens were demoulded after 24 h and left for ambient curing for 28 days. Using compression testing machine (CTM), cubes and cylinders were tested to evaluate the CS of the GPC.

Slump cone test was conducted to study the fresh properties of GPC mixes. The value of slump ranges from 70 to 100 mm.

2.3 Rapid Chloride Permeability Test

Permeability is one of the important factor that allows the transportation of chloride ions to the reinforcement. Lesser the permeability, lesser will be the risks of corrosion of steel. Quality assurance and quality control in the construction stage influences the durability of the concrete.

Table 3 Chloride Ion penetrability based on charge passed as per ASTM C 1202 [14]

Charge passed in coulombs	Chlorine ion penetrability
>4000	High
2000–4000	Moderate
1000–2000	Low
100–1000	Very low
<100	Negligible

The rapid chloride permeability test (RCPT) was performed by passing electric current in the concrete cylindrical disc of size 50 × 100 mm for 6 h. The cylindrical discs were prepared by cutting the GPC cylinder of size 100 mm × 200 mm using cutting machine. In the migration cell containers, concrete disc was placed. In one of the cell containers, discs were immersed in 3% by mass of NaCl in distilled water. The other container was filled with 0.3 N of NaOH solution. A voltage of 60 V perpetuates during entire process for each sample. Table 3 shows the range of chloride ion permeability based on the amount of charge passed through the specimens. RCPT test setup and the GPC specimens after 6 h chloride penetration as shown in Fig. 1a and b. The values were found to be permeable and seems to be satisfactory. The results were given in Table 4.

a   b
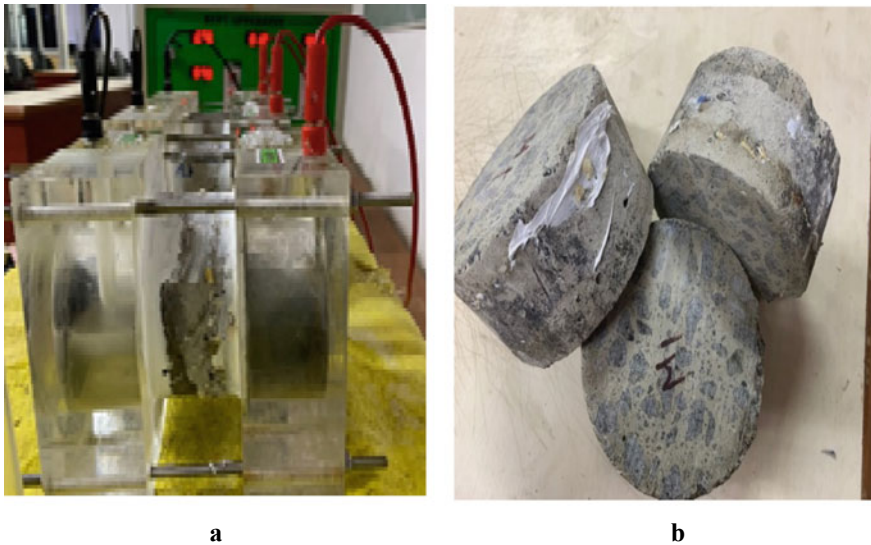
Fig. 1 **a** RCPT setup and **b** GPC sample after 6 h chloride penetration

Table 4 Chloride ion penetrability for GPC mixes

Mix ID	Charge passed in coulombs	Chlorine ion penetrability
GPC 1	2698	Moderate
GPC 2	2479	Moderate

2.4 Resistance to Acid

The cylinder specimens of 100 mm diameter by 200 mm height were immersed in 5% concentrated sulphuric acid as acidic medium. Before immersion, they were weighed and taken as initial weight. The immersed concrete was kept for 28 days, and they were constantly checked to see if any changes occurred in acidic medium. After 28 days, cylinders were taken and kept in open atmosphere for 1 day. They have been weighed and taken as final weight. Then, the CS of the cylinder was taken and compared to the original value (before exposure) of CS and their results are given in Table 5. GPC cylinder specimens immersed in sulphuric acid were shown in Fig. 2a.

Table 5 Test results of acid attack on GPC mixes

Mix ID	Weight (kg)		Increase in weight (%)	Compressive strength (MPa)		Difference in strength (%)
	Initial	Final		After exposure	Before exposure	
GPC 1	3.01	3.84	27	22.4	35.2	36 (decrease)
GPC 2	3.18	3.67	15	35.66	36.3	1.8 (decrease)

a   b
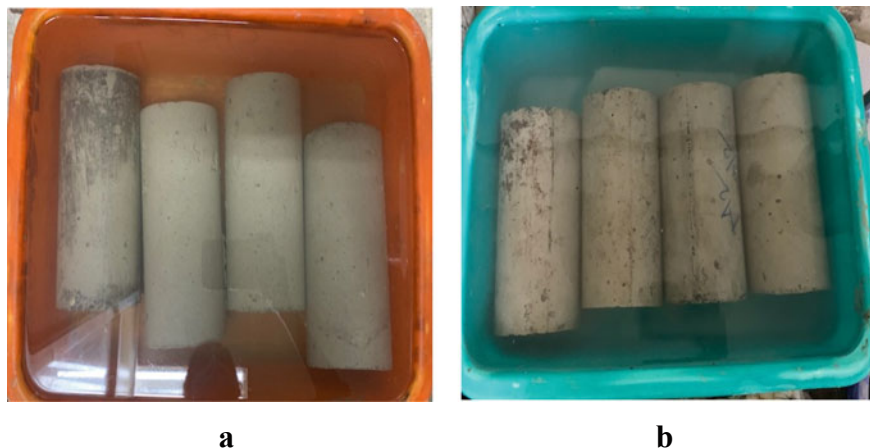
Fig. 2 **a** Immersion of GPC in sulphuric acid and **b** Immersion of GPC in sodium sulphate

Table 6 Results of sulphate attack on GPC mixes

Mix ID	Weight (kg)		Increase in weight (%)	Compressive strength (MPa)		Difference in strength (%)
	Initial	Final		After exposure	Before exposure	
GPC 1	3.01	3.84	21	28.4	35.2	24.11 (decrease)
GPC 2	3.18	3.84	19	34.66	36.32	5.0 (decrease)

2.5 Sulphate Resistance

For sulphate attack test, geopolymer concrete cylinders of size 100 mm diameter by 200 mm height were immersed in 5% Na_2SO_4. Before immersion, they were weighed and taken as initial weight. The immersed concrete was kept for 28 days, and they were constantly checked to see if any changes occurred in alkaline medium. After 28 days, cylinders were taken and kept in open atmosphere for 1 day and weighed which was taken as final weight. The GPC concrete cylinders were tested in CTM, and the concrete CS was calculated. Variations in the CS and weight loss were calculated and shown in Table 6. GPC cylinder specimens immersed in sodium sulphate solution shown in Fig. 2b.

2.6 Water Penetration Test

As per DIN 1048 (part 5) [15], mixes were subjected to hydrostatic pressure of 0.5 MPa for 3 days shown in Fig. 3. Depth of water penetration was measured using

Fig. 3 Water penetration test setup

scale. Specimens exhibited moderate permeability of depth ranging from 5 to 20 mm.

3 Conclusion

This study presented the experimental results of resistance to chloride, sulphuric acid, sodium sulphate and water penetrability of FA-GGBS blend geopolymer concrete. RCPT was conducted for both GPC mixes to evaluate the chloride resistance for period of 6 h. Exposure to acid and sulphate was carried out on both mixes for a period of 28 days. Loss in weight and CS was calculated and compared with conventional GPC specimens. In addition to chemical exposure, penetration of water was also conducted in water penetrability apparatus. The major findings of this article were summarized as follows.

- Under ambient curing condition, structural grade of 40 MPa was achieved by varying ratios of FA-GGBS blend in geopolymer concrete.
- Under RCPT, both mixes showed moderate penetration even though GPC 2 mix had more slag content than GPC 1 mix.
- There were no visible changes as well as efflorescence observed on both the GPC specimens when exposed to H_2SO_4 and Na_2SO_4 solution.
- On exposure to 28 days in 5% H_2SO_4, increase in weight of GPC 1 specimen found to be 45% higher than GPC 2 mix. Whereas in the case of CS, GPC 1 mix had loss of 95% than GPC 2.
- In the case of GPC specimens subjected to alkaline condition, i.e. immersion on 5% sodium sulphate, similar pattern of increase in weight of specimens was observed like immersion on sulphuric acid. Whereas in terms of CS, GPC 1 mix had loss of 80% than GPC 2.
- Loss in compressive strength of GPC 1 mix on both acidic and alkaline environment was due to higher proportion of FA leading to higher porous structure.
- Results pertaining to depth of penetration of water on GPC show moderate penetrability as per DIN 1048 (Part 5).

References

1. Davidovits J (1991) Geopolymers: inorganic polymeric new materials. J Therm Anal Calorim 37(8):1633–1656. https://doi.org/10.1007/bf01912193
2. Alexander MG, Magee BJ (1999) Durability performance of concrete containing condensed silica fume. Cem Concr Res 29(6):917–922. https://doi.org/10.1016/S0008-8846(99)00064-2
3. Bakharev T, Sanjayan JG, Cheng YB (2003) Resistance of alkali-activated slag concrete to acid attack. Cem Concr Res 33(10):1607–1611. https://doi.org/10.1016/S0008-8846(03)00125-X
4. Singh B, Ishwarya G, Gupta M, Bhattacharyya SK (2015) Geopolymer concrete: a review of some recent developments. Constr Build Mater 85:78–90. https://doi.org/10.1016/j.conbuildmat.2015.03.036

5. Temuujin J, Minjigmaa A, Lee M, Chen-Tan N, Van Riessen A (2011) Characterisation of class F fly ash geopolymer pastes immersed in acid and alkaline solutions. Cem Concr Compos 33(10):1086–1091. https://doi.org/10.1016/j.cemconcomp.2011.08.008

6. Singh NB, Middendorf B (2020) Geopolymers as an alternative to Portland cement: an overview. Constr Build Mater 237:117455. https://doi.org/10.1016/j.conbuildmat.2019.117455

7. Gupta S (2021) Durability of flyash based geopolymer concrete. https://www.engineeringcivil.com/durability-of-flyash-based-geopolymer-concrete.html. Accessed 10 Dec 2021

8. Hardjito D, Rangan BV (2005) Development and properties of low-calcium fly ash-based geopolymer concrete. http://hdl.handle.net/20.500.11937/5594

9. Wallah S, Rangan BV (2006) Low-calcium fly ash-based geopolymer concrete: long-term properties. http://hdl.handle.net/20.500.11937/34322

10. Mehta A, Siddique R (2017) Sulfuric acid resistance of fly ash based geopolymer concrete. Constr Build Mater 146:136–143. https://doi.org/10.1016/j.conbuildmat.2017.04.077

11. Albitar M, Ali MM, Visintin P, Drechsler M (2017) Durability evaluation of geopolymer and conventional concretes. Constr Build Mater 136:374–385. https://doi.org/10.1016/j.conbuildmat.2017.01.056

12. Bingöl Ş, Bilim C, Atiş CD, Durak U (2020) Durability properties of geopolymer mortars containing slag. Iran J Sci Technol Trans Civil Eng 1–9. https://doi.org/10.1007/s40996-019-00337-0

13. Srividya T, Rajkumar PK, Sivasakthi M, Sujitha A, Jeyalakshmi R (2021) A state-of-the-art on development of geopolymer concrete and its field applications. Case Stud Constr Mater e00812. https://doi.org/10.1016/j.cscm.2021.e00812

14. ASTM C 1202 (2010) Standard test method for electrical indication of concrete's ability to resist chloride penetration. Annual book of ASTM standards, West Conshohocken, United States

15. DIN 1048 part 5 (1991) Testing of concrete, testing of hardened concrete (Specimens prepared in mould). German Standards

Mechanical Strength Optimization of Geopolymer Concrete Pavement Blocks

Debjit Mitra Roy, Piyali Sengupta, and Satadru Das Adhikary

1 Introduction

In the developing countries like India, the utilization of concrete in the construction field was accelerated over the past few decades. In order to fulfill the requirement of concrete production, ordinary Portland cement (OPC) production has drastically increased widely as primary binder materials. The manufacturing of ordinary Portland cement (OPC) not only consumes a huge amount of natural resources and energy but also emits enormous carbon-di-oxide (CO_2) and greenhouse gases which are primarily responsible for global warming [1]. Global warming is the gravest threat to human civilization, and it is well-depicted that the various greenhouse gases are primarily responsible for global warming. Ordinary Portland concrete (OPC) production not only consumes a huge quantity of natural resources but also contributes to approximately 5–7% of world carbon dioxide (CO_2) emissions which directly influence the global warming [2]. In the existing state of the art, the researchers have put sincere efforts to reduce the emission of ozone-depleting materials that affect global warming. To overcome the environmental hazards, the researchers have started to look into alternative cementitious materials by producing geopolymer concrete (GPC) [1]. Geopolymer concrete is widely acknowledged by past researchers to have minimum global warming developing compared to OPC concrete through various experimental investigations. Production of GPC uses industry by-products,

D. M. Roy (✉) · P. Sengupta · S. D. Adhikary
Department of Civil Engineering, Indian Institute of Technology (ISM), Dhanbad, Jharkhand 826004, India
e-mail: debjit.18dp000397@cve.iitism.ac.in; debjit.nitd@gmail.com

P. Sengupta
e-mail: piyali@iitism.ac.in

S. D. Adhikary
e-mail: satadru@iitism.ac.in

i.e., ground granulated blast furnace slag (GGBS) and fly ash (FA). Many researchers have tried to minimize the utilization of OPC in the production of concrete that in turn will minimize the greenhouse gas emission to control the global warming [3]. Those efforts include the use of supplementary cementing materials and finding the alternative binding materials for partial to complete replacement of OPC with the different ratios of GGBS-FA contents. The GGBS-FA contents at different proportions are activated by alkaline solutions and turned into geopolymer concrete (GPC) [4].

To reuse sustainable industrial by-products, huge prospect is present in the development of geopolymer concrete (GPC). GPC is designated as "green concrete," which is famous in the name of an "inorganic polymer composite" [5]. A huge amount of natural resources was preserved by utilizing alternative cementitious binding materials of geological origin, GGBS and fly ash consisting of higher quantity of silica, alumina with calcium [6]. For the manufacturing of pavements, pavement block or paver blocks or paving blocks became an ideal choice due to its better looks and finish-ability with easy handling and faster laying. The precast pavement blocks are often useful in the upper layer of the road including footpath [7]. In comparison with traditional OPC concrete, GPC pavement blocks are most closable in moderate-dense traffic regions because of more durable with abrasion less surface. So, experimental optimization is very much necessary to check density, compressive strength, and water absorption for the cost-effective cement-less GPC paver blocks. It is well-predicted from the previous research paper that GPC paver blocks possess high compressive strength with better resistance to chemical attacks in comparing to traditional paver block at the same mix proportioning [8–10].

Therefore, in this present research, it is aiming to check the influence of each of different parameters such as ratios of GGBS-FA and AAL/B in the production of low-cost GPC paver block [5]. The GPC paver blocks were evaluated to check mechanical properties with variable compositions of GGBS-FA 40% to 60% and AAS/B 0.42 to 0.45. In the present research, 15 geopolymer paver blocks were developed and cured at ambient environment ($25°C \pm 2°C$) before going to check the compression testing results of the blocks in the compression testing machine [27]. By considering economical aspects, it was noticed that GGBS-Fly ash (50–50%) and 0.425% AAS/B induces relevant design mix proportion w.r.t compressive strength, water absorption and density.

2 Materials

2.1 Coal-Fired Fly ash [11]

Fly ash is an artificial pozzolanic by-products generated from coal-fired thermal power plants. The fly ash (FA), which originated from burning lignite or subbituminous coal, containing calcium oxide (CaO) more than 10% is termed as class-*C* or

calcareous fly ash, usually having both characteristics of hydraulic and pozzolanic. If that CaO remained less than 10%, that FA is known as silica fly ash or class-F fly ash which is usually produced by burning anthracite or bituminous coal and possesses pozzolanic properties only. In respect of unburned quantity of carbon, the color of fly ash may vary from grayish to blackish and spherical structure with few irregular particles. In this present research, Class-*F* FA (less than 10% CaO) from local power plant at Maithan, Jharkhand, was considered.

2.2   *Ground Granulated Blast Furnace Slag (GGBS) [12]*

GGBS is obtained as a waste material from the iron–steel manufacturing factory where natural's resources (such as limestone coke and iron ore) are used as burning materials in the furnace at 1600 C temperature. It accelerates the manufacturing of molten iron and molten slag after melting. As weight of molten slag is smaller than molten iron, it rises to the upper surface of molten iron. The high-pressure water is used to make cooling the molten slag granular. The faster cooling of molten slags makes sure as an outcome of smaller glassy granular particles which consists of 95% alumino-silicate-calcium quantity. Then the fresh granulated slags are made dry and grounded into a required finest powder material. The GGBS, having of off-white or near-white color and rough and angular-shaped particles, has some cementitious pozzolanic properties (Fig. 1).

The combination of GGBS-Fly ash was chosen in this research due to the presence of high alumina-silica resources referred to ASTM C618. The oxide compositions (by weight percentages) of the FA are 50–55% SiO_2, 30–35% Al_2O_3, 5–6% Fe_2O_3, 0.5–1% CaO, 0.5% Na_2O, 0.5% MgO with the ignition loss as 0.40. The mineralogical compositions by weight of the GGBS consume of 30–35% SiO_2, 15–20% Al_2O_3, 35–40% CaO, 2.5–5% Fe_2O_3, 5–10% MgO, 0.3% Na_2O with the ignition loss as 0.30.

(a)   (b)
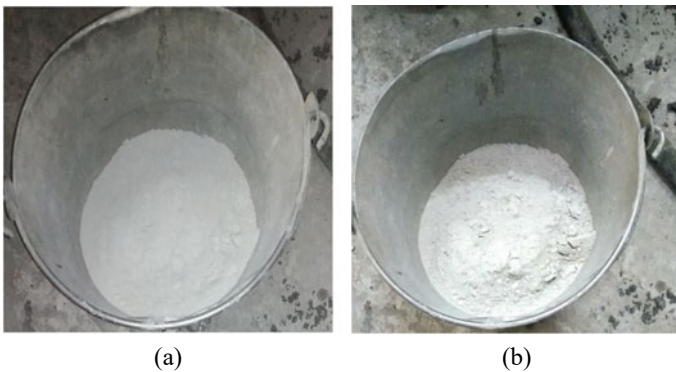
Fig. 1   a Fly ash (FA), **b** GGBS [5]

The important mineralogical components of Fly ash are silica and alumina as per IS 3812 (Part 1): 2013 [11]. It was well-observed that GGBS consisting of silica, alumina, and calcium as per IS 12089: 1987 [12]. It was noteworthy that both the FA and GGBS were selected as combined alumino-silicate materials (silicate, alumina) with the presence of calcium for the development of GGBS-fly ash-based geopolymer concrete paving block, i.e. GPC pavement blocks. According to chemical and geological origin, aluminum oxide (Al_2O_3), silicon dioxide (SiO_2) and calcium oxide (CaO) are naturally present in FA and GGBS and charged by an alkaline activator solution (AAS) [13]. The mineralogical compositions are normally represented as $xAl_2O_3.ySiO_2.zH_2O$.

The following are some major issues that can be controlled when fly ash and GGBS are considered in large quantity in design mix for the development of sustainable alternative binding materials:

- It reduces the larger usage of Portland cement.
- It reduces the emission of CO_2.
- The natural materials/resources like limestone and clay can be conserved, which are used during the cement manufacturing.

2.3 Alkali Activator Solution (AAS)

It was demonstrated from the literature review [14–16] that alkali-activated solution (AAS) is responsible for ensuring the bond between the fly ash and GGBS particles to develop GPC paver block. The main charge particles were an alkaline solution which was developed with the combination of Na_2SiO_3 and predetermined molar solution of NaOH [17–19].

Generally, the NaOH (SH or sodium hydroxide) is available in the shape of solid pellets or flakes. The procured quality of SH is mainly related to its pureness. On that account, SH (of purity 95–96%) is highly suitable for purchasing at its minimum cost. In addition of SH to natural water, the uniform and unvarying liquid-mix of SH with predetermined molar (M) is developed. The SH liquid-mix is considered to charge the solutions of sodium silicate (SS). The SH pellets are mentioned in Fig. 2a [5].

For this research, solutions of SH pellets having a concentration of 1.6 g/mL and SS (Na_2SiO_3) with a specific gravity of 1.4 g/mL (for solution) were used. AAS is required to complete the polymerization reaction with prerequisite time. 7 Molar (M) SH concentrations were generated by adding the calculated weight of SH pallets with portable water. The oxide compositions of Na_2SiO_3 solution were 30.0% SiO_2, 11.6% Na_2O, and 58.4% water. The mass ratio of SiO_2 to Na_2O in the SS (Na_2SiO_3) liquid was 2.61. The final products of AAS are represented in Fig. 2c.
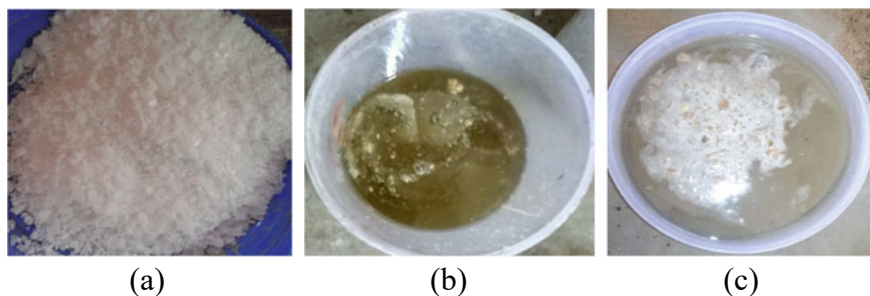
Fig. 2 **a** SH solid flakes, **b** solution of SS, **c** Alkaline activator solution (AAS) [5, 25]

2.4 Aggregate

2.4.1 Fine Aggregate (Fa)

In the present research, the main sources of fine aggregates (Fa) are river sand from Jharkhand surrounding areas and conforming to Zone II, referred to Table 3 of IS: 2386-1968 Part III. According to of table 4 and 5 IS 383-2016, the purchasing sand are passed by IS Sieve 4.75 mm, which are considered for present research [20].

2.4.2 Coarse Aggregate (CA)

Easily purchasable crushing black stone of nominal size 12.5 mm is selected for this research referring to IS 383-2016 [20]. According to of tables 2 and 3 IS 383-2016, physical testing values of coarse agg. Size of 12.5 and 6.3 mm are mentioned (Tables 1 and 2).

3 Experimental Program

3.1 Properties of Pavement Block

The measuring properties of pavement block are mentioned below.

Volume of the paver block = 0.002581 m^3.
Surface area of paver block is 322.578 cm^2.
Depth/thickness of the block = 80 mm.

Table 1 Physical testing results of 12.5, 6.3 mm size coarse agg and 4.75 mm fine agg [13]

Sl. No.	Descriptions	Values obtained			IS 383 recommendations
		Ca-12.5 mm	Ca-6.3 mm	Fa-4.75 mm	
1	Specific gravity	2.73	2.85	2.55	2.5–3
2	Water absorption, %	2.39	3.19	5.19	0.1–2
3	Loose bulk density, kg/m^3	1340.5	1460.5	1590	–
4	Compacted bulk density, %	1570.5	1640.5	1650	–
5	Impact value, %	9.6	–		< 30
6	Crushing strength value, %	6.9	–		< 30
7	Abrasion value, %	24.5	–		< 35

Table 2 Combined gradation of 12, 6 mm size coarse agg

Sl. No.	Sieve size (mm)	Passing %		Passing %			Recommendation for passing % of nominal 12.5 mm size
		Stack (1) 12.5 mm	Stack (2) 6.3 mm	Stack (1) 85%	Stack (2) 15%	Combined 100%	
1	40	100	100	85	15	100	100
2	20	100	100	85	15	100	100
3	12.5	95.5	100	81.17	15	96.17	90–100
4	10	79.7	100	67.74	15	82.74	40–85
5	4.75	0.45	63.2	0.38	9.48	9.86	0–10

3.2 Mix Proportion

In the present series, equal proportions of GGBS and FA were utilized as the solid biding precursor and AAS/B was selected as 0.425 and SS/SH was chosen content as 2 with 7 M of SH solution. Depending on unit volume (1m^3), the compositions of the proposed GPC paver block were designed and the entire binder quantity (GGBS + FA) was remained constant as 438 kg/m^3. The total combined quantity of GGBS and FA which is considered as dust particles (or GGBS + FA) was calculated from the mix-design guideline of IS 10262: 2019 [21]. After deducting the binding dust particles, the complete weight of aggregates was calculated from the remaining amount. Portable water was selected for the mixing purpose while extra water or superplasticizer was not selected for this research.

Table 3 Mix proportion of geopolymer pavement block [21]

Specifications	Dust Particle	Fine agg.	Coarse agg.	H$_2$O	Admixture
By design weight proportioning	1.0	1.813	2.51	0.4246	NA
Material quantities in kg/m³	438	794.12	1099.08	186	NA

Mixture proportions

Nos	MIX	GGBS	AAS/B	*M*	/SH	Concrete mixture quantity (kg/m³)							
						GGBS	FA	SH	SS	SAND (2.36 mm)	CA (20 mm)	(10mm)	w_a
1	70–30	30/70	0.45	7	2	131.40	306.72	65.72	131.53	805.80	757.55	356.50	50.0
2	60–40	40/60				175.25	263.2	65.72	131.53	800.05	752.79	354.20	49.6
3	**50**	**50/50**				**219.15**	**219.15**	**65.72**	**131.53**	**794.12**	**747.35**	**351.73**	**48.3**
4	40–60	60/40				263.2	175.25	65.72	131.53	788.35	741.90	348.10	48.9
5	30–70	70/30				306.72	131.40	65.72	131.53	782.53	736.50	346.60	48.6
6	OPCC	–	0.49 (w/c)			415 (kg/m³) c				794.12	747.35	351.73	48.3

Fig. 3 Experimental
pavement block of surface
area of 0.0322578 m^2 and
depth of 0.080 m
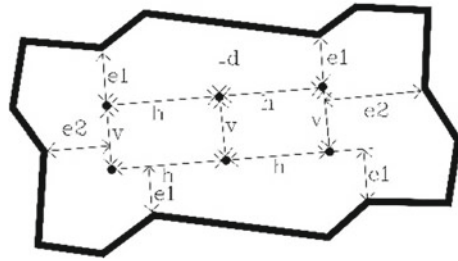
3.3 Testing Program

To make a homogeneous mix among the materials FA, GGBS, fine, and coarse
aggregates were added in a pan-mixer and made combined for 2 min. Then, the
premix solution of AAS was placed to mix the solid dry particles and mixed for
another 2–3 min. Then the developed Fresh GPC was poured into the pavement
block molds of each surface area of 0.0322578 m^2 and thickness of 0.080 m. The
pavement block sample is represented in Fig. 3.

In laboratory environment, the curing temperature of pavement blocks was main-
tained at about of 25° C $\pm$ 2° C with the relative humidity of 60 $\pm$ 5% as per
IS-516: 1959 [22]. After ambient curing of single day, the cast pavement blocks
were unmolded and placed at the laboratory environment up to the testing date. The
compression testing values of the pavement blocks were tested at 28 days from the
casted date in a UTM of 3000 kN capacity with a constant increment of loading at
the rate of 4500 N/s referred to IS: 516–1959 [22].

3.4 Density

From the group of blocks of specified shape, size, and thickness, the GPC Coro-
lock paver block specimens are selected for testing of physical properties. The steel
calipers or steel rule were used to measure the length and width of the paver blocks
across two diagonal sides. Four different positions were chosen to measure the thick-
ness of the pavement block. The thickness of the paver block was written down
according to the average value of measured dimensions and weight, density of the
samples was also determined in kg, kg/mm^3 as shown in Fig. 4. The density of the
sample is determined by dividing the mass of pavement samples in kg to the volume of
that samples in m^3. The density is the key parameter to define the strength of the paver
blocks; as high dense paver blocks can retard the abrasion loss in a better way and
have better resistance to freezing and thawing. As can be seen from the density of the
pavement block is found to be highest for 50% fly ash-50% GGBS at 2,325 kg/m^3 and
also observed that in the mix proportioning of 30% fly ash-70%GGBS, the density
has reached to 2390 kg/cm^2.

Fig. 4 Measuring the mass of tested sample having surface area of 0.0322578 m^2 with a height of 80 mm

Fig. 5 Testing of pavement block under the UTM at the laboratory

3.5 Water Absorption

Water or moisture absorption is considered as a vital parameter for pavement blocks for evaluating the mechanical properties as well as its durability. The GPC pavement blocks were kept under water at an ambient temperature of $25 \pm 2\,°C$ for the duration of 24 ± 2 h. Then the specimens were removed from the water and kept for draining

out for 5 min in the laboratory. Then the dry cotton is used to remove the visible water from the sides of specimens. The specimens were taken their weight and noted down in kgs (W_w). After that all the damp specimens were dried with the help of chamber-heater at a temperature of $105 \pm 5\,°C$ for not less than 24 h. The dry mass of single pavement block (W_d) was taken and written down in kg. The percentage in water absorption were evaluated as follows: $W_{percentage} = [(W_w - W_d)/W_d] \times 100$. As per IS 15658:2006 [23], 24 h water absorption should be less than 7% for every paver block. It was well-observed that GPC paver blocks were shown as very less water absorption percentages. All the specifications blocks met satisfactory results under Indian standard guidelines.

4 Results and Discussion

The present research was experimented to express the ideal and perfect mix proportioning of GPC pavement block to his results of compression testing values, which was evaluated at varying loading conditions. On performance-based design, GGBS and fly ash with 50–50% showed to the GPC pavement block to analyze the optimal mix proportioning of SS/SH and AAS/Binder to produce the ideal quality product.

The compression testing results of GPC and OPC pavement blocks were represented in accordance with IS 3495(Part I):1992.

From Table 4, it was demonstrated the Coro-lock pavement blocks with the results of compression testing values, density, and water absorptions testing results. It was observed that the density of the paver blocks was increased with the increasing in the percentage of fly ash mixes up to an optimum level beyond which it was decreased. As the quantity of fly ash increases further, the bulk density decreases which is mainly due to the increase of the amount of water of consistency with fly ash content in addition to the decreasing the specific gravity of fly ash. The initial AAS/binder ratio shows an impact on the values of the bulk density which is also due to the rate of hydration of fly ash under AAS, and it was observed lower than that of OPC_{CC} paver block, especially at the early ages of hydration. It was noted that 50% fly ash-50%GGBS GPC paver block showed less water absorption than OPC_{CC} paver block.

Table 4 Mechanical and durability property of pavement block made of GPC

Mix proportion					Compressive strength (MPa)		Density (kg/m^3)	Water absorption (%)
MIX-ID	GGBS/FA	AAS/B	M	SS/SH	7 days	28 days		
A50	50/50	0.425	7	2	43 (0.04)	49.5 (0.03)	2325	5.5

Table 5 Cost evaluation of pavement block made of GPC to traditional concrete	Nomenclature [*M*-40 grade]	Compression testing results of block w.r.t manufacturing cost	
		Compression testing values (MPa)	Cost of production (Rupees)
	OPC Pavement block	40.5	3863
	GPC Pavement block	49.5	3552

A production cost of paver block was made comparison between (OPC$_{CC}$) Pavement block and (GPC) Pavement block of M-40 grade based on compression testing results [5, 24] and tabulated in Table 5.

5 Conclusions

Special feature of this research in geopolymer pavement block is for the early gaining strength with better resistivity to chemical attacks. It is well-featured that the manufacturing of geopolymers pavement block was so eco-friendly materials which did not release greenhouse gases during its entire polymerization process. Contrary to OPC, geopolymerization did not necessary calcium-silicate-hydrate (*C-S-H*) gel for matrix establishment to develop the strength but make use of polymerization process among silica, alumina, and calcium precursors to achieve target design strength optimization.

The GPC pavement blocks were developed with the 50–60% of FA and GGBS, respectively, and ratio of SS to SH is 2. Investigational research was accomplished with take care of prime mix proportioning was originated on account of GGBS and FA proportions of 50%, AAL/Binder ratio as 0.425, and molarity of NaOH solutions as 7 M.

Depending on optimal mix proportioning, it was pointed out that the pavement blocks with 50% GGBS in ambient environmental condition generate maximum performance of compressive strength.

From the compressive values, GPC pavement block can be predicted as the appropriate substitute product for construction from both consideration of compression testing values and water absorption tested results. Apart from its higher strength, GPC paver blocks required minimum production cost with higher durability.

Practical implementation of GPC pavement block production was carried out in Indian scenarios under ambient curing condition which is a very good and significant achievement for new product development. It was pointed out that 50% GGBS–50% fly ash was more appropriate than 60% GGBS–40% fly ash, and 40% GGBS–60% fly ash in respect of density, water absorption, and compressive strength.

References

1. Singh NB, Middendorf B (2020) Geopolymers as an alternative to Portland cement: An overview. Constr Build Mater 237:117455. https://doi.org/10.1016/j.conbuildmat.2019.117455
2. Chen C, Habert G, Bouzidi Y, Jullien A (2010) Environmental impact of cement production: detail of the different processes and cement plant variability evaluation. J Clean Prod 18:478–485. https://doi.org/10.1016/j.jclepro.2009.12.014
3. Bondar D, Nanukuttan S, Provis JL, Soutsos M (2019) Efficient mix design of alkali activated slag concretes based on packing fraction of ingredients and paste thickness. J Clean Prod 218:438–449. https://doi.org/10.1016/j.jclepro.2019.01.332
4. Juenger MCG, Winnefeld F, Provis JL, Ideker JH (2011) Advances in alternative cementitious binders. Cem Concr Res 41:1232–1243. https://doi.org/10.1016/j.cemconres.2010.11.012
5. Roy DM, Adhikary SD, Sengupta P (2022) Experimental optimization of GGBS Fly ash-based geopolymer concrete paver blocks. Chapter 13, Springer Science and Business Media LLC. https://doi.org/10.1007/978-981-16-5543-2
6. Saha S, Rajasekaran C (2017) Enhancement of the properties of fly ash-based geopolymer paste by incorporating ground granulated blast furnace slag. Constr Build Mater 146:615–620. https://doi.org/10.1016/j.conbuildmat.2017.04.139
7. Deb PS, Nath P, Sarker PK (2014) The effects of ground granulated blast-furnace slag blending with fly ash and activator content on the workability and strength properties of geopolymer concrete cured at ambient temperature. Mater Des 62:32–39. https://doi.org/10.1016/j.matdes.2014.05.001
8. Nath P, Sarker PK (2017) Flexural strength and elastic modulus of ambient-cured blended low-calcium fly ash geopolymer concrete. Constr Build Mater 130:22–31. https://doi.org/10.1016/j.conbuildmat.2016.11.034
9. Mccann DM, Forde MC (2001) Review of NDT methods in the assessment of concrete and masonry structures. NDT E Int. 34:71–84. https://doi.org/10.1016/S0963-8695(00)00032-3
10. Ling Y, Wang K, Fu C (2019) Shrinkage behavior of fly ash based geopolymer pastes with and without shrinkage reducing admixture. Cement Concr Compos. https://doi.org/10.1016/j.cemconcomp.2019.02.007
11. IS: 3812 (Part-1) (2013) Specification for pulverized fuel ash, for use as Pozzolana in cement, Cement mortar and concrete
12. IS: 12089 (1987) Specification for granulated slag for the manufacturer of Portland slag cement
13. IS 1199 (2004) Indian standard methods of sampling and analysis of concrete
14. Basil MM, Abraham R (2016) Study on geopolymer concrete used for paver blocks. Int J Innov Res Adv Eng 3(9):62–66. https://doi.org/10.6084/m9.figshare.4052382;11. Aaron DV, D'Souza DN, Kaliveer N, Satish KT, Amar SM (2016) Geopolymer paver blocks. In: Proceedings of international conference on advances in civil engineering, pp. 173–178
15. Banupriya C, John S, Suresh R, Divya E, Vinitha D (2016) Experimental investigations on geopolymer bricks/paver blocks. Ind J Sci Technol 9(16):1–5. https://doi.org/10.17485/ijst/2016/v9i16/92209
16. Muthukumar M, Mareeswaran L, Subburaman S, Jeyaprakash B (2019) Evaluation on compressive strength of paver block using geopolymer. Int J Recent Trends Eng Res 5(3):12–20. https://doi.org/10.23883/IJRTER.2019.5018.GFC14
17. Prusty JK, Pradhan B (2020) Multi-response optimization using Taguchi-Grey relational analysis for composition of fly ash-ground granulated blast furnace slag based geopolymer concrete. Constr Build Mater 241:118049. https://doi.org/10.1016/j.conbuildmat.2020.118049

18. Chindaprasirt P, Chareerat T, Sirivivatnanon V (2007) Workability and strength of coarse high calcium fly ash geopolymer. Cem Concr Compos 29:224–229. https://doi.org/10.1016/j.cemconcomp.2006.11.002
19. Somna K, Jaturapitakkul C, Kajitvichyanukul P, Chindaprasirt P (2011) NaOH-activated ground fly ash geopolymer cured at ambient temperature. Fuel 90:2118–2124. https://doi.org/10.1016/j.fuel.2011.01.018
20. IS: 383 (2016) Coarse and fine aggregate for concrete—specification
21. IS 10262 (2019) Concrete mix proportioning—guidelines
22. IS 516 (1959) Method of tests for strength of concrete
23. IS 15658 (2021) Concrete paving blocks—specification
24. Khan HA, Nanda RP (2020) Out-of-plane bending of masonry wallette strengthened with geosynthetic. Constr Build Mater 231:117198. https://doi.org/10.1016/j.conbuildmat.2019.117198
25. Roy DM, Adhikary SD, Sengupta P (2022) Assessment of mechanical and micro-structural characterization of novel ambient cured cement-free composite concrete. Ceram Int. https://doi.org/10.1016/j.ceramint.2022.05.348

Influence of Bay Span Length on Near-Field Seismic Response of Steel Moment Resisting Frames

Bahubali Jayapal Kottalage, Muhamed Safeer Pandikkadavath, and Sujith Mangalathu

1 Introduction

Near-field (NF) seismic disturbances are distinct from far-field (FF) disturbances due to their proximity to faults. They are characterized by short-duration impulsive ground motion and forward directivity pulses having a velocity near the seismic shear waves. The un-damped (due to the proximity to normal fault direction)-rich frequency content makes them capable of releasing high seismic energy that may cause severe damage to structural systems [1]. Past studies showed that the structural response under NF seismic action largely depends on the seismic record pulse period to the fundamental structural period relationship [2–17]. The framed steel structural systems with a time period greater than the NF record pulse period experience early yielding in the upper stories, and as the intensity of the record increases, this yielding demand migrates to the bottom stories, whereas structures with shorter time period maximum cyclic ductility demand always will be at the bottom stories [2]. The presence of velocity pulses in the NF records results in structures exposed to more seismic energy in the first few plastic cycles in contrast to the FF cumulative cyclic demands that may inflict the structure in the later stage of seismic hit [3]. Investigations reported that the structural response prediction under NF records could be made more robust by incorporating relevant inelastic structural response parameters and suitable intensity measure components in the nonlinear analyses [4–6]. In the case of NF sequential seismic actions, the mainshock (MS) peak drift demands itself too large such that the aftershock (AS) action will not increase (further) the drift demands significantly [7, 8]. Likewise, the response of steel moment resisting

B. J. Kottalage · M. S. Pandikkadavath (✉)
Department of Civil Engineering, National Institute of Technology Calicut, Calicut, India
e-mail: msafeerpk@nitc.ac.in

S. Mangalathu
Data Analytics Division, Equifax Inc, Atlanta, GA, USA

frames (SMRFs) to mainshock NF seismic actions shows increased scatter nature (compared to ordinary FF records) with respect to seismic intensity measures (peak ground acceleration, PGA, and spectral acceleration, S_a) [9] and the collapse risk of SMRFs significantly increases as the distance to fault decreases [10]. Similar studies showed that the structural responses are more related to peak ground velocity (PGV) to PGA ratio and the system responses become severe when the structural time period is close to NF pulse period [11, 12]. Most of the investigations adopted maximum inter-storey drift ratio (IDR) and residual (permanent) drift ratio (RDR) for response assessment, and these are nonlinearly related to each other under NF ground motion action [13–16]. Research studies on SMRFs with irregularity showed that values of pulse period to structural period ratio are more relevant to different damage states, and for SMRFs without irregularity experience critical responses when this ratio approaches one [13, 17].

Even if several research studies focused on NF seismic effect on SMRFs (considering different aspects), the influence of beam span length on the NF seismic response of the SMRFs under NF actions is almost not there. The present study attempts to investigate the effect of bay span length on the NF seismic response of SMRF. For the study, eight-storey SMRFs are adopted and the same are designed by equivalent lateral force method for different bay span lengths. The study frame incorporated in a suitable modelling platform and a selected suite of NF seismic records are applied for inelastic time history analyses. Sequentially the seismic response of the SMRFs is assessed in terms of IDR and RDR. The details of the study are presented in the following sections.

2 Building Frame Design and Model

For the study, a three-bay eight-storey frame proposed in past studies are selected [18] and the same is designed as per current US seismic design provisions [19–22]. The frame building is assumed to be located in Los Angeles, USA, and situated in site class-D, taking the bottom of the building is firmly fixed to the soil. The importance factor and occupancy category of the structure are I and II, respectively. The eight-storey building has 5.49 m height at the bottom storey, and all other stories have an equal height of 3.96 m. The building has symmetry in plan and consists of 5 bays along both the longitudinal direction. Three different bay span lengths, namely 6.10 m, 9.14 m and 12.00 m, are accounted for the investigation. Accordingly, the study building plans are 30.10 m × 30.10 m; 45.70 m × 45.70 m; and 60.00 m × 60.00 m, respectively. The lateral earthquake loading-resisting SMRFs are placed symmetrically (three middle frames marked as thick blue in) along the periphery (along both directions) as shown in Fig. 1. The building frames are designed using equivalent lateral force method as per applicable US code provisions. Consequently, the study frames are named as 8S3B-ELF-6.10 (Bay span length of 6.10 m), 8S3B-ELF-9.14 (Bay span length of 9.14 m) and 8S3B-ELF-12.00 (Bay span length of 12.00 m), respectively.
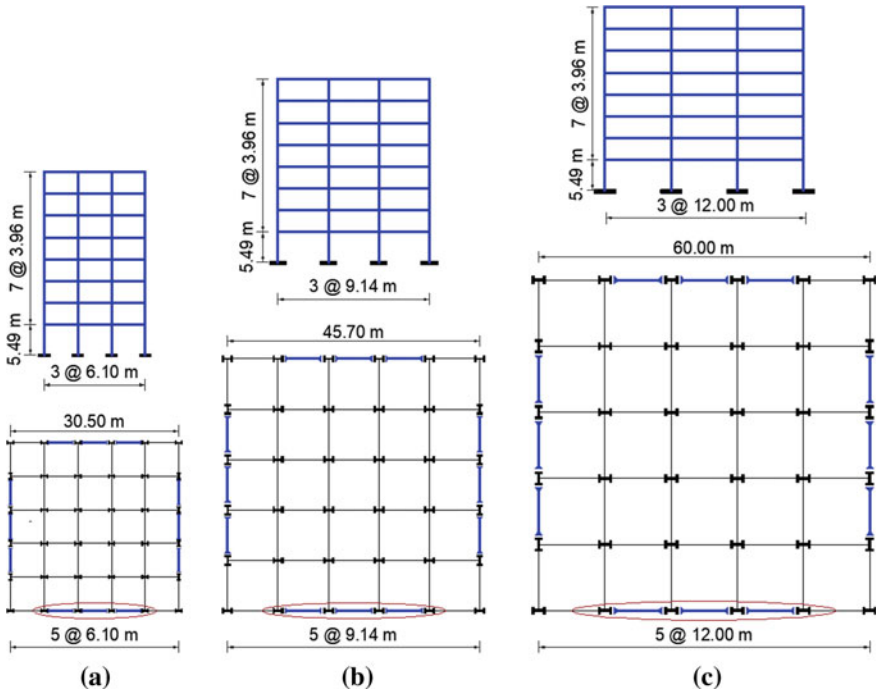
Fig. 1 Plan and elevation views of building models: **a** 6.10 span, **b** 9.14 span and **c** 12.00 m span

The design seismic weights for building frames with spans 6.10 m, 9.14 m and 12.00 m (8S3B-ELF-6.10, 8S3B-ELF-9.14 and 8S3B-ELF-12.00) are found to be 33,452 kN, 75,267 kN and 129,626 kN, respectively. The design spectral response acceleration at short periods and long periods are obtained as 2.09 g and 0.77 g; the design seismic response coefficient and approximate time periods are obtained as 0.0805 and 1.194 s, respectively. Similarly, the response modification coefficient (R) and deflection amplification factor (C_d) are taken as 8 and 5.5 as per the code recommendations. The redundancy factor, ρ, is taken as 1 (since no asymmetry exists), and the column height itself is assumed as the unbraced length of the storey. Young's modulus (E) and material yield strength (f_y) are taken as 200G Pa and 345 MPa (with an overstrength factor of $R_y = 1.1$), respectively, for both beam and column elements [23, 24]. The applicable code recommended load combinations are used to get design cross sections, and all the selected beam and column cross sections are adopted such a way that it will meet the desired code recommendation to behave as highly ductile (slenderness ration criteria) frame components as well as the strong column weak beam design concept. The geometric details of the frames are given in Fig. 1, and the design obtained component cross-sectional information is given in Table 1.

To carry out the nonlinear time history analysis, the study nonlinear 2-D building frame models are developed in OpenSees platform [25]. The concentrated plasticity

Table 1 Beam and column cross-sectional details of study frames

Story	8S3B-ELF-6.10		8S3B-ELF-9.14		8S3B-ELF-12.00	
	Column	Beam	Column	Beam	Column	Beam
1	W33X291	W30X191	W36X441	W33X201	W36X529	W33X291
2	W33X291	W30X191	W36X441	W33X201	W36X529	W33X291
3	W33X263	W30X173	W36X441	W33X201	W36X487	W33X291
4	W33X263	W30X173	W36X441	W33X201	W36X487	W33X291
5	W33X241	W30X132	W36X395	W30X191	W36X395	W33X263
6	W33X241	W30X132	W36X395	W30X191	W36X395	W33X263
7	W33X221	W30X124	W36X395	W30X191	W36X395	W33X263
8	W33X221	W30X124	W36X395	W30X191	W36X395	W33X263

approach is used to model the nonlinearity in the beam–column elements using zero-length spring elements. Structural strength and stiffness deterioration of these springs are accounted in rotational spring by hysteretic behaviour based on Modified Ibarra Krawinkler Deterioration Model (IMK model) [26, 27], and the same has been applied at the beam and column ends suitably. Rigid panel zones are modelled with a suitable number of elastic rigid elements and one multi-linear inelastic rotational spring to represent shear distortions as per the research recommendations [18, 28]. To simulate *P*-Delta effects due to gravity loading, a leaning column at a distance of one bay width is provided to the model and the same is linked to the frame by elastic axial elements (moment release connections at all ends) such that no lateral load sharing or shear lag effect are permitted during the analysis. Rayleigh damping of 2% is assumed for all the modes of frame considering lumped mass approach at receptive nodes for the entire model.

For the NF nonlinear time history analysis, Baker's suite of 80 pulse-like unscaled ground motions is used [29]. This selected suite contains ground motion records with time period varying from 19.90 s to 90 s. The magnitude of these ground motions ranges between 6.19 and 7.62; the distance to faults varies between 1 and 24 km and peak ground acceleration, PGA ranges between 0.10 and 1.08 g. Figure 2 shows the spectra (normalized with respect to acceleration due to gravity, g) of selected ground motion records along with its mean and design spectra of the study frames.

3   Fragility Curves Development

Fragility functions represent the probability of structural demand (*D*) exceeding the capacity (*C*) at a given intensity measure (IM). Inter-storey drift ratio, IDR, and residual drift ratio, RDR, are taken as engineering demand parameters (EDP), and spectral acceleration corresponding to the fundamental time period ($S_{a\text{-}T1}$) is taken as IM. A probabilistic seismic demand model is developed using Eq. (1) [30].

Fig. 2 Spectra for selected ground motions along with their mean and design spectra for the study frames
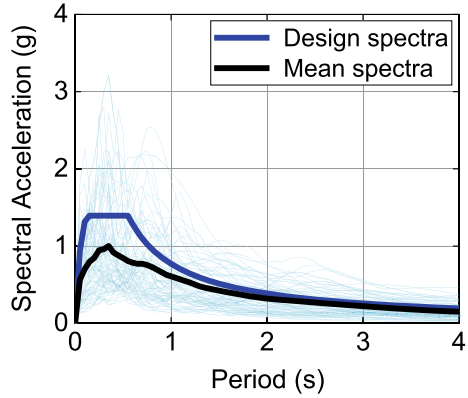
$$P[D \geq C | \text{IM}] = 1 - \Phi\left(\frac{\ln(S_C) - \ln(S_D)}{\sqrt{\beta_{\text{EDP|IM}}^2 + \beta_c^2}}\right) \tag{1}$$

where $\Phi\ (\cdot)$ is the standard normal cumulative distribution function, S_D and S_C are median estimates of demand, D, and capacity, C, respectively. $\beta_{\text{EDP|IM}}$ is the dispersion in the engineering demand parameter at the given intensity measure, and β_C is the dispersion in the capacity. The dispersion in the demand for N ground motion records is estimated using Eq. (2). The dispersion in capacity β_C can be taken as 0.30 as per the recommendation from FEMA P58-1 [31]. The relationship between median demand S_D and IM can be expressed using the power law as given in Eq. (3).

$$\beta_{\text{EDP,IM}} = \sqrt{\frac{\sum(\ln(EDP) - \ln(S_D))^2}{N - 2}} \tag{2}$$

where

$$S_D = a(\text{IM})^b \tag{3}$$

After transforming Eq. (3)

$$\ln(S_D) = \ln(a) + b\ln(\text{IM}) \tag{4}$$

where $\ln(a)$ is intercept and b is the slope and these can be obtained by performing linear regression analysis (in log scale) between response (IDR or RDR) and intensity measure, respectively.

Table 2 Damage states associated with residual drift ratio as per FEMA P58-1

Damage state	Description	Residual story drift ratio (%)
DS1	No structural realignment is necessary for structural stability; however, the building may require adjustment and repairs to non-structural and mechanical components that are sensitive to building alignment (e.g. elevator rails, curtain walls and doors)	0.2
DS2	Realignment of the structural frame and related structural repairs is required to maintain permissible drift limits for non-structural and mechanical components and to limit degradation in structural stability (i.e. collapse safety)	0.5
DS3	Major structural realignment is required to restore the margin of safety for lateral stability; however, the required realignment and repair of the structure may not be economically and practically feasible (i.e. the structure might be a total economic loss)	1
DS4	Residual drift is sufficiently large that the structure is in danger of collapse from earthquake aftershocks (note: this performance point might be considered as equal to collapse but with greater uncertainty)	1–4

Both transient drift (IDR) and permanent drift (RDR) are considered to assess the performance of the structural systems accounted [31, 32]. Under the transient drift, immediate occupancy, IO (0.7% IDR) life safety, LS (2.5% IDR) and collapse prevention CP (5% IDR) are taken as damage states as indicated in FEMA 356 [32]. Permanent drift (residual drift) is also used to assess the performance as it is relevant in post-earthquake repair assessment. FEMA P58-1 [31] Table C-1 identifies four different damage (DS1, DS2, DS3 and DS4) states associated with RDR (for this study these stated approximated as 0.2%, 0.5%, 1% and 4%, respectively) as indicated in Table 2.

4   Analysis Results and Discussion

From the analysis, the fundamental time periods (T_1) are obtained as 1.14 s, 1.52 s and 1.88 s for the frames 8S3B-ELF-6.10, 8S3B-ELF-9.14 and 8S3B-ELF-12.00, respectively. Figure 3 shows the variation of IDR and RDR for all the three frames over the height under the considered suite of nonlinear time history simulations. The maximum mean IDR is observed at the second storey for all the study frames. These values are observed as 0.98%, 1.38% and 1.72% for frames 8S3B-ELF-6.10, 8S3B-ELF-9.14 and 8S3B-ELF-12.00; corresponding standard deviations are found
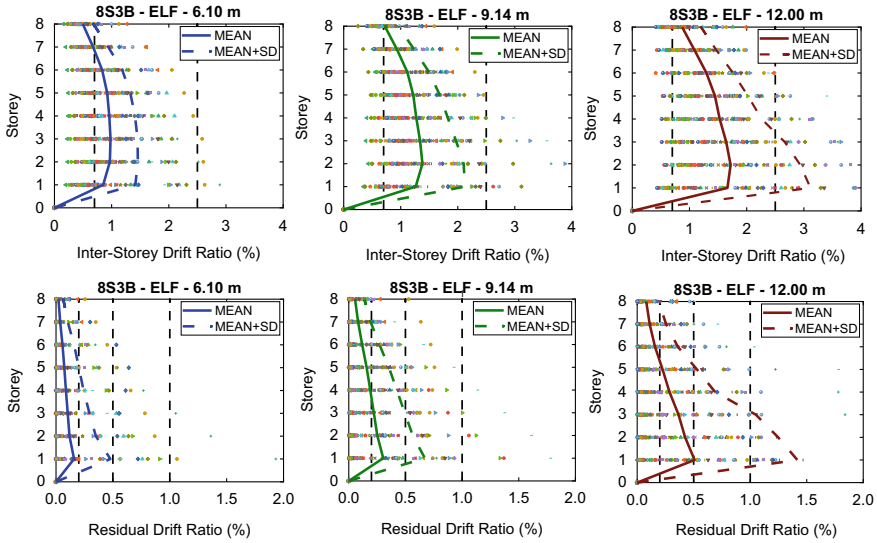
Fig. 3 Inter-storey drift response and residual drift response of SMRFs designed using ELF method

to be 0.47%, 0.72% and 0.85%, respectively. There is an increase of IDR by 40% from 6.00 m span to 9.14 m span frame and a 24% increase from 9.14 m span to 12.00 m span cases. Likewise, the maximum mean RDR values are observed as 0.16%, 0.31% and 0.51% for frames 8S3B-ELF-6.10, 8S3B-ELF-9.14 and 8S3B-ELF-12.00; corresponding standard deviations are found to be 0.32%, 0.37% and 0.53%, respectively (at the first for all the three study frames). There is an increase of RDR by 94% from 6.00 m span to 9.14 m span frame and a 64% increase from 9.14 m span to 12.00 m span cases. The results showed that the drift demands tend to accrue at the bottom storey, and it increases with the increase of bay span length.

The IDR and RDR results from the nonlinear time history analyses are utilized to plot the regression fits between IDR or RDR versus $S_{a\text{-}T1}$ (normalized spectral acceleration corresponding to the first mode time period of the frames) in logarithmic scale. Figure 4 shows these linear regression fits developed between frames responses IDR or RDR and $S_{a\text{-}T1}$ for frames accounted for the investigation. Likewise, Table 3 shows the various regression parameters obtained corresponding respective plots in Fig. 4. The IDR fit showed a better R^2 value compared to RDR fit with $S_{a\text{-}T1}$, and these results are further presented in the following section.

To scale the frame seismic hazard level fragility curves are developed (derived from regression fits only) using probabilistic seismic demand model as given in Eq. (1). Figure 5 shows the fragility curves for IDR and RDR responses for different damage states. Tables 4 and 5 show the probability of exceeding the given damage states for IDR and RDR responses, respectively, at $S_{a\text{-}T1} = 1.0$ g and $S_{a\text{-}T1} = 1.5$ g, respectively.
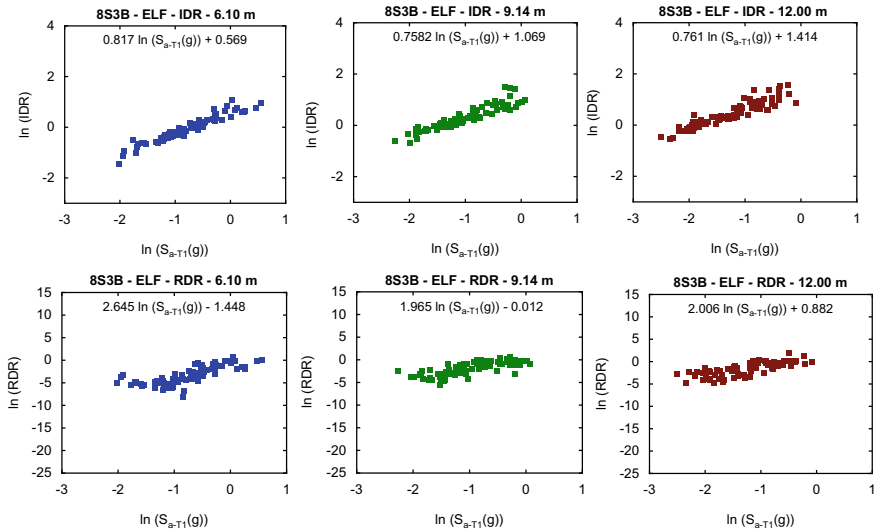
Fig. 4 Regression fits for IDR or RDR versus $S_{a\text{-}T1}$ for the study frames

Table 3 Regression parameters for IDR and RDR response

	IDR response				RDR response			
Frame ID	$\ln(a)$	b	$\beta_{IDR|Sa\text{-}T1}$	β	$\ln(a)$	b	$\beta_{RDR|Sa\text{-}T1}$	β
ELF-6.10 m	0.567	0.816	0.141	0.38	−1.448	2.645	1.328	1.37
ELF-9.14 m	1.069	0.752	0.176	0.39	−0.012	1.964	1.014	1.07
ELF-12.00 m	1.414	0.761	0.191	0.40	0.882	2.006	0.993	1.05

For 8S3B-ELF-6.10 frame the probability of exceeding immediate occupancy (IO), life safety (LS) and collapse prevention (CP) damage states are found to be 99.79%, 14.71% and 0.08%; at $S_{a\text{-}T1} = 1.0$ g; the same damage state vulnerability is found to be 99.99%, 48.0% and 1.61% at $S_{a\text{-}T1} = 1.5$ g, respectively. Likewise, for 8S3B-ELF-9.14 frame, the above limit states exceedance is obtained as 99.99%, 66.99% and 6.0% at $S_{a\text{-}T1} = 1.0$ g; for $S_{a\text{-}T1} = 1.5$ g the same is observed as 99.99%, 90.62% and 24.94%, respectively. For 8S3B-ELF-12.00 frame at $S_{a\text{-}T1} = 1.0$ g, these exceedance values are found to be 99.99%, 91.67% and 29.35% and at $S_{a\text{-}T1} = 1.5$ g the same is noted as 99.99%, 98.95% and 62.38%, respectively. Based on RDR response the probability of exceeding damage states (DSi) DS1, DS2, DS3 and DS4 for 8S3B-ELF-6.10 frame at $S_{a\text{-}T1} = 1.0$ g are 54.71%, 28.95%, 14.36% and 2.0%; at $S_{a\text{-}T1} = 1.5$ g, they are 1.86%; 81.786%, 59.22%, 39.13% and 9.77%, respectively. For 8S3B-ELF-9.14 frame, these values are 93.45%, 74.01%, 49.52% and 9.28% at $S_{a\text{-}T1} = 1.0$ g; and 98.82%, 91.88%, 77.08% and 28.44% at $S_{a\text{-}T1} = 1.5$ g, respectively. Finally for 8S3B-ELF-12.00 frame the same damage state exceedance values under RDR are 99.18%, 93.55%, 80.24% and 31.36% at $S_{a\text{-}T1} = 1.0$ g; 99.92%, 98.93%,
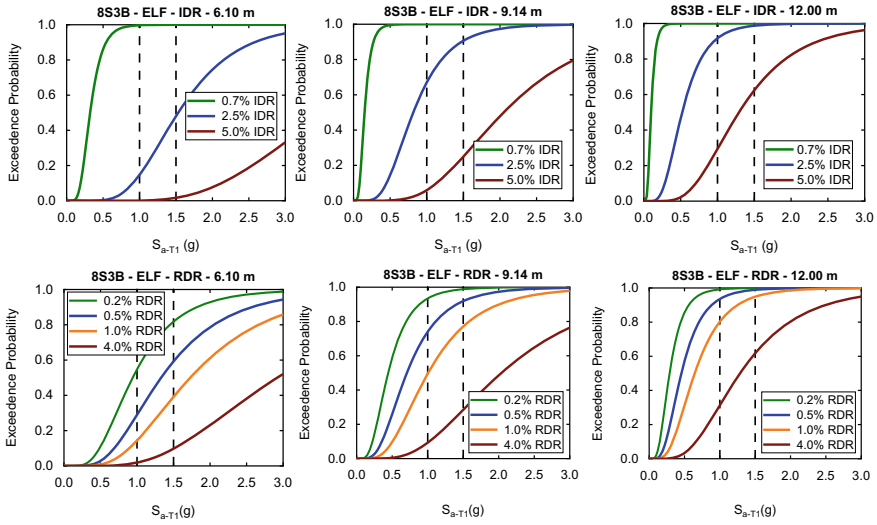
Fig. 5 Fragility curves for IDR or RDR response for the study frames

Table 4 Probability of exceeding damage states for IDR response

Frame	$S_{a\text{-}T1} = 1.0$ g			$S_{a\text{-}T1} = 1.5$ g		
	DS1	DS2	DS3	DS1	DS2	DS3
8S3B-ELF-6.10	0.99	0.15	0.00	0.99	0.48	0.02
8S3B-ELF-9.14	0.99	0.67	0.06	0.99	0.91	0.25
8S3B-ELF-12.00	0.99	0.92	0.29	0.99	0.98	0.62

Table 5 Probability of exceeding damage states for RDR response

Frame	$S_{a\text{-}T1} = 1.0$ g				$S_{a\text{-}T1} = 1.5$ g			
	DS1	DS2	DS3	DS4	DS1	DS2	DS3	DS4
8S3B-ELF-6.10	0.55	0.29	0.14	0.02	0.82	0.59	0.39	0.09
8S3B-ELF-9.14	0.94	0.74	0.49	0.09	0.98	0.92	0.77	0.28
8S3B-ELF-12.00	0.99	0.94	0.80	0.32	0.99	0.98	0.94	0.62

94.89% and 61.73% at $S_{a\text{-}T1} = 1.5$ g, respectively. These results are tabulated in Tables 4 and 5, respectively.

5 Conclusions

Nonlinear time history analysis is carried out on eight-storey three-bay steel special moment frames for different span lengths (designed using equivalent lateral force method) under 80 near-field ground motion records. The frames response is studied in terms of inter-storey drift ratio, IDR, and residual drift ratio, RDR. Cloud analysis based on simple regression relation between demand (IDR or RDR) and intensity measure (spectral acceleration) is carried out (in logarithmic scale). Fragility plots are derived based on the probabilistic seismic demand model (PSDM) by taking IDR and RDR as engineering demand parameters. Maximum of mean IDR and RDR are observed more at bottom stories, and these responses are observed to increase with the increase of span length. The fragility curves corresponding to different damage states in terms of IDR and RDR also showed similar trends.

References

1. Somerville PG, Smith NF, Graves RW, Abrahamson NA (1997) Modification of empirical strong ground motion attenuation relations to include the amplitude and duration effects of rupture directivity. Seismol Res Lett 68:199–222
2. Alavi B, Krawinkler H (2004) Behaviour of moment-resisting frame structures subjected to near-fault ground motions. Earthq Eng Struct Dynam 33:687–706
3. Kalkan E, Kunnath SK (2006) Effect of fling step and forward directivity on seismic response of buildings. Earthq Spect 22(2):367–390
4. Makris N, Psychogios T (2006) Dimensional response analysis of yielding structures with first-mode dominated response. Earthq Eng Struct Dynam 35:1203–1224
5. Tothong P, Cornell CA (2008) Structural performance assessment under near-source pulse-like ground motions using advanced ground motion intensity measures. Earthq Eng Struct Dynam 37:1018–1037
6. Karavasilis TL, Makris N, Bazeos N, Beskos DM (2010) Dimensional response analysis of multi storey regular steel MRF subjected to pulselike earthquake ground motions, J Struct Eng ASCE 136(8), 150.140.254.66
7. Riuz-Grcia J, Nagrete-Manriquez JC (2011) Evaluation of drift demands in existing steel moment resisting frames under as-recorded far-field and near-fault mainshock-aftershock seismic sequences. Eng Struct 33:621–634
8. Aljawhari K, Gentile R, Freddi F, Galsso C (2020) Effect of ground-motion sequences on fragility and vulnerability of case-study reinforced concrte frames. Bull Earthq Eng. https://doi.org/10.1007/s10518-020-01006-8
9. Sehhati R, Rodriguez-Marek A, ElGawady M, Cofer WF (2011) Effects of near-fault ground motions and equivalent pulses on multi-story structures. Eng Struct 33:767–779
10. Tzimas AS, Kamaris GS, Karavasilis GS, Galasso C (2016) Collapse risk and resiudual drift performance of steel buildings using post-tensioned MRFs and viscous dampers in near-fault regions. Bull Earthq Eng 14:1643–1662
11. Fang C, Zhong Q, Wang W, Hu S, Qiu C (2018) Peak and residual responses of steel moment-resisting and braced frames under pulse-like near-fault earthquakes. Eng Struct 177:579–597
12. Ruiz-Garcia J, Ramos-Cruz JM (2020) Assessment of permanent drift demands in steel moment-resisting steel buildings due to recorded near-fault forward directivity earthquake ground motions and velocity pulse models. Structures 27:1260–1273

13. Mashhadi S, Homaei F, Asadi A, Tajammolian H (2021) Fragility analysis of steel MRFs: Effects of frequency-content components of near-fault pulse-like ground motions and setbacks. Structures 33:3655–3666
14. Gutiérrez-Urzúa LF, Freddi F, Di Sarno L (2021) Comparative analysis of code based approaches for the seismic assessment of existing steel moment resisting frames. J Constr Steel Res 181:106589
15. Elettore E, Freddi F, Latour M, Rizzano G (2021) Design and analysis of a seismic resilient steel moment resisting frame equipped with damage-free self-centering column bases. J Constr Steel Res 179:106543
16. Elettore E, Lettieri A, Freddi F, Latour M, Rizzano G (2021) Performance-based assessment of seismic-resilient steel moment resisting frames equipped with innovative column bases connections. Structures 32:1646–1664
17. Homaei F, Mashhadi S (2021) The effect of pulse-like ground motion on the performance-based confidence level of setback special steel moment-resisting frames. J Build Eng 44:103327
18. Gupta A, Krawingler H (1999) Seismic demands for performance evaluation of steel moment resisting frame structures, The SAC Joint Venture, Report No. 132, The John A. Blume Earthquake Engineering Centre, Stanford University, Stanford, CA
19. ASCE/SEI 7–16 (2017) Minimum design loads and associated criteria for buildings and other structures. American Society of Civil Engineers, Reston, VA
20. ANSI/341-16 (2016) Seismic provisions for structural steel buildings. American Institute of Steel Construction, Chicago, IL
21. ANSI/358-16 (2016) Prequalified connections for special and intermediate steel moment frames for seismic applications. American Institute of Steel Construction, Chicago, IL
22. ANSI/360-16 (2016) Specification for structural steel buildings. American Institute of Steel Construction, Chicago, IL
23. Pandikkadavath MS, Sahoo DR (2016) Analytical investigation on cyclic performance of buckling restrained braces with short yielding core segments. Int J Steel Struct 16(4):1273–1285
24. Pandikkadavath MS, Sahoo DR (2017) Mitigation of seismic drift response of braced frames using short yielding-core BRBs. Steel Compos Struct 23(3):285–302
25. Mazzoni S, McKenna F, Scott MH, Fenves GL (2006) OpenSees command language manual, Pacific Earthquake Engineering Research (PEER) Centre. University of California Berkeley, California
26. Ibarra LF, Medina RA, Krawinkler H (2005) Hysteretic models that incorporate strength and stiffness deterioration. Earthquake Eng Struct Dynam 34(12):1489–1511
27. Lignos DG, Krawinkler H (2011) Deterioration modeling of steel components in support of collapse prediction of steel moment frames under earthquake loading. J Struct Eng ASCE 137(11):1291–1302
28. Krawinkler H. (1978). Shear in beam-column joints in seismic design of steel frames. Eng J-Am Inst of Steel Constr Inc 15(3):82–91
29. Baker JW, Ling T, Shahi SK, Jayaram N (2011) New ground motion selection procedures and selected motions for the PEER transportation research program. University of California, Berkeley, CA, Pacific Earthquake Engineering Research Centre
30. Cornell C, Jalayer F, Hamburger R, Foutch D (2002) Probabilistic basis for 2000 SAC Federal Emergency Management Agency steel moment frame guidelines. J Struct Eng ASCE 128:526–533
31. FEMA P58–1 (2018). Seismic performance assessment of buildings Vol. 1—Methodology. Federal Emergency Management Agency, Washington, DC
32. FEMA 356 (2000) Prestandard and Commentary for the seismic rehabilitation of buildings. Federal Emergency Management Agency, Washington, DC

Influence of Span Length on Seismic Mainshock—Aftershock Response of RC Bridges Pre-Exposed to Scouring

K. K. Jithiya, Muhamed Safeer Pandikkadavath, Praveen Nagarajan, and Sujith Mangalathu

1 Introduction

Seismic action on RC bridges pre-exposed to flood-scouring is a multi-hazard scenario. Flood-induced soil erosion, here referred to as flood-scouring, causes the loss of all-around lateral support offered by soil at bridge foundations. Scouring can alter the dynamic characteristics of the bridges and may affect the seismic behaviour of RC bridges adversely [1–3]. Mostly seismic mainshock (MS) invokes several imminent aftershocks (AS) even before the repair or retrofitting required time frame. These AS impact on MS impaired structure escalates the damage risk even under moderate level seismic activities. That is, the seismic response evaluation considering MS alone can lead to underestimation of actual bridge damage risk [4–9]. The case of MS-AS activity on the flood-scouring affected bridges makes this scenario more awful. For reliable response evaluation of bridges, that are located in flood vulnerable seismically susceptible regions, multi-hazard scenarios by considering flood-induced scour along with MS-AS effects need to be accounted for [10].

The present study aims to evaluate the effect of span length on the seismic MS-AS response of scour-affected RC bridges. The variation in bridge span length affects the seismic mass, consequently on the seismic response of the bridge structure. For the investigation, two-span bridges with the same cross-sectional details and different span lengths are considered. A limiting value of flood-induced scour depth reported from the past studies is assimilated for all the bridges. Bridges are modelled in a suitable modelling platform, and nonlinear time history analyses are carried out under MS-only cases and MS-AS sequential cases taking suitable ground motion records.

K. K. Jithiya · M. S. Pandikkadavath (✉) · P. Nagarajan
Department of Civil Engineering, National Institute of Technology Calicut, Kerala, India
e-mail: msafeerpk@nitc.ac.in

S. Mangalathu
Data Analytics Division, Equifax Inc, Atlanta, GA, USA

Subsequently, MS alone and MS-AS responses of bridges are evaluated with the help of probabilistic seismic demand models using applicable structural engineering demand parameter and seismic intensity measure corresponding to different damage states.

2 Description of Bridges

A two-span bridge having an equal span length, L of 39.6 m used in prior studies [1, 10] is selected as a basic structure for the investigation. The bridge deck is made of a prestressed hollow box girder having a width of 12.9 m and a depth of 2.1 m. The bridge pier is a single column circular bent with a diameter of 2.4 m and a length of 19.8 m; the substructure foundation system comprises a group of 40 piles each having a length of 18.3 m and a diameter of 0.38 m, respectively. The schematic plot that shows the geometric details of the study bridge are given in Fig. 1, and the corresponding cross-sectional details are provided in Fig. 2. Apart from the 39.6 m span case, three additional span lengths (keeping all other parameters the same) of 20, 40 and 50 m are considered for the investigation. All the study bridges are accounted for flood-induced scour conditions judiciously. For the flood-scour inflicted case,

Fig. 1 Schematic view of bridges considered
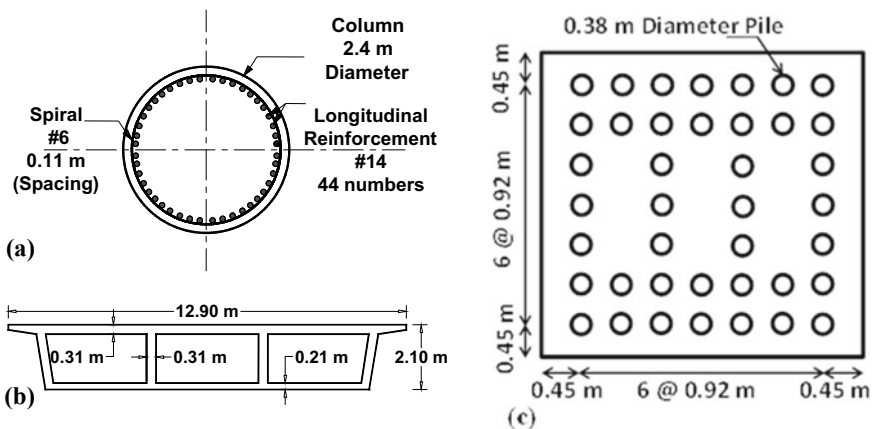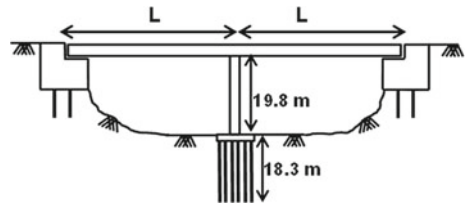
Fig. 2 Cross-sectional details of **a** Pier, **b** deck and **c** foundation

Fig. 3 Ground motion
spectra of the selected suite
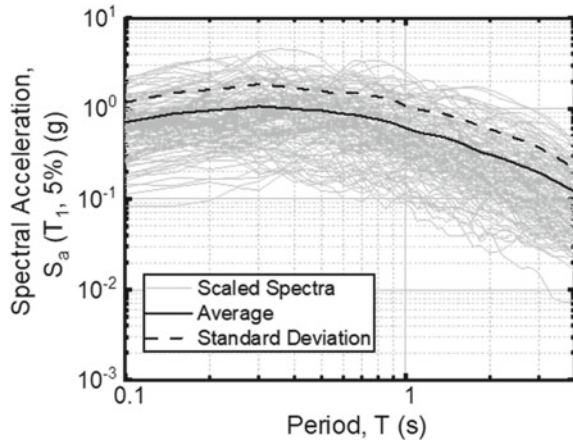
limiting scour depth corresponding to maximum response variation observed case
(5-year flood-scour depth of original bridge) is incorporated [1, 10].

3   Seismic Hazard

For nonlinear time history analysis, a suite of 124 ground motions that come
under different hazard levels is considered. The records comprise both natural
and simulated records including 20 ground motion records of design level earth-
quakes (DBE): having 10% exceeding probability in 50 years [11], same numbers
of maximum considered level earthquakes (MCE): having exceedance probability
of 2% in 50 years [11], 44 records developed by FEMA P695 guidelines [12] and
40 records from broadband ground motion (BBGM) set—1A developed for Pacific
Earthquake Engineering research program [13]. Magnitudes of the ground motions
considered range between 6.0 and 7.9; peak ground acceleration, PGA is in the range
of 0.08 g to 1.33 g. All these 124 ground motions are considered for MS evaluation.
For AS sequence, the records are selected from the same suite randomly which falls
between 0.7 and 0.9 times the PGA of MS [14, 15]. The response spectra of the
ground motion suite along with its mean are shown in Fig. 3.

4   Flood-Induced Scour

The scour depth estimate at a bridge location is highly dependent on the flow velocity
and thus the flood discharge. Flood hazard curves can give the flood discharge vulner-
ability at any given region, and it provides the annual peak discharge values of flood
events corresponding to different exceedance probabilities. Flood frequency analysis

is can be used for the development of a flood hazard curve. For flood frequency analysis, annual peak discharge data recorded for the selected site for the last 113 years (from 1907 to 2019) is obtained from the United States Geological Survey (USGS) National Water Information System [16]. Using an empirical approach, a flood hazard curve is developed and relation between annual peak discharge and corresponding annual exceedance probability is established. More details about this flood hazard curve can be found in the literature [10]. From the flood hazard curve, the 5-year flood discharge, Q is obtained as 675 m^3/s. The stream cross section is assumed as a rectangle, and the width of the stream is considered as the length of the bridge. Using the dimensions of the original bridge, the velocity, V, and depth of flow, h corresponding to flood event is calculated with the help of Eqs. (1) and (2) [17].

$$Q = bhy_1 \tag{1}$$

$$V = \frac{1}{n}\left[\frac{by_1}{b + 2y_1}\right]^{2/3} S^{1/2} \tag{2}$$

where b is the width of the stream and y_1 is the depth of flow. Manning's roughness coefficient, n that represents the frictional effect in the channel to flow is taken as 0.08; similarly slope of the bed stream, S is adopted as 0.001 based on previous study recommendations [1, 10]. The soil profile has three different regions starting with 11.7 m deep top silty sand layer, followed by 5.5 m deep silt and 1 m sand layer for the bottom-most location along with the depth [1, 2]. The local scour around all the piers are assumed to be the same at a given hazard level. The pile cap is assumed to be at ground level, and the scour depths are calculated from the top of the pile cap [18]. Using the flow velocity, V, and flow depth, y_1 obtained using Eq. (1) and Eq. (2), scour depths are calculated for different levels of flood hazards with the help of Eq. (3) [19].

$$Y_s = 2y_1 K_1 K_2 K_3 \left(\frac{a_1}{y_1}\right)^{0.65} Fr_1^{0.43} \tag{3}$$

where a_1 is the width of the pier, y_1 is the depth of flow directly upstream to the bridge pier; K_3, K_2 and K_1 are correction factors for bed condition, angle of flow attack and nose shape of the pier, respectively. Fr_1 is the Froude number at the upstream of the pier, which is defined as $V/(gy_1)^{0.5}$, where V is the upstream mean velocity and g is the acceleration due to gravity. Since the pier is circular, the K_1 value is taken as 1.0. The angle of attack of flow is assumed to be zero, so K_2 is taken as 1, and assuming clear water conditions K_3 is taken 1.1. For $y_1/a < 0.8$, additional correction factor K_w also applied conveniently [19].

The scour depth estimation procedure discussed provides a quick reasonable estimate of scour around the bridge piers due to flood events. But for the exact magnitudes of scour, a detailed hydraulic analysis of these bridges at each pier is required, which is beyond the scope of the present investigation.

5 Modelling and Nonlinear Analysis

5.1 Deck and Pier

The nonlinear analyses of the example two-dimensional bridges are carried out using SAP2000 [20]. The bridge girders are modelled as linear beam-column elements aligned along the centreline of the decks. A monolithic rigid connection is assumed between pier and girder. At the abutment locations, girders are assumed to be free to translate in the longitudinal direction. The degrees of freedom in the transverse direction are fully restrained and only in-plane rotations are allowed [2, 3, 10]. During earthquake excitations, this arrangement allows to development of maximum bending moments at the pier ends and induces the formation of plastic hinges in these locations. At these critical locations, Pivot hysteretic model adopted plastic hinges are assigned to depict the inelastic response of the bridge [21]. The validation of this model with the test results is given in Fig. 4a. The corresponding Pivot hysteretic model parameters are $\alpha_1 = \alpha_2 = 5$ and $\beta_1 = \beta_2 = 0.2$ and $\varepsilon = 0$, respectively [20]. This Pivot hysteretic model used a plastic hinge ensured to pursue the design derived from multi-linear moment rotation relation parameters [22]. The relevant moment, rotation and stiffness values are yield moment, $M_y = 36,493$ kNm, ultimate moment, $M_u = 41,490$ k Nm, yield rotation, $\theta_y = 0.00373$ rad, ultimate rotation, $\theta_u = 0.03415$ rad, elastic stiffness of the pier, $K_{Elastic} = 9.78 \times 106$ kNm/rad and post-yield stiffness, $K_{PY} = 1.66 \times 10^5$ k Nm/rad (post-yield to elastic stiffness ratio is 0.017), respectively [2, 3, 10]. From the so modelled structure, the horizontal displacement obtained displacement ductility at top of the pier (at superstructure level) is considered for estimating the probability of bridge damage under the earthquakes.
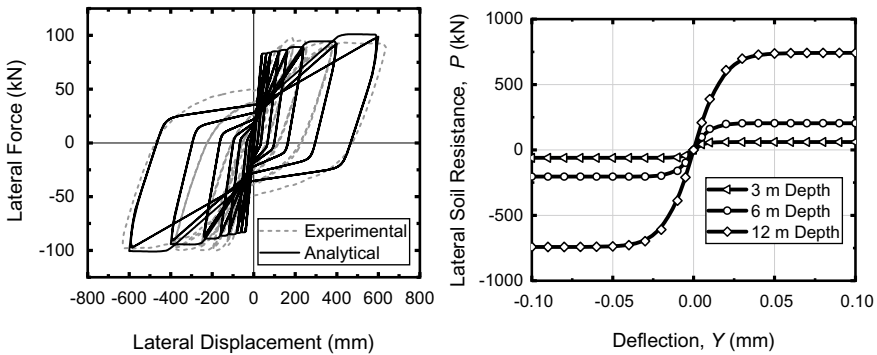
Fig. 4　a Pivot plastic hinge model and **b** sample P–Y curves of soil springs

5.2   Soil Structure Interaction

The soil–structure interaction represents the nonlinear lateral resistance offered by soil during the ground motions propagation. The foundation system consists of 40 numbers of 0.38 m diameter piles below the pier. To avoid the complexity involved in modelling the pile group system, an equivalent single pile concept is utilized. The pile group is replaced by a single pile (equivalent pile) having the same bending stiffness as that of the entire pile group system [23]. The pile foundation may have a rocking or/and sway motion during the earthquakes. In these conditions, the lateral load–deflection characteristics and bending stiffness of the pile group (EI_G) will be different. For sway motions, the bending stiffness value of equivalent pile (EI_{eq}) can be calculated by the following expression [23]:

$$EI_{eq} = EI_G = n_p EI_p \tag{4}$$

For rocking motion bending stiffness value of equivalent pile (EI_{eq}) can be calculated using Eq. (5):

$$EI_{eq} = EI_G = \sum_{i=1}^{n_p} \left\{ EI_P + EA_P \left(x_{pi} - x_0 \right)^2 \right\} \tag{5}$$

Here E is the modulus of elasticity of the material of pile, I_G is the moment of inertia of entire pile group, and I_{eq} is the moment of inertia of equivalent pile cross section; I_p is the moment of inertia of single pile; n_p is the number of piles in the pile group; (x_{pi}–x_0) denotes the relative distance of a given single pile from the centroid of the pile group;A_p denotes the cross-sectional area of individual piles, respectively. In the present study, the pile group is represented by a single equivalent pile using the literature-recommended method. For the sway condition, the diameter of the equivalent pile (d_{eq}) obtained is 0.97 m, and for the rocking condition, it is obtained as 4.2 m. The length of the equivalent pile is taken the same as that of individual piles (18.3 m) in any case accounted. The lower bound value of $d_{eq} = 0.97$ m is considered for modelling.

During the seismic ground motion hit, lateral deflection occurs in an equivalent pile system. The soil interaction offers resistance against this displacement. This soil–structure interaction is dependent on the characteristics of the surrounding soil. The relation between the lateral load resistance offered by soil (P) and corresponding deflection in the pile (Y) of cohesionless soil at any depth H (P-Y curve) can be determined using Eq. (6) [24]:

$$P = A \times P_u \times \tanh\left[\frac{k \times H}{A \times P_u} \times Y \right] \tag{6}$$

where factor A narrates for loading condition and for cyclic loading, A can be taken as 0.9 [24]. P_u is the ultimate lateral resistance at a given depth H, which can be taken as the minimum value obtained from Eqs. (7) and (8). k is the initial modulus of subgrade reaction, and its value is taken as 11,970 k N/m^3 [1, 2].

$$P_u = (C_1 H + C_2 d)\gamma H \tag{7}$$

$$P_u = (C_3 d)\gamma H \tag{8}$$

Equations (7) and (8) represent the ultimate lateral resistance for shallow and deep foundation conditions, respectively. The coefficients C_1, C_2 and C_3 are functions of the friction angle of the soil [23]. A friction angle for the soil profile considered is 30^0 and corresponding values of C_1, C_2 and C_3 are 1.9, 2.65 and 28, respectively [24]. The effective soil weight (γ) was taken as 9.02 kN/m^3 assuming submerged conditions [1, 2].

Elastic linear beam-column elements are used to model the equivalent single pile that represents the foundation of the example bridges [1, 2]. The soil–pile interaction is incorporated using nonlinear P–Y springs. These springs are provided along the length of the equivalent pile at 0.3 m intervals. Nonlinear elastic spring links are utilized in SAP2000 to incorporate this condition, and the properties are determined using Eq. (6). Initially, lateral soil resistance changes nonlinearly with lateral deflection, and then it becomes constant. The P–Y curve of soil springs at four representative depths (3, 6 and 12 m) is shown in Fig. 4. It is observed that lateral soil resistance increases as the depth increases.

If scouring has occurred, there won't be any lateral soil resistance up to this scour depth. So, to model the loss of surrounding lateral support due to scour, soil springs are taken out down up to the scour depth Y_s measured from the top of the ground surface. Here 3.3 m scour is considered based on the past study reports, and hence, soil springs are removed up to a depth of 3.3 m from the ground surface for such a situation in the model. Pinned end support scenario is assumed at the bottom tip of piles as per the research recommendations [1, 2].

In the present study, all the models are assumed to be inflicted with scouring. The detailed no-scour inelastic response results can be found in the literature [1–3, 10]. Modal analysis is performed, and it is observed that the fundamental period increases as the span length increases. For the original two-span bridge (span, L = 39.6 m), at 3.3 m scour the first mode fundamental time period is found to be 2.65 s. For bridges with spans 20 m, 30 m and 50 m the first mode fundamental times period corresponding to 3.3 m scour depth is obtained as 2.05 s, 2.55 s and 3.41 s, respectively.

5.3 *Nonlinear Time History Analysis*

For nonlinear analyses, the mainshock is applied in continuation of gravity load case, then the aftershock is applied sequentially to the mainshock. For each ground motion, the nonlinear time history of longitudinal displacement at the pier top (superstructure level) is extracted. The measured displacements are transformed to displacement ductility (μ_Δ), which is the ratio of the bridge pier displacement to the yield displacement, and the same is utilized to assess the seismic response assessment of the bridge structures.

6 Fragility Analysis

The fragility curve gives the conditional probability, that the response of a particular structure (or component) may exceed the capacity limit at a given ground motion intensity.

The probabilistic seismic demand models (PSDM) define the demand (D) side of the problem. To establish the resistance side of the problem, capacity (C) limit states need to be quantified in terms of engineering demand parameters (EDPs). The lognormal distribution is assumed for both D and C for developing the PSDM [25–27]. A fragility function designates the probability of a demand, D to exceed the capacity, C for a specific found motion intensity measure, IM. Fragility curves for different damage states can be expressed using the closed-form solution outlined in Eq. (9) [28].

$$P[D > C|IM] = \Phi\left[\frac{\ln\left(S_d/S_c\right)}{\sqrt{\beta_{D|IM}^2 + \beta_C^2}}\right] \tag{9}$$

where $\Phi(\bullet)$ is the standard normal cumulative distribution function, S_d is the median of demand, S_c is the median value of capacity and βc is capacity dispersion. β_{dIIM} is referred to as the dispersion of the demand conditioned over IM.

6.1 *Probabilistic Seismic Demand Model*

PSDMs are developed using regression analysis between D and IM in log-transformed space using Eq. (10). Where $\ln(a)$ and b are regression coefficients. If N numbers of responses are recorded for a suit of N ground motions, the dispersion of the demand β$_{D|IM}$ can be determined using Eq. (11)

$$\ln(S_d) = \ln(a) + b \cdot \ln(IM) \tag{10}$$
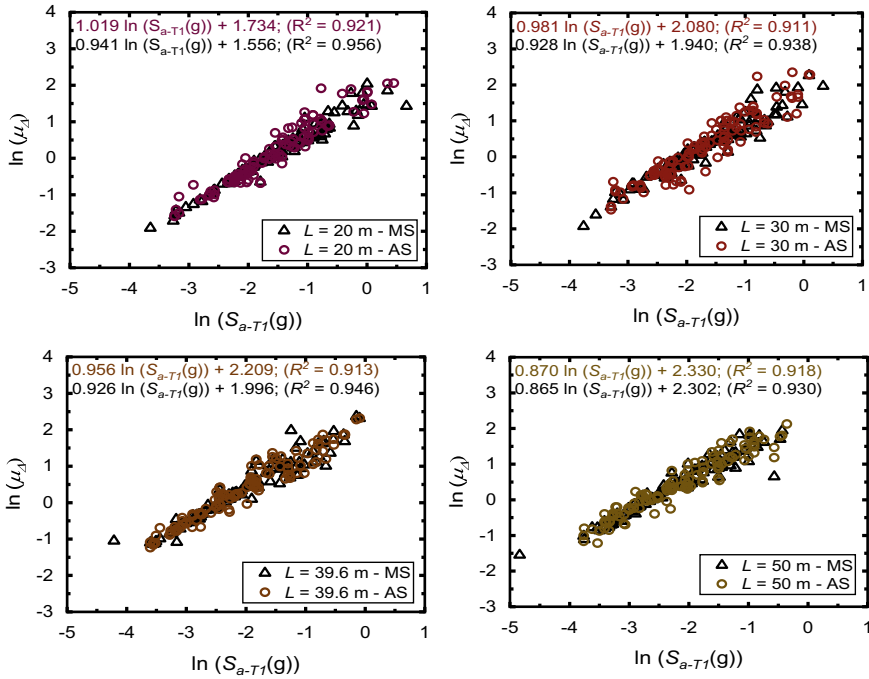
Fig. 5 PSDMs for the considered cases

$$\beta_{d|IM} = \sqrt{\sum_{i=1}^{N} \frac{(\ln(di) - \ln(S_d))^2}{N-2}} \tag{11}$$

Here spectral acceleration at first mode fundamental period of bridge model, $S_{\text{a-T1}}$ is considered as IM. Peak displacement ductility, μ_{Δ} corresponding to respective seismic records are considered as demand parameters. Using values of μ_{Δ} and correspond to each ground motion $S_{\text{a-T1}}$ for each bridge model with different spans PSDMs are developed, and they are shown in Fig. 5. Successively $\beta_{\text{D|IM}}$ is estimated for all cases, and the same is utilized to get the fragility curves.

6.2 Capacity Limits

Limit state definition is integral part in the fragility analysis. As pointed out earlier the capacity distribution is also assumed to be lognormal with the values of median, S_c and dispersion, β_c. Five damage states, namely minor (slight), moderate, major (severe) and complete collapse are accounted as the capacity limits for the fragility analyses. Definitions of these damage states follow the HAZUS-1999 description of

bridge damage states [29]. Since the responses are evaluated in terms of displacement ductility (μ_Δ), the median values of damage thresholds (S_c) also need to express in terms of μ_Δ. The S_c values for the damage thresholds (DTs) are 2.25, 2.9, 4.6 and 5 for minor, moderate and major, complete damage states respectively [1, 2, 29]. Dispersion β_c is taken as 0.35 for all the damage states as per the recommendations [25, 26].

6.3 Fragility Curves

Using the PSDMs, fragility curves are developed for different damage states using Eq. (9). Developed fragility curves for the considered bridges are shown in Fig. 6, and median values of the fragility curves are compared as shown in Fig. 7.

Median value of fragility curve for complete damage state is 1.06 g for bridge-1 ($L = 20$ m), 0.70 g for bridge-2 ($L = 30$ m), 0.52 g for bridge-3 ($L = 39.6$) and 0.45 g for bridge-4 ($L = 50$), respectively, under MS case. For MS-AS sequential case, the median values corresponding to complete damage states are 0.88 g, 0.62 g, 0.50 g and 0.44 g for bridges with the span length 20 m, 30 m, 39.6 m and 50 m, respectively. A 50% reduction in span length ($L = 20$ m) from the original span (39.6 m) lead to a 104% increase in median value; 25% reduction in span lead to a 32% increase in median value, and a 25% increase in span caused 14% reduction in median value for MS case from the basic case. A similar trend was observed for the MS-AS case as well (for all damage states also). The results show that span length change influences the vulnerability corresponding to any given damage state. A nonlinear relation is observed between damage state vulnerability and span length. For all damage states, median values are lower for the MS-AS case compared to the MS case. This indicates that MS-AS vulnerability for any given damage state is higher than the corresponding MS vulnerability.

7 Conclusion

This study assesses the seismic mainshock–aftershock performance of RC bridges subjected to flood-induced scour. Four two-span bridges with identical cross-sectional features and varying span lengths are considered. A specific value of flood-induced scour depth is considered for all the bridges. Bridges are modelled in a suitable software platform by incorporating applicable soil–structure interaction. Nonlinear time history analyses were carried out under MS-only cases and MS-AS sequential cases using selected ground motion records. Subsequently, fragility curves are developed and compared. From this study, the following key conclusions are made:
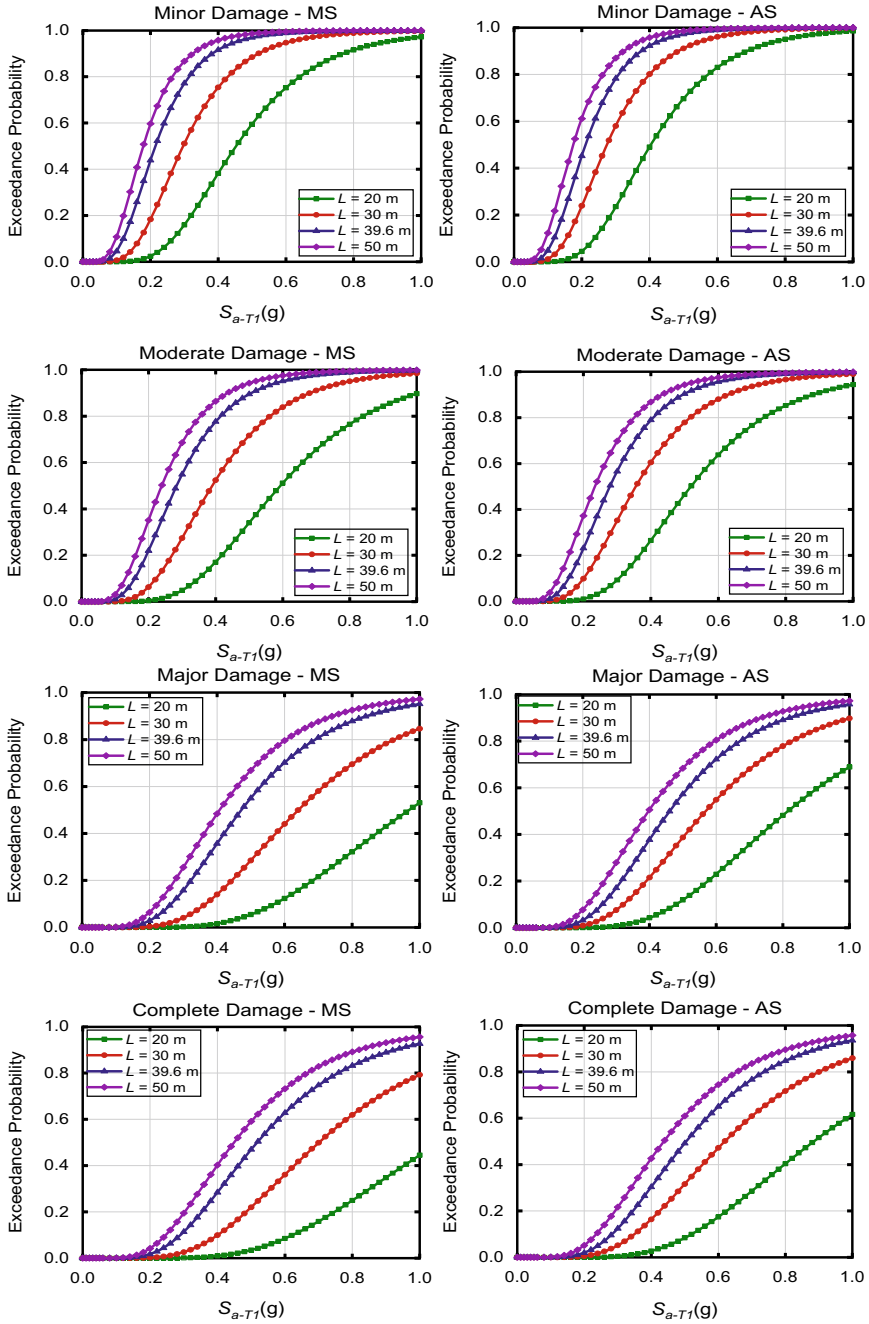
Fig. 6 Fragility curves for the considered cases
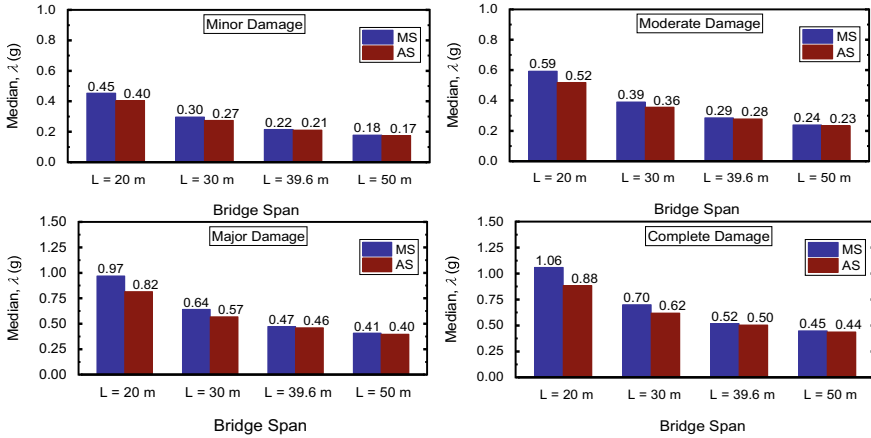
Fig. 7 Comparison of median values of fragility curves

- Compared to the mainshock alone case, mainshock–aftershock sequence events cause higher vulnerability to bridges in the presence of flood-induced scour.
- Span length change is influential on the fragility characteristics of the bridge. The vulnerability of bridges nonlinearly increases with an increase in span length.
- Nonlinear analyses neglecting the effects of seismic mainshock–aftershock sequence and flood-instigated scour may lead to the underestimation of the actual vulnerability of the bridges located in flood-prone seismically active regions.

References

1. Prasad GG, Banerjee S (2013) The impact of flood-induced scour on seismic fragility characteristics of bridges. J Earthq Eng 17:803–828
2. Banerjee S, Prasad GG (2013) Seismic risk assessment of reinforced concrete bridges in flood-prone regions. Struct Infrastruct Eng 9(9):952–968
3. Yilmaz T, Banerjee S, Johnson PA (2016) Performance of two real-life California bridges under regional natural hazards. ASCE J Bridge Eng 21(3):04015063
4. Alessandri S, Giannini R, Paolacci F (2013) Aftershock risk assessment and the decision to open traffic on bridges. Earthq Eng Struct Dyn 42:2255–2275
5. Kumar R, Gardoni P (2014) Effect of seismic degradation on the fragility of reinforced concrete bridges. Eng Struct 79:267–275
6. Dong Y, Frangopol DM (2015) Risk and resilience assessment of bridges under mainshock and aftershock incorporating uncertainties. Eng Struct 83:198–208
7. Ghosh J, Padget JE, Silva MS (2015) Seismic damage accumulation in high bridges in earthquake-prone regions. Earthq Spectra 31(1):115–135
8. Omranian E, Abdelnaby AE, Abdollazadeh G (2018) Seismic vulnerability assessment of RC skew bridges subjected to the mainshock-aftershock sequence. Soil Dyn Earthq Eng 114:186–197

9. Gidaris I, Padgett JE, Misra S (2020) Probabilistic fragility and resilience assessment and sensitivity analysis of bridges incorporating aftershock effects. Sustain Resil Infrastruct. https://doi.org/10.1080/23789689.2019.1708174
10. Jithiya KK, Pandikkadavath MS, Mangalathu S, Nagarajan P (2020) Seismic mainshock-aftershock vulnerability assessment of reinforced concrete bridge exposed to flood-induced scour. Recent Adv Earthq Eng Lect Notes Civ Eng 175:211–221
11. Somerville P, Smith N, Punyamurthala S, Sun J (1997) Development of ground motion time histories for phase 2 of the FEMA/SAC steel project. Report no: SAC/BD-97/04, 1997, SAC joint venture
12. FEMA (2009) Quantification of building seismic performance factors—FEMA P695. Federal Emergency Management Agency, Washington DC
13. Baker JW, Lin T, Shahi SK, Jayaram N (2011) New ground motion selection procedures and selected ground motions for the PEER transportation research program. PEER report No. 2011/03, Pacific Earthquake Engineering Research Centre, University of California, Berkeley.
14. Jeon JS, DesRoches R, Lowes LN, Brilakis I (2015) Framework of aftershock fragility assessment–case studies older California reinforced concrete building frames. Earthq Eng Struct Dynam 44:2617–2636
15. Managlathu S, Shokrabadi M, Burton HV (2019) Aftershock seismic vulnerability and time-dependent risk assessment of bridges. PEER report No. 2019/4, 2019; Pacific Earthquake Engineering Research Center, University of California, Berkeley.
16. USGS. (2020). National water information system. http://nwis.waterdata.usgs.gov/nwis, (accessed on 18 September 2020.)
17. Gupta RS (2017) Hydrology and hydraulic systems, 4th edn. Illinois, Waveland Press Inc
18. Bennett CR, Lin C, Parsons R, Han J (2009) Evaluation of behaviour of a laterally loaded bridge pile group under scour conditions. In: Proceedings of SEI 2009 structures congress, Texas, pp 290–299
19. Arneson LA, Zevenbergen LW, Lagasse PF, Clopper PE (2012) Evaluating scour at bridges. Publication No. FHWA-HIF-12–003, Hydraulic Engineering Circular (HEC) No.18, Federal Highway Administration United States Department of Transportation, Washington DC
20. CSI (2013) SAP2000, User guide. Computers and Structures Inc., Berkly, CA, USA
21. Dowell RK, Seible F, Wilson EL (1998) Pivot hysteresis model for reinforced concrete members. ACI Struct J 95(5):607–617
22. Priestley MJN, Seible F, Calvi GM (1996) Seismic design and retrofit of bridges. John Wiley and Son Inc., New York
23. Yin Y, Konagai K (2001) A simplified method for expression of the dynamic stiffness of large-scaled grouped piles in sway and rocking motions. J Appl Mech JSCE 4:415–422
24. API (2000) Recommended practice for planning, designing and constructing fixed offshore platforms. API recommended Practice 2A-WSD (RP 2A). American Petroleum Institute, Washington, DC
25. Ramanathan K, Padgett JE, DesRoches R (2015) Temporal evolution of seismic fragility curves for box-girder bridges in California. Eng Struct 95:29–46
26. Mangalathu S, Jeon JS, DesRoches R, Padgett JE (2016) ANCOVA-based grouping of bridge classes for seismic fragility assessment. Eng Struct 123:379–394
27. Managlathu S, Shokrabadi M, Burton HV (2019) Aftershock seismic vulnerability and time-dependent risk assessment of bridges. PEER Report No. 2019/4, Pacific Earthquake Engineering Research Center, University of California, Berkeley
28. Cornell C, Jalayer F, Hamburger R, Foutch D (2002) Probabilistic basis for 2000 SAC Federal Emergency Management Agency steel moment frame guidelines. J Struct Eng ASCE 128(4):526–533
29. Hazus (1999) Earthquake loss estimation methodology, Technical Manual SR2. Federal Emergency Management Agency (through agreement with National Institute of Building Science), Washington DC

Nonlinear Finite Element Analysis and Artificial Intelligence (ANN)-Based Predictions for RC Beam Members Strengthened with CFRP Laminates

Sagnik Mukhopadhyay and Subhashish Roy Chowdhury

1 Introduction

Fibre-reinforced polymers (FRP) belong to a class of composite materials. The majority of FRP materials are composed of continuous fibres of high strength embedded in a polymer matrix (resin). The embedded fibres serve as the primary reinforcing components, while the polymer matrix acts as a binder, preserving the fibres and facilitating load transmission to and between them. Fibre-reinforced polymer (FRP) materials exhibit a wide range of behaviours based on the fibre type and polymer matrix. Retrofitting reinforced and unreinforced masonry walls, retrofitting earthquake-resistant bridges and other structures, repairing or improving concrete structures, metal-and-timber girders, or slabs, and restoring historic monuments and offshore platforms are all possible applications for FRP materials. Concrete surfaces must be prepped before FRP plates and sheets may be attached to them using grinding, sandblasting or water jetting. This method of external reinforcement can be swiftly applied due to its simplicity.

Neural networks are made up of neurons, also known as nodes or units, which are the basic computational units. It receives input from other nodes or an external source. Weight (w) for each input in the equation is assigned based on how significant it is in relation to other inputs. The main components of neural network are input nodes (layer), hidden nodes (layer) where most of the calculations take place and the output nodes (layer).

Experiments on the influence FRP have on flexural, shear, torsional and axial reinforcement in reinforced concrete structural component have garnered attention in recent years from both academic and industry researchers. In 1998, Ritchie et al. [1] tested adhesively bonded GFRP and CFRP plates to failure on 2.75 m long

---

S. Mukhopadhyay (✉) · S. R. Chowdhury
Department of Civil Engineering, Jadavpur University, West Bengal, Kolkata 700032, India
e-mail: sagnik.mukhopadhyay.ju@gmail.com

reinforced RC beams that were exposed to flexural impacts. Meier [2] conducted a study in 1992 on 60 small-scale RC beams in a four-point bend configuration. CFRP sheets of 200 mm in width and 0.3 mm thick were used to reinforce these beams. There were experiments performed by Arduini and Nanni [3] that involved the use of CFRP sheets to reinforce pre-cracked RC beams. Hussain et al. [4] conducted research on RC-columns of three distinct forms wrapped with GFRP. El-Gamal's et al. [5] research work involved casting 10 full-scale RC beams and reinforcing them in flexure with different FRP materials. Anil et al. [6] in 2013 conducted tests on 12 FRP-strengthened reinforced concrete slabs. Ceroni et al. [7] carried out flexural tests on 21 RC beams reinforced with NSM bars and CFRP plates.

Researchers have shown that artificial neural networks (ANNs) may be used to calculate displacement in reinforced concrete beams as an alternative to traditional techniques. For example, Naderpour et al. [8] predicted concrete's compressive strength; Ahmadi et al. [9] predicted the axial strength of composite columns; and Khademi [10] evaluated the displacement of RC buildings using ANN. Using ANN, Kaczmarek and Szyma'nska [11] calculated displacement in reinforced concrete and the findings were highly accurate. An investigation conducted by Tuan Ya et al. [12] found that the result was extremely accurate when using the ANN technique to forecast displacement in cantilever beams.

Although previous work has been carried out on strengthening beams with FRP, the area to be laminated and the position of placing the FRP over the beam can be a scope of study. How the different strength parameters, crack pattern and other behavioural changes occur with the positioning of the FRP, and varying the area of lamination can be further studied. Prediction of the behaviour of these kinds of beams can be done using ANN and will help the structural engineering professional to assess the extent of improvement that can be achieved by the strengthening process. But to understand the behavioural changes due to FRP, it requires a huge number of numerical experiments. It can be avoided if ANN models can predict those parameters based on some developed data.

2 Numerical Modelling

2.1 Finite Element Modelling

A nonlinear analysis is performed when applied forces and displacements for a structural component are not linearly related. As a result, unlike in linear analysis, the stiffness matrix does not remain constant during the load application process. Thus, the nonlinear analysis requires a different solution method and, consequently, a separate solver. Loading of a structure results in varying stresses at different places in the structure. With the help of modern analytic software tools, nonlinear issues can now be analysed. In this work, the commercial software package ABAQUS has been used for nonlinear analysis of RC beam strengthened with FRP laminates.

The concrete damage plasticity model has been used for analysis of concrete and reinforcement, and the Hashin damage model for analysis of CFRP. The concrete damaged plasticity model in ABAQUS can simulate behaviour of concrete and other quasi-brittle materials in various kinds of constructions (beams, trusses, shells and solids). It is also used with rebar to model concrete reinforcement. The CDP model has been developed for applications where concrete is subjected to monotonic, cyclic and/or dynamic loads.

Concrete elements are modelled using C3D8R meshing, i.e. 8-node linear brick, reduced integration and hourglass control. Reinforcements are meshed using T3D2: a 2-node linear 3-D truss is used, and for CFRP element S4R (a 4-node doubly curved thin or thick shell, reduced integration, hourglass control, finite membrane strains) mesh is used.

2.2 ANN Modelling

It is the neurons in the model that process input data and predict output in artificial neural networks (ANNs) or deep learning models. Neurons can have more than one layer. The model predicts the output using weights and other activation functions that are sent through the model's neurons along with each input. This is known as "forward propagation". The training dataset is a pair of (x, y) where x denotes the features and y denotes the expected output. The predicted output is evaluated against the expected output "y". Now we evaluate the performance of the model using a loss function between the predicted output and "y" (actual output). The loss function is the measure of the difference between the actual and predicted outputs. The loss function could be log-loss, mean-squared-error or any other function. The weights associated with the input and other neural network layers are randomly initialised and are adjusted repeatedly with the help of the loss function. The weights are so adjusted to minimise the loss function. The gradient of the loss function with respect to the parameters is computed. Using this gradient, the weights in each layer are adjusted. This process of adjusting weights, starting from the last layer to the input layer, is known as "back-propagation". There is a learning rate associated with the weight gradients that determine the influence of the gradients in adjusting weights. Once the weights are adjusted, the model is again evaluated to get the loss function and the weights are readjusted. This process goes on till the loss functions are minimised.

3 Results and Discussion

3.1 Loading Condition 1: Beam Subjected to Concentrated Load at Mid-Span

A sample RCC beam with the following specification has been taken for modelling:

Cross section: 100 mm × 200 mm, Length: 2 m.

Reinforcement: Main reinforcement: Top-12 mm @ 2 Nos, Bottom-12 mm @ 2 Nos. Stirrups: 8 mm @ 150 *c/c* (Fig. 1).

On the given beam, incremental load has been induced at the centre till the RCC beam reached the plastic state. Carbon fibre-reinforced polymer (CFRP) has been wrapped at different places on the beam (Figs. 2, 3, 4, 5, 6 and 7).

When the load is low, the lines almost completely overlap (Fig. 8), but as the load increases, the difference in displacement widens significantly. It is seen in this graph that the deflection values for the two configurations, *S2* and *S3*, are nearly identical across the whole region. 125 kN yielded a deflection of 4.69 mm on *S3* sides and
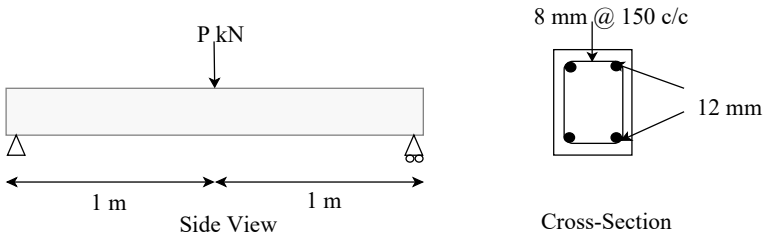
Fig. 1 Sketch of simply supported beam

Fig. 2 Different combinations of CFRP strengthening
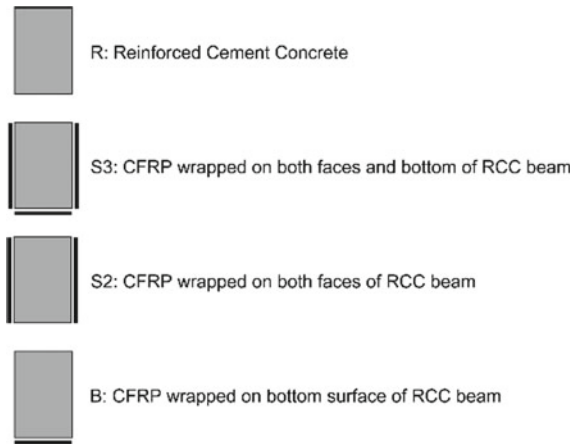
Fig. 3 Stress flow in CFRP in *B* (top), *S*2 (centre) and *S*3 (last*)*
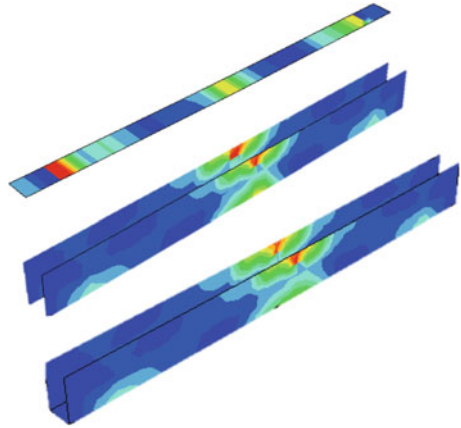
Fig. 4 Crack propagation for RCC
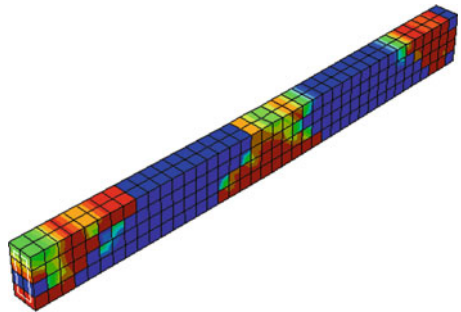
Fig. 5 Crack propagation for CFRP at bottom (*B*)
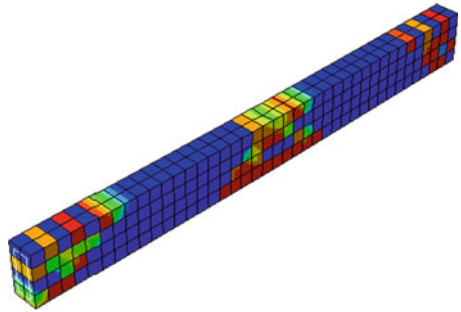
4.96 mm on *S*2. Even at a larger load, the change is only 0.27 mm, which is not that significant. As a result, it is preferable to use CFRP on both sides (*S*2) rather than all three, which makes it less cost-effective (Table 1).

It may be deduced that one of the most efficient ways to apply CFRP is to wrap it on both faces. Further different combinations of wrapping of CFRP on both sides of the beam have been done, which are depicted below (Fig. 9).

Fig. 6 Crack propagation for CFRP on both sides (*S2*)
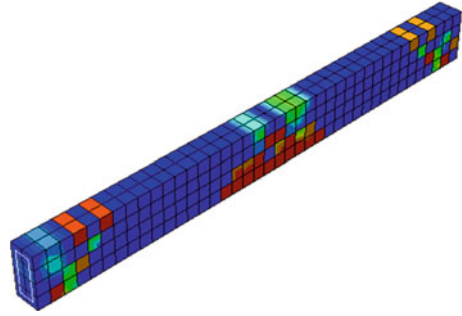
Fig. 7 Crack propagation for CFRP on 3 sides (*S3*)
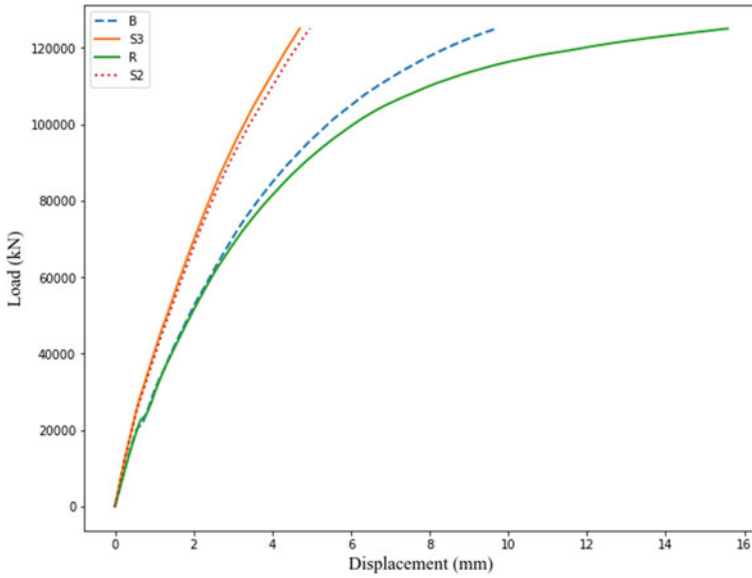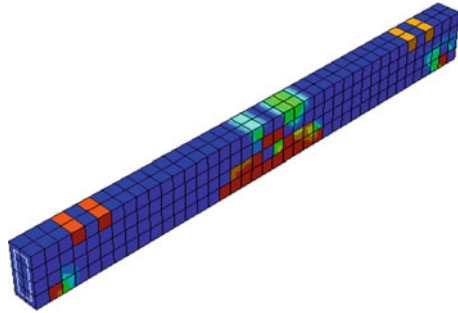
Fig. 8 Load–displacement graph under concentrated loading for different CFRP strengthening modes

Table 1 Comparison of load–deflection responses

	125 kN		100 kN	
	Δ (mm)	% reduction in Δ	Δ (mm)	% reduction in Δ
R: RCC	15.58	–	6.25	–
B: CFRP on bottom	9.7	38	5.58	11
*S*2: CFRP on both faces	4.96	68	3.44	45
*S*3: CFRP on 3 sides	4.69	70	3.28	48
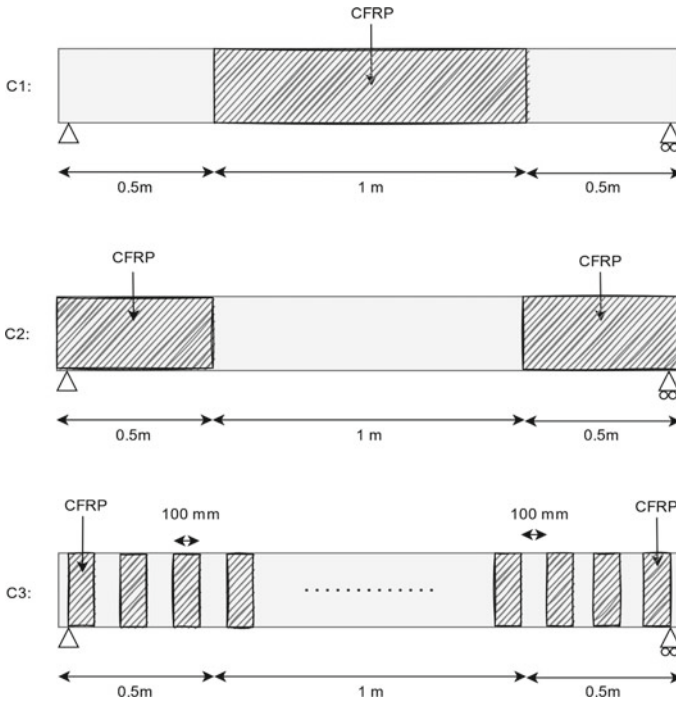
Fig. 9 Different combinations of CFRP wrapping on sides

*C*1: CFRP of total length *L*/2 wrapping at mid-section.
*C*2: CFRP of total length *L*/2, with *L*/4 wrapped at two ends.
*C*3: CFRP of total length *L*/2, with each segment having a width of 100 mm and 100 mm spacing in between.

Except for *S*2, the same length of CFRP has been applied on all the other combinations, i.e., *C*1, *C*2 and *C*3, but the difference in deflection is quite significant. While the best possible combination is *C*1, which has a merely 7.2% increment from *S*2, *C*2 is the worst combination with a drastic 90.9% increment over *S*2 (Table 2).

Table 2 Load–deflection comparison of $C1$, $C2$ and $C3$ with respect to $S2$

	P = 125 kN	
	Δ (mm)	% increment in Δ w.r.t $S2$
R: RCC	15.58	–
$S2$: CFRP on sides	4.96	–
$C1$: CFRP $L/2$ middle	5.31	7.2
$C2$: CFRP $L/4$ both edges	9.47	90.9
$C3$: CFRP gap graded	8.26	66.5

Gain in Strength of RCC beam may be represented as: $S3 > S2 > C1 > C3 > C2 > B$.

3.2 Loading Condition 2: Beam Subjected to Pressure Load of Different Magnitude

Pressure load of different magnitude applied on the same simply supported beam (mentioned earlier) (Figs. 10 and 11).

$S3$ and $S2$ give the best results (Table 3) with maximum reduction in deflection,

Fig. 10 Abaqus model of RC beam under pressure loading
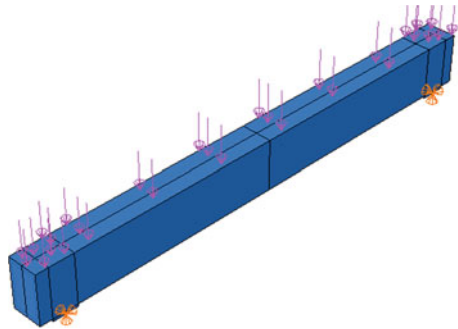
Fig. 11 Crack propagation of RC beam under pressure load
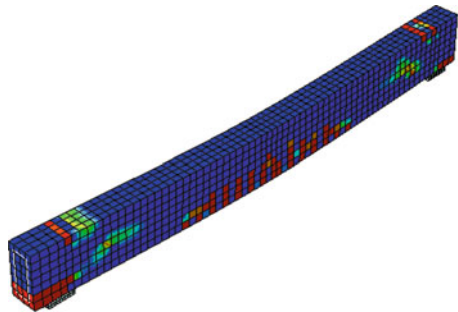
Table 3
Pressure–displacement
comparison

	Pressure = 1.8 MPa	
	Δ (mm)	% Reduction in Δ
R: RCC	9.91	–
B: CFRP on bottom	6.28	36.7
*S*2: CFRP on both faces	3.99	59.7
*S*3: CFRP on 3 sides	3.65	63.1
*C*1: CFRP @ *L*/2 middle	7.50	24.3
*C*2: CFRP @*L*/4 on both edges	4.07	58.9
*C*3: CFRP gap graded	4.41	55.5

but one major difference that has been found is that *C*2 and *C*3 perform better when pressure load is applied, unlike in concentrated loading at the midpoint (Figs. 12, 13). So, it can be concluded that for pressure loading *S*3, *S*2 performs the best, followed by *C*2 and *C*3. *C*2 will be the most economical way of strengthening for pressure loading.
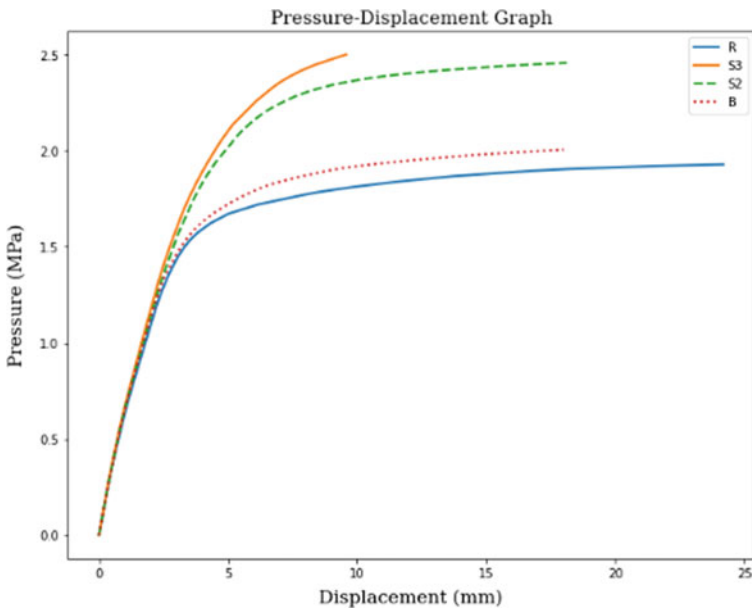
Fig. 12 Pressure–displacement graph for *R*, *B*, *S*2 and *S*3
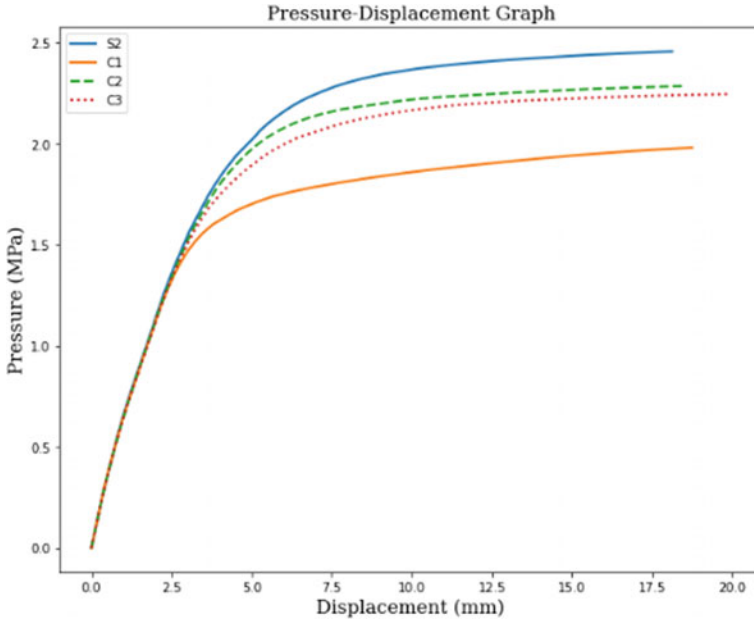
Fig. 13 Pressure–displacement graph for $S2$, $C1$, $C2$, $C3$

Gain in strength of RCC beam may be represented as: $S3 > S2 > C2 > C3 > B > C1$.

Variation of Load and Deflection of Beam With Thickness of CFRP
The thickness of CFRP has also been changed and the variation in loading capacity and reduction in deflection has been observed. The ultimate loading capacity of the beam increases significantly as the thickness of the CFRP increases (Fig. 14). The deflection of the beam reduces if the thickness is increased. Though the reduction is greater initially, the rate of reduction in deflection decreases after 2.4 mm (Figs. 15, 16, and 17). The slope of the graphs decreases with an increase in thickness, which signifies that the rate of reduction decreases.

Validation of FEM Model Using Artificial Neural Network
FEM data obtained from Abaqus was trained with the deep neural network (DNN) model, to learn the constitutive law of the carbon fibre-reinforced composite. DNN learns the constitutive law in a form-free manner. The learned result automatically satisfies the equilibrium and kinematics equations, which avoids inaccuracies associated with the presumed functions in the constitutive laws. All the models were trained for different combinations of CFRP wrapping in Python (using Keras) and MATLAB. The dataset consists of one feature, i.e. load or pressure, and one target variable, i.e. displacement. The splitting of dataset has been done into training (70%), testing (20%) and validation (10%) using train_test_split () function from sklearn. Training
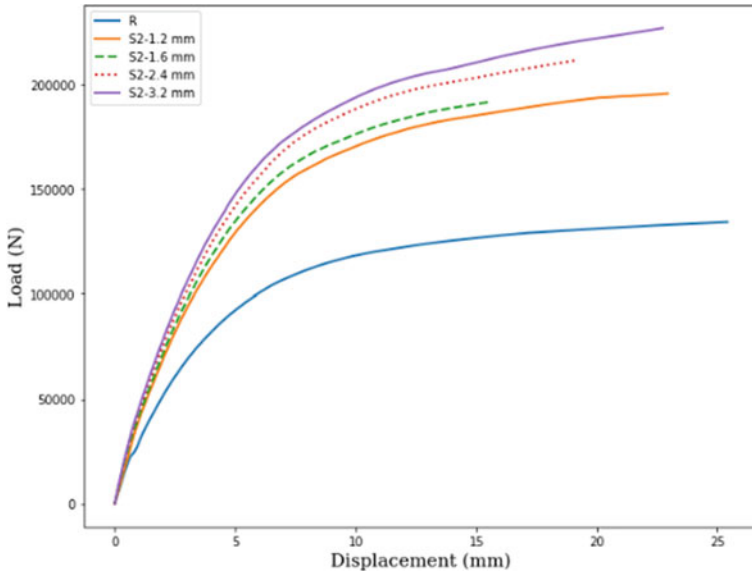
Fig. 14 Load–displacement curve of *S*2 for different thickness of CFRP
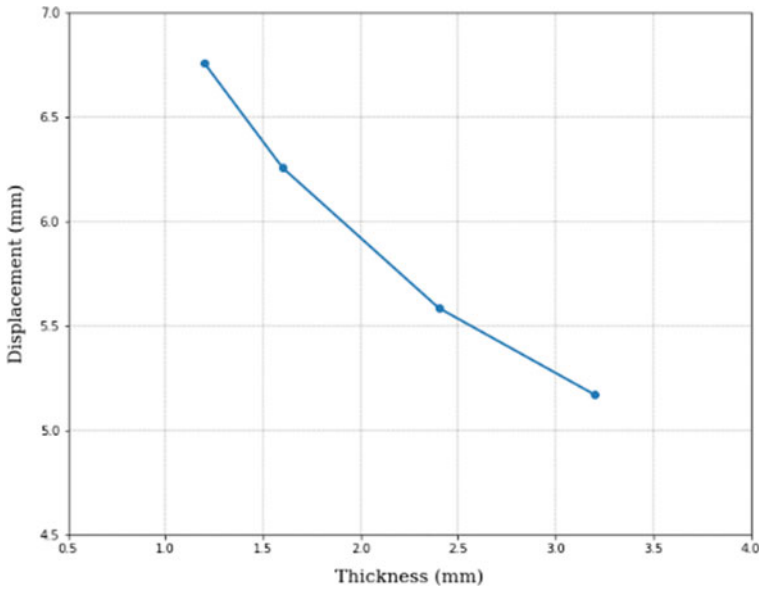
Fig. 15 Thickness (CFRP)–displacement graph for *S*2 model at 150 kN load
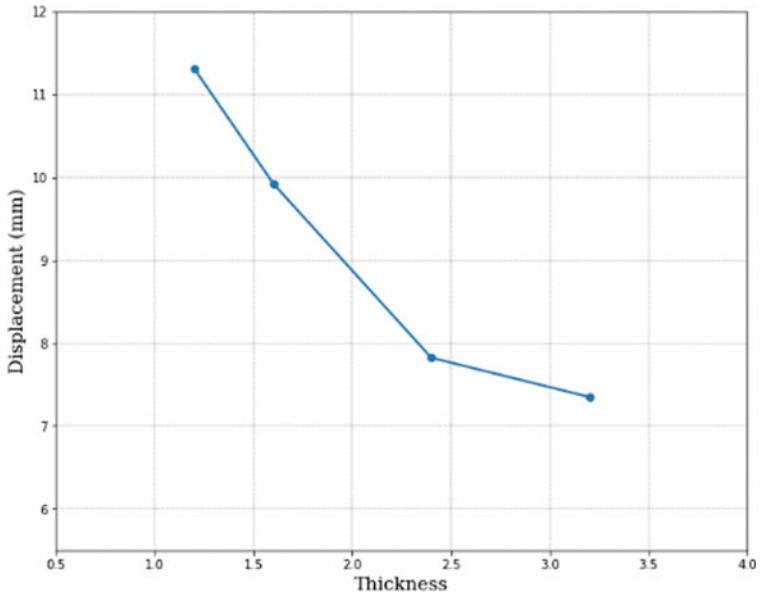
Fig. 16 Thickness (CFRP)–displacement graph for $S2$ model at 175 kN load
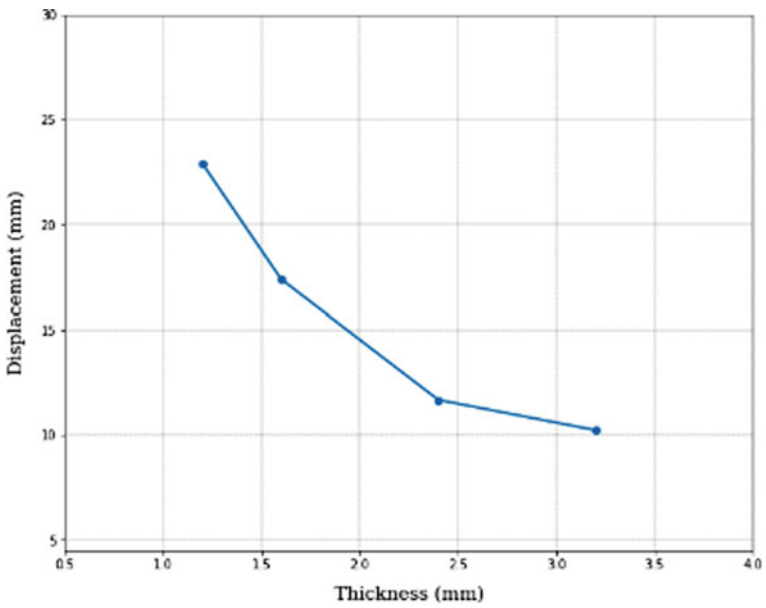
Fig. 17 Thickness (CFRP)–displacement graph for $S2$ model at 195 kN load

Fig. 18 ANN architecture

Input Layer

Hidden Layer

Hidden Layer

Output Layer
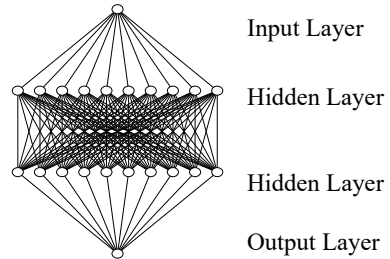
of the neural network with different hyper-parameters has shown that the best activation function is "tanh" and the best optimization function is Adam. Two hidden layers were used with 10 and 20 nodes. The model architecture is given in Fig. 18. The input node consists of one node (since the dataset has one feature), then there are two hidden layers of 10 neurons followed by one output node. In MATLAB, two different neural network models have been used, cascade forward back-propagation (CFB) and Elman back-propagation (EB). The difference in displacement values for FEM and both the ANN models have been calculated (Tables 4, 5) and the values have been plotted (Figs. 19, 20, 21, 22, 23 and 24) to get an idea of the variations from FEM model.

The average R-square value for ANN is 0.99. There is a strong correlation between the two results. With an error rate of less than 1% on average, ANN's predictions reveal a very low and acceptable level of precision in prediction. Moreover, the plots also show that predicted values follow a nonlinear trend (Figs. 21, 22, 23, and 24). Most of the predicted values are in agreement with the Abaqus data.

Table 4 Relative error of ANN model (load-Δ) for $C1$

$C1$	FEM	ANN		% Error	
Load (N)	Δ (mm)	CFBΔ (mm)	EB Δ (mm)	CFB	EB
0	0.00	0.02	0.04	–	–
12,500	0.26	0.25	0.23	0.36	9.81
25,000	0.55	0.55	0.56	0.12	1.55
50,781	1.38	1.38	1.39	0.07	0.20
60,290	1.73	1.73	1.73	0.34	0.18
75,276	2.31	2.31	2.31	0.02	0.20
100,364	3.60	3.64	3.61	1.30	0.28
120,013	5.08	5.08	5.09	0.02	0.26
125,000	5.58	5.54	5.49	0.69	1.51

Table 5 Relative error of ANN model (pressure-Δ) for $C1$

C1	FEM	ANN		% Error	
Pressure (MPa)	Δ (mm)	CFB Δ (mm)	EB Δ (mm)	CFB	EB
0.00	0.00	0.00	0.01	-	-
0.20	0.27	0.27	0.27	0.00	0.48
0.63	0.95	0.95	0.95	0.01	0.18
1.01	1.77	1.77	1.77	0.00	0.03
1.41	2.82	2.81	2.83	0.24	0.41
1.61	4.51	4.51	4.48	0.02	0.65
1.72	7.66	7.66	7.64	0.00	0.18
1.80	11.86	11.82	11.83	0.30	0.26
1.90	21.82	21.80	21.87	0.11	0.21
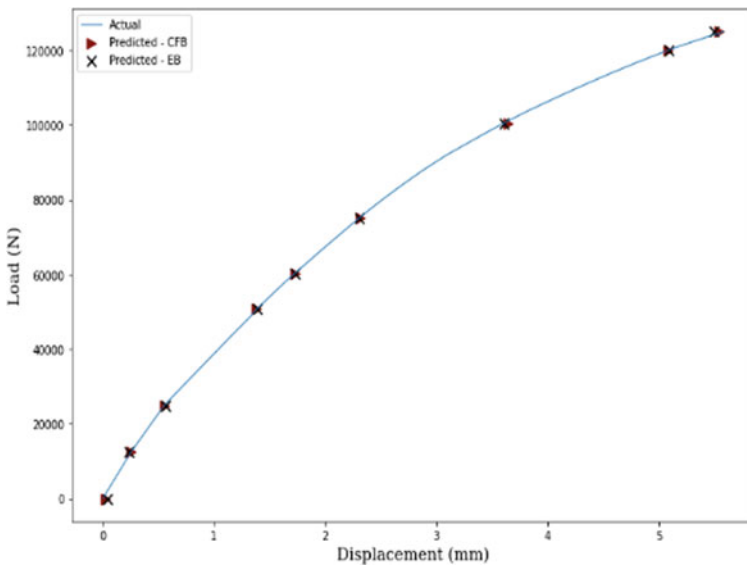
Fig. 19 Actual versus predicted load–displacement curve for $C1$

4 Conclusion

- Under concentrated loading, 48% and 45% reductions in displacement over the control RC beam have been found for CFRP wrapped on three sides ($S3$) and CFRP wrapped on both faces ($S2$), respectively.
- In the case of the RC beam under concentrated load, CFRP of length $L/2$ wrapped on both sides at mid-span ($C1$) has shown to be one of the most effective and
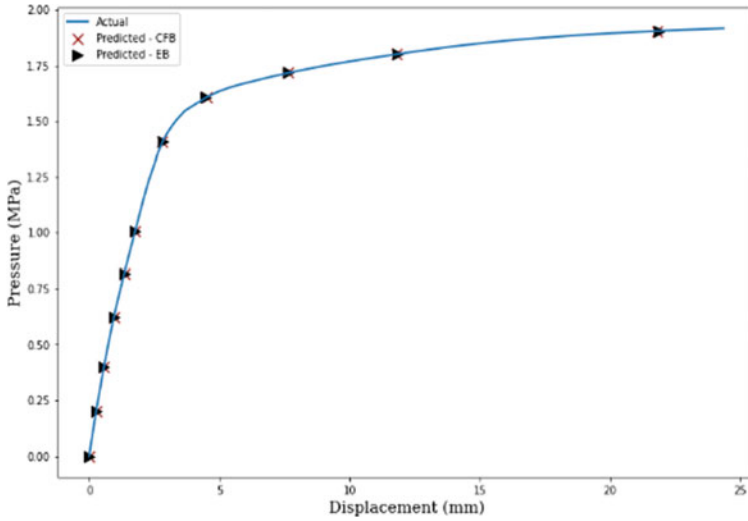
Fig. 20 Actual versus predicted pressure–displacement curve for $C1$
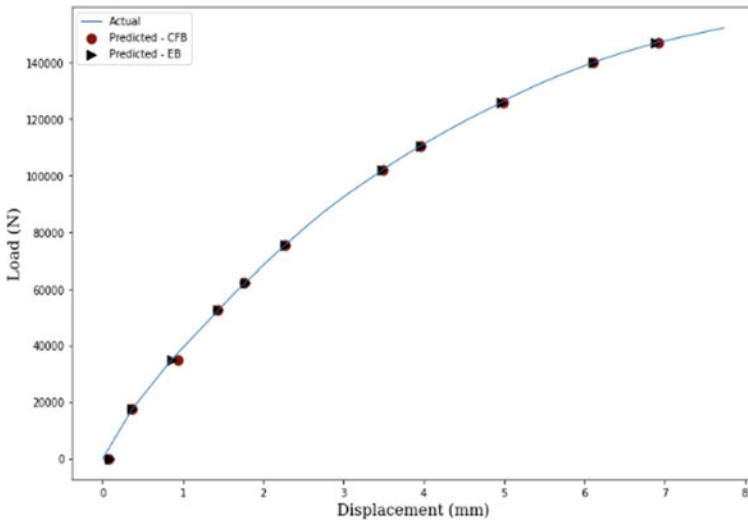
Fig. 21 Actual versus predicted load–displacement curve for $S2$

economical means of wrapping since the increase in deflection was only 7.2% compared to S2 (fully wrapped on both faces).

- Under pressure loading, it has been observed that $S3$ and $S2$ perform best, with a reduction in the displacement of 63.1% and 59.7% over the control beam, respectively. Apart from full-length wraps, $C2$ (wrapped $L/4$ at edges on both sides of
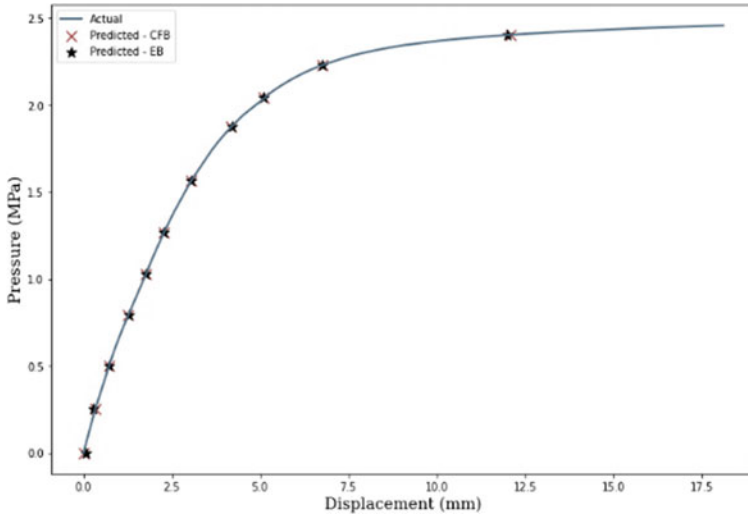
Fig. 22 Actual versus predicted pressure–displacement curve for $S2$
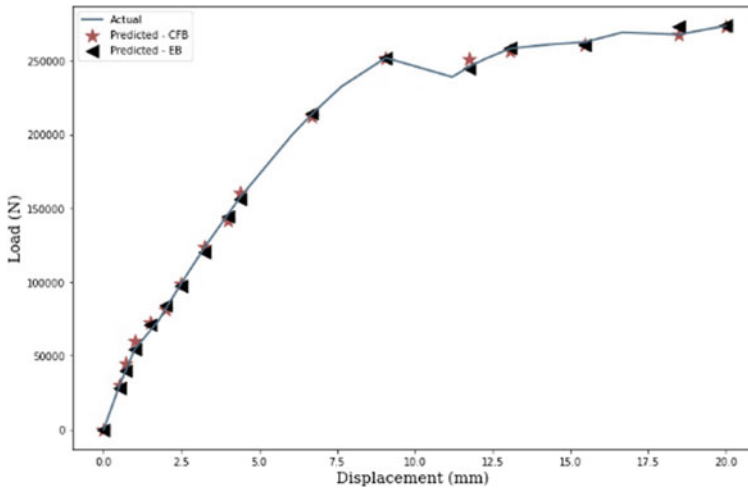
Fig. 23 Actual versus predicted of ultimate load for RCC

the beam) and $C3$ (CFRP gap graded) produce better results, with a reduction of 58.5% and 55.5% over the control beam, respectively.

- With an increase in the thickness of CFRP, there is a considerable amount of reduction in the deflection of the beam, but the rate of reduction in deflection decreases after a certain point even if the thickness of CFRP is kept on increasing.
- It can be concluded that when the load is concentrated at the mid-span of a beam, then the most efficient way of strengthening is to wrap CFRP of length $L/2$ at the
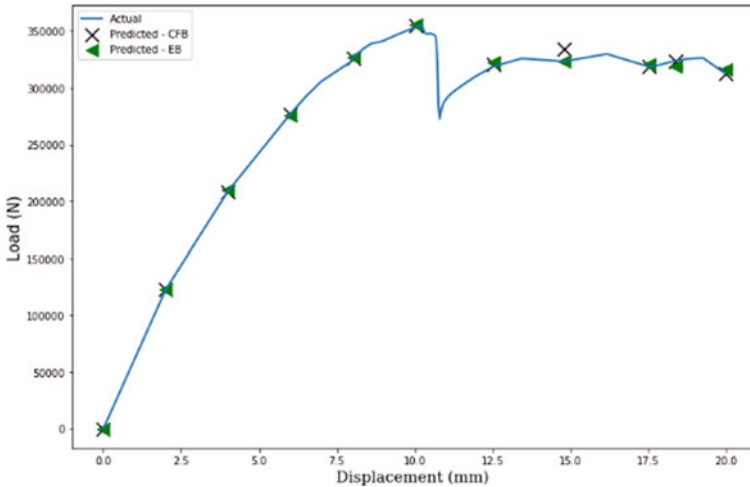
Fig. 24 Actual versus predicted ultimate load for *S*2

mid-span on opposite faces. But when the beam is under pressure load then CFRP of length *L*/4 wrapped near the ends is the most efficient way of strengthening.

- The ANN model predicts the nonlinearity of the models with very high accuracy. An average value of *R* score of 0.999 indicates that the two results are consistent. Both the ANN model could predict the ultimate load as well as unknown deflection with high accuracy.

References

1. Ritchie PA, Thomas DA, Lu L-W, Connelly GM (1988) External reinforcement of concrete beams using fiber reinforced plastic
2. Meier U (1992) Carbon fiber-reinforced polymers: modern materials in bridge engineering. Struct Eng Int 2:7–12
3. Arduini M, Nanni A (1997) Parametric study of beams with externally bonded FRP reinforcement. ACI Struct J 94:493–501
4. Hussain SM, Loganathan C, Arun AS An experimental investigation and finite element modeling of RCC columns confined with FRP sheets under axial compression.
5. El-Gamal SE, Al-Nuaimi A, Al-Saidy A, Al-Lawati A (2016) Efficiency of near surface mounted technique using fiber reinforced polymers for the flexural strengthening of RC beams. Construct Build Mater 118:52–62
6. Anil Ö, Kaya N, Arslan O (2013) Strengthening of one way RC slab with opening using CFRP strips. Constr Build Mater 48:883–893
7. Ceroni F (2010) Experimental performances of RC beams strengthened with FRP materials. Constr Build Mater 24:1547–1559
8. Naderpour H, Kheyroddin A, Amiri GG (2010) Prediction of FRP-confined compressive strength of concrete using artificial neural networks. Compos Struct 92:2817–2829

9. Ahmadi M, Naderpour H, Kheyroddin A (2014) Utilization of artificial neural networks to prediction of the capacity of CCFT short columns subject to short term axial load. Arch Civil Mech Eng 14:510–517
10. Khademi F, Akbari M, Nikoo M (2017) Displacement determination of concrete reinforcement building using data-driven models. Int J Sustain Built Environ 6:400–411
11. Kaczmarek M, Szymańska A (2016) Application of artificial neural networks to predict the deflections of reinforced concrete beams
12. Ya TT, Alebrahim R, Fitri N, Alebrahim, M (2019) Analysis of cantilever beam deflection under uniformly distributed load using artificial neural networks. In: MATEC Web of Conferences, 2019

A Critical Review of Utilization of Sugarcane Bagasse Ash in Concrete as Partial Replacement to Cement

Debadrita Das, T. Jothi Saravanan, K. I. Syed Ahmed Kabeer, and Kunal Bisht

1 Introduction

Concrete is the most essential building material used throughout the world in large quantities. Cement is the major component of concrete and world-wide requirement of cement is approximately 4.0 billion tons per year and increases every year [1]. Manufacturing process of cement is a high contributor to the release of CO_2 and global climate change. The manufacture of one ton of ordinary Portland cement (OPC) produces around 0.9 ton of CO_2 [2]. To resolve this, industrial and agricultural wastes can be focused upon to replace cement [3]. Pozzolanic materials improve the inherent properties of concrete when incorporated in them. Because of the pozzolanic interaction with $Ca(OH)_2$ created during hydration of cement, adding these has a beneficial impact on the mechanical and durability qualities of concrete [4, 5].

India is among the world's major sugarcane growers, with a production of 30.2 million tons in the year 2020–21 which lead to the generation of large quantities of sugarcane bagasse ash (SBA). SBA is the residue produced from the combustion of sugarcane waste which in most cases is dumped in landfills [1]. The utilization of SBA is very minimal compared to its increasing production which makes it an easily available pozzolan. Its usage as a partial alternative of cement in concrete or mortar will decrease the amount of waste that goes into landfills while also preserving resources and lowering carbon emissions. Hence, this paper discusses the gainful

D. Das (✉) · T. J. Saravanan
School of Infrastructure, Indian Institute of Technology Bhubaneswar, Bhubaneswar, India
e-mail: dd15@iitbbs.ac.in

K. I. S. A. Kabeer
School of Architecture and Interior Design, SRM Institute of Science and Technology, Kattankulathur, India

K. Bisht
Department of Civil Engineering, KIET Group of Institutions, Delhi NCR, Ghaziabad, India

667

SBA usage in concrete as a partial replacement for cement, highlighting its hydration characteristics along with its impact on various concrete parameters.

2   Review Methodology

The purpose of the study was to get a thorough and comprehensive knowledge of the use of BA as a partial replacement for cement in concrete. The existing literature in the field of interest was first gathered, followed by filtering, and was ultimately assessed. Reliable publications in peer-reviewed journals from search engines using different keywords were collected. A detailed evaluation of the acquired material was done, and the article's objectives were set based on the findings and comprehension of the data received. A detailed comparative analysis was performed to report about the comprehensive study of the properties and tests done in this research topic. The article was prepared by integrating the qualitative and quantitative data obtained from the understanding of the literature. The mix designs of the reviewed papers is presented in Table 1.

3   Chemical Composition and Microstructure

SBA has an appreciable pozzolanic response, according to several researches, and may be used as a replacement to cement in concrete. On studying the oxide composition of OPC and SBA it is seen that silicon dioxide (SiO_2) constitutes majority of bagasse ash's chemical makeup which is three times that of OPC. The high silicon dioxide content covers amorphous and crystalline silica from SBA and some sand contamination.

Apart from silica, the other constituent oxides of SBA are of aluminium, iron and calcium. For usage as a supplement for cementitious material, ASTM C618 [17] mentions that at least 70% of the ash to be made up of SiO_2, Al_2O_3 and Fe_2O_3. It has been observed in almost all the studies that the sum of sulphur dioxide, aluminium and iron oxides is above 70% making it a good pozzolanic material. Also, the content of oxide essential for pozzolanic reaction is high is ground SBA as compared to ordinary SBA irrespective of the LOI. The LOI values of concrete with GBA substitution increased with increase in percentage of replacement. Despite them exceeding the 10% weight limit [17] (LOI < 10%), SBA might be used in concrete as an OPC replacement [8]. The oxide compositions of the SBA and cement have been tabulated in Table 2.

The unprocessed SBA particles are flaky, large and irregularly sized while grinding improves the fineness and decreases the porosity of the particles. Ordinary SBA was found to have lower specific gravity than grounded SBA due to the reduction of porosity of SBA after grinding [13].

Table 1 Mix proportions of the concrete mixes used in the various studies reviewed here. [1, 4, 6–16]

Mix Design	W/B ratio	Cement	Bagasse ash	Fine aggregates	Fly ash	Micro Silica	Coarse aggregate	Super plasticizer content (%)
Rukzon and Chindaprasirt [9]								
CT	0.3	560	–	710			924	7.5
10BA	0.3	504	56	717			896	6
20BA	0.3	448	112	711			888	10
30BA	0.3	392	168	708			885	19.5
Rerkpiboon et al. [10]								
CT	0.45	450	0	750			955	0
BA10	0.45	405	45	740			945	1.8
BA20	0.45	360	90	735			935	3.15
BA30	0.45	315	135	730			925	4.5
BA40	0.45	270	180	720			915	6.3
BA50	0.45	225	225	710			905	9
Gar et al. [9]								
CC		365	–	740	–		1110	–
SBA5		330	36	740	–		1110	–
SBA10		292	73	740	–		1110	–
SBA15		255	110	740	–		1110	–
SBA20		220	146	740	–		1110	–
SBA25		183	183	740	–		1110	–
Somna et al. [12]								
CON	0.45	424	–	767			–	–
RB00	0.45	424	–	733			936	–
RB20	0.45	339	85	719			922	2.5
RB35	0.45	276	148	708			908	4.6
RB50	0.45	212	212	697			893	8.5
Montakarntiwong et al. [13]								
CON	0.5	350	–	808			1049	1.7
OBL-20	0.5	280	70	798			1035	2.1
OBL-30	0.5	245	105	791			1027	4
OBL-40	0.5	210	140	783			1024	4.5
GBL-20	0.5	280	70	801			1041	1.8
GBL-30	0.5	245	105	785			1019	2.1
GBL-40	0.5	210	140	768			997	2.5

(continued)

Table 1 (continued)

Mix Design	W/B ratio	Cement	Bagasse ash	Fine aggregates	Fly ash	Micro Silica	Coarse aggregate	Super plasticizer content (%)
GBH-20	0.5	280	70	798			1035	1.7
GBH-30	0.5	245	105	791			1027	2.5
GBH-40	0.5	210	140	783			1024	4.4
Rajashekar et al. [4]								
CM	0.18	1	0					
BA50	0.18	0.95	0.05					
BA10	0.18	0.9	0.1					
BA15	0.18	0.85	0.15					
BA20	0.18	0.8	0.2					
Ríos-Parada et al. [14]								
C		410	–	727	–		1015	2.7
*T*0		328	–	727	82		1015	1.6
*T*1		287	41	727	82		1015	3.1
*T*2		246	82	727	82		1015	4.9
Ganesan et al. [15]								
*B*0	0.53	383	0	575			1150	
*B*1	0.53	364	19	575			1150	
*B*2	0.53	345	388	575			1150	
*B*3	0.53	326	57	575			1150	
*B*4	0.53	306	77	575			1150	
*B*5	0.53	287	96	575			1150	
*B*6	0.53	268	115	575			1150	
Zareei et al. [16]								
OCBA								
CTL	0.4	400	0	760		10	900	15
OCBA5	0.4	380	5	760		10	900	15
OBBA10	0.4	360	10	760		10	900	15
OCBA15	0.4	340	15	760		10	900	15
OCBA20	0.4	320	20	760		10	900	15
OCBA25	0.4	300	25	760		10	900	15
LWCBA							Pumice	
CTL	0.4	450	0	500		10	360	15
LWCBA5	0.4	428	5	500		10	360	15

Table 1 (continued)

Mix Design	W/B ratio	Cement	Bagasse ash	Fine aggregates	Fly ash	Micro Silica	Coarse aggregate	Super plasticizer content (%)
LWCBA10	0.4	405	10	500		10	360	15
LWCBA15	0.4	383	15	500		10	360	15
LWCBA20	0.4	360	20	500		10	360	15
LWCBA25	0.4	338	25	500		10	360	15
Praveenkumar et al. [6]								
P1		200	0	600				
P2		190	10	600				
P3		180	20	600				
P4		170	30	600				
P5		160	40	600				
P6		150	50	600				
P7		140	60	600				
Cordeiro et al. [22]								
CC-REF		366	–	–	725		1001	–
CC-SCBA20%		293	73	–	724		1001	–
CC-RHA20%		293	–	73	724		1001	0.54
CC-TER		220	73	73	724		1001	–
HS-REF		478	–	–	860		905	1.4
HS-SCBA20%		382	96	–	860		906	1.23
HS-RHA20%		382	–	96	858		903	2.39
HS-TER		287	96	96	859		904	1.91
Chindaprasirt et al. [1]								
0.4CT		500	0	670	0		961	0.7
0.4BA50		250	250	600	0		950	2.5
0.4BA60		200	300	590	0		944	3
0.4BA70		150	350	578	0		940	4.1
0.4BA50FA10		200	250	590	50		950	2.3
0.4BA60FA10		150	300	580	50		944	2.8
0.4BA50FA20		150	250	585	100		945	2.6
CT	0.45	400	0	880			920	2.4
Klathae et al. [8]								
10BA50	0.45	200	200	845			885	4.4
10BA65	0.45	140	260	835			875	6

(continued)

Table 1 (continued)

Mix Design	W/B ratio	Cement	Bagasse ash	Fine aggregates	Fly ash	Micro Silica	Coarse aggregate	Super plasticizer content (%)
10BA80	0.45	80	320	830			865	8.4
15BA50	0.45	200	200	845			885	6.3
15BA65	0.45	140	260	835			875	7.5
15BA80	0.45	80	320	830			865	9.3
20BA50	0.45	200	200	845			885	7.4
20BA65	0.45	140	260	835			875	8.7
20BA80	0.45	80	320	830			865	10.4

The energy-dispersive X-ray spectroscopy (EDX) spectrum of SBA shows that silicon is present as a primary compound and other metal ions like aluminum, calcium, iron, magnesium and potassium are also present [4]. The wide scattering peaks (hump) noted in the X-Ray diffraction pattern of SBA are indicative of the presence of amorphous silica which is an effective pozzolanic material with favorable thermal properties [11]. High amount of quartz is shown as well in the XRD and it is due to the presence of sand adhered to the sugarcane. The qualitative analysis using XRD for microstructure of cementitious pastes showed an increase in the intensity of C–S–H peak and a decrease in the intensity of C–H peak indicating the occurrence of pozzolanic reaction (crystallization of CSH, consumption of CH) after 28 days on inclusion of SBA [14] (Fig. 1).

4 Properties of Concrete Containing Bagasse Ash

4.1 Workability

The fresh characteristics of concrete are affected by the physical properties of SBA particles incorporated. Somna et al., Rerkpiboon et al., Montakarntiwong et al., and Klathae et al. [8, 10, 12, 13] reported an increase in the amount of plasticizer needed to keep up the workability with increase in the percentage replacement of SBA. They have explained that irregular shape, rough surface and high porosity of the ground SBA particles was responsible for the reduced flow value.

Montakarntiwong et al. [13] used grounded SBA and ordinary SBA with two different LOI and observed that the plasticizer content required for ground SBA was lesser because it had lower porosity when compared to ordinary SBA. SBA with higher LOI needed a higher plasticizer when compared to SBA with lesser LOI. This is because the higher LOI makes the particles more porous leading to higher absorption of water into particles. Similarly Klathae et al. results also were in line

Table 2 Oxide compositions of SBA and cement used in the various studies reviewed here [1, 4, 6, 8–13, 15, 16, 18]

	References	SiO$_2$ (%)	Al$_2$O$_3$ (%)	Fe$_2$O$_3$ (%)	CaO (%)	MgO (%)	K$_2$O (%)	SO$_3$ (%)	LOI (%)	SiO$_2$ + Al$_2$O$_3$ + Fe$_2$O$_3$ (%)
Cement	Ganesan et al. [15]	19.25	5.04	3.16	63.61	4.56	0.51		3.12	27.45
	Rukzon and Chindaprasirt [9]	25.1	5.5	5.9	55	3.4	0.5	2.7	0.9	36.5
	Somma et al. [12]	20.9	4.8	3.4	65.4	1.3	0.4	2.7	1	29.1
	Montakarntiwong et al. [13]	20.9	4.7	3.4	65.4	1.2	–	2.7	0.9	29
	Corderio et al. [22]	20.9	4.2	5.3	63.5		0.4	2.4	1.1	30.4
	Rerkpiboon et al. [10]	20.8	5.5	3.16	64.97	1.06	0.55	2.96	2.89	29.46
	Parada et al. [14]	20.67	4.87	3.57	60.3	1.5	0.85	4.95	8.4	29.11
	Rajasekar et al. [4]	25	4	0.6	63	4	1.3	2.1	2.5	29.6
	Zareei et al. [16]	21.5	6	2.5	66.1	2	0.6			30
	Chindaprasirt et al. [1]	20.6	4.8	3.2	63.6	1.1	0.8	2.7	2.1	28.6
	Praveenkumar et al. [6]	17.99	2.64	4.03	70.93	0.85	1.52		0.8	24.66
	Klathae et al. [8]	20.5	4.7	3.3	64.2	1.3	0.3	2.7	2.8	28.5
	Ganesan et al. [15]	64.15	9.05	5.52	8.14	2.85	1.35		4.9	78.72
Grounded Bagasse Ash	Rukzon and Chindaprasirt [9]	65	4.8	0.9	3.9	–	2	0.9	10.5	70.7
	Somma et al. [12]	55	5.1	4.1	11	0.9	1.2	2.2	19.6	64.2

(continued)

Table 2 (continued)

References	SiO$_2$ (%)	Al$_2$O$_3$ (%)	Fe$_2$O$_3$ (%)	CaO (%)	MgO (%)	K$_2$O (%)	SO$_3$ (%)	LOI (%)	SiO$_2$ + Al$_2$O$_3$ + Fe$_2$O$_3$ (%)
Montakarntiwong et al. [13]	76.8	4.4	8	5.4	0.9	–	0.1	3.3	89.2
Montakarntiwong et al. [13]	67.1	5.7	2.5	2.9	0.5	–	0	20.4	75.3
Corderio et al. [22]	78.3	8.9	3.6	2.2		3.5		0.4	90.8
Rerkpiboon et al. [10]	55.04	5.14	4.06	11.03	0.91	1.22	2.16	19.6	64.24
Setayesh Gar et al. [9]	69.94	3.34	1.25	2.27	6.68	5.83	0.42	2.35	74.53
Parada et al. [14]	66.12	15	7.16	2.57	1.19	3.52	0.26	9	88.28
Rajasekar et al. [4]	86.79	2.45	1.75	3.42	1.46	3.83	0.3	7	90.99
Zareei et al. [16]	64.233	9.08	5.47	8.17	2.97	1.32			78.78
Praveenkumar et al. [6]	55.49	4.92	8.29	8.74	7.96	8.3		5.4	68.7
Chindaprasirt et al. [1]	65.1	8.2	3.2	6.5	2.1	2.4	2.1	12.1	76.5
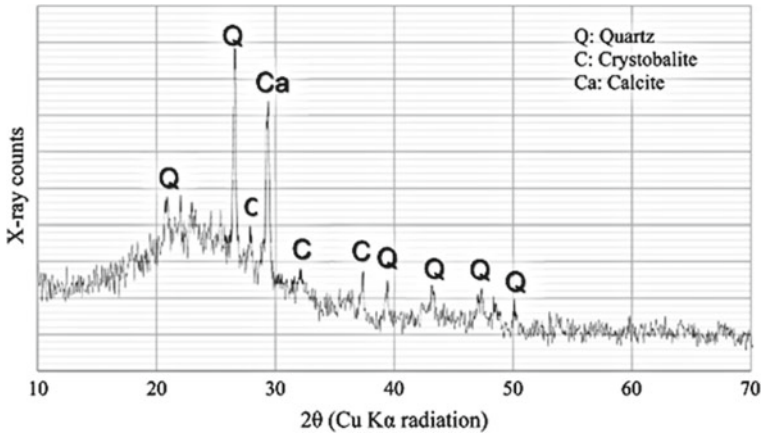
Fig. 1 X-ray diffraction pattern of SBA sample [16]

with the results shown by Montakarntiwong et al. [8, 13]. Klathae et al. also stated that the ternary blend required less super plasticizer due to the additional fly ash which increases the spherical particles in the cement thereby increasing the fluidity and workability [8].

Contrastingly Rajashekar et al., Zareei et al. and Praveenkumar et al. reported that with a rise in the amount of BA incorporated, there was an increase in the workability/ slump value/ flow value of concrete formed for which the fineness of BA particles could be a plausible reason [4, 16, 19].

4.2 Hardened Properties

The porosity of the concrete was reported to rise with increase in the percentage of SBA incorporated. This was ascribed to the effect of pore refinement and the fact that SBA particles have non-uniform shape and are porous [1, 9]. When equal amount of cement was substituted from the mix, the porosity of concrete with ternary mix with fly ash (FA) was lower than when only SBA was incorporated, as FA particles are spherical in shape and possess a smooth surface.

As the ground SBA with high LOI possesses larger porosities, the drying shrinkage of concrete incorporated with high volume ground SBA rose with the increase of LOI. Incorporation of high volume ground SBA of any LOI in concrete improved its drying shrinkage as compared to that of control mix [8].

4.3 Mechanical Properties

4.3.1   Flexural and Tensile Strengths

Setayesh Gar et al. [9] stated that the highest flexural strength is that of control mixture at room temperature. As replacement and temperature increased the flexural strength decreased. Least flexural strength was observed at 25% replacement, 400 degrees elevated temperature (Fig. 2).

According to Zareei et al. [13] with an increase in the percentage of SBA replacement the tensile strength decreased. For lightweight concrete with SBA replacement the strength remained constant for 5% replacement and decreased for 10%, 15% and 20% and there was a 2% increase for 25% replacement. The maximum reduction occurred for ordinary concrete with SBA replacement of 25%. The tensile strength to compressive strength ratio rose marginally by incorporating 50 to 65% of SBA as cement replacement in concrete [7]. Because of the poor compressive strength of SBA incorporated concretes, replacing OPC with 80 weight % of SBA of binder gave a large ratio of tensile strength to compressive strength. The tensile strength of concrete was unaffected by the various LOIs of SBA and by the use of large volume BA with and without FA in the binder [1] (Fig. 3).
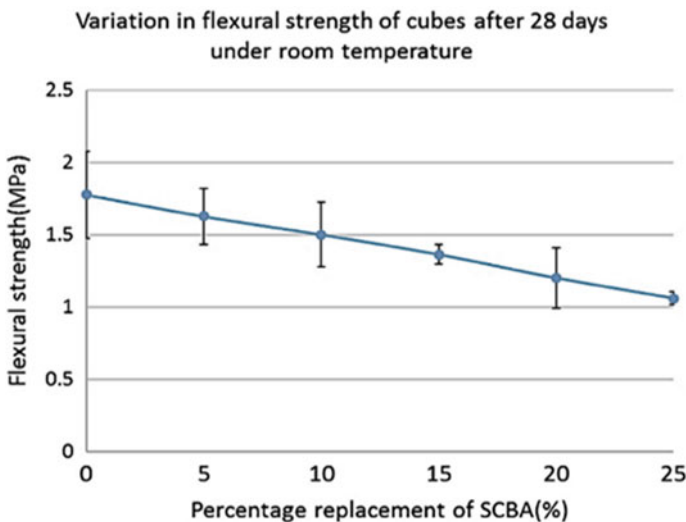
Fig. 2 Variation of flexural strength with increase in SBA [11]
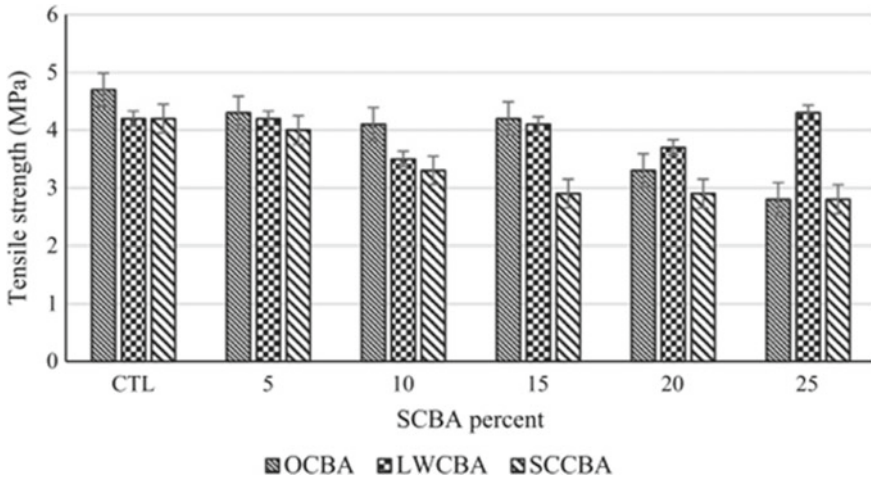
Fig. 3 Variation of split tensile strength with increase in SBA [16]

4.3.2 Compressive Strength

The 28-day normalized compressive strength of concrete from the various studies have been displayed in Fig. 1. The compressive strength typically manifested a decreasing trend as the replacement ratio of SBA increased. The cement concentration in the mixture dropped as replacement increased, resulting in a reduction in $Ca(OH)_2$ from the hydration process. As a result, the amount of $Ca(OH)_2$ required for the pozzolanic reaction was insufficient, resulting in poor compressive strength. However, there were notable outliers in several experiments where the replacement amount was 10%–20%, that generated the strongest hardened mixes [4, 9, 15, 16]. The abundant silica content, fineness, amorphous phase, high surface area, responsiveness of SBA, and pozzolanic interaction between calcium hydroxide and silica present in SBA may all contribute to the improvement in compressive strength of concrete up to 20% SBA substitution. Chindaprasirt and Rerkpiboon et al. reported that 10–30% of BSA produced concretes with compressive strengths higher than that of control mix [12, 17]. Low early age strength and later age strength development was observed in concrete with SBA incorporated. Somna et al. used recycled aggregates which resulted in lower compressive strength irrespective of the SBA incorporation [11].

Montakarntiwong et al. reported that the compressive strength increased with increase in grounding of SBA. Ground SBA with high LOI considerably decreases the compressive strength of concrete when compared to ground SBA with low LOI [8]. Heat treatment shows higher compressive strength than normal and steam curing. It might be due to the formation of long CSH chains during heat curing. This in turn was due to SBA pozzolanic activity and the development of hydration products [4]. Replacement of cement with FA gave higher values of compressive strength,
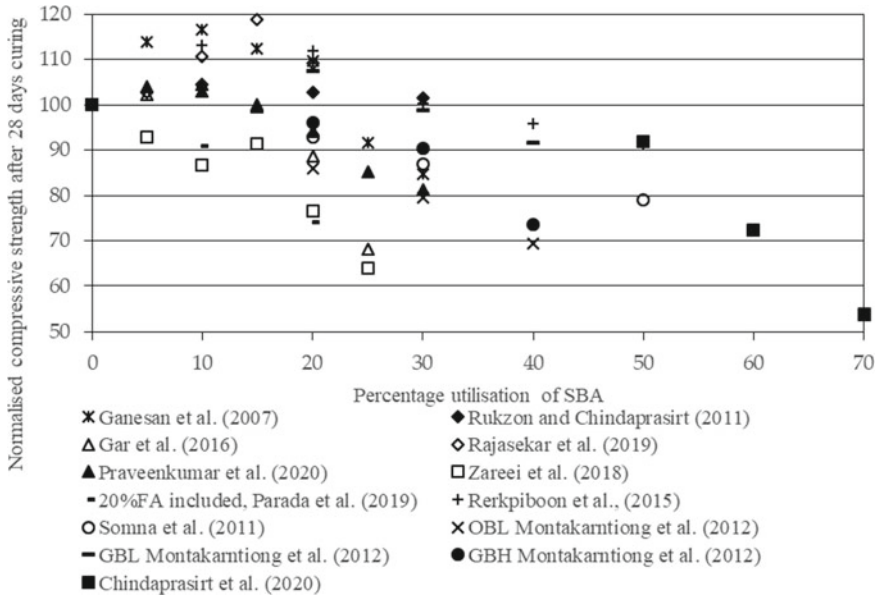
Fig. 4 Impact of BA replacement percentage on the 28-day normalized compressive strength of concrete [1, 4, 8–13, 15, 18, 19]. *Note:* GBL – Ground BA with low LOI; OBL – Ordinary BA with low LOI; GBH – Ground BA with high LOI.

yet further replacement of SBA after replacing with FA reduced the compressive strength values due to the presence of lower amount of SiO_2 in SBA when compared to FA. When both FA and SBA were used as replacement, for the same amount of replacement, mix replaced with higher FA gave better values than the ones replaced with higher SBA [1] (Fig. 4).

4.4 Durability Properties

4.4.1 Water Absorption

Ganesan et al. [15] and Zareei et al. [16] reported that the percentage of water absorption increased with increasing BA content at 28 days curing. This is because of the finer nature of SBA and the fact that it is hygroscopic in nature, whereas it decreased significantly after 90 days curing, due to the progressive closing of pores. Similarly, Somna et al. [12] stated that due to the embedded mortar on the face of recycled aggregate that acts as a conduit for water moving through, the water permeability coefficient of natural aggregate concrete is lesser than that of recycled aggregate concrete without SBA. Contrastingly Praveenkumar et al. [6] stated that there was a decrease in the coefficient of water permeability with increase

in replacement as the particles of SBA acted as a filler material and occupied the voids causing reduction in water permeability.

According to Ganesan et al. [15] with increasing SBA concentration, sorptivity diminishes, and it is only at 30% SBA that there is a considerable rise. The levels are similarly lower after 90 days of curing, showing that prolonged curing up to 90 days might be advantageous in this regard. Similarly, Rajasekar et al. [4] reported that as per ASTM C1585-13 the rate of water absorption was determined by performing sorptivity test. As replacement of bagasse ash was increased, decrease in sorptivity was observed. The minimum sorptivity was obtained 1.74 mm/s$^{1/2}$ which was equal for normal, heat and steam curing with 20% replacement of bagasse ash at the age of 28 days. These results show that sorptivity decreased by incorporation of fine particles and made the concrete highly impermeable.

4.4.2   Rapid Chloride Ion Penetration

SBA incorporation was specifically extremely beneficial in reducing chloride penetrability. According to Ganesan et al. [15], Rukzon and Chindaprasirt [9], Rerkpiboon et al. [10], Rajashekar et al. [4] and Chindaprasirt et al. [1] with increasing replacement, the charge flowing through SBA mixed concrete specimens continues to decrease. When 15% to 50% of SBA is used to replace OPC, the resultant concrete has very low chloride ion penetrability (100–1000 coulombs). The pozzolanic reaction of the components in bagasse ash improved the chloride resistance of concrete. This was due to the fact that concrete containing SBA had a higher concentration of hydration products, which allowed the increased surface area of reaction products to adsorb a greater quantity of chloride. The charge transmitted by the ternary blend mix was lower than that of the binary blend mix at the same high level of replacement. The synergistic impact of pozzolan minerals was responsible for the decreased permeability. Cordeiro et al. [22] reported that the usage of ultrafine SBA in the ordinary concrete decreases the electrical charge. Performance against chloride resistance was highest when heat curing was used and followed normal and steam curing. Because steam curing causes an irregular distribution of hydration products as well as a comparatively higher porous microstructure, greater chloride permeability is achieved [4].

4.5   Environmental and Economic Benefits

When SBA is used instead of cement, it lowers landfill trash, reduces cement consumption, and hence reduces CO_2 emissions. It encourages research into the use of alternative residual substances and the resolution of energy issues. Pozzolanic material is generally less expensive than OPC. SBA has a very low to nil cost, and even if the grinding process costs money, it is still less expensive than grinding cement clinker [13].

According to Klathae et al. [8] bagasse ash is harmful to the environment because it resembles dust, is light in weight, and easily scatters by wind. Using High Volume Ground SBA provides a number of advantages, including reduced disposal space, increased value, lower concrete production costs, and a suitable alternative for lowering CO_2 emissions owing to reduced cement use.

Chindaprasirt et al. [1] stated that concrete incorporating SBA or FA is a cost efficient and environmentally beneficial material. The addition of an adequate quantity of pozzolan to concrete increased its durability while also saving money. The results suggested that the incorporation of high-volume SBA with additional FA was more attractive in terms of economy and environment.

5   Conclusions

This paper examined the characteristics and potential functions of SBA in concrete:

- Incorporation of SBA increases the super plasticizer content required to keep up the workability.
- SCBA is a reactive pozzolan that may be used in a variety of cement-based products. A suitable dose (less than 20%) can significantly improve the strength metrics and reduce the cement usage. With increase in the LOI of SBA incorporated the compressive strength decreased.
- FA is more efficient in increasing the compressive strength than SCBA. At the same level of replacement ternary mixes have better compressive strength.
- Porosity and drying shrinkage increased with increase in replacement level.
- Usage of SBA resulted in increase in tensile to compressive strength ratios due to the drastic fall in compressive strength values on higher extent of incorporation.

The review concludes that SBA could be suitably used as a partial replacement for cement in various construction materials application upon appropriate grinding and with proper LOI. This could reduce the adverse environmental effects caused due to excessive cement usage and reduce the problems faced during the disposal of agricultural waste.

References

1. Chindaprasirt P, Kroehong W, Damrongwiriyanupap N, Suriyo W, Jaturapitakkul C (2020) Mechanical properties, chloride resistance and microstructure of Portland fly ash cement concrete containing high volume bagasse ash. J Build Eng 31:101415. https://doi.org/10.1016/j.jobe.2020.101415
2. Kore SD, Vyas AK, Kabeer KISA (2019) A brief review on sustainable utilisation of marble waste in concrete. Int J Sustain Eng 13:1–16. https://doi.org/10.1080/19397038.2019.1703151

3. Agrawal A, Saravanan TJ, Bisht K, Kabeer KISA (2021) Synthesis of cement composites utilizing ceramic waste as a partial replacement for Portland cement: literature review. J Hazard Toxic Radioact Waste 25:1–18. https://doi.org/10.1061/(ASCE)HZ.2153-5515.0000637

4. Rajasekar A, Arunachalam K, Kottaisamy M, Saraswathy V (2018) Durability characteristics of Ultra High Strength Concrete with treated sugarcane bagasse ash. Constr Build Mater 171:350–356. https://doi.org/10.1016/j.conbuildmat.2018.03.140

5. Rukzon S, Chindaprasirt P (2018) Strength, chloride penetration and corrosion resistance of ternary blends of Portland cement self-compacting concrete containing bagasse ash and rice husk-bark ash. Chiang Mai J Sci 45:1863–1874

6. Praveenkumar S, Sankarasubramanian G (2020) Synergic effect of sugarcane bagasse ash based cement on high performance concrete properties. Silicon. https://doi.org/10.1007/s12633-020-00832-4

7. Cordeiro GC, Filho RDT, Fairbairn EMR (2010) Ultrafine sugar cane bagasse ash: high potential pozzolanic material for tropical countries, IBRACON. Struct Mater 3:50–67

8. Klathae T, Tanawuttiphong N, Tangchirapat W, Chindaprasirt P, Sukontasukkul P, Jaturapitakkul C (2020) Heat evolution, strengths, and drying shrinkage of concrete containing high volume ground bagasse ash with different LOIs. Constr Build Mater 258:119443. https://doi.org/10.1016/j.conbuildmat.2020.119443

9. Rukzon S, Chindaprasirt P (2012) Utilization of bagasse ash in high-strength concrete. Mater Des 34:45–50. https://doi.org/10.1016/j.matdes.2011.07.045

10. Rerkpiboon A, Tangchirapat W, Jaturapitakkul C (2015) Strength, chloride resistance, and expansion of concretes containing ground bagasse ash. Constr Build Mater 101:983–989. https://doi.org/10.1016/j.conbuildmat.2015.10.140

11. Gar PS, Suresh N, Bindiganavile V (2017) Sugar cane bagasse ash as a pozzolanic admixture in concrete for resistance to sustained elevated temperatures. Constr Build Mater 153:929–936. https://doi.org/10.1016/j.conbuildmat.2017.07.107

12. Somna R, Jaturapitakkul C, Rattanachu P, Chalee W (2012) Effect of ground bagasse ash on mechanical and durability properties of recycled aggregate concrete. Mater Des 36:597–603. https://doi.org/10.1016/j.matdes.2011.11.065

13. Montakarntiwong K, Chusilp N, Tangchirapat W, Jaturapitakkul C (2013) Strength and heat evolution of concretes containing bagasse ash from thermal power plants in sugar industry. Mater Des 49:414–420. https://doi.org/10.1016/j.matdes.2013.01.031

14. Ríos-Parada V, Jiménez-Quero VG, Valdez-Tamez PL, Montes-García P (2017) Characterization and use of an untreated Mexican sugarcane bagasse ash as supplementary material for the preparation of ternary concretes. Constr Build Mater 157:83–95. https://doi.org/10.1016/j.conbuildmat.2017.09.060

15. Ganesan K, Rajagopal K, Thangavel K (2007) Evaluation of bagasse ash as supplementary cementitious material. Cem Concr Compos 29:515–524. https://doi.org/10.1016/j.cemconcomp.2007.03.001

16. Zareei SA, Ameri F, Bahrami N (2018) Microstructure, strength, and durability of eco-friendly concretes containing sugarcane bagasse ash. Constr Build Mater 184:258–268. https://doi.org/10.1016/j.conbuildmat.2018.06.153

17. ASTM C 618 (2019) Standard specification for coal fly ash and raw or calcined natural pozzolan for use in concrete. https://doi.org/10.1520/C0618-19.2

18. Cordeiro GC, Tavares LM, Toledo Filho RD (2016) Improved pozzolanic activity of sugar cane bagasse ash by selective grinding and classification. Cem Concr Res 89:269–275. https://doi.org/10.1016/j.cemconres.2016.08.020

19. Praveenkumar S, Sankarasubramanian G, Sindhu S (2020) Strength, permeability and microstructure characterization of pulverized bagasse ash in cement mortars. Constr Build Mater 238:117691. https://doi.org/10.1016/j.conbuildmat.2019.117691

20. Praveenkumar S, Sankarasubramanian G (2019) Mechanical and durability properties of bagasse ash-blended high-performance concrete. SN Appl Sci 1:1–7. https://doi.org/10.1007/s42452-019-1711-x

21. Chindaprasirt P, Sujumnongtokul P, Posi P (2019) Durability and mechanical properties of pavement concrete containing bagasse ash. Mater Today Proc 17:1612–1626. https://doi.org/10.1016/j.matpr.2019.06.191

22. Cordeiro GC, Toledo Filho RD, Tavares LM, Fairbairn EMR (2012) Experimental characterization of binary and ternary blended-cement concretes containing ultrafine residual rice husk and sugar cane bagasse ashes. Constr Build Mater 29:641–646. https://doi.org/10.1016/j.conbuildmat.2011.08.095

A Short Review of Innovation in Autonomous Car in Combination with Mechanical and Electronics

Sahil Negi, Kulwant Singh , and Anuj Kumar Sehgal

1 Introduction

Vehicles were previously thought to be the domain of mechanical engineers [1]. However, extraordinary advances in automotive and information technology have transformed a typical car from conventional transportation into a fully-fledged, intelligent, infotainment-rich computer machine on the go [2]. The features and qualities provided both high-tech communications and computer technology, as well as the proliferation of high-end vehicles, give groundwork for the implementation of smart vehicles. These vehicles have been dubbed "autonomous vehicles" [3]. An autonomous automobile is a computer-controlled vehicle capable of navigating, acquaint itself with its environment, make judgments, and function completely autonomously. The requirement for driver and driving safety, population expansion, growing infrastructure, an increased traffic, a requirement for the efficient administration of time, active utilization of sources, are key reasons behind the introduction of autonomous automobiles [4]. In today's scenario transport infrastructure is poor, whether it be roads or parking lots to petrol stations and charging stations. Governments have taken substantial steps to improve road safety in recent decades, in abundance that includes both stationary and flexible mechanics like closed circuit television cameras (CCTVs), street sensors, and more [5]. Linked automobiles and autonomous vehicles are alternative technologies that are being investigated for the elimination of human mistakes and life-threatening condition on the road [6]. The development and emergence of self-driving automobiles are the product of outstanding research findings from disciplines of radio intelligence, installed regularities, sensors, temporary web technology, distribution, and analysis of data. The

S. Negi · K. Singh (✉) · A. K. Sehgal
Department of Mechanical Engineering, University Institute of Engineering, Chandigarh University, Mohali, Punjab, India
e-mail: kskookna@gmail.com; kulwant.e11668@cumail.in

concept of self-driving automobiles began in the 1920s with "phantom autos," which were operated by a remote control unit [7]. The "Prometheus Project" was sponsored back in 1987 by Mercedes [8], clearing each significant success by the construction concerning the first robot vehicle for monitoring the traffic signals and additional carriers. Despite the fact, it was not entirely autonomous at the time but the capability to switch lanes autonomously was a significant development. The growing interest in self-driving automobiles in the twenty-first century has been spurred with less expensive technology, which works well in a variety of domains [9]. It is critical to distinguish between two opposing concepts: the automated automobile and a self-governing car [10]. The level of driving automation has been illustrated in Fig. 1. A general outlook of both terms conveys the idea of allowing these cars to be independent. The first, however, refers to a machine-controlled vehicle that may require human interference. Autonomous vehicles make use of the notion of linked automobile technologies [3]. The connected vehicle uses the technology of vehicular ad hoc (VANET) network, in which the onboard unit (OBU) is introduced. These automobiles are able to interact with one another only when available in the sphere of communication through the standard short-term communication protocol (DSRC) [11]. In contrast to Google, Microsoft has formed a partnership with Volvo and Toyota to create autonomous automobiles. NVidia has demonstrated great passion in self-driving vehicles. NVidia Drive PX2 has launched their flagship which is GPU-based a dominant processing program for self-driving vehicles [12]. Companies like Uber and Apple are also emerging players in the self-driving vehicle market. TATA, KIA, Nissan, and Hyundai are significant Asian businesses funding the scheme, production, and research of self-driving automobiles. Vehicle ownership has increased tremendously over the previous several decades as their costs have dropped; likewise, individuals pride automobiles further accessible as their earnings rise. However, this speed of car acquisition contributes to increased contamination and transportation obstruction [13].

In 2010 this globe was home to one billion automobiles, and the figure is predicted to double in 2030, necessitating a critical requirement for increased supplies and infrastructural assistance to accommodate this massive growth in the number of transportation [14]. Over 1.25 million people are losing their life every year in traffic accidents as reported by World Health Organization (WHO) [15], with the death
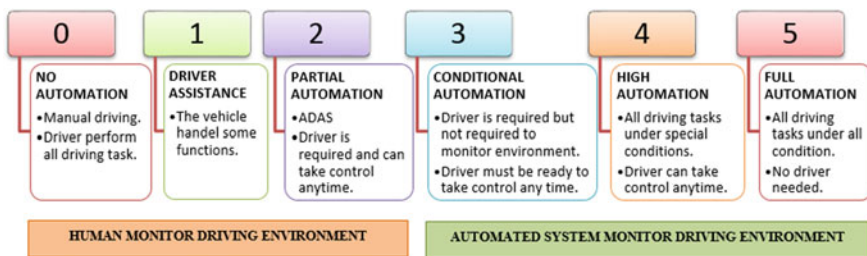

Fig. 1 Level of driving automation

toll expected to grow to 1.8 million by 2030 [14]. As a result, there is an urgent demand for a technologically sophisticated, completely automated, dependable, and safe mode of transportation, and the autonomous car sector has been working hard to achieve these expectations. After nearly five decades, the quality of the automatic transmission system had improved and the cost had been decreased to the point where it could be used in most vehicles [16]. The same logic applies to electric and hybrid cars [17]. In a word, owing of its initial high price and limited dependability, autonomous automobile technology will take time to become available and accessible to customers. However, vehicle makers must overcome these difficulties before autonomous cars can be successful and transform the automotive industry. In this paper, the recent developments in autonomous car technology are summarized and current concerns and challenges in development of autonomous vehicles has been reviewed.

2   The Autonomous Car

Driving an autonomous car needs support, mainly in the case of sudden vehicle action. Therefore, showing these findings and their predicted movements is very important to understand the situation [18]. The design of a standalone vehicle should take into account size, speed, character, heterogeneity, and real-time info environment [19]. Its deserving mentioning that various automakers use onboard sensors and controlling technology for a variety of optimal applications. However, the ability to function independently is a crucial necessity at the heart of autonomous automobile design [20]. In other words, the autonomous automobile must-have capabilities allow it to anticipate, determine, and maneuver safely and reliably following a plan. The key components of a high-performance autonomous vehicle system are shown in Fig. 2. The tiered structure comprises data collecting conducted with hardware parts such as sensors (in-car and onboard), radar (long-range and short-range), LIDAR, cameras, and transceivers [21]. The data obtained by those elements is analyzed by a central computer system of an independent vehicle, which is following used by the resolution guide operation. The autonomous car is activated by the decision support system [22]. This is important to note that condition awareness is achieved using both short and long-distance thinking systems such as detectors, LIDAR, and cameras. These regions comprised by these sections are shown in Fig. 3. Different levels of situational awareness are appropriate for different applications and have been attained through various components [3]. Infrared technologies, for example, avoid front and rear bumper collisions, while short-range radars give lane-change warning, short-distance object recognition, and construction of traffic viewing [23]. The self-driving car is also outfitted with several cameras to provide a 360° picture of its surroundings, as well as LIDAR for collision avoidance and emergency braking. Long-range radars enable cooperative cruise control and the building of long-range traffic views [24]. An autonomous automobile must go through a sequence of steps: the car must sense and become aware of its surroundings, plan a route, operate, also
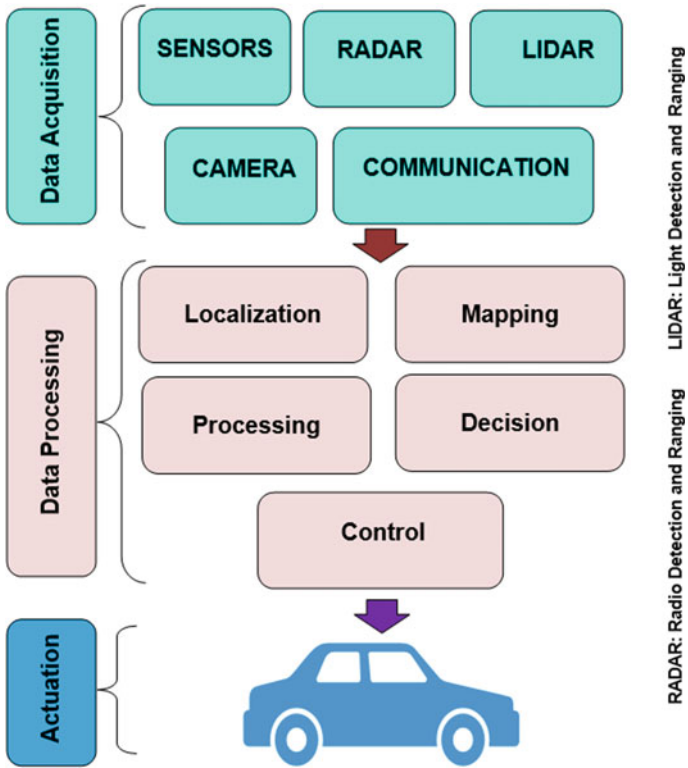
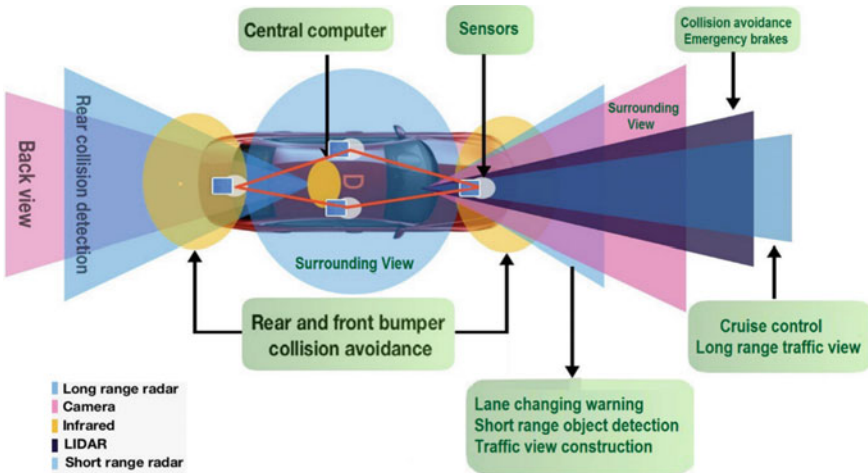**Fig. 2** Autonomous cars: functional architecture [27]

Fig. 3 Autonomous cars: system architecture [27, 28]

perform the controlled movement on the path [25]. Major stages involved in carrying out the aforesaid activities [26] in an autonomous vehicle are as follows:

- Situational and Environmental Awareness
- Navigation and Path Planning
- Maneuver Control.

2.1 Environmental and Situational Awareness

The primary plus most crucial stage in self-driving cars is to become aware of their surroundings, which adds target monitoring, self-positioning, and plane finding [29]. These automobiles need to be able to sense what is ahead of them, as well as have 360° neighborhood awareness [30]. As previously stated, a variety of hardware components, ranging from onboard and in-car cameras to common and short-distance detectors, are utilized for this purpose [31]. However, each of these components has advantages and disadvantages. Cameras can help people become more aware of their surroundings and the environment. However, the amount and rate of real-time info needed for area recognition are required in terms of automotive computing [32]. Radar technology performs much more effectively at tracing an object than cameras in this context, giving it one of the most effective vehicle modes [33]. LIDAR tracking is employed in an autonomous vehicle. LIDAR's key features include 360° visualization and tracking of long-distance efficiency. As result, a LIDAR device may be put on the automobile to provide a comprehensive picture of the surroundings [34]. However, it is important to note that LIDAR does not perform well in obtaining a solid object, such as collision-resistant parking, avoiding a collision, and bump protection [35]. Instead, for the aforementioned functions, specialized radars are positioned in the front, back, and sides of the vehicle. The data collected by these gadgets aid independent vehicle decision-making systems to control speed, use brakes, switch lanes, and navigate. The info collected by these methods are utilized in sophisticated software to create a three-dimensional representation of the surrounding area [36].

2.2 Navigation and Path Planning

The fundamental role of navigation or guiding in an autonomous car is to let the car drive in the direction you want. If the self-driving vehicle knows its surroundings, it should determine its route according to its purpose [3]. The automobile constructs a time-dependent path between the present place and the destination using navigation technology as a well-known global positioning system (GPS) control system [37]. Due to its precision, efficiency, and compacted hardware, architecture (on-chip), cheap cost, and usage, GPS is the principal method of routing for the automobile. Furthermore, the path is dynamically recalculated in the event of specific occurrences such as road closures, detours, and soon. The navigation system in the automobile

must be strong enough to accommodate abrupt and consequent adjustments to the path by changing the path made by the computer in the past. Path networks are substantially predetermined, and the self-driven vehicle's steering system compares car continuity in a regular study [38]. Various research initiatives were carried out and evaluated real-world data which produces a map for self-driving automobiles [13]. The results are encouraging and will help in the first phase of self-driving car sales.

2.3 Maneuver Control

The autonomous automobile begins its trip when it observes its surroundings and uses this knowledge, coupled with its destination information [39]. For a smooth, safe (or at least unsuccessful) journey along the way, various motions should be properly regulated [40]. As previously noted, the autonomous vehicle is outfitted with a plethora of detector and controller. Most auto components are electronically commanded by Electronic Control Units (ECUs) [41]. During its voyage, the autonomous car has to do a few things like taking care of the road, the distance from bump to bump, sudden brakes, jumping, and stopping on-road signals. This movement requires hardware/software support, as well as large-scale communication and real-time data exchange across multiple vehicle control systems [42].

3 Autonomous Cars Major Advantages

Despite its complexity, the autonomous car idea offers up new apps to innovate and provide users with security, efficiency, convenience, and additional aids. In this part, there is a need to go over some of the primary advantages of self-driving vehicles as well as prospective uses for self-driving automobiles.

3.1 Improved Security

Safety is a character with many features in the automotive environment, where people's lives are at the forefront when it comes to driving. One of the most essential uses of self-driving vehicles is safe driving for its passengers [40, 43]. With high-tech sensors onboard, the autonomous automobile can correctly detect its rightful owner and issue an alarm to the owner in the event of an uncomfortable circumstance [44]. Biometric such as fingerprints, retina scans, speech recognition software, and/or synthetic telepathy might be used in self-driving automobiles [24].

3.2 Usefulness and Convenience

Another advantage of self-driving automobiles is their simplicity of use and convenience [42]. People are sometimes unable to drive an automobile due to medical/disability issues or drunkenness. Self-driving car may be an appropriate form of transportation for the elderly, young people who do not have a driving license, and individuals who cannot meet the expense of a car [45].

3.3 Improved Traffic Conditions

Autonomous vehicles will improve traffic conditions by increasing the occupancy of each vehicle and reducing the number of automobiles on the highways [46]. Self-driving cars can assist in more accurately complying with traffic regulations, minimizing the need for traffic cops on the road. In situations such as excessive running, erratic driving, starting and stopping, and rapid braking self-driving car may prevent unpredictable driving habits that result in fuel inefficiency [45, 47].

3.4 Autonomous Parking

The growing number of vehicles, overcrowded people, spaces between cars in parking lots are one of the main problems in metropolitan centers today [48]. After dropping off passengers, autonomous cars can park even in the smallest of available parking spaces (where people will look for larger parking spaces for each car) [42].

3.5 Customer-Centered Experience

Drivers will be able to relax, sit down, and enjoy the journey of self-driving cars. It is worth mentioning that Tesla, the electric automobile company, has already made strides in these areas, including "summon" [48] applications in its high-end models [36]. Autonomous vehicles will open the way for a slew of passenger-centered apps, allowing passengers to tailor their travel experience depending on factors such as speed, amount of danger, in-car entertainment, and so on [49].

4   Design and Implementation Issues

Security, durability, good demolition, environment failure, hardware/software archi-
tectures, and user satisfaction will determine the future of self-driving automobiles
[2]. However, in order to accomplish these objectives, the concept and production
of self-driving vehicles must provide maximum accuracy, protection, and substan-
tiality, as human lives are directly dependent on them. Road acquisition is one of the
most important mobile vehicle needs and is often seen with various sensors such as
radar, LIDAR, location, sonar, advanced sensors, and softwares are all used in the
self-driving automobile. The conceptual and implementation concerns are summa-
rized in Table 1. In this part, there's a discussion over design and use-issues that
the autonomous car industry is facing. Existing validation tools has been described
(such as simulators) for simulating and testing various components of the autonomous
vehicle.

4.1   Cost

The cost of hardware and software is a key impediment to the widespread manu-
facture of self-driving automobiles [50]. Earlier LIDAR hardware costs roughly US
$75,000, which is significantly more expensive than the automobile itself, but with
technological advancement currently, it cost US $7500 [51]. As a result, it is fair
to expect that hardware costs will be critical in the design and implementation of
self-driving automobiles.

4.2   Maps

The maps utilized for self-driving cars differ those created by regular GPS systems
[52, 53]. These maps make extensive use of road features including lane length,
distance from pedestrians, and steep elevation. Using big data technology to solve
these difficulties may be an option you can consider in the future [13]. Data is gathered
by various sensors like 3-D LiDAR [34], odometer sensors, and economical GPS;
nevertheless, changing landscapes and road constructions continue to pose challenges
for effective mapping [54].

4.3   Software Complexity and Quality

The accuracy of the system generated by the software must be extremely reliable
[44]. The level of expertise in self-driving car software must be able to reflect a

Table 1 Summary of design and implementation issues

Aspect	Challenge	Possible solutions	References
Cost	• Hardware cost • Software cost • Management cost • Maintenance and testing are expensive	• Mass production	[50, 51]
Maps	• Massive processing resources required for real-time map production • Storage expense • Unpredictable weather circumstances • Dynamic environment as well as road layouts	• Big data applications • Collaborative mapping with neighbors	[34, 52, 54]
Software complexity	• Testing as well as verification • Requirements remain incomplete • Natural challenges cause software inconsistency • Program expense • Program protection • Difficult to get permission to use the software	• Fail-safety profiles and driving qualities • Put a greater emphasis on AI as well as deep learning-based technologies	[3, 42, 55, 56, 70, 71]
Validation and testing	• No comprehensive list of prerequisites • Strong and uncomplicated activities • Complication of action • Aim-demanding quality	• Restricted operating paradigms • Pedagogical guidance as well as machine learning methodologies • Error prevention • Logical division of programming modules	[57–61, 70]
Security and reliability	• The similarity of a person's level of self-reliance requires many resources • Distance traveled during test drives has no bearing on loyalty measure is imprecise • Removal of abortion work is dangerous • Uncertain verification period	• Appropriate short-term objectives • Comprehensive inefficient systems • Developing sophisticated algorithms for small tasks • Using machine learning, deep learning, and artificial intelligence	[39, 62–67, 70–72]

(continued)

Table 1 (continued)

Aspect	Challenge	Possible solutions	References
Sensors management	• Data of several sensors need to be handled in the problem-solving moment • In-depth learning algorithms that store and operate a computer • Lack of data, external factors, and granularity from sensory data • Verification of observed data	• Increasing computation and transmission means • Finding crowds and seeing crowds • Sensory data sharing throughout all units • The trade-off between the number of sensory inputs and the speed	[2, 21, 50, 70, 73]

person's mind and/or behavior [55, 56]. With self-driving cars, the driver is not there, necessitating even more strict procedures to maintain the greatest software quality [3]. As a result, it is significant for independent software developers to ensure that the software retorts to a variety of unexpected events [56].

4.4 Validation and Testing

There are many verification methods and testing methods available, from bug fixes to full quality tests [57]. On the other hand, the design/actuator design will help with the demand problem and provide fail-safe modes for autonomous vehicles [58]. The third option is an error vaccine, which can help in the certification of autonomous cars. Koopman and Wagner [59] proposed that at least in part, the complicated requirements difficulties may be minimized by restricting the autonomous car's operating principles [60]. The present testing methodologies for autonomous vehicles, while large and concrete, it cannot cover the entire safety spectrum and operational requirements, as well as the unpredictable behavior displayed by autonomous vehicles [61].

4.5 Safety and Reliability

The safety and dependability of self-driving automobiles is vital problem to overcome [28, 62]. It is arguable that before the commercialization of autonomous cars, couple hundred millions of kilometers testing must to complete [63]. The time necessary for autonomous automobile technology to drive itself safely is in the tens, if not

hundreds, of years [64]. This is a massive test run for a self-driving automobile [65]. The autonomous automobile must be able to work on its own without personal involvement, even during testing [66]. The automated car's safety and dependability are still in their start, and it will take time to satisfy the rules of security and accuracy. The safety benefits of autonomous cars can be brought about by the installation of idle safety features in the integrated safety system [39]. The in-vehicle network must also be secured form attacks [67].

4.6 Sensor Management

Autonomous vehicles contain several sensors that create a massive quantity of info in actual time. This info is utilized by several automotive components to work properly [21]. Currently, the major issue for self-driving cars is not efficiency. As a result, crowd sourcing and crowd sensing will be demanding in the improvement of autonomous vehicles afterward [2]. In other words, rather than having a big number of detectors, having a complete number of detectors and exchanging sensory info between neighbors is likely to produce superior results. In addition, a trading solution to this problem can be reached by reaching an agreement on the value of these detectors, the number of detectors, and the expenses they put into data processing and decision-making processes [51].

5 Limitations

If an object is at an angle nearly perpendicular to the sensor, the limited resolution of the LiDAR may cause consecutive points in the scan to be measured at far away different distances, causing the check to fail even though the object is actually connected. This is a fundamental limitation of LiDAR information; there is no way to determine based on the sensor data whether the object is fully [68]. Ethical and ethical considerations are taken into account when developing program that determines what step a car takes in certain casualty [40]. Susceptibility of navigation system of the car to different types of weather (snowy conditions, floods, heavy rain, etc.) is also a major limitation factor [69].

6 Conclusion

In this modern era, autonomous technology and vehicles are becoming fast-growing technology. Various automakers like technology business owners are experimenting with them. The complete functional cycle of an autonomous vehicle is divided into various patterns such as situational awareness, planning, control, and inclination. The

principal advantages concerning self-driving vehicles incorporate increased security for passengers, fresh business possibilities, upgraded traffic situations, learners, and the creation of customer participation. Notwithstanding certain advantages, still, there are few design and applications difficulties which are needed to be solved before these practical autonomous vehicles can be completely deployed. The software complexity and quality, object detection accuracy, sensor management, decision-making, actuation, and testing were looked at along with the security and authenticity of these vehicles. In addition, nontechnical difficulties were examined like variety, customer support, unpredictable expenses of autonomous vehicles, and sociological hurdles: for instance, human behavior upon driving, as well as moral and honest implications. Ultimately, presented ideas to assist designers and policymakers in developing viable regulations for the design, construction, and deployment of autonomous vehicles were explored. This must be acceptable to consumers as well. Despite the outstanding accomplishments obtained with autonomous automobile technology thus far, still a bit too hasty to predict the commercial phase of the driverless vehicle. Nonetheless, it is expected that more research findings will propel the autonomous vehicle sector toward commercialization in the near future. The summarized conclusions and future outlook are:

- Radar is the most effective technology to trace an object in autonomous vehicles.
- LIDAR is lacking to provide collision-resistant parking, avert a collision, and provide bump protection.
- The maps make considerable use of road characteristics such as lane length, pedestrian distance, and steep elevation. Big data technologies implementation for road characteristics can be explored for more understanding.
- Road acquisition is one of the most significant requirements for mobile vehicles, and it is generally accomplished using a variety of sensors such as radar, LIDAR, position, sonar, sensors, and software optimization.
- The navigation system which can be explored for more understanding of accommodating abrupt and consequent variations in the path by altering the path taken previously by the computer.
- It may also be worthwhile to secure in-vehicle network from attacks.
- Autonomous vehicle has a large number of detectors to exchanging sensory information. It could a great innovation to develop superior structure having a small number of detectors.
- Lastly, software used in autonomous vehicles should capable of responding to a wide range of unforeseen circumstances.

References

1. Wagg DJ, Worden K, Barthorpe RJ, Gardner P (2020) Digital twins: state-of-the-art and future directions for modeling and simulation in engineering dynamics applications. ASME J Risk Uncertainty Part B 6(3):030901

2. Fagnant DJ, Kockelman K (2015) Preparing a nation for autonomous vehicles: opportunities, barriers and policy recommendations. Transp Res Part A Policy Pract 77:167–181
3. Paden B, Čap M, Yong SZ, Yershov D, Frazzoli E (2016) A survey of motion planning and control techniques for self-driving urban vehicles. IEEE Trans Intell Veh 1:33–55
4. Martínez-Díaz M, Soriguera F (2018) Autonomous vehicles: theoretical and practical challenges. Transp Res Procedia 33:275–282
5. Guerreroibanez JA, Zeadally S, Contreras-Castillo J (2015) Integration challenges of intelligent transportation systems with connected vehicle, cloud computing, and internet of things technologies. IEEE Wirel Commun 22:122–128
6. Cunneen M, Mullins M, Murphy F (2019) Autonomous vehicles and embedded artificial intelligence: the challenges of framing machine driving decisions. Appl Artif Intell 33(8):706–731
7. Lafrance A (2016) Our grandmother's driverless car. https://www.theatlantic.com/technology/archive/2016/06/beep/489029/
8. Schmidhuber J. Robot car history. http://people.idsia.ch/juergen/robotcars.html
9. Howard D, Dai D (2014) Public perceptions of self-driving cars: the case of Berkeley, California. In: Transportation research board 93rd annual meeting, vol 14, no 4502
10. Okuda R, Kajiwara Y, Terashima K (2014) A survey of technical trend of ADAS and autonomous driving. In: Proceedings of technical program—2014 international symposium on VLSI technology, systems, and application (VLSI-TSA), Apr 2014, pp 1–4
11. Zeadally S, Hunt R, Chen Y-S, Irwin A, Hassan A (2012) Vehicular ad hoc networks (VANETS): status, results, and challenges. Telecommun Syst 50:217–241
12. Lopez N (2016) Nvidiaannounces a 'super computer' GPU and deep learning platform for self-driving cars. https://thenextweb.com/author/napierlopez/.tnwG6F0jhzi
13. Contreras-Castillo J, Zeadally S, Ibanez JAG (2016) Solving vehicular adhoc network challenges with big data solutions. IET Netw 5(4):81–84
14. Gross M (2016) A planet with two billion cars. Curr Biol 26(8):R307–R310
15. WHO (2016) The road traffic death rate by who region and income level. http://www.who.int/gho/roadsafety/en/
16. Mehar S, Zeadally S, Remy G, Senouci SM (2015) Sustainable transportation management system for a fleet of electric vehicles. IEEE Trans Intell Transp Syst 16(3):1401–1414
17. Zamboni G, Dressino L, Boileau H (2020) A tool for the assessment of the potential benefits of electric and hybrid cars for emissions reduction in urban areas. Int J Environ Stud 77(4):703–723
18. Wiegand G, Weber T, Hussmann H, Schmidmaier M, Liu Y (2019) I drive—you trust: explaining driving behavior of autonomous cars. https://doi.org/10.1145/3290607.3312817
19. Guo Y, Sayed T, Essa M (2020) Real-time conflict-based Bayesian Tobit models for safety evaluation of signalized intersections. Accid Anal Prev 144:105660
20. Tavakoli M, Carriere J, Torabi A (2020) Robotics, smart wearable technologies, and autonomous intelligent systems for healthcare during the COVID-19 pandemic: an analysis of the state of the art and future vision. Adv Intell Syst 2(7):2000071
21. Shi W, Alawieh MB, Li X, Yu H (2017) Algorithm and hardware implementation for visual perception system in autonomous vehicle: a survey. Integr VLSI J 59:148–156
22. Ballentine M et al (2021) Conceptualising and prototyping a decision support system for safer urban unmanned aerial vehicle operations. Urban Plann Transp Res 1–21
23. Pandey N, Duggal G, Ram SS (2020) Database of simulated inverse synthetic aperture radar images for short range automotive radar. In: 2020 IEEE international radar conference (RADAR). IEEE
24. Antony MM, Whenish R (2021) Advanced driver assistance systems (ADAS). In: Automotive embedded systems. Springer, Cham, pp 165–181
25. De Ryck M, Versteyhe M, Debrouwere F (2020) Automated guided vehicle systems, state-of-the-art control algorithms and techniques. J Manuf Syst 54:152–173
26. Panagiotopoulos I, Dimitrakopoulos G (2018) An empirical investigation on consumers' intentions towards autonomous driving. Transp Res Part C Emerg Technol 95:773–784

27. Hussain R, Zeadally S (2018) Autonomous cars: research results, issues, and future challenges. IEEE Commun Surv Tutor 21(2):1275–1313
28. Jo K, Kim J, Kim D, Jang C, Sunwoo M (2014) Development of autonomous car (part I): distributed system architecture and development process. IEEE Trans Ind Electron 61:7131–7140
29. Soldatov MA et al (2021) Self-driving laboratories for development of new functional materials and optimizing known reactions. Nanomaterials 11(3):619
30. Nikitas A, Njoya ET, Dani S (2019) Examining the myths of connected and autonomous vehicles: analysing the pathway to a driverless mobility paradigm. Int J Automot Technol Manage 19(1–2):10–30
31. Ahangar MN et al (2021) A survey of autonomous vehicles: enabling communication technologies and challenges. Sensors 21(3):706
32. Rahman AU et al (2020) Context-aware opportunistic computing in vehicle-to-vehicle networks. Veh Commun 24:100236
33. Clunie T et al (2021) Development of a perception system for an autonomous surface vehicle using monocular camera, LIDAR, and marine RADAR. In: 2021 IEEE international conference on robotics and automation (ICRA). IEEE
34. Carless D et al (2019) Mapping landscape-scale peatland degradation using airborne lidar and multispectral data. Landscape Ecol 34(6):1329–1345
35. Vora S et al (2020) Pointpainting: sequential fusion for 3D object detection. In: Proceedings of the IEEE/CVF conference on computer vision and pattern recognition
36. Narula L, Iannucci PA, Humphreys TE (2020) Automotive-radar-based 50-cm urban positioning. In: 2020 IEEE/ION position, location and navigation symposium (PLANS)
37. Guo R et al (2020) Time-dependent urban customized bus routing with path flexibility. IEEE Trans Intell Transp Syst 22(4):2381–2390
38. Lim W et al (2018) Hierarchical trajectory planning of an autonomous car based on the integration of a sampling and an optimization method. IEEE Trans Intell Transp Syst 19(2):613–626
39. Mík AJ, Bouchner BP (2020) Safety of crews of autonomous cars. In: 2020 smart cities symposium, Prague. IEEE. ISBN 978-1-7281-68210/20/$31.00
40. Ondruš J, Kolla E, Vertal P, Šaric Ž (2020) How do autonomous cars work? Horizons of autonomous mobility in Europe. Transp Res Procedia 44:226–233
41. örs Yalçın SB, Soltekin MME (2021) Designing and implementing secure automotive network for autonomous cars. In: 2021 29th signal processing and communications applications conference (SIU). IEEE
42. Bagloee SA, Tavana M, Asadi M, Oliver T (2016) Autonomous vehicles: challenges, opportunities, and future implications for transportation policies. J Mod Transp 24:284–303
43. Ramsey M (2015) Self-driving cars could cut down on accidents. https://www.wsj.com/articles/self-driving-cars-could-cut-down-onaccidentsstudy-says-1425567905
44. Marini S et al (2020) ENDURUNS: an integrated and flexible approach for seabed survey through autonomous mobile vehicles. J Mar Sci Eng 8(9):633
45. Acheampong RA, Cugurullo F (2019) Capturing the behavioural determinants behind the adoption of autonomous vehicles: conceptual frameworks and measurement models to predict public transport, sharing and ownership trends of self-driving cars. Transp Res F Traffic Psychol Behav 62:349–375
46. Simoni MD et al (2019) Congestion pricing in a world of self-driving vehicles: an analysis of different strategies in alternative future scenarios. Transp Res Part C Emerg Technol 98:167–185
47. Fu M, Song W, Yi Y, Wang M (2015) Path planning and decision making for autonomous vehicle in urban environment. In: 2015 IEEE 18th international conference on intelligent transportation systems, Sept 2015, pp 686–692
48. Pierce D (2016) Tesla summons hints at how the world of self-driving cars will work.https://www.wired.com/2016/01/tesla-summon/
49. Brenner W, Herrmann A (2018) An overview of technology, benefits and impact of automated and autonomous driving on the automotive industry. In: Digital marketplaces unleashed, pp 427–442

50. Bechtel MG et al (2018) Deeppicar: a low-cost deep neural network-based autonomous car. In: 2018 IEEE 24th international conference on embedded and real-time computing systems and applications (RTCSA). IEEE
51. Hecht J (2018) Lidar for self-driving cars. Opt Photonics News 29(1):26–33
52. Liu Y et al (2018) An innovative information fusion method with adaptive Kalman filter for integrated INS/GPS navigation of autonomous vehicles. Mech Syst Signal Process 100:605–616
53. Jo K, Sunwoo M (2014) Generation of a precise road way map for autonomous cars. IEEE Trans Intell Transp Syst 15:925–937
54. Bresson G, Alsayed Z, Yu L, Glaser S (2017) Simultaneous localization and mapping: a survey of current trends in autonomous driving. IEEE Trans Intell Veh 2:194–220
55. Joy J, Gerla M (2017) Internet of vehicles and autonomous connected car privacy and security issues. In: 2017 26th international conference on computer communication and networks (ICCCN), July 2017, pp 1–9
56. Hubmann C, Becker M, Althoff D, Lenz D, Stiller C (2017) Decision making for autonomous driving considering interaction and uncertain prediction of surrounding vehicles. In: 2017 IEEE intelligent vehicles symposium (IV), June 2017, pp 1671–1678
57. Abraham H, Lee C, Brady S, Fitzgerald C, Mehler B, Reimer B, Coughlin JF (2016) White paper: autonomous vehicles, trust, and driving alternatives: a survey of consumer preferences. Tech. Rep. 2016-6, June 2016. MIT AgeLab, Massachusetts Institute of Technology, Cambridge, MA
58. Campbell M, Egerstedt M, How JP, Murray RM (2010) Autonomous driving in urban environments: approaches, lessons and challenges. Philos Trans R Soc Lond Ser A 368(1928):4649–4672
59. Koopman P, Wagner M (2017) Autonomous vehicle safety: an interdisciplinary challenge. IEEE Intell Transp Syst Mag 9:90–96
60. Koopman P, Wagner M (2016) Challenges in autonomous vehicle testing and validation. SAE Int J Trans Saf 4:15–24
61. Aeberhard M, Rauch S, Bahram M, Tanzmeister G, Thomas J, Pilat Y, Homm F, Huber W, Kaempchen N (2015) Experience, results and lessons learned from automated driving on Germany's highways. IEEE Intell Transp Syst Mag 7:42–57
62. Jo K, Kim J, Kim D, Jang C, Sunwoo M (2015) Development of autonomous car (part II): a case study on the implementation of an autonomous driving system based on distributed architecture. IEEE Trans Ind Electron 62:5119–5132
63. Hulse LM, Xie H, Galea ER (2018) Perceptions of autonomous vehicles: relationships with road users, risk, gender and age. Saf Sci 102:1–13
64. Parkinson S, Ward P, Wilson K, Miller J (2017) Cyber threats facing autonomous and connected vehicles: future challenges. IEEE Trans Intell Transp Syst 18(11):2898–2915
65. Hars A (2016) Misconception 7: to convince us that they are safe, self driving cars must drive hundreds of millions of miles. http://driverlessfuture.com/?cat=32
66. Fisher DL, Lohrenz M, Moore D, Nadler ED, Pollard JK (2016) Humans and intelligent vehicles: the hope, the help, and the harm. IEEE Trans
67. Groza B, Murvay S (2018) Security solutions for the controller area network: bringing authentication to in vehicle networks. IEEE Veh Technol Mag 13(1):40–47
68. Guajardo U, Bryan A, Arechiga N, Campos S, Chow J, Jackson D, Kong S, Litt G, Pollock J (2021) Certified perception for autonomous cars. In: 6th workshop on monitoring and testing of cyber-physical systems
69. Kalašová A, Ondruš J, Kubíková S (2018) Inteligentné dopravné systémy, 1st edn. Žilinská univerzita v Žiline, Žilina, 302 p. ISBN 978-80-554-1493-5
70. Janai J,Güney F, Behl A, Geiger A (2017) Computer vision for autonomous vehicles: problems, datasets and state-of-the-art. CoRR. vol abs/1704.05519
71. Gonzalez A, Vazquez D, Lopez AM, Amores J (2017) On-board object detection: multicue, multimodal, and multiview random forest of local experts. IEEE Trans Cybern 47:3980–3990

72. Claussmann L, Revilloud M, Glaser S, Gruyer D (2017) A study on al-based approaches for high-level decision making in highway autonomous driving. In: 2017 IEEE international conference on systems, man, and cybernetics (SMC), Oct 2017, pp 3671–3676
73. Chen X, Kundu K,Zhu Y, Ma H, Fidler S, Urtasun R (2016) 3D object proposals using stereo imagery for accurate object class detection. CoRR, vol abs/1608.07711

Use of Super Absorbent Polymer with GGBS in Normal Concrete

T. J. Rajeeth, B. M. Sagar, R. Arpitha, M. S. Shashank, and Manu S. Gowda

1 Introduction

Concrete has long been recognized as a well-known construction material in India, particularly for infrastructural development. The practice of using add-on cementitious constituents such as ground granulated blast furnace slag, silica fume, rice husk ash, and pulverized fly ash in concrete has been shown to reduce the amount of cement required to achieve the desired compressive strength and other properties for use in all construction. Ground granulated blast furnace slag (GGBS) is by-product obtained from blast furnace in the iron and steel industries, which will be produced in the same proportion as iron [1]. The slag contains lime, silica, and alumina, which bind like Portland cement. In its saturated form, the super absorbent polymer (SAP) [2] functions as a humidity generator, which aids in the hydration of the cement. SAP is primarily used to prevent self-desiccation (autogenous shrinkage) of concrete and to liberate free water from the concrete mix.

External curing will hydrate only the exterior surface of the concrete, as water can penetrate just a few millimetres from the exposed surface due to depreciation, and the interior does not achieve its potential. Whereas in internal curing, there is excess water that is not part of the mix. This water forms reservoirs of water as depicted, which enables the hydration of concrete from the inside out, providing additional hydration products that increase the strength and reduce micropores, thereby increasing

T. J. Rajeeth (✉) · B. M. Sagar · R. Arpitha · M. S. Shashank
Department of Civil Engineering, Vidyavardhaka College of Engineering, Mysuru, Karnataka 570 002, India
e-mail: tjrajeeth@vvce.ac.in

M. S. Gowda
Department of Civil Engineering, Maharaja Institute of Technology Thandavapura, Mysuru, Karnataka 571 302, India

699

concrete durability. Hence, by incorporating SAP as a self-curing agent, concrete can be cured internally to achieve maximum hydration.

2   Literature Review

The concrete produced with SAP has many beneficial properties, particularly in reducing early-age autogenous shrinkage problems. Many researchers have attempted to check the feasibility of the usage of SAP in concrete applications, and some of them are discussed here. The strength properties are nearly identical whether water is added to the paste or entrained by SAP [3]. By adding SAP, high-performance concrete compressive strength is reduced while correcting for void volume [4]. The internal curing degree determines the swelling peak, and the autogenous shrinkage is not fully compensated [5, 6]. Internally cured high-performance mortars with SAP have lower apparent densities. This can influence the paste microstructure and water to cement ratio [7]. A prediction model for the working water to cement ratio was derived, which may be used to forecast IRH fluctuations in early-age concrete internally cured with SAP and could minimize early-age autogenous shrinkage [8–10]. The concrete made up of SAP could be able to resist cyclic loads [11]. With increasing levels of SAP, the compressive strength and stiffness, indicated by the modulus of elasticity, increased statistically [12]. The shrinkage of concrete with the use of SAP is less. This is because of internal curing [13]. The dosage of SAP should be as low as possible and be selected for optimal particle size to get better strengths [14]. The SAP affected zone had a greater indentation modulus and fewer C-S-H interlayer pores. [15]. Internal SAP curing reduces the danger of concrete cracking by two classes, ensuring that both cracking stress and net cracking time are in the low-risk category [16, 17]. At optimum dosage, the SAP can reduce autogenous shrinkage, resulting in more durable, high-performance mortar and concrete [18–20]. The cement paste plays a vital role and, due to the increased consistent availability of moisture, internal curing may also improve hydration and compressive strength at later ages [21, 22]. The water stored can work on several physical or chemical principles, each with its own potential. Some of the strategies described have yet to be tested. SAP increases the thermodynamic and kinetic availability of water for cementitious reactions, which is crucial for all approaches [23, 24]. It is observed from literature that the utilization of supplementary cementitious materials and durability aspects have not been tried. Hence, in our work, an attempt is being made to make use GGBS along with SAP in normal concrete production.

3 Objectives

The main objective is to study the strength characteristics of GGBS concrete with the application of SAP and to compare the mechanical strength characteristics and durability properties for different curing periods.

4 Materials and Methodology

The materials used in this research work are cement of grade OPC 43 grade, since the OPC is not blended with any type of pozzolonic materials during its manufacture and to get the detrimental effect of GGBS usage. The manufactured sand as fine aggregate, 20 mm and 10 mm size coarse aggregate, potable drinking water for mixing and curing, GGBS, and sodium polyacrylate polymer (chemical structure of SAP, SAP powder, and swollen SAP are shown in Figs. 1, 2 and 3) of medical grade were used. The tests on the ingredients were done as per Bureau of Indian Standards specifications. According to IS 10262:2019 [25], M20 grade concrete with a 1:2.4:3.2 proportion is designed. The w/c ratio of the mix is adopted as 0.5. Experimental measurements were performed to predict the fresh and hardened properties of concrete containing SAP and with the partial replacement of cement by GGBS at a range of 10–50% (at an interval of 10%). The workability of concrete in terms of compaction factor [IS: 1199-1959 (Reaffirmed 2004)] [26], and compressive [IS: 516-1959 (Reaffirmed 2004)] [27], flexural [IS: 516-1959 (Reaffirmed 2004)] [27],

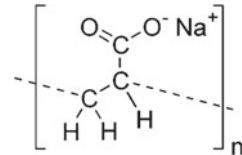**Fig. 1** Structure of sodium polyacrylate monomer
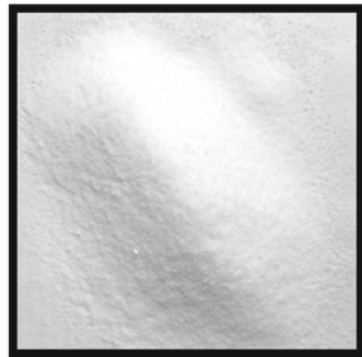

Fig. 2 SAP powder

Fig. 3 Swollen SAP

split tensile tests [IS: 5816-1999 (Reaffirmed 2004)] [28], and durability tests [ASTM C642-06] [29] like water absorption, apparent porosity, and acid resistance tests [ASTM C1898-20] [30] were performed at different curing periods.

5 Results

The test results were tabulated for seven types of concrete mixes based on the dosage of SAP, GGBS, and curing methods adopted. Firstly, the workability of fresh concrete in terms of compaction factor value was noted since concrete mix has less workability. The results are given in Table 1. To check the strength of hardened concrete, various mix proportions and at different curing periods were tested, the results are shown in Fig. 4. The results obtained on the flexural and split strength of concrete are presented in Table 2. The durability tests like water absorption and apparent density

Table 1 Compaction factor values for various mix proportions

S. No.	Type of mix	GGBS (%)	SAP (%)	Curing method	Compaction factor
1	Mix-I	0	0	External (water curing)	0.78
2	Mix-II	0	0.3	Internal (open air curing)	0.79
3	Mix-III	10	0.3	Internal (open air curing)	0.80
4	Mix-IV	20	0.3	Internal (open air curing)	0.87
5	Mix-V	30	0.3	Internal (open air curing)	0.87
6	Mix-VI	40	0.3	Internal (open air curing)	0.88
7	Mix-VII	50	0.3	Internal (open air curing)	0.89
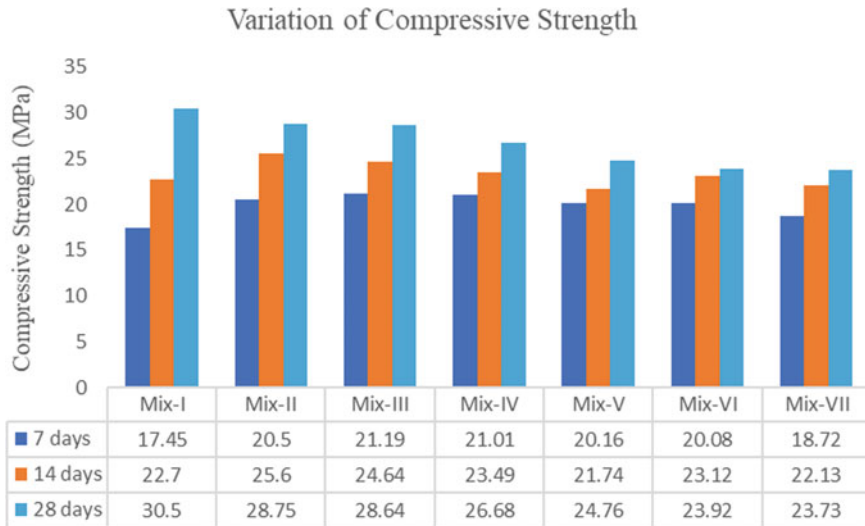
Fig. 4 Compressive strength variation for various mix proportions

Table 2 Flexural and split tensile strength values at 28 days

S. No.	Type of mix	Flexural strength (N/mm^2)	Split tensile strength (N/mm^2)
1	Mix-I	3.40	2.65
2	Mix-II	3.24	2.61
3	Mix-III	3.10	2.58
4	Mix-IV	3.01	2.44
5	Mix-V	2.99	2.40
6	Mix-VI	2.80	2.27
7	Mix-VII	2.78	2.16

are on hardened concrete. The results obtained are presented in Table 3. The effect of on acid environment (HCl solution) on hardened concrete in terms of strength and weight loss is presented in Table 4.

6 Discussion

The concrete property in a fresh state was expressed in terms of the compaction factor (Table 1), since the concrete mixture felt dry and the slump cone did not yield acceptable results. From the results, it is observed that as the GGBS percentage increases, the workability also increases. Since the GGBS has more fineness than the cement, the workability can be further enhanced by adding the proper dose of

Table 3 Water absorption and apparent density of concrete at 28-days

S. No.	Type of mix	Water absorption (%)	Apparent density (g/cc)
1	Mix-I	2.79	2.58
2	Mix-II	2.50	2.49
3	Mix-III	2.82	2.48
4	Mix-IV	2.83	2.45
5	Mix-V	2.85	2.41
6	Mix-VI	2.89	2.38
7	Mix-VII	2.91	2.34

Table 4 Effect of acid on weight loss and compressive strength of concrete at 28 day

S. No.	Type of mix	Loss in weight (%)	Compressive strength (MPa)
1	Mix-I	1.79	27.37
2	Mix-II	1.65	26.94
3	Mix-III	1.60	26.54
4	Mix-IV	1.64	25.62
5	Mix-V	1.68	23.50
6	Mix-VI	1.70	21.46
7	Mix-VII	1.60	21.82

super plasticizer. Based on a previous study, concrete with SAP attained a strength nearly equal to normal curing concrete, up to a certain dosage, and in the present study, the dosage of 0.3% is fixed throughout. The mechanical strength properties like compressive strength on cubes are determined and presented in Fig. 4, and it is observed that with the replacement of cement with GGBS, the compressive strength decreased marginally. The SAP concrete yields an acceptable compressive strength value because of internal curing and by providing additional water for full hydration of the cement. The compressive strength obtained for 10% and 50% GGBS is 1% and 17%, respectively, on par with reference mix without GGBS and SAP. The flexural and split tensile strengths (Table 2) are almost on par with the conventional mix. The durability properties are presented in Tables 3 and 4, and it is observed that the mix with 10–20% of GGBS with 0.3% SAP yields the acceptable values.

7 Conclusions

In this study, an attempt was made to establish the suitability of SAP with manufactured sand and GGBS as a replacement for cement. Based on the analysis conducted and the results obtained, the following conclusions may be drawn:

- As the replacement of GGBS increases, also the workability of concrete increases due to increase in fineness of GGBS compared OPC.
- With the increase in replacement of cement by GGBS, there is a decrease in compressive strength for all mixes.
- The addition of super absorbent polymer (SAP) leads to the maximum hydration of cement with a slight decrease in compressive strength and yields an acceptable results.
- The compressive strength of concrete with 0.3% of SAP yields 28.75 MPa compared to conventional concrete with 30.50 MPa.
- The compressive strength of concrete with 20% GGBS yields 26.68 MPa, which is more than the required target compressive strength for M20 grade concrete.
- The durability properties of SAP cured concrete were comparable to those of the reference mix with water-curing concrete, and the values are within acceptable limits.
- SAP can be used in the case of water scarcity areas to do external curing of concrete.
- The strength and durability properties tests must be performed at longer curing periods to know exactly the detrimental effect of SAP usage in concrete applications, and one can use this type of concrete where there is a scarcity of water.

References

1. El-Chabib H (2020) Properties of SCC with supplementary cementing materials. Self-Compacting Concr Mater Prop Appl 1:284–308
2. Wong HS (2018) Concrete with superabsorbent polymer. Eco-efficient Repair Rehabil Concr Infrastruct 1:467–469
3. Assmann A, Reinhardt HW (2014) Tensile creep and shrinkage of SAP modified concrete. Cem Concr Res 58:179–185
4. Olawuyi BJ, Babafemi AJ, Boshoff WP (2021) Early-age and long-term strength development of high-performance concrete with SAP. Constr Build Mater 267:121798
5. Desineni BOR, Kommineni HR (2020) An experimental study on strength characteristics of self-curing concrete with manufacture sand using super absorbed polymer. Mater Today Proc 33:333–337
6. Craeye B, Geirnaert M, De Schutter G (2011) Super absorbing polymers as an internal curing agent for mitigation of early-age cracking of high-performance concrete bridge decks. Constr Build Mater 25:1–13
7. Mönnig S, Lura P (2007) Superabsorbent polymers—an additive to increase the freeze-thaw resistance of high strength concrete. In: Advances in construction materials, pp 351–358
8. Shen D, Wanga M, Chen Y, Wang W, Zhang J (2017) Prediction of internal relative humidity in concrete modified with super absorbent polymers at early age. Constr Build Mater 149:543–552
9. Shen D, Liu C, Jiang J, Kang J, Li M (2020) Influence of super absorbent polymers on early-age behavior and tensile creep of internal curing high strength concrete. Constr Build Mater 258:120068
10. Shen D, Wena C, Zhu P, Wua Y, Yue W (2020) Influence of Barchip fiber on early-age autogenous shrinkage of high-strength concrete internally cured with super absorbent polymers. Constr Build Mater 264:119983

11. Xie F, Cai D, Ji L, Zhang C, Ruan J (2021) Experimental study on the mechanical properties of internally cured concrete with super absorbent polymer under monotonic and cyclic loads. Constr Build Mater 270:121495
12. Gao D, Heimann RB, Alexandert SDB (1997) Box-Behnken design applied to study the strengthening of aluminate concrete modified by a superabsorbent polymer/clay composite. Adv Cem Res 9:93–97
13. AzariJafari H, Kazemian A, Rahimi M, Yahia A (2016) Effects of pre-soaked super absorbent polymers on fresh and hardened properties of self-consolidating lightweight concrete. Constr Build Mater 113:215–220
14. Ding H, Zhang L, Zhang P (2017) Factors influencing strength of super absorbent polymer (SAP) concrete. Trans Tianjin Univ 23:245–257
15. Liu J, Farzadnia N, Shi C (2021) Microstructural and micromechanical characteristics of ultra-high-performance concrete with superabsorbent polymer (SAP). Cem Concr Res 149:106560
16. Yang J, Guo Y, Shen A, Chen Z, Qin X, Zhao M (2019) Research on drying shrinkage deformation and cracking risk of pavement concrete internally cured by SAPs. Constr Build Mater 227:116705
17. Fan J, Shen A, Guo Y, Zhao M, Yang X, Wang X (2020) Evaluation of the shrinkage and fracture properties of hybrid fiber-reinforced SAP modified concrete. Constr Build Mater 256:19491
18. De Meyst L, Mannekens E, Van Tittelboom K, De Belie N (2021) The influence of super-absorbent polymers (SAPs) on autogenous shrinkage in cement paste, mortar and concrete. Constr Build Mater 286:122948
19. Hasholt MT, Jensen OM, Kovler K, Zhutovsky S (2012) Can superabsorent polymers mitigate autogenous shrinkage of internally cured concrete without compromising the strength? Constr Build Mater 31:226–230
20. Mejlhede JO (2013) Use of superabsorbent polymers in concrete. Concr Int 1:48–52
21. Geiker MR, Bentz DP (2004) Mitigating autogenous shrinkage by internal curing, SP-218–9, pp 143–148
22. Jensen OM, Hansen PF (2001) Water-entrained cement-based materials: I. Principles and theoretical background. Cem Concr Res 31:647–654
23. Jensen OM, Lura P (2006) Techniques and materials for internal water curing of concrete. Mater Struct 39:817–825
24. Faxiang X, Dingpeng C, Lin J, Chuanlong Z, Jing R, Xiao L (2021) Combined compression-shear performance, and failure criteria of internally cured concrete with super absorbent polymer. Constr Build Mater 266:120888
25. IS 10262: 2019 Guidelines for concrete mix proportioning (second revision), Bureau of Indian Standards, New Delhi
26. IS 1199: 1959 Methods for sampling and analysis of concrete (Reaffirmed 2004), Bureau of Indian Standards, New Delhi
27. IS 516: 1959 Methods for tests for strength of concrete (Reaffirmed 2004), Bureau of Indian Standards, New Delhi
28. IS: 5816-1999 Splitting tensile strength of concrete—method of test (Reaffirmed 2004), Bureau of Indian Standards, New Delhi
29. ASTM C642-06 (2013) Standard test method for density, absorption, and voids in hardened concrete, ASTM, International
30. ASTM C1898-20 (2020) Standard test methods for determining the chemical resistance of concrete products to acid attack, ASTM, International

Towards Enhancing Properties of Concrete Mixed with Silica

Adnan Khan, Moinul Haq, and Tabassum Naqvi

1 Introduction

Silica fume (SF) is a silicon metal industry processing by-product used in the metal industry that would have been initially assumed to be a waste. Nowadays, it may be used in concrete to boost strength properties and also helps in optimizing mechanical and durability qualities [1]. One of the best amorphous silica powders is SF. Because of its fine granularity, it functions as a filler ingredient, fitting into the spaces between the cement particles in the same manner as sand occupies the gap between coarse sand particles in traditional concrete [2, 3]. The existence of silica fume affects the thickness of the transition phase and the degree of orientation of generated calcium hydroxide (C–H) particles in it. The possible mechanism is linked to the formation of complexes of calcium silicate hydrate (C–S–H) at the interface, as well as the polarity, porosity and thickness of the transition zone microstructure (i.e. C–H) [1, 4]. Silica fume is a remarkably reactive pozzolanic substance owing to its fineness and high amorphous content of silicon dioxide. It accelerates the hydration processes in cement paste throughout all the stages. The compatibility of condensed silica fume (CSF) with Portland cement (PC) is determined by adding it in conventional concrete [5, 6]. To examine the durability characteristics, the study was carried out using CSF and blast furnace slag. We have seen that CSF was found to be more compatible than blast furnace slag for improvement of mechanical and durability characteristics. Owing to increased water demand, a high percentage of replacement is restricted

A. Khan (✉) · M. Haq · T. Naqvi
Department of Civil Engineering, Z.H. College of Engineering and Technology, Aligarh Muslim University, Aligarh 202001, India
e-mail: adnankhansirsa@gmail.com

M. Haq
e-mail: mmhaq2010@gmail.com

due to fineness that would alter the workability of concrete mix at constant water–binder ratio without employing super plasticizer [3]. The appropriate silica fume replacement ratio for maximal 28-day strength in M30 mixes usually ranges from 10 to 20% [7]. Silica present in concrete reacts with the calcium hydroxide released during cement hydration to overproduce C–S–H, which strengthens the concrete's mechanical performance. When compared to standard concrete, a variable water–binder ratio enhanced compressive strength (CS) by 11.56–18.89% [8]. To validate the relative importance of the physical and pozzolanic effects of silica fume, carbon black is used. Physical impacts may be ascribed to the influence on concrete CS at 7 days, but by 28 days, both physical and chemical effects become substantial. The workability and CS of high-performance concrete were reported to be unaffected by a 10% cement substitution with silica fume [9]. The appropriateness of SF and its influence upon workability of the concrete are examined; minimal change in workability was reported among all cases of SF concrete mix [7].

To study the effect of silica fume with several additive ratios and to compare the CS between controlled concrete and concrete with SF, recommendation was given to add silica fume to 15% for maximum CS for high performance [10]. Due to greater development of pozzolanic activity in the latter period, there was a loss in early strength compared to seven days and late considerable gains as long as 56 days after infusing silica fume in plain concrete [11, 12]. There is an efficient silica fume substance that ranges from 15 to 20% (1:1 partial substitution in concrete by weight) that produces the best responses by increasing compactness at the transition zone and improving pore structure, which results in high-performance concrete [13]. It is determined by visual investigation that the failure plane of SAC cubes passes through the aggregates body during crushing for strength measurement, but not along the interfacial zone due to high strength of paste-aggregate bonding then ordinary. The mean percentage of SF used to modify concrete was found to be 12% based on the data obtained from the statistical analysis, which is more effective in improving strength of high-strength concrete (HSC) [14]. The favourable effect of SF started seeming after the 7 days period and its complete consequence occurs at the 90 days period [15]. When concrete was replaced with SF, the mechanical properties of the concrete improved significantly [11, 16–18] which can also be validated using various non-destructive methods [19–21]. SF is having surface area of 100,000 cm^2/g very higher than OPC having 3000–3500 cm^2/g, due to smaller area accumulate inside the pore spaces of cement, reaching high dense state, increases the CS and flexural strength up to 10% [22]. Experimentally determined that for low water–binder ratio the impact of SF replacement is noticed higher for CS [23]. CS was enhanced to 15% at 7 and 14 days due to the addition of silica fume, which facilitates bond strength of concrete [24, 25]. According to some studies, SF has a lot more potential for use in the building sector as a cement substitute in concrete [25]. Even when 1.0% SF is added to concrete, the CS increases after 7, 14 and 28 days [26]. At 7.5% replacement with water-to-cement ratio of 0.45 when compared to reference concrete at 7 days and 28 days, 11.5% and 10.8% greater CS values are obtained, respectively [27]. The average w/c ratio for SAC was determined to be about 0.4 after statistical modelling of thousands of CS data in the range of 4–100 MPa [14].

The pores filled with hydration products with later ages increase the volume fraction of the solid phase. The connected solid phases give the higher value of ultrasonic pulse velocity of the specimen with the condition that concrete should be flawless [28].

The purpose of this study was to compare the CS of regular concrete versus silica fume admixed concrete. The suitability of silica fume was investigated by substituting silica fume for cement at various percentages while keeping the water-to-binder (W/B) ratio constant, and the strength measures were analysed. It is anticipated from past studies that with increasing value of W/B ratio the CS value decreases going after an increase in silica fume constituent level and is one of the reason for keeping W/B ratio lower in this research work. It was also observed that strength is increasing either by addition or replacement of SF in concrete at different W/B ratios, but maximum values lie between 10 and 20% replacement with or without super-plasticizer. The goals of this research include (a) determining under room temperature, without using superplasticizer at constant W/B ratio of 0.45, which percentage replacement is most suitable for strength enhancement as compared to referral concrete, (b) determining how the strength gain/loss is varying with the age of concrete from 0 to 90 days, for this various NDT and destructive tests were performed.

2 Experimental Investigation

2.1 Material Used for Work

2.1.1 Cement

In all of the mixtures, OPC of 43 grade conforming to IS: 8112-2013 [29] was employed. The properties related to the cement are shown in Table 1.

Table 1 OPC properties

S. No.	Measured property	Units	Value
1	Consistency of cement	%	32.5
2	Final setting time	min	305 (minimum; 600 min)
3	Initial setting time	min	42 (maximum; 30 min)
4	Fineness of cement	m^2/kg	340
5	Specific gravity	–	3.15

Table 2 Sieve analysis of 20 mm coarse aggregates

IS sieve size	Weight retained (g)	Percentage wt. retained (%)	Cumulative percentage wt. retained
20 mm	2380	47.60	47.60
10 mm	2610	52.20	99.80
4.75 mm	10	0.20	100
2.36 mm	0	0	100
1.18 mm	0	0	100
600 μm	0	0	100
300 μm	0	0	100
150 μm	0	0	100

Table 3 Sieve analysis of 10 mm coarse aggregate

IS sieve size	Weight retained (g)	Percentage wt. retained (%)	Cumulative percentage wt. retained
10 mm	1813	36.26	36.26
4.75 mm	2337	46.74	83.00
2.36 mm	850	17.00	100
1.18 mm	0	0	100
600 μm	0	0	100
300 μm	0	0	100
150 μm	0	0	100

2.1.2   Coarse Aggregate

The crushed aggregate utilized complied with IS: 383-2016 [30]. The aggregates computed specific gravity equals to 2.84. The fineness moduli (FM) of 10 and 20 mm aggregates are 6.19 and 7.47, respectively (refer to Table 2).

2.1.3   Fine Aggregate

Natural sand that was locally accessible and conformed to IS: 383-2016 [30] was utilized. The fine aggregate utilized had a specific gravity of 2.50, a FM of 2.73 and had been classified as zone ii according to IS 456: 2000 [31] (refer to Table 3).

2.1.4   Water

Concrete examples were mixed and cured using water that had a pH of almost 7 and met the requirements of IS: 456-2000 [31].

Table 4 Properties of silica fumes

Property	Units	Values
Specific gravity	–	2.2–2.4
Size	Mm	0.17
Bulk density	kg/m^3	600
Specific surface area	m^2/g	202
Al$_2$O$_3$	%	0.005
SiO$_2$	%	99.88
Moisture content	%	0.8
pH value	–	4.12

Table 5 Mix proportioning

Materials	Quantity (kg/m^3)
OPC	483.2
Coarse aggregate	1131.92
Fine aggregate	639.80
Water	191.6

2.1.5 Silica Fume

SF is being used to substitute cement in concrete mixes. The physical and chemical quality standards for SF specified in IS: 15388-2003 [32] are met to consider ones by the qualities as stated in Table 4.

2.2 *Mix Proportioning*

Concrete proportioning is an essential aspect of any concrete structural composition because proportioning helps in achieving the requisite quality and cost-effectiveness. The first stage in achieving the aim of designing concrete with specified performance characteristics is to choose component materials; the second step is to use a methodology called mix design to find the finest possible mix of ingredients. The mix design procedure utilized to generate M30 grade concrete in this research complies with IS 10262-2009 [33]. The concrete mix percentage is shown in Table 5.

3 Experimental Procedures

The detailed experimental procedure adopted is shown in flowchart in Fig. 1. The CS of a typical concrete cube with a side length of 150 mm was determined using both destructive testing and non-destructive testing. Rebound hammer (RH) and portable

Fig. 1 Summary of
experimental procedure
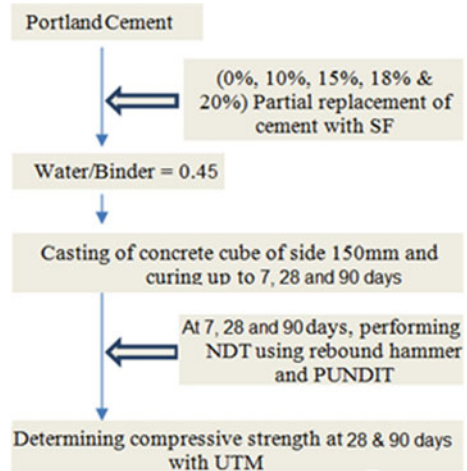
ultrasonic non-destructive indicating tester (PUNDIT) were used in non-destructive testing, whereas universal testing machine (UTM) was utilized in destructive tests. With each percentage of silica fume replacement, three specimens were examined for 7, 28 and 90 days non-destructively. Destructive tests were performed for getting 28 and 90 days strength. The percentage of replacement varies between 0 and 20%. The water–binder ratio used was 0.45 (binder = cement + partial replacement of silica fume by weight). In three rounds, concrete were poured, each of which was compacted with a tamping rod before being smoothed off at the vibrating table. After 24 h, the specimens were de-moulded after one day, wetted for 7, 14, 28 and 90 days and then evaluated for CS according to Indian Standards (Fig. 2).

4   Test Results and Analysis

Dependency on just one test method will not give accurate results, so we adopted different tests and at the end matched test results with universal testing method. RH test was carried out confirming to IS: 13311(Part 2)-1992 [34]. Strength was determined by relating rebound index and CS by the graph provided on the body of Schmidt's instrument. The ultrasonic pulse velocity was determined, confirming to IS: 13311(Part 1)-1992 [35], depending upon the concrete matrix through which they pass. Eventually, crushing CS was determined to compare value with other tests performed. In Fig. 3a, b, the graph between CS derived from RH versus age (days) was drawn for various percentages of cement substitution with SF. From the plot, an increasing pattern of curve with increasing percentage replacement of silica fume is observed irrespective of vertical or horizontal usage of the hammer. This pattern starts from 0%, goes up to 15% and afterwards decreases continuously.
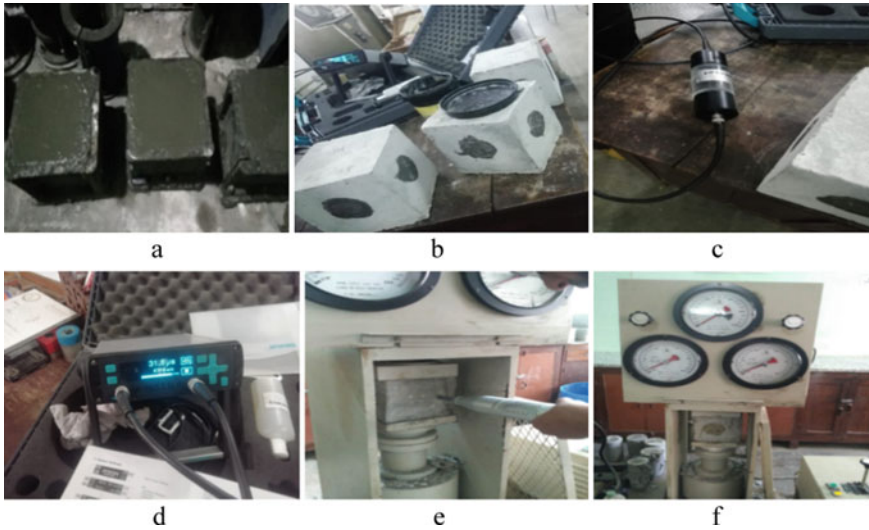
Fig. 2 Specimen preparation and testing: **a** Cube casting, **b** Cubes ready for NDT using PUNDIT, **c** Calibration of PUNDIT, **d** Pulse velocity measurement in PUNDIT, **e** RH testing and **f** Destructive CS testing by UTM
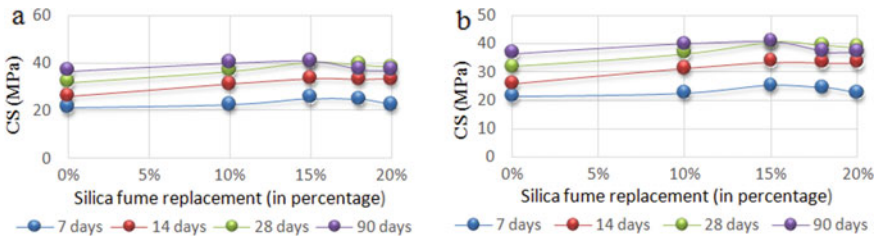

Fig. 3 **a** CS determined by RH taken horizontally, **b** CS determined by RH taken vertically

The CS values determined by taking RH horizontally and vertically are plotted in Fig. 3a, b, respectively. Figure 3a shows that replacing 10%, 15% and 18% of cement with silica fumes results in 2.97%, 13.43% and 7.27% increase in CS values as compared to the concrete having 0% SF replacement and also shows that CS values obtained for 0 and 20% replacement are found to be almost similar. The pulse velocity values represented in the graphical form in Fig. 4a for 0–20% replacement blocks range from 3.5 to 4.5, indicating good concrete quality grading according to Table 2 of IS: 13311(1st part), which was developed to characterize the quality of concrete in construction. The average pulse velocity increases from 4.22 to 4.36 km/s at 7 days and from 4.60 to 4.83 km/s at 28 days after casting as the silica replacement content increases from 0 to 18%. For both 7 and 28 days, the value of pulse velocity increases more beyond 15% replacement, the peak value is observed at 18% and after that declination takes place. Figure 4b shows the CS value obtained using correlation
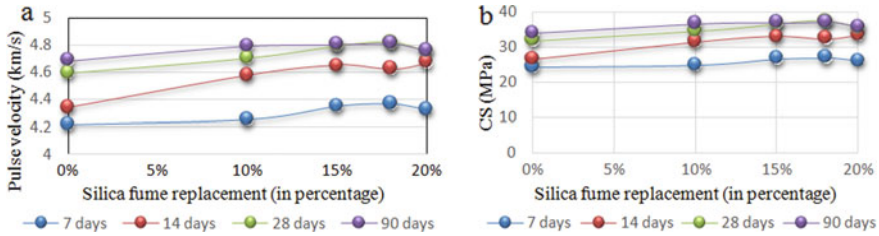
Fig. 4 **a** Pulse velocity determined by PUNDIT, **b** CS determined by pulse velocity

between CS and pulse velocity that follows the same trend as of pulse velocity [36]. The result of destructive testing also shows that crushing CS value is greater at 28 and 90 days for 15% replacement of silica fume. Also, the crushing CS values plotted in Fig. 5a at 28 and 90 days match with RH's CS values obtained at 15% replacement. The vertical bars in Fig. 5b representing CS values measured through different techniques show that values at 15 and 18% at 28 days seem almost similar except CS values obtained from UTM, which are found to be greater for 15%. At 18% replacement values are getting reduced at 90 days, especially for RH vertical part.

The minimal error can be clearly seen in the values of CS obtained from PUNDIT. The strength of traditional concrete is generally less than the strength of cement paste due to weak aggregate paste bonding. The inclusion of silica fume, on the other hand, reinforces the cement paste-aggregate bond and creates a less porous and more homogenous microstructure in the interfacial area, overcoming this weak link. With an increase in SF percentage substitution, the values of ultrasonic pulse velocity and CS significantly improved. As a result, silica fume concrete outperforms silica fume cement paste. The chemical impacts of SF assimilation in concrete are attributed to pozzolanic activity, whereas the physical effect is related to micro-filler response. The loss of strength in concrete is induced by injecting SF in excess of that required for pozzolanic and filler activities.
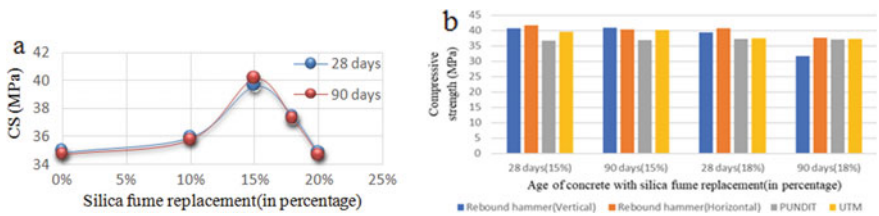

Fig. 5 **a** CS (destructive) measured using UTM, **b** CS values with age obtained with different test performed

5   Conclusions

The replacement of cement with silica fumes will lead to increase of CS and homogeneity. The optimal point of CS obtained from RH, PUNDIT and UTM lies in the range near to 15%. The strength diminishes when the silica fume substitution exceeds the optimal level. When compared to the referral concrete, the CS of concrete with silica fume improves significantly both at 28 and 90 days. The percentage increase in strength was 13.43% at 28 days and 15.44% at 90 days, indicating that slow development of pozzolanic response and its continuation beyond 28 days contributes to strength development [11]. Mineral admixture like micro-silica has property to consume free water and decrease in relative humidity of the system known as self-desiccation due to which the continuous medium for pulse velocity got somewhat disturbed and take more time to travel cube length, may be occurring after optimum percentage replacement therefore pulse velocity generally seems decreasing after the same. The pulse velocity value increases with age of concrete but the percentage change is very less. The reason behind this mechanism is that the density of the concrete remains constant with age, so we should not solely depend on pulse velocity test in case of substituting silica fume.

References

1. Khan MI, Siddique R (2011) Utilization of silica fume in concrete: review of durability properties. Resour Conserv Recycl 57:30–35. https://doi.org/10.1016/j.resconrec.2011.09.016
2. Cong X, Gong S, Darwin D, McCabe SL (1990) Role of silica fume in compressive strength of cement paste, mortar, and concrete
3. Sounthararajan VM, Srinivasan K, Sivakumar A (2013) Micro filler effects of silica-fume on the setting and hardened properties of concrete. Res J Appl Sci Eng Technol 6:2649–2654. https://doi.org/10.19026/rjaset.6.3753
4. Siddique R (2011) Utilization of silica fume in concrete: review of hardened properties
5. Alexander MG, Magee BJ (1999) Durability performance of concrete containing condensed silica fume
6. Khan RA, Haq M (2020) Long-term mechanical and statistical characteristics of binary- and ternary-blended concrete containing rice husk ash, metakaolin and silica fume. Innovative Infrastruct Solutions 5(2):1–14. https://doi.org/10.1007/s41062-020-00303-0
7. Srivastava V, Kumar R, Agarwal VC, Mehta PK (2014) Effect of silica fume on workability and compressive strength of OPC concrete. J Environ Nanotechnol 3:32–35. https://doi.org/10.13074/jent.2014.09.143086
8. Mehta RJD, PK Chemical and physical effects of silica fume on the mechanical behavior of concrete. ACI Mater J 86. https://doi.org/10.14359/2281
9. Duval R, Kadri EH (1998) Influence of silica fume on the workability and the compressive strength of high-performance concretes. Cem Concr Res 28:533–547. https://doi.org/10.1016/S0008-8846(98)00010-6

10. Ahmad OA (2017) Production of high-performance silica fume concrete. Am J Appl Sci 14:1031–1038. https://doi.org/10.3844/ajassp.2017.1031.1038
11. Khedr SA, Abou-Zeid MN (1994) Characteristics of silica-fume concrete. J Mater Civ Eng 6:357–375. https://doi.org/10.1061/(asce)0899-1561(1994)6:3(357)
12. Jain A, Pawade NPY (2015) Characteristics of silica fume concrete. Int J Comput Appl 975–8887
13. Pradhan D, Dutta D (2013) Influence of silica fume on normal concrete. Int J Eng Res Appl 3:79–82
14. Burhan L, Ghafor K, Mohammed A (2019) Modeling the effect of silica fume on the compressive, tensile strengths and durability of NSC and HSC in various strength ranges. J Building Pathol Rehabil 4. https://doi.org/10.1007/s41024-019-0058-4
15. K VB, Hanumesh BM, Varun BK, Harish AB (2008) The mechanical properties of concrete incorporating silica fume as partial replacement of cement. Int J Emerg Technol Adv Eng
16. Imam A, Kumar V, Srivastava V (2018) Review study towards effect of silica fume on the fresh and hardened properties of concrete. https://doi.org/10.12989/acc.2018.6.2.145
17. Selvapriya R (2019) Silica fume as partial replacement of cement in concrete. Int Res J Multi Technovation 325–333. https://doi.org/10.34256/irjmtcon43
18. Pashankar KA, Patil AS, Thorat PM (2020) A literature review on study of silica fume as partial replacement of cement in concrete. Int J Sci Res Eng Trends 6:275–278
19. Ibrahim YE, Al-Akhras N, Al-Kutti W (2014) Destructive and nondestructive testing on silica fume concrete. In: Advanced Materials Research vol 919, pp 9211890–9211893. https://doi.org/10.4028/www.scientific.net/AMR.919-921.1890
20. Mohammed BS, Adamu M, Liew MS (2018) Evaluating the effect of crumb rubber and nano silica on the properties of high volume fly ash roller compacted concrete pavement using non-destructive techniques. Case Stud Constr Mater 8380–391. https://doi.org/10.1016/j.cscm.2018.03.004
21. Haq M, Bhalla S, Naqvi T (2020) Fatigue damage and residual fatigue life assessment in reinforced concrete frames using PZT-impedance transducers. Cem Concr Compos 114103771. https://doi.org/10.1016/j.cemconcomp.2020.103771
22. Saini LK, Saini LK, Nayak JR (2019) An experimental investigation on the mechanical properties of concrete with grade m55 and m60 by partial replacement with silica fume. Int J Recent Trends Eng Res 5:9–15. https://doi.org/10.23883/ijrter.2019.5080.roqjv
23. Behnood A, Golafshani EM (2018) Predicting the compressive strength of silica fume concrete using hybrid artificial neural network with multi-objective grey wolves. J Clean Prod 202:54–64. https://doi.org/10.1016/j.jclepro.2018.08.065
24. V P, Priyadharshini S, R S, Selvan S (2019) Studies on effect of silica fume on workability and strength of concrete. Int Res J Multi Technovation 165–171. https://doi.org/10.34256/irjmtcon21
25. Chouhan P, Jamle S, Varma M (2017) Experimental investigation of silica fume as partial replacement of cement for M25 grade of concrete. IJSART 5:714–717
26. Ranjitham M, Prabhakaran RA, Dhanusuya J (2020) Effect of silica fumes on properties of concrete. Int Res J Eng Technol
27. Tripathi D, Kumar R, Mehta PK, Singh A (2020) Silica fume mixed concrete in acidic environment. Mater Today: Proc 27:1001–1005. https://doi.org/10.1016/j.matpr.2020.01.311
28. Hong G, Oh S, Choi S, Chin WJ, Kim YJ, Song C (2021) Correlation between the compressive strength and ultrasonic pulse velocity of cement mortars blended with silica fume: an analysis of microstructure and hydration kinetics. Materials 14. https://doi.org/10.3390/ma14102476
29. BIS 8112 (2013) Ordinary portland cement, 43 grade specification. Bureau of Indian Standards, New Delhi, India
30. IS: 383 (2016) Coarse and fine aggregates for concrete-Specification (Third revision). Bureau of Indian Standards, New Delhi, India
31. IS-456 (2000) Indian standard plain and reinforced concrete-Code of practice. Bureau Indian Standards, New Delhi, India

32. IS: 15388 (2003) Silica fume-specification. Bureau of Indian Standards, New Delhi, India. pp 1–13
33. IS: 10262 (2019) Concrete mix proportioning-guidelines. Bureau of Indian Standards (BIS) Second Rev, pp 1–40
34. IS: 13311 (1992) Non-destructive testing of concrete—Methods of test, Part 2: Rebound Hammer, Bureau of Indian Standards, New Delhi, India
35. IS: 13311 (1992) Non-destructive testing of concrete—Methods of test, Part 1: Ultrasonic pulse velocity test. Bureau of Indian Standards, New Delhi, India
36. Jain A, Kathuria A, Kumar A, Verma Y, Murari K (2013) Combined use of non-destructive tests for assessment of strength of concrete in structure. Proc Eng 54:241–251. https://doi.org/10.1016/j.proeng.2013.03.022

Long-Span Through-Beam RCS System for Fast Construction of Industrial Buildings in Low-Seismic Zones

M. Adil Dar, Abhishek Verma, Sze Dai Pang, and Jat-Yuen Richard Liew

1 Introduction

Reinforced concrete (RC) is the most commonly used construction material used for building construction. Over the past decades, traditional reinforced concrete construction has transitioned towards precast construction to improve onsite productivity. Figure 1 shows the installation of a lotus root precast column to beam connection [1]. In industrial buildings, lifting of precast beams can be a challenge due to their long spans and high deadweight. Moreover, the column reinforcement is often highly congested, making the onsite installation cumbersome and inefficient. Steel–concrete composite frames have been used for decades in construction due to their excellent structural performance under severe loading conditions [2]. One such frame is the reinforced concrete column and steel beam system (RCS). RCS makes the best use of the two materials. Concrete has a lower cost per unit strength and stiffness and thus is more efficient in taking compressive axial loads in columns. On the other hand, steel has higher strength and ductility per unit weight, making it suitable for long-span structural members. It also leads to a reduction in story weights, resulting in reduced load on columns and foundations. The use of composite decks and steel beams in RCS frames can significantly reduce the use of formwork, enhance the rate of construction and further reduce the story weight.

Steel beams are connected to RC columns through moment-resisting or simple connections. Simple connections are preferred for gravity frames due to their ease of construction. However, moment-resisting connections are essential in lateral load -resisting frames. RCS structures broadly comprise two types of beam-to-column moment-resisting connections: through-beam and through-column. As the

M. A. Dar (✉) · A. Verma · S. D. Pang · J.-Y. R. Liew
Department of Civil and Environmental Engineering, National University of Singapore, Singapore 117576, Singapore
e-mail: dar.adil@nus.edu.sg

Fig. 1 Installation of lotus root precast beam–column connection [1]

name suggests, through-beam connections feature steel beams continuously passing through the columns [3]. The continuity of the beams results in ductile moment-resisting behaviour at the ends of the beams. For through-column connections, the beams are discontinued and connected outside the column. Thus, the columns are continuous through a story. The use of full moment-resisting connections can also be advantageous in gravity frames. It can considerably reduce the beam weight, especially in long-span beams under heavy gravity loads. Composite action of the steel beam and the slab can increase beam stiffness and further economise the steel section. However, usually heavy onsite bolting or welding is required to achieve moment-resisting connections.

During the 1980s and early 1990s, the USA and Japan conducted many RCS beam-to-column connections tests. Over 400 RCS connection subassemblies were tested in Japan and 17 in the USA [4]. Many of the joints tested in Japan were of proprietary details sponsored by Japanese construction companies, with the primary goal being to validate specific joint details. It had limited research value to quantify the internal force transfer mechanisms of the joint. Most of the RCS joints tested in the past have transverse reinforcement at the joint obstructed by the beam web. These reinforcements are either required to pass through predrilled holes or require onsite welding, which is not only labour-intensive but also affects onsite productivity. Cover plates can be used at the joint to eliminate the need for transverse reinforcements

and act as permanent formwork for onsite concrete casting. Experimental studies have demonstrated the efficacy of cover plates to eliminate the need for transverse reinforcement at the joint. Bugeja et al. [5] tested internal RCS joints with 380 × 380 mm columns. The steel beams were continuous in one direction and discontinuous in the other. The beam in the discontinuous direction utilised simple bolted web connections inside the joint. The first two specimens used 'overlapping cross-ties' in the joint region, whereas specimen 3 utilised a 10 mm bent cover plate and band plate to replace the transverse reinforcement. The cover plate was reported to have improved the constructability and enhanced the performance of the joint. Continuation of the beam was also found to have better strength and ductility. The continuous beams in all the cases developed beam hinges, whereas, in the other direction, failure was observed in the joint region due to bearing and elongation mechanisms.

Parra-Montesinos and Wight [6] tested RCS joints with exterior columns. One of the specimens utilised a 6 mm cover plate (6.3% of the joint volume) to replace transverse reinforcement. A 13% increase in the joint strength compared to the control specimen was observed. This increase was attributed to the high level of confinement of the concrete at the joint. An increase in the peak average bond stress for vertical reinforcement (from 3.3 to 4.5 MPa) was also observed. Liang and Parra-Montesinos [7] tested RCS joints, two with interior and two with exterior columns. Smaller ties replaced the transverse reinforcement in the joint region, and band plates were introduced in the specimens' second pair. Only minor to moderate joint damage was reported for this pair under severe cyclic lateral loads, which is acceptable for implementation in low-seismic regions. Despite extensive experimental investigations conducted to understand the behaviour of an RCS system, the exploration of its application in low-seismic regions has been limited. Existing design and detailing recommendations [8] aim at enhancing the strength and ductility of the joint for large lateral drifts. If this system is intended to be used only to resist gravity loads, the stringent detailing of the joint can be relaxed to improve construction productivity. Making this system highly suited for long-span industrial application in low seismic regions.

Past experimental research has primarily focused on the construction sequence adopted in the USA, which utilises steel erection columns with onsite column casting, resulting in composite RC columns. In many parts of the world, especially in southeast Asia, precast concrete construction is highly preferred. Hence, it is essential to investigate joint detailing that can be smoothly adopted in this region. This study first conducts a material saving and cost–benefit analysis of moment-resisting beam–column connections in RCS systems designed as gravity frames in long-span industrial buildings. A joint detailing and its construction sequence are then proposed to improve productivity and enhance construction safety, focusing on the construction practices in Southeast Asia. A large-scale experimental investigation of the proposed through-beam RCS sub-assembly under gravity frame type loading is presented. The load–deflection behaviour and failure modes are presented. This experiment is a preliminary test that is a part of a more extensive study that aims to develop design guidelines for RCS frames in low-seismic regions of Asia.

2 Material Saving and Cost-Benefit Analysis

The use of precast RC beams for industrial buildings (long spans and heavy loading) is challenging due to its high deadweight. Adopting steel beams can prove more practical and efficient for such buildings. RCS systems have been championed for their optimised use of material: reinforced concrete for the columns under compressive loading and steel beams as lightweight solutions for long spans. This section compares the material utilisation and its cost implications for steel and RCS frames. In addition, beam-to-column connections are varied as either simple or fully moment-resisting.

A four-storey industrial building with a 4×4 bays layout was modelled in the commercially available building analysis and design software, ETABS. The height of each storey was assumed to be 5 m, while the beam spans were taken as 12 m. For simplicity, no secondary beams were considered. Industrial floor loading of 15 kN/m^2 was applied. A total of four cases were considered with varying frame types (steel frame and RCS frame) and types of beam-to-column connections (simple and full moment-resisting connections). An isometric view of the industrial building modelled in ETABS is shown in Fig. 2a. Steel and concrete design tools were used to optimise the beams and columns based on Eurocode [9, 10] strength and deflection requirements.

The weights of the structural elements obtained from the software and their costs are tabulated in Table 1. The rates of the materials were taken from BCA's publication (last updated 2017) [11]. For steel, S$ 7.2/kg was assumed to consider the structural steel section price (S$ 5.10/kg) and off-site surface treatment (S$ 2.10/kg). The cost of a precast concrete column was taken as S$ 1093.3/kg. This price includes the cost of the concrete with steel reinforcement, hoisting and casting, inclusive of all labour, material, formwork, accessories and jointing. Figure 2b shows the percentage difference in total cost between the four types of framing systems, with the RCS-simple (i.e. simple beam-to-column connections) taken as the base case. It
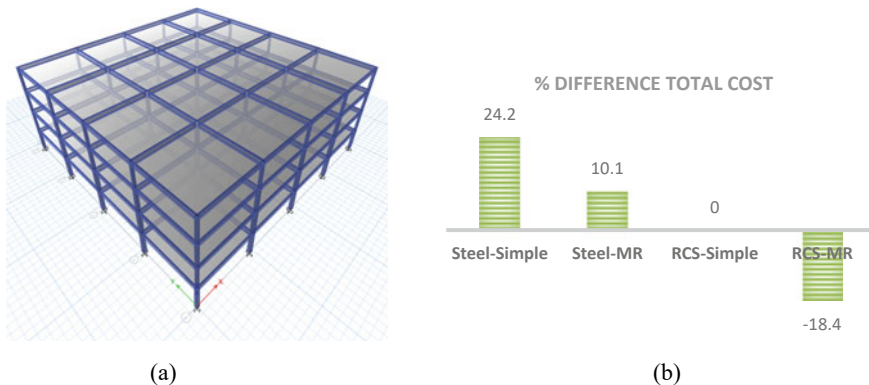

Fig. 2 **a** ETABS model for cast analysis. **b** Difference in material cost for different frames

Table 1 Weight and cost of framing systems

Frame type	Steel-simple	Steel-MR[a]	RCS-simple	RCS-MR[a]
Column weight (tonne)	116	145	427	505
Beam weight (tonne)	435	343	418	332
Total concrete weight (tonne)			427	505
Total steel weight (tonne)	551	488	418	332
Total frame weight (tonne)	551	488	845	837
Cost of column (S$)	833,663	1,043,272	179,388	212,170
Cost of beam (S$)	3,130,368	2,471,004	3,011,721	2,393,350
Cost of concrete (S$)			179,388	212,170
Cost of steel (S$)	3,964,031	3,514,276	3,011,721	2,393,350
Total cost (S$)	3,964,031	3,514,276	3,191,109	2,605,520

[*] MR = Moment Resisting

was observed that using moment-resisting connections instead of simple connections results in a cost reduction of about 20%. The steel frame structures are about 25% more expensive than their RCS counterpart.

3 Proposed Fast Connection

This study proposes the connection shown in Fig. 3 to promote the adoption of moment-resisting RCS systems for low-seismic regions for improving construction productivity, sustainability and safety. The moment-resisting connection is achieved by making the steel beam pass through the column. This allows for the use of lighter beam sections compared to simple beam-to-column connections. Steel cover plates are provided at the exterior of the joint to eliminate the labour-intensive installation of transverse reinforcement at the joint. The installation of the transverse reinforcement would require the labour to complete this task at a certain height from the ground (at the joint location). This elimination will lead to better safety for site workers. The cover plate also acts as permanent formwork for onsite wet works, further increasing construction productivity.

The joint detailing required to achieve a moment-resisting connection results in a considerable obstruction for the column longitudinal reinforcement bars. This will result in bundling reinforcement bars at the corners for industrial columns with a high percentage of longitudinal reinforcement. This in turn, will demand greater lap lengths for these bundles. Hence, a balanced approach is adopted for the proposed connection by providing an extended plate connection in the orthogonal direction of the through-beam (henceforth referred to as secondary direction). This results in a traditional simple connection outside the joint for easy installation. For columns where sufficient reinforcement can be provided even after obstructions by the beams
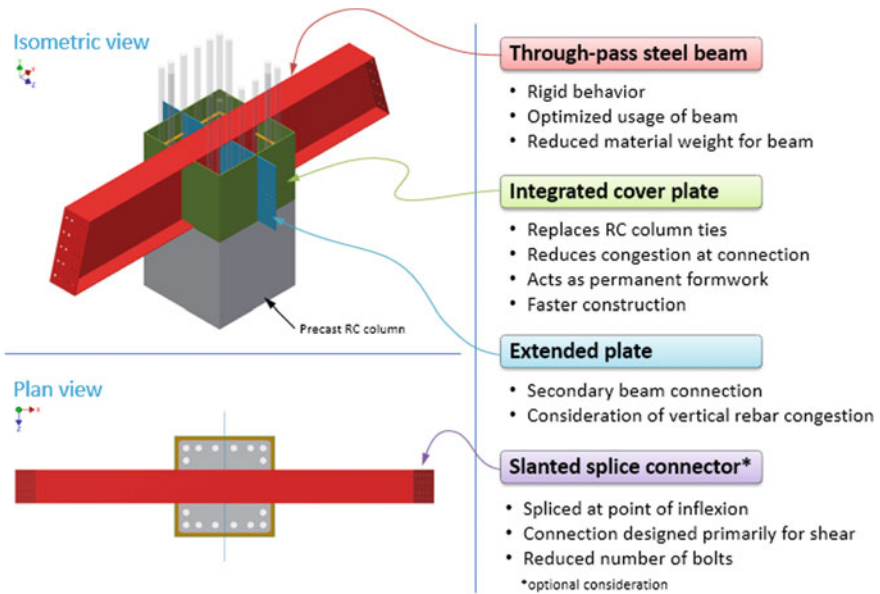
Isometric view

Through-pass steel beam
- Rigid behavior
- Optimized usage of beam
- Reduced material weight for beam

Integrated cover plate
- Replaces RC column ties
- Reduces congestion at connection
- Acts as permanent formwork
- Faster construction

Precast RC column

Extended plate
- Secondary beam connection
- Consideration of vertical rebar congestion

Plan view

Slanted splice connector*
- Spliced at point of inflexion
- Connection designed primarily for shear
- Reduced number of bolts
  *optional consideration

Fig. 3 Proposed joint detailing for RCS joints

from both directions, moment-resisting connections in both directions could be a viable option. Any standard beam splicing technique may be utilised to connect the beams outside the joint region. However, the slanted beam splicing connections near the expected flexural inflexion point can be a good choice due to its easy installation and lower force demand on the connection.

4 Construction Sequence

The proposed connection aims to improve construction productivity and safety through the fast assembly and installation procedure discussed in this section. Figure 4 shows the proposed construction sequence. This procedure is considered the most widely adopted practice in Singapore, where precast concrete columns are connected onsite at each story level. The steel beams and cover plates may be transported to the site as separate components for ease of packing and improved logistics.

Currently, the maximum permissible beam length that can be conveniently transported through roads in Singapore is 12 m. Thus, the steel beams would be transported in lengths shorter than the full span for buildings with longer beam spans. The beams and the cover plates are assembled on the ground before lifting for installation. The cover plates could be either bolted or welded to the preinstalled steel plates welded to the web of the steel beam. Installation of two column-heads (see Fig. 4) on top of
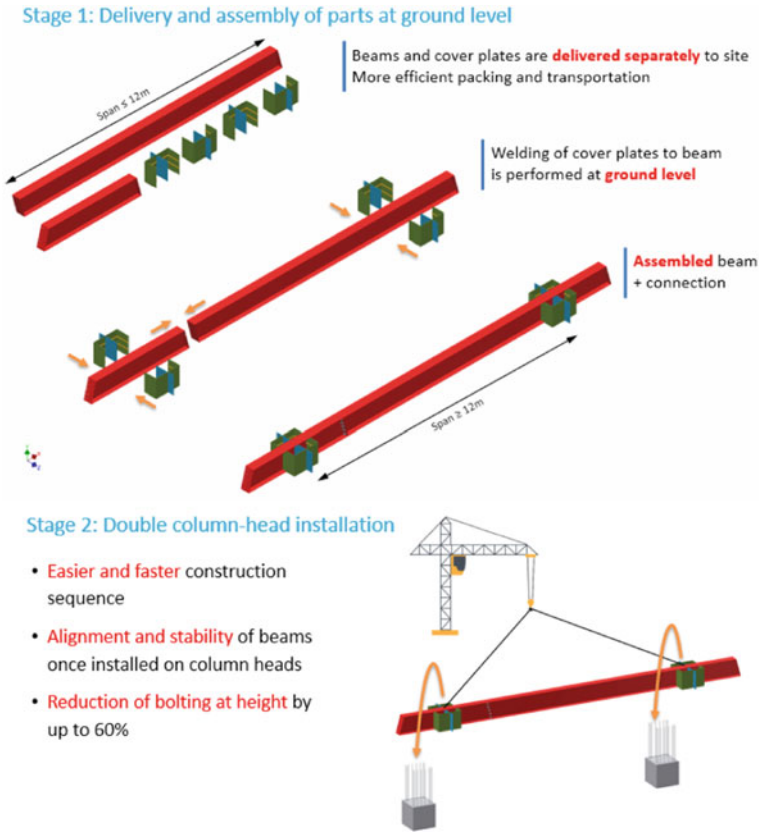
Fig. 4 Proposed construction sequence for RCS frames

the precast columns for the first span can provide better stability to the beam before the in-situ casting of the joint is carried out. This installation process can reduce the splicing of beams at height by 50% for the through-beam direction, leading to enhanced safety and increased productivity.

5 Experimental Study

An experimental investigation was conducted to investigate the performance of the proposed connection under extreme gravity loading. Figure 5 shows the schematic representation of the experimental set-up. The dimension and the specimen size was adopted by downscaling a realistic loading condition in an industrial building. Figure 6 (left side of the diagram) shows a schematic representation of the loading on the beam of an RCS system and its internal forces. The beam can be considered to
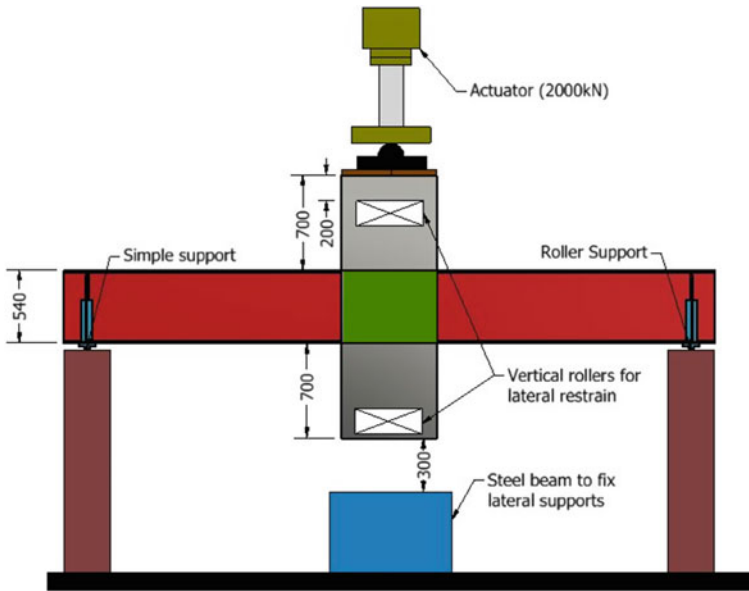
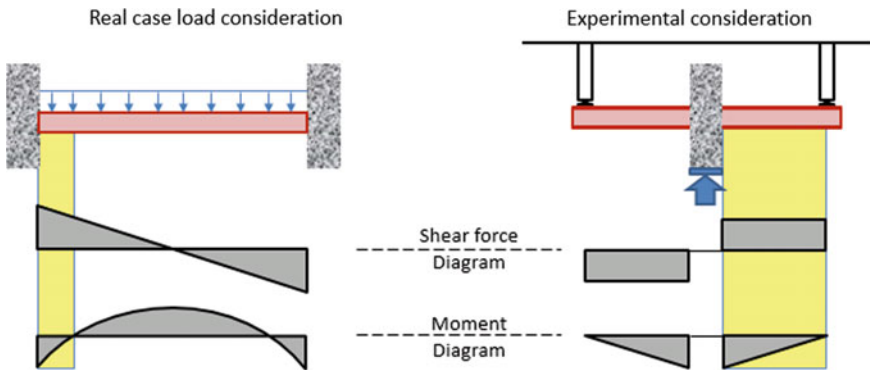**Fig. 5** Schematic diagram of the experimental set-up

Fig. 6 Loading and boundary conditions considered in the experiment

be clamped at both ends. On the right side of the diagram, it is the inverted representation of the experimental set-up. The diagram compares the bending moment and shear force distribution for the highlighted (yellow) portion between the actual and experimental conditions.

An industrial building with a clear beam span of 12 m was considered with an unfactored gravity load of 15 kN/m^2. The beam was designed assuming fixed end conditions using Eurocode 3 [10]. The cover plate thickness was calculated to avoid deformation while pouring wet concrete at the site. A scaling factor of 3/4 was

utilised for calculating the specimen dimensions. The joint detailing conforms to the recommendation by ASCE 1994 [8]. Figure 7 shows the specimen dimensions and detailing. Concrete grade C40/50 was used for the concrete column. The average compressive strength of the concrete observed from the cube tests was 57 MPa. The beam demonstrated the yield stress and ultimate stress of 460 MPa and 591 MPa, respectively. The specimen was whitewashed to inspect concrete cracks and excessive deformation in steel components visually. As shown in Fig. 5, one of the end support was simply supported and the other was roller support. Lateral supports were used to restrain the concrete column in the desired plane. A hydraulic actuator was attached to the column through a ball and socket arrangement to avoid moment transfer while pushing the column downwards. The specimen was unloaded two times each after pushing it down to 6, 12 and 18 mm before reloading it. Henceforth, the specimen was loaded monotonically to 70 mm. Such cyclic loading in the elastic stage of
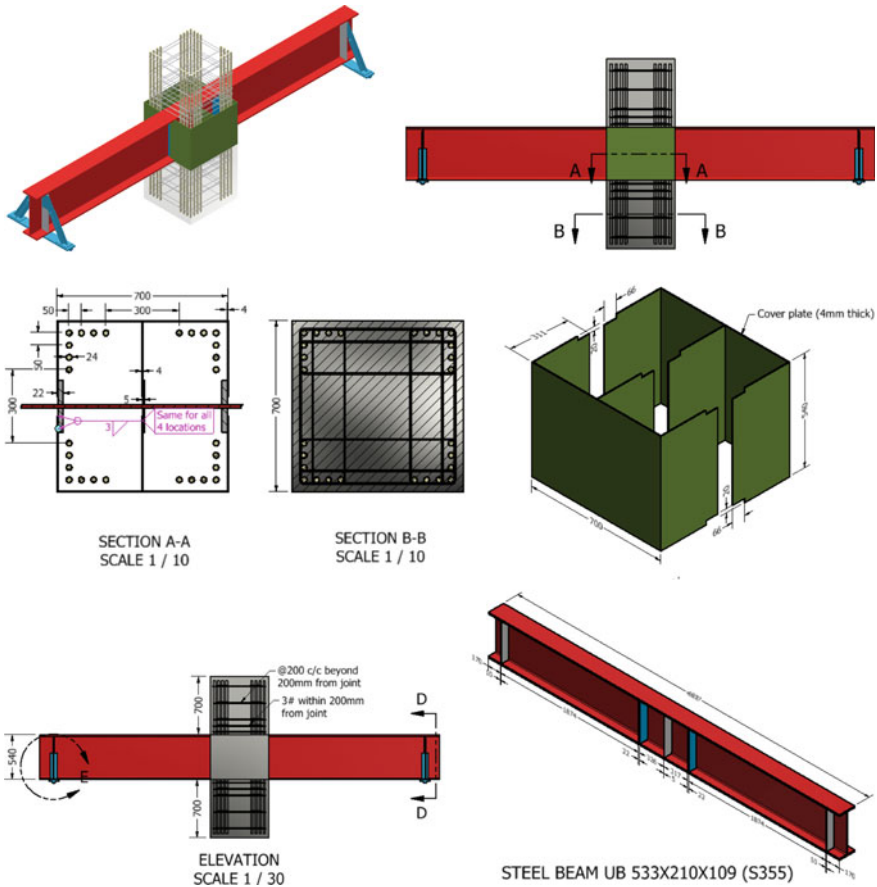

Fig. 7 Structural details of the specimen

(a)   (b)

Fig. 8 Images of the specimen showing **a** flange yielding and **b** flange local buckling at the beam plastic hinge region

the specimen was included to simulate the effect of service loads. Linear variable displacement transducers (LVDTs) were installed to record the vertical displacement of the four bottom corners of the column. An average of the four LVDTs was used to calculate the mean displacement of the column. A total of 10 strain gauges were installed on the cover plate and 4 on the beam flanges.

The RCS joint demonstrated full moment resistance with no yielding, cracking or damage observed within and around the joint. Figure 9a shows the load–deflection behaviour of the specimen. The cyclic loading in the elastic stage did not result in loss of stiffness. The specimen exhibited excellent ductility and strength. Flexural yielding of the steel beam was observed outside the joint at about 18 mm displacement and a vertical load of 810 kN. Figure 8a shows the marks in the whitewash at the beam flange, which represents flexural plastic deformation in the steel beam. Significant local buckling of the flange under compression was observed at a deflection of around 70 mm (shown in Fig. 8b). This local deformation occurred gradually and did not lead to any sudden drop in the load-carrying capacity of the beam. However, this event resulted in the flattening of the load–deflection curve. The experiment was terminated at a deflection of 80 mm, which corresponds to 0.04 rad rotation in the beam. These results demonstrated that the simplified detailing of the steel beam-to-RC column adopted in this study can enhance on-site construction productivity and be structurally robust. This preliminary study will be followed by experiments at the National University of Singapore to investigate the more critical loading scenarios in peripheral RCS joints with varying joint details.

6 Conclusions

This study proposes a simplified moment-resisting joint detailing and a construction sequence for RC column and steel beam (RCS) frames to enhance construction productivity and ensure structural robustness of the frame. The cost-savings in terms
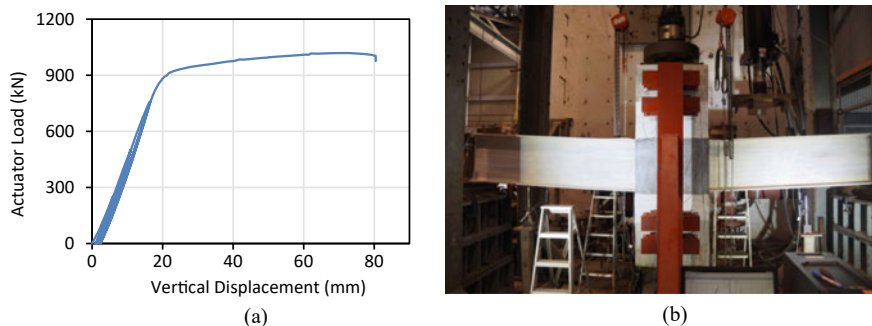
Fig. 9 **a** Load–displacement response and **b** the deformed shape of the specimen

of material cost are presented through an example frame. Finally, the findings of a preliminary test of RCS sub-assembly are presented. The following conclusion can be made from this study:

1. Adopting moment-resisting connections in RCS gravity frames instead of the commonly adopted simple connections can result in a material cost-savings of about 15–20%. Additionally, higher on-site productivity can lead to further cost-saving and reduction in construction time.
2. The experimental results demonstrated that the simplified RCS connection adopted in this study is structurally robust. The joint performed similar to a full moment-resisting connection. Plastic hinges developed in the steel beams outside the joint region. No cracks or damage was observed in the concrete up to a beam rotation of 0.04 rad.

References

1. BCA (2018) Connections for advanced precast concrete system. Singapore: building and construction authority
2. Khaloo A, Bakhtiari RB (2018) Seismic performance of precast RC column to steel beam connections with variable joint configurations. Eng Struct 160:408–418
3. Nguyen XH, Nguyen QH, Le DD, Mirza O (2017) Experimental study on seismic performance of new RCS connection. Structures 9:53–62
4. Deierlein GG, Noguchi H (2004) Overview of U.S.–Japan research on the seismic design of composite reinforced concrete and steel moment frame structures. J Struct Eng 130:361–367
5. Bugeja MN, Bracci JM, Moore WP (2000) Seismic behavior of composite RCS frame systems. J Struct Eng 126:429–436
6. Parra-Montesinos G, Wight JK (2000) Seismic response of exterior RC column-to-steel beam connections. J Struct Eng 126:1113–1121
7. Liang X, Parra-Montesinos GJ (2004) Seismic behavior of reinforced concrete column-steel beam subassemblies and frame systems. J Struct Eng 130:310–319
8. ASCE Task Committee on design criteria for composite structures in steel and concrete (1994) guidelines for design of joints between steel beams and reinforced concrete columns. J Struct Eng 120:2330–2357

9. EN1922-1-1, Eurocode 2 (2004): Design of concrete structures-Part 1–1: General rules and rules for buildings. British Standards Institution, Brussels
10. EN 1993-1-1, Eurocode 3 (2005): Design of steel structures-Part 1–1: General rules and rules for buildings. British Standards Institution, Brussels
11. BCA, (2017) Unit rates for construction. Building and Construction Authority, Singapore